4.11 Nitrogen dioxide – NO_2

Nitrogen dioxide (NO_2) is a major air pollutant in the troposphere, and is produced mainly by fossil fuel burning (*via* production of NO, see *Section 4.10*). Natural sources of tropospheric NO_2 involve lightning, bacterial processes in soil and water, and biomass burning. The main source of NO_2 in the stratosphere is the oxidation of N_2O, also originating from soil emissions (see *Section 4.4*), followed by downward transport of upper atmospheric NO_x in the winter polar vortex (up to 9%). Stratospheric NO_2 is considered an ozone depleting substance through the catalytic NO_x cycle. At the same time, NO_2 acts as a buffer against halogen-catalyzed ozone loss by converting reactive chlorine, bromine, and hydrogen compounds into stable reservoir substances ($ClONO_2$, $BrONO_2$, HNO_3). The removal of nitrogen from the stratosphere, as observed in the SH polar vortex during the formation and sedimentation of polar stratospheric clouds (PSCs), is a key microphysical process in the formation of the Antarctic polar ozone hole during spring.

Stratospheric NO_2 variations are controlled by the sunlight-driven equilibrium between NO_x (NO, NO_2) on one hand and the reservoir substances (N_2O_5, HNO_3, $ClONO_2$) on the other hand. In particular, the strong diurnal NO_2 cycle complicates a comparison of satellite-based NO_2 measurements that correspond to different LSTs. **Figure 4.11.1** shows examples of the diurnal NO_2 cycle as a function of LST for three different pressure levels as derived with a chemical box model [*McLinden et al.*, 2010]. As seen in these plots there are large differences between day and night-time NO_2, with a steep gradient at sunrise and sunset. Solar occultation measurements are always made at SZA = 90° and can therefore be compared amongst each other. Limb scattering and emission measurements however, can correspond to different SZAs, and a direct comparison of the climatologies is not meaningful in most cases unless the dependence on the SZA is taken into account.

4.11.1 Availability of NO_2 measurements

The first vertically resolved satellite NO_2 measurements were made by LIMS in 1978/1979. SAGE II and HALOE provide the longest continuous NO_2 datasets, both ending in 2005. A number of more recent satellite missions have been measuring NO_2 from 2002 onwards. Solar occultation measurements are available from SAGE II, HALOE, POAM II, POAM III, SAGE III and ACE-FTS. Periods of maximum overlap are 1994-1996 (SAGE II, HALOE, and POAM II) and 2005 (SAGE II, HALOE, POAM III, SAGE III, and ACE-FTS). NO_2 measurements by limb emission and scattering techniques are available for OSIRIS, SCIAMACHY, and MIPAS from 2002 onward, while GOMOS provides stellar occultation measurements for the same time period. Additionally, HIRDLS data for 2005-2007 and LIMS data for 1978-1979 exist. **Table 4.11.1** summarises information on the available NO_2 measurement record including time period and vertical range.

The solar occultation climatologies can be compared directly if separated into local sunrise and local sunset measurements. Note that there is a difference between the sunrise/sunset as seen from a satellite and the local sunrise/sunset that determines the chemical state of the measured air mass, and is therefore used to categorise the measurements. The corresponding data files are labelled as am/pm with am LST generally corresponding to local sunrise and pm LST generally corresponding to local sunset. One deviation from the photochemical conditions at local sunrise can occur when a satellite crosses the terminator towards the polar day area at high latitudes. During such observations, the photochemical conditions of the atmosphere at local surise may be completely different than that of a typical sunrise observation because the area is continuously illuminated during polar day. The same situation can occur when the satellite crosses the terminator towards polar night. **Table 4.11.2** summarises the local sunrise/sunset climatologies.

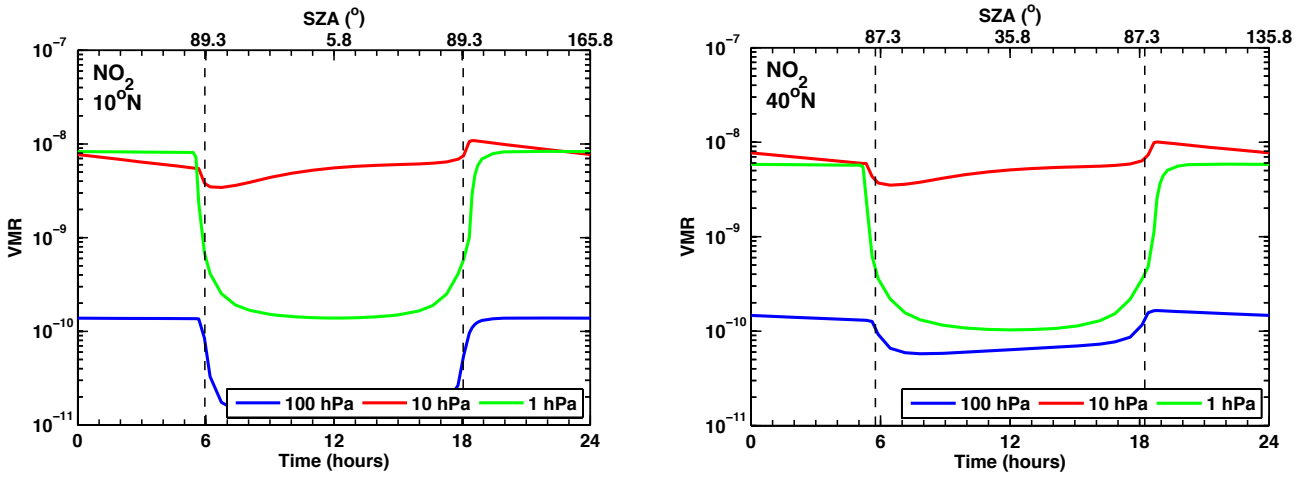

Figure 4.11.1: Diurnal NO_2 cycle. *NO_2 variations as function of LST are shown at 10°N and 40°N at 1, 10 and 100 hPa for March 15.*

NO_2 measurements by limb emission and scattering techniques correspond approximately to a fixed LST if the instrument has a sun-synchronous orbit (*e.g.*, MIPAS measurements correspond to 10am and 10pm LST). The measurement LST can vary from instrument to instrument, and may also vary for some instruments between seasons and latitudes. In order to compare other instruments (OSIRIS, SCIAMACHY, ACE-FTS) with MIPAS, their measurements have been scaled to LST 10am and 10pm with the help of a chemical box model [*McLinden et al.*, 2010].

Table 4.11.1: Available NO_2 measurement records from limb-sounding satellite instruments between 1978 and 2010. *The red filling of the grid boxes indicates the temporal and vertical coverage of the respective instrument. Instruments are grouped according to their measurement LST into the group of solar occultation instruments (upper panel) and the group of limb emission/scattering and stellar occultation instruments (lower panel).*

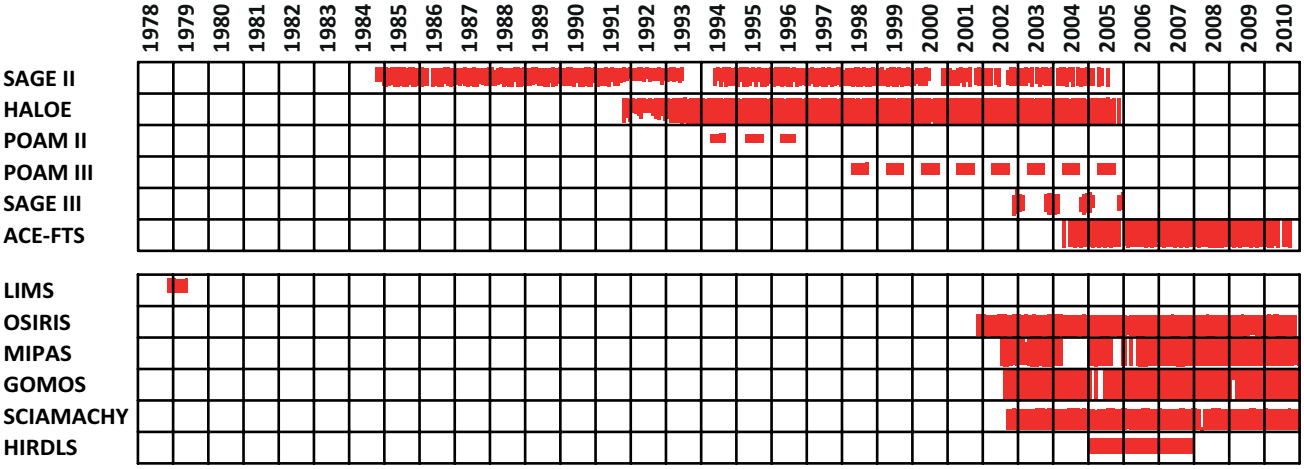

Table 4.11.2: Overview of available NO_2 local sunrise and local sunset climatologies. *For local sunrise/sunset climatologies, the instrument name, the method used to derive the climatology, the corresponding LST and the satellite orbit are given. Detailed information on the corresponding LST depending on month and latitude can be found in the data files.*

Instrument	**Local sunrise climatologies**		**Local sunset climatologies**		Satellite orbit
	Method	Corresponding LST	Method	Corresponding LST	
SAGE II	**Local sunrise**	am (mixed times)	**Local sunset**	pm (mixed times)	non-sun-synchronous
HALOE	**Local sunrise**	am (mixed times)	**Local sunset**	pm (mixed times)	non-sun-synchronous
POAM II	**Local sunrise**	am (mixed times)	**Local sunset**	pm (mixed times)	sun-synchronous
POAM III	**Local sunrise**	am (mixed times)	**Local sunset**	pm (mixed times)	sun-synchronous
SAGE III	**Local sunrise**	am (mixed times)	**Local sunset**	pm (mixed times)	sun-synchronous
ACE-FTS	**Local sunrise**	am (mixed times)	**Local sunset**	pm (mixed times)	non-sun-synchronous

Table 4.11.3: Overview of available NO_2 daytime and night-time climatologies including the 10am/pm climatologies. *For daytime and night-time climatologies, the instrument name, the method used to derive the climatology, i.e., scaling measurements or sorting measurements according to LST, orbit or SZA, and the corresponding LST range are given. Climatologies corresponding to 10am and 10pm LST are printed in bold face. Detailed information on the corresponding LST depending on month and latitude can be found in the data files.*

Instrument	**Daytime climatologies**		**Night-time climatologies**	
	Method	Corresponding LST	Method	Corresponding LST
LIMS	Ascending orbit	~1pm	Descending orbit	~11pm
OSIRIS	am LST	Mixed times	pm LST	Mixed times
	Scaled	**10am**	**Scaled**	**10pm**
SCIAMACHY	No adjustments	~8am - 2pm		
	Scaled	**10am**	**Scaled**	**10pm**
MIPAS	**am LST**	**10am**	**pm LST**	**10pm**
GOMOS			**No adjustments**	**10pm**
HIRDLS	SZA < 90°	~3pm	SZA > 90°	00:30am
	Scaled	**10am**	**Scaled**	**10pm**
ACE-FTS	**Scaled**	**10am**	**Scaled**	**10pm**

For OSIRIS, scaling is done profile-by-profile, with the initialisation of the model using the measured trace gas abundances and temperature. The scaling for SCIAMACHY and ACE-FTS on the other hand, is done based on lookup tables calculated from the photochemical box model initialised with climatological inputs (see *Section 3.2.1*). GOMOS provides stellar occultation measurements at 10pm. These are evaluated with the group of limb emission and scattering instruments. The ACE-FTS climatology derived from data scaled to 10am/pm provides an opportunity to compare one solar occultation dataset with the measurements based on emission and scattering techniques. HIRDLS data from June 2005 to May 2006 have been scaled to 10am/pm with the SD-WACCM Version 3548 (SD stands for Specified Dynamics using GEOS5.1) [*Garcia et al.*, 2007]. **Table 4.11.3** summarises all available daytime and night-time NO_2 climatologies including the original available daytime and night-time climatologies and the ones scaled to 10am/pm LST. All instruments listed in **Table 4.11.3**, except for ACE-FTS, are in sun-synchronous orbits. **Table 4.11.4** compiles information on all NO_2 measurements, including time period, vertical range and resolution, and references relevant for the data product used in this report.

4.11.2 NO_2 evaluations: Zonal monthly mean cross sections and vertical profiles of local sunrise/sunset climatologies

Local sunrise NO_2 climatologies from the solar occultation instruments SAGE II, HALOE, ACE-FTS, SAGE III, POAM II, and POAM III are displayed in **Figure 4.11.2**. The annual zonal mean climatologies are calculated over the respective lifetime of each instrument. In general, the zonal mean distribution shows the largest NO_2 abundances around 10 hPa, with maximum values at high latitudes. The three solar occultation instruments in a non-sun-synchronous orbit (SAGE II, HALOE, ACE-FTS) offer near-global coverage over the course of a year, while the three instruments in a sun-synchronous orbit (SAGE III, POAM II, and POAM III) provide measurements in a narrow range at high latitudes. The higher annual mean abundances reported by the first group of instruments when compared to the latter may be the result of varying seasonal coverage instead of an actual measurement bias. One example of the complications arising from the varying data coverage is the evaluation of 1994-1996 POAM II local sunrise monthly zonal means that show no direct overlap with any of the other datasets. (Note that the overlap of the annual means visible in **Figure 4.11.2** does not necessarily correspond to an overlap of the monthly zonal means.) Moreover, the instruments with near-global coverage over the course of a year or season (SAGE II, HALOE and ACE-FTS) have strongly varying data coverage from month to month. Therefore, the comparison of annual zonal means, as carried out for the long-lived trace gases, may not be meaningful, and instead a comparison of monthly zonal means will be presented. Note that the data coverage problem is intensified by the necessary separation into local sunrise and sunset data.

Table 4.11.4: Time period, vertical range, vertical resolution, references and other comments for NO_2 measurements.

Instrument	Time period	Vertical range	Vertical resolution	References	Additional comments
LIMS V6.0	Nov 78 – May 79	Cloud top – 50 km (+ mesosphere for polar night)	3.7 km	*Remsberg et al.*, 2010	
SAGE II V6.2	Oct 84 – Aug 05	Cloud top – 50 km	1.0 km (< 38 km) 5.0 km (> 38 km)	*Cunnold et al.*, 1991	Only satellite SS data are used
HALOE V19	Oct 91 – Nov 05	up to 50 km	2.5 km	*Grooß and Russell*, 2005	
POAM II V6.0	Oct 93 – Nov 96	20 – 40 km	1.5 – 2.5 km	*Lumpe et al.*, 1997 *Randall et al.*, 1998	
POAM III V4.0	Apr 98 – Dec 05	20 – 40 km	1.5 – 2.5 km	*Lumpe et al.*, 1997 *Randall et al.*, 1998	
OSIRIS V3-0	Oct 01 –	13 – 45 km	2 km	*Brohede et al.*, 2007a *Brohede et al.*, 2007b	
SAGE III V4.0	May 02 – Dec 05	Cloud top – 50 km	0.5 ~ 1.0 km		Only solar occultation products used
MIPAS V15 V220	 Mar 02 – Mar 04 Jan 05 – Apr 12	 12 – 50/70 km (day/night)	 3 – 6 km 2.5 – 6 km	 *Funke et al.*, 2005a *Funke et al.*, 2005b	 Change in spectral resolution in 2005
GOMOS V5.0	Mar 02 – Apr 12	20 – 50/70 km	4 km	*Kyrölä et al.*, 2010a	
SCIAMACHY V3-1	Sep 02 – Apr 12	11 – 42 km	3 – 5 km	*Bauer et al.*, 2012	
ACE-FTS V2.2	Mar 04 –	7 – 52 km	3 – 4 km	*Kerzenmacher et al.*, 2008	
HIRDLS V6.0	Jan 05 – Jan 08	20 – 50 km	1 km	*Gille and Gray*, 2011	

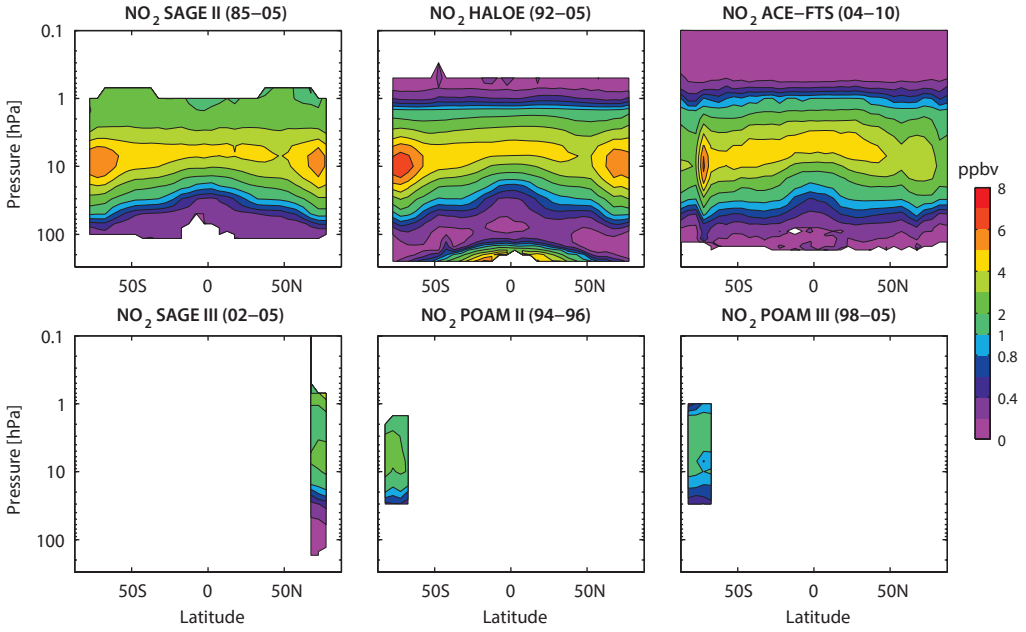

Figure 4.11.2: Cross sections of annual zonal mean, local sunrise NO_2 for solar occultation instruments. *Annual zonal mean, local sunrise NO_2 cross sections are shown for the SAGE II (1985-2005), HALOE (1992-2005), ACE-FTS (2004-2010), SAGE III (2002-2005), POAM II (1994-1996), and POAM III (1998-2005).*

As a first step, the evaluations of local sunrise and sunset climatologies will focus on the comparison of the two longer time series from SAGE II and HALOE during their overlap time period 1992-2005. The other instruments will be compared to SAGE II and HALOE for time periods that allow as many instruments as possible to be included (1994-1996 for POAM II, 2004-2005 for ACE-FTS, POAM III, SAGE III).

SAGE II and HALOE (1992-2005)

Figure 4.11.3 shows NO_2 local sunrise and sunset monthly mean climatologies for SAGE II and HALOE for April and October. The monthly multi-annual means of the two datasets overlap in both hemispheres. The sunset climatologies show notably more NO_2 than the sunrise climatologies as a result of N_2O_5 photolysis, which is driven by the available

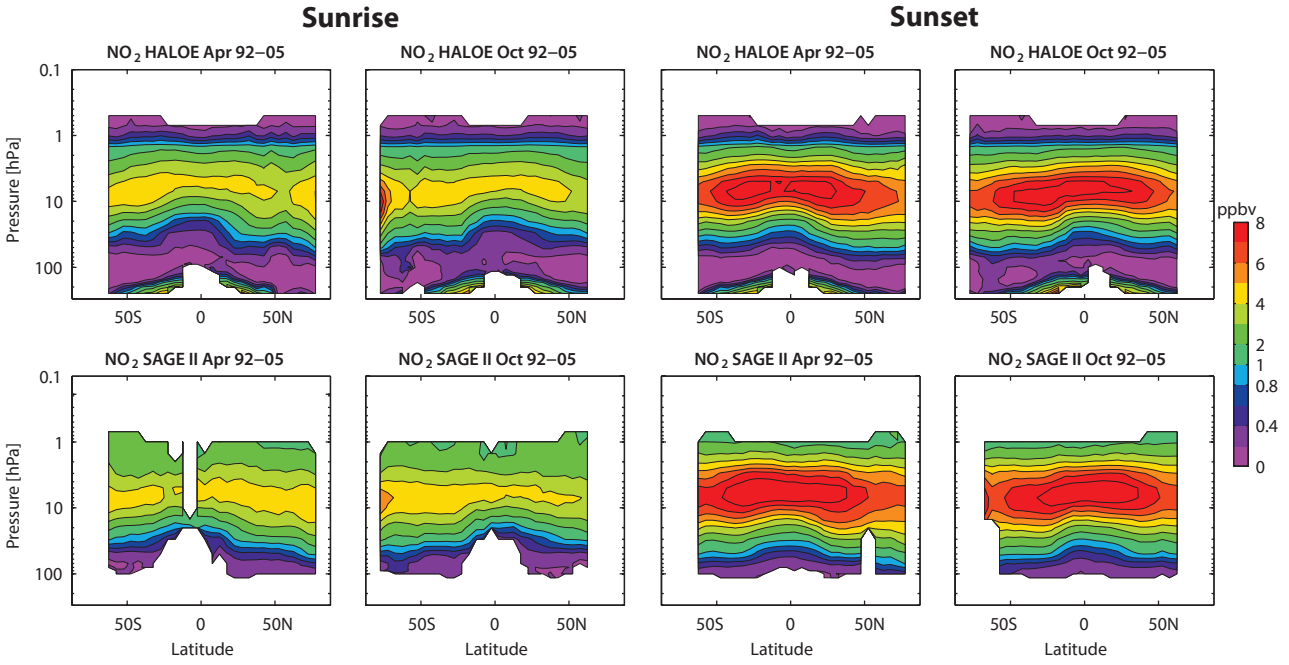

Figure 4.11.3: Cross sections of monthly zonal mean, local sunrise and sunset NO_2 for 1992-2005. *Monthly zonal mean, local sunrise (column 1 and 2) and local sunset (column 3 and 4) NO_2 cross sections for April and October are shown for HALOE (upper row) and SAGE II (lower row).*

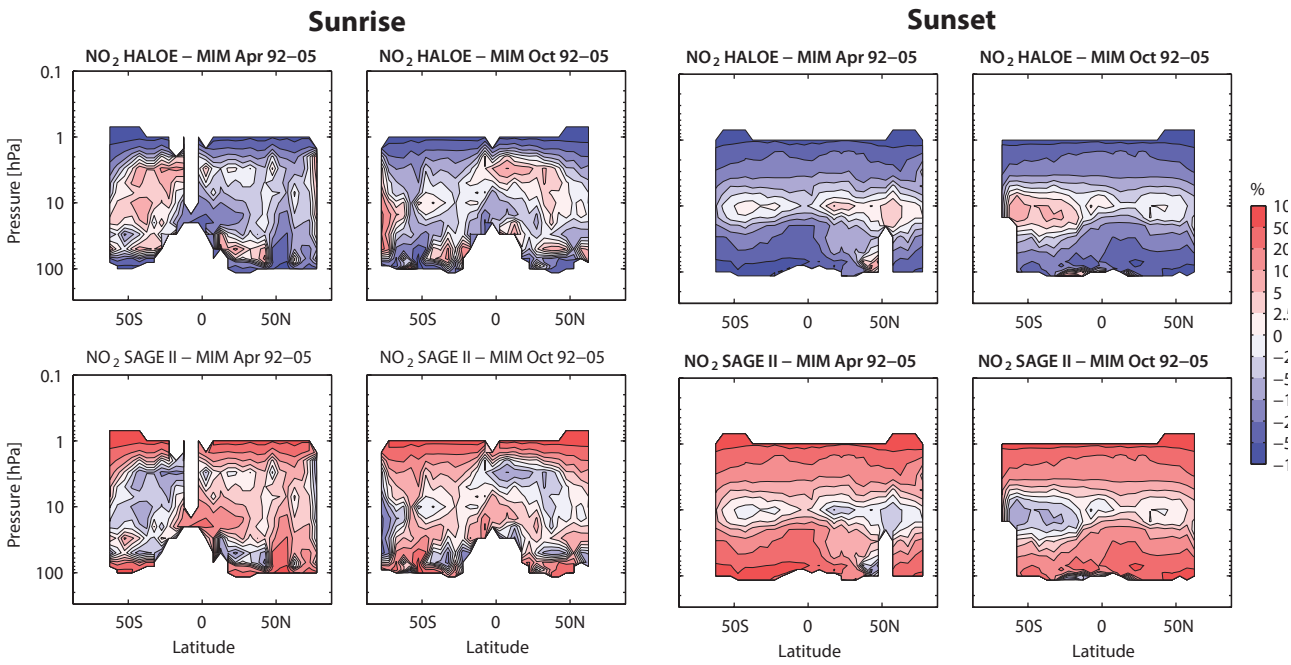

Figure 4.11.4: Cross sections of monthly zonal mean, local sunrise and sunset NO_2 differences for 1992-2005. *Monthly zonal mean, local sunrise (column 1 and 2) and local sunset (column 3 and 4) NO_2 differences for April, and October between the individual instruments (SAGE II, HALOE) and their MIM are shown.*

sunlight and reactivates NO_2 from its reservoir species. The N_2O_5 photolysis during daytime is fast enough that by sunset nearly all N_2O_5 is converted to NO_2, leading to a nearly symmetric distribution at the equator independent of the time of year. The N_2O_5 production during nighttime is somewhat slower, and as a result larger NO_2 sunrise abundances are observed for shorter nights (*e.g.*, in the SH during October).

The relative differences of SAGE II and HALOE from their MIM in April and October are displayed in **Figure 4.11.4**. At the level of maximum NO_2 abundance (10 hPa), the two datasets agree well with differences from the MIM of up to ±10% (corresponding to differences of 20% between the two instruments). Above and below this level, the relative differences increase steadily reaching values of up to ±50% at 2 hPa and 20/50 hPa for local sunset/sunrise climatologies. The steadily increasing differences below and above the maximum are related to the smaller vertical gradients in SAGE II NO_2 compared to HALOE. At around 10 hPa, HALOE detects more NO_2 than SAGE II, but above and below the maximum it quickly reaches lower values due to its stronger gradients and shows mostly negative differences when compared to SAGE II. Exceptions to this pattern are the local sunrise climatologies in the summer (**Figure A4.11.2** in *Appendix A4*) and autumn hemispheres (**Figure 4.11.4**) when HALOE shows positive differences from the MIM everywhere below 2 hPa. Overall, the NO_2 local sunrise and sunset evaluations give a consistent picture, however, some small differences exist (*e.g.*, sunset differences

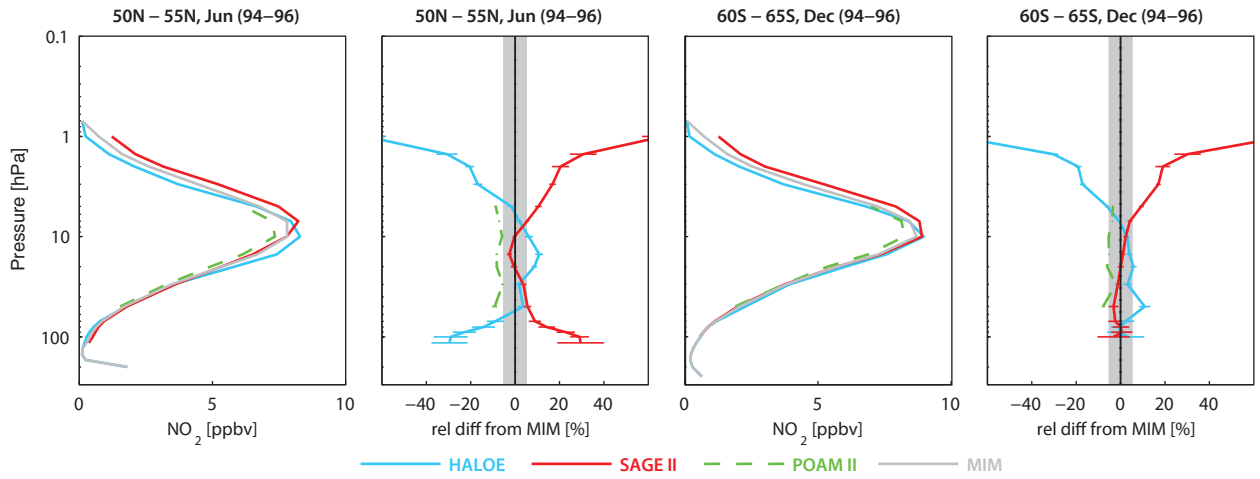

Figure 4.11.5: Profiles of zonal mean, local sunset NO_2 for 1994-1996. *Zonal mean, local sunset NO_2 profiles for 50°N-55°N for June and 60°S-65°S for December are shown with their differences from the MIM. Bars indicate the uncertainties in each climatological mean based on the SEM. The grey shaded area indicates where relative differences are smaller than ±5%.*

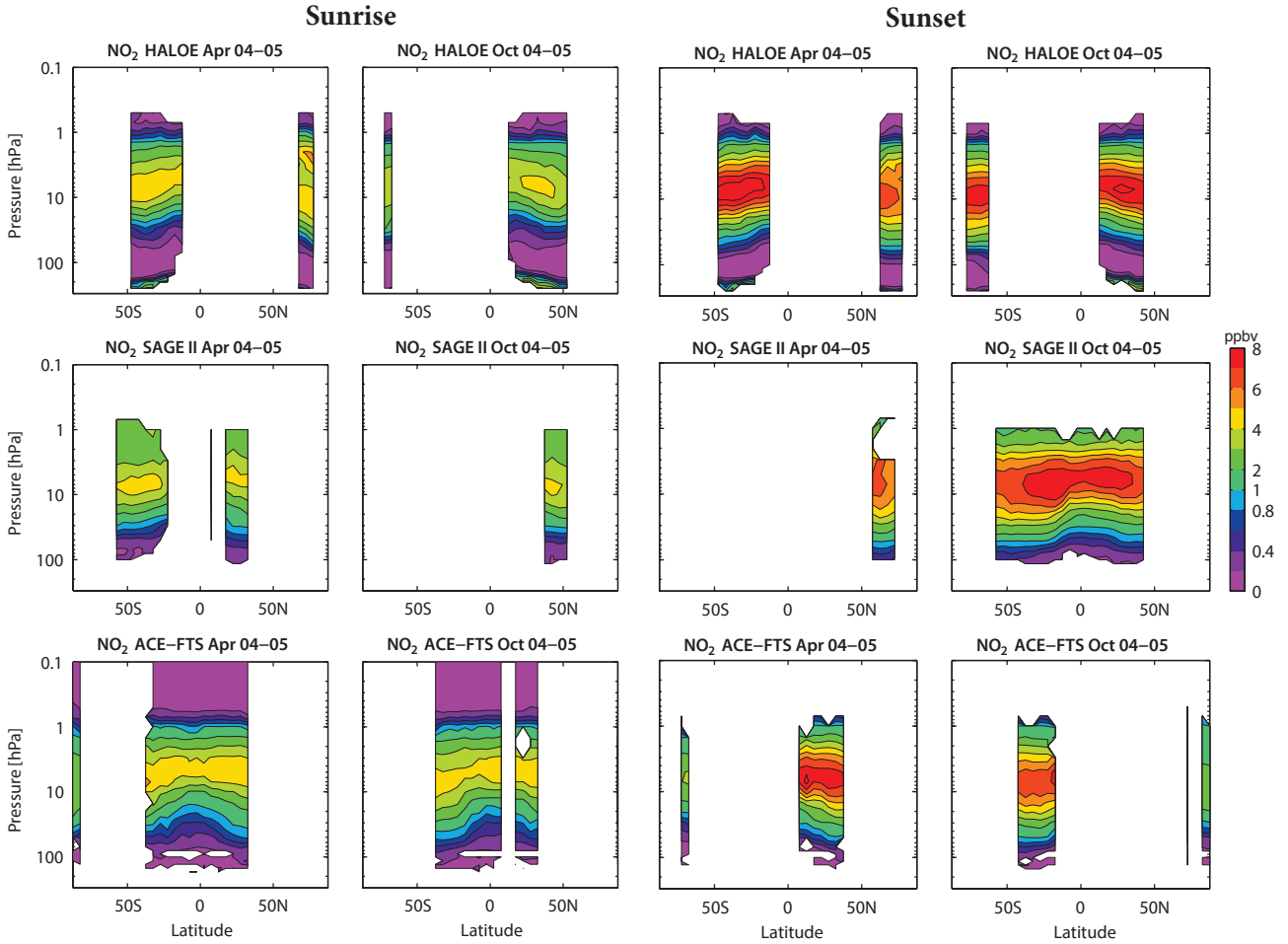

Figure 4.11.6: Cross sections of monthly zonal mean, local sunrise and sunset NO_2 for 2004-2005. *Monthly zonal mean, local sunrise (column 1 and 2) and local sunset (column 3 and 4) NO_2 cross sections for April and October are shown for the HALOE, SAGE II, and ACE-FTS.*

show a stronger hemispheric symmetry consistent with the same feature observed for the sunset mixing ratios).

SAGE II, HALOE, and POAM II (1994-1996)

As a consequence of the gaps in temporal and spatial coverage of POAM II, a direct comparison of local sunrise NO_2 climatologies from POAM II and the other two instruments is not possible. However, for NO_2 sunset measurements, some months and latitude bands exist where all three datasets overlap, allowing for a direct comparison of POAM II, SAGE II and HALOE. Vertical profiles from all three instrument local sunset climatologies and their relative differences from the MIM are displayed in **Figure 4.11.5**. In both latitude bands (NH and SH mid-latitudes), the POAM II climatology reports smaller values than SAGE II and HALOE, with differences with respect to the MIM of -10%. Above 7 hPa, POAM II agrees better with HALOE than with SAGE II, while below 7 hPa the situation is reversed.

SAGE II, HALOE, POAM III, SAGE III, and ACE-FTS (2004-2005)

For the period 2004-2005, the long NO_2 time series from SAGE II and HALOE overlap with the more recent data from ACE-FTS. Also available during this period are datasets from SAGE III and POAM III, which focus on narrow latitude ranges. A comparison of SAGE III and POAM III zonal monthly mean cross sections is not possible, therefore the evaluation of these two climatologies will be based on vertical profiles.

Figure 4.11.6 shows NO_2 local sunrise and sunset monthly mean climatologies for SAGE II, HALOE, and ACE-FTS for April and October. Note that SAGE II and HALOE have less latitudinal coverage for 2004-2005 (the last two years of their lifetimes) when compared to earlier time periods (*e.g.*, **Figure 4.11.3**). The respective relative differences between the individual datasets and their MIM are presented in **Figure 4.11.7**. Overall, the magnitude and spread of the relative differences are similar to those already discussed for the long-term comparison of SAGE II and HALOE, with the smallest differences (up to ±10%) around 10 hPa, and larger differences (up to ±50%) above 2 hPa and below 50 hPa. Note that for some cases the differences are below ±20% for the complete altitude range from 1 to 100 hPa (*e.g.*, sunset differences of SAGE II and ACE-FTS to their MIM for SH October). For the local sunrise climatologies, ACE-FTS shows the largest, and HALOE the lowest NO_2 abundances. For the local sunset climatologies, SAGE II show the largest and HALOE the lowest NO_2 abundances, with ACE-FTS values between the other two

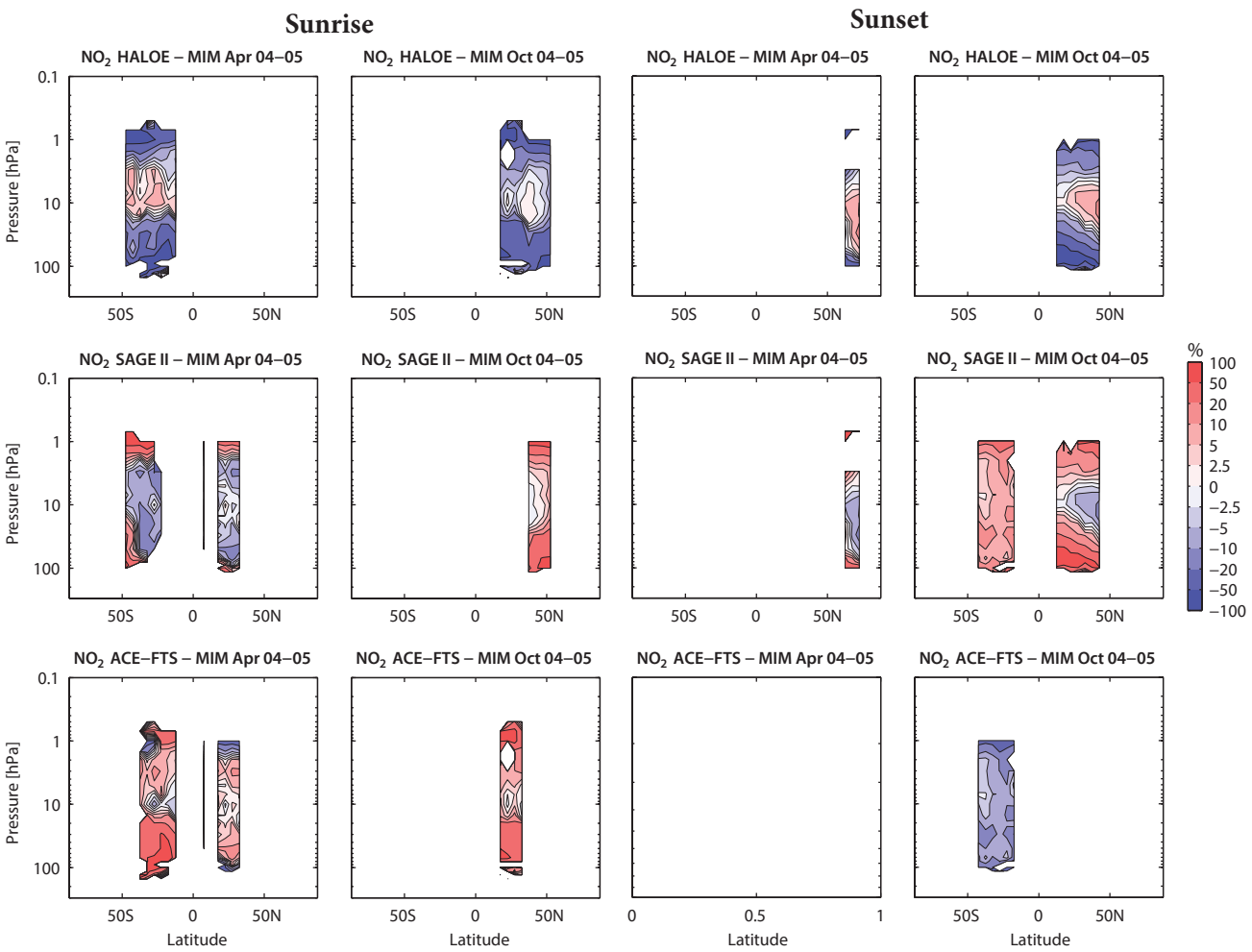

Figure 4.11.7: Cross sections of monthly zonal mean, local sunrise and sunset NO_2 differences for 2004-2005. *Monthly zonal mean, local sunrise (column 1 and 2) and local sunset (column 3 and 4) NO_2 differences for April and October between the individual instruments (HALOE, SAGE II, ACE-FTS) and their MIM are shown.*

instruments. The only exception is found at 10 hPa where HALOE detects a larger NO_2 peak than the other two datasets, consistent with the evaluations of the earlier time period. Overall, ACE-FTS agrees better with SAGE II than with HALOE.

A comparison of POAM III and SAGE III with the other datasets is shown in **Figure 4.11.8** as vertical profiles and their relative differences from the MIM. The months and latitude bands used for this comparison are chosen because the coverage includes the maximum number of datasets available. The profiles confirm the good agreement of all instruments

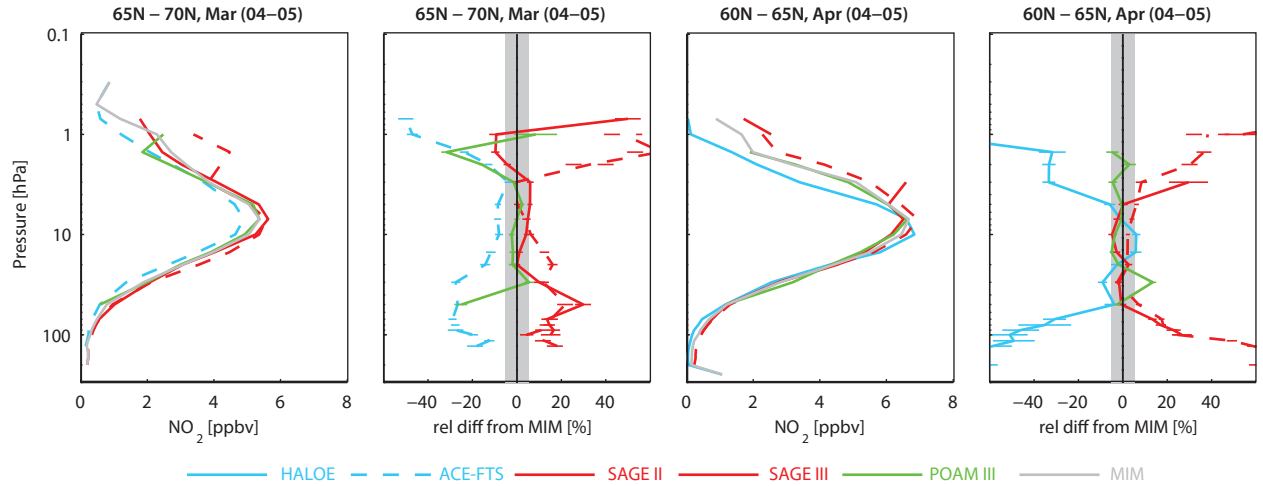

Figure 4.11.8: Profiles of zonal mean, local sunset NO_2 for 2004-2005. *Zonal mean, local sunset NO_2 profiles for 65°N-70°N for March and 60°N-65°N for April are shown together with their differences from the MIM. Bars indicate the uncertainties in each climatological mean based on the SEM. The grey shaded area indicates where relative differences are smaller than ±5%.*

in the MS with differences often below ±5%, except for a divergence between ACE-FTS and SAGE III in March which show differences from the MIM of up to ±10%. Differences are large in the LS and USLM consistent with low NO_2 abundances. However, there is a much better agreement between 50 and 10 hPa (below the NO_2 VMR peak) compared to between 5 and 1 hPa (above the NO_2 peak) for similar NO_2 background abundances. In general, SAGE III is similar to SAGE II and shows larger NO_2 values than the other datasets, while POAM III values reside mostly in the middle.

4.11.3 NO_2 evaluations: Zonal monthly mean cross sections of 10am/pm climatologies

NO_2 measurements by limb emission and scattering techniques and from stellar occultation have been sorted according to LST or scaled with the help of chemical box models (see *Section 4.11.1* for details). Additionally, the solar occultation dataset from ACE-FTS has been scaled to allow for a first-step comparison between the two groups of instruments. In the following, climatologies corresponding to 10am and 10pm will be compared with each other. For a better understanding of the scaling effects, the initial climatologies are also shown. Note that the 10am/pm climatologies are part of the larger groups of daytime/night-time climatologies as explained in **Table 4.11.3**.

OSIRIS, SCIAMACHY, MIPAS, GOMOS, HIRDLS, and ACE-FTS (2005-2007)

Figure 4.11.9 shows the NO_2 10am climatologies for October 2005-2007 that can be directly compared to each other: MIPAS (corresponding to 10am LST) and ACE-FTS, OSIRIS, SCIAMACHY, and HIRDLS, all scaled to 10am LST (labelled as s10am in the figure titles). Additionally, unscaled daytime data from SCIAMACHY and OSIRIS (corresponding to a range of LSTs), HIRDLS daytime measurements (corresponding to 3pm), and ACE-FTS local sunrise measurements are shown. The overall NO_2 distribution shows flat isopleths and maximum abundances in the subtropics between 5 and 10 hPa. Note that the elevated values observed by MIPAS at very high NH latitudes are related to small changes of the LST from 10am and the timing of sunsets/sunrises (near 10am) during October. Similarly, MIPAS shows elevated values at high SH latitudes for April (see **Figure A4.11.6** in *Appendix A4*).

The MIM is calculated based on MIPAS and scaled ACE-FTS, OSIRIS, SCIAMACHY, and HIRDLS climatologies

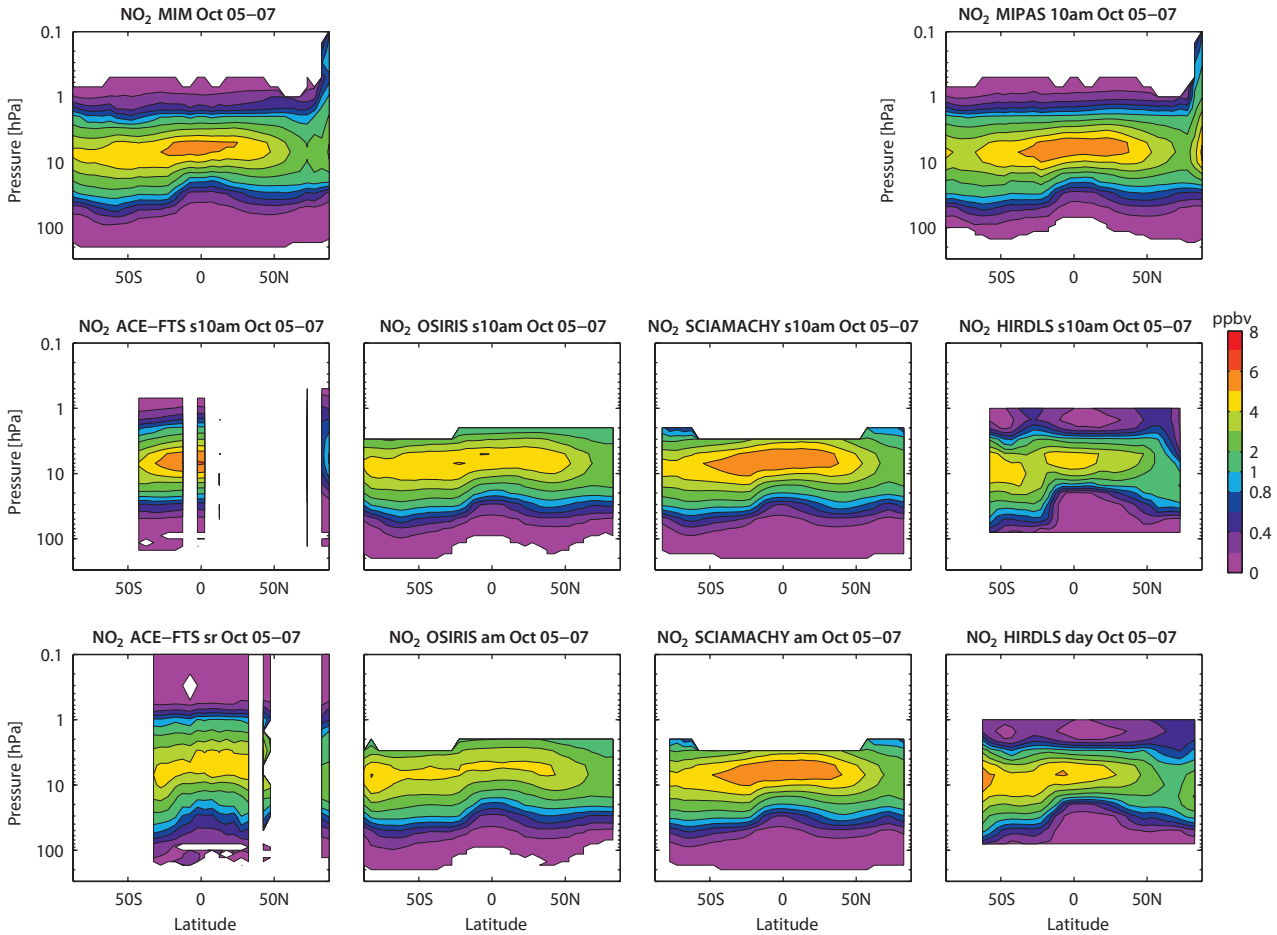

Figure 4.11.9: Cross sections of zonal mean daytime NO_2 for October 2005-2007. *Monthly zonal mean NO_2 cross sections for October 2005-2007 are shown for the MIM (upper left panel) and the individual instruments. Measurements correspond to 10am LST (MIPAS) or are scaled to 10am LST. Note that scaled HIRDLS data are only available for June 2005 – May 2006. In addition, unscaled data from ACE-FTS, OSIRIS, SCIAMACHY, and HIRDLS are shown.*

for 2005-2007. Differences of the individual datasets from the MIM for October 2005-2007 are shown in **Figure 4.11.10**. In general, the differences in the MS vary strongly, from ±5% in some regions to ±50% in others. MIPAS and SCIAMACHY show similar features and observe larger NO_2 abundances than the other instruments, leading to deviations from the MIM in the MS of around +20%, and locally +50%. One exception is the SH extra-tropics where both instruments show negative differences from the MIM of up to -20%. While MIPAS and SCIAMACHY are on the high side, HIRDLS observes values at the lower end of the range, producing large negative deviations from the MIM of up to -50% (and locally -100%). An exception to this behaviour is again the SH extra-tropics where HIRDLS detects larger NO_2 abundances than the other instruments. OSIRIS is mostly in the middle range; deviations from the MIM change sign depending on the latitude band and exceed ±50% only occasionally. ACE-FTS also observes deviations of mixed signs, mostly opposite to HIRDLS with particularly large negative deviations where HIRDLS shows a positive difference. Note that at high SH latitudes, where only MIPAS, OSIRIS and SCIAMACHY measurements are available, the three instruments agree considerably better, with deviations from their MIM of only up to ±20%, while in regions where all five instruments provide measurements, deviations can reach ±50% to ±100%. Evaluations of January, April, and July climatologies (see **Figure A4.11.6** in *Appendix A4* for April evaluations) give a consistent picture for all four seasons. The main difference from the October evaluations discussed above is that MIPAS and HIRDLS show more differences of mixed signs. While in the SH spring and summer, MIPAS is mostly positive and HIRDLS mostly negative, MIPAS deviations from the MIM in the NH spring and summer are negative almost everywhere below 10 hPa. The pattern of OSIRIS deviations from the MIM changes from month to month. Note that scaled HIRDLS data are only available for June 2005 – May 2006, and that the evaluation of this one-year long time period (not shown) gives very similar results to the evaluation presented above.

For a better understanding of the scaling effects, the initial climatologies are also shown. The unscaled OSIRIS and ACE-FTS datasets have a considerably larger bias compared to the scaled datasets, indicating that scaling is necessary in order to compare the climatologies. SCIAMACHY shows similar differences for the scaled and unscaled datasets, which can be explained by the fact that the LST of the original SCIAMACHY dataset is 10am at the equator and only changes slightly when moving to higher latitudes. For some regions (*e.g.*, SH in March) the scaled dataset shows somewhat larger differences from the MIM than the unscaled

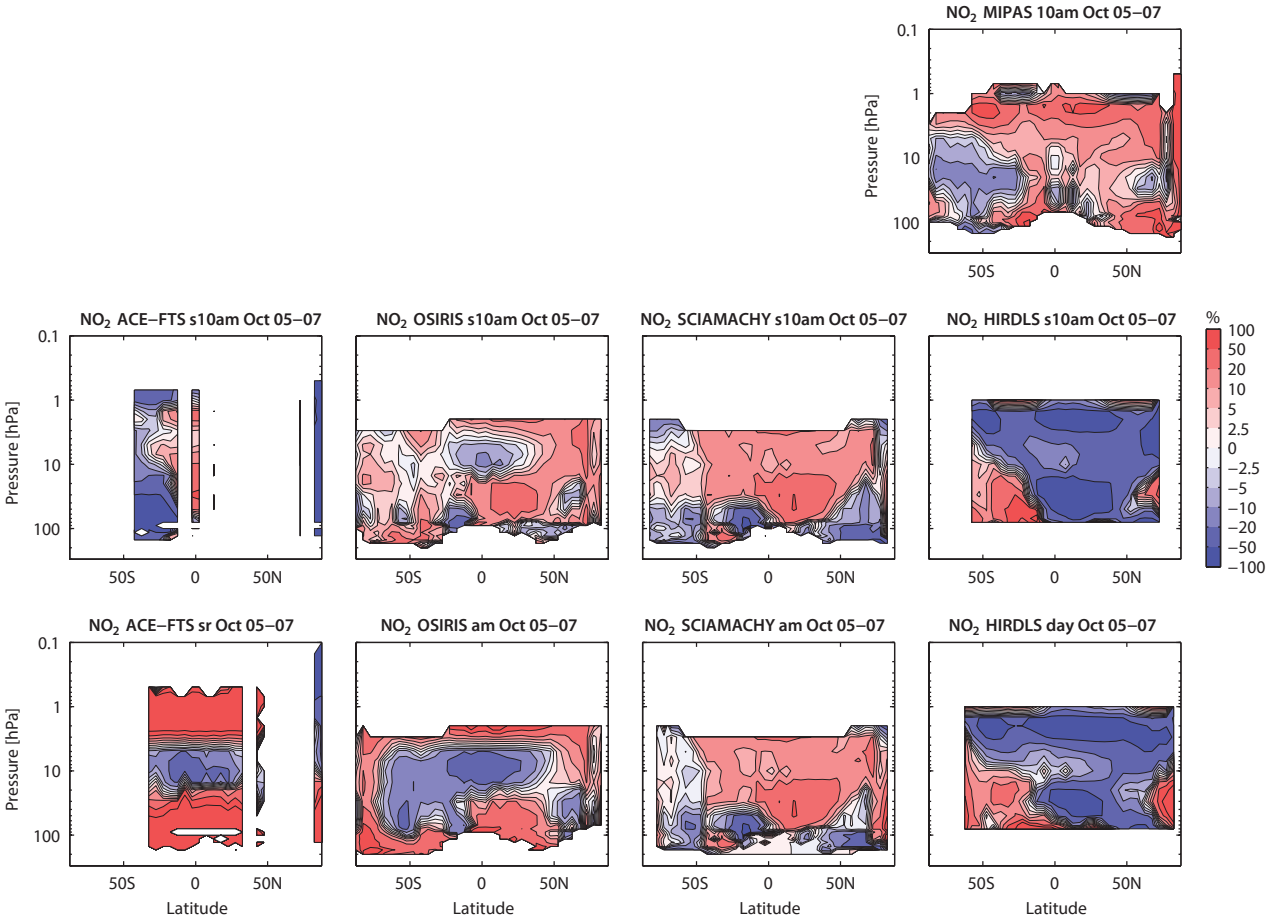

Figure 4.11.10: Cross sections of zonal mean daytime NO_2 differences for October 2005-2007. *Monthly zonal mean NO_2 differences from the MIM for October 2005-2007 are shown. Measurements correspond to 10am LST (MIPAS) or are scaled to 10am LST. Note that scaled HIRDLS data are only available for June 2005 – May 2006. In addition, unscaled data from ACE-FTS, OSIRIS, SCIAMACHY, and HIRDLS are shown.*

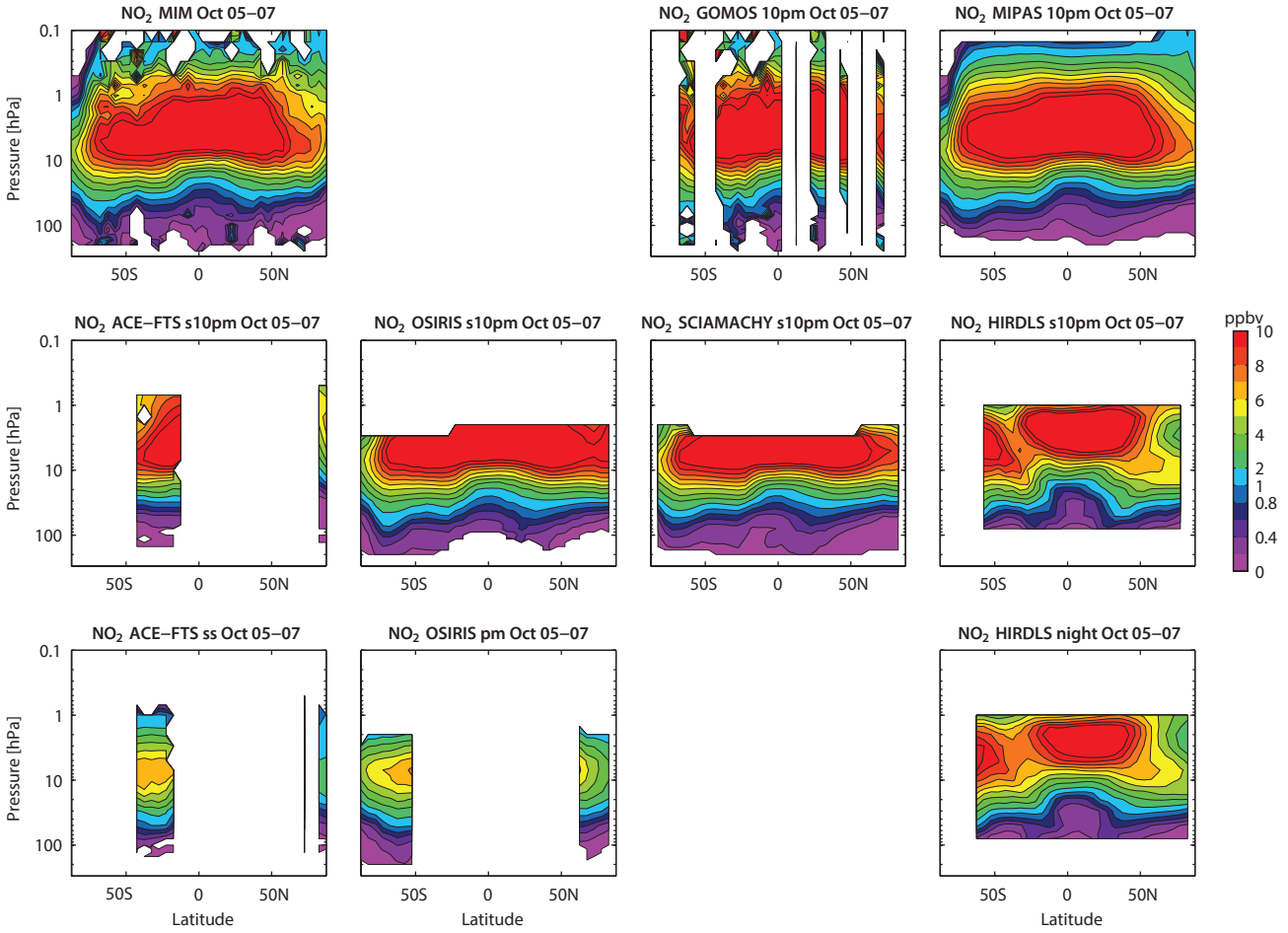

Figure 4.11.11: Cross sections of zonal mean night-time NO_2 for October 2005-2007. *Monthly zonal mean NO_2 cross sections for October 2005-2007 are shown for the MIM (upper panel) and the individual instruments. Measurements correspond to 10pm LST (MIPAS, and GOMOS) or are scaled to 10pm LST. Note that scaled HIRDLS data are only available for June 2005 – May 2006. In addition, unscaled data from ACE-FTS, OSIRIS, and HIRDLS are shown.*

dataset, unlike the results from OSIRIS. In these cases, it is possible that the errors introduced by the scaling based on look up tables outweigh the improvement achieved by the correction to a specific LST. For HIRDLS, large negative deviations are apparent in the scaled and unscaled datasets, indicating that the differences are related to measurement differences and cannot be corrected by accounting for the measurement LST.

NO_2 night-time climatologies for October 2005-2007 are shown in **Figure 4.11.11**. NO_2 abundances are considerably larger for the night-time climatologies than for daytime climatologies, as expected from the diurnal cycle. Maximum NO_2 values can be observed in the SH mid-latitudes and tropics between 1 and 10 hPa. As for the daytime climatologies, MIPAS data (corresponding to 10pm LST) as well as scaled ACE-FTS, OSIRIS, SCIAMACHY and HIRDLS data (all scaled to 10pm LST) are available and can be compared directly. Additionally, GOMOS measures night-time NO_2 at 10pm LST. Also shown in **Figure 4.11.11** are the unscaled OSIRIS night-time climatology (corresponding to a range of LSTs), the HIRDLS night-time climatology (corresponding to approximately 00:30am) and the ACE-FTS local sunset climatology. Note that for SCIAMACHY no measurements during the night exist and that the scaled 10pm SCIAMACHY climatology is based on daytime SCIAMACHY measurements.

Differences of the individual night-time climatologies from the MIM are displayed in **Figure 4.11.12**. The MIM is based on the climatologies corresponding directly to 10pm LST (MIPAS, GOMOS), and scaled to 10pm LST (ACE-FTS, OSIRIS, SCIAMACHY and HIRDLS). MIPAS and SCIAMACHY have positive deviations in the MS and negative deviations in the LS, and agree well with each other and with OSIRIS. The climatologies from HIRDLS and ACE-FTS show lower values for most latitude bands, with deviations from the MIM of up to -50%. The GOMOS dataset is somewhat noisier than the other climatologies but shows small differences from the MIM (up to ±10%) between 10 and 1 hPa. In the LS, MIPAS, SCIAMACHY and ACE-FTS observe the lowest values while GOMOS and OSIRIS show positive deviations from the MIM. Differences can become as large as ±100% locally. Note that SCIAMACHY data scaled to 10pm represent a scaling to completely different illumination conditions, namely from day to night, while the scaling of SCIAMACHY data to 10am is a daytime to daytime scaling, with only slightly different illumination conditions. The fact that the SCIAMACHY night-time climatology does not show larger differences from the MIM

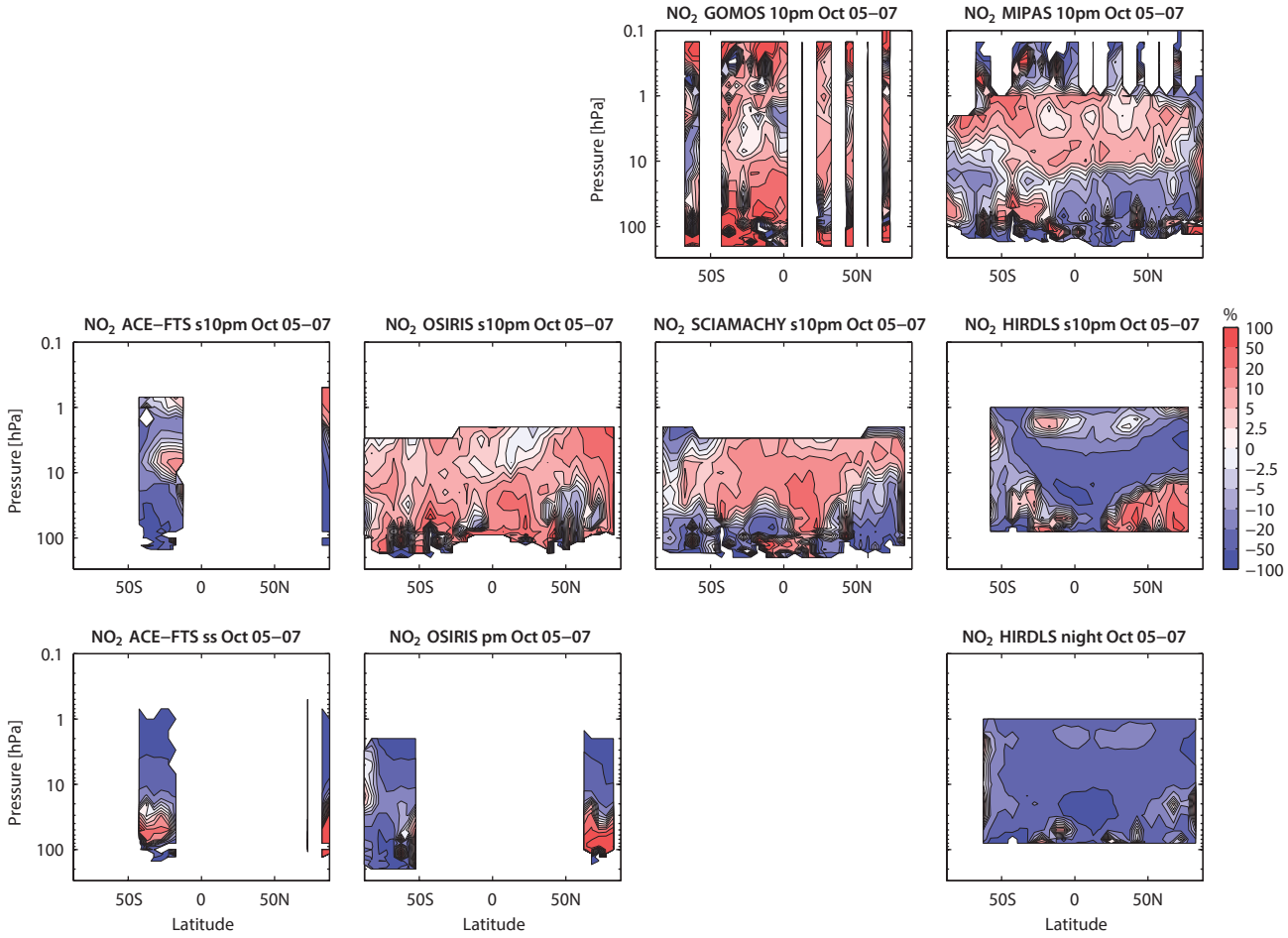

Figure 4.11.12: Cross sections of zonal mean night-time NO_2 differences for October 2005-2007. *Monthly zonal mean NO_2 differences from the MIM for October 2005-2007 are shown. Measurements correspond to 10pm LST (MIPAS, and GOMOS) or are scaled to 10pm LST. Note that scaled HIRDLS data are only available for June 2005 – May 2006. In addition, unscaled data from ACE-FTS, OSIRIS, and HIRDLS are shown.*

than the daytime climatology suggests that no large errors have been introduced by this scaling procedure.

A comparison of the night-time climatologies without GOMOS (see **Figure A4.11.9** in *Appendix A4*) shows that the observed differences are quite similar to the daytime evaluations, and that both sets of climatologies provide a consistent picture. Note that differences are slightly smaller between the night-time climatologies than between the daytime climatologies, which might be related to the larger NO_2 abundances during night-time.

In addition to the NO_2 datasets discussed above, which cover the time period after 2000, the very first satellite borne NO_2 profile measurements from the limb emission instrument LIMS are available for 1978/1979. The LIMS daytime climatology corresponds to 1pm at low and mid-latitudes and shifts to late afternoon at higher latitudes, while the LIMS night-time climatology corresponds approximately to 11pm LST. Since there are no daytime or night-time NO_2 measurements available before 2002, LIMS will be compared to the 2005-2007 climatologies presented above. Note that the stratospheric aerosol content is very low for both time periods, which facilitates the comparison of LIMS NO_2 with the other datasets.

Figure 4.11.13 shows the relative differences of LIMS day- and night-time climatologies to the respective 10am/pm 2005-2007 MIM from the evaluations above. LIMS shows good agreement in a narrow pressure range between 10 and 5 hPa, with differences mostly between ±10%. Below this level differences increase quickly, reaching +100% in the LS. Above this level, the daytime climatologies differ by up to -50% while the night-time climatologies show slightly better agreement, with differences of up to -20%. Note that LIMS measurements are not taken at 10am or 10pm LST, and it is therefore not possible to easily separate the differences attributable to a real measurement bias, and the effects of the diurnal NO_2 cycle.

4.11.4 NO_2 evaluations: Seasonal cycles

NO_2 exhibits a strong seasonal cycle in the extra-tropics due to the effects of sunlight on the partitioning of the NO_y family. Seasonal cycles of the NO_2 daytime and night-time climatologies will be evaluated below. Since the seasonal variations of the sunset and sunrise climatologies from the solar occultation instruments can be difficult to analyse due to sparse data coverage, they are not shown here.

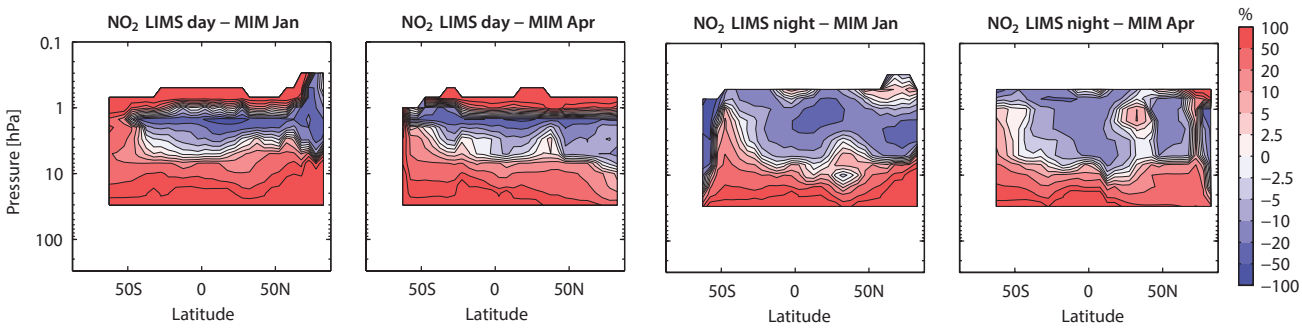

Figure 4.11.13: Cross sections of zonal mean daytime/night-time NO_2 differences between LIMS (1978-1979) and MIM (2005-2007). *Monthly zonal mean NO_2 differences between LIMS (1978-1979) and the MIM (2005-2007) are shown for January and April. Measurements correspond to 1pm for LIMS and 10am for the MIM (left panels) and the 11pm for LIMS and 10pm for MIM (right panels). The MIM is based on the 10am/pm climatologies for 2005-2007 presented above.*

Figure 4.11.14 shows the seasonal cycle of 2005-2007 daytime NO_2 climatologies for the NH and SH mid-latitudes at 10 hPa and the SH tropics at 3 hPa. The five datasets evaluated here (MIPAS and scaled ACE-FTS, OSIRIS, SCIAMACHY, and HIRDLS) correspond to 10am LST. The mid-latitude seasonal cycle with maximum values in summer and minimum values in winter is reproduced by all instruments. The datasets agree better during the summer, and show a larger spread during the hemispheric winter. The seasonal cycles from HIRDLS and ACE-FTS have larger amplitudes than the other datasets in both hemispheres, particularly in the NH mid-latitudes. In contrast, the seasonal cycle observed by MIPAS shows the smallest amplitude. Note that OSIRIS does not provide data for the SH winter months, leading to a flattening of the fitted seasonal cycle. In the tropics, seasonal variations are weak and the instruments have problems reproducing the signal. MIPAS and SCIAMACHY display the same seasonal cycle, with a maximum in April and a minimum in August/September. The seasonal cycle observed by OSIRIS agrees reasonably well but has a slightly larger amplitude and earlier minimum (July). The largest deviations are observed by HIRDLS, which shows a stronger amplitude and a weak second maximum in January/February, indicating a semiannual oscillation. Note that ACE-FTS in the SH tropics provides data only at the beginning and end of the year, and therefore does not offer sufficient information to fit the seasonal cycle. While ACE-FTS values for January and August are close to MIPAS and HIRDLS, the ACE-FTS values for February, April and October do not follow the seasonal signal suggested by the other instruments, indicating that the scaled ACE-FTS data observe at best a weak annual cycle.

Comparing the scaled climatologies in **Figure 4.11.14** with the seasonal cycle of the respective unscaled climatologies (**Figure A4.11.10** in *Appendix A4*) demonstrates a strong improvement in agreement of the seasonal cycle for OSIRIS, HIRDLS, and ACE-FTS for the SH and NH mid-latitudes, compared to each other and with MIPAS and SCIAMACHY. In the tropics, however, OSIRIS observes the same mean values and the same seasonal signal as MIPAS before the scaling, while the scaled dataset has lower mean values and a slightly shifted phase. Similarly, HIRDLS in

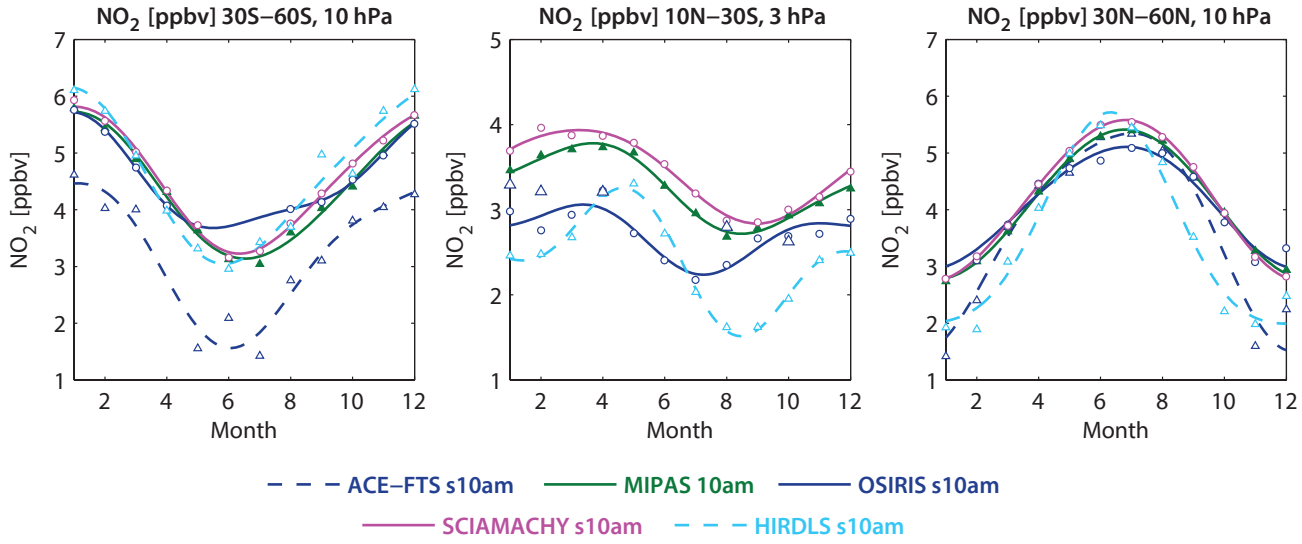

Figure 4.11.14: Seasonal cycle of daytime NO_2 for 2005-2007. *Seasonal cycle of monthly zonal mean NO_2 for 30°S-60°S at 10 hPa (left panel), 10°S-30°S at 3 hPa (middle panel) and 30°N-60°N at 10 hPa (right panel). Measurements correspond directly to 10am LST (filled symbols) or are scaled to 10am LST (open symbols). Note that scaled HIRDLS data are only available for June 2005 – May 2006. ACE-FTS in the SH tropics does not provide sufficient data coverage to estimate a fit of the seasonal cycle.*

the tropics has more similarities with the other instruments before the scaling in the sense that it shows no semiannual component. Finally, tropical unscaled ACE-FTS data have the same signal as MIPAS and SCIAMACHY as opposed to the scaled dataset.

Figure 4.11.15 displays the seasonal cycle of night-time NO_2 for 2005-2007. Although the general shape of the seasonal cycle is very similar to the one derived from daytime measurements, the instruments show a much larger spread in the signal. Excellent agreement is found between SCIAMACHY and GOMOS for the SH mid-latitudes. In this region, MIPAS and HIRDLS show the same phase but HIRDLS has a stronger amplitude than MIPAS. Similar to the daytime measurements, OSIRIS has little data available during SH winter, and the seasonal fit displays a flattened and shifted peak. In the NH mid-latitudes, the instruments disagree on the timing of the maximum, from June (HIRDLS), over July (MIPAS, SCIAMACHY) and August (OSIRIS), to September (GOMOS). Additionally, there is considerable spread in the amplitude of the seasonal signal, with HIRDLS displaying the largest amplitude and MIPAS and OSIRIS the smallest. The tropical seasonal cycles of MIPAS, GOMOS and SCIAMACHY agree well, while OSIRIS has a shifted phase and HIRDLS has an amplitude that is too strong.

4.11.5 NO_2 evaluations: Interannual variability

Apart from the climatological differences between the datasets it is of interest to evaluate how well the instruments detect signals of interannual variability. **Figure 4.11.16** shows the time series of daytime NO_2 mean values (upper panels) and deseasonalised anomalies (lower panels) for the tropical latitude band 20°S-20°N at 10 hPa. Datasets corresponding to 10am LST are displayed in the left panels and the original datasets are displayed in the right panels. The anomalies of the scaled datasets are calculated in an additive sense by subtracting monthly multi-year mean values for each month. Such additive anomalies, however, might also display a diurnal cycle and are therefore not suitable evaluation tools for the unscaled datasets. Instead, the anomalies of the unscaled climatologies are calculated in a multiplicative sense as percentage deviations from the monthly multi-year mean values, a quantity that is less affected by the diurnal variations.

In the tropics, NO_2 shows strong interannual variability dominated by an approximately two year long cycle, which is linked to the QBO-modulated transport of NO_y [*Zawodny and McCormick*, 1991]. MIPAS, OSIRIS and SCIAMACHY anomalies in the tropics agree extremely well and display the expected QBO cycle. Note that although unscaled OSIRIS mean values display strong deviations from MIPAS and SCIAMACHY, their multiplicative anomalies agree as well as the additive anomalies of the scaled datasets, creating confidence in the method applied. The scaled ACE-FTS climatology does not show a QBO signal and reveals only very little interannual variability. However, the unscaled ACE-FTS anomalies display a QBO signal very similar to the other instruments indicating that the missing interannual variability must be introduced by the scaling procedure. The scaled HIRDLS dataset is only available from June 2005 to May 2006 and does not provide any information on interannual variability. The unscaled HIRDLS climatology covers 3 years and shows similar interannual signals as the other datasets but with larger month-to-month variations. Evaluations of tropical nighttime climatologies (not shown) give very similar results.

Figure 4.11.17 shows the evaluation of the interannual anomalies of the longer time series from SAGE II and HALOE in comparison with the interannual variability of

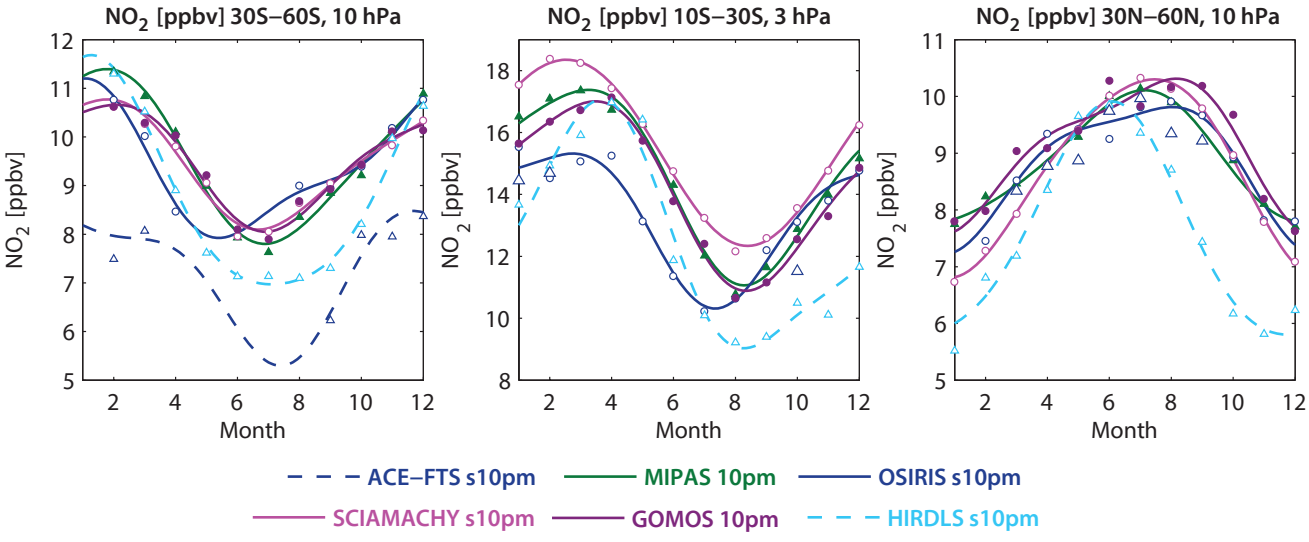

Figure 4.11.15: Seasonal cycle of night-time NO_2 for 2005-2007. Seasonal cycle of monthly zonal mean NO_2 for 30°S-60°S at 10 hPa (left panel), 10°S-30°S at 3 hPa (middle panel) and 30°N-60°N at 10 hPa (right panel). Measurements correspond directly to 10pm LST (filled symbols) or are scaled to 10pm LST (open symbols). Note that scaled HIRDLS data are only available for June 2005 – May 2006. ACE-FTS in the SH tropics and NH mid-latitudes does not provide sufficient data coverage to estimate a fit of the seasonal cycle.

ACE-FTS, MIPAS, OSIRIS and SCIAMACHY. Since no scaled versions of SAGE II and HALOE data are available, the comparison focuses on multiplicative anomalies of the sunrise/daytime NO_2 climatologies including the SAGE II, HALOE, and ACE-FTS local sunrise datasets as well as the MIPAS, OSIRIS, and SCIAMACHY 10am datasets. The comparison of the mean values (upper panel) shows very good agreement of MIPAS and scaled SCIAMACHY measurements, and good agreement of sunrise SAGE II, HALOE and ACE-FTS data for the overlap period 2004-2005. Scaled OSIRIS data lie between the two sets of climatologies and, surprisingly, are slightly closer to the local sunrise measurements rather than the 10am climatologies from MIPAS and SCIAMACHY, as one would expect. From 2003 onwards the multiplicative anomalies of all datasets display the expected QBO signal, with the best agreement between MIPAS, OSIRIS and SCIAMACHY. While HALOE agrees with the minimum values in 2003 and 2005 and maximum values in 2004, it shows much stronger month-to-month fluctuations. Also, while HALOE data indicate a QBO signal from 1993 to 1998, it has rather low variability and no clear QBO cycle for 1998 to 2002. SAGE II has similar month-to-month variability compared to HALOE, but shows no clear indication of a QBO signal, possibly as a result of its relatively sparse data coverage intensified by the separation into sunrise/sunset measurements. Note that the evaluation of the local sunset/night-time climatologies (**Figure A4.11.11** in *Appendix A4*) give similar results with excellent agreement of the interannual anomalies of MIPAS, SCIAMACHY, OSIRIS, and GOMOS. One difference to the local sunrise/daytime evaluations is that SAGE II and HALOE sunset climatologies agree better on their interannual variability and display the QBO signal over the whole time period.

In the mid-latitudes, NO_2 shows less interannual variability and the datasets show less good agreement (**Figure A4.11.12** in *Appendix A4*) when compared to the tropics. The largest deviations are found for GOMOS and HIRDLS, which display strong month-to-month fluctuations. The evaluation of interannual anomalies at SH polar latitudes (**Figure A4.11.13** in *Appendix A4*) is based on multiplicative anomalies calculated relative to the monthly mean values of the time period 2003-2005 (in order to include POAM III local sunrise) and on multiplicative anomalies calculated relative to the time period 2005-2007 (in order to include MIPAS). Interannual variations are most pronounced during the SH winter, but the datasets do not always agree on sign or magnitude of the anomalies. For the comparison relative to the time period 2003-2005, POAM III shows the largest anomalies, and for the comparison relative to the later time period 2005-2007, the MIPAS anomalies are strongest. Note that the evaluation of the polar anomalies might be impacted by sampling artefacts., *e.g.*, compared to SCIAMACHY, MIPAS observes higher latitudes of the SH in winter and might see less NO_2 due to polar vortex denitrification.

4.11.6 NO_2 evaluations: Downward transport of NO_2 during polar winter

In the polar mesosphere, NO_x is produced by ionizing Energetic Particle Precipitation (EPP) [*Barth*, 1992; *Solomon et al.*, 1982]. Observations have shown that inside the polar vortex NO_x is transported downwards into the stratosphere [*Funke et al.*, 2005b; *Seppälä et al.*, 2007] causing elevated NO_2 levels during polar winter with strong year-to-year variability. How well the limb-viewing satellite datasets

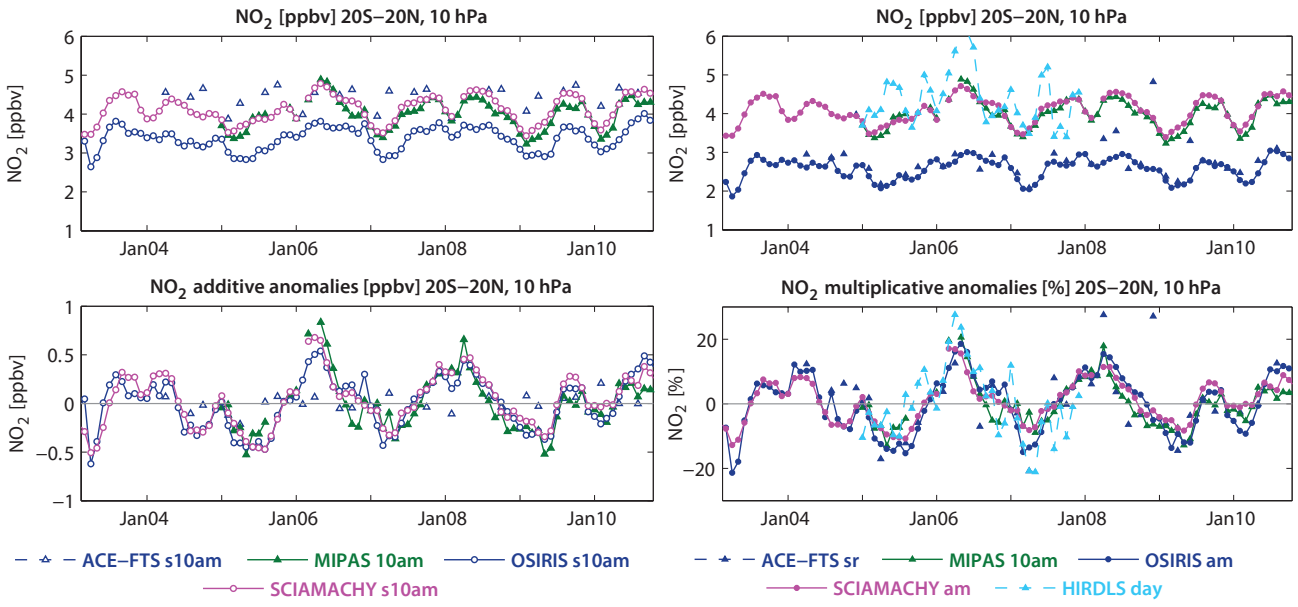

Figure 4.11.16: Time series of daytime tropical NO_2 mean values and anomalies for 2003-2010. *Monthly mean values (upper panels) and deseasonalised anomalies (lower panels) of NO_2 between 20°S – 20°N at 10 hPa. The 10am climatologies (left panel) correspond directly to 10am LST (filled symbols) or are scaled to 10am LST (open symbols). The daytime climatologies (right panel) correspond to a variety of LSTs as described in Table 4.11.3. The anomalies are calculated in an additive manner for the 10am and in a multiplicative manner for the daytime climatologies, as further explained in the text.*

agree on this phenomenon is evaluated in **Figure 4.11.18**, which shows NO_2 time series in the USLM (1 hPa) for nighttime climatologies at high NH and SH latitudes. Since at sunrise/sunset most of the atmospheric NO_x is available as NO and not NO_2, solar occultation measurements of NO_2 do not show very strong EPP signals. Therefore, the following comparison focuses on emission and star occultation measurements from HIRLDS, MIPAS and GOMOS. As the only exception, scaled ACE-FTS data are included allowing for the evaluation of the EPP signal in sunrise/sunset NO_2 by scaling it to 10pm NO_2 abundances.

In both hemispheres, measurements during the polar winter reveal very large NO_2 values (up to 10 times higher than the 10 hPa maximum in the summer hemisphere) related to the polar winter descent of NO_x. In the NH, MIPAS and GOMOS data show very good agreement on the timing and magnitude of the elevated NO_2 values for most years with stronger month-to-month fluctuations for GOMOS. In the SH, the two datasets also agree very well for the winter months, however, larger deviations are found before and after the winter, when MIPAS values decay but GOMOS values remain high or increase even further. Note that GOMOS does not provide any measurements during the SH polar summer and one can therefore not compare the winter NO_2 abundance to the annual mean state. HIRDLS measurements in both hemispheres show elevated values during the winter months very similar to MIPAS and GOMOS, except for the SH winter 2007 and the NH winter 2007/2008 when HIRDLS is low. During the rest of the year, HIRDLS NO_2 decays only slightly compared to the winter months, in contrast to MIPAS data, which is very low in the spring and summer. Since the HIRDLS nighttime climatology includes only measurements at SZA>90° with a measurement time varying around 0:30am, the absolute HIRDLS values cannot be compared directly with MIPAS or GOMOS. Very likely the larger NO_2 abundances observed by HIRDLS in summer are due to the fact that the HIRDLS climatology contains no measurements at illuminated conditions when NO_2 is rapidly transformed into NO. Based on the MIPAS NO_x climatologies in the same region we would expect the overall NO_x abundance to be ~7-8 ppbv during the NH summer 2005 (see **Figure 4.12.9** in *Section 4.12*), which is roughly consistent with the HIRDLS NO_2 values during this time. Scaled ACE-FTS data, although less frequent, shows the same signal as MIPAS data with elevated NO_2 in winter between 5 and 10 ppbv and very low NO_2 in summer with less than 1 ppbv. Note that unscaled ACE-FTS data do not reveal any elevated wintertime NO_2 levels, as expected due to the NO/NO_2 partitioning in the LM at sunrise/sunset.

The elevated NO_2 abundances caused by EPP in the mesosphere propagate downward into the upper and middle stratosphere during the polar winter as evident from MIPAS and GOMOS observations in **Figure 4.11.19**. The time-altitude cross sections show that elevated NO_2 exists for every winter but show a large interannual variability throughout the whole LM and US. Particularly strong events have been observed for 2004 and 2005 by both instruments. For the two last winters

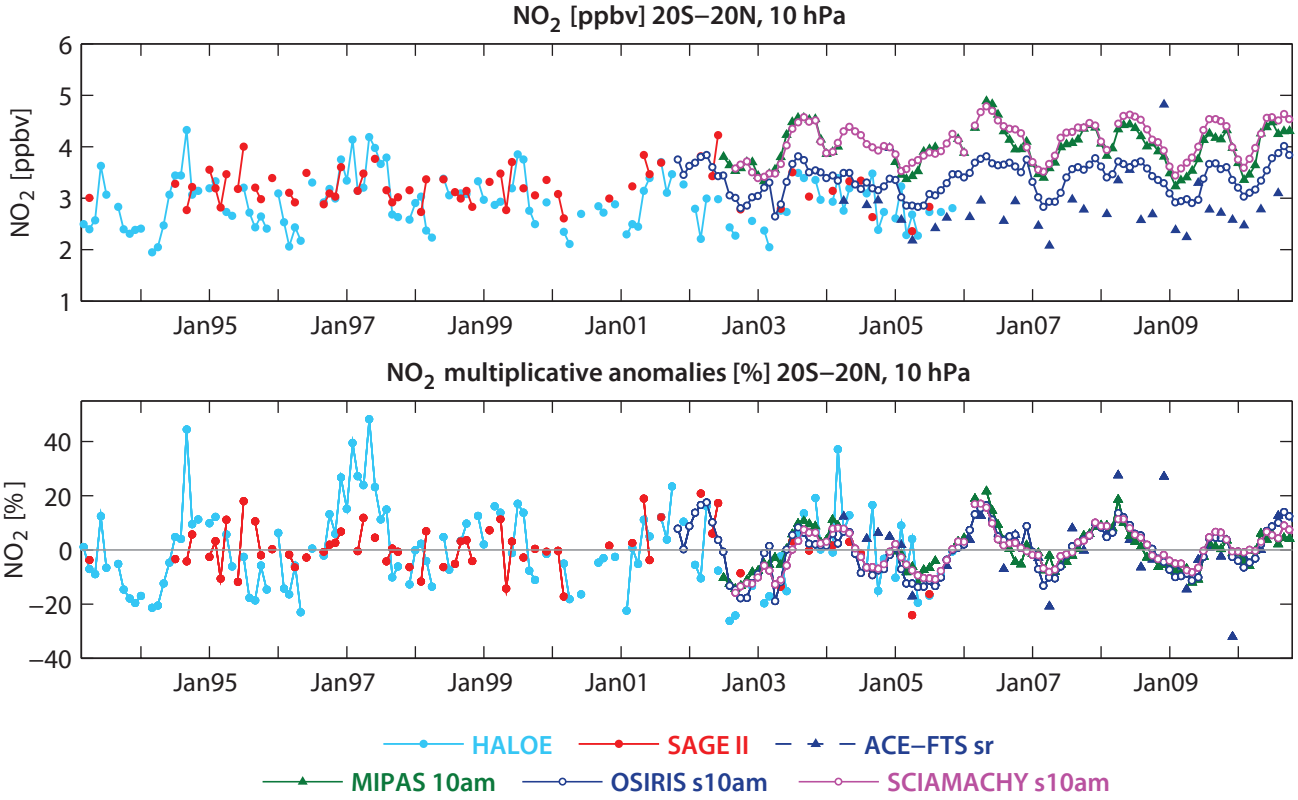

Figure 4.11.17: Time series of tropical local sunrise and daytime NO_2 mean values and anomalies for 1993-2010. *Monthly mean values (upper panels) and deseasonalised anomalies (lower panels) of NO_2 between 20°S – 20°N at 10 hPa. Datasets correspond to local sunrise or to 10am LSTs as described in the text.*

of the time series, MIPAS measurements show only slightly elevated NO_2 abundances, while the GOMOS time series includes some larger values that are, however, somewhat isolated in the noisy dataset. Differences of the two instruments to their MIM are of changing sign reaching ±50%. Overall, during periods of elevated abundances, MIPAS detects less NO_2 than GOMOS with the exception of early 2004.

Note that LIMS measurements in the NH winter 1978/1979 also reveal elevated NO_2 abundances from the LM down to 20 hPa. Due to the strong interannual variability of EPP indirect effects, LIMS observations belonging to a different period are not directly comparable to the other datasets. Additional to the elevated NO_2 in the US and LM there is an apparent excess of LIMS NO_2 at 10 hPa at high latitudes. This could partly be due to the fact that there were large wave-1 events in January 1979 that moved the vortex off the Pole and brought some NO_2 to high latitudes.

4.11.7 Summary and conclusions: NO_2

A comprehensive comparison of NO_2 profile climatologies from 12 satellite instruments (LIMS, SAGE II, HALOE, POAM II, POAM III, OSIRIS, SAGE III, MIPAS, GOMOS, SCIAMACHY, ACE-FTS, and HIRDLS) has been carried out. Overall findings on the systematic uncertainty in our knowledge of the NO_2 mean state and important characteristics of the individual datasets are presented in the following summary including two synopsis plots. The first summary plot (**Figure 4.11.20**) provides information on the NO_2 mean state at local sunrise (am LSTs), local sunset (pm LSTs), 10am and 10pm. Additionally, the uncertainty derived from the spread between the datasets is given for all four illumination conditions. The second summary plot (**Figure 4.11.21**) shows specific inter-instrument differences in the form of the deviations of the instrument climatologies from the MIM climatology. For each region, four separate evaluations for the four different "illumination conditions" are included. For each LST, instrument and selected region the deviation to the MIM is given in form of the median (mean) difference over all grid points in this region. Additionally, for each instrument the spread of the differences over all grid points in this region is presented. Note that both pieces of information (average deviation and spread) are important for a meaningful assessment of inter-instrument differences. A detailed description of the summary plot evaluations can be found in *Section 3.3.5*.

Atmospheric mean state

Middle stratosphere (30-5 hPa)

The uncertainty in our knowledge of the atmospheric NO_2 annual mean state is smallest in the tropical and

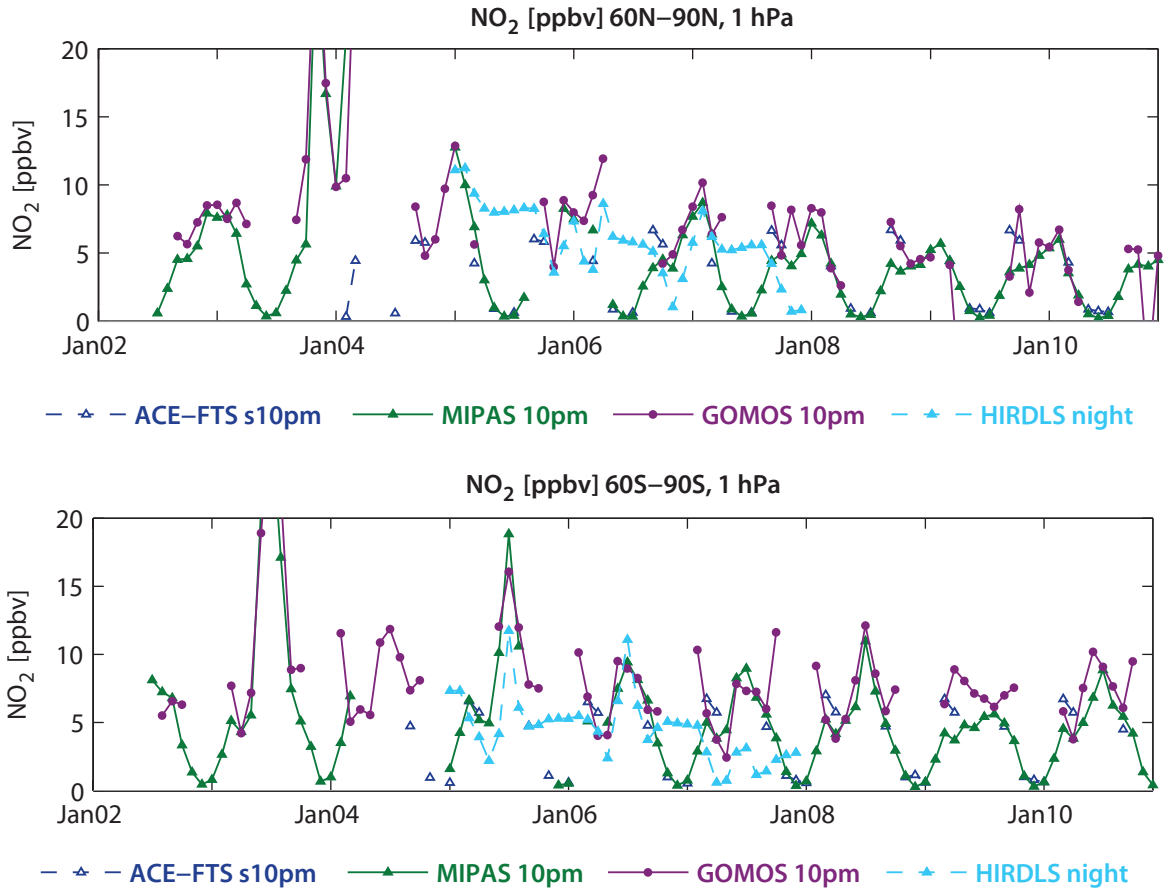

Figure 4.11.18: Time series of polar night-time NO_2 for 2002-2010. *Time series of night-time NO_2 at 1 hPa for 60°N-90°N (upper panel) and for 60°S-90°S (lower panel) from 2002 to 2010 are shown.*

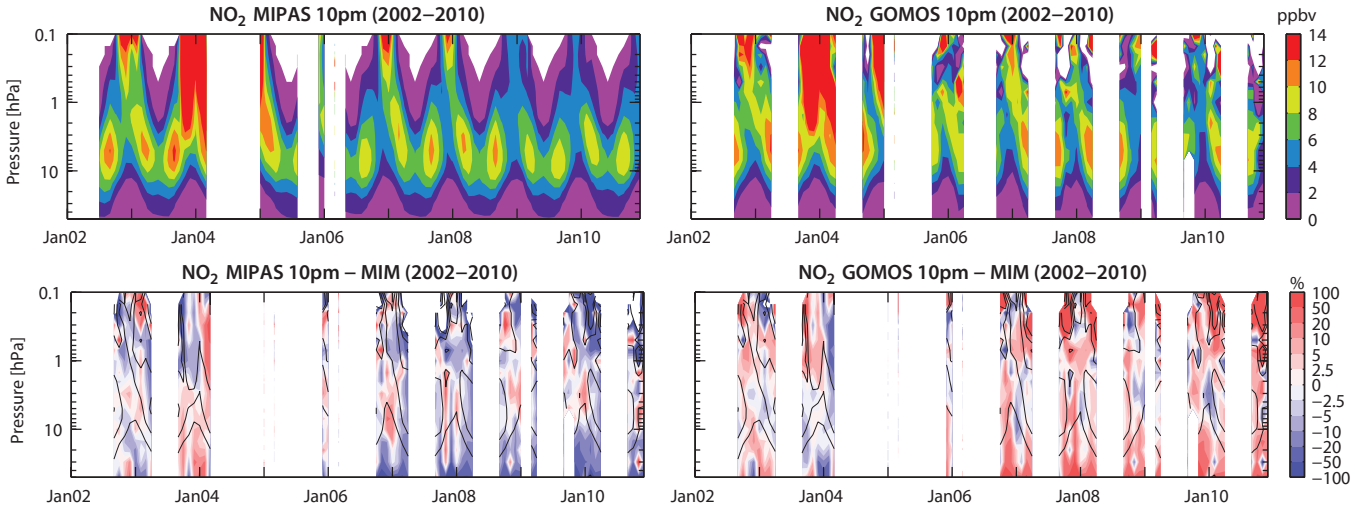

Figure 4.11.19: Altitude time evolution of NO_2 mean values and differences to the MIM in the Arctic. *Altitude-time sections of monthly zonal mean NO_2 (upper panels) and differences to the MIM (lower panels) corresponding to 10pm for 60°N-90°N from 2002 to 2010 are shown. The differences to the MIM are displayed by colour contours while the overlaid black contours show the MIM NO_2 field.*

mid-latitude MS. The evaluation of three solar occultation local sunrise/sunset datasets for 2004-2005 reveals a 1σ multi-instrument spread in this region of ±5% to ±10% (**Figure 4.11.20**, right panel). The datasets corresponding to 10am/pm LST give a slightly larger spread in the MS of ±10% to ±20%. Note that the latter comparison is based on climatologies derived by scaling measurements with a chemical box model to a common LST.

Lower stratosphere (100-30 hPa)

In the LS, the NO_2 abundances decrease quickly and the local sunrise/sunset climatologies from the solar occultation instruments show a large spread (1σ of ±50%), while a slightly better agreement is found for the daytime/nighttime climatologies (1σ of ±10% to ±50%). In particular, the 10am climatologies show a good agreement in the NH mid-latitudes down to 100 hPa.

Upper stratosphere (5-1 hPa)

In the US, the best agreement is found for the climatologies corresponding to 10pm LST, which give a multi-instrument spread in the tropics and mid-latitudes of ±5% to ±10%. Larger deviations are found for the other sets of climatologies, in particular above 2 hPa with a 1σ spread of up to ±30%.

High latitudes

At high latitudes, the instruments show larger deviations than at lower latitudes. In the MS, best agreement is found for the local sunrise datasets (1σ of ±10% to ±20%) while all other sets of climatologies give a larger uncertainty of the mean state (1σ of ±50%). In the USLM, the high latitude annual mean NO_2 abundance is dominated by the polar night NO_x descent, which is best reported by the limb emission instruments.

Instrument-specific conclusions

Local sunrise/sunset climatologies from solar occultation instruments

SAGE II, HALOE and ACE-FTS show very good to good agreement in the MS, with mean differences below ±5% for their local sunset climatologies and below ±10% for their local sunrise climatologies (**Figure 4.11.21**). Above and below this level, the relative differences increase steadily reaching mean values of up to ±20% in the US and up to ±50% in the LS. For most regions, the NO_2 local sunrise and sunset evaluations give a consistent picture, however, some differences exist (*e.g.*, for ACE-FTS and SAGE II in the tropical LS). Despite their sparser data coverage when compared to other limb sounders, all three solar occultation instruments observe the tropical QBO cycle except for the SAGE II sunrise climatologies, in which no QBO signal can be identified. One important characteristic of the solar occultation climatologies is the stronger month-to-month fluctuations. A comparison of the long-term climatologies from SAGE II and HALOE (1992-2005) leads to similar results as the comparison of their short-term climatologies (2004-2005) discussed above.

- When compared to the other solar occultation datasets, **SAGE II** detects mostly larger NO_2 abundances, with the exception of the MS local sunrise climatologies, for which SAGE II is lowest. In the US, a relatively large regional spread (over all US grid points) of the SAGE II differences is found, indicating individual monthly mean differences larger than +50%.
- **HALOE** detects less NO_2 than the other two instruments except around 10 hPa where, depending on the latitude bin, it can show larger values. Evaluations of the HALOE local sunrise and sunset climatologies give consistent results.

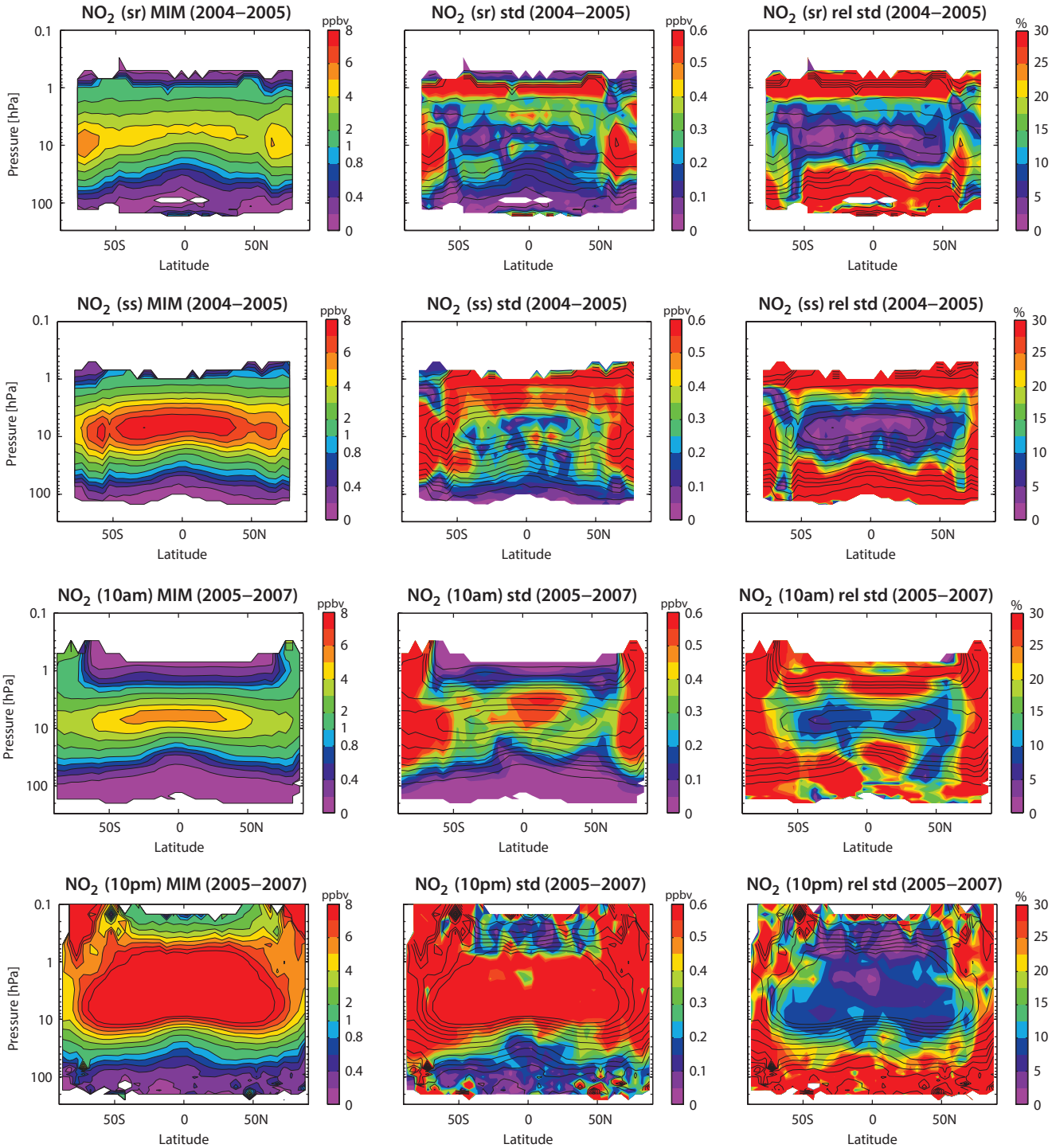

Figure 4.11.20: Summary of NO_2 annual zonal mean state for 2004-2005 and 2005-2007. *Annual zonal mean cross sections of the NO_2 MIM are shown in the left panels for local sunrise (upper row), local sunset (second row), 10am (third row) and 10pm (lower row) illumination conditions. The local sunrise and sunset mean state for 2004-2005 are based on SAGE II, HALOE and ACE-FTS. The mean state at 10am for 2005-2007 is based on MIPAS at 10am and OSIRIS, SCIAMACHY, ACE-FTS, and HIRDLS scaled to 10am. The mean state at 10pm for 2005-2007 is based on MIPAS and GOMOS at 10pm and OSIRIS, SCIAMACHY, ACE-FTS, and HIRDLS scaled to 10pm. Additionally, for all four illumination conditions, the standard deviation over all respective instruments is presented in the middle panel. Relative standard deviation (calculated by dividing the absolute standard deviation by the MIM) is shown in the right panel. Black contour lines in the right panels give the MIM distribution. The MIM and standard deviation are only displayed for regions where at least two instruments provide measurements.*

- The **ACE-FTS** NO_2 local sunset climatologies are in the mid-range between the other two instruments. ACE-FTS local sunrise climatologies in the LSMS, however, display largest NO_2 abundances.
- **SAGE III**, **POAM II**, and **POAM III** provide measurements over a narrow range at high latitudes. The POAM II climatology for 1994-1996 reports smaller values than SAGE II and HALOE with differences from

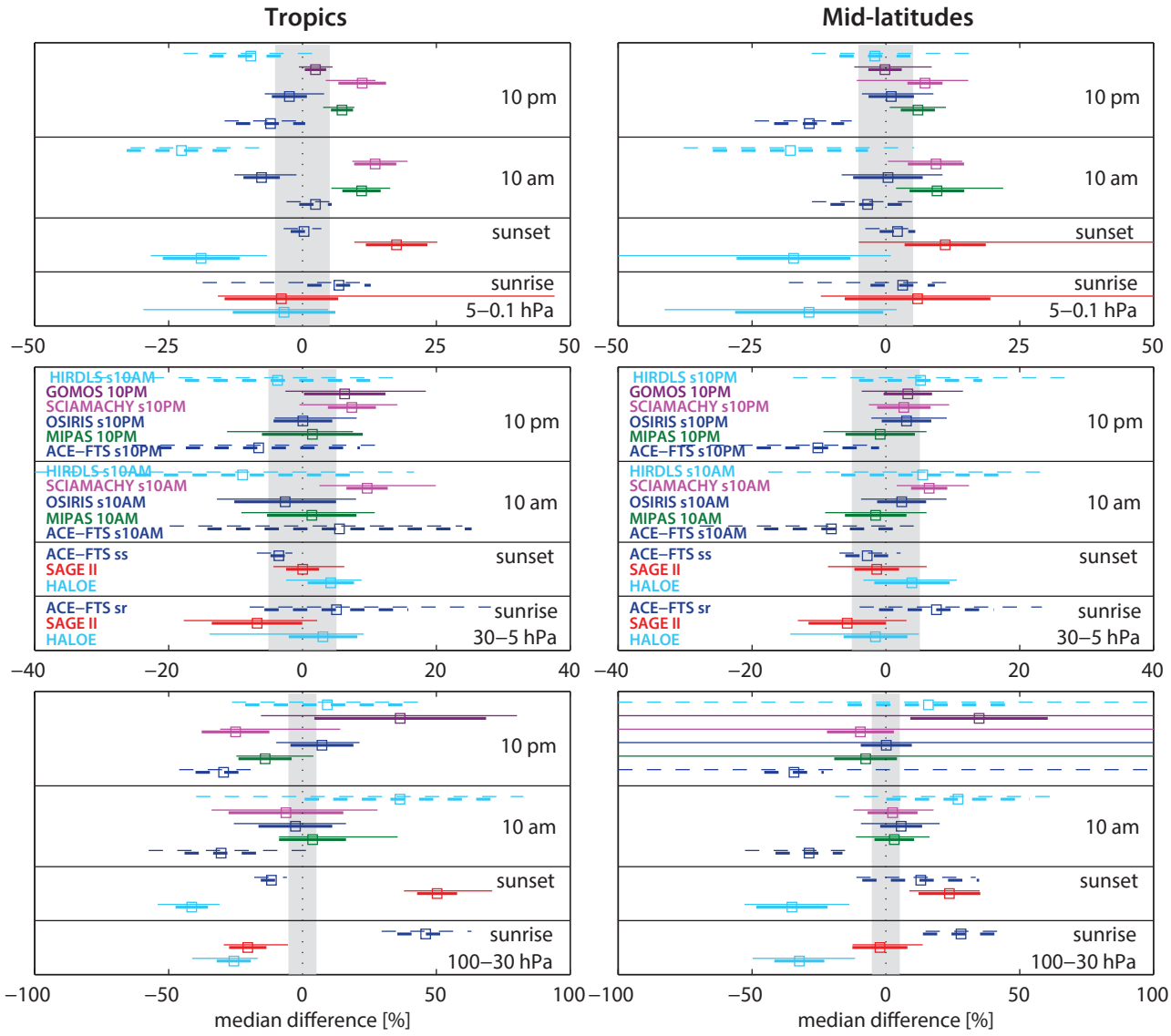

Figure 4.11.21: Summary NO_2 differences for 2004-2005. *Over a given latitude and altitude region the median (squares), median absolute deviation (MAD, thick lines), and the standard deviation (thin lines) of the monthly mean relative differences between an individual instrument-climatology and the MIM are calculated. Results are shown for the tropics (30°S-30°N) and mid-latitudes (30°S-60°S and 30°N-60°N) and for three different altitude regions from the UT up to the LM between 300 and 0.1 hPa for the reference period 2004-2005.*

the MIM of around -10%. The comparison of POAM III and SAGE III to the other instruments for 2004-2005 yields a good agreement in the MS with differences often below ±5% except for a divergence between ACE-FTS and SAGE III in March (±10%). In general, SAGE III is similar to SAGE II and shows larger NO_2 values than the other datasets, while POAM III mostly resides in the mid-range.

10am/pm climatologies

The limb emission and scattering instruments MIPAS, OSIRIS, SCIAMACHY, and HIRDLS are evaluated based on their 10am/pm climatologies, with the latter three derived from scaling with a chemical box model. Additionally, a 10pm climatology from the stellar occultation instrument GOMOS and 10am/pm climatologies from the scaled local sunrise/sunset measurements of the solar occultation instrument ACE-FTS are included in the evaluation. All climatologies show a good agreement in the MS with mean differences of ±5% to ±10%. In particular MIPAS, GOMOS, OSIRIS and SCIAMACHY agree very well with differences below ±5% and in some cases even below ±2% (*e.g.*, for 10pm climatologies in mid-latitudes). In the LS, overall mean differences can be as large as ±40%, however, MIPAS, OSIRIS, and SCIAMACHY are very close to each other with differences among them in the range of ±5% for most cases (±20% for the 10pm climatologies in the tropics). In the US, the inter-instrument spread is about ±25%, with the lower end of the range given by HIRDLS or ACE-FTS depending on latitude and LST. OSIRIS and GOMOS in the middle range agree very well (±2%) and the same is true for MIPAS and SCIAMACHY (±2%) at the upper end of the measurement range. Monthly zonal mean cross sections (**Figures 4.11.9 – 4.11.12**) reveal that for most climatologies the deviations from the MIM can change sign

depending on the latitude band and month. All 10am/pm climatologies show the tropical QBO signal with the best agreement found between MIPAS, OSIRIS, SCIAMACHY and GOMOS.

- **MIPAS** measurements correspond directly to 10am/pm and have not been scaled for the evaluations presented in this chapter. The MIPAS climatologies, when compared to other datasets, are mostly in the middle range, with slightly larger NO_2 abundances and only small deviations from the MIM of up to +5% in MS and up to +15% in the US. Only in the LS, MIPAS shows negative deviations (-15%).
- The **OSIRIS** climatologies, based on measurements scaled to 10am/pm, agree very well with the MIM. Largest deviations are found in the tropical US where OSIRIS data corresponding to 10am show a mean difference of -7%. In the LS, a relatively large spread between all datasets is observed with OSIRIS in the middle range.
- The scaled **SCIAMACHY** climatologies agree overall very well with MIPAS and OSIRIS. Notable differences occur in the tropical US, where SCIAMACHY sets the upper end of the range of climatological values with mean differences from the MIM of +15%. In the tropical LS, SCIAMACHY values scaled to 10pm are on the low side with deviations from the MIM of up to -25%. Note that the SCIAMACHY daytime climatology does not show smaller differences to the MIM than the evaluation of the night-time climatologies (except for the tropical LS) although the latter is based on a scaling to completely different illumination conditions.
- **GOMOS** stellar occultation measurements are only available in the night. The GOMOS 10pm climatology is in the middle range of the other measurements in the US, where they compare very well with OSIRIS and also in the MS, where they are very close to MIPAS, OSIRIS and SCIAMACHY. In the LS, however, GOMOS observes more NO_2 than all other datasets resulting in large mean deviations from the MIM of up to +40%. Additionally, large deviations of GOMOS from the MIM in the mid-latitudes below 100 hPa cause a large inter-instrument spread whenever GOMOS measurements are present and therefore large variations of the differences of the other instruments from the MIM over the mid-latitude LS. GOMOS interannual anomalies in the mid-latitudes are characterised by strong month-to-month fluctuations.
- Scaled **HIRDLS** data agree well with the other datasets in the mid-latitude MS. Here, mean differences are less than 5%, however, a relatively wide regional spread (over all MS mid-latitude grid points) of the differences is found, indicating individual monthly mean differences larger than ±20%. In the US, there is a notable difference between HIRDLS 10am and HIRDLS 10pm climatologies with the latter agreeing quite well (up to -10%) while the first show mean differences to the MIM of up to -30%. The reverse is true for the LS, where the HIRDLS 10pm climatologies are in the middle range while the 10am climatologies show large positive differences of up to +40%. The NO_2 seasonal cycle derived from HIRDLS data often show stronger amplitude than suggested by the other instruments; the HIRDLS interannual anomalies also generally exhibit larger month-to-month fluctuations than the other observations.
- In the US and tropical MS, scaled 10am **ACE-FTS** data show a good agreement with the other datasets with small differences from the MIM (1% in the US, 5% in the MS). Scaled 10pm ACE-FTS data, on the other hand, are low and close to HIRDLS in the tropical MS/US (-5%) and well below all other datasets in the mid-latitude US. This inconsistency between ACE-FTS 10am and 10pm climatologies is not observed in the LS and mid-latitude MS, where both climatologies are always on the low side with differences of up to -40% in the LS.

Comparing local sunrise/sunset measurements and 10am/pm climatologies

The ACE-FTS climatologies are available in unscaled form where they can be compared to local sunrise/sunset climatologies from solar occultation instruments, and in scaled form where they can be compared to the 10am/pm climatologies from limb emission and scattering instruments. In the tropical MS, ACE-FTS agrees well with the 10am/pm climatologies and with the sunrise/sunset climatologies with differences up to ±5% (except for SAGE II local sunrise data). This agreement suggests that all available measurements at different LSTs are consistent with each other in this region. In the mid-latitude MS, ACE-FTS agrees quite well with SAGE II and HALOE but is on the lower side of the 10am/pm climatologies with differences of up to -10%. One needs to keep in mind that such differences could have been introduced by scaling the ACE-FTS data. However, if one assumes no errors from the scaling, then the solar occultation instruments would observe less NO_2 than the emission and scattering instruments in the mid-latitude MS. In the US, the same approach would place SAGE II measurements in the middle range with slightly positive differences and would give negative difference for HALOE versus most other datasets. In the LS, SAGE II and HALOE would both be on the low side when compared to the other instruments *via* ACE-FTS (except for SAGE II sunset data).

4.12 Nitrogen oxides – NO_x

Nitric oxide (NO) and nitrogen dioxide (NO_2) are together known as the nitrogen family NO_x. Sources of tropospheric NO_x include fossil fuel burning, lightning, chemical processes in soils, and biomass burning (see *Sections 4.10* and *4.11*). The primary source of NO_x in the stratosphere is the oxidation of N_2O also originating from soil emissions (see *Section 4.4*), which is transported from the troposphere into the stratosphere. NO_x is an efficient catalyst for the destruction of stratospheric ozone [*Crutzen*, 1970; *Johnston*, 1971]. While chlorine- and bromine-containing halocarbons have been successfully reduced by the Montreal Protocol and its Amendments and Adjustments,

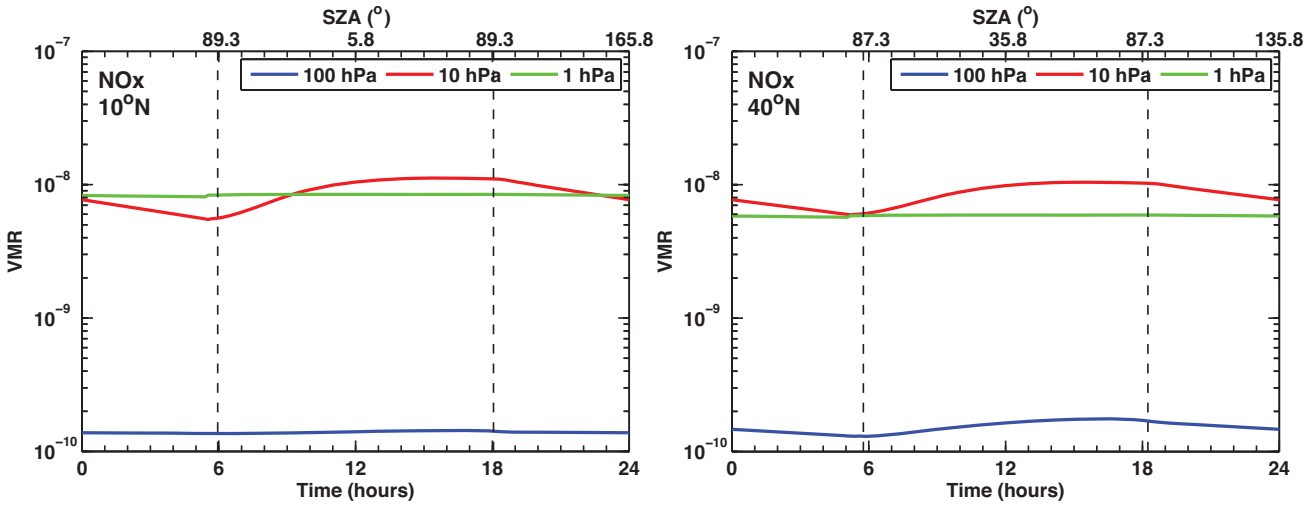

Figure 4.12.1: Diurnal NO_x cycle. *NO_x variations as function of LST are shown at 10°N and 40°N for at 1, 10 and 100 hPa for March 15.*

N_2O emissions are unregulated and are expected to become the most important ozone-depleting emission during the 21st century [*Ravishankara et al.*, 2009] on the basis of NO_x driven catalytic ozone loss. The second important source of stratospheric NO_x is the enhancement of upper atmospheric NO_x through ionizing Energetic Particle Precipitation [*Barth*, 1992; *Solomon et al.,* 1982] and the NO_x downward transport inside the polar vortex [*Funke et al.*, 2005b; *Seppälä et al.*, 2007]. This mechanism is enabled by the absence of solar radiation during the polar winter when chemically long-lived NO_x is dominated by atmospheric transport and has been suggested to impact global ozone variability [*e.g.*, *Vogel et al.*, 2008; *Reddmann et al.*, 2010].

Stratospheric NO_x, given as the sum of NO_2 and NO, displays a weak diurnal cycle in the LS and MS. **Figure 4.12.1** shows the diurnal NO_x cycle as a function of LST for three different pressure levels as derived from a chemical box model [*McLinden et al.*, 2010].

4.12.1 Availability of NO_x measurements

HALOE, ACE-FTS and MIPAS measure both NO and NO_2 and can therefore provide vertically resolved NO_x climatologies based on the sum of the two trace gases. OSIRIS and SCIAMACHY measure NO_2 but not NO. For these two instruments the NO_x climatologies are compiled based on their NO_2 measurements and on NO profiles derived from a chemical box model [*McLinden et al.*, 2010]. Both of these NO_x datasets as well as ACE-FTS data are afterwards scaled to 10am/pm in order to be comparable to MIPAS measurements. For OSIRIS, the scaling of NO_2 to NO_x at 10am/pm is done profile-by-profile with the photochemical box model initialised with measured trace gas abundances and temperature. The scaling for SCIAMACHY and ACE-FTS on the other hand is performed based on lookup tables calculated from the photochemical box model initialised with climatological inputs (see *Section 3.1.2*). In addition to the climatologies corresponding to 10am/pm, solar occultation measurements from HALOE and ACE-FTS can be compared directly if separated into local sunrise and sunset data. The two instruments overlap during 2004-2005.

Table 4.12.1 summarises all available NO_x climatologies derived from satellite measurements including time period and vertical range. Information on NO and NO_2 measurements used for deriving the NO_x climatologies, including time period, vertical range and resolution, and relevant references are given in *Sections 4.10* and *4.11*.

4.12.2 NO_x evaluations: Zonal mean cross sections

HALOE and ACE-FTS (2004-2005)

For the time period 2004-2005, the long NO_x time series from HALOE overlaps with the more recent time series from ACE-FTS. **Figure 4.12.2** shows the HALOE, and

Table 4.12.1: Available NO_x datasets based on measurements from limb-sounding satellite instruments between 1978 and 2010. *The red filling of the grid boxes indicates the temporal and vertical coverage of the respective instrument.*

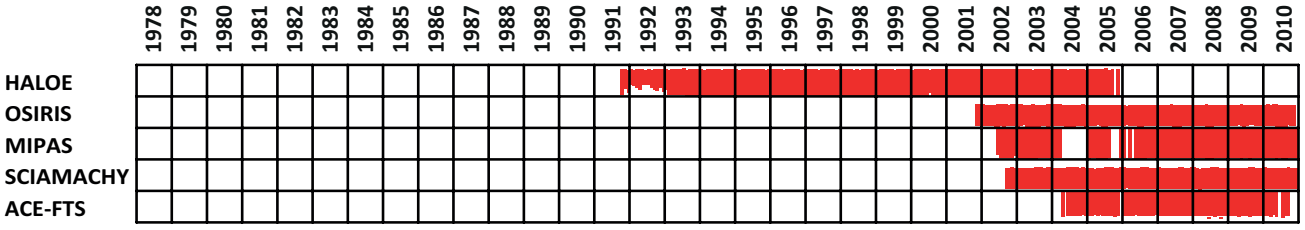

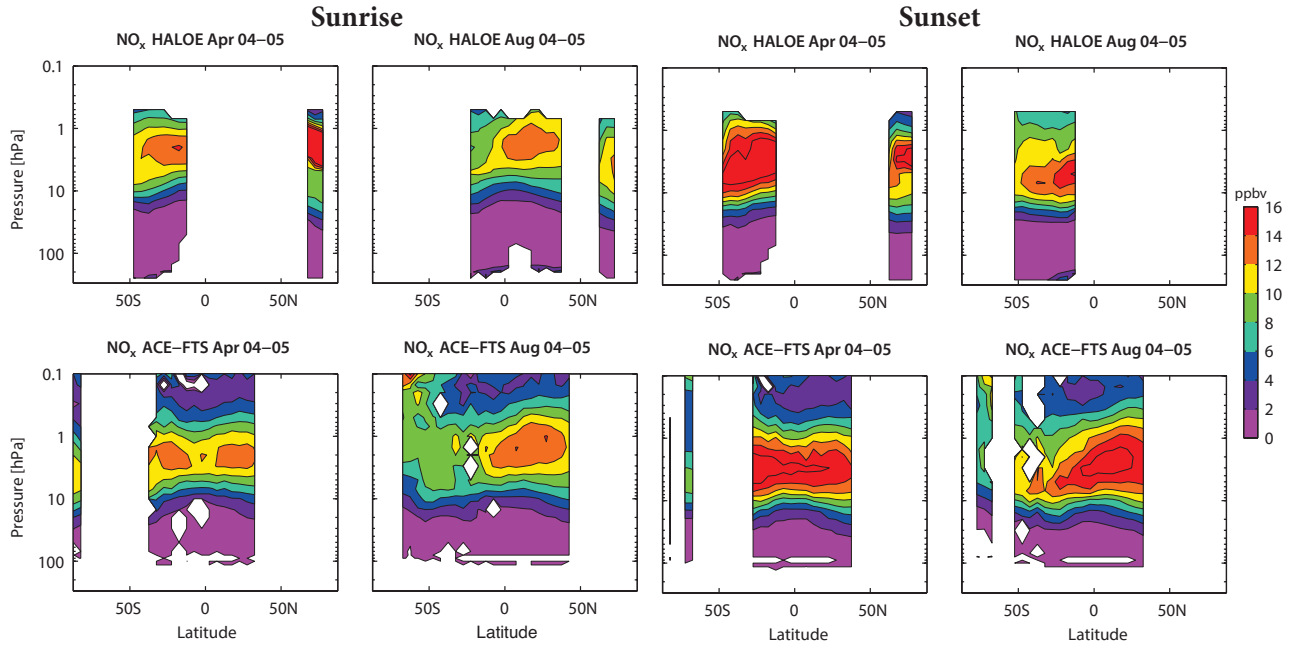

Figure 4.12.2: Cross sections of monthly zonal mean, local sunrise and sunset NO_x for 2004-2005. *Monthly zonal mean, local sunrise (column 1 and 2) and sunset (column 3 and 4) NO_x cross sections for April and August are shown for HALOE (upper row) and ACE-FTS (lower row).*

ACE-FTS local sunrise and sunset NO_x climatologies for April and August, while **Figure 4.12.3** shows the differences of both instruments from their MIM. Note that we use the comparison of both datasets to their MIM (and not a direct comparison) in order to stay consistent with other parts of the report. Departures from the mean in the MS and US are small and mostly below ±10%. HALOE shows larger values than ACE-FTS in the MS (and also in the US for April) and lower values otherwise. In the tropical LS, the relative differences increase to up to ±50%. Evaluations for the rest of the year agree in general with the April and August differences. However, the vertical extent of the region where HALOE shows larger NO_x values compared to ACE-FTS can differ with season and latitude and can sometimes extend through the whole MS and US. Note that there is less overlap between the two instruments for the other months of the year. While some month-to-month variations of the differences exist, the deviations between the local sunrise measurements are consistent with the comparison of the local sunset measurements over the same month and latitude.

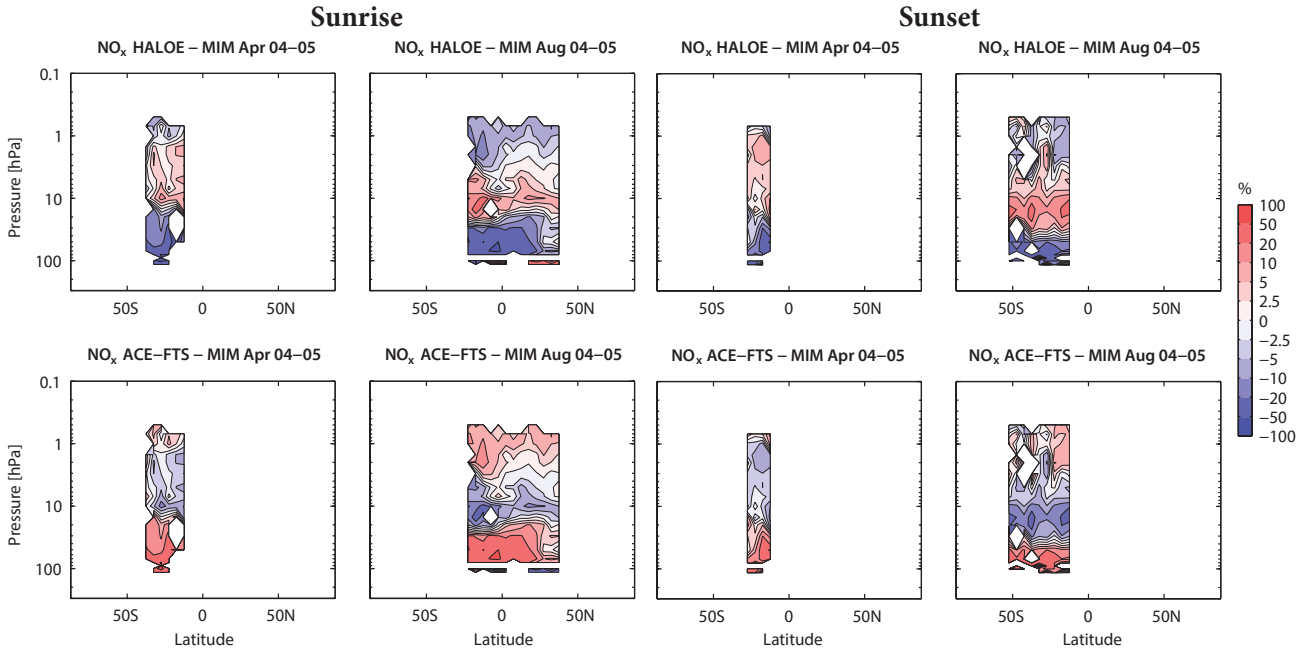

Figure 4.12.3: Cross sections of monthly zonal mean, local sunrise and sunset NO_x differences for 2004-2005. *Monthly zonal mean, local sunrise (column 1 and 2) and sunset (column 3 and 4) NO_x differences for April and August between the individual instruments (HALOE and ACE-FTS) and their MIM are shown.*

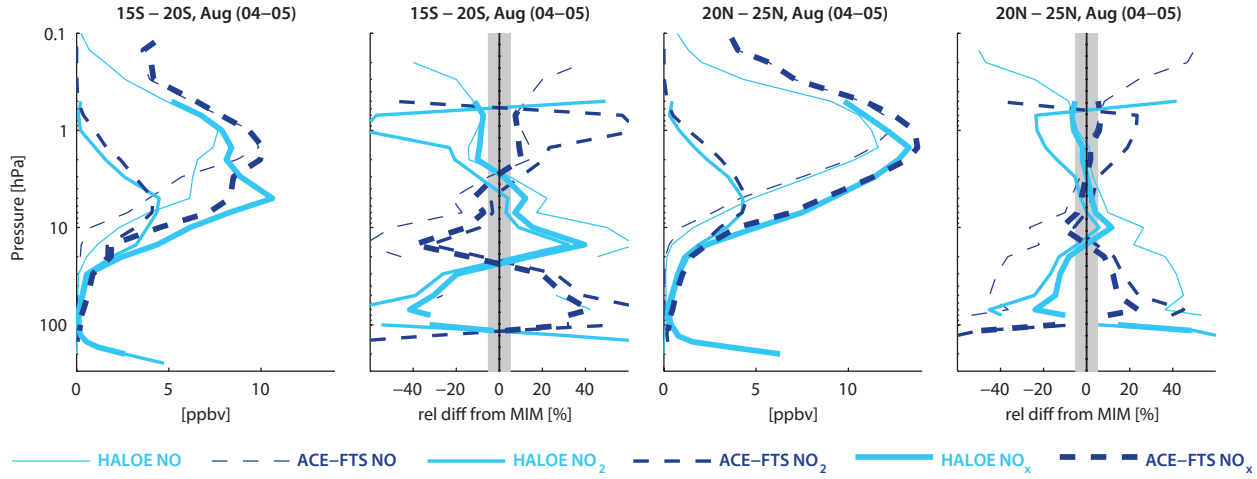

Figure 4.12.4: Profiles of monthly zonal mean, local sunrise NO, NO_2, and NO_x for 2004-2005. *Zonal mean NO, NO_2, and NO_x profiles for 15°S-20°S and 20°N-25°N for August are shown together with their differences from the MIM.*

For both local sunrise and sunset measurements, the evaluation of NO_2 from HALOE and ACE-FTS shows in general the same features as the evaluation of NO_x from the two instruments, as illustrated in **Figure 4.12.4** for individual profile comparisons. For NO_2, HALOE is larger than ACE-FTS only between 20 and 3 hPa but lower otherwise, in agreement with the results from the NO_x deviations. In addition to the NO_2 and NO_x profiles, the corresponding NO data are shown in **Figure 4.12.4**. NO differences are consistent with NO_x in the US and MS, but not in the LS where HALOE measures more NO, but less NO_2 and NO_x.

OSIRIS, SCIAMACHY, MIPAS, and ACE-FTS (2005-2010)

Figure 4.12.5 shows the NO_x 10am and 10pm climatologies for August 2005-2010. The datasets correspond to either 10am or 10pm LST, with scaled ACE-FTS, OSIRIS and SCIAMACHY (labelled as s10am and s10pm in the figure titles), and can be directly compared to each other. The four datasets corresponding to 10am or 10pm LST, respectively, show a similar NO_x distribution. However, some differences exist (*e.g.*, different meridional gradients around 10 hPa for SCIAMACHY). MIPAS 10am and 10pm measurements during the polar night above 10 hPa reveal very large NO_x values related to the polar winter descent of NO_x produced by energetic particle precipitation in the upper atmosphere.

Differences of the individual datasets from their respective MIM for August 2005-2010 are displayed in **Figure 4.12.6**. In general, the differences for the 10am climatologies in the MS are below ±10%, and reach values of ±10 to ±20% only in some regions, similar to the comparison of the solar occultation instruments. MIPAS is in the middle of the measurement range, with deviations in the MS of only up to ±5%. ACE-FTS and OSIRIS display opposite structures in their deviations from the MIM, with strong negative (positive) deviations in the SH extra-tropics. The structure of the differences is similar to that found for the comparison of the NO_2 climatologies (see **Figure A4.12.1** in *Appendix A4*). However, the NO_x climatologies, in particular the ones from MIPAS, agree better than the NO_2 climatologies and show smaller differences from their respective MIM.

NO_x 10pm climatologies show deviations of around ±10 to ±20% in the MS. Overall, the deviations are consistent with the ones derived for the 10am climatologies. While the results for SCIAMACHY and OSIRIS are very similar, some inconsistencies can be observed for MIPAS, for which negative deviations of -20(50)% are found in the MS(LS) that do not exist for the 10am climatologies. Since most of the 10pm NO_x is present as NO_2, the differences of the NO_x climatologies resemble the differences of the NO_2 climatologies (see **Figure A4.12.1** in *Appendix A4*). Not only do they display the same structure but they are also of similar or slightly larger magnitude, in contrast to the 10am climatologies where the relative differences for NO_x are smaller than those for NO_2. A comparison of climatologies for other months reveals similar differences (see **Figures A4.12.2** and **A4.12.3** in *Appendix A4*). The yearly mean climatologies and their relative differences with respect to the MIM (see **Figures A4.12.4** and **A4.12.5** in *Appendix A4*) show a similar structure but overall larger differences.

For both 10am and 10pm climatologies, the departure of unscaled datasets (*e.g.*, unscaled OSIRIS data corresponding to a variety of LSTs) from the MIM is quite different to that of the scaled data. This indicates that, although the diurnal cycle is weaker for NO_x than for NO or NO_2, the NO_x climatologies corresponding to the different LSTs cannot easily be compared unless the dependence on the LST is taken into account. A comparison of the two local sunrise/sunset datasets from HALOE and ACE-FTS to the four datasets corresponding to 10am/pm LST will be complicated by the diurnal cycle, and deviations cannot be attributed to actual measurement differences. Therefore, such a comparison is not provided here.

4.12.3 NO_x evaluations: Seasonal cycles

NO_x exhibits a strong seasonal cycle due to the effects of sunlight on the partitioning of the nitrogen family.

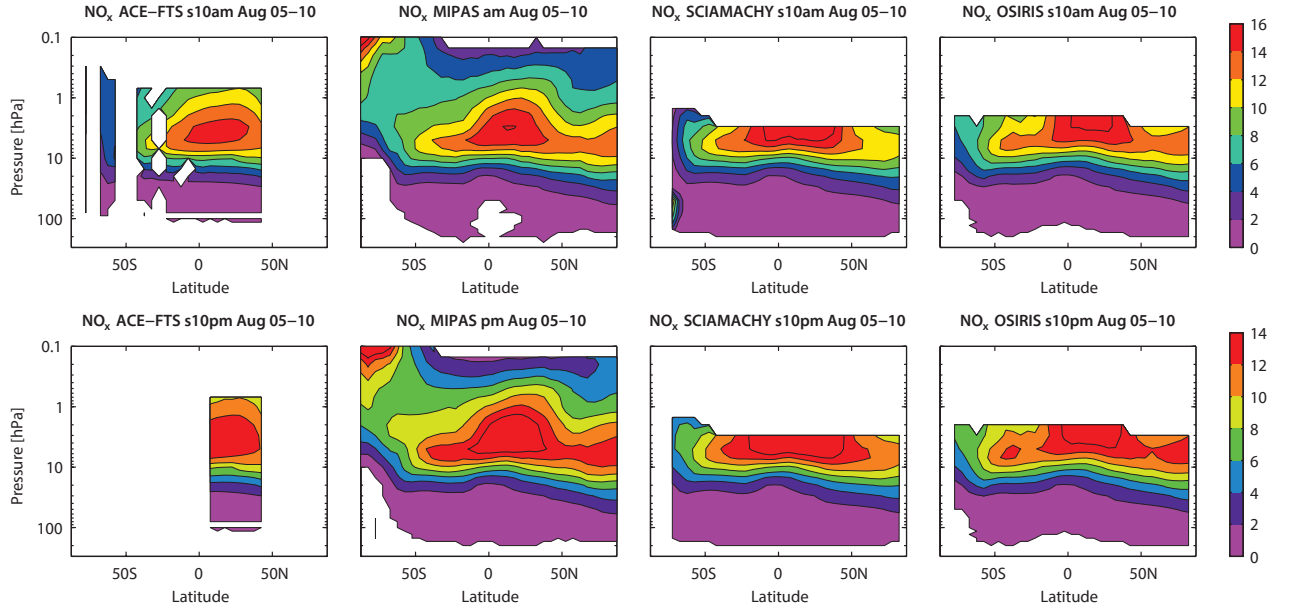

Figure 4.12.5: Cross sections of monthly zonal mean NO_x for August 2005-2010. *Monthly zonal mean NO_x cross sections of 10am (upper panels) and 10pm (lower panels) climatologies for August 2005-2010 are shown.*

Figure 4.12.7 displays the seasonal cycle of the 10am (upper panels) and 10pm (lower panels) NO_x climatologies for NH and SH mid-latitudes and tropics.

In the SH mid-latitudes, all four datasets agree very well on the seasonal cycle, with maximum values in summer and minimum values in winter. The best agreement is found for MIPAS and SCIAMACHY, which both show the same amplitude and phase, in particular for the 10am climatologies. For OSIRIS, the phase is shifted by one month (with a minimum in May) due to missing data coverage in June and July, as well as slightly elevated values in August compared to the other two datasets. The phase shift is more pronounced for the OSIRIS 10pm climatologies. ACE-FTS mean values are lower and show a larger spread around the fitted seasonal cycle, but still display very similar amplitude and phase. Note that for the ACE-FTS 10pm climatology there are no data during the SH autumn and winter, and only the September value constrains the seasonal cycle. The resulting amplitude agrees very well with that based on 10pm SCIAMACHY data, with both datasets producing an amplitude that is approximately 10% larger than that detected by MIPAS and OSIRIS.

In the NH mid-latitudes, the 10am MIPAS, OSIRIS and SCIAMACHY climatologies show the same annual cycle, with only slight differences in the amplitude of the seasonal signal. While OSIRIS has the smallest and SCIAMACHY the largest amplitude, MIPAS is in the middle range between the two instruments. ACE-FTS at 10am agrees on the

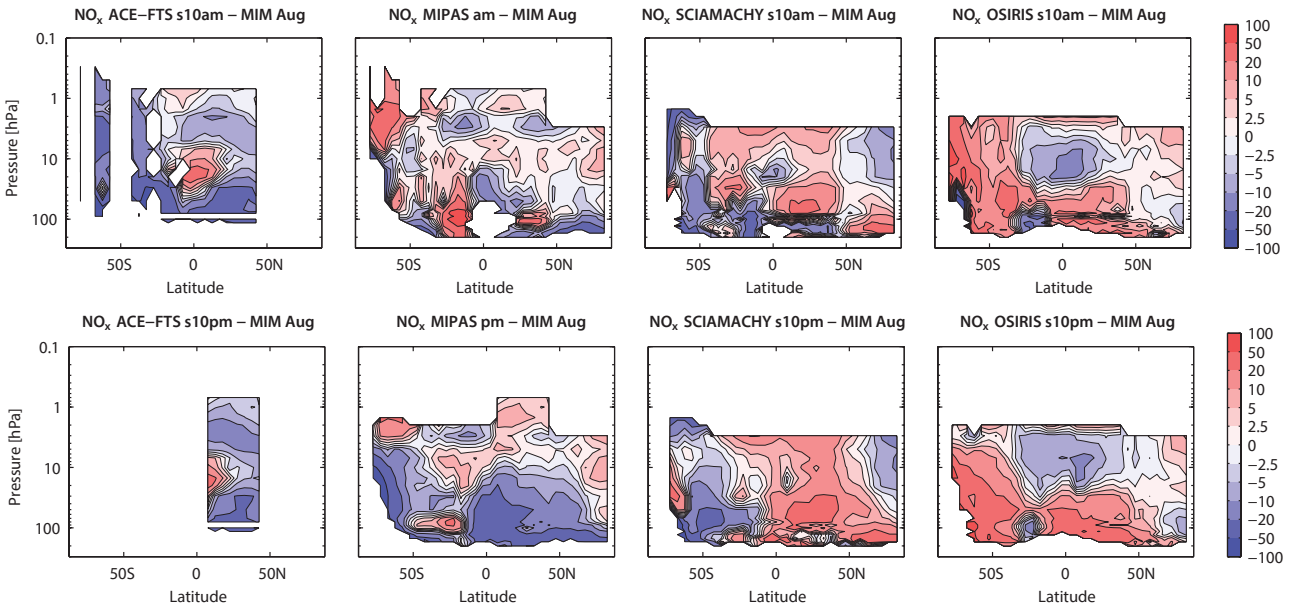

Figure 4.12.6: Cross sections of monthly zonal mean NO_x differences for August 2005-2010. *Monthly zonal mean NO_x differences from the MIM of 10am (upper panels) and 10pm (lower panels) climatologies for August 2005-2010 are shown. The MIM is based on all displayed climatologies corresponding to the respective LST.*

general structure of the seasonal signal but shows a larger amplitude due to low values in January and November. The 10pm datasets all show a very similar phase, including ACE-FTS. Here, the largest deviations to the evaluation of the 10am climatologies are the pronounced differences in the amplitude of the seasonal cycle. SCIAMACHY observes an amplitude four times larger than ACE-FTS, while MIPAS and OSIRIS agree very well in the middle range.

In the SH tropics, all four instruments detect a seasonal cycle with maximum values in the SH summer/early autumn, however they disagree on the details of the cycle. SCIAMACHY has larger mean values than the other datasets for most of the year (particularly pronounced for the 10pm climatologies) but a seasonal cycle very similar to the one detected by MIPAS. OSIRIS shows a slightly smaller amplitude than SCIAMACHY and MIPAS and a flattened maximum extending over 5 months. The largest deviations of the 10am seasonal cycle are found for ACE-FTS, which does not show the expected minimum in August but detects lowest NO_x in November. ACE-FTS at 10pm does not provide sufficient data to fit a seasonal cycle.

For SCIAMACHY, large deviations are found in the US at high latitudes (**Figure A4.12.6** in *Appendix A4*), where it does not produce the minimum in winter as observed by the other datasets. Note that this deficiency is not related to the choice of a wide latitude band (60°-90°) as similar results are obtained by analysing narrower latitude bands (60°-65°).

4.12.4 NO_x evaluations: Interannual variability

In addition to the absolute differences between the climatologies, it is of importance to evaluate how well the instruments detect signals of interannual variability. **Figure 4.12.8** shows the time series of 10am and local sunrise NO_x mean values (upper panels) and deseasonalised anomalies (lower panels) from 2003 to 2010. Datasets corresponding to 10am LST (MIPAS, scaled OSIRIS, scaled SCIAMACHY) and the two local sunrise datasets (ACE-FTS and HALOE) are compared in the tropics (20°S-20°N) at 10 hPa and NH mid-latitudes (40°N-50°N) at 7 hPa. The anomalies of the climatologies are calculated in a multiplicative sense as

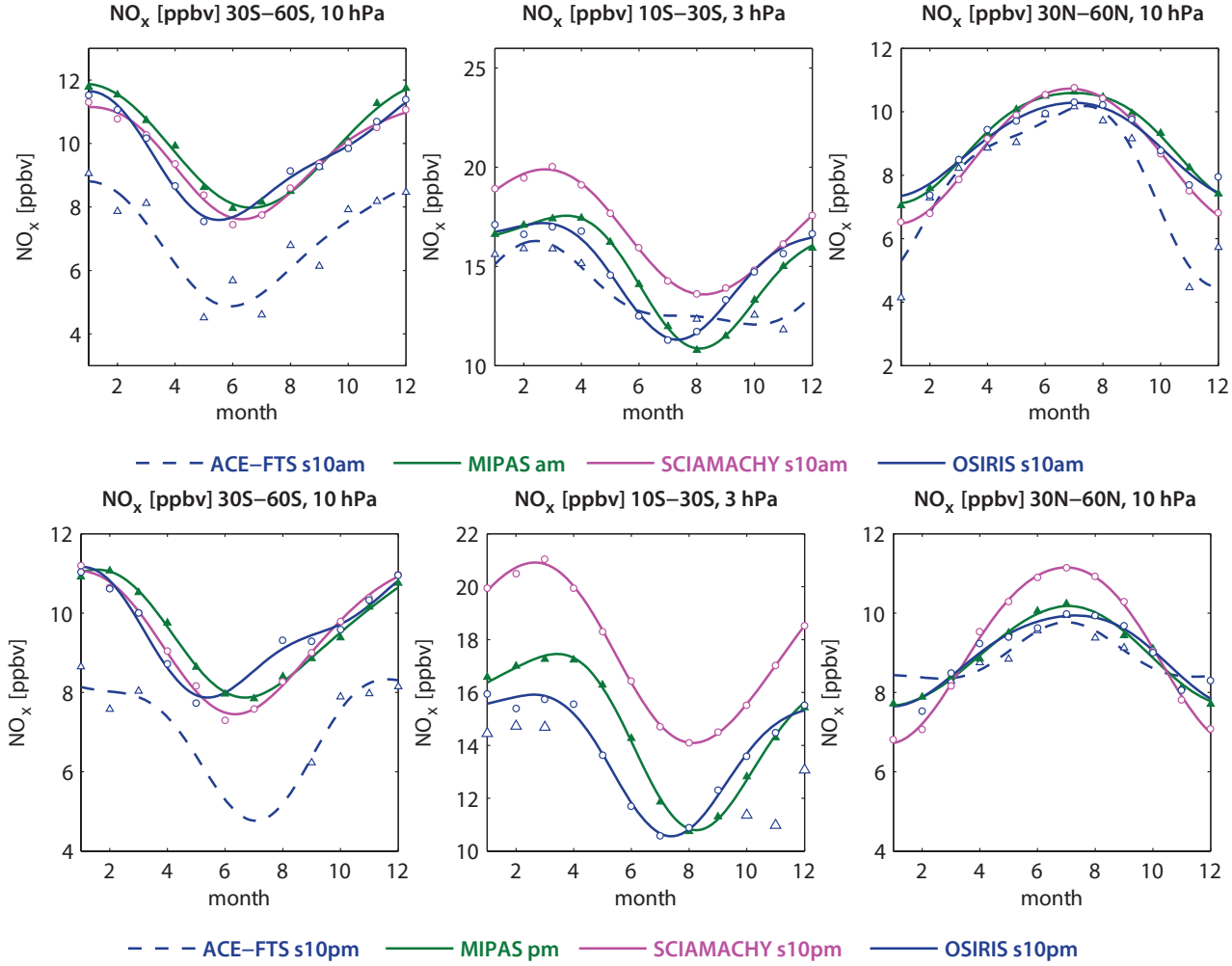

Figure 4.12.7: Seasonal cycle of 10am and 10pm NO_x for 2005-2010. *Seasonal cycle of monthly zonal mean NO_x for 30°S-60°S at 10 hPa (left column), 10°S-30°S at 3 hPa (middle column) and 30°N-60°N at 10 hPa (right column) for 10am (upper row) and 10pm (lower row) climatologies. Measurements correspond directly to 10am/pm LST (filled symbols) or are scaled to 10pm/am LST (open symbols). ACE-FTS scaled to 10pm in the SH tropics does not provide sufficient data coverage to estimate a fit of the seasonal cycle.*

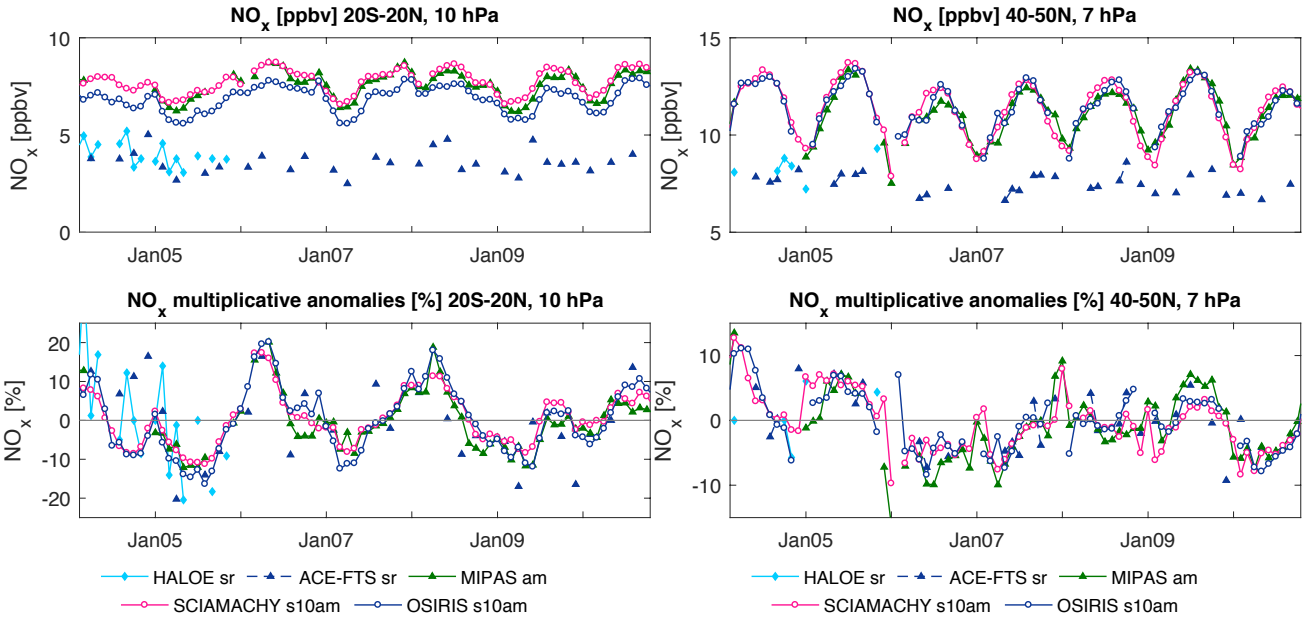

Figure 4.12.8: Time series of 10am and local sunrise NO_x mean values and anomalies for 2003-2010. *Monthly mean values (upper panels) and deseasonalized anomalies (lower panels) of NO_x at 10 hPa for 20°S – 20°N and at 7 hPa for 40°N-50°N. Measurements correspond to local sunrise conditions (ACE-FTS sr, HALOE sr), to 10am LST (MIPAS am) or are scaled to 10am LST (SCIAMACHY s10am, OSIRIS s10am).*

percent deviations from the monthly multi-year mean values, a quantity that is less affected by the diurnal variations than anomalies calculated in an additive sense.

In the tropics, NO_x is dominated by an approximately two year long cycle which is linked to the QBO (see *Section 4.11*). MIPAS, OSIRIS, and SCIAMACHY anomalies in the tropics agree very well and display the expected QBO cycle. Unscaled ACE-FTS and HALOE data show a QBO signal similar to the other datasets but also exhibit stronger month-to-month variability. The interannual variability of the scaled ACE-FTS data (not shown here) do not agree as well with the other datasets compared to the unscaled ACE-FTS data, similar to the results for NO_2.

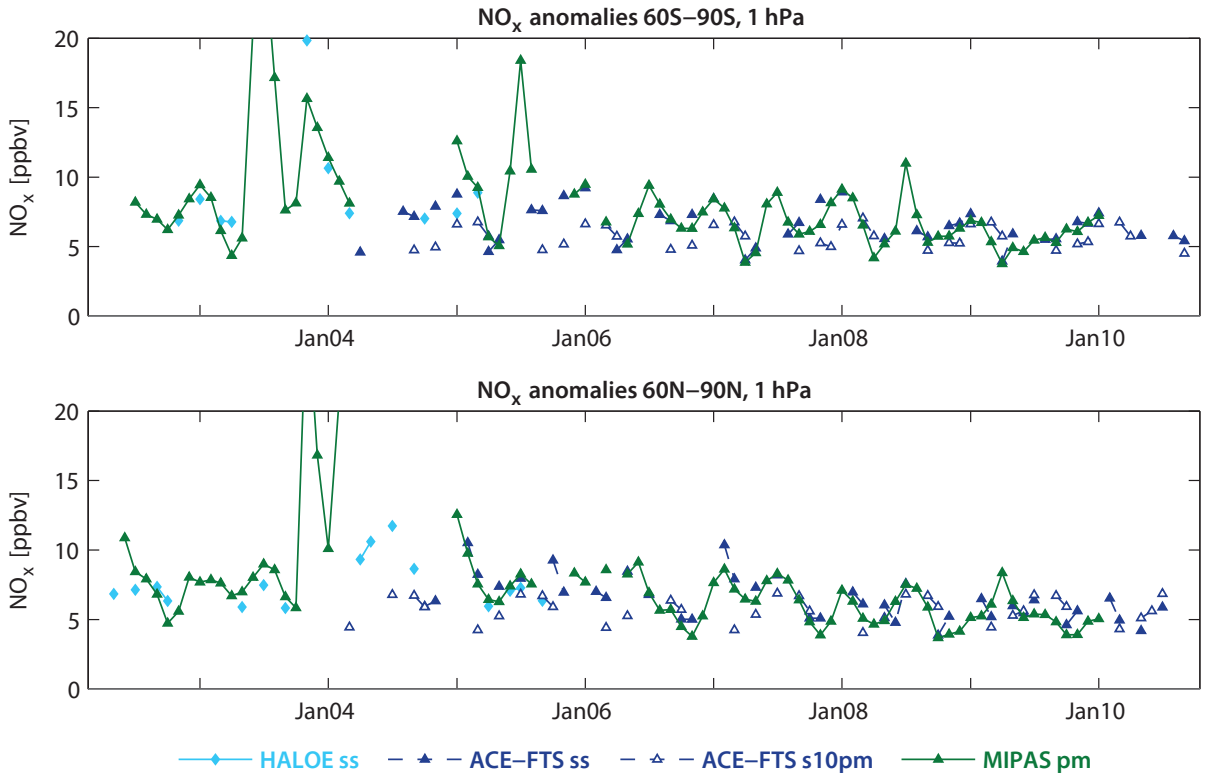

Figure 4.12.9: Time series of polar NO_x for 2003-2010. *Time series of polar 10pm and local sunset NO_x for 60°S-90°S (upper panel) and 60°N-90°N (lower panel) at 1 hPa from 2003 to 2010 are shown.*

In the mid-latitudes, the dataset anomalies show similar signals related to interannual variability, although the agreement is not as good compared to the tropics, consistent with results from the evaluations of the NO_2 interannual variability. Again, the scaled ACE-FTS data (not shown here) mostly fail to reproduce the interannual signal observed by the other instruments.

Most features observed for deseasonalised 10am and local sunrise NO_x also hold for the 10pm and local sunset NO_x time series (see **Figure A4.12.7** in *Appendix A4*). The tropical anomalies show a very similar QBO signal that agrees quite well between all instruments. Overall, the three 10pm datasets agree better with each other than with ACE-FTS and HALOE. In the SH mid-latitudes, SCIAMACHY shows smaller anomalies than the other datasets for some years (*e.g.*, 2007).

4.12.5 NO_x evaluations: Downward transport of NO_x during polar winter

In the polar mesosphere, NO_x is produced by EPP [*Barth*, 1992; *Solomon et al.*, 1982]. Observations have shown that NO_x in the polar mesosphere is transported downwards into the stratosphere inside the polar vortex [*Funke et al.*, 2005b; *Seppälä et al.*, 2007] causing elevated NO_x levels during polar winter. How well the limb-viewing satellite datasets agree on this phenomenon is evaluated in **Figure 4.12.9**, which shows NO_x time series in the USLM (1 hPa) for local sunrise and 10pm climatologies at high NH and SH latitudes.

MIPAS shows very high NO_x abundances for the SH winters 2003 and 2005, and for the NH winters 2003/2004 and 2004/2005. For most of these pronounced events HALOE and ACE-FTS do not provide the monthly zonal means, so that a direct comparison is not possible. The only exception is the NH winter 2004/2005, for which sunset ACE-FTS in February confirms high NO_x values exceeding 10 ppbv as observed by MIPAS. For the rest of the observation time period the polar NO_x time series shows a semi-annual oscillation with a maximum in summer due to a build up from reservoirs and (for most years) a maximum in winter due to EPP events. For the NH winters 2006/2007 and 2007/2008, MIPAS and sunset ACE-FTS datasets both confirm elevated NO_x values, while for the remaining winters a direct comparison is more complicated due to missing data coverage for ACE-FTS. Note that scaled ACE-FTS NO_x data show no clear signals of EPP events opposite to scaled ACE-FTS NO_2 data (*Section 4.11*).

4.12.6 Summary and conclusions: NO_x

A comprehensive comparison of NO_x profile climatologies from five satellite instruments (HALOE, OSIRIS, MIPAS, SCIAMACHY, and ACE-FTS) has been carried out. Overall findings on the systematic uncertainty in our knowledge of the NO_x mean state and important characteristics of the individual datasets are presented in the following summary, including three synopsis plots. The first summary plot (**Figure 4.12.10**) provides information on the NO_x mean state at 10am and 10pm. Additionally, the uncertainty

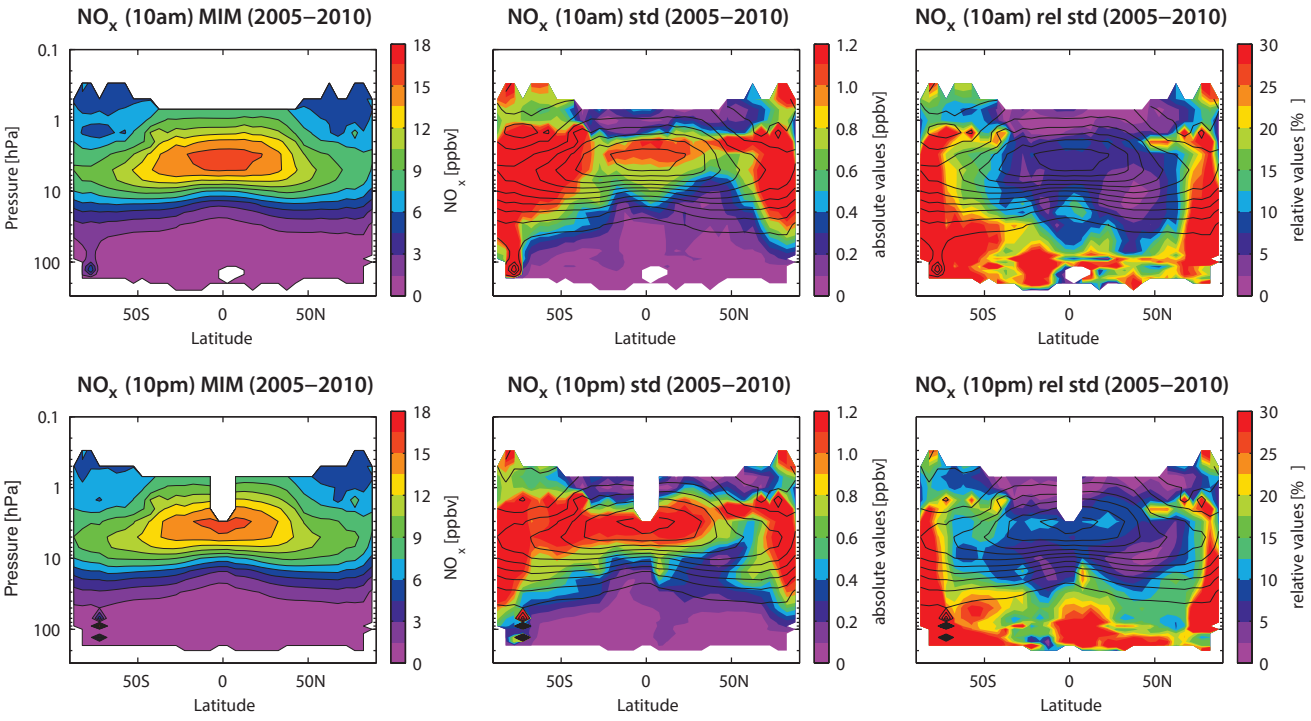

Figure 4.12.10: Summary of NO_x annual zonal mean state for 2005-2010. *Annual zonal mean cross sections of the NO_x MIM are shown in the left panels for10am (upper row) and 10pm (lower row) illumination conditions. The NO_x mean state at 10am (pm) is based on MIPAS at 10am (pm), ACE-FTS scaled to 10am (pm) and OSIRIS and SCIAMACHY derived from NO_2 with a chemical box model and scaled to 10am (pm). For both illumination conditions, the standard deviation over all respective instruments is presented in the middle panel, and the relative standard deviation in the right panel. Black contour lines give the MIM distribution. The MIM and standard deviation are only displayed for regions where at least two instruments provide measurements.*

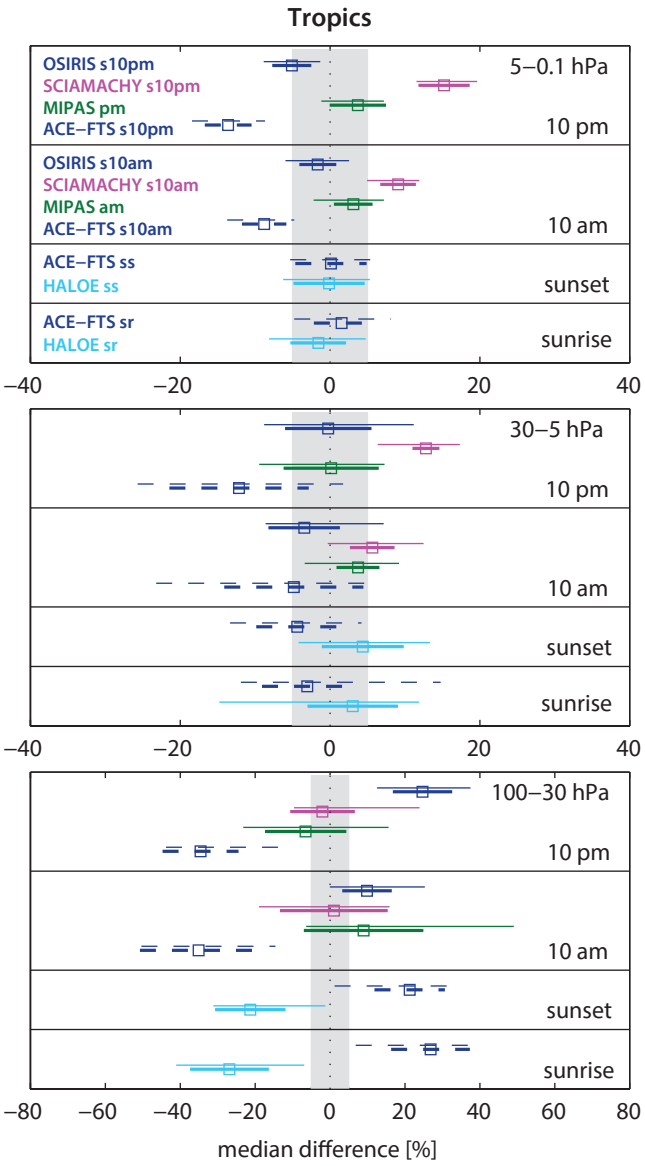

Figure 4.12.11: Summary NO_x differences in the tropics for 2004-2005. *Over a given latitude and altitude region the median (squares), median absolute deviation (MAD, thick lines), and the standard deviation (thin lines) of the monthly mean relative differences between an individual instrument-climatology and the MIM are calculated. Results are shown for the tropics (30°S-30°N) for three different altitude regions from the UT up to the LM between 100 and 0.1 hPa for the reference period 2004-2005.*

derived from the spread between the datasets is given for both illumination conditions. The second summary plot (**Figures 4.12.11** and **4.12.12**) shows specific inter-instrument differences in form of deviations of the instrument climatologies from the MIM climatology. For each region four separate evaluations for the four different illumination conditions (10am, 10pm, ss, sr) are included. For each LST, instrument and selected region, the deviation from the MIM is given in form of the median (mean) difference over all grid points in this region. Additionally, for each instrument the spread of the differences over all grid points in this region is presented. Note that both pieces of information (average deviation and spread) are important for a meaningful assessment of inter-instrument differences. A detailed description of the summary plot evaluations can be found in *Section 3.3.5*.

Atmospheric mean state

The assessment of the atmospheric NO_x annual mean state is based on four climatologies corresponding to 10am and 10pm, respectively. Note that three out of four climatologies have been derived by scaling the individual measurements with a chemical box model to 10am/pm LST.

Middle and upper stratosphere (30-1 hPa)

The uncertainty in our knowledge of the atmospheric NO_x annual mean state is smallest in the tropical and NH mid-latitude MS/US (**Figure 4.12.10**, right panel), with a 1σ multi-instrument spread in this region of up to ±10%. In particular, in the NH mid-latitude MS, the instruments agree very well (1σ of ±5%). In the SH subtropics, the inter-instrument spread is comparable to the tropics (up to ±10%), but deviations increase in the SH mid-latitudes, in particular for the 10am climatologies (up to ±20%).

Lower stratosphere (100-30 hPa)

In the LS, the NO_x abundances decrease quickly with decreasing altitude and large deviations of up to ±30% are found in the SH mid-latitudes and for the 10pm climatologies also in the tropics. The instruments show a better agreement in the NH mid-latitudes and SH subtropics with a spread of up to ±20%.

High latitudes

At high latitudes, the instruments show larger deviations than at lower latitudes. In the MS, the best agreement is found for the 10pm climatologies in the NH where a spread larger than ±20% is found only north of 80°N. In the USLM, the high latitude annual mean NO_x abundance is dominated by the polar night NO_x descent, causing an increase of the inter-instrument spread for levels above 1 hPa.

Instrument-specific conclusions

Local sunrise/sunset climatologies from solar occultation instruments

HALOE and **ACE-FTS** show an excellent agreement in the US with mean differences below ±2.5% for their local sunset and sunrise climatologies (**Figures 4.12.11** and **4.12.12**). In the MS, HALOE detects slightly larger NO_x abundances than ACE-FTS resulting in differences with respect to their MIM of ±5%. The only exception to this is the comparison of the local sunset climatologies in the mid-latitude MS where both instruments show differences of up to ±10%. In the LS, the relative differences increase steadily, reaching mean values of up to ±30% with HALOE on the

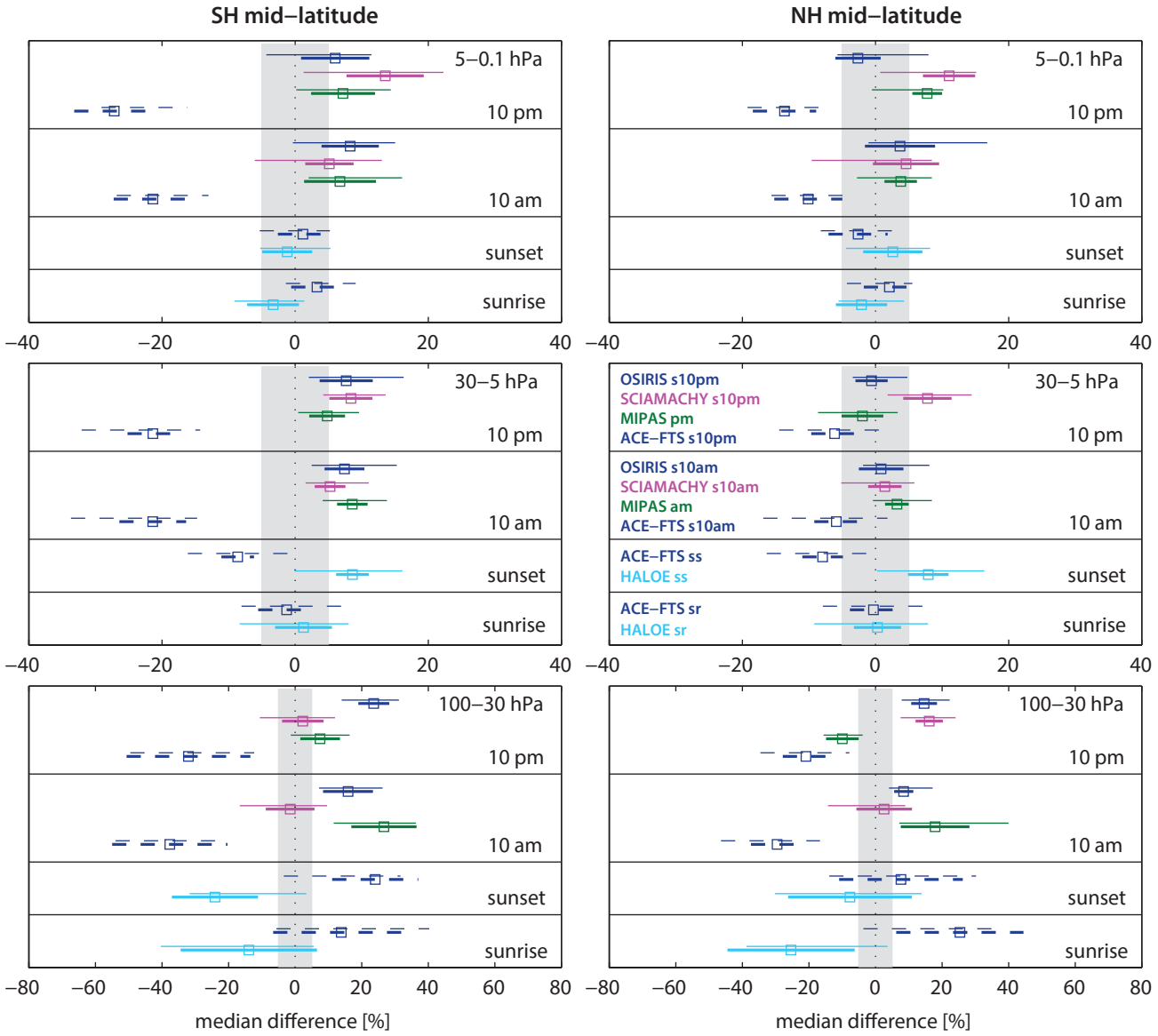

Figure 4.12.12: Summary NO_x differences in the mid-latitudes for 2004-2005. *Over a given latitude and altitude region the median (squares), median absolute deviation (MAD, thick lines), and the standard deviation (thin lines) of the monthly mean relative differences between an individual instrument-climatology and the MIM are calculated. Results are shown for the NH mid-latitudes (30°N-60°N) and for the SH mid-latitudes (30°S-60°S) for three different altitude regions from the UT up to the LM between 100 and 0.1 hPa for the reference period 2004-2005.*

low side and ACE-FTS on the high side. In particular in the mid-latitude LS, both datasets show a large regional spread (over all grid points in this region) indicating that the deviations are not well defined. Overall, the NO_x local sunrise and sunset evaluations give a consistent picture, with the exception of the mid-latitude MS. Despite their lower data coverage when compared to other limb sounders, both solar occultation instruments display important signals of interannual variability like the tropical QBO cycle. At the same time they show stronger month-to-month fluctuations probably related to sampling impacts.

10am/pm climatologies

The limb emission and scattering instruments MIPAS, OSIRIS, and SCIAMACHY, are evaluated based on their 10am/pm climatologies, with the latter two derived from scaling with a chemical box model. Additionally, 10am/pm climatologies from the scaled local sunrise/sunset measurements of the solar occultation instrument ACE-FTS are included in the evaluation. All climatologies show a good agreement in the tropical and NH mid-latitude MS with mean differences of ±5% to ±10%. In particular, the 10am climatologies from MIPAS, OSIRIS, and SCIAMACHY agree very well in the mid-latitude MS and US with differences of less than ±5%. Monthly zonal mean cross sections (**Figure 4.12.6**) reveal that for most climatologies the deviations from the MIM can change sign depending on the latitude band and month. All 10am/pm climatologies show the tropical QBO signal with the best agreement found between MIPAS, OSIRIS, and SCIAMACHY.

MIPAS measurements correspond directly to 10am/pm and have not been scaled for the evaluations presented in

this chapter. The MIPAS climatology, when compared to other datasets, is mostly in the middle range with relatively small deviations with respect to the MIM of up to ±10%. Only the 10am climatologies in the LS show negative deviations of up -20% in agreement with a similar finding for the MIPAS NO_2 climatologies.

The 10am **SCIAMACHY** climatology agrees very well with the MIM with differences of up to ±5% in most cases. The 10pm climatology, however, shows larger values than the other datasets with deviations of up to +10% in the MS and +15% in the US. This could be caused by the larger impact of the scaling procedure on the 10pm climatology for which SCIAMACHY measurements need to be scaled to completely different illumination conditions. Note, however, that for NO_2, which shows a much more pronounced diurnal cycle, no such severe differences in the performance of the 10am/pm climatologies exist.

OSIRIS is in the middle of the range in the MS and US, but shows larger deviations in the LS where it sets the upper measurement range and displays differences of up to +30% for the 10pm climatologies. The fact that in the tropical LS, OSIRIS 10am climatology agrees within ±5% with MIPAS and SCIAMACHY, while the OSIRIS 10pm climatology is 20-30% larger than the other two datasets, is consistent with the NO_2 evaluations.

Scaled ACE-FTS in the tropical and NH mid-latitude MS agrees well with the other datasets, with deviations of ±5% to ±10% in the MS and deviations of up to ±15% in the US. However, in the SH mid-latitudes, scaled ACE-FTS data are considerably lower than the other datasets, with differences of up to -30%. This inconsistency between NH and SH mid-latitudes causes the larger inter-instrument spread in the latter region, apparent also in **Figure 4.12.10**. In the LS, scaled ACE-FTS sets the lower end of the measurement range with differences of up to -40%.

4.13 Nitric acid – HNO_3

Nitric acid (HNO_3) is a member of the total reactive nitrogen family NO_y and has a large impact on stratospheric ozone destruction in the polar regions through its role in PSC formation. HNO_3 contributes to the composition of nitric acid trihydrate (NAT), forming Type Ia PSCs [*Toon et al.*, 1986; *Hanson and Mauersberger*, 1988], and to supercooled ternary solution particles ($H_2SO_4/H_2O/HNO_3$), forming Type Ib PSCs [*Carslaw et al.*, 1994; *Lowe and MacKenzie*, 2008]. Heterogeneous reactions occurring on PSC surfaces convert halogens from relatively inert reservoir species into their reactive forms, driving halogen-catalyzed ozone loss in polar spring [*e.g.*, *Peter*, 1997; *Solomon*, 1999]. HNO_3 is irreversibly removed if the solid PSC particles grow to large sizes and sediment out of the stratosphere [*Fahey et al.*, 2001], a process that is referred to as denitrification. If PSC particles do not sediment out of the stratosphere but eventually evaporate, the photolysis of HNO_3 will cause increasing NO_2 concentrations, thus enhancing the halogen deactivation process in polar springtime.

Stratospheric HNO_3 displays a weak diurnal cycle in the US that increases in the LM. **Figure 4.13.1** shows the diurnal HNO_3 cycle as a function of LST for three different pressure levels as derived from a chemical box model [*McLinden et al.*, 2010].

4.13.1 Availability of HNO_3 measurements

The first stratospheric HNO_3 measurements were made by LIMS, covering the end of 1978 and the first half of 1979. The next vertically resolved HNO_3 satellite measurements included in the SPARC Data Initiative came from UARS-MLS, covering the years 1991 to 1999. After 2001, several HNO_3 datasets became available from limb emission and solar occultation instruments. The time period 2005-2010 is covered by SMR, MIPAS, ACE-FTS, and Aura-MLS

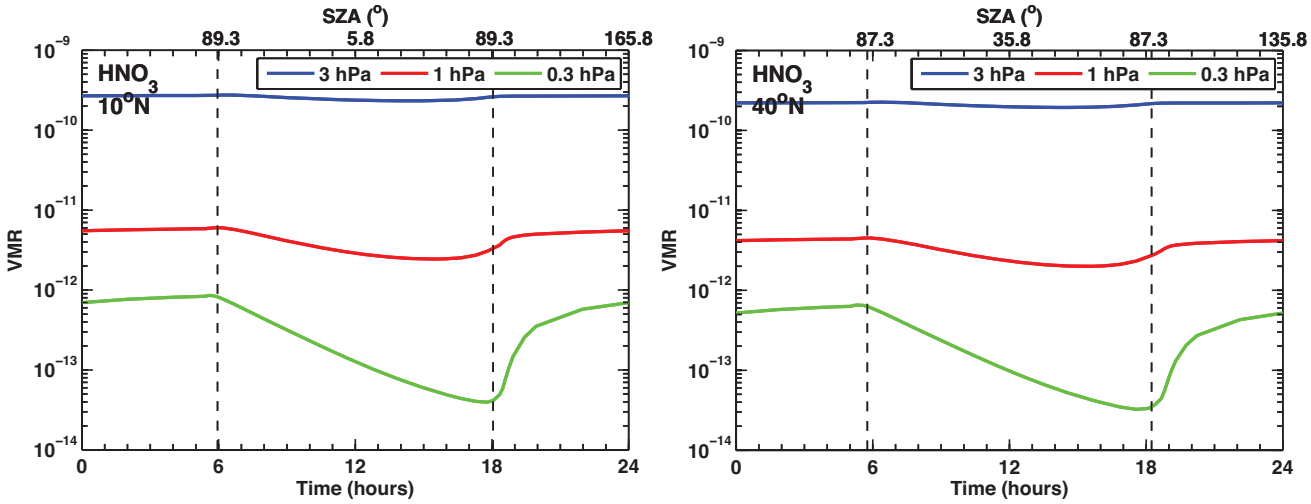

Figure 4.13.1: Diurnal HNO_3 cycle. *HNO_3 variations as function of LST are shown at 10°N and 40°N at 0.3, 1 and 3 hPa for March 15.*

allowing for an inter-instrument comparison maximising the number of instruments and number of years. HIRDLS measurements (2005-2007) are also included in the basic 2005-2010 comparison since sensitivity tests show that the results are not affected by HIRDLS covering a shorter time period. **Tables 4.13.1** and **4.13.2** compile information on the availability of HNO_3 measurements, including time period, altitude range, vertical resolution, and references relevant for the data product used in this report.

4.13.2 HNO_3 evaluations: Zonal mean cross sections and vertical profiles

SMR, MIPAS, ACE-FTS, Aura-MLS, and HIRDLS (2005-2010)

Zonal mean cross sections and vertical profiles are first compared for the overlap period 2005-2010. **Figure 4.13.2** shows all annual mean HNO_3 climatologies, which have maxima in the MS (around 20-30 hPa) at the mid- and high latitudes of both hemispheres. While the datasets agree very well on the overall distribution at low latitudes, they show large differences at polar latitudes, in particular in the SH. Here, ACE-FTS observes much higher and SMR much lower abundances than MIPAS in the annual zonal mean distribution. Examining monthly zonal mean cross sections (*e.g.*, **Figure A4.13.1** in *Appendix A4*) reveals that for ACE-FTS this feature is related to the sampling coverage of this region, which varies over the year resulting in an annual mean cross section that is not representative. In contrast, the zonal mean evaluations for SMR yield similar results to the annual mean evaluations.

Figure 4.13.3 shows the relative differences of the five instruments with respect to their MIM. For most instruments, the differences have a pronounced vertical gradient (negative and positive) and change sign between 30 and 10 hPa. At higher altitudes, *i.e.*, above the HNO_3 maximum, Aura-MLS and HIRDLS abundances are lower than the MIM, with differences that can reach up to -50%. ACE-FTS is larger, with differences of up to +50%, while MIPAS and SMR are also larger than the MIM but exhibit less extreme differences. In the LS, the situation is reversed

Table 4.13.1: Available HNO_3 measurement records from limb-sounding satellite instruments between 1978 and 2010. *The red filling of the grid boxes indicates the temporal and vertical coverage of the respective instrument.*

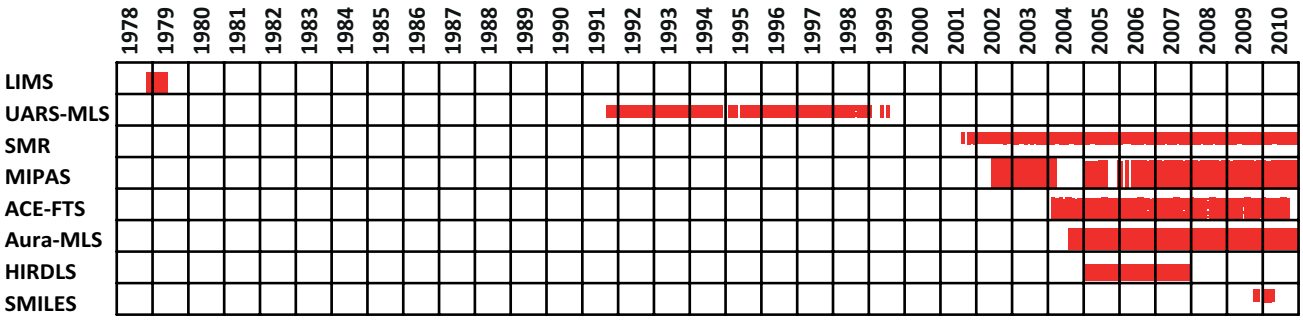

Table 4.13.2: Data version, time period, vertical range, vertical resolution, references and other comments for HNO_3 datasets participating in the SPARC Data Initiative.

Instrument and data version	Time period	Vertical range	Vertical resolution	References	Additional comments
LIMS V6.0	Nov 78 – May 79				
UARS-MLS V6	Oct 91 – Oct 99	100 – 4.6 hPa	5 – 10 km	*Livesey et al.*, 2003	Significant low bias (1-3 ppbv) exists for p<15 hPa. Some evidence for high bias below VMR peak.
SMR V2-0	Jul 01 –	18 – 45 km	1.5 – 2 km	*Urban et al.*, 2006 *Urban et al.*, 2009	Empirical scaling correction applied (see *Urban et al.*, 2009)
MIPAS **MIPAS(1)** V9 **MIPAS(2)** V220	 Mar 02 – Mar 04 Jan 05 – Apr 12	6 km (cloud top altitude) – 70 km	 4 – 6 km 3 – 5 km	*Mengistu Tsidu et al.*, 2005 *Wang et al.*, 2007 *von Clarmann et al.*, 2009a	
ACE-FTS V2.2	Mar 04 –	5 – 37 km	3 – 4 km	*Wolff et al.*, 2008	
Aura-MLS V3-3	Aug 04 –	147 – 1 hPa	3 – 5 km	*Santee et al.*, 2007 *Livesey et al.*, 2013 *Fiorucci et al.*, 2013	
HIRDLS V6.0	Jan 05 – Mar 08	215 – 7.5 hPa	1 km	*Gille and Gray*, 2011	Latitude range 63°S-80°N
SMILES V2-0-1	Oct 09 – April 10	18 – 45 km	3 – 4 km	*Kreyling et al.*, 2013	Bias due to problems in spectroscopic parameter and altitude shift (corrected for in v3-0-0).

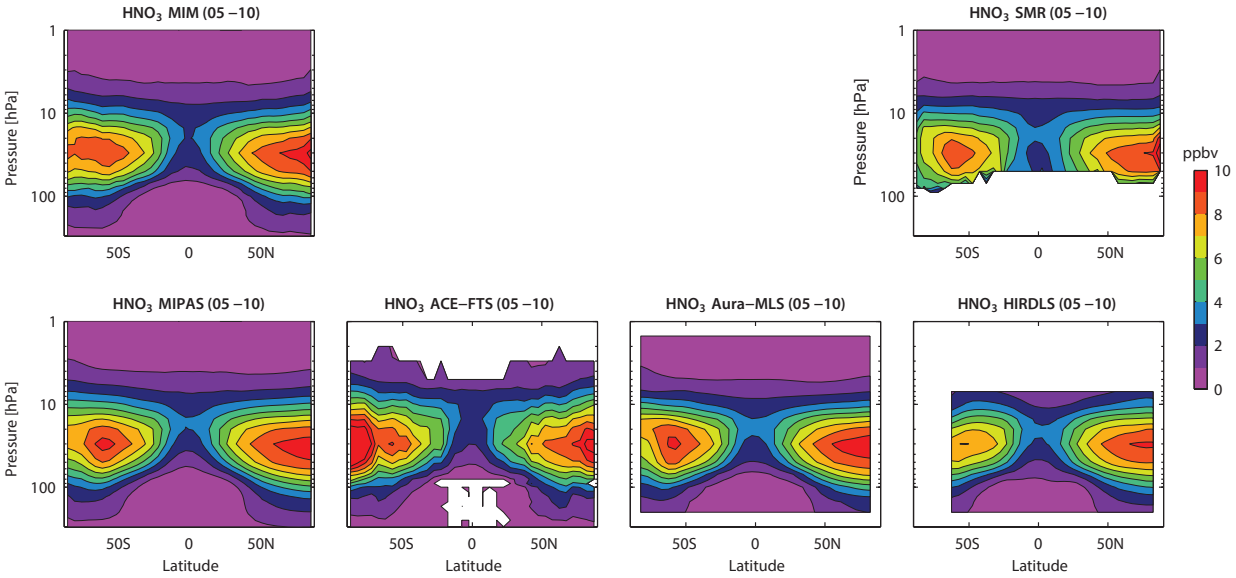

Figure 4.13.2: Cross sections of annual zonal mean HNO_3. *Annual zonal mean HNO_3 cross sections for 2005-2010 are shown for the MIM in the upper left, SMR in the upper right and MIPAS, ACE-FTS, Aura-MLS, and HIRDLS in the lower panels.*

with Aura-MLS values being high and ACE-FTS values low. Such a tendency between the Aura-MLS and ACE-FTS profiles was already noted in the Aura-MLS data quality documentation by *Livesey et al.* [2013], although the average coincident profile differences discussed there are somewhat smaller than the differences mentioned here. The smallest deviations are found for SMR, MIPAS, and HIRDLS in the mid-latitudes. At high latitudes, monthly mean cross sections need to be analysed instead of annual means, since the latter can be impacted strongly by the sampling patterns of the instruments. Overall, differences are largest in the SH polar winter, and spring at latitudes higher than 60°S (see **Figure A4.13.2** in *Appendix A4*), with MIPAS reporting more and Aura-MLS and SMR less HNO_3.

Detailed evaluations of monthly zonal mean differences for individual latitude bands are shown in **Figure 4.13.4**. At high SH latitudes (75°S-80°S) in July, all instruments clearly show the removal of HNO_3 from the gas phase. However, the signal is much stronger in Aura-MLS and SMR than in MIPAS, leading to differences of up to ±50% relative to the MIM at around 50 hPa. Very likely, this can be attributed to the higher sensitivity of infrared emission sounders like MIPAS to PSCs, leading to a more rigorous rejection of PSC-contaminated measurements and thus to higher HNO_3 mean values during the Antarctic winter conditions. In the 65°S-70°S latitude band, the HNO_3 contribution to PSC formation is smaller but MIPAS still clearly shows higher HNO_3 abundances than the other instruments (differences of up to +40%). Above 30 hPa, ACE-FTS shows better agreement with MIPAS. The Aura-MLS profile at high latitudes is characterised by small oscillations not found for any of the other instruments. In the tropics (0°N-5°N for January), the strongest disagreement is found for HIRDLS, which is larger than all other datasets in the LS and MS. The positive deviations of up to +80% (of small values) at

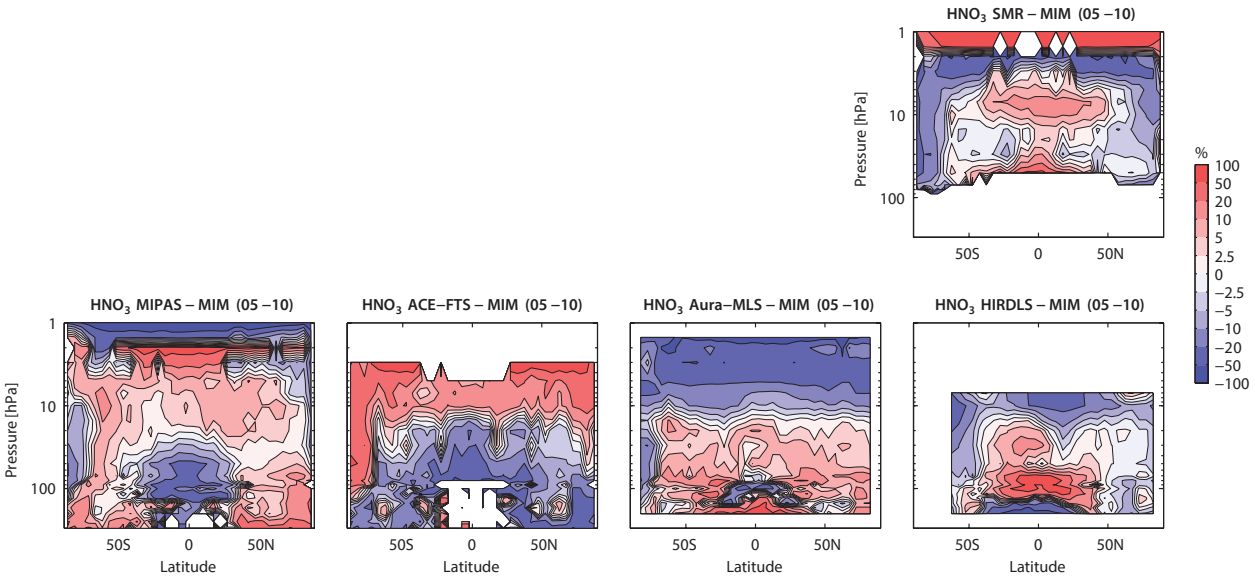

Figure 4.13.3: Cross sections of annual zonal mean HNO_3 differences. *Annual zonal mean HNO_3 differences for 2005-2010 between the individual instruments (SMR, MIPAS, ACE-FTS, Aura-MLS, and HIRDLS) and the MIM are shown.*

around 70 hPa are probably due to the lack of correction for aerosol emission in V6. The comparison of the NH mid-latitude profiles (50°N-55°N for May) confirms very good agreement in a wide altitude range from 200 to 15 hPa. Above this level, Aura-MLS falls off faster than HIRDLS and ACE-FTS, leading to differences of up to ±30% at 5 hPa. In the tropics and mid-latitudes, SMR has a positive vertical gradient between 3 and 1 hPa, where all other datasets approach zero, resulting in large deviations at these upper levels.

LIMS, UARS-MLS, and SMILES

For LIMS and UARS-MLS, no direct comparison for HNO_3 is possible, thus we include a comparison to the 2005-2010 MIM (restricted to January-April for the LIMS evaluation). The resulting differences can be caused by inter-instrument differences or by long-term changes in HNO_3, therefore clear attribution of the differences is not possible. The trend in N_2O is expected to lead to an upward trend in all nitrogen species, modulated by shifts in the total reactive nitrogen family partitioning due to changes in ozone, temperature, halogens, and possibly aerosol loading [*Fish et al.*, 2000; *McLinden et al.*, 2001].

Cross sections of LIMS (January-April 1979) show, as expected, considerably smaller HNO_3 abundances than the 2005-2010 MIM (**Figure 4.13.5**). The difference between the two (**Figure 4.13.6**) is mostly negative (up to -100% in the tropical LS), except for the mid-latitude LS and the US. At NH high latitudes, deviations are relatively small (up to ±5%), suggesting similar HNO_3 abundance in 1979 and 2005-2010 during Arctic winter and spring.

UARS-MLS detects less HNO_3 for the time period 1991-1998 compared to the annual mean 2005-2010 cross sections (**Figure 4.13.5**). Particularly evident is the reduced HNO_3 amount at high SH latitudes during the 1990s, consistent with strong PSC formation during this time period. The deviations between UARS-MLS and the 2005-2010 MIM are negative over a large range (**Figure 4.13.6**). A negative bias in UARS-MLS HNO_3 was also noted in comparsion with ATMOS and Improved Limb Atmospheric Spetrometer (ILAS) data for pressures less than 15 hPa [*Livesey et al.*, 2003]. In the mid-latitude LS and the NH

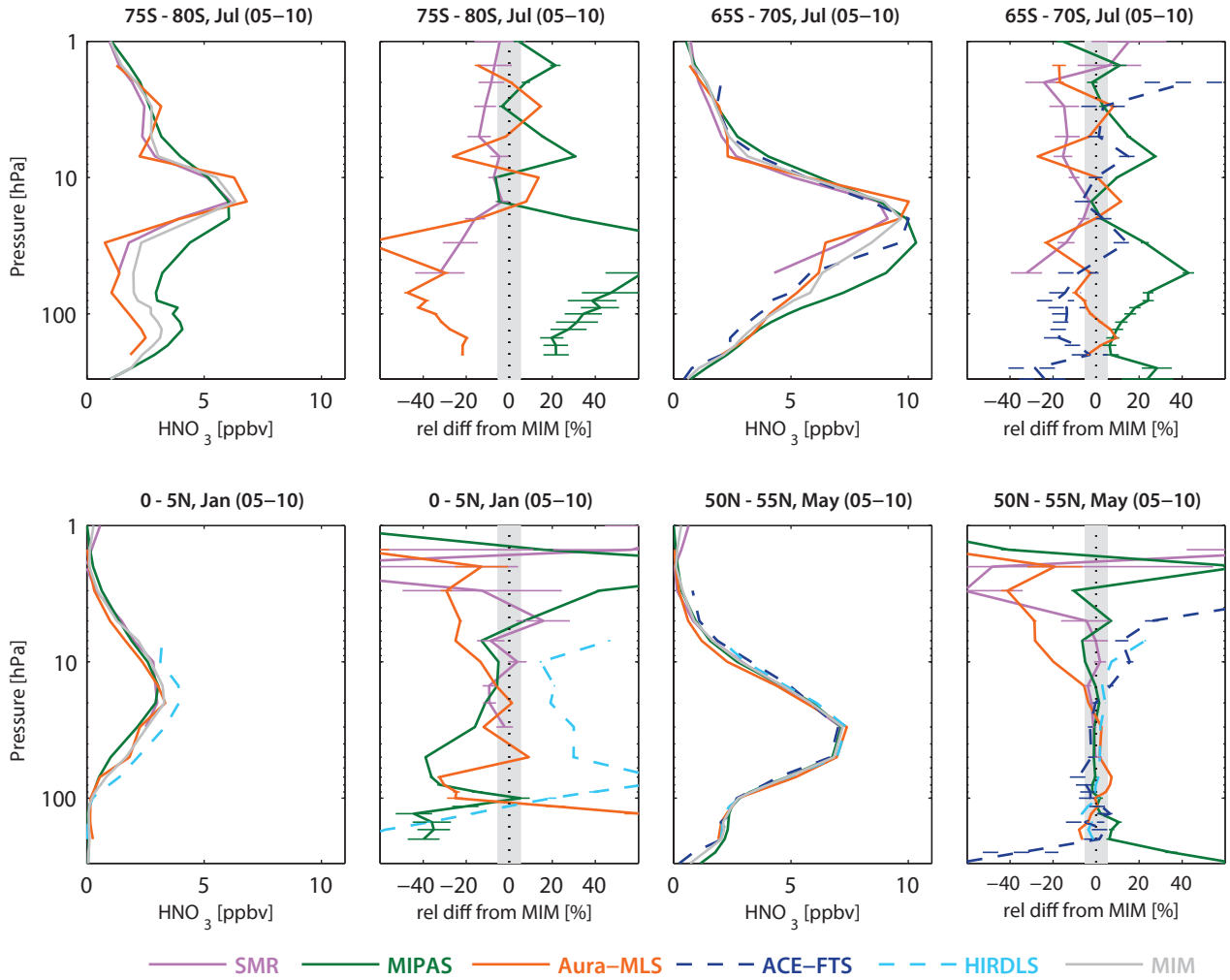

Figure 4.13.4: Vertical profiles of monthly zonal mean HNO_3 for 2005-2010. *Zonal mean HNO_3 profiles for 75°S-80°S and 65°S-70°S in July, 0°N-5°N in January, and 50°N-55°N in May are shown in columns 1 and 3. Differences between the individual instruments and the MIM profiles are shown in columns 2 and 4. Bars indicate the uncertainties in each climatological mean based on the SEM. The grey shaded area indicates where relative differences are within ±5%.*

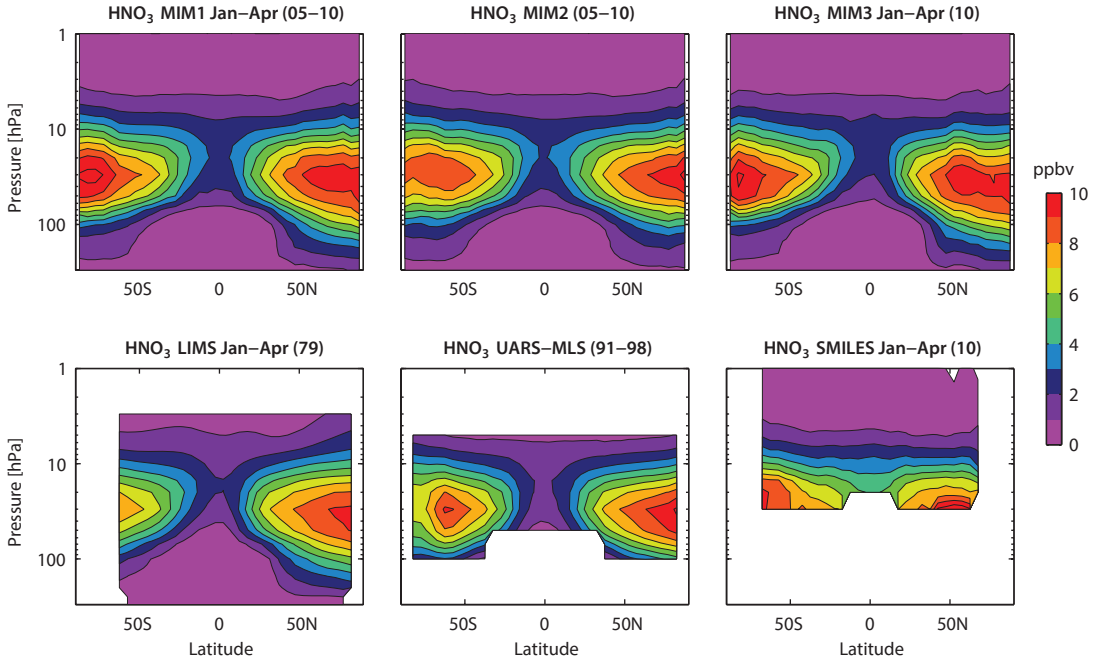

Figure 4.13.5: Cross sections of zonal mean HNO_3. *Zonal mean HNO_3 cross sections of the MIM1 (January-April 2005-2010), MIM2 (2005-2010) and MIM3 (January-April 2010), all based on SMR, MIPAS, ACE-FTS, Aura-MLS, and HIRDLS, are shown in the upper panels. Cross sections of LIMS (January-April 1979), UARS-MLS (1991-1998), and SMILES (January-April 2010) are displayed in the lower panels.*

high latitude LS, UARS-MLS is larger than the 2005-2010 MIM. Such positive deviations of an older dataset *versus* the newer datasets in the mid-latitude LS are also evident in the comparison of LIMS *versus* the 2005-2010 MIM but are not consistent with the expected positive NO_y trend. They could be related to inter-instrument differences caused by factors such as different altitude resolutions, to shifts in the nitrogen partitioning or possibly to changes in transport and mixing properties. More detailed comparisons *versus* models would be necessary to help investigate such issues.

The most recent satellite HNO_3 dataset is from SMILES and a comparison to the MIM of SMR, MIPAS, ACE-FTS, and Aura-MLS for the time period January-April 2010 is given in **Figures 4.13.5** and **4.13.6**. SMILES detects much higher abundances of up to ±50% in the MS, likely related to line mixing spectroscopic parameters and an altitude shift.

4.13.3 HNO_3 evaluations: Seasonal cycles

Figure 4.13.7 shows the HNO_3 seasonal cycles at high and tropical latitudes at 50 hPa. HNO_3 exhibits a strong seasonal cycle in the high latitude LS due to chemistry and transport effects. In winter, descending air masses transport HNO_3 downwards into the LS. This dynamical effect is counteracted by PSC formation, which removes HNO_3 from the gas phase and leads to a HNO_3 minimum at the end of winter/beginning of spring in the SH. During SH spring and summer, HNO_3 recovery through renitrification occurs, slowed down by the conversion between HNO_3 and the other nitrogen species. Comparison with the NO_y seasonal cycle (**Figure 4.17.5** in *Section 4.17*) further indicates that nearly the entire amplitude of the Antarctic HNO_3 seasonal cycle (around 8 ppbv between maximum and minimum) is related to the HNO_3 heterogeneous chemistry. Amplitudes derived from MIPAS and Aura-MLS seasonal cycles

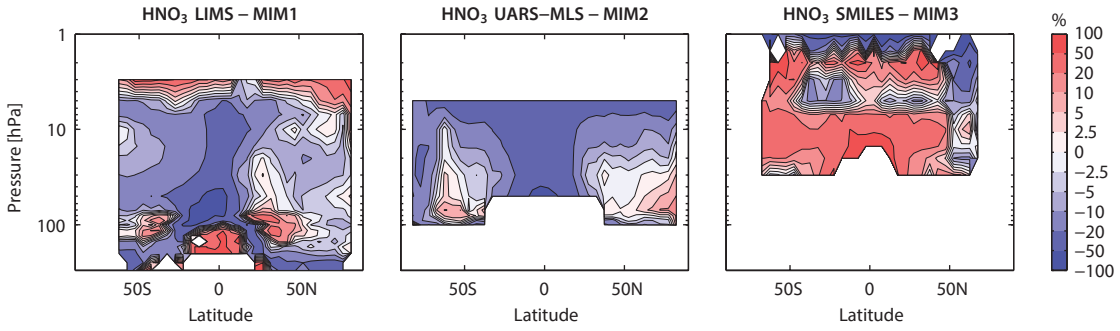

Figure 4.13.6: Cross sections of zonal mean HNO_3 differences. *Annual zonal mean HNO_3 differences between the individual instruments LIMS, UARS-MLS, SMILES and MIM1, MIM2, and MIM3, respectively, are shown. Time periods for the individual instruments and the MIMs are given in Figure 4.13.5.*

agree well and are relatively large. ACE-FTS and SMR have smaller amplitudes, but their total values show a considerable offset towards each other for most months, with smaller values from SMR. At these high southern latitudes, MIPAS shows minima and maxima of the HNO_3 seasonal cycle with a delay of about 1 and 2 months, respectively, compared to Aura-MLS and SMR.

In the NH high latitudes, the HNO_3 seasonal cycle is also impacted by the conversion between HNO_3 and NO_x as well as by heterogeneous chemistry, as evidenced by the much smaller chemistry-caused seasonal cycle in NO_y (**Figure 4.17.5** in *Section 4.17*). All HNO_3 datasets show a very similar phase but HIRDLS and SMR have smaller amplitudes than the other instruments. While the seasonal cycles in HNO_3 and NO_y are consistent for ACE-FTS and MIPAS, the same is not true for SMR, indicating that inconsistencies are introduced by the compilation of the Odin NO_y climatology, which is partially based on photochemically modelled member species (see *Section 4.17*).

In the tropics, transport variations are expected to cause a weak annual cycle as seen by MIPAS, Aura-MLS, and HIRDLS. Again, HIRDLS is affected by the uncorrected effects of tropical aerosols (see also *Section 4.5*). MIPAS and Aura-MLS agree very well on the amplitude and phase of the seasonal cycle but show a large offset. There is no agreement of the ACE-FTS and SMR seasonal signals with the other instruments. The ACE-FTS sampling is sparser in the tropics than at higher latitudes, which is probably largely responsible for apparent differences in this region.

4.13.4 HNO_3 evaluations: Interannual variability

Interannual variability of HNO_3 at polar latitudes (60°N-90°N and 60°S-90°S) at 50 hPa and in the tropics (10°S-10°N) at 30 hPa is shown in **Figure 4.13.8**. The 2005-2010 time series of deseasonalised anomalies in the tropics at 30 hPa shows an excellent agreement between MIPAS, Aura-MLS, and ACE-FTS. The pronounced QBO signal is recorded with the same amplitude and phase by the three satellite datasets. SMR and HIRDLS also detect the QBO signal but show some deviations compared to the other datasets. SMR has a lower QBO amplitude, particularly at the beginning of 2007 and the end of 2009/beginning of 2010. HIRDLS has unrealistic January anomalies due to a too high January value in 2005 at the beginning of the measurement period. Note that the 2005 January HIRDLS value is based on two days of measurements only and will be omitted in future HIRDLS data versions. Furthermore, HIRDLS shows positive anomalies at the end of 2007 while the other datasets have negative anomalies during this time period. Note that a comparison of the anomalies for the 2005-2007 time period leads to very similar results.

At polar latitudes, the datasets show good agreement, but some outliers in the anomaly time series can be found as well. For most years the largest anomalies occur during polar winter, related to the strong interannual variability of chemical and dynamical processes impacting the polar stratospheric nitrogen budget. In the Arctic, the largest differences coincide with the largest anomalies in January. The smallest differences are found during NH summer when the smallest anomalies occur. In general, the maximum anomalies are followed by a slow decay of the anomalies over the following months until next autumn. This seasonal persistence is also found in the Antarctic where the interannual anomalies are more pronounced. MIPAS shows largest deviations in June and SMR displays stronger month-to-month fluctuations.

4.13.5 Summary and conclusions: HNO_3

A comprehensive comparison of eight HNO_3 profile climatologies has been carried out. Overall findings on the systematic uncertainty in our knowledge of the HNO_3 mean state and important characteristics of the individual datasets are presented in the following summary including two synopsis plots. The first summary plot (**Figure 4.13.9**) provides information on the HNO_3 mean state and the

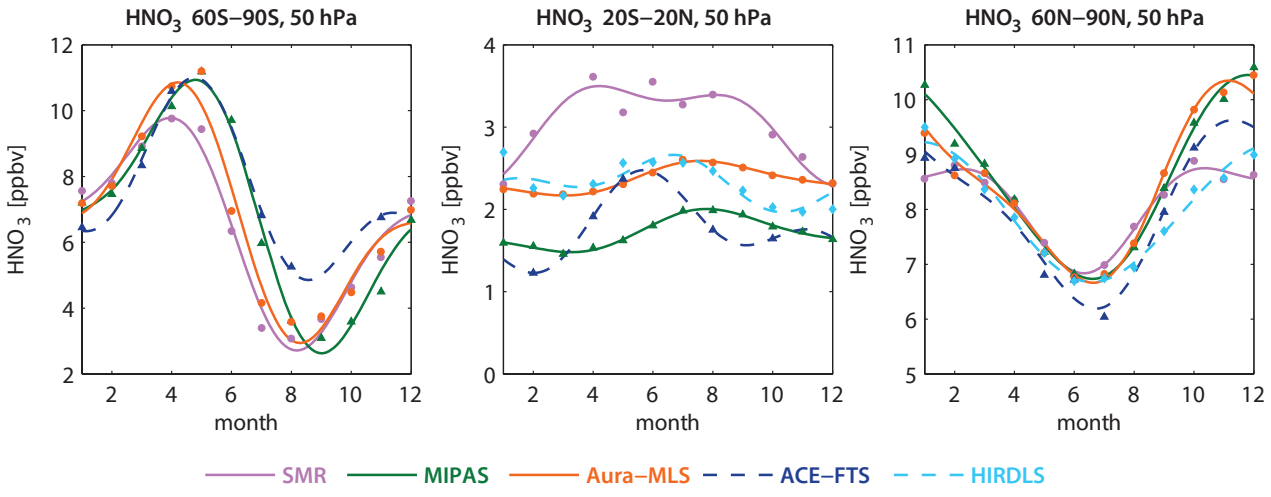

Figure 4.13.7: Seasonal cycle of HNO_3 for 2005-2010. *Seasonal cycle of monthly zonal mean HNO_3 for 60°S-90°S (left column), 20°S-20°N (middle column) and 60°N-90°N (right column) at 50 hPa.*

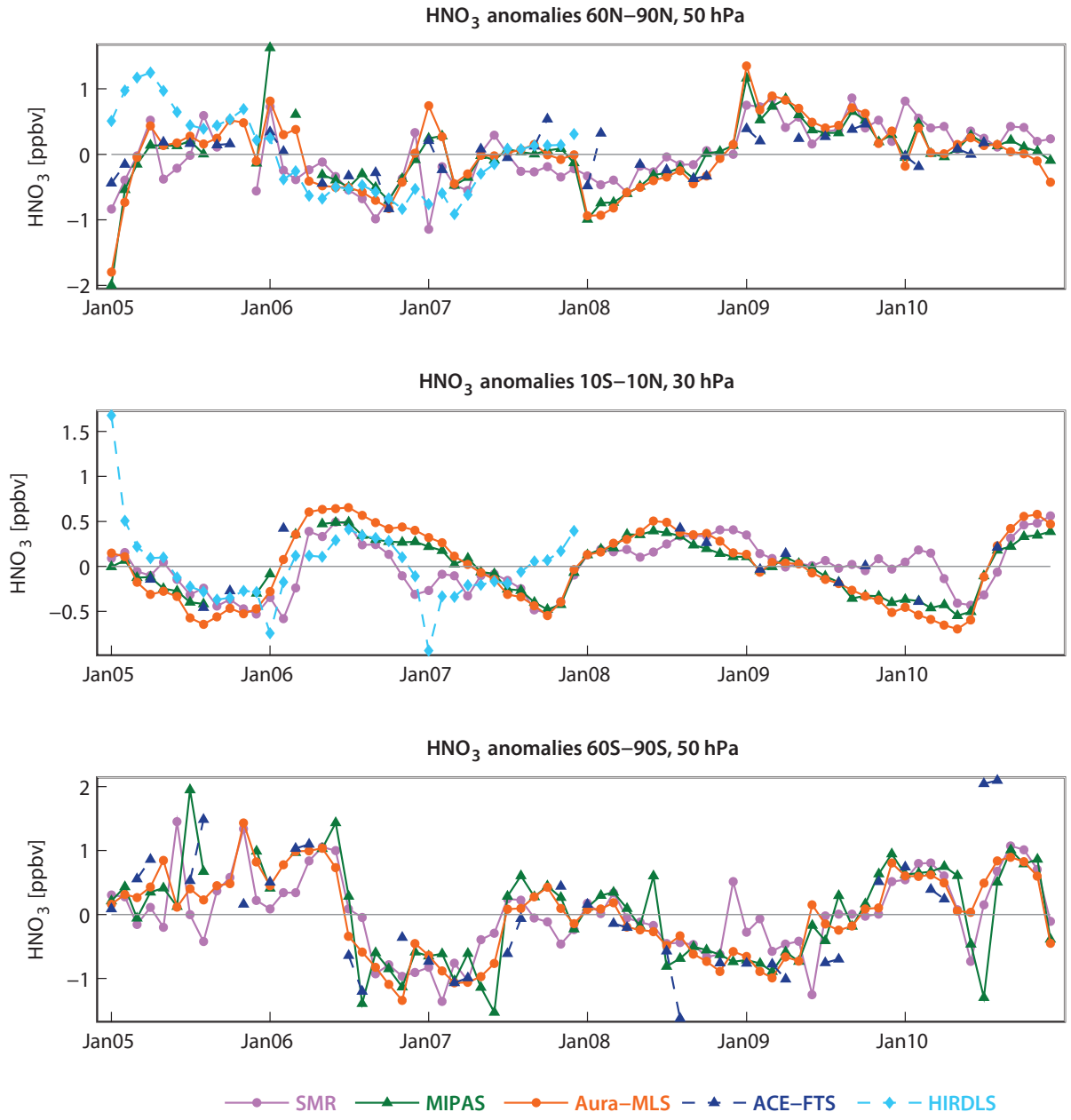

Figure 4.13.8: Time series of HNO_3 anomalies for 2005-2010. *Monthly zonal mean deseasonalised HNO_3 anomalies at 50 hPa for 60°N-90°N and 60°S-90°S, and at 30 hPa for 10°S-10°N.*

uncertainty derived from the spread between the datasets. The second summary plot (**Figure 4.13.10**) shows specific inter-instrument differences in form of deviations of the instrument climatologies relative to the MIM climatology. For each instrument and selected region, the deviation to the MIM is given as the median (mean) difference over all grid points in this region. Additionally, for each instrument the spread of the differences over all grid points in this region is presented. Note that both pieces of information (average deviation and spread) are important for a meaningful assessment of inter-instrument differences. A detailed description of the rationale behind the summary plot evaluations can be found in *Section 3.3.5*.

Atmospheric mean state

The assessment of the atmospheric HNO_3 annual mean state is based on five climatologies overlapping for the time period 2005-2010.

Middle stratosphere (30-5 hPa)

The uncertainty in our knowledge of the atmospheric HNO_3 annual mean state is smallest in the MS (**Figure 4.13.9**, right panel) with a 1σ multi-instrument spread in this region between ±5% and ±15%. However, in the SH at the highest latitude bands (south of 80°S), the spread can reach values of ±30% partially related to larger deviations

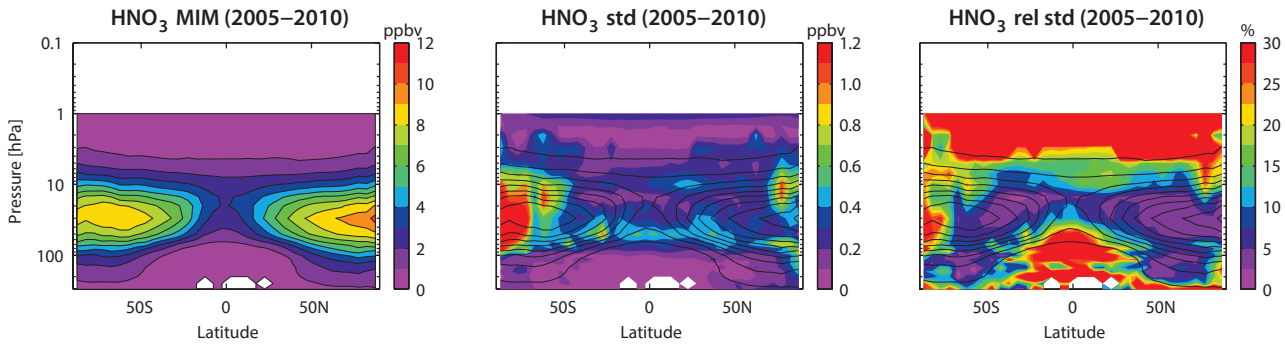

Figure 4.13.9: Summary of HNO_3 annual zonal mean state for 2005-2010. *Shown are the annual zonal mean cross section for the MIM of HNO_3 (left panel), the standard deviation over all instruments (middle panel), and the relative standard deviation with respect to the MIM (right panel). Black contour lines in the two rightmost panels give the MIM distribution. Instruments included are SMR, MIPAS, ACE-FTS, Aura-MLS, and HIRDLS. The MIM and standard deviation are only displayed for regions where at least two instruments provide measurements.*

during Antarctic winter. In addition, the larger deviations at the SH high latitudes are related to the fact that for some instruments (ACE-FTS) annual mean fields are not representative and evaluations in this region should be based on monthly mean fields.

Upper troposphere/lower stratosphere (300-30 hPa)

In the tropical UT and LS, the HNO_3 abundances decrease with decreasing altitude to very low values and the datasets show a large relative spread of up to ±50%. A much better agreement (±5% to ±10%) is found in the mid-latitude LS where the HNO_3 mixing ratios are larger compared to the tropics. In the mid-latitudes between 300-100 hPa, HNO_3 decreases and the values are comparable to the tropical LS; however, the deviations are considerably smaller giving an inter-instrument spread of around ±10%.

Upper stratosphere (5-1 hPa)

Above 3 hPa, the inter-instrument spread reaches very large values of ±50% to ±100% probably related to low HNO_3 mixing ratios close to the detection limit. In addition, diurnal variations become important above this level which can further impact the inter-instrument differences.

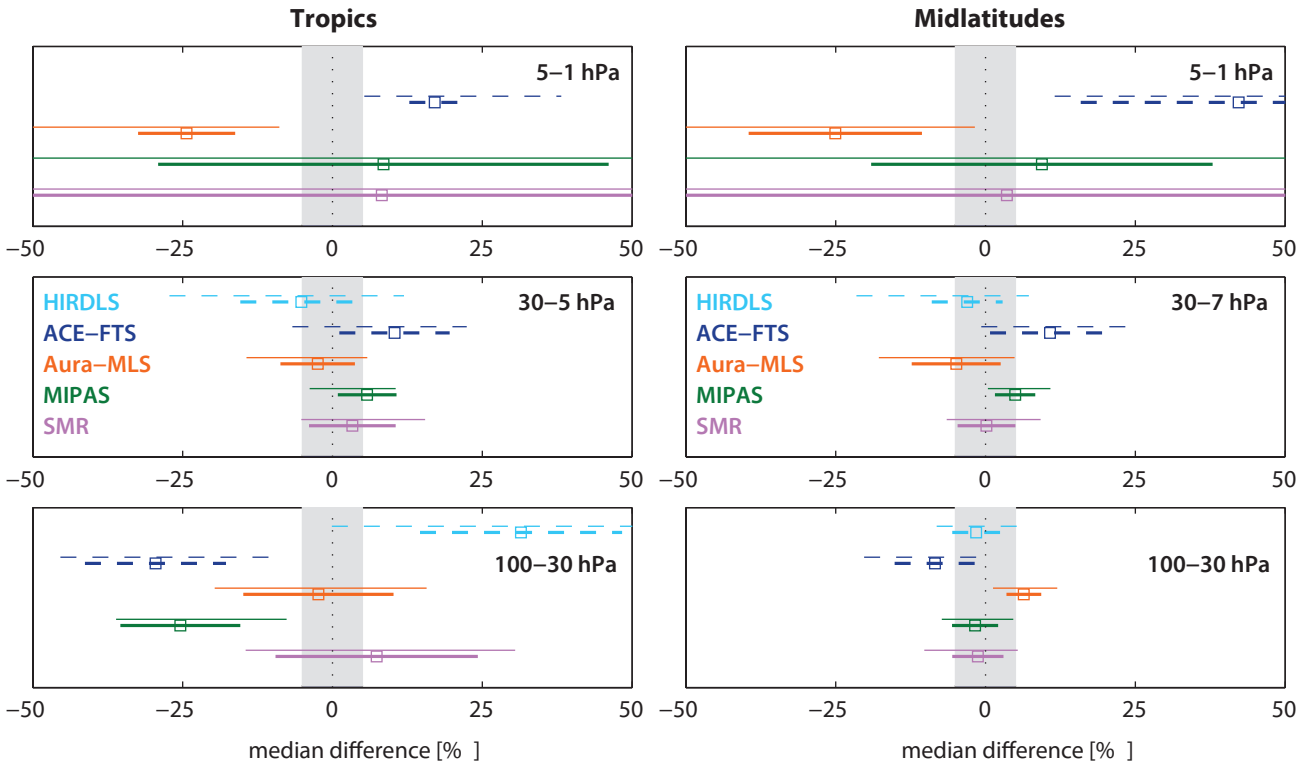

Figure 4.13.10: Summary of HNO_3 differences for 2005-2010. *Over a given latitude and altitude region the median (squares), median absolute deviation (MAD, thick lines), and the standard deviation (thin lines) of the monthly mean relative differences between an individual instrument-climatology and the MIM are calculated. Results are shown for the tropics (20°S-20°N) and midlatitudes (30°S-60°S and 30°N-60°N) and for three different altitude regions from the LS up to the US between 100 and 1 hPa for the reference period 2005-2010. The grey shaded area indicates where relative differences are within ±5%.*

Instrument-specific conclusions

LIMS and **UARS-MLS** provide the oldest HNO_3 satellite measurements available to the SPARC Data Initiative, and show negative deviations with respect to the later datasets covering 2005-2010. This difference is very likely attributable to the N_2O induced trend in HNO_3. At mid-latitudes and NH high latitudes in the LS, the deviations relative to the 2005-2010 data are positive, which is possibly related to changes in transport and mixing.

SMR shows excellent agreement with the MIM in the mid-latitude LS and MS, with differences smaller than ±2.5%. In the tropical MS, SMR is still in the middle range with differences smaller than +5%. In the tropical LS and in the US, SMR shows mostly positive deviations (smaller than +10%) and has a very large regional spread indicating a wide distribution of the relative differences around their mean.

The **MIPAS** climatology shows very similar behaviour to the SMR dataset, except for the tropical LS where MIPAS has a negative offset of -25%. MIPAS agrees well with the other datasets in terms of seasonal cycle and interannual variability, except for the Antarctic winter when it shows different anomalies. During Antarctic winter, MIPAS reports larger HNO_3 monthly mean values than the other instruments, very likely related to the rejection of PSC-impacted measurements.

Overall, **ACE-FTS** shows the largest deviations relative to the MIM that change from negative in the LS (up to -30%) to positive in the US (up to +40%). The mean and median of the deviations in the US are well defined with a low spread as opposed to SMR and MIPAS.

In the tropical LSMS, **Aura-MLS** is mostly in the middle of the range, but in the US it shows negative deviations of up to -25%. At mid-latitudes, Aura-MLS is towards the end of the range given by all measurements, with mean differences varying between +6% in the LS and -25% in the US.

HIRDLS is mostly in the middle of the range, except for the tropical LS where it shows large positive deviations. At high latitudes, the HIRDLS seasonal cycle has a much smaller amplitude than the other instruments.

4.14 Peroxynitric acid – HNO_4

Peroxynitric acid (HNO_4) acts as a reservoir of NO_x and has very low atmospheric mixing ratios. It is thought to be formed exclusively in the gas phase by the reaction of HO_2 with NO_2 and a collision partner [*DeMore et al.*, 1997], and thus has indirect tropospheric sources such as soil emissions and fossil fuel burning (see *Section 4.11*). HNO_4 easily decomposes back into its precursor species and has a local lifetime of minutes to days depending on temperature. In the stratosphere, the reaction of HNO_4 with OH can lead to NO_x-catalysed loss of odd hydrogen radicals, presenting a significant sink of the latter [*Brasseur and Solomon,* 2005]. HNO_4 has a strong diurnal cycle in the US but is relatively constant in the LS and MS as demonstrated by examples of the diurnal HNO_4 cycle for three different pressure levels (**Figure 4.14.1**) derived with a chemical box model [*McLinden et al.*, 2010].

4.14.1 Availability of HNO_4 measurements

The assessment of the atmospheric HNO_4 annual mean state is based on the climatologies from ACE-FTS and MIPAS. **Tables 4.14.1** and **4.14.2** compile information on the availability of HNO_4 measurements, including time period, altitude range, vertical resolution, and references relevant for the data products used in this report. ACE-FTS measurements are split into local sunrise and sunset data, and MIPAS measurements are split into 10am and 10pm data in order to identify differences between the datasets attributable to different LSTs.

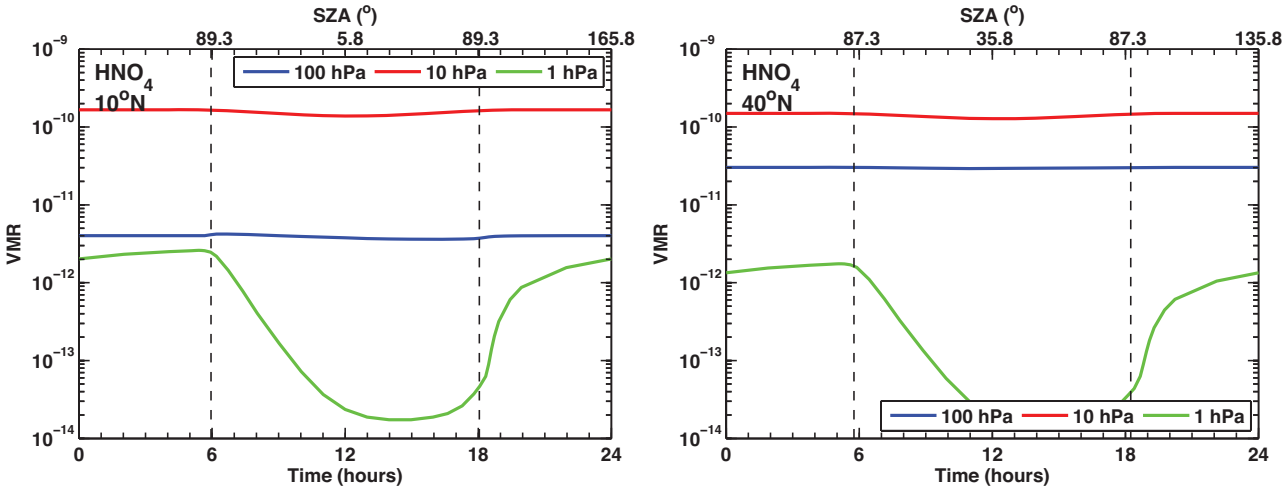

Figure 4.14.1: Diurnal HNO_4 cycle. *HNO_4 variations as function of LST are shown at 10°N and 40°N at 1, 10 and 100 hPa for March 15.*

Table 4.14.1: Available HNO_4 measurement records from limb-sounding satellite instruments between 1978 and 2010. The red filling of the grid boxes indicates the temporal and vertical coverage of the respective instrument.

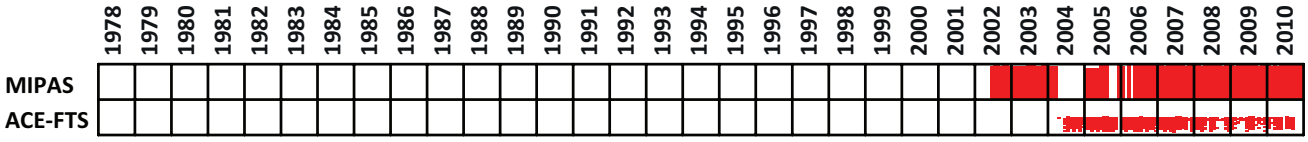

Table 4.14.2: Data version, time period, vertical range, vertical resolution, references, and other comments for HNO_4 datasets participating in the SPARC Data Initiative.

Instrument and data version	Time period	Vertical range	Vertical resolution	References	Additional comments
MIPAS **MIPAS(1)** V12 **MIPAS(2)** V220	 Mar 02 – Mar 04 Jan 05 – Apr 12	Cloud top – 55 km	MIPAS(1): 4 – 6 km below 40 km; 10 – 15 km above MIPAS(2): 3 – 8 km below 40 km; 10 – 15 km above	*Stiller et al.*, 2007	
ACE-FTS V2.2	Mar 04 –	12 – 25 km	3 – 4 km	*Jones et al.*, 2011	Research product used here.

4.14.2 HNO_4 evaluations: Zonal mean cross sections and vertical profiles

Zonal mean cross sections are compared for the overlap period 2005-2010. As a first step, the annual mean MIPAS 10am and 10pm climatologies are compared to each other in order to identify the regions where varying LSTs may cause differences. **Figure 4.14.2** shows the cross sections of the two datasets, revealing very similar HNO_4 distributions below 10 hPa and significant differences above 10 hPa. For both LSTs the HNO_4 maximum is found in the tropical and subtropical LS to MS. While for the 10pm climatologies the maximum extends all the way through the MS with a steep gradient above, the 10am data decrease gradually above 10 hPa.

Differences of the MIPAS 10am and MIPAS 10pm datasets from their MIM are caused primarily by diurnal variations and are shown in **Figure 4.14.3**. Between 70 and 10 hPa, differences are very small (<±2.5%) suggesting only a very weak diurnal cycle in this region in accordance with the results from the chemical box model (**Figure 4.14.1**). At around 100 hPa in the tropics, slightly larger differences are found, increasing up to ±20%. The diurnal cycle has a large impact above 10 hPa causing differences of up to ±100% between the datasets corresponding to different LSTs. In the US, the 10pm measurements result in higher HNO_4 mixing ratios than the 10am measurements, while the situation is reversed in the LM. Differences around 100 hPa in the tropics and above 1 hPa are large in percentage units but should not be over interpreted since the mixing ratios here are very small as are the absolute diurnal variations.

A direct comparison between the MIPAS and ACE-FTS climatologies needs to be restricted to regions below 10 hPa and in the tropics to regions between 70 and 10 hPa. Outside of this range, different LSTs will cause differences in the HNO_4 mixing ratios. This conceals the true inter-instrument spread as the evaluations of MIPAS 10am and MIPAS 10pm climatologies have demonstrated. As the ACE-FTS datasets cover 130-20 hPa (70-20 hPa in the tropics), the comparison can be undertaken for the whole measurement range. **Figure 4.14.4** shows the annual zonal mean mixing ratios of the two MIPAS (10am and 10pm) and the two ACE-FTS (local sunrise and local sunset) datasets. While there is a good agreement on the magnitude of the HNO_4 mixing ratios and on the overall distribution, smaller differences exist leading to deviating tracer isopleths. While for MIPAS the tracer isopleths slope downwards from the tropics to the mid-latitudes, for ACE-FTS isopleths larger than 0.1 ppbv seem to slope upwards. Additionally, the ACE-FTS isopleths are noisier, which is very likely related to noisier profiles (compared to other ACE-FTS species) and to smaller sample sizes for the calculation of the monthly zonal mean values (compared to MIPAS mean values).

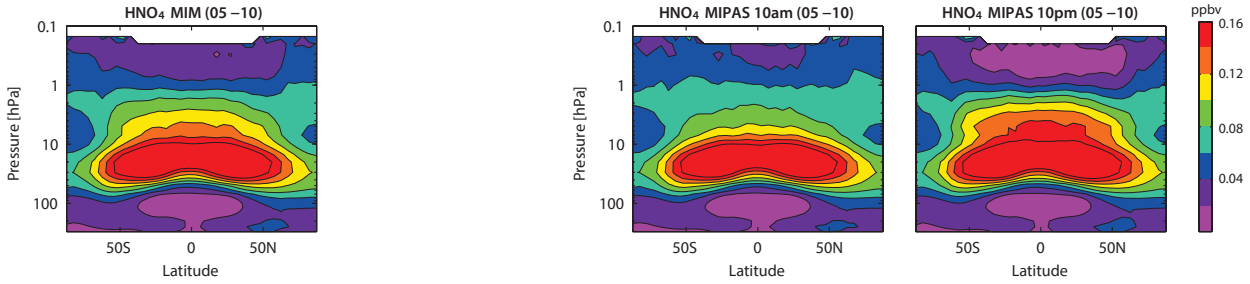

Figure 4.14.2: MIPAS cross sections of annual zonal mean HNO_4 for 2005-2010. Annual zonal mean HNO_4 cross sections are shown for MIPAS 10am and MIPAS 10pm in the right panels and for their MIM in the left panel.

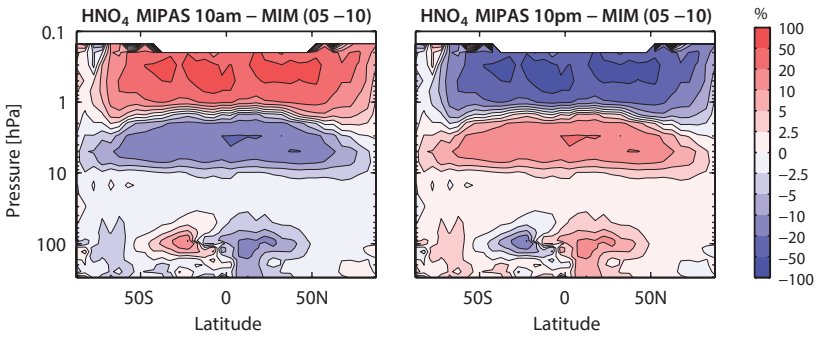

Figure 4.14.3: MIPAS cross sections of annual zonal mean HNO_4 differences for 2005-2010. *Annual zonal mean HNO_4 differences between MIPAS 10am, MIPAS 10pm and their MIM are shown.*

Differences between the four datasets and their MIM are shown in **Figure 4.14.5**. ACE-FTS detects smaller HNO_4 mixing ratios than MIPAS, leading to differences of up to ±50%. In all cases the differences between the two different instruments are larger than the differences caused by varying LSTs, as identified above. The only exception is at SH high latitudes where ACE-FTS local sunset data show much lower HNO_4 mixing ratios than ACE-FTS local sunrise data. This is likely due to the specific months that are sampled by sunrises and sunsets throughout the year.

4.14.3 Summary and conclusions: HNO_4

HNO_4 climatologies are available from two limb sounders, namely, ACE-FTS and MIPAS, with measurements at local sunrise/sunset and measurements at 10am/pm, respectively. The strong diurnal cycle above 10 hPa prevents a thorough comparison of the datasets in this region. Below 10 hPa, diurnal variations are weak allowing for a direct comparison of the datasets corresponding to different LSTs. For nearly all cases, ACE-FTS detects smaller and MIPAS larger HNO_4 mixing ratios leading to differences of up to ±50%. Comparisons of seasonal variations or interannual

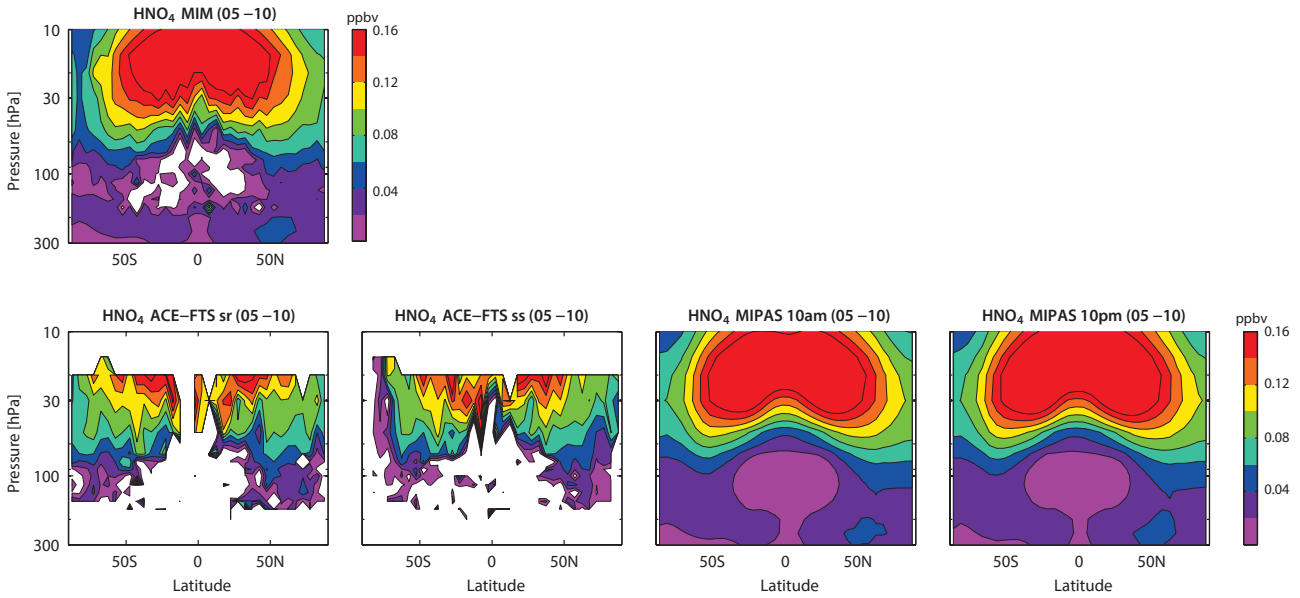

Figure 4.14.4: Cross sections of annual zonal mean HNO_4 for 2005-2010. *Annual zonal mean HNO_4 cross sections are shown for the MIM, ACE-FTS local sunrise (sr), ACE-FTS local sunset (ss), MIPAS 10am and MIPAS 10pm.*

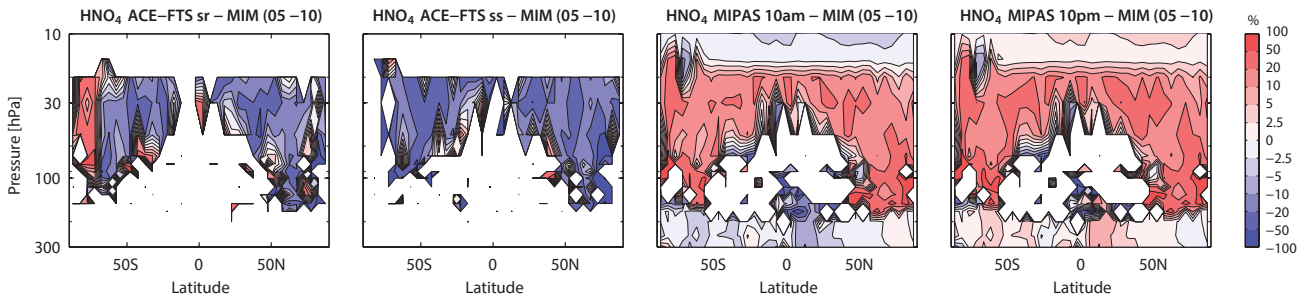

Figure 4.14.5: Cross sections of annual zonal mean HNO_4 differences for 2005-2010. *Annual zonal mean HNO_4 differences between the individual datasets and their MIM are shown.*

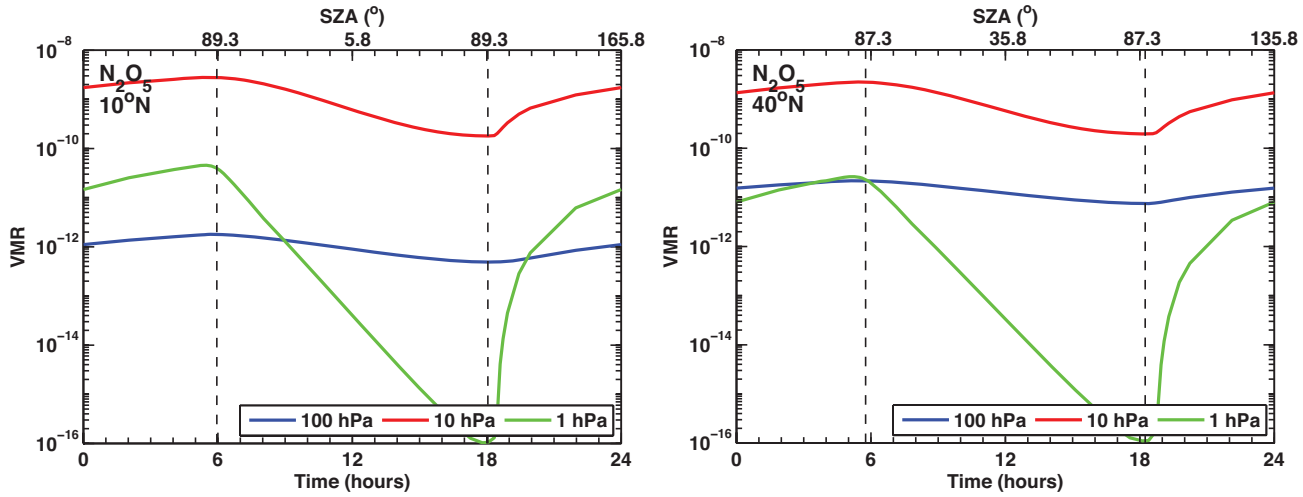

Figure 4.15.1: Diurnal N_2O_5 cycle. *N_2O_5 variations as function of LST are shown at 10°N and 40°N at 1, 10 and 100 hPa for March 15.*

variability are not possible due to the sparse ACE-FTS sampling pattern.

4.15 Dinitrogen pentoxide – N_2O_5

Dinitrogen pentoxide (N_2O_5) is a dominant night-time reservoir for the reactive nitrogen family. N_2O_5 is formed by the reaction of NO_2 with NO_3 and a collision partner, and thus has indirect tropospheric sources such as soil emissions and fossil fuel burning (see *Section 4.11*). Since NO_3 and N_2O_5 itself are rapidly photolysed by sunlight, N_2O_5 can only be formed and accumulated at night, reaching a maximum just before sunrise. During polar night, a significant fraction of NO_y in the lower to mid stratosphere will be available in the form of N_2O_5. In the presence of polar stratospheric clouds or volcanic aerosols, N_2O_5 can be converted to HNO_3, which has a large impact on stratospheric ozone destruction and can be irreversibly removed from the stratosphere by denitrification (see *Section 4.13*). The diurnal cycle of N_2O_5 for three different pressure levels derived with a chemical box model [*McLinden et al.*, 2010] is shown in **Figure 4.15.1**.

4.15.1 Availability of N_2O_5 measurements

The assessment of the atmospheric N_2O_5 annual mean state is based on the climatologies from ACE-FTS and MIPAS. **Tables 4.15.1** and **4.15.2** compile information on the availability of N_2O_5 measurements, including time period, altitude range, vertical resolution, and references relevant for the data product used in this report. ACE-FTS measurements are split into local sunrise and sunset data, and MIPAS measurements are split into 10am and 10pm data in order to identify differences between the datasets attributable to different LSTs.

4.15.2 N_2O_5 evaluations: Zonal mean cross sections and vertical profiles

Zonal mean cross sections are shown for the overlap period 2005-2010 for ACE-FTS local sunrise and sunset data and for MIPAS 10am and 10pm data (**Figure 4.15.2**). As expected from the diurnal cycle, ACE-FTS local sunrise data report overall the highest and ACE-FTS local sunset data the lowest N_2O_5 mixing ratios. MIPAS data at 10am

Table 4.15.1: Available N_2O_5 measurement records from limb-sounding satellite instruments between 1978 and 2010. *The red filling of the grid boxes indicates the temporal and vertical coverage of the respective instrument.*

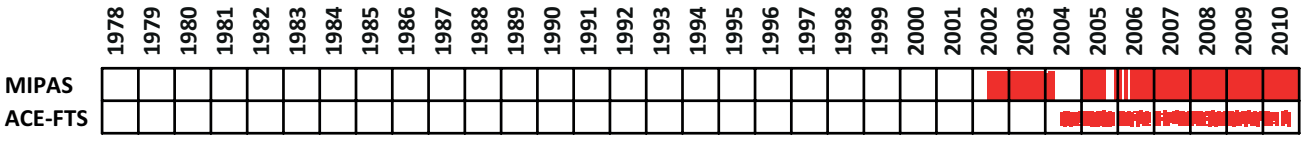

Table 4.15.2: Data version, time period, vertical range, vertical resolution, references and other comments for N_2O_5 datasets participating in the SPARC Data Initiative.

Instrument and data version	Time period	Vertical range	Vertical resolution	References	Additional comments
MIPAS **MIPAS(1)** V10 **MIPAS(2)** V220	 Mar 02 – Mar 04 Jan 05 – Apr 12	 cloud top altitude - 0.3 hPa (52 km)	 5 – 7 km below 2 hPa, 9 – 10 km above	 *Mengistu Tsidu et al.*, 2004	
ACE-FTS V2.2	Mar 04 –	15 – 40 km	3 – 4 km	*Wolff et al.*, 2008	

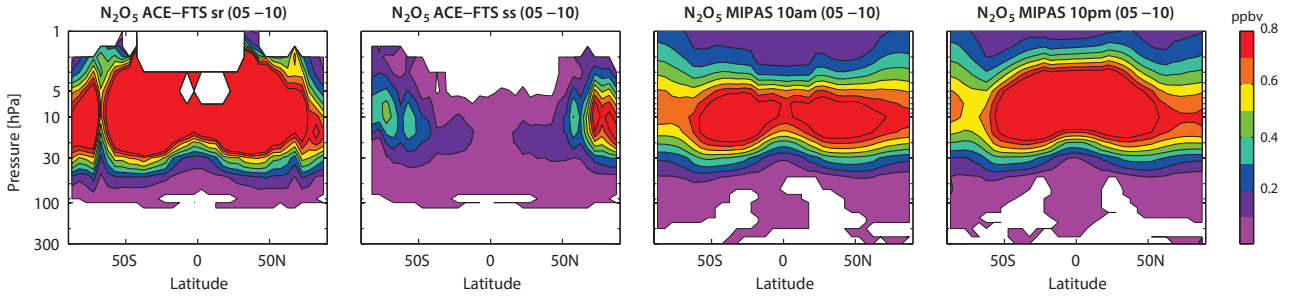

Figure 4.15.2: Cross sections of annual zonal mean N_2O_5 for 2005-2010. *Annual zonal mean N_2O_5 cross sections are shown for ACE-FTS local sunrise (sr), ACE-FTS local sunset (ss), MIPAS 10am, and MIPAS 10pm.*

and at 10pm are mostly in the middle of the range. An exception occurs at high latitudes. For example, in the NH at polar latitudes, ACE-FTS local sunset data are higher than both MIPAS climatologies, and in the US are also higher than ACE-FTS local sunrise data. These unexpectedly large values of the ACE-FTS local sunset dataset are caused by the fact that the annual mean includes more NH winter months, when N_2O_5 is higher, than the other three datasets. Similarly, at the SH polar latitudes, the annual mean ACE-FTS local sunset data are lower than expected related to the fact that not as much data from the SH winter is available and contributing to the annual mean. The comparison demonstrates that the annual mean ACE-FTS data at high latitudes, and in particular the local sunset data, are not representative and monthly means need to be evaluated instead.

Figure 4.15.3 shows monthly mean N_2O_5 profiles for NH high latitudes (65°N-70°N) during winter. The ACE-FTS local sunrise profiles show the largest values throughout most of the stratosphere, as expected from the diurnal cycle. Below 20 hPa, ACE-FTS local sunrise data are smaller than the two MIPAS profiles, contradicting the expectations based on N_2O_5 diurnal variations. Overall, differences in the MS and US are about ±20% between ACE-FTS local sunrise and MIPAS 10am/pm profiles and about ±50% between ACE-FTS local sunrise and local sunset profiles. In the latitude band 60°N-65°N, the instruments show a completely different picture, with MIPAS 10am profiles that are larger than ACE-FTS local sunrise data throughout the whole stratosphere (**Figure 4.15.4**). Similarly, at high SH latitudes in July and August, the ACE-FTS local sunrise data are lower than the MIPAS 10am and 10pm climatologies. Based on the current knowledge of the N_2O_5 diurnal cycle, the local sunrise data should give larger values than the other measurements. Therefore the comparisons in the 60°N/S-65°N/S latitude bands point to an inconsistency in either the MIPAS or the ACE-FTS data. Note, however, that local sunrise in this latitude band is between 8:30 and 9:30am reducing the diurnal variation-driven difference between ACE-FTS local sunrise and MIPAS 10am measurements. Furthermore, these latitude bands are characterised by large latitudinal gradients, and sparse sampling can have an impact on the representativeness of the monthly zonal mean values. As a result, sampling-driven differences can be larger than deviations caused by different LSTs causing the inconsistencies observed in the 60°N/S-65°N/S latitude bands. This assumption is further supported by the fact that the ACE-FTS sample size for the latitude bin 65°N-70°N is about 4 times larger than for the latitude bin 60°N-65°N.

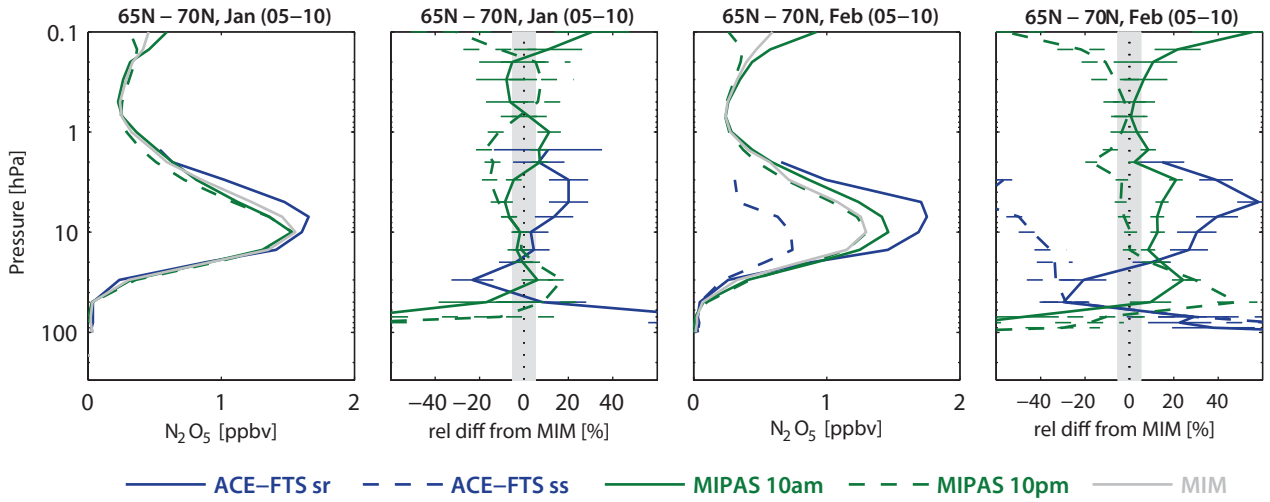

Figure 4.15.3: Vertical profiles of monthly zonal mean N_2O_5 for 2005-2010. *Zonal mean N_2O_5 profiles for 65°N-70°N in January and February are shown together with the differences between the individual instruments and the MIM profiles. Bars indicate the uncertainties in each climatological mean based on the SEM. The grey shaded area indicates where relative differences are within ±5%.*

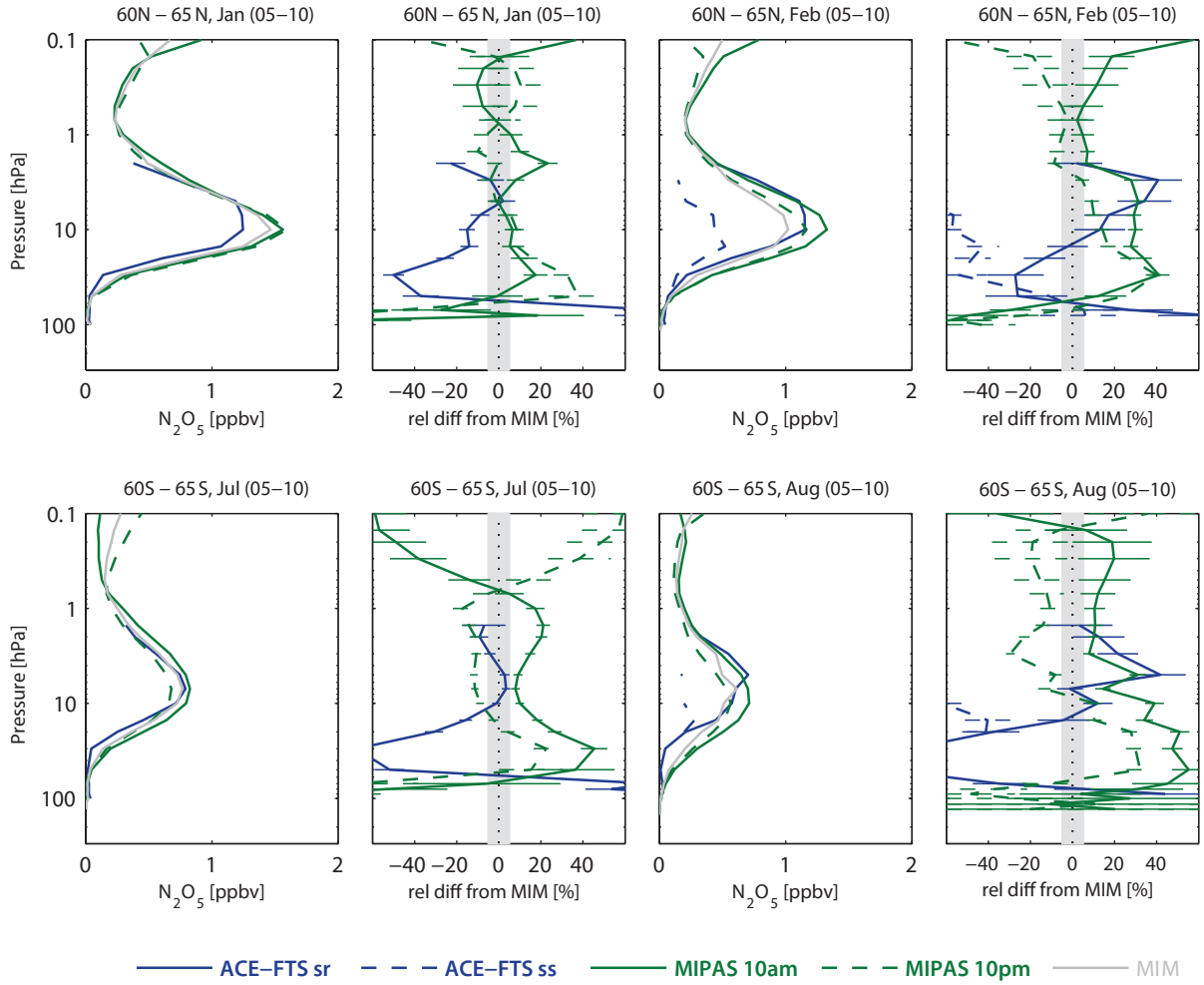

Figure 4.15.4: Vertical profiles of monthly zonal mean N_2O_5 for 2005-2010. *Zonal mean N_2O_5 profiles for 60°N-65°N in January and February and 60°S-65°S in July and August are shown in columns 1 and 3. Differences between the individual instruments and the MIM profiles are shown in columns 2 and 4. Bars indicate the uncertainties in each climatological mean based on the SEM. The grey shaded area indicates where relative differences are within ±5%.*

4.15.3 Summary and conclusions: N_2O_5

N_2O_5 climatologies are available from the limb sounders ACE-FTS and MIPAS, with measurements at local sunrise/sunset and measurements at 10am/pm, respectively. The strong diurnal cycle above 100 hPa prevents a thorough comparison of the datasets in this region. Below 100 hPa, diurnal variations are weak and the mixing ratios are low. For nearly all cases, ACE-FTS local sunrise detects the largest and ACE-FTS local sunset the lowest N_2O_5 mixing ratios, consistent with the diurnal cycle. ACE-FTS local sunrise is lower than the MIPAS 10am/pm datasets during winter at higher latitudes, in contradiction to the diurnal cycle. However, this issue may be attributable to sampling artefacts due to the latitudinal gradient, which is particularly pronounced in the latitude bins investigated. When using the datasets of trace gases with strong diurnal cycles, we recommend that additional information such as average latitude, day of month, sample size and LST (provided in the data files) should be taken into account.

4.16 Chlorine nitrate – $ClONO_2$

Chlorine nitrate ($ClONO_2$) is a reservoir species for stratospheric nitrogen and chlorine and therefore is important for ozone chemistry. $ClONO_2$ is produced from NO_x by reaction with ClO and a collision partner. During the daytime, $ClONO_2$ is photolyzed at ultraviolet wavelengths and reaches minimum abundances. During polar night, the presence of $ClONO_2$ reduces the amount of active chlorine and nitrogen and thus chemical ozone destruction. In the presence of polar stratospheric clouds, however, $ClONO_2$ can undergo heterogeneous reactions with H_2O and HCl to release chlorine into its chemically active form. The diurnal cycle of $ClONO_2$ for three different pressure levels derived with a chemical box model [*McLinden et al.*, 2010] is shown in **Figure 4.16.1**.

4.16.1 Availability of $ClONO_2$ measurements

The assessment of the atmospheric $ClONO_2$ annual mean state is based on the climatologies from ACE-FTS and MIPAS. **Tables 4.16.1** and **4.16.2** compile information on

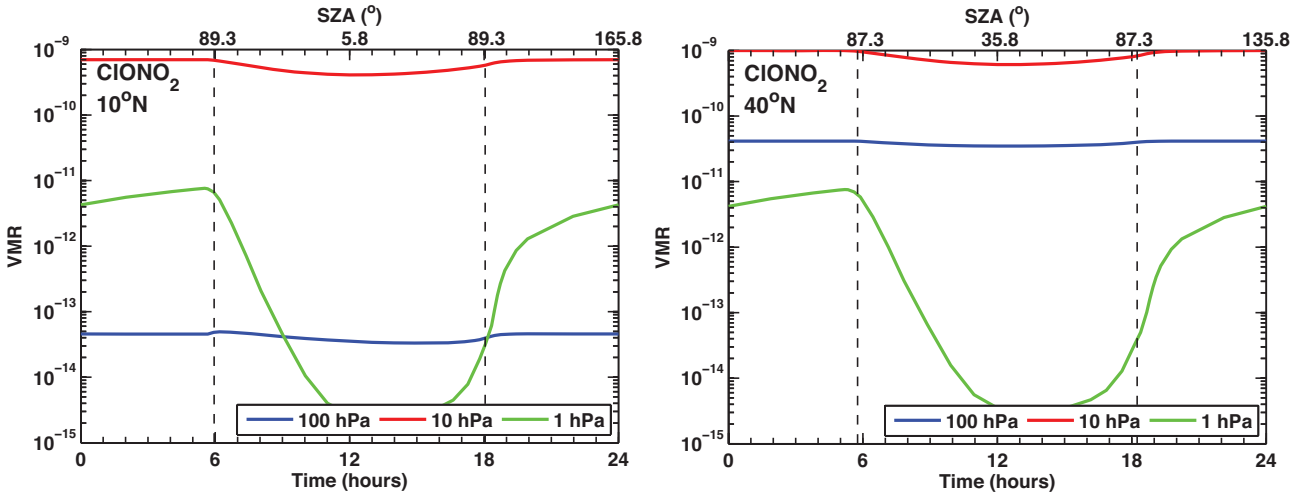

Figure 4.16.1: Diurnal $ClONO_2$ cycle. *$ClONO_2$ variations as function of LST are shown at 10°N and 40°N at 1, 10 and 100 hPa for March 15.*

the availability of $ClONO_2$ measurements, including time period, altitude range, vertical resolution, and references relevant for the data product used in this report. ACE-FTS measurements are split into local sunrise and sunset data, and MIPAS measurements are split into 10am and 10pm data in order to identify differences between the datasets attributable to different LSTs.

4.16.2 $ClONO_2$ evaluations: Zonal mean cross sections and vertical profiles

Zonal mean cross sections are shown for the overlap period 2005-2010 for ACE-FTS local sunrise and sunset data and for MIPAS 10am and 10pm data in **Figure 4.16.2**. The annual mean $ClONO_2$ distribution shows maxima at the mid-latitudes between 50 and 10 hPa. For the ACE-FTS local sunrise measurements, the maxima extend higher (up to 5 hPa). As expected from the diurnal cycle, the local sunrise data are overall the highest, whereas the ACE-FTS local sunset data and MIPAS 10am data show the lowest $ClONO_2$ mixing ratios in most regions. At high latitudes, the annual mean climatologies compare in a different way, and at the NH polar latitudes ACE-FTS local sunset data are higher than the other three datasets. Note that the same characteristic was found for the N_2O_5 climatologies (see *Section 4.15*). For both gases, the unexpectedly high values of the ACE-FTS local sunset datasets are caused by the fact that the annual mean includes more NH winter months, when $ClONO_2$ and N_2O_5 are higher than during the rest of the year. The comparison demonstrates that the annual mean ACE-FTS data at high latitudes, and in particular the local sunset data, are not representative and monthly means need to be evaluated instead.

Annual mean differences between the datasets and their MIM (**Figure 4.16.3**) in the low- and mid-latitudes show that in the LS, where the diurnal variations are expected to have only a small impact, the datasets agree quite well with differences of up to ±10%. Consistent with the diurnal cycle estimated from box model calculations, differences become significantly larger in the MS, in particular above 20 hPa for local sunrise and 10am measurements and above 10 hPa for local sunset and 10pm measurements. Differences below 100 hPa are also larger than in the LS. However, at these levels the impact of the diurnal cycle is supposed to be negligibly small and cannot explain the large deviations. Thus, the relative differences in the UT (or below 100 hPa) appear

Table 4.16.1: Available $ClONO_2$ measurement records from limb-sounding satellite instruments between 1978 and 2010. *The red filling of the grid boxes indicates the temporal and vertical coverage of the respective instrument.*

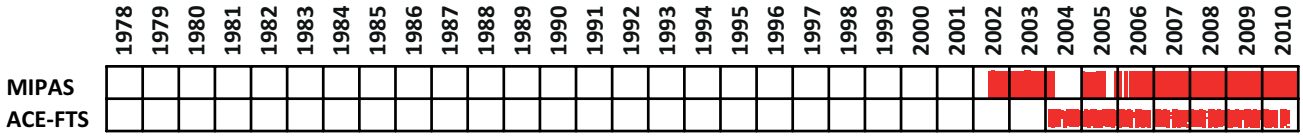

Table 4.16.2: Data version, time period, vertical range, vertical resolution, references and other comments for $ClONO_2$ datasets participating in the SPARC Data Initiative.

Instrument and data version	Time period	Vertical range	Vertical resolution	References	Additional comments
MIPAS					
MIPAS(1) V10	Mar 02 – Mar 04	8 – 65 km	3.2 – 8.5 km	*Höpfner et al.*, 2004, 2007	
MIPAS(2) V220	Jan 05 – Apr 12	8 – 65 km	2.5 – 9 km	*von Clarmann et al.*, 2009a	
ACE-FTS V2.2	Mar 04 –	12 – 35 km	3 – 4 km	*Wolff et al.*, 2008	

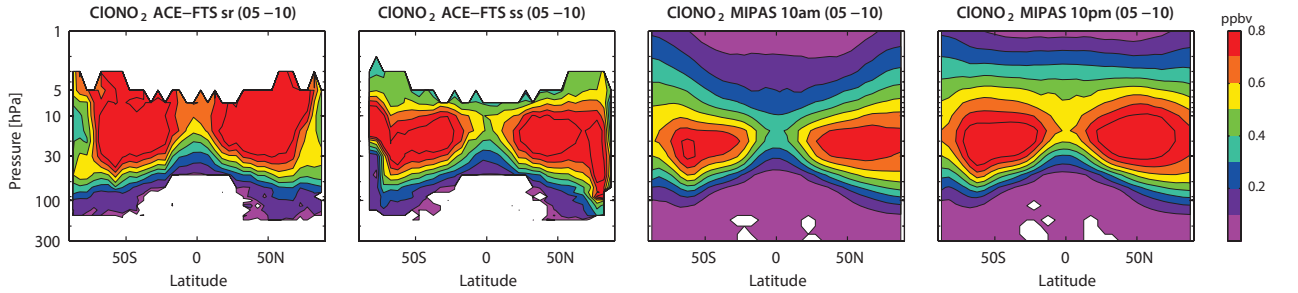

Figure 4.16.2: Cross sections of annual zonal mean $ClONO_2$ for 2005-2010. *Annual zonal mean $ClONO_2$ cross sections are shown for ACE-FTS local sunrise (sr), ACE-FTS local sunset (ss), MIPAS 10am and MIPAS 10pm.*

to be real inter-instrument differences further amplified by the small mixing ratios in this region.

Figure 4.16.4 shows monthly zonal mean cross sections for April and October. At the SH high latitudes, the April climatologies show maxima at 50 and 5 hPa. After the polar summer, the $ClONO_2$ mixing ratios are low and only start to increase with decreasing solar radiation. This increase is faster at around 5 hPa than at 10 hPa, possibly related to more nitrogen being available at the higher level. Together with the persistence of the summer time maximum at 50 hPa, this results in a vertical structure with a local minimum at around 10 hPa. ACE-FTS local sunrise measurements, available in the latitude band between 80°S and 90°S, confirm the structure observed by MIPAS. At the NH polar latitudes, the October climatologies from MIPAS show a very broad maximum and no local minimum as their SH autumn counterpart. ACE-FTS local sunrise data, however, suggest a similar structure in the NH with a local minimum around 10 hPa.

Differences of the monthly mean datasets with respect to their MIM (**Figure A4.16.1** in *Appendix A4*) are similar to the differences of the annual mean climatologies. Only at high latitudes, ACE-FTS monthly mean differences are smaller than the annual mean differences demonstrating the impact of irregular sampling on the annual mean evaluations at these latitudes.

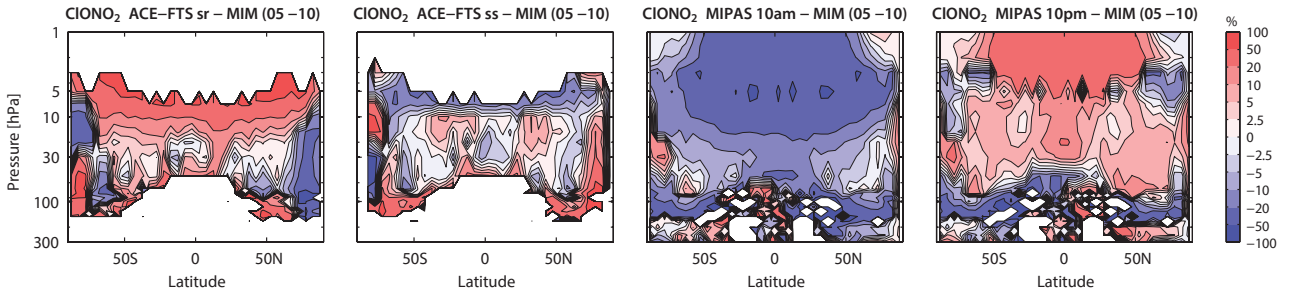

Figure 4.16.3: Cross sections of annual zonal mean $ClONO_2$ differences. *Annual zonal mean $ClONO_2$ differences for 2005-2010 between the datasets and the MIM are shown.*

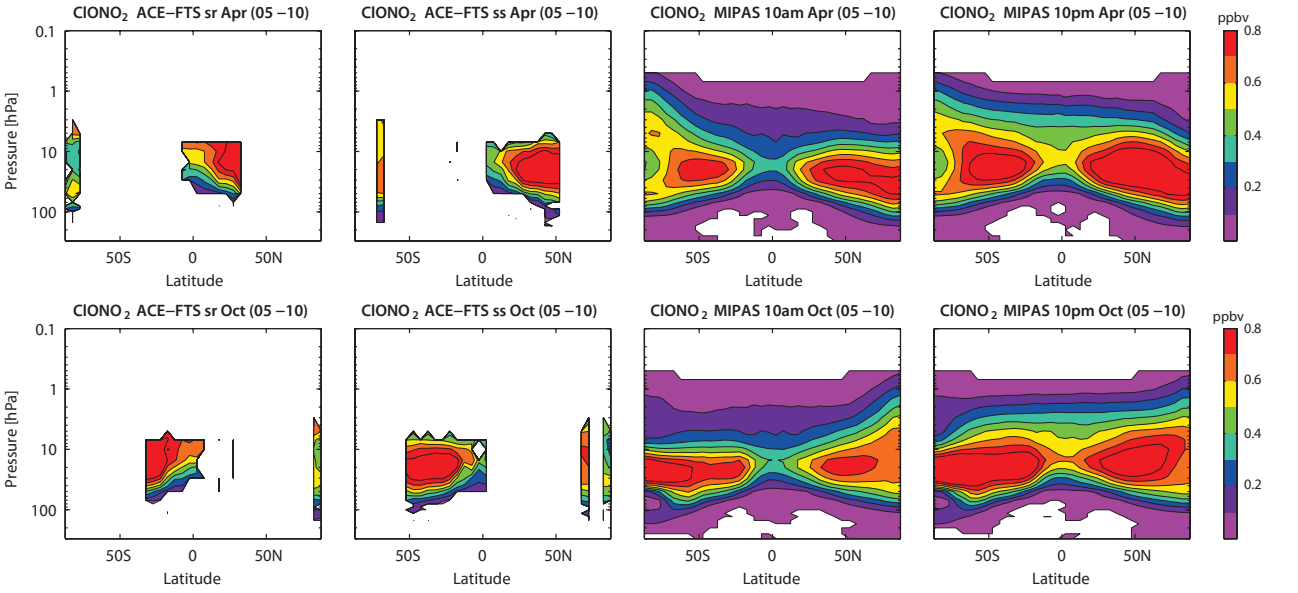

Figure 4.16.4: Cross sections of monthly zonal mean $ClONO_2$ for April and October. *Monthly zonal mean $ClONO_2$ cross sections are shown April (upper panels) and October (lower panels) 2005-2010 for ACE-FTS local sunrise (sr), ACE-FTS local sunset (ss), MIPAS 10am and MIPAS 10pm.*

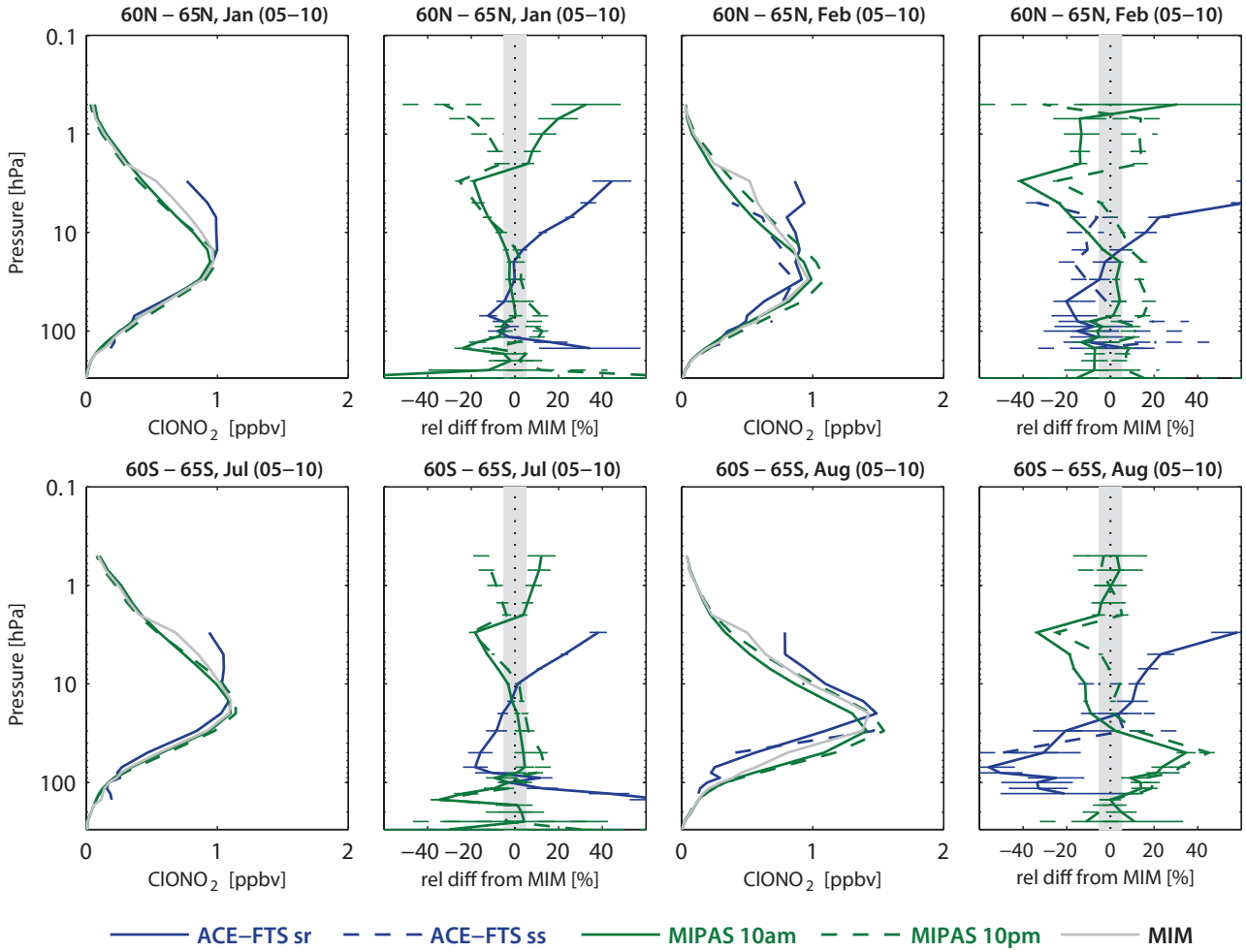

Figure 4.16.5: Vertical profiles of monthly zonal mean $ClONO_2$ for 2005-2010. *Zonal mean $ClONO_2$ profiles for 60°N-65°N in January and February and 60°S-65°S in July and August are shown in columns 1 and 3. Differences between the individual instruments and the MIM profiles are shown in columns 2 and 4. Bars indicate the uncertainties in each climatological mean based on the SEM. The grey shaded area indicates where relative differences are within ±5%.*

Figure 4.16.5 shows monthly mean $ClONO_2$ profiles at high latitudes (60°N-65°N and 60°S-65°S) during winter. The rapid increase of the deviations of ACE-FTS local sunrise data in the MS to US identify the level above which the diurnal cycle significantly impacts the climatology comparison. In the LS, where $ClONO_2$ has a longer lifetime, the ACE-FTS local sunrise profile seems to be shifted with regard to the MIPAS profiles, with the largest shift at 60°S-65°S in August. As a result the ACE-FTS local sunrise climatology is smaller than the MIPAS 10am and 10pm climatologies between 100 and 20 hPa. This larger difference, when compared to the July evaluations, could be related to the fact that considerably less data points are available for the construction of the ACE-FTS 60°S-65°S mean value in August than in July.

4.16.3 Summary and conclusions: $ClONO_2$

$ClONO_2$ climatologies are available from the limb sounders ACE-FTS and MIPAS with measurements at local sunrise/sunset and measurements at 10am/pm, respectively. The strong diurnal cycle in the MS and US prevents a thorough comparison of the datasets in this region. Below 10 hPa, diurnal variations are quite weak and the datasets agree well with differences from their MIM of up to ±10%. In the LS, however, relative differences are large partially related to the low mixing ratios. For nearly all cases, ACE-FTS local sunrise detects largest and MIPAS 10am lowest $ClONO_2$ mixing ratios consistent with the diurnal cycle. Only at higher latitudes during winter, ACE-FTS local sunrise is lower than the MIPAS 10am/pm datasets; a difference that cannot be explained by the diurnal cycle.

4.17 Total reactive nitrogen – NO_y

Total reactive nitrogen (NO_y) is the sum of all atmospheric reactive nitrogen species (NO_y = NO + NO_2 + NO_3 + HNO_3 + HNO_4 + $2N_2O_5$ + $ClONO_2$ + $BrONO_2$ + aerosol nitrate + …). Tropospheric NO_y originates largely from sources of NO and NO_2 released by fossil fuel burning, lightning, chemical processes in soils, and biomass burning (see *Sections 4.10* and *4.11*). The primary source of NO_y in the stratosphere is the oxidation of N_2O also originating from soil emissions (see *Section 4.4*). The dominant sink of stratospheric NO_y is through HNO_3 wash-out and sedimentation of HNO_3-containing PSCs. Reactive nitrogen species play an important role in stratospheric ozone

Table 4.17.1: Available NO_y measurement records from limb-sounding satellite instruments between 1978 and 2010. The red filling of the grid boxes indicates the temporal and vertical coverage of the respective instrument.

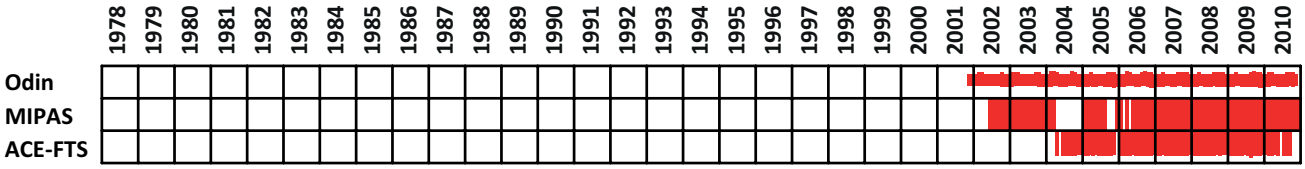

chemistry through different mechanisms. First, NO_x is an ozone-depleting substance due to the catalytic NO_x cycle [*Crutzen*, 1970; *Johnston*, 1971]. Second, the presence of HNO_3 in an air parcel supports the formation of type I PSCs, which in turn enhance the release of chlorine from reservoir species into its ozone-destroying reactive form (see *Section 4.13*). Third, NO_2 reduces halogen-catalyzed ozone loss by converting reactive chlorine, bromine, and hydrogen compounds into more stable reservoir substances ($ClONO_2$, $BrONO_2$, HNO_3). The overall impact of reactive nitrogen on stratospheric ozone chemistry is determined by the balance of the different processes that are ultimately coupled since the amount of available NO_2 is, among other things, controlled by HNO_3 photolysis.

4.17.1 Availability of NO_y measurements

The assessment of the atmospheric NO_y annual mean state is based on the climatologies from ACE-FTS, MIPAS, and Odin. For ACE-FTS [*Jones et al.*, 2011] and MIPAS [*Funke et al.*, 2014] the climatologies are compiled from NO, NO_2, HNO_3, HNO_4, $2\times N_2O_5$, and $ClONO_2$ (six species climatologies) all directly measured by the instruments. The Odin climatology [*Brohede et al.*, 2008] is based on NO_2 from OSIRIS, HNO_3 from SMR and NO, $2\times N_2O_5$ and $ClONO_2$ taken from scan-based chemical box model simulations [*McLinden et al.*, 2010], while HNO_4 is not included (five species climatology). In addition, a MIPAS climatology not including HNO_4 is available (five species climatology) and analysed in the cross section evaluations in *Section 4.17.2*. For the remainder of *Section 4.17*, the MIPAS climatology based on six species is used. In all figures the instrument names will be augmented by lower indices indicating the number of species used to compile the climatology, *e.g.*, $MIPAS_5$ for the MIPAS five species climatology. Note that the ACE-FTS and Odin NO_y products are daytime climatologies and do not include polar night data, in contrast to MIPAS.

Table 4.17.1 summarises all available NO_y climatologies derived from satellite measurements, including time period and vertical range. Information on individual nitrogen species measurements used for deriving the NO_y climatologies, including time period, vertical range and resolution, and relevant references have been given in *Sections 4.10-4.16*.

4.17.2 NO_y evaluations: Zonal mean cross sections and vertical profiles

Zonal mean cross sections and vertical profiles are compared for the overlap period 2005-2010. **Figure 4.17.1** displays all annual mean NO_y climatologies. Note that the MIM consists of the six species climatologies from MIPAS and ACE-FTS and the five species climatology from Odin. The five species climatology from MIPAS is not included in order to prevent double counting of the MIPAS data. The two MIPAS climatologies are very similar and show differences from their MIM of less than 1% above 170 hPa and differences of less than 5% between 300 and 170 hPa. The small differences between the two climatologies suggest that the impact of HNO_4 is negligible in most regions, and that Odin can be compared directly to the six species climatologies from MIPAS and ACE-FTS.

Similar to the NO_2 distribution, the maximum values are found between 10 and 5 hPa with downward sloping isopleths towards higher latitudes due to isentropic mixing between the ascending and descending branches of the Brewer-Dobson circulation. Above 5 hPa, the distribution becomes more uniform with relatively flat isolines. Overall, the NO_y distributions of the three datasets agree very well with each other. The noisier isolines and the large values at the highest latitudes in ACE-FTS are related to sampling issues, *i.e.*, the region south of 85°S is only covered by ACE-FTS in March and April, resulting in anomalously high values when compiling annual means.

Figure 4.17.2 shows the differences of the three instruments from their MIM. Below 2 hPa, ACE-FTS is clearly lower than MIPAS with differences from the MIM ranging from -10% (ACE-FTS) to +10% (MIPAS), respectively. The Odin climatology changes from positive differences (below 10 hPa) to negative differences (above 10 hPa), mostly in the range of ±10%. Overall, there is good agreement between the three datasets, which is confirmed by the evaluation of the monthly mean climatologies (**Figure A4.17.1** and **A4.17.2** in *Appendix A4*) and consistent with evaluations [*Jones et al.*, 2011]. Above 2 hPa, only ACE-FTS and MIPAS data are available and differences can be larger reaching even ±50% at the high latitudes. The differences show a strong latitudinal gradient with ACE-FTS on the high side and MIPAS on the low side in the tropics and subtropics and *vice versa* poleward of about 50°.

Detailed evaluations of monthly zonal mean differences for individual latitude bands (0°N-5°N and 70°S-75°S for August) are shown in **Figure 4.17.3**. The comparison of the tropical profiles confirms the very good agreement in a wide altitude range from 40 to 0.3 hPa. While ACE-FTS and MIPAS agree also very well below 40 hPa, Odin shows clearly larger values with differences of up to +30%. The maximum at 5 hPa as seen by MIPAS is about 5 to 10% too large when compared to the other two climatologies.

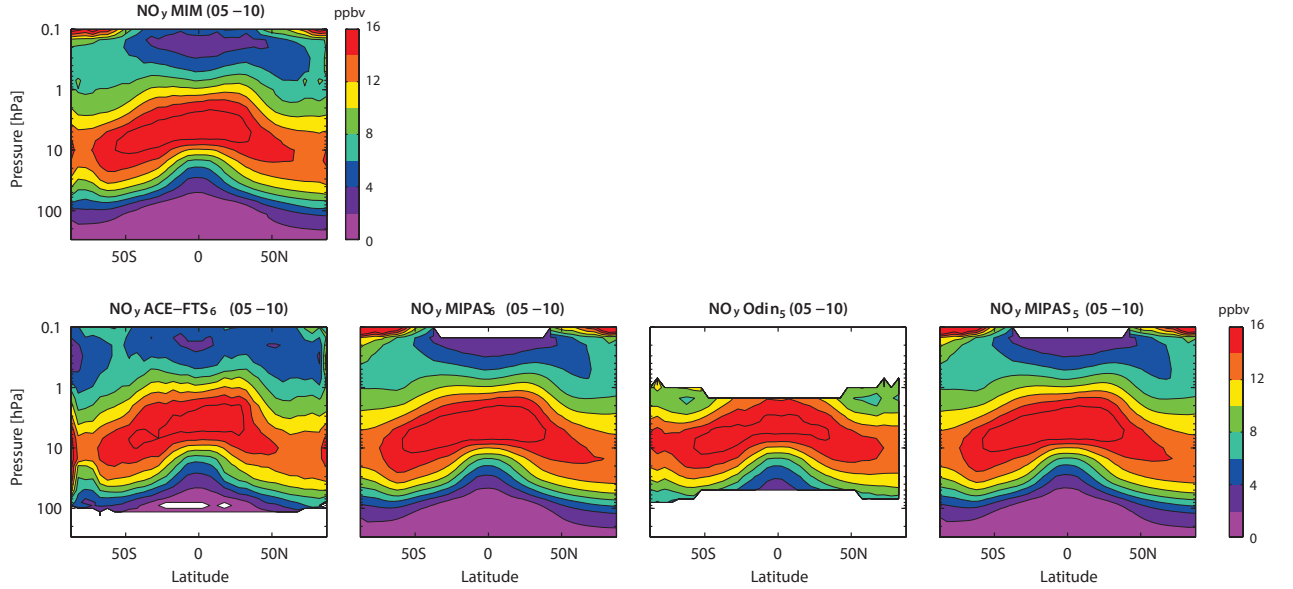

Figure 4.17.1: Cross sections of annual zonal mean NO_y for 2005-2010. *Annual zonal mean NO_y cross sections are shown for the MIM in the upper panel and for ACE-FTS_6, $MIPAS_6$, $Odin_5$ and $MIPAS_5$ in the lower panels. Note that $MIPAS_5$ is not included in the MIM.*

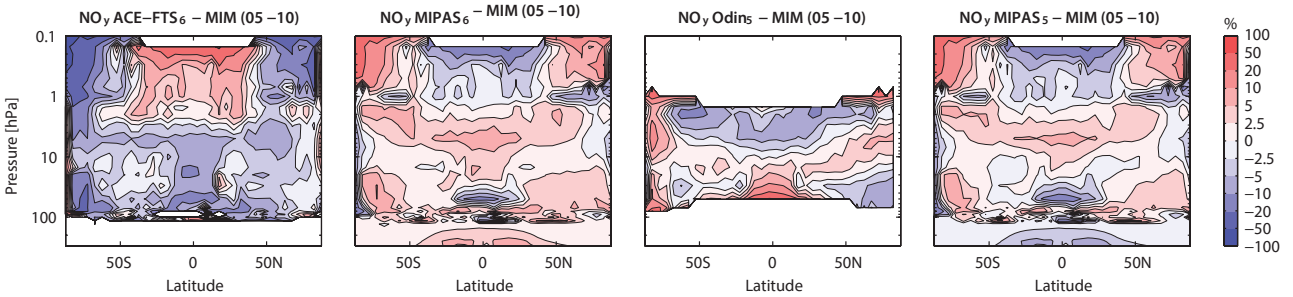

Figure 4.17.2: Cross sections of annual zonal mean NO_y differences for 2005-2010. *Annual zonal mean NO_y differences between the individual instruments and the MIM are shown. Note that $MIPAS_5$ is not included in the MIM.*

At high latitudes, the datasets agree less well than in the tropics. In the SH high latitude winter displayed here, NO_y has an S-shaped profile caused by Energetic Particle Precipitation NO_y intrusions, which is seen differently by the three instruments. In particular, the position of the MS maximum varies between 20 hPa (ACE-FTS and Odin) and 3 hPa (MIPAS). Furthermore, Odin shows the USLM minimum at a much lower level (2 hPa) than the other two instruments (0.5-0.2 hPa). Overall, the high latitude differences range between ±20% except for the LS where ACE-FTS has a large offset of around -60%. The similarity of the August monthly mean deviations and the annual mean deviations indicates that the negative offset found for annual mean ACE-FTS at the SH high latitudes between 100 and 50 hPa (**Figure 4.17.2**) is not related to annual sampling patterns.

At 1 hPa, the largest fraction of NO_y is located in the NO_x family while the other nitrogen species have smaller atmospheric abundances. Both nitrogen families, NO_y and NO_x, are available from MIPAS and ACE-FTS and are displayed in **Figure 4.17.4** as meridional profiles at 1 hPa for April 2005-2010. The NO_y profiles from the two instruments (upper row) agree very well, with differences of less than ±5% except for the high latitudes. The comparison of the NO_x profiles (middle row) also shows good agreement, but slightly larger relative differences of up to ±10% are found. The 1 hPa level has been chosen here because of the low diurnal variations NO_x displays at this level (±5%) in the tropics and mid-latitudes. The remaining fraction of the NO_y family (lower row) is calculated here as the difference between the NO_y and NO_x fields and is referred to as the residual in the following. The residual consists basically of the sum of HNO_3, HNO_4, $2N_2O_5$ and $ClONO_2$ and is expected to have similar (but inverted) diurnal variations as NO_x itself. The absolute differences of the MIPAS and ACE-FTS residuals are smaller than the absolute differences of the NO_y and NO_x families. As expected, the residuals act to remove the impact of the diurnal cycle and reduce the differences between the two instruments found in NO_x when added to give NO_y. Relative to NO_x the residual deviations are quite small (~5%) and are therefore consistent with deviations expected due to the diurnal cycle in the species and different LSTs of the measurements.

4.17.3 NO_y evaluations: Seasonal cycles

Figure 4.17.5 displays the NO_y seasonal cycles at high and tropical latitudes at 50 hPa. NO_y exhibits a strong seasonal cycle in the SH high latitude LS due to chemistry and transport effects. During polar night, descending air masses

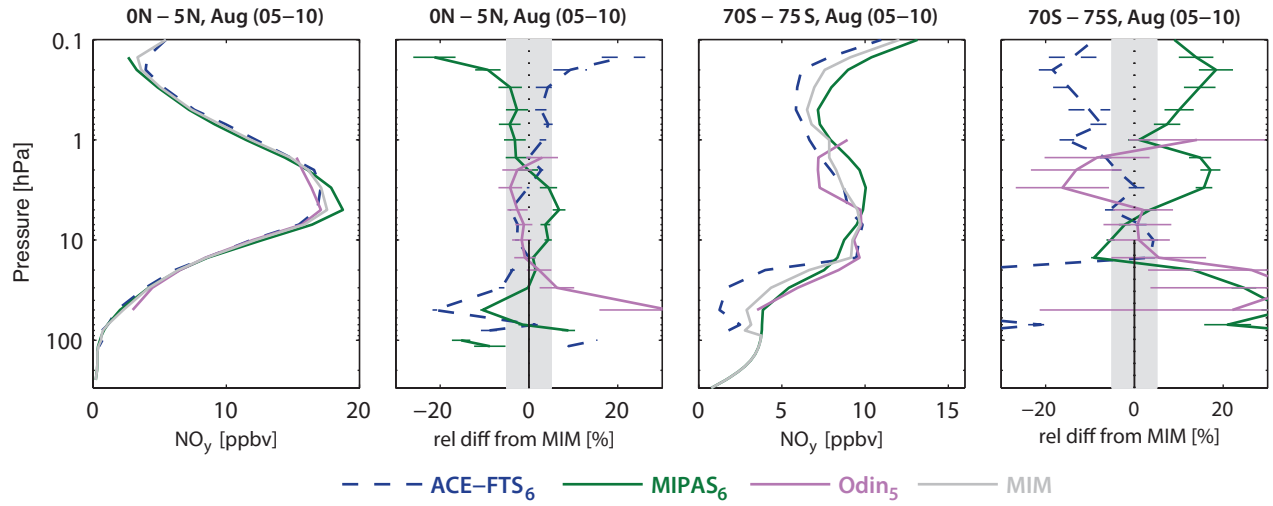

Figure 4.17.3: Vertical profiles of monthly zonal mean NO_y for 2005-2010. *Zonal mean NO_y profiles for 0°N-5°N and 70°S-75°S for August are shown in panels 1 and 3. Relative differences between the individual instruments and the MIM profiles are shown in panels 2 and 4. Bars indicate the uncertainties in each climatological mean based on the SEM. The grey shaded area indicates where relative differences are within ±5%.*

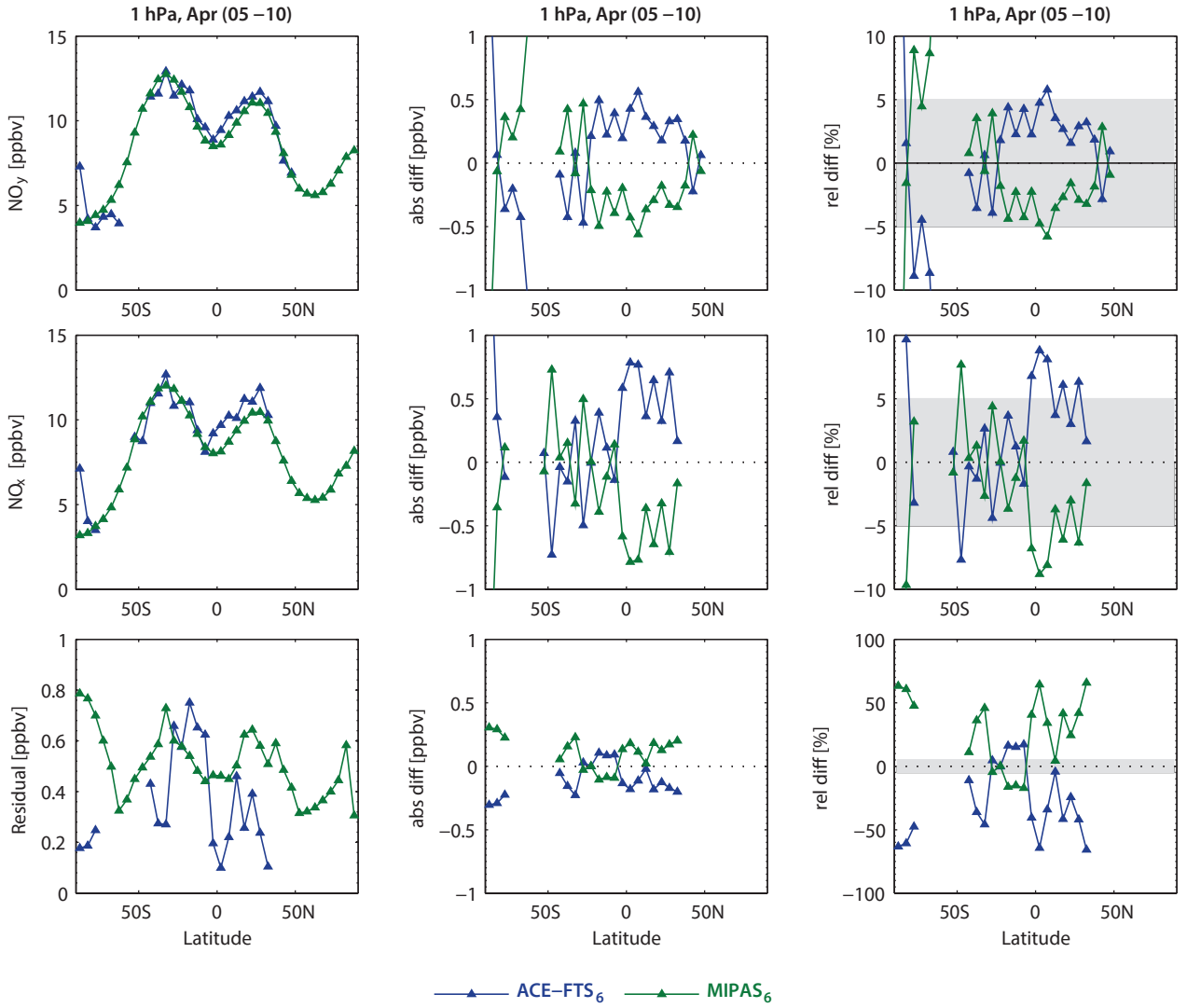

Figure 4.17.4: Meridional profiles of monthly zonal mean NO_y, NO_x, and their residual for 2005-2010. *Meridional profiles of monthly zonal mean NO_y, NO_x, and their residual at 1 hPa for April 2005-2010 are shown in the left column. Absolute (middle column) and relative (right column) differences between the two instruments (ACE-FTS and MIPAS) and their MIM are also shown for the two nitrogen families and the residual. The grey shaded area indicates where relative differences are smaller than ±5%.*

within the polar vortex bring higher NO_y concentrations into the LS, but this increase is counteracted by the formation of type I PSCs, which removes HNO_3 particles from the gas phase and causes a pronounced minimum in SH winter/spring. All three datasets show the same overall shape of the seasonal cycle. However, there are some differences in SH summer after renitrification when values stay approximately constant over three months; NO_y from ACE-FTS is smaller than from the other two datasets. There are also differences in SH winter when Odin shows larger values, and does not report the same level of HNO_3 removal as the other two datasets.

In the NH polar regions, the less frequent PSC type I formation leads to the opposite seasonal cycle. Here the downward transport dominates in autumn, producing a weak maximum at the beginning of winter. Later in the NH winter, removal of HNO_3 leads to a weak decline of the total nitrogen, which levels off in May. The main difference from the Antarctic counterpart is that there is no indication of strong renitrification in late spring and summer. MIPAS and ACE-FTS agree reasonably well in terms of amplitude but show some offset regarding phase and absolute values - MIPAS is larger and starts to decline earlier. Odin, on the other hand, displays an opposite seasonal cycle with a minimum in winter and spring that is not consistent with our understanding of polar processes determining the NO_y abundance. Note that the SMR HNO_3 seasonal cycle in this region is in general consistent with the other HNO_3 datasets with slightly smaller values during NH winter (see **Figure 4.13.7** in *Section 4.13*). Additionally, the OSIRIS NO_2 seasonal cycle in this region agrees very well with the other NO_2 datasets. Thus the deviations of the Odin NO_y seasonal cycle are not consistent with the underlying SMR HNO_3 or OSIRS NO_2 data, but are very likely introduced through the use of the photochemical model during the climatology compilation.

In the tropics, transport variations are expected to cause a weak annual cycle as seen by MIPAS. In addition to the relatively large absolute deviations between the datasets, there is no agreement on the seasonal signal, and both ACE-FTS and Odin show a semi-annual cycle with maxima in June/July and December/January, respectively. Note that 50 hPa is at the lower edge of the SMR measurement range for the HNO_3 product used to derive the Odin NO_y climatology. At higher levels (*e.g.*, 30 hPa) in the tropics, the Odin seasonal cycle agrees better with MIPAS, exhibiting the expected annual cycle. However, in the NH polar regions Odin agrees better with the other two datasets only above 10 hPa.

4.17.4 NO_y evaluations: Interannual variability

In addition to the absolute differences between the climatologies, it is important to evaluate how well the instruments detect signals of interannual variability. **Figure 4.17.6** shows the deseasonalised NO_y anomaly time series from 2005 to 2010 at polar and tropical latitudes at different pressure levels. The comparison in the tropics (10°S-10°N) at 10 hPa shows excellent agreement between the three datasets with only occasional deviations for ACE-FTS. The pronounced QBO signal is recorded with the same amplitude and phase by all satellite datasets.

At polar latitudes, the datasets also agree well, but stronger deviations between the three anomaly time series can be seen. For most years, the largest interannual anomalies occur during polar winter, related to the strong interannual variability of the chemical and dynamical processes that impact the polar stratospheric nitrogen budget. In both hemispheres, differences between ACE-FTS and MIPAS are also largest in polar winter months, a time period that is not covered by Odin. The maximum anomalies in winter are followed by a slow decay of the signal during spring and summer until the next autumn, which is a characteristic of HNO_3 (see *Section 4.13*). During spring and summer the three instruments agree better, and in most cases follow the winter anomaly signal given by MIPAS and not the one suggested by ACE-FTS.

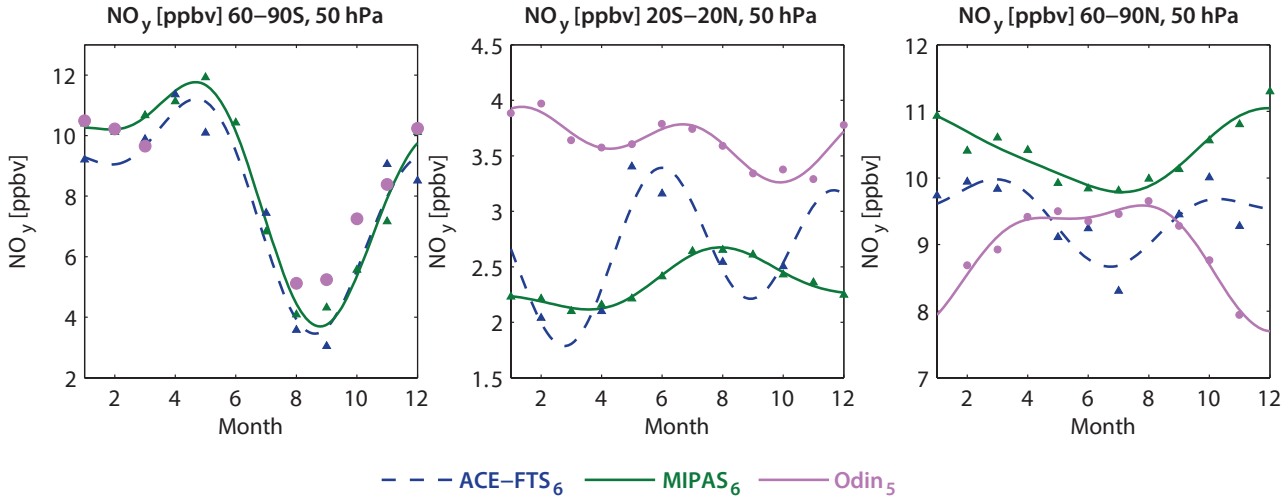

Figure 4.17.5: Seasonal cycle of NO_y for 2005-2010. *Seasonal cycle of monthly zonal mean NO_y for 60°S-90°S (left column), 20°S-20°N (middle column) and 60°N-90°N (right column). At SH high latitudes at 50 hPa, Odin does not provide sufficient coverage for fitting a seasonal cycle.*

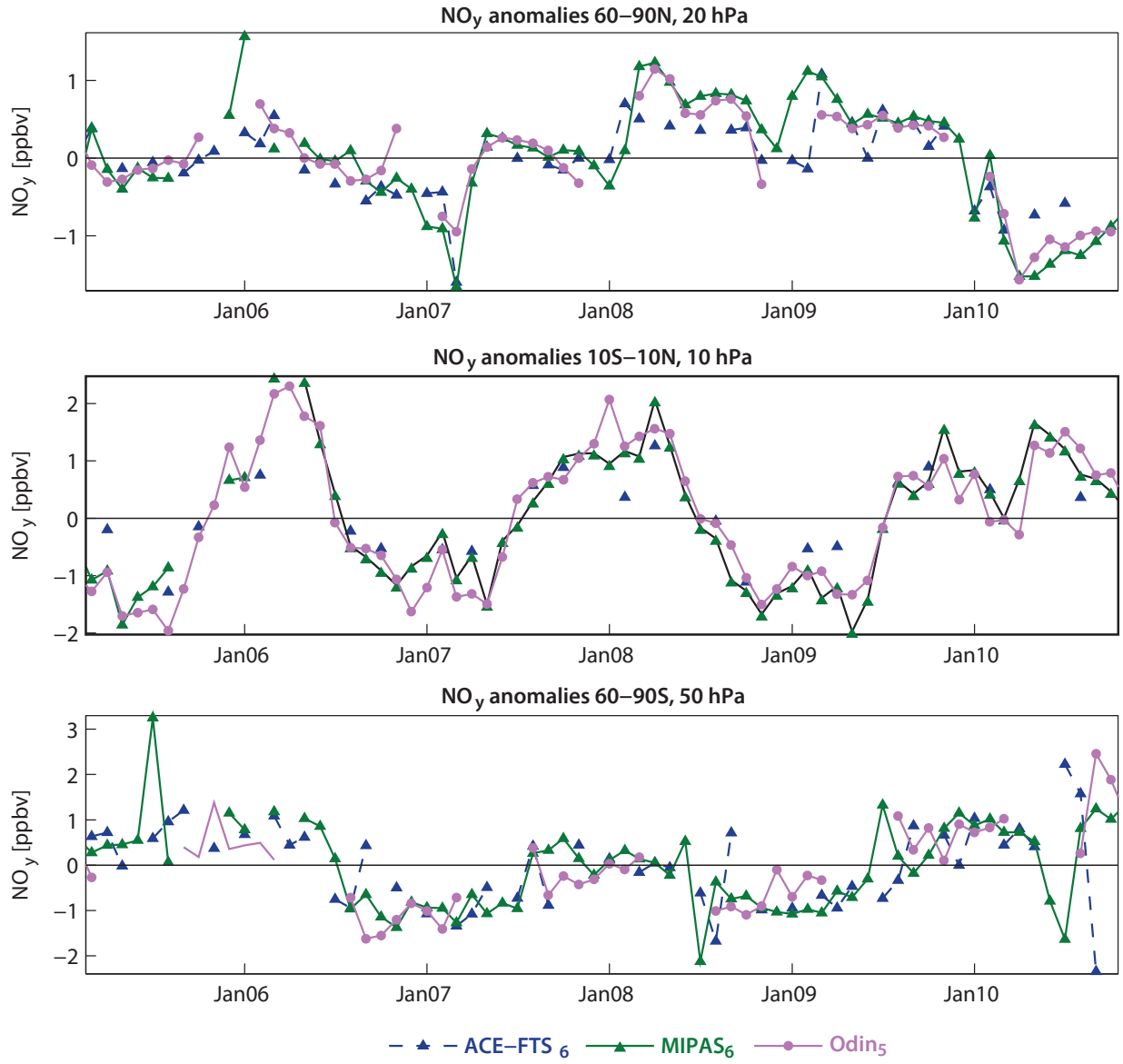

Figure 4.17.6: Time series of NO_y anomalies for 2005-2010. *Monthly zonal mean deseasonalised NO_y anomalies at 20 hPa for 60°N–90°N, at 10 hPa for 10°S-10°N, and at 50 hPa for 60°S-90°S.*

4.17.5 Summary and conclusions: NO_y

A comprehensive comparison of three NO_y profile climatologies (from ACE-FTS, MIPAS, and Odin) has been carried out. Overall findings on the systematic uncertainty in our knowledge of the NO_y mean state and important characteristics of the individual datasets are presented in the following summary in the form of two synopsis plots. The first summary plot (**Figure 4.17.7**) provides information on the NO_y mean state and the uncertainty derived from the spread between the datasets. The second summary plot (**Figure 4.17.8**) shows specific inter-instrument differences in the form of the deviations of the instrument climatologies relative to the MIM climatology. For each instrument and selected region, the deviation relative to the MIM is given in form of the median (mean) difference over all grid points in this region. Additionally, for each instrument the spread of the differences over all grid points in this region is presented. Note that both pieces of information (average deviation and spread) are important for a meaningful assessment of inter-instrument differences. A detailed discussion of the rationale behind these summary plot evaluations can be found in *Section 3.3.5*.

Atmospheric mean state

The assessment of the atmospheric NO_y annual mean state is based on three climatologies with two datasets (ACE-FTS, MIPAS) constructed purely from measurements while the other dataset (Odin) is based upon NO_2 and HNO_3 measurements and chemical box model simulations of the remaining NO_y species.

Lower stratosphere (100-30 hPa)

In the LS, the NO_y abundance decreases with decreasing altitude, but the agreement in the mid-latitudes and NH polar latitudes is overall very good, with a spread of ±5%. The

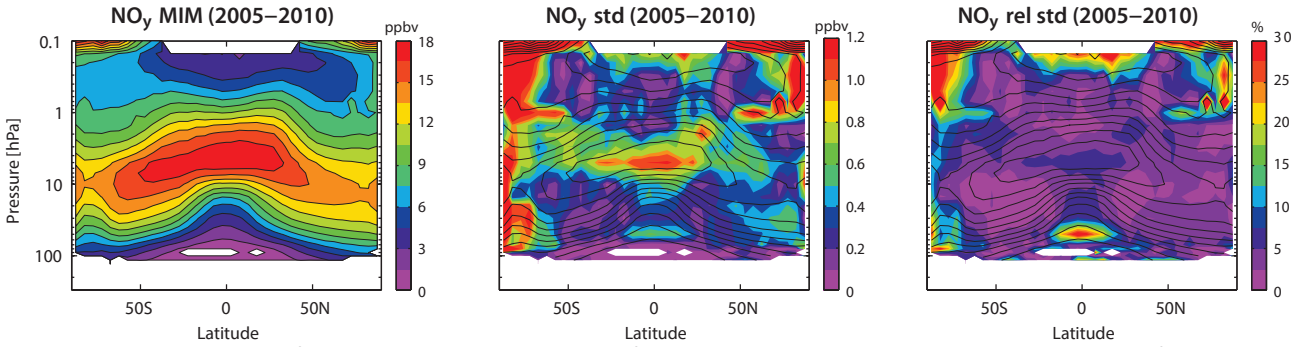

Figure 4.17.7: Summary of NO_y annual zonal mean state for 2005-2010. *Annual zonal mean cross section of the NO_y MIM for 2005-2010 is shown in the left panel. Additionally, the standard deviation over all three instruments is presented in the middle panel. Relative standard deviation (calculated by dividing the absolute standard deviation by the MIM) is shown in the right panel. Black contour lines in the right panels give the MIM distribution. Instruments included are ACE-FTS$_6$, MIPAS$_6$ and OSIRIS/SMR(Odin$_5$). The MIM and standard deviation are only displayed for regions where at least two instruments provide measurements.*

three datasets show a larger spread in the tropical LS with an inter-instrument spread of up to ±30% and at the SH high latitudes related to large deviations during polar winter.

Middle and upper stratosphere (30-1 hPa)

The uncertainty in our knowledge of the atmospheric NO_y annual mean state is smallest in the MS/US (**Figure 4.17.7**, right panel) with a 1σ multi-instrument spread in this region of mostly up to ±5%, in some regions up to ±7.5%. In the SH highest latitude bands (south of 80°S) the spread can reach values of ±12.5%.

Lower mesosphere (1-0.1 hPa)

At high latitudes, and in particular in the SH, the instruments show larger deviations with a spread of up to ±30%. In the mid-latitudes and tropics, on the other hand, the datasets agree very well and deviations are comparable to the MS/US.

Instrument-specific conclusions

ACE-FTS is generally lower compared to MIPAS and Odin, with mean deviations of around -5% except for the tropical and mid-latitude US and LM, where it shows positive deviations from MIPAS. The solar occultation instrument displays a similar seasonal cycle as MIPAS at high latitudes but an unrealistic semi-annual cycle in the tropical LS. Inter-annual anomalies from ACE-FTS differ from MIPAS in polar winter in a way that might be unrealistic considering the development of the anomaly in the following months.

MIPAS measurements are mostly on the high side (+5%) except for the tropical and mid-latitude US and LM. A

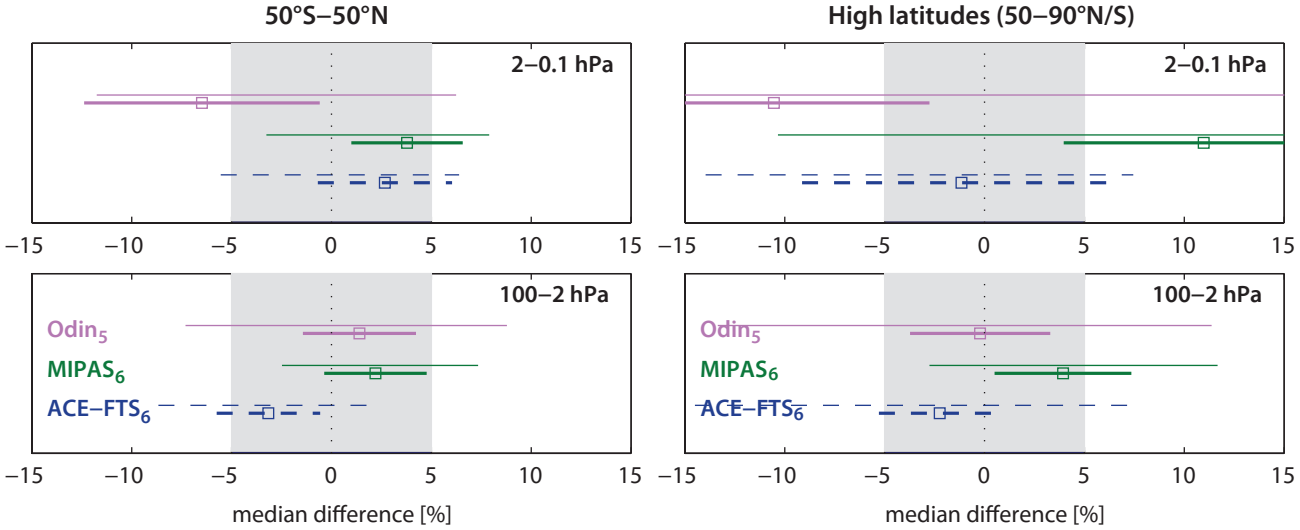

Figure 4.17.8: Summary NO_y differences for 2005-2010. *Over a given latitude and altitude region the median (squares), median absolute deviation (MAD, thick lines), and the standard deviation (thin lines) of the monthly mean relative differences between an individual instrument-climatology and the MIM are calculated. Results are shown for the lower (50°S-50°N) and the higher (50°S-90°S and 50°N-90°N) latitudes and for two different altitude regions from the LS up to the LM between 100 and 0.1 hPa for the reference period 2005-2010. The grey shaded area indicates where mean and median relative differences are within ±5%.*

comparison of the MIPAS and ACE-FTS nitrogen families (NO_y and NO_x) at 1 hPa suggests that the NO_y differences between the two instruments are consistent with the slightly larger NO_x differences, which are within the uncertainty given by the diurnal variations and differences in local times of measurements.

The **Odin** NO_y climatology covers the LS to US and is mostly in the mid-range between the other two datasets. In SH winter/spring, Odin reports higher values compared to ACE-FTS and MIPAS but shows similar signals of interannual variability. In the NH middle and upper stratosphere, the NO_y seasonal cycle from Odin shows severe differences compared to the other two datasets.

4.18 Hydrogen chloride – HCl

Hydrogen Chloride (HCl) is the main reservoir gas for reactive chlorine in the Earth's atmosphere. In the troposphere, the main sources of HCl are the ocean (acidification of salt spray) and volcanic activity; however, HCl is readily removed by wet scavenging, and hence it has a short lifetime and a relatively low concentration in the troposphere. In the stratosphere, HCl is the most abundant inorganic chlorine species with a lifetime of approximately one month. Its main source is the photolysis of anthropogenic chlorofluorocarbons (CFCs, see *Sections 4.5* and *4.6*) or hydrochlorofluorocarbons (HCFCs) and the subsequent reaction of the generated Cl-radical with methane (CH_4, see *Section 4.3*). HCl is processed on polar stratospheric clouds (PSCs) during winter, thereby releasing reactive chlorine atoms that can destroy ozone, and create the Antarctic ozone hole during SH springtime. Hence, the abundance of HCl (scaled to yield total reactive chlorine Cl_y) in the stratosphere is often used as a diagnostic for chemistry-climate models [*SPARC*, 2010].

4.18.1 Availability of HCl measurements

Measurements of HCl available to the SPARC Data Initiative start in 1991. The longest time series comes from HALOE, and the only instruments that overlap with this data record and have ongoing measurements are ACE-FTS and Aura-MLS. SMILES offers two HCl isotopologue products (from $H^{35}Cl$ and $H^{37}Cl$, named SMILES(1) and SMILES(2), respectively) for comparison during its mission time between October 2009 and April 2010.

Tables 4.18.1 and **4.18.2** compile information on the availability of HCl measurements including time period, height range, vertical resolution, and references relevant for the data product used in this report.

4.18.2 HCl evaluations: Zonal mean cross sections, vertical and meridional profiles

The HCl zonal mean cross section evaluations have been carried out using climatologies averaged over the years

Table 4.18.1: Available HCl measurement records from limb-sounding satellite instruments between 1978 and 2010. *The red filling in each grid box indicates the temporal and vertical coverage (within the pressure range 300-0.1 hPa) of the respective instrument.*

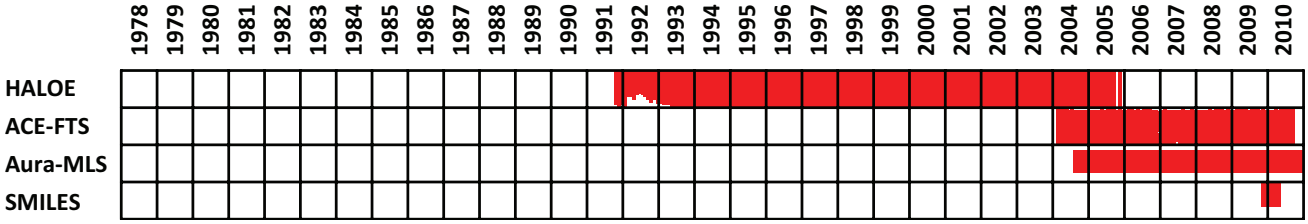

Table 4.18.2: Time period, vertical range, vertical resolution, references and other comments for HCl measurements.

Instrument	Time period	Vertical range	Vertical resolution	References	Additional comments
HALOE V19	Oct 91 – Nov 05	up to 70 km	3.5 km	*Grooß and Russell*, 2005	
Aura-MLS V3.3	Jul 04 –	100 – 0.32 hPa (16 - 57 km)	3 km (in LS) 4 – 6 km (above 1 hPa)	*Froidevaux et al.*, 2008b (for V2.2) *Livesey et al.*, 2011 (for V3.3 update)	The MLS continuous band 14 HCl data used here are not suitable for upper stratospheric trend studies (see refs.). Values at 147 hPa are biased very high at low latitudes, but are probably more useful at high latitudes; all values below 100 hPa were flagged with bad value (-999.) for the current climatology.
ACE-FTS V2.2	Mar 04 –	8 – 57 km	3 – 4 km	*Mahieu et al.*, 2008	
SMILES HCl-35 V2.1.5 SMILES(1) HCl-37 V2.1.5 SMILES(2)	Oct 09 – Apr 10	100 hPa – 0.0001 hPa (16 – 110 km)	3 km	*Kreyling et al.*, 2013	Diurnal variation is observed.

2002-2008. HCl exhibits relatively small trends during this time period and averaging over a longer time period decreases the sampling bias. As shown in **Figure A4.18.1** in *Appendix A4*, the instruments show similar although somewhat noisier behaviour when only the year 2005 is considered. Additionally, vertical and meridional profiles are evaluated.

Note that SMILES measured over only a few months during 2009 and 2010 and hence was not included in the calculation of the MIM. SMILES(1) HCl is based on $H^{35}Cl$ isotopologue data and multiplied with a scaling factor of 1/0.7578, while SMILES(2) is based on $H^{37}Cl$ isotopologue data and multiplied with scaling factor of 1/0.2422. The scaling factors account for the natural isotopic abundance in the atmosphere.

HALOE, ACE-FTS, Aura-MLS, and SMILES (2002-2008)

Figure 4.18.1a shows the annual zonal mean HCl climatologies for 2002-2008. The relative differences between the instruments and the MIM are displayed in **Figure 4.18.1b**. **Figure 4.18.1a** reveals that HCl is a mostly stratospheric trace gas exhibiting very low mixing ratios in the troposphere. HCl increases with increasing altitude, opposite to its source gases that consist mostly of CFCs (see *Sections 4.5* and *4.6*). Below 5 hPa, the trace gas isopleths slope downwards between the tropics and the extra-tropics as expected for intermediate to long-lived trace gases. The instruments seem to agree well through most of the LS and MS, however show less agreement in the USLM. ACE-FTS, for example, shows much larger values at highest altitudes than the other instruments providing measurements in this region. This is a known feature reported in *Froidevaux et al.* [2008b] and this difference is reduced in the more recent ACE-FTS data version 3. The two SMILES datasets reveal very similar structures to the overall HCl distributions, however do not show increasing values in the LM as seen in the other instruments.

The difference plots in **Figure 4.18.1b** reveal upon close inspection that Aura-MLS and ACE-FTS show excellent agreement within ±2.5% through most of the stratosphere and into the LM up to the altitudes where Aura-MLS is available. Exceptions to this are the Southern Hemisphere polar region and the LS, where ACE-FTS (Aura-MLS) shows a slightly larger negative (positive) departure from the MIM of ±20%. The larger differences in these regions may be due to sampling bias (as suggested by smaller monthly values seen in **Figure A4.18.2** in *Appendix A4*). HALOE exhibits negative departures from the MIM with values below -10%. Validation studies of earlier versions of HALOE (v17) have already pointed toward a low bias in HALOE when compared to other correlative measurements such as balloon and ATMOS measurements, with differences between 10% and 20% [*Russell et al.*, 1996b]. The somewhat low HALOE (v19) HCl values have also been discussed in a number of previous studies, including those by *Froidevaux et al.* [2006; 2008b] for Aura-MLS versus HALOE, by *McHugh et al.* [2005] and *Mahieu et al.* [2008] for ACE-FTS versus HALOE, and by *Lary et al.* [2007], who used various space-based measurements in a neural network analysis. Both SMILES data products used in the SPARC Data Initiative show similar values as HALOE, with negative deviations from the MIM through most of the USLM. However, a newer version of SMILES with a better altitude registration tends to increase HCl, so that the differences versus Aura MLS are much smaller. Therefore, HALOE can be considered typically lower than all other three instrument retrievals. In the UTLS, SMILES shows structures in the deviations from the MIM that resemble the impact of different QBO phases on trace gas distributions [*cf., Randel et al.*, 1999]. Indeed a strong easterly phase was observed during 2009/2010. An evaluation of monthly cross sections

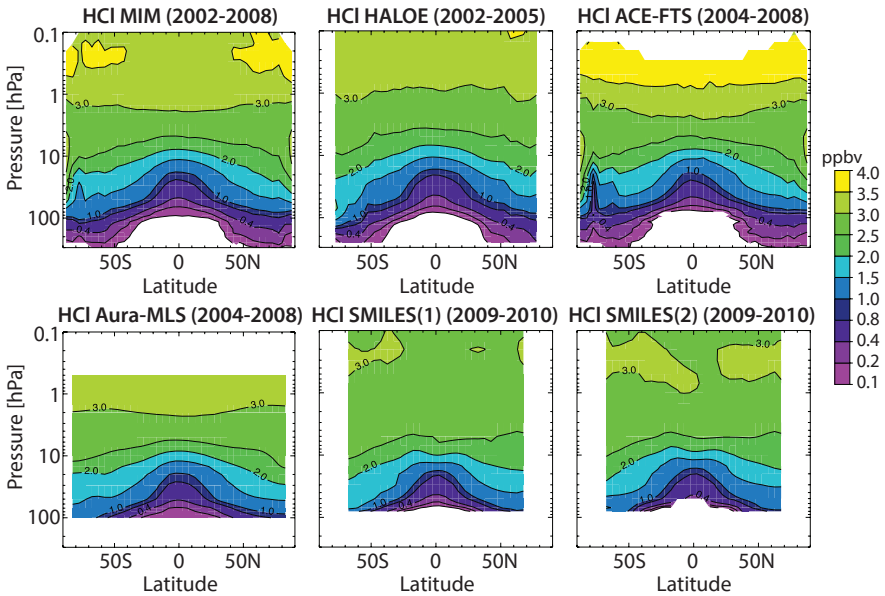

Figure 4.18.1a: Cross sections of annual zonal mean HCl for 2002-2008. *Annual zonal mean HCl cross sections are shown for 2002-2008 for the MIM, HALOE, ACE-FTS, Aura-MLS and SMILES. Note that the instruments provide data for different time periods as indicated in the panel titles. SMILES data have not been included in the MIM.*

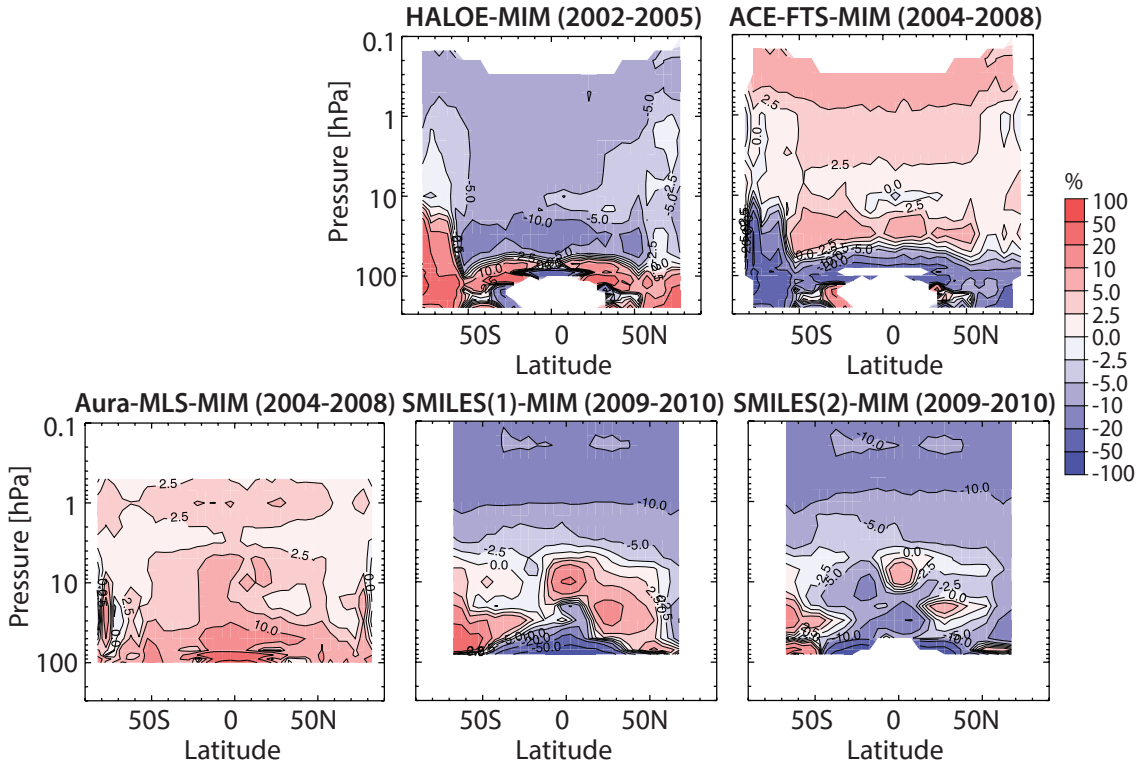

Figure 4.18.1b: Cross sections of annual zonal mean HCl differences for 2002-2008. *Annual zonal mean HCl differences between the individual instruments (HALOE, ACE-FTS, Aura-MLS, and SMILES) and the MIM are shown. SMILES data have not been included in the MIM.*

in the years 2009 and 2010 shows that these QBO-like structures disappear in the SMILES deviations from the MIM (see **Figure A4.18.2** in *Appendix A4*).

The altitude profiles shown in **Figure 4.18.2** support the above findings and reveal further structural details on shorter (monthly) time scales. ACE-FTS and Aura-MLS

Figure 4.18.2: Vertical profiles of zonal mean HCl for 2002-2008. *Zonal mean HCl profiles for January 25°S-30°S and April 25°N-30°N (upper panels), and for April 60°S-65°S and September 65°N-70°N (lower panels) are shown together with their differences from the MIM. The grey shading indicates the ±5% difference range. Bars indicate the uncertainties in the relative differences (expressed here as ±1 SEM). SMILES is not included in the MIM since it measures during a limited time period in 2009-2010 only.*

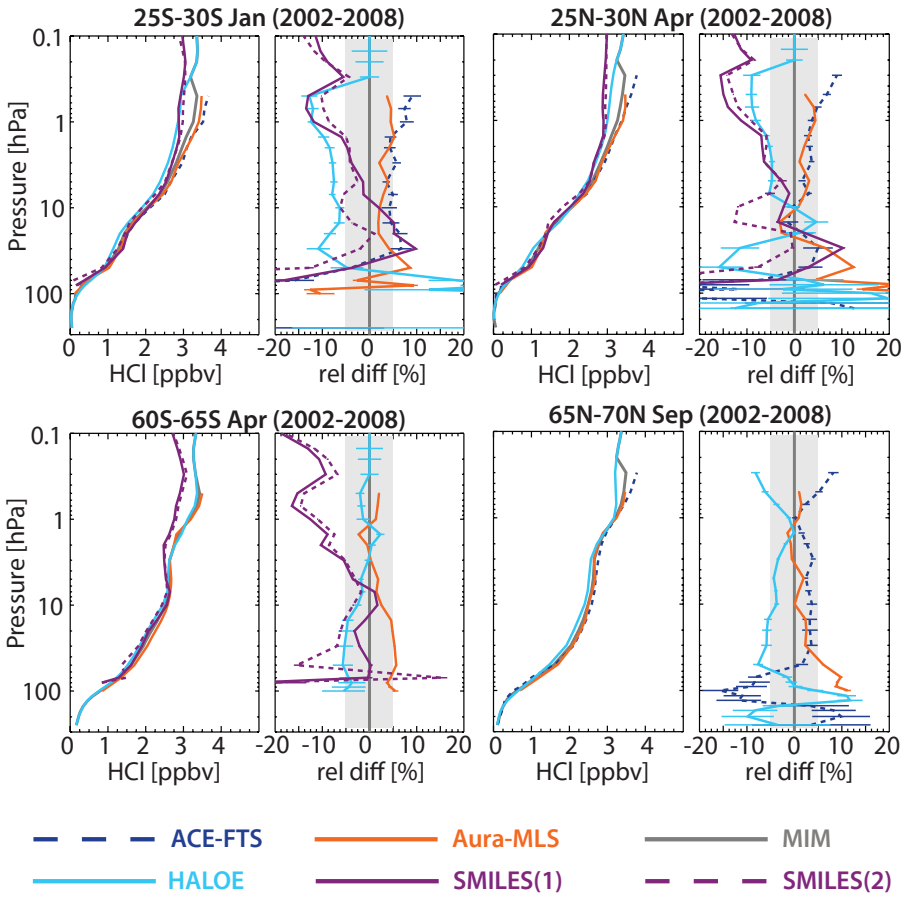

agree well throughout the stratosphere and the LM for all months for which ACE-FTS is available, while HALOE is biased low by about 10%-15% except for the SH high latitudes. In the LS, however, ACE-FTS and Aura-MLS drift apart, with ACE-FTS (Aura-MLS) showing negative (positive) departures from the MIM as already seen in the annual mean cross sections. HALOE also shows a positive departure from the MIM in the UTLS. Both SMILES products tend to agree with ACE-FTS and Aura-MLS in the LS, but show negative deviations from the MIM above, with values more similar to those of HALOE. Monthly deviations can exceed annual mean deviations locally.

The meridional profiles in **Figure 4.18.3** illustrate how the relative differences from the MIM are decreasing with increasing altitude. At 100 hPa, HALOE and Aura-MLS show relative differences from the MIM in the extra-tropics and tropics of up to ±25% and ±80%, respectively. All instruments show relative differences around ±15% at 10 hPa, and around ±8% at 1 hPa. The relative differences increase again above 1 hPa. Note that the improved SMILES retrieval of HCl is expected to bring SMILES closer to Aura-MLS and ACE-FTS.

4.18.3 HCl evaluations: Latitude-time evolution

Figure 4.18.4 shows the latitude-time evolution of HCl at 50 hPa. Only Aura-MLS has frequent enough spatial and temporal sampling to provide year-around coverage at all latitudes. Nevertheless, the comparison with the interpolated fields from HALOE and ACE-FTS show consistent features. Generally, there is not much intra-annual variability seen in the field (except in the polar regions). As expected from the annual zonal mean cross sections, the isopleths are shaped by the Brewer-Dobson circulation, with lower values in the tropics than in the extra-tropics. In the tropics, HALOE shows somewhat lower values than Aura-MLS. However, a strong minimum in HCl is found in the polar vortex region during Southern Hemisphere winter, a feature consistently reproduced by Aura-MLS and ACE-FTS, and to some extent by HALOE. The physical explanation for the minimum in HCl is the build-up of polar stratospheric clouds (PSCs) during winter, on which HCl (together with HNO_3) reacts to release active chlorine [*e.g.*, *Santee et al.*, 2008]. The activation of chlorine atoms then leads to the severe catalytic depletion of ozone (and the Antarctic ozone hole) during polar spring.

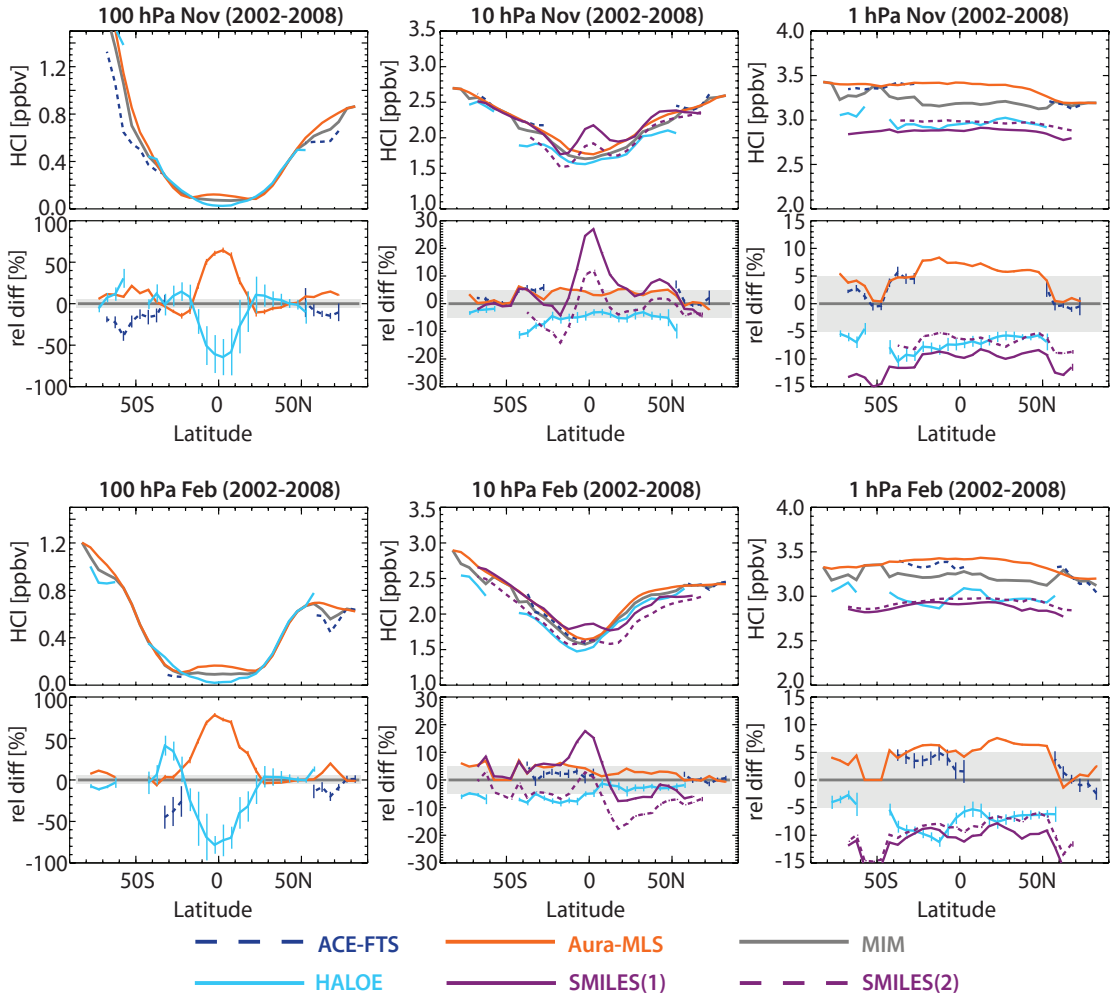

Figure 4.18.3: Meridional profiles of zonal mean HCl for 2002-2008. *Meridional zonal mean HCl profiles at 100, 10, and 1 hPa for November (upper row) and February (lower row). Differences between the individual instruments (HALOE, ACE-FTS, Aura-MLS, and SMILES) and the MIM are shown in the lower panels. The grey shading indicates the ±5% difference range. Bars indicate the uncertainties in the relative differences (expressed here as ±1 SEM). Note, SMILES is not included in the MIM.*

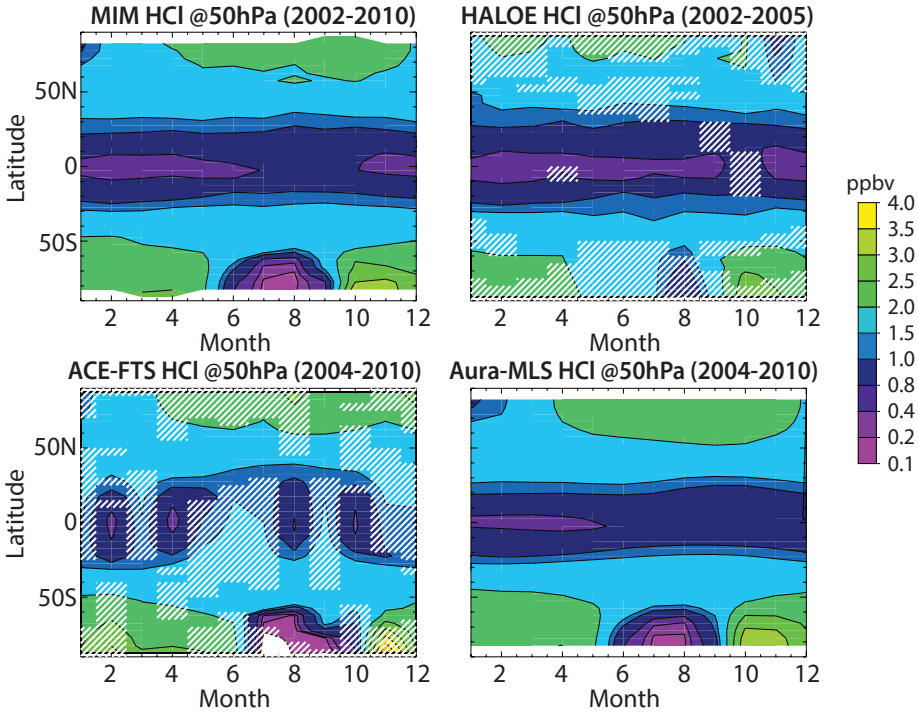

Figure 4.18.4: Latitude–time evolution of HCl at 50hPa. *The latitude-time evolution of HCl at 50 hPa is shown for the MIM (2002-2010 average) in the leftmost upper panel and the instruments HALOE, ACE-FTS, and Aura-MLS. HALOE and ACE-FTS show interpolated fields, with hatched regions indicating where no measurements are available.*

4.18.4 HCl evaluations: Interannual variability

In addition to climatological differences, the instrument performances in reproducing interannual variability is tested. While there is not enough overlap to thoroughly evaluate HALOE versus the later instruments and SMILES does not provide a long enough time series to be included in the comparison, one can deduce some information from the comparison on the behaviour of Aura-MLS and ACE-FTS. **Figure 4.18.5** shows anomalies for the different instruments at different pressure levels in the polar region of the Northern Hemisphere. Aura-MLS and ACE-FTS agree well, although ACE-FTS exhibits less frequent sampling and incomplete

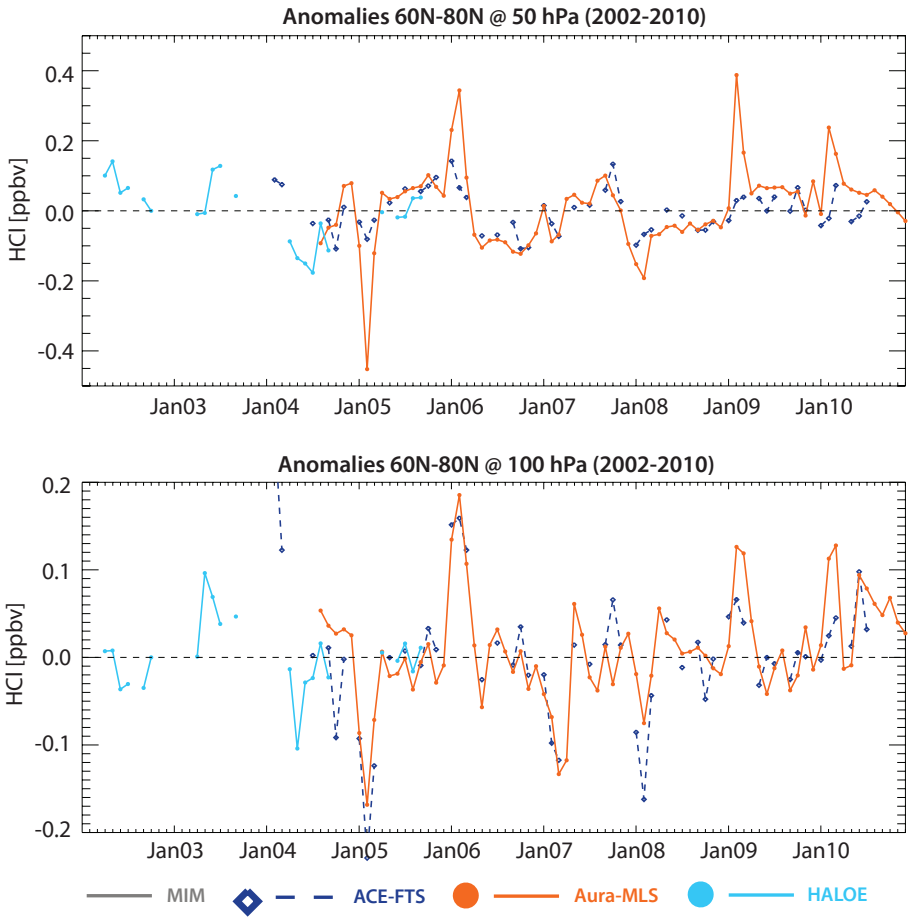

Figure 4.18.5: Time series of deseasonalised HCl anomalies in the Northern Hemisphere extra-tropics. *Deseasonalised HCl anomalies are shown for 60°N-80°N at 50 hPa (upper panel) and 100 hPa (lower panel).*

annual information. January maxima and minima in the data record are somewhat better resolved by ACE-FTS at 100 than at 50 hPa. The observed maxima stem from the descent of HCl-rich air during warmer winters, while the minima indicate strong processing on polar stratospheric clouds. The temperatures during the 2004/2005 Arctic winter for example were at a record low, with much higher PSC abundances than in other years. In the NH polar latitudes, the anomalies show the strongest disagreement during the winter months. This could be related to a different sampling of the polar vortex by the two instruments. Note that ACE-FTS is only of limited use when looking at interannual variability in the tropics, where the instrument's temporal coverage is more limited.

4.18.5 Summary and conclusions: HCl

HCl climatologies from four limb-sounders (HALOE, ACE-FTS, Aura-MLS, and SMILES) have been compared within the SPARC Data Initiative. SMILES measures two isotopologues ($H^{35}Cl$ and $H^{37}Cl$), which have been evaluated separately (using the SMILES(1) and SMILES(2) notation). Overall findings on the systematic uncertainty in our knowledge of the HCl mean state and important characteristics of the individual datasets are presented in the following summary including two synopsis plots as discussed in the previous trace gas sections and detailed in *Section 3.3.5*.

Atmospheric mean state

The uncertainty in our knowledge of the atmospheric HCl annual mean state as derived from the four satellite instruments and measured by the multi-instrument spread is smallest in the MS and US, and smaller in the polar regions (±4%) than in the tropics (±8%) (see **Figure 4.18.6**). Good knowledge is obtained in the LM and tropical LS, where the uncertainty is about ±10-15%. The uncertainty is largest

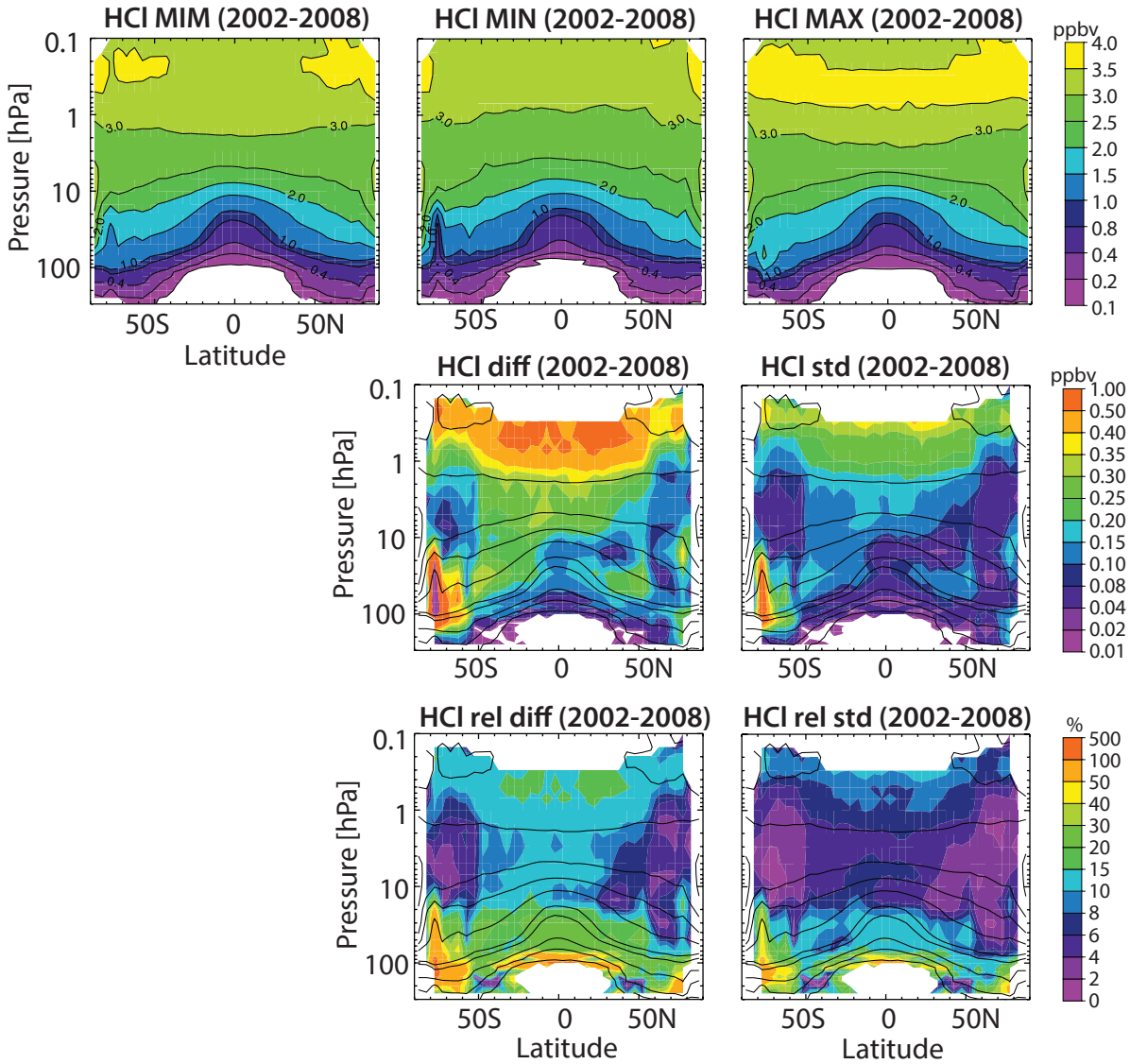

Figure 4.18.6: Summary of HCl annual zonal mean state for 2002-2008. *Annual zonal mean cross sections for 2002-2008 of the MIM, minimum (MIN), and maximum (MAX) HCl values are shown in upper row. The absolute and relative differences over all instruments (MAX-MIN) and the absolute and relative standard deviations over all instruments are presented in the middle and lower row, respectively. Black contours in lower panels repeat the MIM distribution. Instruments considered are ACE-FTS, Aura-MLS, and HALOE. Note SMILES(1) and SMILES(2) are not included in the MIM due to their limited sampling.*

in the Southern Hemisphere polar vortex region and the UTLS (reaching values higher than ±50%). The large uncertainty in the UTLS may be explained by the relatively small HCl mixing ratios that the instruments have to be able to detect.

Performance by region

In the USLM (0.1-5 hPa), median values are well defined as indicated by small MADs. The derived inter-instrument differences, which lie mostly within ±10%, are therefore well defined as well. SMILES shows somewhat larger deviations from the MIM, especially in the tropics.

In the MS (5-30 hPa), excellent agreement is found between the instruments in the extra-tropics. In the tropics, the uncertainty increases to ±8%. However, large MADs indicate that these inter-instrument differences are not well defined and local difference can be much larger.

In the LS (30-100 hPa), good agreement within ±10% is found in the extra-tropics, but considerable disagreement with inter-instrument differences of up to ±40% is found in the tropics.

In the UT (100-300 hPa), only HALOE and ACE-FTS provide measurements. HALOE (ACE-FTS) shows mostly positive (negative) differences in this region reaching mean values of up to ±20%. Note that the median values are not well defined as seen in relatively large MADs. Also, Aura-MLS HCl data at these lower altitudes may be useful at high latitudes, but they have a high bias at low latitudes [see *Froidevaux et al.*, 2008b] and hence were not included in the SPARC Data Initiative climatologies. This issue could also explain the tendency for Aura-MLS HCl values at 100 hPa to be on the high side in the tropics.

Instrument-specific conclusions

HALOE shows a negative bias throughout the stratosphere and the LM, with relative differences with respect to the MIM of between -5% and -10%. The negative bias in HALOE is known from previous studies and also agrees in magnitude [*Russell et al.*, 1996b; *Lary et al.*, 2007]. For pressures larger than 100 hPa, HALOE shows a positive deviation from the MIM (which is mostly determined by the comparison to ACE-FTS).

Below 30 hPa, **ACE-FTS** shows much lower values than the other instruments in the extra-tropical UTLS. Above 30 hPa, however, it shows excellent agreement with the Aura-MLS dataset.

As noted previously, **Aura-MLS** and ACE-FTS show excellent agreement with each other, except in the LS where Aura-MLS shows much higher values than ACE-FTS.

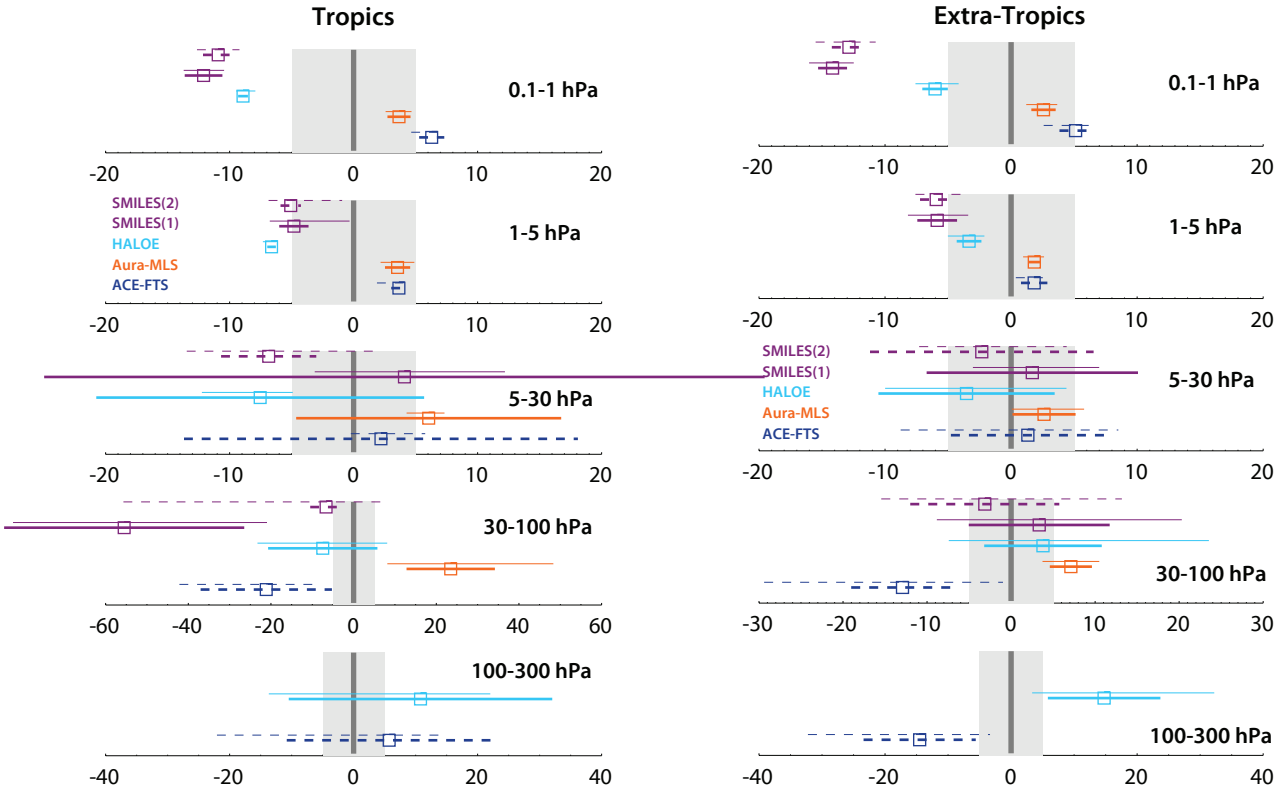

Figure 4.18.7: Inter-instrument differences in HCl calculated for the tropics (left) (20°S–20°N) and (right) extra-tropics (40°S–80°S and 40°N–80°N) and for five different altitude regions from the UT up to the LM. *Shown are the median (squares), median absolute deviations (MAD, thick lines), and the mean ±1σ ranges (thin lines) of the relative differences between each individual instrument and the MIM calculated over a given latitude and altitude region. The reference period is 2002-2008. Note SMILES(1) and SMILES(2) are not included in the MIM due to their limited sampling.*

SMILES(1) and **SMILES(2)** versions available to the SPARC Data Initiative are very similar in their overall structure, except in the tropical LS. Here, SMILES(1) shows a large negative bias with deviations from the MIM of around 50%. In the USLM, the two datasets generally are showing even larger negative deviations from the MIM than HALOE, which is known to exhibit a low bias. Note that an improved version of SMILES HCl has become available in the meantime, which largely removes the low bias and makes the retrieved values closer to those measured by Aura-MLS and ACE-FTS.

4.18.6 Recommendations: HCl

The long-term monitoring capability for stratospheric HCl hinges on two instruments (ACE-FTS and Aura-MLS), which are both past their expected lifetimes. New height-resolved measurements are needed to maintain this capability in order to be able to fulfill obligations to the Montreal Protocol.

4.19 Chlorine monoxide – ClO

Chlorine monoxide (ClO) is one of the most important reactive chlorine species involved in chlorine-catalyzed destruction of stratospheric ozone. The primary sources of ClO are CFCs (see *Sections 4.5* and *4.6*), but also hydrochlorofluorocarbons (HCFCs), methyl chloride (CH_3Cl), and carbon tetrachloride (CCl_4). These source gases reach the stratosphere, and are transported by the stratospheric circulation to higher altitudes, where they are photolyzed by UV radiation and release atomic chlorine (Cl). Cl then reacts with ozone to form ClO. In the upper stratosphere, ClO represents a substantial fraction of total available stratospheric chlorine. However, in the lower and middle stratosphere, reactive chlorine (ClO and Cl) is mostly tied up in the reservoir species HCl and $ClONO_2$ that do not directly destroy ozone. It is only during winter/spring in polar regions that HCl and $ClONO_2$ are converted back into ClO via heterogeneous chemical reactions on polar stratospheric clouds; these processes create enhanced levels of ClO that are a precursor to ozone destruction [*Solomon et al.*, 1986; *Molina and Molina*, 1987].

ClO exhibits a relatively strong diurnal cycle in the LS and MS, however, a less pronounced diurnal cycle in the US. **Figure 4.19.1** shows two examples of the diurnal ClO cycle as a function of local solar time or solar zenith angle for three different pressure levels as derived from a chemical box model [*McLinden et al.*, 2010]. A comparison of satellite-based ClO measurements corresponding to different local solar times would, ideally, account for this dependence on SZA.

4.19.1 Availability of ClO measurements

The assessment of ClO is based on the climatologies from SMR, Aura-MLS, MIPAS, and SMILES observations available to the SPARC Data Initiative. The climatologies start in 2001, with SMR currently providing the longest record. Both night-time and daytime ClO climatologies are available for the instruments used here, but only daytime measurements are presented and evaluated in this chapter. Measurements used from MIPAS correspond roughly to 10am, from Aura-MLS to about 1:30pm, from SMR to 6:30am (SMR(1))and also 6:30am measurements scaled to 1:30pm (SMR(2)), while SMILES measurements are taken throughout the day.

Older measurements are available from UARS-MLS, but are not included in the comparisons shown here, partly because significant trends are expected in atmospheric ClO concentrations between the 1990s and the 2000s as a result of reductions of chlorine source gas emissions following the Montreal Protocol regulations. Moreover, a careful selection of UARS-MLS data is needed as local time varies during each month complicating the creation of regular monthly datasets at all latitudes. This is due to periodic satellite yaws, which change the global viewing geometry of UARS-MLS roughly every 36 days. *Nedoluha et al.* [2011]

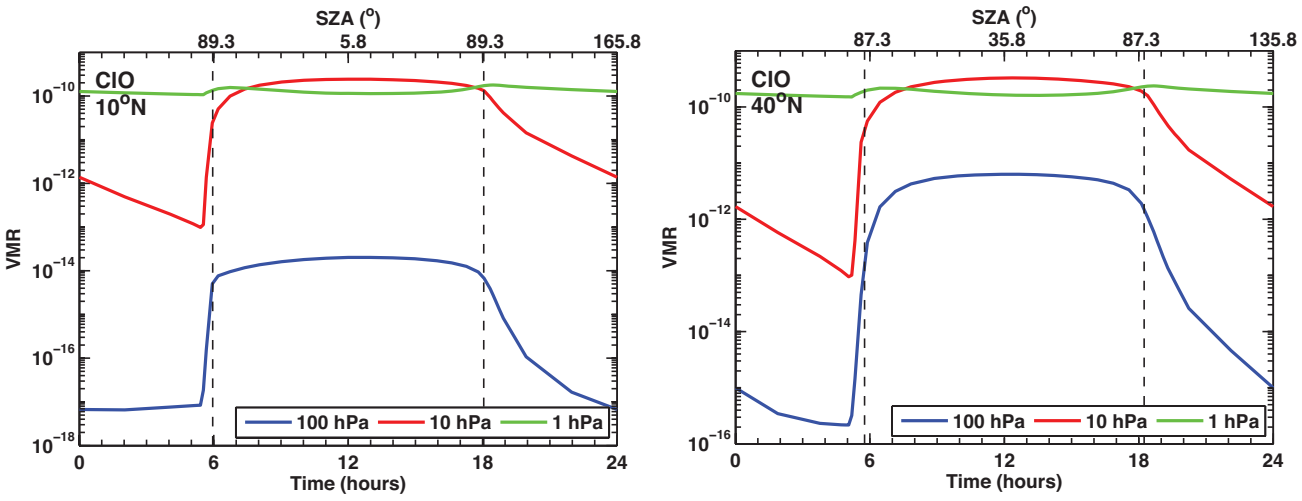

Figure 4.19.1: Diurnal cycle in ClO. *ClO diurnal variations are shown as a function of LST or SZA at 10°N (left panel) and 40°N (right panel) for 1, 10 and 100 hPa. The diurnal cycle is derived using a chemical box model [McLinden et al., 2010].*

Table 4.19.1: Available ClO measurement records from limb-sounding satellite instruments between 1978 and 2010. The red filling of the grid boxes indicates the temporal and vertical coverage of the respective instrument.

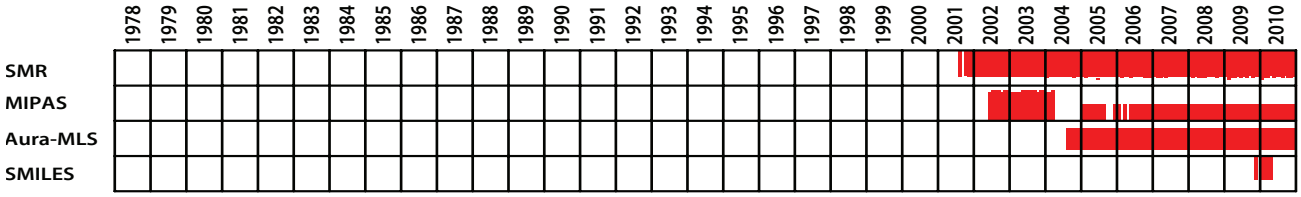

Table 4.19.2: Data version, time period, vertical range, vertical resolution, references and other comments for ClO measurements.

Instrument	Time period	Vertical range	Vertical resolution	References	Additional comments
Aura-MLS V3.3	Aug 2004 –	130 – 1 hPa	3 – 4.5 km	*Santee et al.,* 2008 *Livesey et al.,* 2013	about 1:30am/pm (but changes towards high latitudes)
SMR V2.1	Jul 2001 –	20 – 50 km (variable range depending on minimum mixing ratios)	2.5 – 3 km	*Urban et al.,* 2005b *Urban et al.,* 2006 *Khosravi et al.,* 2013	6:30am/pm; am/pm climatologies scaled to 1:30am/pm are also available
MIPAS **MIPAS(1)** V11 **MIPAS(2)** V220	 Mar 02 – Apr 04 Jan 05 – Apr 12	 10 – 45 km 10 – 30 km	 4 km (below 25 km) > 8 km (above 25 km) 3.3 – 7.5 km	 *Glatthor et al.,* 2004 *von Clarmann et al.,* 2009a	10am/pm; close to detection limit; measurement mode switched in 2005 from high spectral to high vertical resolution; Note that for single measurement profiles, use of a restricted altitude range of 10 – 30 km is recommended for both products.
SMILES V2.1	Nov 2009 – Apr 2010	100 – 0.01 hPa	3 – 5 km (stratosphere) 5 – 8 km (mesosphere)	*Sato et al.,* 2012 *Sagawa et al.,* 2013	C-band measurements

compared daytime portions of the UARS-MLS and Aura-MLS datasets versus time series of (daytime) ground-based profiles in the upper stratosphere and found no significant adjustment need between these two satellite datasets in this region, given their inferred average agreement of 1% ± 4%.

Tables 4.19.1 and **4.19.2** compile information on the availability of ClO measurements, including data version, time period, height range, vertical resolution, and references relevant for the data product used in this report.

4.19.2 ClO evaluations: Zonal mean cross sections

Monthly zonal mean cross sections will be analysed for daytime climatologies in order to investigate mean biases between the various datasets. Daytime climatologies are chosen, since the ClO diurnal cycle is smaller during the day than the night.

SMR(1), SMR(2), MIPAS(2), Aura-MLS, and SMILES (2009-2010), and MIPAS(1) (2002-2004)

Figure 4.19.2a shows the monthly zonal mean ClO climatologies for the reference period 2009-2010 chosen for all available measurements. MIPAS(1) measured during an earlier time period (2002-2004), but is here also compared to the 2009-2010 MIM reference. Note that in the following, SMR(1) is not included in the calculation of the MIM, but that the SMR(2) scaled product is considered in the limited region available.

The ClO distribution indicates a maximum in the upper stratosphere, representing a major contribution to total chlorine apart from HCl. The maximum values around 3-5 hPa reach around 800 pptv. ClO decreases towards the LM and also the LS to values smaller than 5 pptv, which is close to most instruments' detection limit. A localised maximum in the ClO distribution is found in the LS polar vortex region during winter/spring, indicating the enhancement of ClO through heterogeneous reactions on polar stratospheric clouds.

The different instruments' monthly climatologies look very similar, although MIPAS(1) shows somewhat larger values than the other instruments, especially across the US in the tropics. The higher values may be at least partially attributable to a negative trend in stratospheric ClO over the 2000s, the consequence of the successful implementation of the Montreal Protocol regulations on chlorine source gases. At the other end, SMR(1) shows lowest ClO mixing ratios, consistent with its local measurement time being slightly

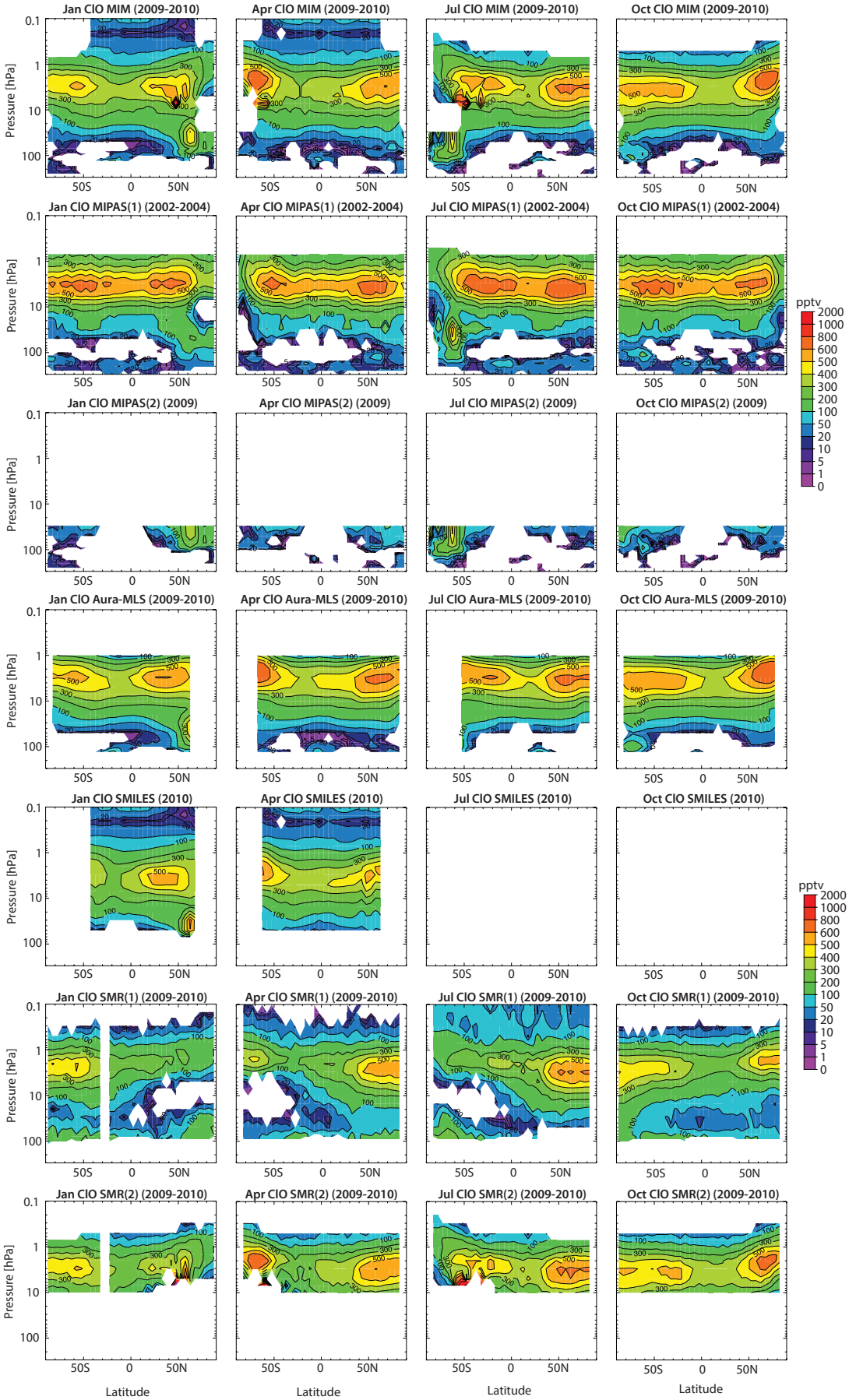

Figure 4.19.1a: Cross sections of monthly zonal mean ClO for 2009-2010. *ClO cross sections for 2009-2010 (or according to availability as indicated) are shown for the MIM, MIPAS(1) (2002-2004), MIPAS(2) (2009), Aura-MLS, SMILES (2010), SMR-am data unscaled (SMR(1)) and scaled to 1:30pm (SMR(2)). Note, MIPAS(1) and SMR(1) are not included in the MIM.*

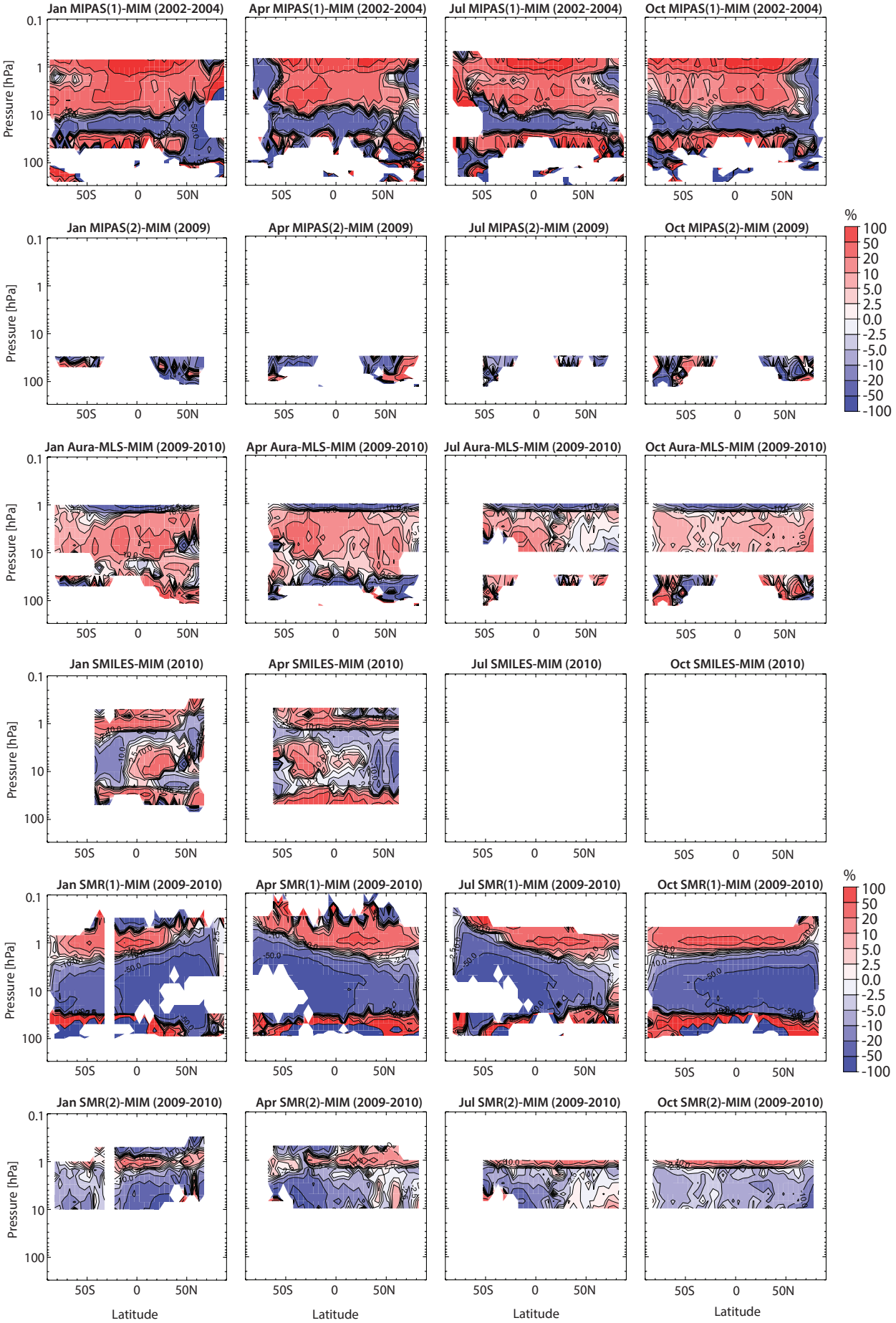

Figure 4.19.1b: Cross sections of monthly zonal mean ClO differences for 2009-2010. *ClO relative differences with respect to the MIM are shown for the individual instruments as in Figure 4.19.2a.*

before the maximum daily values are reached (which then are more or less constant through the day).

The corresponding relative differences of the instruments with respect to the MIM are displayed in **Figure 4.19.2b** The figure quantifies the qualitative discussion on instrument differences above. Note that the white bar in the Aura-MLS difference climatology between 30 and 10 hPa during July and October is due to the fact that the MIM at these altitudes consists of Aura-MLS data only (MIPAS(1) and SMR(1) are not considered in the MIM). Aura-MLS, SMILES, and the scaled SMR(2) climatologies agree reasonably well, mostly within ±10-20%, confirming earlier validation studies [*Sagawa et al.*, 2013; *Kreyling et al.*, 2013]. Aura-MLS and SMR(2) agree even better than ±10% (as seen for July and October). This result is in good agreement with an earlier comparison by *Livesey et al.* [2013] who used tight coincidence criteria in terms of SZA for Aura-MLS and SMR profiles and who showed differences within 10-15% (except at 68 to 100 hPa where both datasets are subject to larger biases, and for which no comparison could be made here). The good quality of Aura-MLS ClO is supported by comparisons versus ground-based observations. Antarctic spring (year 2005) enhanced Aura-MLS ClO profiles, appropriately convolved to match the coarser vertical resolution of ground-based microwave ClO profiles, have been shown by *Connor et al.* [2007] to agree, on average, with the ground-based profiles (coincident in space and local time) near the lower stratospheric peak (within 11 ± 8%, and within the combined 2σ uncertainties); Aura-MLS values are slightly lower than the ground-based values.

The unscaled SMR climatology, SMR(1), shows large negative relative differences from the MIM throughout most of the LS and MS (reaching more than -50%), which is expected from its measurement time at 6:30am shortly before values reach their daily maximum. Note that around 1 hPa, the SMR(1) differences are positive, which again can be expected from the diurnal cycle, which is different than at lower altitudes and shows localised maxima just after 6am and 6pm (see **Figure 4.19.1**).

MIPAS(1) shows large positive differences reaching more than +20% in the US, with a band of large negative differences reaching -20% just below in the MS. Note that a comparison between MIPAS(1) and SMR(2) over the same time period (2002-2004; not shown) does not yield better agreement between the instruments, despite avoiding a potential temporal sampling issue.

4.19.3 ClO evaluations: Vertical and meridional profiles

The vertical and meridional profiles shown in **Figures 4.19.3** and **4.19.4** emphasise details in the structure of the differences in the monthly zonal mean cross sections.

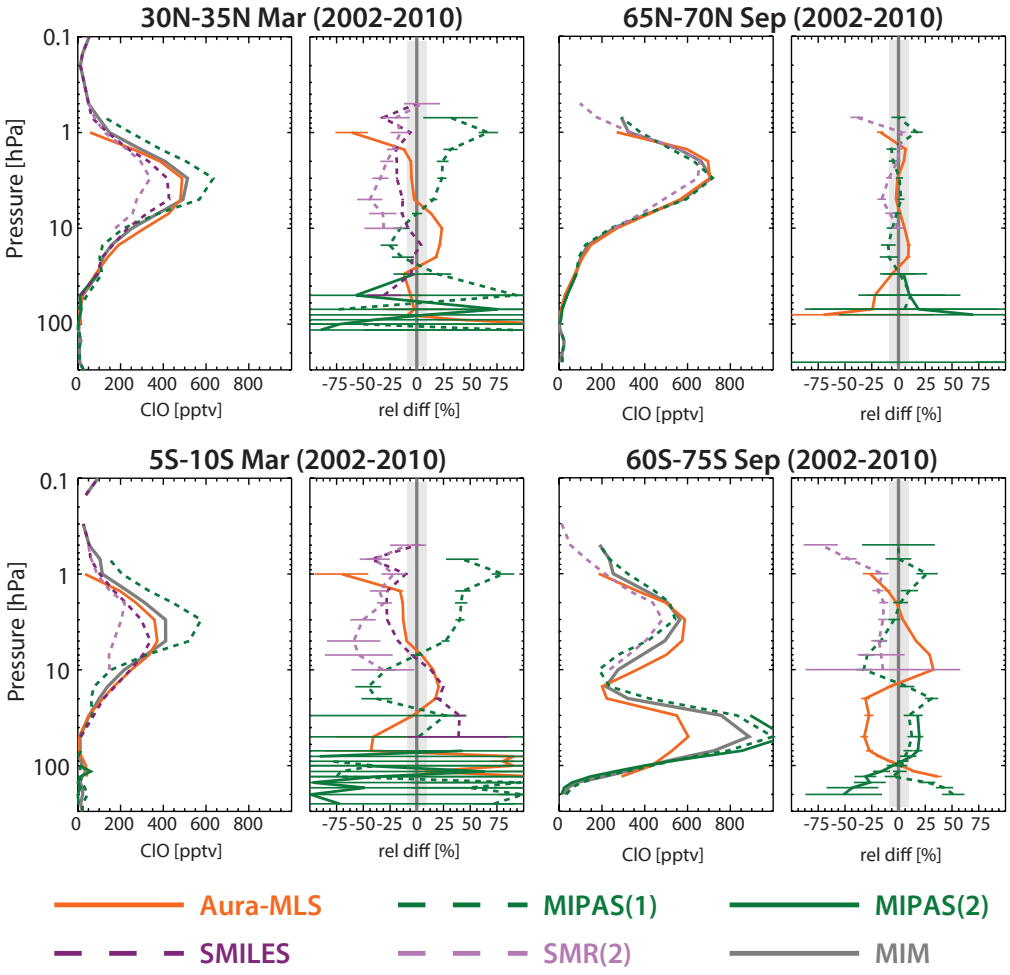

Figure 4.19.2: Vertical profiles of monthly zonal mean ClO for 2002-2010. *Vertical ClO profiles for March 30°N-35°N and 5°S-10°S (left panels), and for September 65°N-70°N and 60°S-75°S (right panels) are shown together with their differences from the MIM for both. Note, while MIPAS(1) and MIPAS(2) are included in the MIM, SMR(2) is not. The grey shading indicates where the relative differences are smaller than ±10%. Bars indicate the uncertainties in the relative differences based on the SEM of each instrument's climatology.*

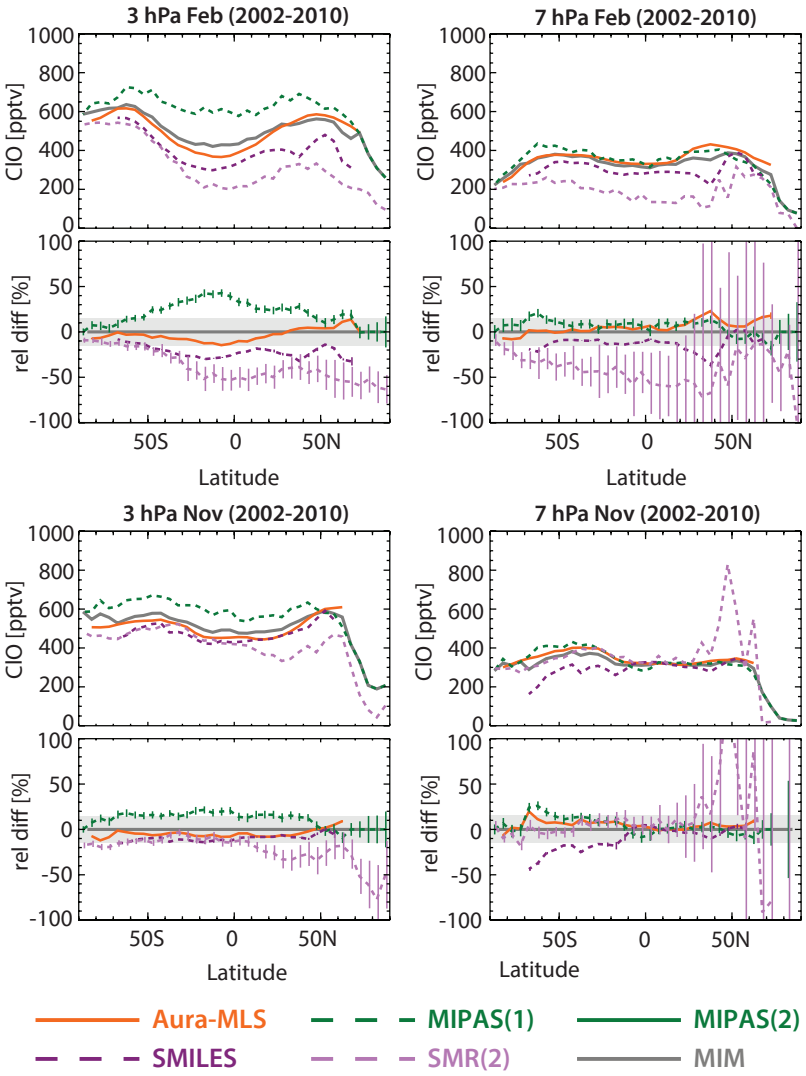

Figure 4.19.3: Meridional profiles of monthly zonal mean ClO for 2002-2010. *ClO profiles are shown at 3 and 7 hPa for February (upper row) and November (lower row) averaged over 2002-2010. Relative differences between the individual instruments (SMR(2), MIPAS(1), SMILES, and MLS) and the MIM profiles are shown in the lower panels. Note, SMR(2) is not included in the MIM. The grey shading indicates where the relative differences are smaller than ±15%. Bars indicate the uncertainties in the relative differences based on the SEM of each instrument's climatology.*

Good agreement and smallest relative differences of ±10% are found between the different instruments during September in the northern high-latitudes, when stratospheric dynamics is rather quiet and as a consequence geophysical variability is small. Small variability is also expected in the tropics throughout the year, however, the vertical profiles at 5°S-10°S show fairly large relative differences between the instruments. An exception is Aura-MLS and SMILES, which show very good agreement over most of the MS and US and similar maximum values around 3 hPa. The high bias in MIPAS(1) in the upper stratosphere may be partially explained by the expected trend in the chlorine loading between the early and late 2000s.

Only reasonably good agreement to considerable disagreement is found for March at northern mid-latitudes and September at southern high-latitudes. These are dynamically and chemically active seasons and sampling issues may play a stronger role in determining the relative differences between the instruments, especially for such a short-lived species as ClO that shows in addition strong interannual variability. In the face of the high natural variability it is hence difficult to draw firm conclusions about the instruments' retrievals during these dynamically active seasons. Note also that for Aura-MLS daytime data at higher latitudes, the local time is shifted away from 1:30pm to around 3:30pm, so that the diurnal change effect will tend to introduce larger biases than anticipated when comparing to the SMR product scaled to 1:30pm.

Meridional monthly zonal mean ClO profiles for 2002-2010 are shown in **Figure 4.19.4** for two levels in the MS (7 hPa) and US (3 hPa). At these levels, MIPAS(1), SMILES, and Aura-MLS show generally good to reasonable agreement (between ±10 and ±20%). The scaled SMR(2) product is, despite the diurnal adjustment, still on the low side of the other instruments' climatologies and also shows much larger SEM values, *i.e.,* its mean is not as clearly defined. MIPAS(1) is generally on the high side.

4.19.4 Summary and conclusions: ClO

ClO climatologies are available from four limb satellite instruments: MIPAS, SMR, Aura-MLS, and SMILES. While SMILES observes the full diurnal cycle, MIPAS measurements are made at about 10am/pm, Aura-MLS at about 1:30am/pm, and SMR at 6:30am/pm respectively. The observations allow therefore for the compilation of both daytime and night-time climatologies. Only daytime climatologies are evaluated here, since the diurnal cycle is deemed to cause

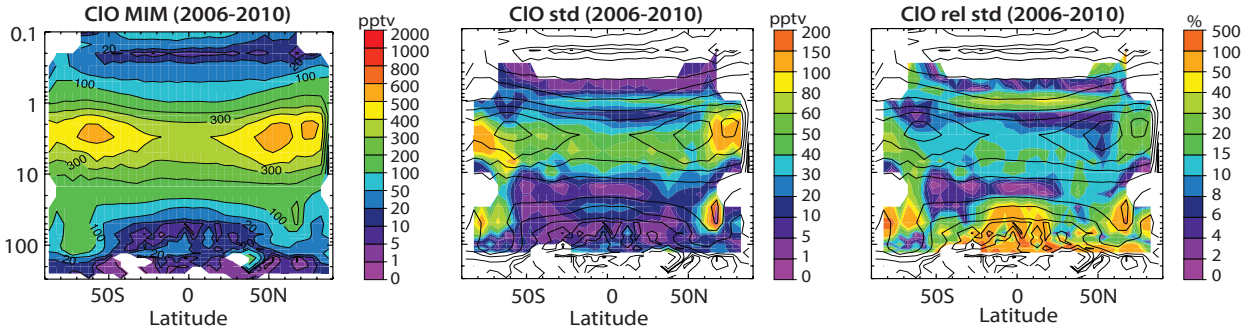

Figure 4.19.4: Summary of ClO annual zonal mean state for 2006-2010. *Annual zonal mean cross sections for 2006-2010 of the MIM, the absolute, and the relative standard deviations over all instruments are presented from left to right. Black contours in right-hand panels repeat the MIM distribution. Instruments considered are MIPAS(2), Aura-MLS, SMILES, and the scaled SMR product (SMR(2)). MIPAS(1) has not been included since its measurement period does not overlap with the rest of the instruments.*

smaller variations during the day than during night, and since lower stratospheric night-time values are much smaller (and harder to measure) than daytime values in this region.

Both the unscaled and scaled SMR climatologies are on the low side of the other instruments. It has been found that SMR am measurements scaled to 1:30pm improve the comparison with the other instruments, but generally still underestimate ClO mixing ratios through most of the stratosphere and LM. Nevertheless, the differences between the scaled SMR and Aura-MLS climatologies are generally well below 10-20% (or ±5-10% with respect to the MIM) in our zonal monthly mean comparisons between 10 and 1 hPa (the range the scaled SMR product is available for), indicating very good to good agreement. This result agrees with averaged coincident ClO profile differences between SMR and Aura-MLS (see *Livesey et al.*, 2013).

SMILES introduces somewhat larger differences compared to these two instruments, with values around ±10% with respect to the MIM depending on the region, with the results being largely consistent with *Sagawa et al.* [2013]. The high-spectral resolution MIPAS climatology, MIPAS(1), exhibits generally somewhat larger values (±20% with respect to the MIM) than those of the other instruments, with a contribution to the differences of only 3-5% likely attributable to the decreasing trend in stratospheric total chlorine following the Montreal Protocol regulations.

The overall agreement between the satellite ClO measurements excluding MIPAS(1) (see **Figure 4.19.5**) and as expressed by the relative standard deviation is very good to good throughout the MS and US (5-15%), and especially in regions where maximum values are found (US around 3 hPa at high latitudes). The uncertainty in the atmospheric mean state increases towards regions where ClO mixing ratios are close to the detection limit of the instrument (*e.g.*, tropical UTLS, or LM) with relative standard deviations larger than 50% (or absolute mixing ratios of only 20 pptv).

The above results and comparison with earlier validation literature highlight the general usefulness of the climatological validation approach even for shorter-lived species, yielding complementary information on latitude-height dependent measurement differences to that obtained from profile coincidences. For ClO, expected diurnal variations are relatively small during the day, so that most instruments can be compared directly with each other using daytime climatologies. An exception to this is SMR, which measures shortly before the 'stable' daytime ClO mixing ratios are reached, and for which scaling to mid-day values improves the comparisons significantly. Note that in regions where ClO variability is higher or daytime sampling differs from the stated equator crossing time (as in the case for Aura-MLS measurements at high latitudes), larger differences are found. To minimise such effects, validation and related inter-comparisons necessitate a lot of care and the use of selected coincident profiles (in terms of SZA and location) from either ground-based or satellite data.

4.20 Hypochlorous acid – HOCl

Hypochlorous acid (HOCl) in the stratosphere and LM is a short-lived reservoir gas for active chlorine (ClO_x) and hydrogen oxide (HO_x) species [*von Clarmann et al.*, 2012]. HOCl is photolyzed or reacts with atomic oxygen or hydroxyl radicals (OH) to form reactive chlorine, thereby contributing to ozone loss in the HOCl catalytic cycle [*Johnson et al.*, 1995]. HOCl is produced by the reaction between ClO and HO_2 (see *Sections 4.19* and *4.23*, respectively). The build-up of HOCl depends on the abundance of HO_2 relative to atomic oxygen (which competes for ClO to form the chlorine radical Cl), and available sunlight (which determines the rate of HOCl photolysis). HOCl can also be transformed into reactive chlorine species in heterogeneous processes on polar stratospheric clouds. Increases in upper stratospheric polar HOCl abundances following strong solar proton events have been observed in satellite data (MIPAS and Aura-MLS), as discussed by *von Clarmann et al.* [2005] and *Damiani et al.* [2012]. There is also some tropospheric HOCl chemistry in the marine boundary layer that produces HOCl, however, tropospheric concentrations remain very small because the HOCl lifetime (determined by wet scavenging there) is even shorter than in the stratosphere.

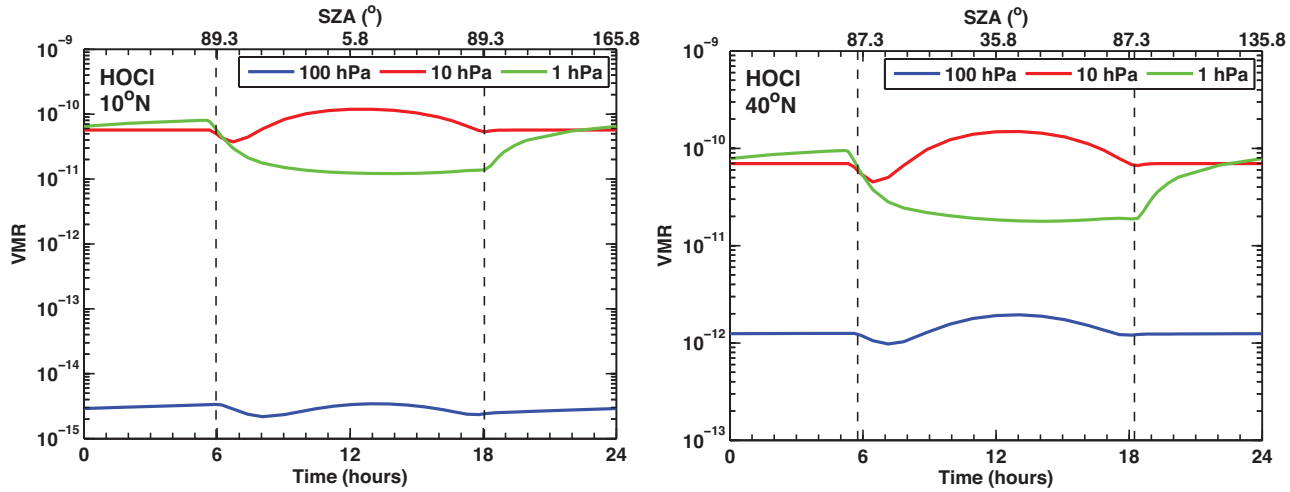

Figure 4.20.1: Diurnal cycle in HOCl. *HOCl diurnal variations are shown as function of LST or SZA at 10°N (left panel) and 40°N (right panel) for 1, 10 and 100 hPa. The diurnal cycle is derived using a chemical box model [McLinden et al., 2010].*

Figure 4.20.1 shows the diurnal cycle in HOCl at two different latitudes as a function of local solar time or solar zenith angle and for three different pressure levels as derived from a chemical box model [*McLinden et al.*, 2010]. The diurnal cycle in HOCl varies with altitude, depending on the relative strengths of formation and destruction reactions of HOCl and the abundances of species that lead to HOCl formation (in particular HO_2 and ClO). A quantification of the increases in night-time HOCl found in the US due to the reaction ClO + HO_2 -> HOCl is presented in *Kuribayashi et al.* [2014]. An evaluation of the diurnal cycle from SMILES measurements can be found in *Kreyling et al.* [2013]. A comparison of satellite-based HOCl measurements, which correspond to different local solar times would hence ideally account for the dependence of HOCl on the SZA.

4.20.1 Availability of HOCl measurements

The assessment of HOCl is based on the climatologies from Aura-MLS, MIPAS, and SMILES observations. **Tables 4.20.1** and **4.20.2** compile information on the availability of HOCl measurements, including data version, time period, altitude range, vertical resolution, and references relevant for the data product used in this report. Measurements of HOCl are available for the high-spectral MIPAS measurements between 2002-2004, Aura-MLS from 2004 onwards, and SMILES between October 2009 and April 2010. The Aura-MLS measurement range is limited to the US. Measurements are available for both night-time and daytime, but only night-time measurements will be presented and evaluated in this chapter because of a smaller diurnal cycle amplitude during the night. A data-comparison taking

Table 4.20.1: Available HOCl measurement records from limb-sounding satellite instruments between 1978 and 2010. *The red filling of the grid boxes indicates the temporal and vertical coverage of the respective instrument.*

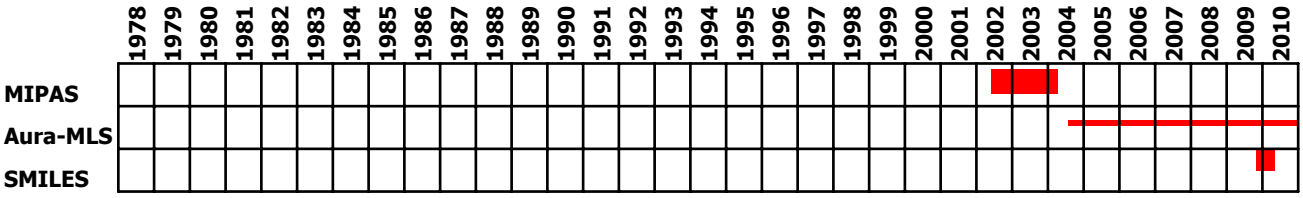

Table 4.20.2: Data version, time period, vertical range, vertical resolution, references and other comments for HOCl measurements.

Instrument	Time period	Vertical range	Vertical resolution	References	Additional comments
Aura-MLS V3.3	Jul 2004 –	10 – 2.2 hPa	3 – 6 km	*Khosravi et al.*, 2013	2am/pm
MIPAS V4	Mar 2002 – Apr 2004	20 – 70 km (50 – 0.04 hPa)	9 km	*von Clarmann et al.*, 2006 *von Clarmann et al.*, 2009b	10am/pm
SMILES V2.1.5	Nov 2009 – Apr 2010	30 – 70 km	3 – 6 km	*Kreyling et al.*, 2013 *Khosravi et al.*, 2013 *Kuribayashi et al.*, 2014	day-/night-time Band A

into account the HOCl diurnal cycle has been presented by *Khosravi et al.* [2013], however with a focus on tropical data at three different altitude levels only.

4.20.2 HOCl evaluations: Zonal mean cross sections

Monthly mean zonal mean HOCl cross sections derived from night-time measurements for the time period 2002-2010 are compared in order to investigate mean biases between the various datasets. We choose to compare the night-time climatologies, since the diurnal cycle (at least below 10 hPa) shows weakest changes during the night. Measurements from MIPAS correspond roughly to 10pm, measurements from Aura-MLS correspond roughly to 2am and SMILES measurements take place over the whole nighttime.

MIPAS (2002-2004), Aura-MLS (2004-2010), and SMILES (2009-2010)

Figure 4.20.2a shows the monthly zonal mean HOCl night-time climatologies averaged over 2002-2010 for available measurements. The evaluation of the monthly mean instead of the annual mean datasets is chosen to avoid sampling biases for SMILES, which only covers a few months of the year. The MIM monthly mean climatologies for NH late autumn to early spring show highest values in the US at pressure levels between 5 and 2 hPa. Two distinct maxima are found at mid-latitudes of each hemisphere reaching up to about 200 pptv, and with somewhat higher values in the winter hemisphere than in the summer hemisphere. The maximum values increase towards the equinoxes. HOCl

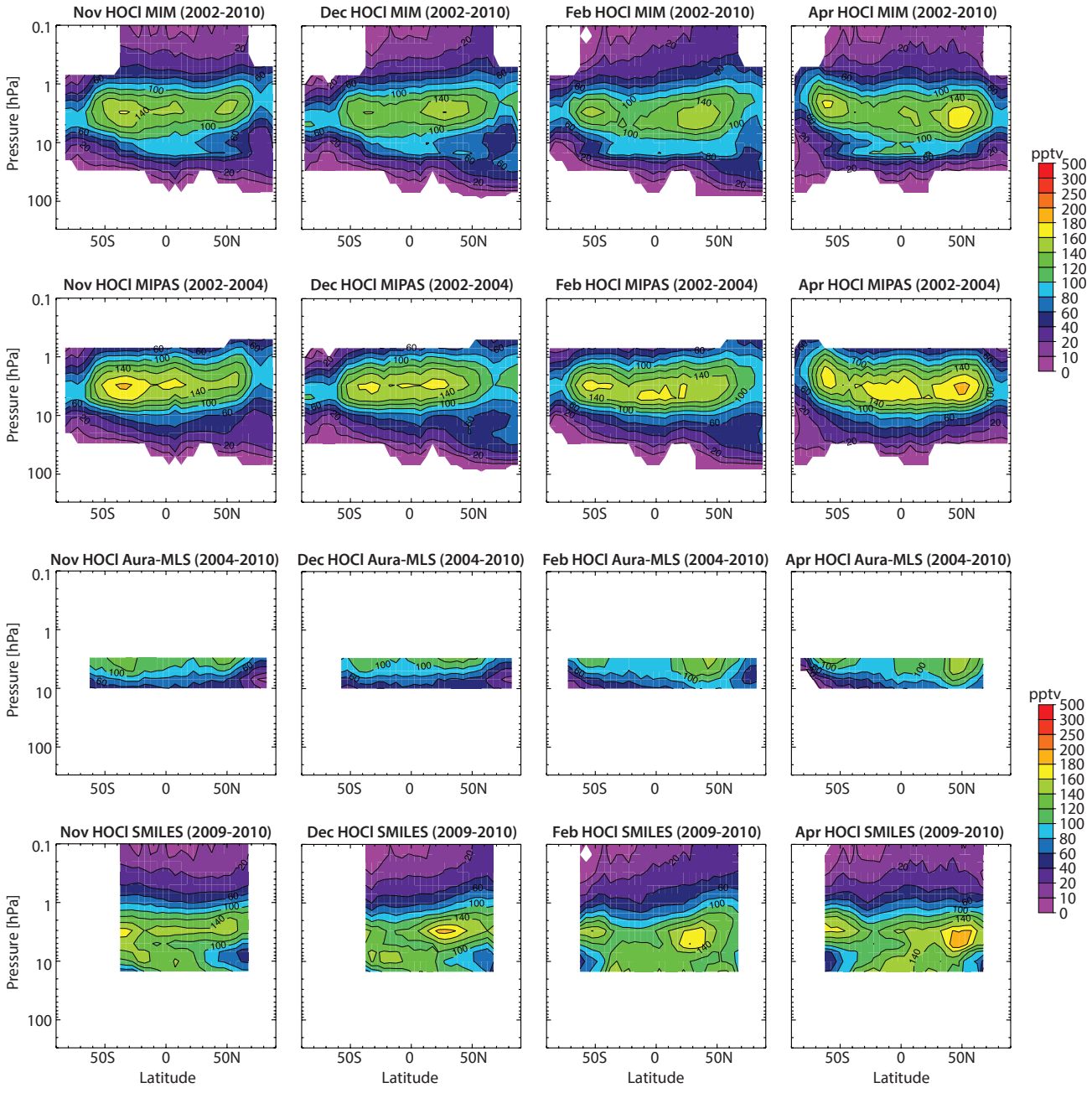

Figure 4.20.2a: Cross sections of monthly zonal mean HOCl for 2002-2010. *Monthly zonal mean HOCl cross sections for November, December, February and April over 2002-2010 are shown for the MIM, MIPAS, Aura-MLS, and SMILES.*

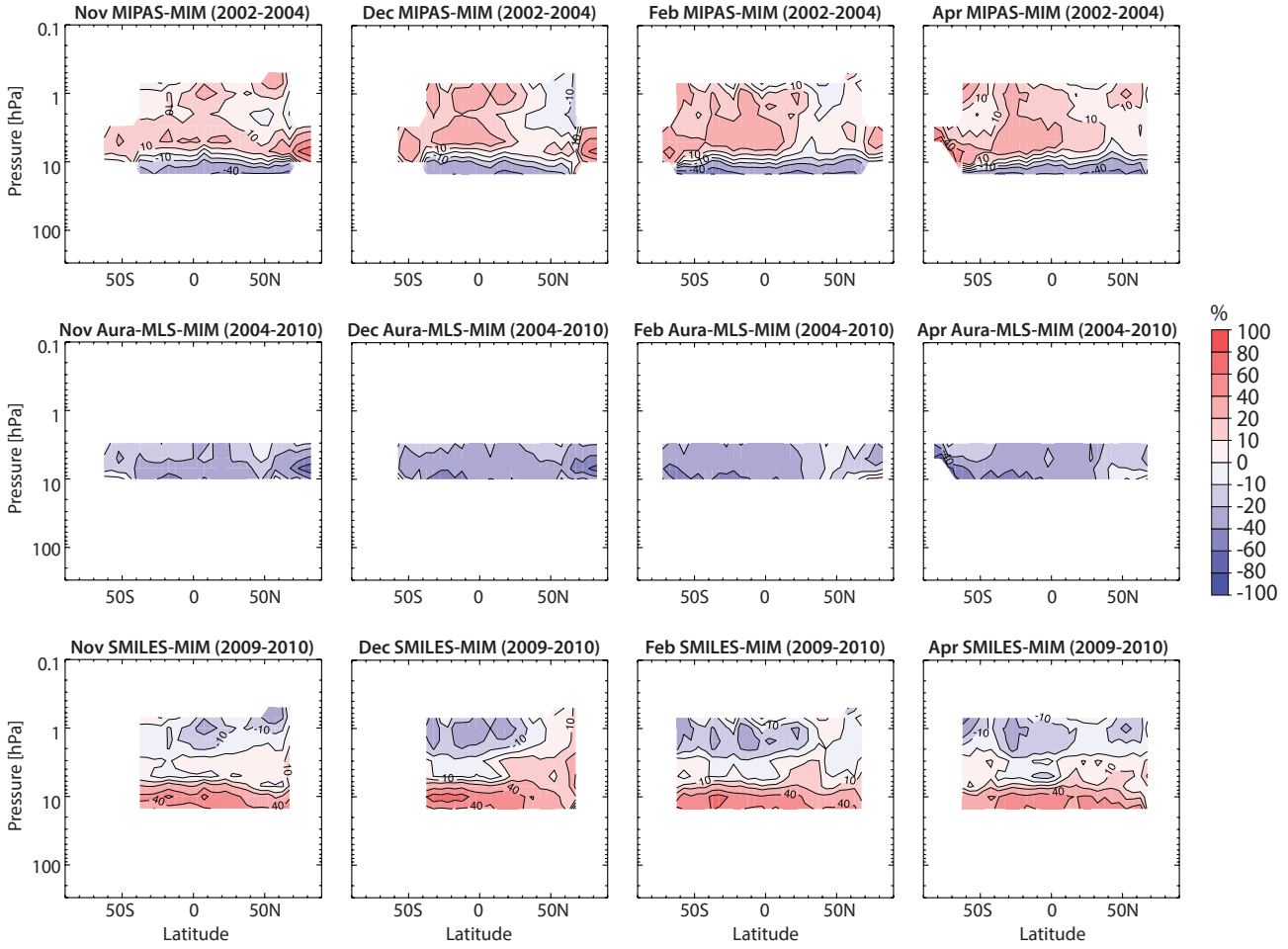

Figure 4.20.2b: Cross sections of monthly zonal mean HOCl differences for 2002-2010. *Monthly zonal mean HOCl differences for 2002-2010 between the instrument climatologies and the MIM are shown. From top to bottom: MIPAS, Aura-MLS, and SMILES.*

quickly drops to below 60 pptv in the LM above 1 hPa, and in the LS below 30 hPa. MIPAS indicates a third maximum in the tropical US region, which is not as pronounced in the SMILES observations. SMILES values, on the other hand, do not decrease as quickly below 10 hPa as seen in MIPAS (or Aura-MLS at its lower boundary). Differences are likely due to a decrease in the sensitivity of SMILES data below 10 hPa, which arises from a low signal-to-noise ratio attributable to contamination from pressure broadened ozone lines and air continuum absorption as described in *Kreyling et al.* [2013].

The differences in the instruments' HOCl climatologies relative to the MIM are displayed in **Figure 4.20.2b** and reflect the features seen in SMILES and MIPAS discussed above. The differences are strongly positive (and are opposite of what would be expected from the diurnal cycle) for MIPAS in the tropical US and for SMILES below about 6 hPa, consistent in sign with the results by *Khosravi et al.* [2013]. However, our evaluations indicate somewhat smaller differences than found in their study despite the fact that they attempted to take the diurnal cycle effects into account. Aura-MLS HOCl is slightly low throughout its limited measurements range when compared to the other two instruments' climatologies. Note the differences between Aura-MLS and SMILES are the same when looking only at the 2009/2010 months for which SMILES took measurements, so are not resulting from looking at different years. The negative trends in stratospheric chlorine since the late 1990s will contribute (by a few percent) to the positive differences seen in MIPAS data when compared to SMILES and Aura-MLS values for later years.

4.20.3 HOCl evaluations: Vertical and meridional profiles

The vertical profiles shown in **Figure 4.20.3** for subtropics (25°N-30°N) and mid-latitudes (50°N-55°N) further illustrate details in the vertical structure of the differences found in the monthly mean cross sections. In the US and LM, MIPAS and SMILES agree well or reasonably well within 10-20% except in April at mid-latitudes. This agreement is better than indicated in *Khosravi et al.* [2013], which may be partially due to their evaluation being performed in the deeper tropics. Aura-MLS shows decreasing negative differences with respect to the MIM with increasing altitude.

HOCl meridional mean profiles for 2002-2010 are shown in **Figure 4.20.4**. This evaluation highlights that MIPAS and SMILES generally agree reasonably well (within 20%) in the USLM, but that MIPAS agrees better with Aura-MLS in the MS with differences within 20%. Note that the meridional profiles also show somewhat better agreement at

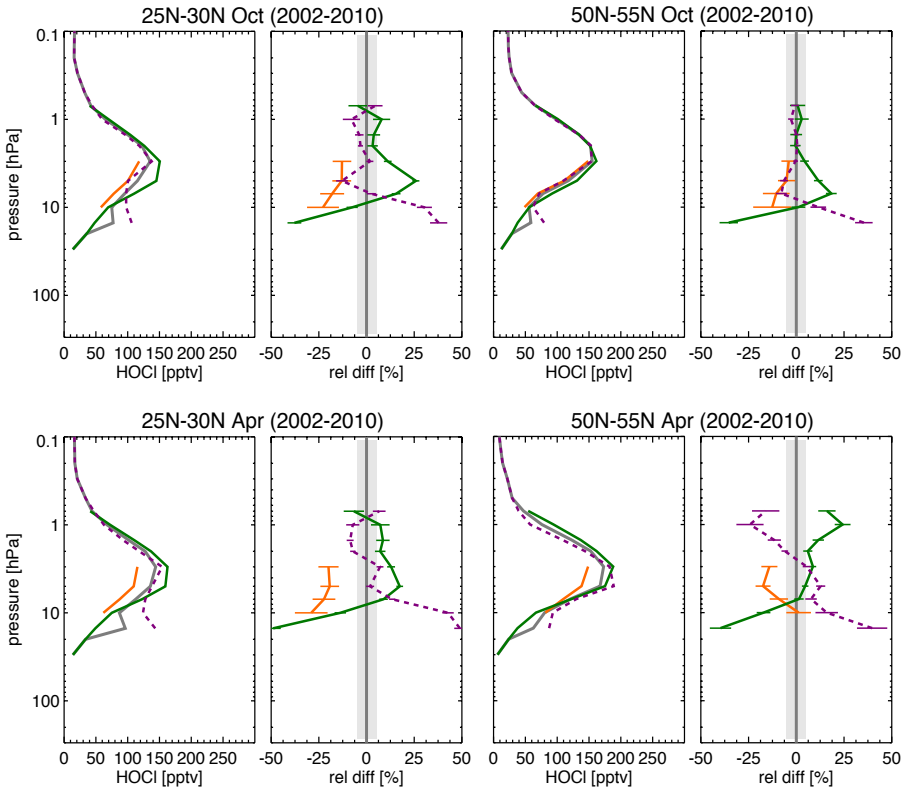

Figure 4.20.3: Vertical profiles of zonal mean HOCl for 2002-2010. *Vertical zonal mean HOCl profiles for October and April 25°N-30°N (left panels) and 55°N-60°N (right panels) are shown together with their differences from the MIM. MIPAS, Aura-MLS, and SMILES climatologies are averaged over the years 2002-2004, 2004-2010, and 2009-2010, respectively.*

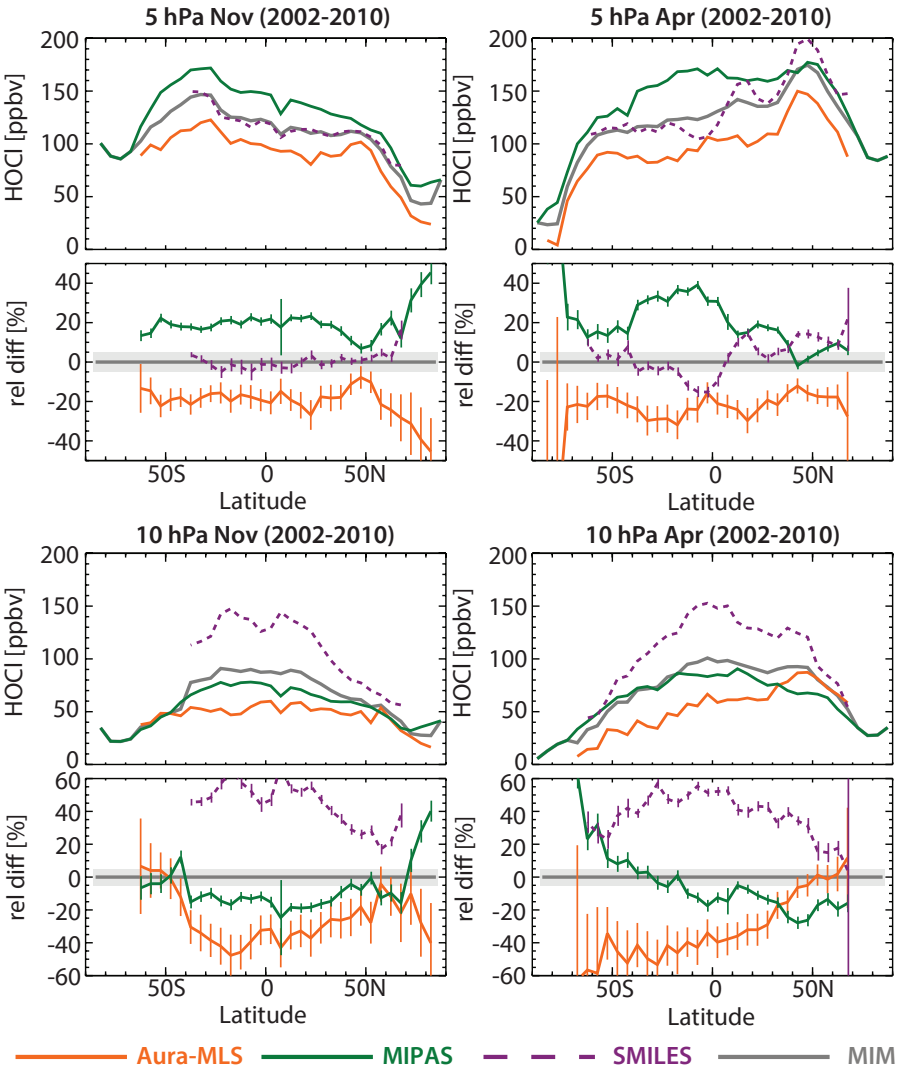

Figure 4.20.4: Meridional profiles of zonal mean HOCl for 2002-2010. *Meridional zonal mean HOCl profiles are shown for November (left) and April (right) at 5 hPa (upper row) and at 10 hPa (lower row). The climatologies are averaged over different time periods between 2002 and 2010 (see caption of Fig. 4.20.3). Differences between the individual instruments' (MIPAS, Aura-MLS, and SMILES) HOCl and the MIM profiles are shown in the lower panels.*

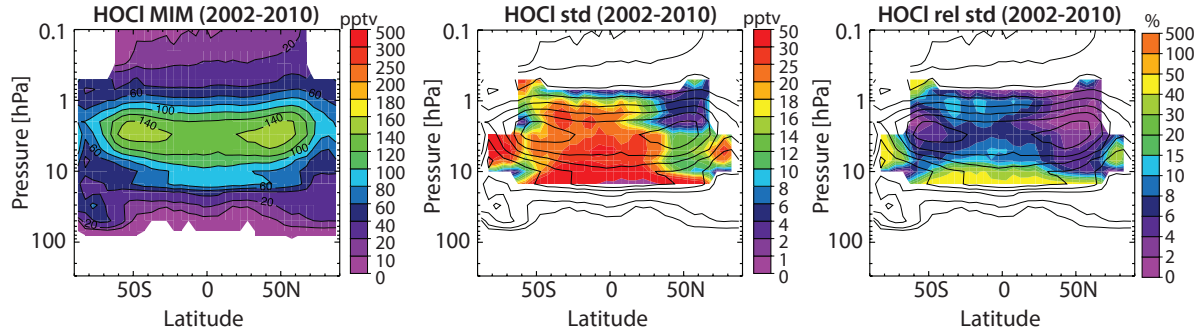

Figure 4.20.5: Summary of HOCl annual zonal mean state for 2002-2010. *Annual zonal mean cross sections for 2002-2010 of the MIM, the absolute, and the relative standard deviations over all instruments are presented from left to right, respectively. Black contours in right-hand panels repeat the MIM distribution. Instruments considered are MIPAS, Aura-MLS, and SMILES.*

mid-latitudes and the extra-tropics than in the inner tropics (20°S-20°N) where *Kohsravi et al.* [2013] chose to perform their comparison.

4.20.4 Summary and conclusions: HOCl

HOCl climatologies are available from three limb satellite instruments: MIPAS, Aura-MLS, and SMILES. While SMILES observes the full diurnal cycle, MIPAS measurements are made at about 10am/pm and Aura-MLS at about 2am/pm, respectively. The observations allow therefore for the compilation of both day- and night-time climatologies. Only the latter were evaluated here, since the impact of the diurnal cycle on night-time comparisons is deemed smaller (or even negligible below 10 hPa). The overall agreement between the instruments (see **Figure 4.20.5**) is better in the US than in the MS, despite the expectation that the diurnal cycle in HOCl may lead to a larger impact on the night-time comparison at higher altitudes.

In the US, MIPAS and SMILES agree reasonably well to within mostly 20%. In the MS, MIPAS agrees better with Aura-MLS (largely to within 30%). This can be explained by SMILES loosing sensitivity below about 10 hPa, which leads to a decrease in the quality of its HOCl product [*Kreyling et al.*, 2013]. Aura-MLS is generally on the low side of the other two instruments, with a few percent of the differences to MIPAS being explained by negative trends in stratospheric chlorine between the measurement periods of MIPAS (2002-2004) and Aura-MLS (2004-2010).

4.21 Bromine oxide – BrO

Bromine oxide (BrO) is another important reactive species involved in the catalytic destruction of stratospheric ozone, especially in the LS below about 20 km [*Brasseur and Solomon*, 1986]. While stratospheric abundances of inorganic bromine (Br_y) are much smaller than those of inorganic chlorine, bromine is around 60 times more effective in destroying ozone on a per-atom basis when compared to chlorine [*Sinnhuber et al.*, 2009]. The primary sources of stratospheric BrO are organic bromine-containing compounds including the longer-lived methyl-bromide (CH_3Br; from both anthropogenic and natural sources), halons (*e.g.*, CF_2ClBr, $CBrF_3$; from anthropogenic sources), and very short-lived bromine-containing source gases such as CH_2Br_2, $CHBr_3$, $CHBr_2Cl$ (mainly from natural sources) that are transported from Earth's surface into the stratosphere [*Carpenter et al.*, 2014]. In the stratosphere, these compounds are photolyzed by UV into bromine, which then reacts with ozone to form BrO. BrO is the most abundant inorganic bromine species in the LS and MS during daylight, making up to 50% of total inorganic bromine (Br_y; *Brasseur and Solomon*, 2005). Total inorganic bromine entering the stratosphere in 2012 as derived from tropospheric observations was 20.1 pptv, with a contribution from very-short lived substances of around 5 pptv [*WMO*, 2014].

BrO exhibits a relatively strong diurnal cycle in the LS and MS, and a somewhat smaller diurnal cycle in the US. **Figure 4.21.1** shows examples of the diurnal cycle of BrO at two different latitudes and as a function of local solar time or solar zenith angle for three different pressure levels as derived from a chemical box model [*McLinden et al.*, 2010]. A comparison of satellite-based BrO measurements corresponding to different local solar times would, ideally, account for this dependence on SZA.

4.21.1 Availability of BrO measurements

The assessment of BrO is based on the climatologies from OSIRIS, SCIAMACHY, and SMILES observations available to the SPARC Data Initiative. The climatologies start in 2001, with OSIRIS providing the longest record. Even where both night-time and daytime BrO climatologies are available for an instrument, only daytime measurements are evaluated here since diurnal variations are smaller during the day (see **Figure 4.21.1**). OSIRIS measurements available for 6:30am and scaled to 10am, SCIAMACHY measurements available for 10am (equator crossing time) and scaled to 10am (note that the local time is substantially different at higher latitudes), and SMILES daytime measurements are used.

Other BrO measurements are produced from Aura-MLS over a limited altitude range between 10 and 4.6 hPa [*Millán et al.*, 2012], although these were not provided as part of this comparison work; the latter authors note that for the 10 hPa level

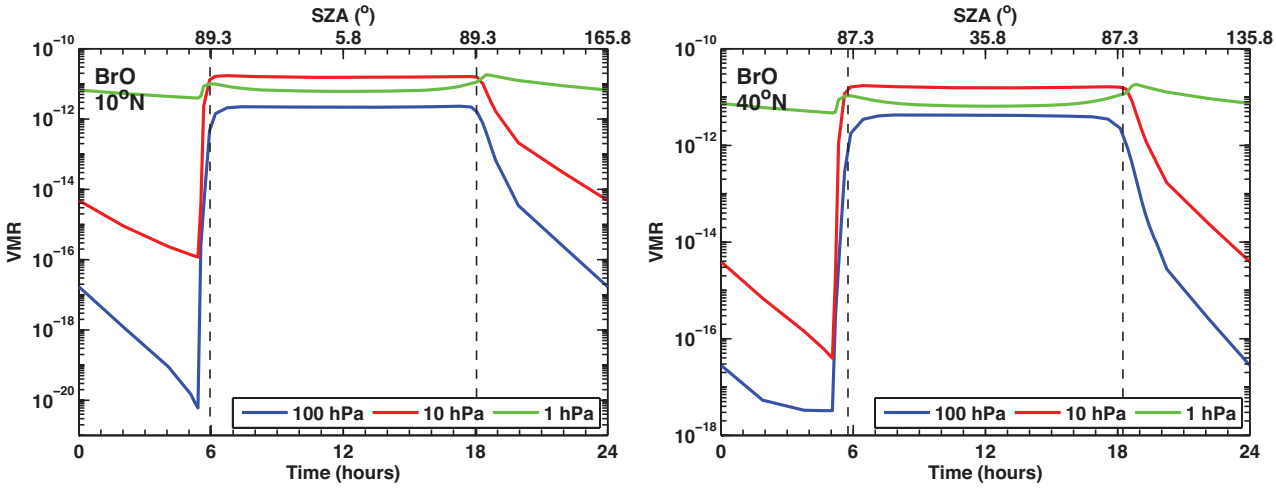

*Figure 4.21.1: **Diurnal cycle in BrO.** BrO diurnal variations are shown as function of LST or SZA at 10°N (left panel) and 40°N (right panel) for 1, 10 and 100 hPa. The diurnal cycle is derived using a chemical box model [McLinden et al., 2010].*

of overlap, MLS BrO generally agrees, within the respective uncertainties, with OSIRIS and SCIAMACHY BrO.

Tables 4.21.1 and **4.21.2** compile information on the availability of BrO measurements, including time period, height range, vertical resolution, and references relevant for the data product used in this report.

4.21.2 BrO evaluations: Monthly zonal mean cross sections

Monthly zonal mean cross sections are analysed for daytime climatologies in order to investigate mean biases between the various datasets. Daytime climatologies are chosen, since variations in the BrO diurnal cycle are smaller during the day than the night.

SMILES (2009-2010), OSIRIS, and SCIAMACHY (2003-2010)

Figure 4.21.2a shows the monthly zonal mean BrO climatologies for 2003-2010 (except for SMILES, 2009-2010) of all instruments available as derived from their daytime measurements and with the data for OSIRIS and SCIAMACHY scaled to 10am. The SMILES measurement range does not overlap substantially with OSIRIS or SCIAMACHY, so the comparison in the USLM is basically between the two SMILES products themselves as derived from the A-band (SMILES(1)) versus C-band (SMILES(2)) measurements. The comparison between OSIRIS and SCIAMACHY is further limited by the seasonally varying latitude coverage of OSIRIS.

The multi-instrument mean (MIM) reveals the structure of BrO throughout the domain, however it should be kept in

*Table 4.21.1: **Available BrO measurement records from limb-sounding satellite instruments between 1978 and 2010.** The red filling of the grid boxes indicates the temporal and vertical coverage of the respective instrument.*

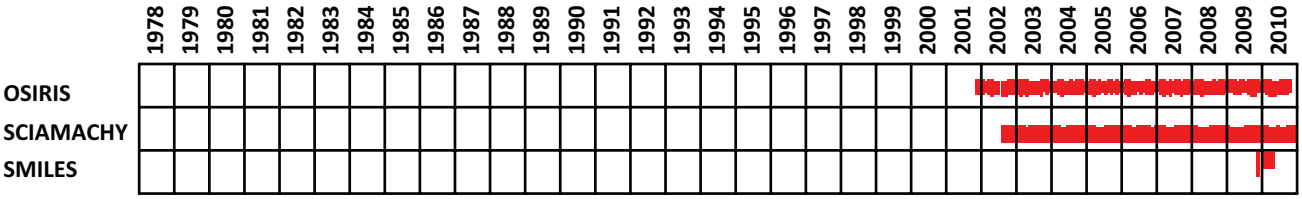

Table 4.21.2: Time period, vertical range, vertical resolution, references and other comments for BrO measurements.

Instrument	Time period	Vertical range	Vertical resolution	References	Additional comments
OSIRIS V5.0	Oct 01 –	16 – 36 km (100 – 5 hPa)	3 – 5 km	*McLinden et al.*, 2010	Zonally averaged spectra with 10° lat bins; 6:30am/pm and scaled to 10am/pm
SCIAMACHY V4.1	Sep 2002 – Apr 2012	14 – 30 km (150 – 10 hPa)	3 – 5 km	*Rozanov et al.*, 2011	10am (LT of crossing at equator) and scaled to 10am/pm
SMILES V2.1.5	Oct 2009 – Apr 2010	30 – 60 km (10 – 0.2 hPa)	4 – 5 km (stratosphere) 5 – 8 km (mesosphere)	*Kreyling et al.*, 2013 *Kasai et al.*, 2013	Band A (SMILES(1)) and C (SMILES(2)) measurements day/night

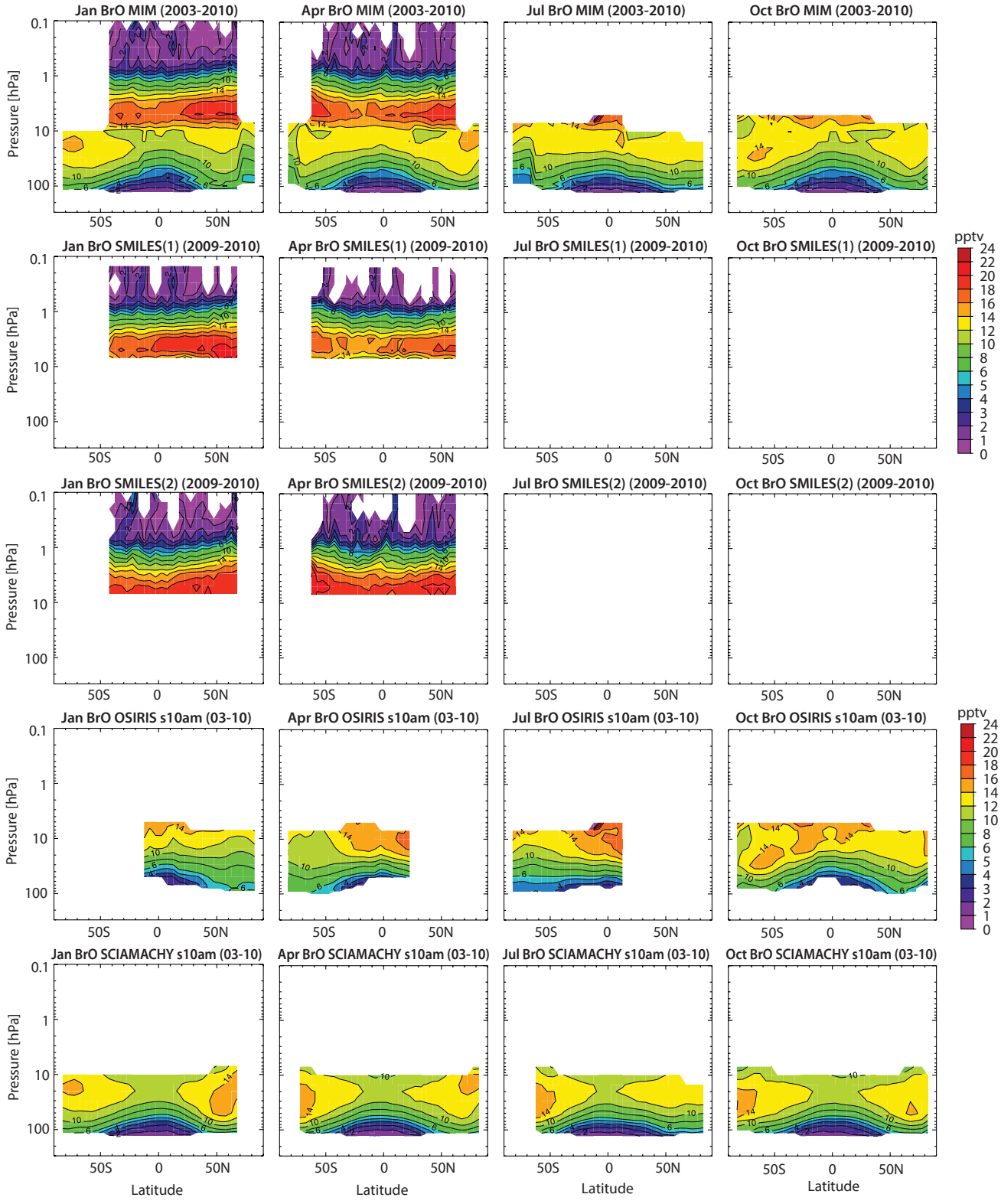

Figure 4.21.2a: Cross sections of monthly zonal mean BrO for 2003-2010. *Monthly zonal mean BrO cross sections are shown for the MIM, daytime SMILES(1) and SMILES(2) (2009-2010) measurements, OSIRIS 6:30am measurements scaled to 10am (2003-2010), and SCIAMACHY 10am measurements scaled to 10am (2003-2010).*

mind that this distribution exhibits considerable uncertainty because it is based on at most two instruments (just one in the USLM). Very low mixing ratios (< 1 pptv) are found in the tropical UT. Beyond the tropopause, and for the first few kilometers in the LS, mixing ratios are steadily increasing (with values up to around 8 pptv), and with isopleths that are seen to roughly follow the tropopause shape as expected from a trace gas with longer-lived tropospheric gases as its source. A band of high BrO values (with a maximum of about 18 pptv) is found between 30 and 5 hPa before mixing ratios decrease again towards the LM. This behaviour is similar to that seen in ClO (see *Section 4.19*).

Figure 4.21.2b shows the differences of the monthly zonal mean climatologies from the MIM. In the MS (except around 20 hPa where the instruments agree very well), SCIAMACHY (OSIRIS) shows negative (positive) differences from the MIM of around ±10%. On the other hand in the LS, SCIAMACHY (OSIRIS) shows positive (negative) differences from the MIM that are up to ±20% and larger. The structure and magnitude of the differences is observed for all months and is consistent with the study by *McLinden et al.* [2010]. In the US, the two A-band and C-band climatologies derived from SMILES agree very well to within ±2.5% at least during April. The differences between the two products are larger during January (up to ±10%) and also increase towards the LM. As can be seen in **Figure A4.21.1** in *Appendix A4*, the scaled climatologies when compared to those that are unscaled do not lead to a considerable improvement in the agreement between the instruments' monthly climatologies. This is likely because the diurnal variations during daytime are very small.

4.21.3 BrO evaluations: Vertical and meridional profiles

The vertical and meridional profiles shown in **Figures 4.21.3** and **4.21.4** provide more detailed information on inter-instrument differences, here considering only single-month evaluations in 2009 and 2010 during the time period when SMILES was operating.

Figure 4.21.3, which shows vertical profiles at different latitudes, indicates that the three instruments' climatologies seem not to agree on the altitude level where a maximum in BrO is found. SCIAMACHY indicates a maximum around 20 hPa, OSIRIS at around 10 hPa. SMILES, although it

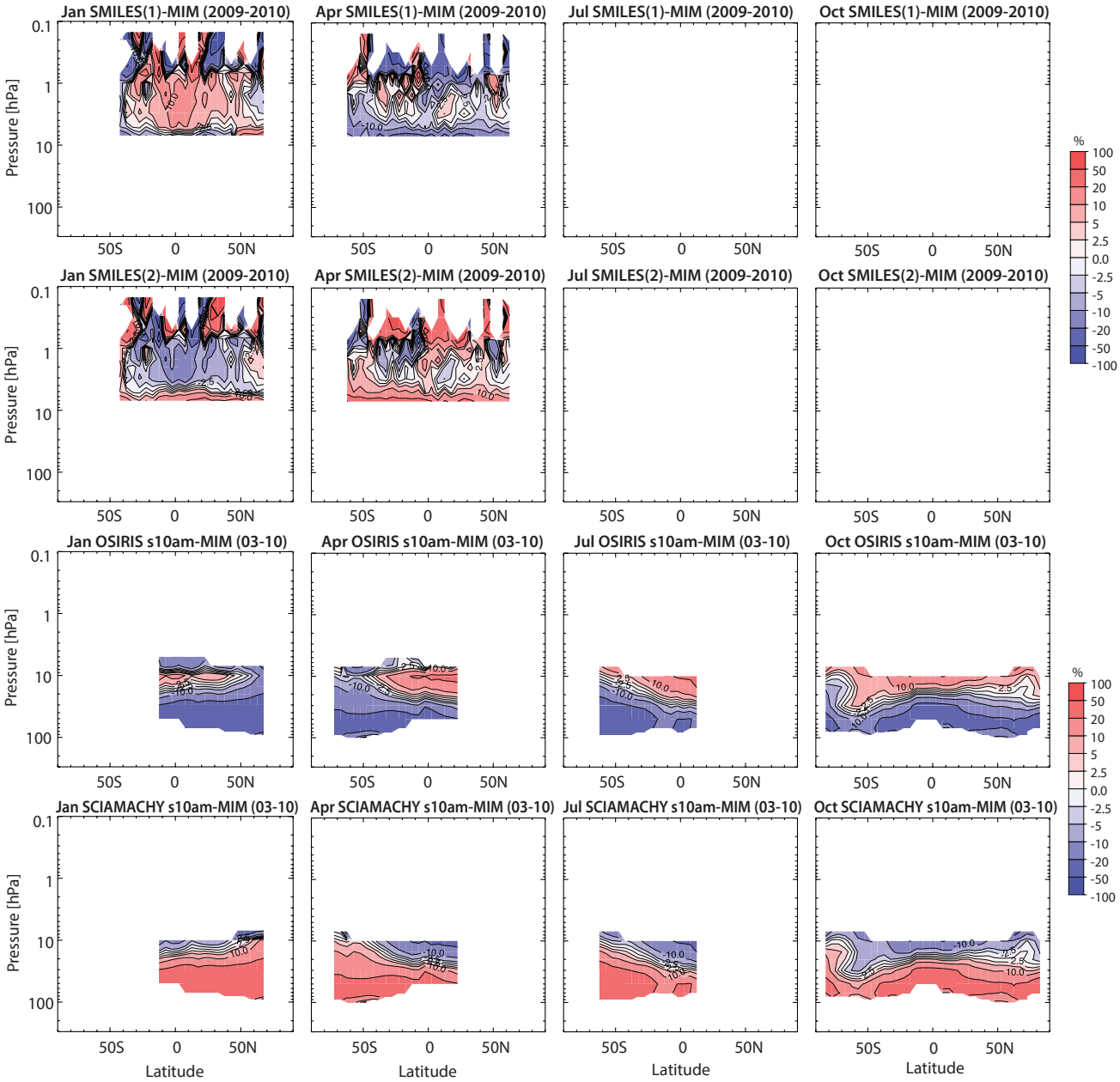

Figure 4.21.2b: Cross sections of monthly zonal mean BrO differences for 2003-2010. *Monthly zonal mean BrO differences between the individual instruments (SMILES, OSIRIS, and SCIAMACHY) and the MIM are shown.*

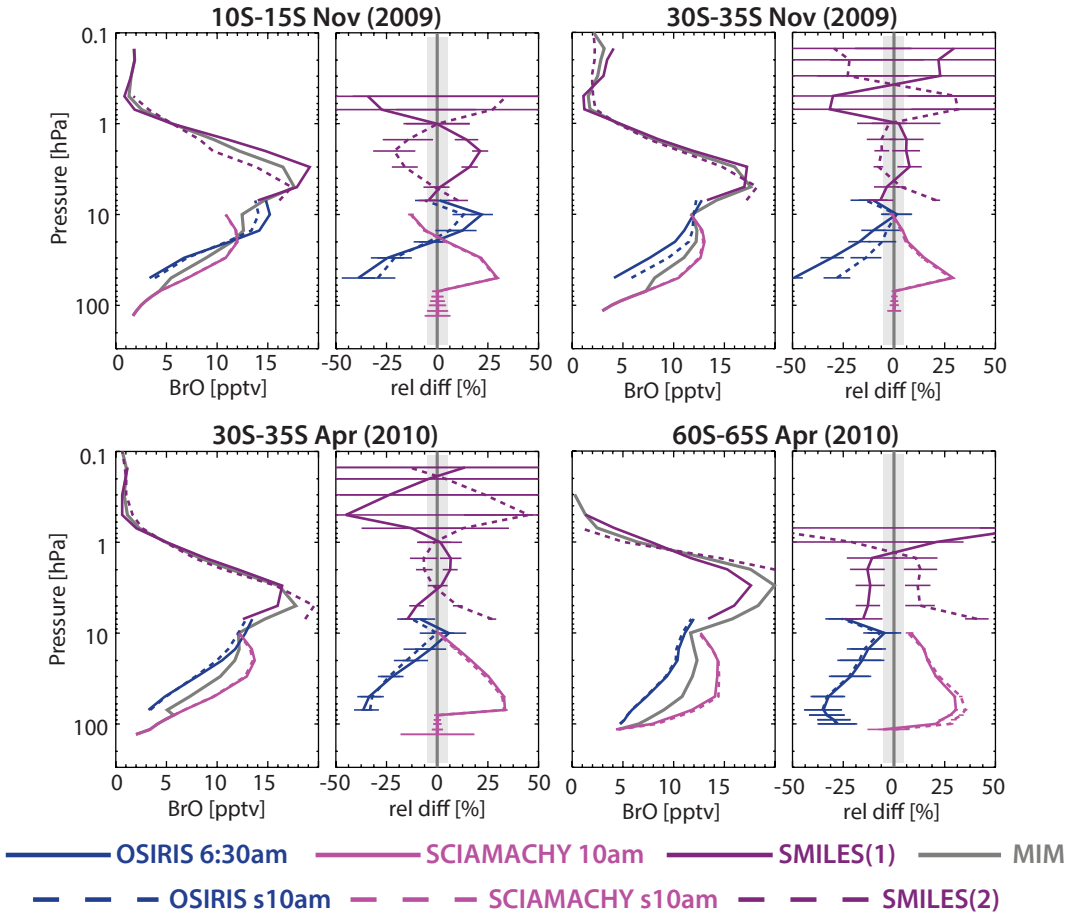

Figure 4.21.3: Vertical profiles of zonal mean BrO for 2009/2010. *Vertical zonal mean BrO profiles for November 2009 (upper panels) and April 2010 (lower panels) are shown for different latitude bands, together with their differences from the MIM. Note, the unscaled OSIRIS and SCIAMACHY products are excluded from the MIM.*

has no coverage below 10 hPa and hence cannot confirm or disprove the existence of a maximum at lower altitudes, shows a maximum at around 3 hPa (which is confirmed by Aura-MLS BrO data, although not shown here, see *Millán et al.*, 2012). The figure highlights again that SCIAMACHY and OSIRIS show only reasonably good agreement (±20% from the MIM) throughout most of the LS, but somewhat better agreement in the MS. The scaling of the climatologies in general leads to an improvement in the agreement of around 10%. The differences between these two instruments are mostly consistent during different months and at different latitudes.

Figure 4.21.4 finally shows meridional profiles during September 2009 and February 2010 at different altitudes. The figure indicates that the large differences in the LS (at 50 hPa) are statistically significant using the SEM as indicator for the uncertainty in the climatology, whereas the smaller differences in the MS (at 20 hPa) during both months lie within the range of the observational uncertainty across most latitudes except the polar region. In the limited measurement range where OSIRIS and SMILES show overlap, the scaled OSIRIS and the SMILES(1) agree mostly very well (within ±5%). Note that despite good agreement between the two SMILES products at 5 hPa, this result is not representative for higher altitudes (see **Figure 4.21.3**).

4.21.4 Summary and conclusions: BrO

BrO climatologies are available from three limb satellite instruments: OSIRIS, SCIAMACHY, and SMILES. While SMILES observes the full diurnal cycle, OSIRIS measurements are made at about 6:30am/pm and SCIAMACHY at about 10am local time at equator crossing, respectively. The observations allow therefore for the compilation of both day- and night-time climatologies. Only the daytime are evaluated here, since the impact of the diurnal cycle on daytime comparisons is deemed smaller (or even negligible). OSIRIS and SCIAMACHY cover the lower altitude range (LS and MS), while SMILES covers the higher altitude range (US and LM). SMILES offers two different BrO products (A-band and C-band retrievals), which are compared in this region.

The overall structure in BrO indicates a minimum in the tropical tropopause region, increasing mixing ratios with increasing altitude in the LS and MS, and a maximum in the US (around 5 hPa) with values around 18 pptv. The BrO distribution thereby resembles strongly the ClO distribution (see *Section 4.19*).

OSIRIS and SCIAMACHY show considerable disagreement in the LS with differences from the MIM of up to

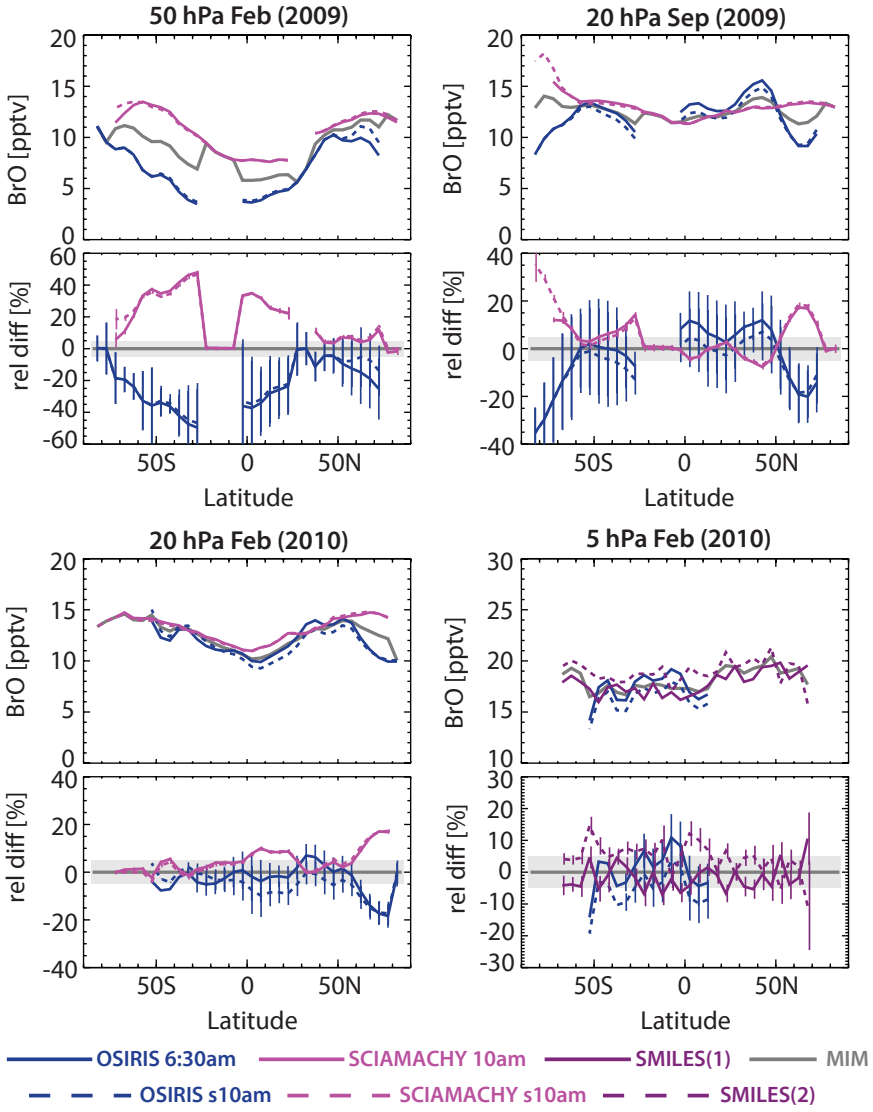

Figure 4.21.4: Meridional profiles of zonal mean BrO for 2009/2010. *Meridional zonal mean BrO profiles for September 2009 at 50 hPa and 20 hPa (upper panels), and for February 2010 at 20 hPa and 5 hPa (lower panels) are shown together with their differences from the MIM. Note, the unscaled OSIRIS and SCIAMACHY products are excluded from the MIM.*

±30%. Note, BrO mixing ratios are relatively low (around a few pptv) in the LS, hence the instruments measure near their detection limit in this region. On the other hand, good agreement (±10%) between the two instruments is found in the MS (except at high latitudes). Good to very good agreement is found between OSIRIS and SMILES(1) where their measurements overlap (around 5 hPa), whereas somewhat larger differences are found between OSIRIS and SMILES(2).

4.22 Hydroxyl radical – OH

The hydroxyl radical (OH) is one of the most reactive molecules in the atmosphere and of great importance to both tropospheric and stratospheric chemistry. OH is known as the cleansing agent of the atmosphere, since it helps in the destruction of many air pollutants and greenhouse gases. However, it is also involved in the catalytic reaction cycles of the HO_x family (OH, HO_2, H) that destroy stratospheric ozone. The HOx cycle was the first catalytic reaction cycle to be identified [*Bates and Nicolet*, 1950]. The primary source of OH in the stratosphere is the reaction of $O(^1D)$ (from the photolysis of O_3) with H_2O. In the mesosphere, another relevant source is the photolysis of water vapour. The OH abundance is generally not dominated by transport (except in polar night), and it depends mainly on local source gas abundances. OH responds very quickly to changes in available sunlight (UV radiation), which leads to OH variations on daily (see **Figure 4.22.1**), seasonal, and longer timescales (*e.g.*, following the 11-year solar cycle variations).

4.22.1 Availability of OH measurements

Measurements of OH are available to the SPARC Data Initiative only from the Aura-MLS instrument and currently only between 2004 and 2009. The climatologies discussed here are derived from daytime measurements (near 1:30pm local time at low- to mid-latitudes). Other OH measurements have been performed in the past on balloon soundings, such as from the Middle Atmosphere High-Resolution Spectograph Investigation (MAHRSI) in 1994 and 1997 [*Conway et al.*, 1999; 2000], the Far-Infrared Spectrometer (FIRS-2) [*Jucks et al.*, 1998], and the Balloon OH (BOH) instrument [*Pickett et al.*, 2006]. There have been other measurements of mesospheric OH from space, namely by the Spatial Heterodyne Imager for Mesospheric Radicals

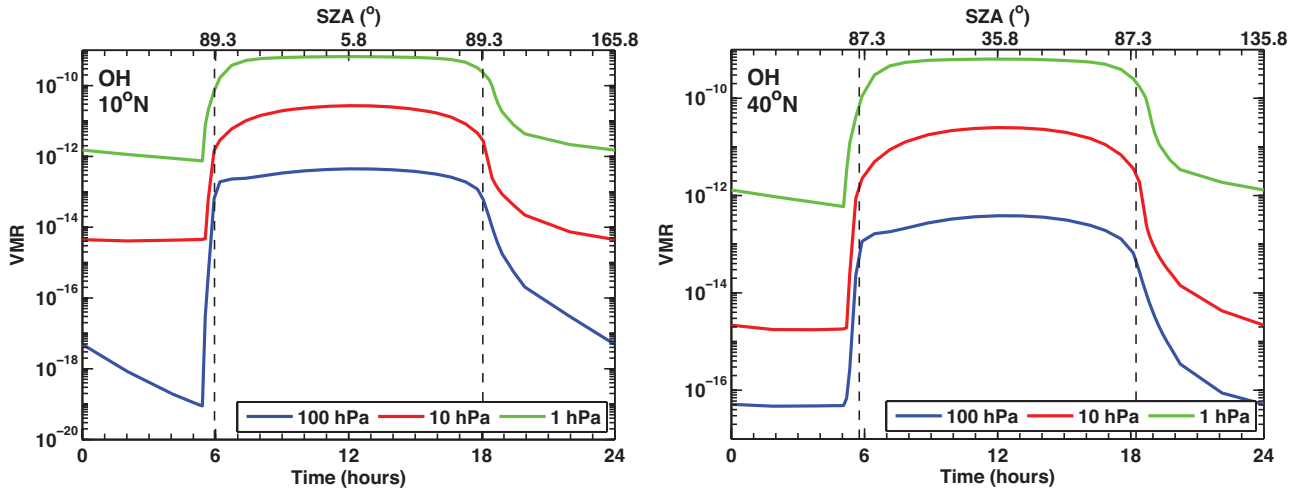

Figure 4.22.1: Diurnal cycle of OH. *OH variations as a function of LST are shown at 10°N and 40°N at 1, 10 and 100 hPa for March 15. The diurnal cycle is derived using a chemical box model [McLinden et al., 2010].*

(SHIMMER), between March 2007 and October 2009, and analyses of this dataset have been provided by *Englert et al.* [2008; 2010] and *Siskind et al.* [2013]. Good agreement (within 10-20%) between mesospheric OH profiles from SHIMMER and Aura-MLS was generally observed (at various latitudes and time periods), although the MLS values were found to be lower than SHIMMER values by more than 20% near 63-67 km [*Englert et al.*, 2010]. However, most of the altitude range for SHIMMER OH retrievals is above the range of the data files included in the SPARC Data Initiative (with a top pressure level at 0.1 hPa).

Validation of the Aura-MLS measurements has been described by *Pickett et al.* [2006] in terms of comparisons versus balloon-borne data, and by *Wang et al.* [2008] for column OH comparisons versus ground-based data. No major issues have been noted, and the MLS OH data are generally quite consistent with the few other correlative datasets. The 11-year solar cycle variation impacts on OH have also been described by *Wang et al.* [2013], using both ground-based data and the Aura-MLS dataset.

Tables 4.22.1 and **4.22.2** compile information on the availability of OH measurements, including time period, height range, vertical resolution, and references relevant for the data product used in this report.

4.22.2 OH zonal mean cross sections

Satellite OH measurements were only made available to the SPARC Data Initiative from the Aura-MLS instrument, hence there are no comparisons herein with other instruments. Instead, we show annual and monthly zonal mean cross sections from Aura-MLS daytime OH data with the aim to illustrate the general behaviour of and variability in OH in the atmosphere as known from the measurements from this instrument. Note that a correction was applied to the daytime zonal means, by subtracting long-term night-time averages, for the bottom few pressure levels (32 to 10 hPa), where this correction is non-negligible. This is done because the night-time values should be very small, and non-zero MLS night-time averages are more an indication of instrument systematics than real night-time values. The corrected daytime values are found in the SPARC Data Initiative (daytime) data files.

Notable in both the annual and monthly zonal mean OH cross sections are the rather flat distributions of the OH isopleths throughout the tropics and mid-latitudes. No strong seasonality is observed in these regions. At latitudes closer to the poles (higher than approx. 50°N or 50°S) a somewhat stronger seasonality in OH is observed, as further illustrated in the next section. In particular, OH mixing ratios

Table 4.22.1: Available OH measurement records from limb-sounding satellite instruments between 1978 and 2010. *The red filling of the grid boxes indicates the temporal and vertical coverage of the respective instrument.*

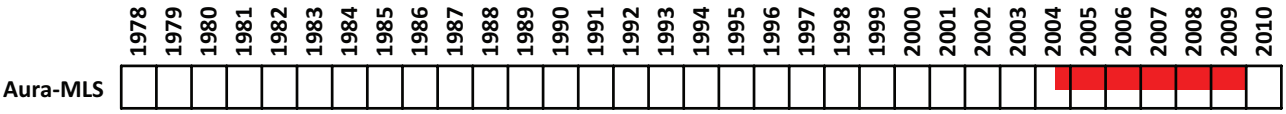

Table 4.22.2: Time period, vertical range, vertical resolution, references and other comments for OH measurements.

Instrument	Time period	Vertical range	Vertical resolution	References	Additional comments
Aura-MLS V3.3	Jul 2004 – Dec 2009	32 – 0.0046 hPa	2.5 km at most pressure levels	*Pickett et al.*, 2008 *Wang et al.*, 2008 *Livesey et al.*, 2013	Only daytime measurements are considered here

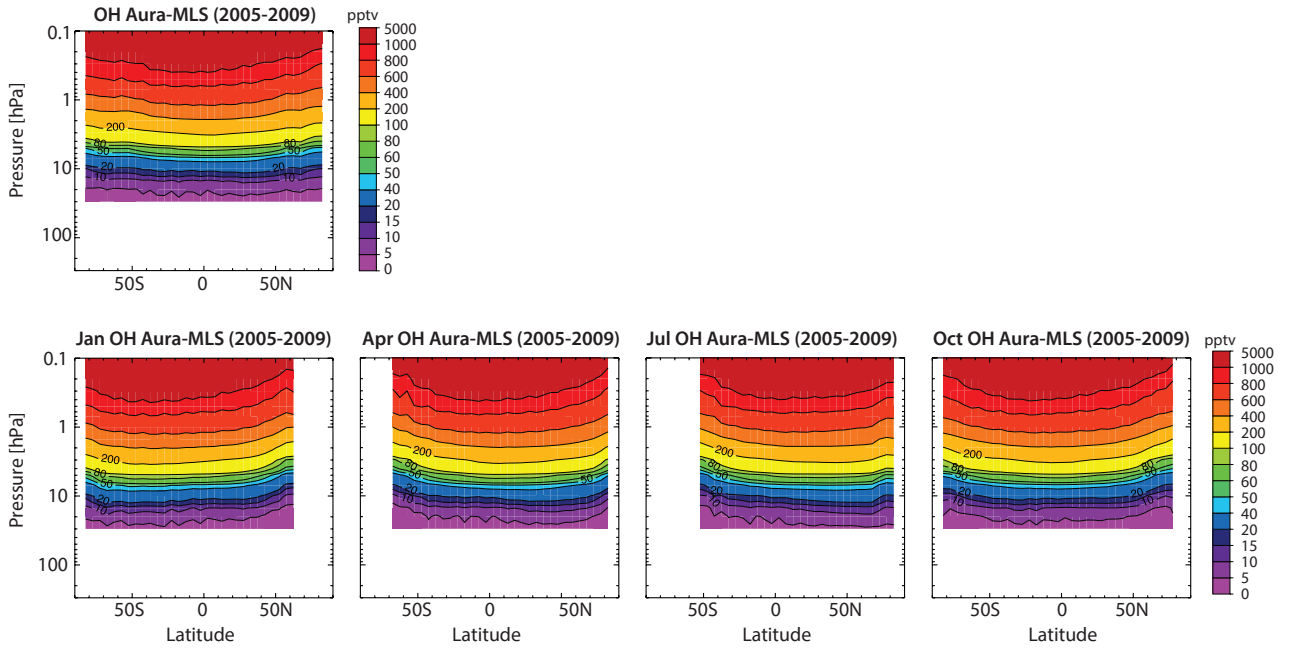

Figure 4.22.2: Zonal mean cross sections. *The annual zonal mean cross section from Aura-MLS averaged over measurements between 2005 and 2009 is shown in the upper left corner. Monthly zonal mean cross sections are shown for January, April, July, and October.*

decrease towards the poles during autumn/early winter. Changes in OH are largely driven by variations in sunlight (solar zenith angle).

4.22.3 OH vertical profiles from Aura-MLS

Aura-MLS zonal mean vertical profiles of OH illustrate the seasonality identified in the above cross sections more quantitatively. Again, in the tropics, there is basically no seasonality. The OH seasonal cycle becomes larger when moving towards higher latitudes, with decreases in the OH mixing ratios at mid-latitudes between July and January by approximately 30%, and in the NH polar region between July and October by up to 50%. The SH mid-latitude region exhibits a somewhat stronger OH decrease during winter than that in the NH.

4.22.4 Summary and conclusions: OH

Aura-MLS is the only instrument providing OH measurements within the SPARC Data Initiative. Aura-MLS OH climatologies are available between 2004 and 2009 and consist of daytime measurements (near 2pm local time, for low- to mid-latitudes). The seasonality in daytime OH is discussed. However, no comparisons with other OH measurements are provided here. An earlier version of the Aura-MLS OH data was validated by *Pickett et al.* [2006, 2008], including estimated uncertainties and comparisons with balloon-borne OH datasets. Based on this work, MLS stratospheric OH systematic uncertainties of about 10% are implied.

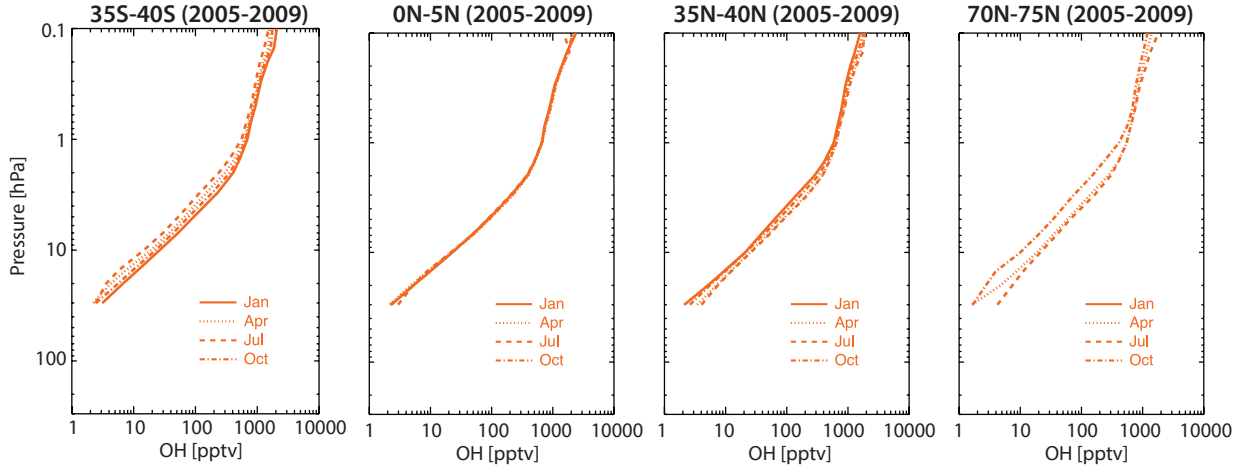

Figure 4.22.3: Zonal mean vertical profiles of daytime OH. *Zonal mean vertical profiles of OH averaged over 2005-2009 from Aura-MLS are shown for different months and latitude bands (SH mid-latitudes and NH equatorial, mid-latitude, and polar region). Note, there is no data during polar night.*

4.23 Hydroperoxy radical – HO_2

The hydroperoxy radical (HO_2) together with the hydrogen atom (H) and hydroxyl radical (OH; see *Section 4.22*) forms the HO_x family. HO_2 is formed in the reaction between a hydrogen atom and molecular oxygen (O_2), or between O_3 and an OH molecule. HO_2 is a highly reactive molecule and plays an important role in stratospheric ozone chemistry through its role in the HO_x catalytic reaction cycles that destroys ozone. The HO_x cycle was the first catalytic reaction cycle to be identified [*Bates and Nicolet*, 1950]. HO_x chemistry dominates ozone destruction above 40 km, while NO_x dominates ozone destruction in the lower stratosphere.

HO_2 exhibits relatively strong day-night differences (see **Figure 4.23.1**), in particular in the lower stratosphere. The relative differences decrease with increasing altitude. Maximum values are found during the day and are relatively constant, minimum values are found before sunrise with more or less steadily decreasing values during the night, when the main reservoir for HO_x is H_2O_2 (hydrogen peroxide), produced from the reaction between two HO_2 radicals. The daytime photolysis of H_2O_2 releases HO_x, and a rapid photochemical equilibrium is set up between OH and HO_2. Two-monthly climatologies of diurnal variations are provided from SMILES observations by *Kreyling et al.* [2013]. *Kuribayashi et al.* [2014] discussed in detail the night-time decrease in HO_2 due to the reaction HO_2 + ClO -> HOCl.

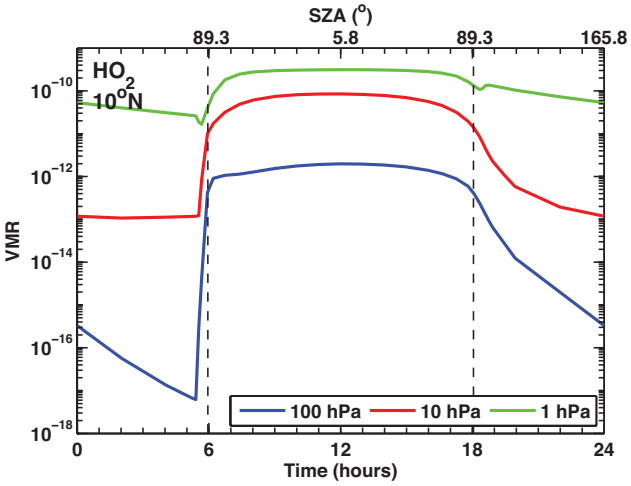

Figure 4.23.1: Diurnal cycle of HO_2. *HO_2 variations as a function of LST are shown at 10°N at 1, 10 and 100 hPa for March 15. The diurnal cycle is derived using a chemical box model [McLinden et al., 2010].*

4.23.1 Availability of HO_2 measurements

Measurements of HO_2 are available within the SPARC Data Initiative from three limb emission satellite instruments, SMILES, SMR, and Aura-MLS, which measure in the sub-mm/microwave wavelength bands. Other available stratospheric HO_2 datasets are restricted to balloon campaigns, such as from the Middle Atmosphere High-Resolution Spectograph Investigation (MAHRSI) in 1994 and 1997 [*Conway et al.*, 1999; 2000] and Far-Infrared Spectrometer (FIRS-2) [*Jucks et al.*, 1998]. There is no temporal overlap of the measurements from the three satellite instruments, since SMR currently provides HO_2 data only as a research product during 2003 and 2004, while the SMILES mission lasted from October 2009 to April 2010. Another difficulty in comparing the observations of these three instruments stems from the fact that they measure at different solar zenith angles, which poses a problem for all short-lived species with strong diurnal cycles. Aura-MLS and SMR are in sun-synchronous orbits and measure at about 1:30am/pm and 6:30am/pm, respectively. SMILES on the ISS was in a non-sun-synchronous orbit and hence measured the full diurnal cycle. For HO_2, no attempt is made here to correct for the differences in local measurement times. However, we focus on the daytime climatologies of SMILES and Aura-MLS, since the HO_2 abundances are larger and fairly constant during the day, and on SMR-am data, which are expected to be closer to daytime values than the SMR-pm data (compare **Figure 4.23.1**). For the MLS HO_2 daytime data, instrumental biases obtained from the night-time values have been subtracted, following the data usage recommendations from the MLS team [see *Pickett et al.*, 2008; *Livesey et al.*, 2013].

Tables 4.23.1 and **4.23.2** compile information on the availability of HO_2 measurements, including time period, height range, vertical resolution, and references relevant for the data product used in this report.

4.23.2 HO_2 evaluations: Zonal mean cross sections

Monthly zonal mean cross sections are analysed to investigate mean biases between the various datasets. Note that the climatologies of the different instruments are not representative of the same years or solar zenith angles, which likely explains some of the differences found between the datasets. SMILES daytime, Aura-MLS 1:30pm, and SMR 6:30am climatologies are used. A study by *Khosravi et al.* [2013] accounts for the diurnal cycle in the validation of the three instruments, however for limited pressure levels, seasons, and latitudes only.

SMR (2003-2004), Aura-MLS (2004-2010), and SMILES (2009-2010)

Figure 4.23.2 shows the comparison of the monthly zonal mean HO_2 climatologies from the different instruments in November and April, averaged over their respective observation periods. As seen in the MIM, mixing ratios are similar in both months in the tropics, indicating a weak seasonal cycle in the daily values in this region, where solar zenith angles do not vary very much with season. Lowest mixing ratios are found in the polar regions of the winter hemisphere (during high solar zenith angle conditions), indicating a more pronounced seasonal cycle in the daily values in these regions.

Table 4.23.1: Available HO_2 measurement records from limb-sounding satellite instruments between 1978 and 2010. The red filling of the grid boxes indicates the temporal and vertical coverage of the respective instrument.

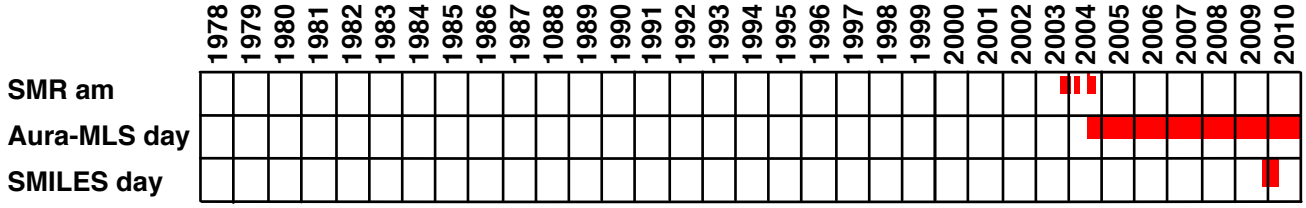

Table 4.23.2: Time period, vertical range, vertical resolution, references and other comments for HO_2 measurements.

Instrument	Time Period	Vertical range	Vertical resolution	References	Comments
MLS Aura V3.3	Jul 04 –	22 – 0.046 hPa	4 – 10 km	*Pickett et al.,* 2006 *Pickett et al.,* 2008 *Khosravi et al.,* 2013	SPARC Data Initiative files are daytime zonal monthly means (corrected by subtracting the small means from night climatology)
SMILES V2.0.1	Oct 09 – Apr 10	26 – 95 km (20 – 0.001 hPa)	4 – 5 km	*Kreyling et al.,* 2013 *Khosravi et al.,* 2013 *Kuribayashi et al.,* 2014 *Millán et al.,* 2015	
SMR V2.1	Oct 03 – Oct 04	30 – 60 km (10 – 0.3 hPa)	4 – 8 km	*Khosravi et al.,* 2013	

The differences between the SMILES and Aura-MLS instruments show distinct features. Aura-MLS exhibits lower values than SMILES by 10-20% through most of the stratosphere and LM, indicating a good to reasonably good agreement between the two instruments, similar to the differences found in *Khosravi et al.* [2013]. Differences are somewhat larger in the respective autumn hemisphere. Aura-MLS (SMILES) show positive (negative) differences at higher latitudes and the lowest/highest altitude regions covered by the SPARC Data Initiative climatologies. Note that using only years for which the instruments overlap yields somewhat better agreement between the datasets, but the overall structures in the differences remain similar. The SMR monthly zonal mean climatologies are based on a few days of data only for each of the chosen months and hence were not included in the calculation of the MIM. SMR exhibits lower values throughout the USLM by more than 50%. Since sunset observations can be more than 100% smaller than daytime measurements, scaling the SMR to daytime values for the comparison would be expected to yield better comparison results. *Khosravi et al.* [2013] have compared these three instruments' measurements in the tropics at three different pressure levels, scaling the data with a model (via local SZA), and find relatively good agreement (within about 10-20%, and also for SMR); this is better than their combined systematic uncertainty estimates (which are at least 15-20%).

4.23.3 HO_2 evaluations: Vertical profiles

The vertical profiles in **Figure 4.23.3** reveal further details of the structure in the differences of the monthly mean cross sections. In order to minimise sampling biases, we here compare the instruments during years of overlap only. Aura-MLS and SMR profiles are compared for August (65°N-70°N) and September (0°S-5°S) for the year 2004. Aura-MLS and SMILES are then compared for November (55°N-60°N) in 2009, and for April (10°S-15°S) in 2010.

For SMR, the time-consistent comparison yields better results than the multi-annual monthly mean comparison in *Section 4.23.2*. Due to its small number of profiles going into the monthly mean, SMR shows however large fluctuations in HO_2 mixing ratios with altitude, and a larger SEM in its differences from the MIM. SMR does not exhibit consistently lower values than Aura-MLS, as would be expected from its sampling times, although the overall behaviour *versus* pressure for this species with strong vertical gradients and small abundances is matched fairly well. For August at northern high latitudes, differences between SMR and Aura-MLS are mostly within 50%. For the September comparison in the Southern Hemisphere tropics, larger differences up to 100% are found, but SMR shows larger SEM values, leading to the differences not being statistically significant.

The comparisons between Aura-MLS and SMILES vertical profiles show consistent structures in their relative differences as in the zonal monthly mean cross section evaluation over the longer time period, with very good agreement in the tropical stratosphere during April. Relative inter-instrument differences lie mostly within 20% except for the lowest levels of the measurement range (with small mixing ratios) (around 10 hPa), where the differences increase to over 100%.

4.23.4 Summary and conclusions: HO_2

HO_2 climatologies are available from three limb-sounders: SMR, Aura-MLS, and SMILES. Here, we compare daytime climatologies from Aura-MLS and SMILES, since daytime HO_2 values are fairly constant allowing for a meaningful comparison despite different local sampling times. For SMR,

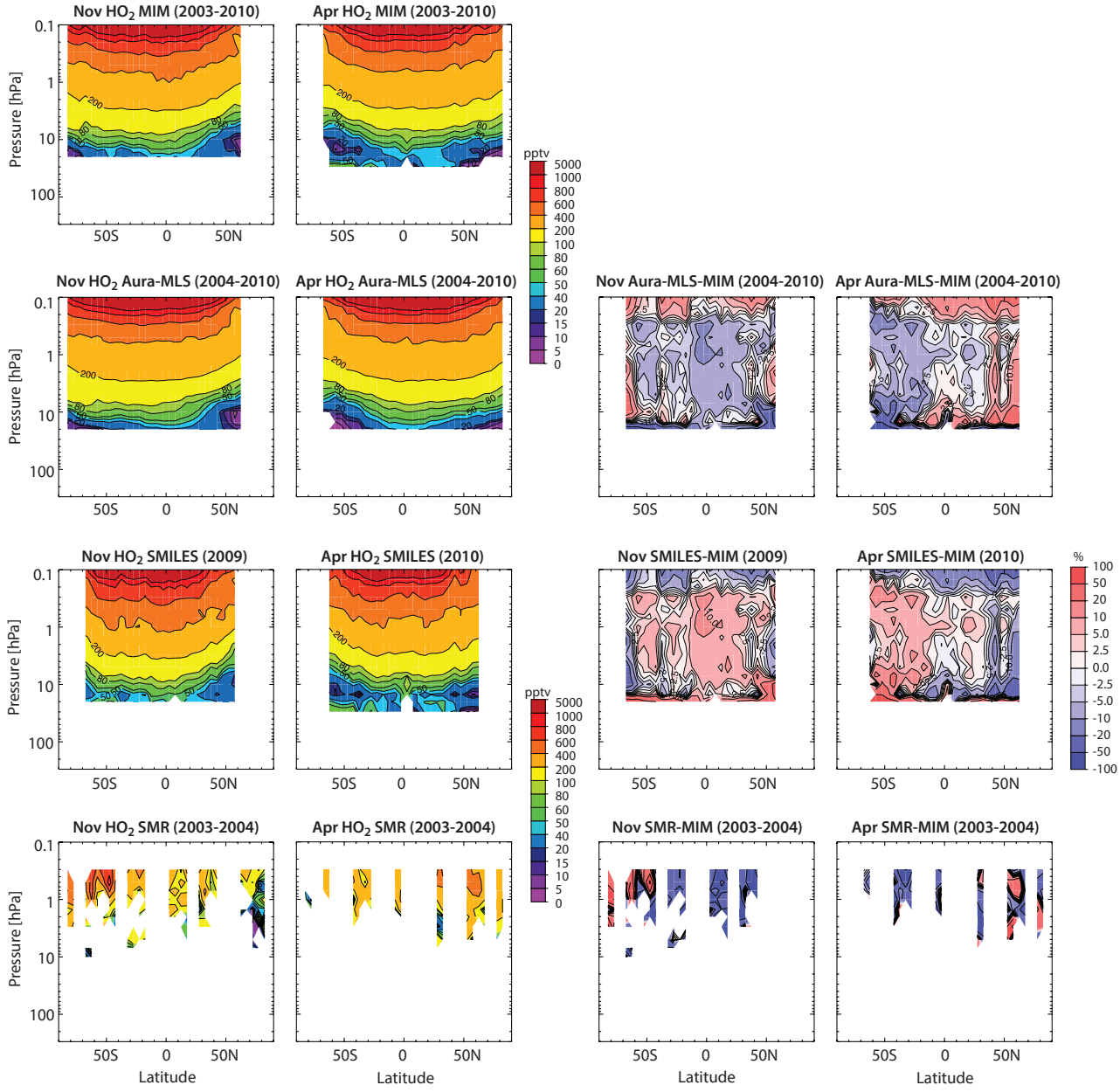

Figure 4.23.2: Cross sections of monthly zonal mean HO_2 and differences from the MIM. *Monthly zonal mean HO_2 cross sections (left two columns) and their differences from the MIM (right two columns) for the different instruments are shown for November and April as averaged over available years. Note SMR is excluded from the MIM due to its limited number of profiles in these monthly zonal mean climatologies.*

we use the climatologies derived from am-measurements, since they are expected to be closer to the daytime measurements than the pm-measurements, although on the low side of those due to the increase in HO_2 when sunlight starts appearing. Note that for a more detailed comparison of SMR with SMILES and Aura-MLS, scaling towards the daytime measurement would have to be applied [see *Khosravi et al.*, 2013]. Overall findings on the systematic uncertainty in our knowledge of the HO_2 mean state are presented in the following summary including the discussion of **Figure 4.23.4**.

Atmospheric mean state

Knowledge of the atmospheric HO_2 annual mean state presented here is based mainly on Aura-MLS, with the information being corroborated primarily by comparison with SMILES. The uncertainty in the annual mean state as derived from the two satellite instruments is smallest in the LM, and also in the tropical MS and US with values smaller than ±10%. The uncertainty increases towards the mid-latitudes with inter-instrument spreads of ±30%. Largest uncertainties are found at the lowest levels at which measurements are available (around 20 hPa). Here, HO_2 mixing ratios are very low (around 40 pptv) and differences increase to up to ±100%. The annual mean results are consistent with single-month comparisons.

Overall, the comparisons between Aura-MLS and SMILES daytime climatologies show promising results and good agreement over much of the altitude range the measurements cover (with inter-instrument differences mostly well

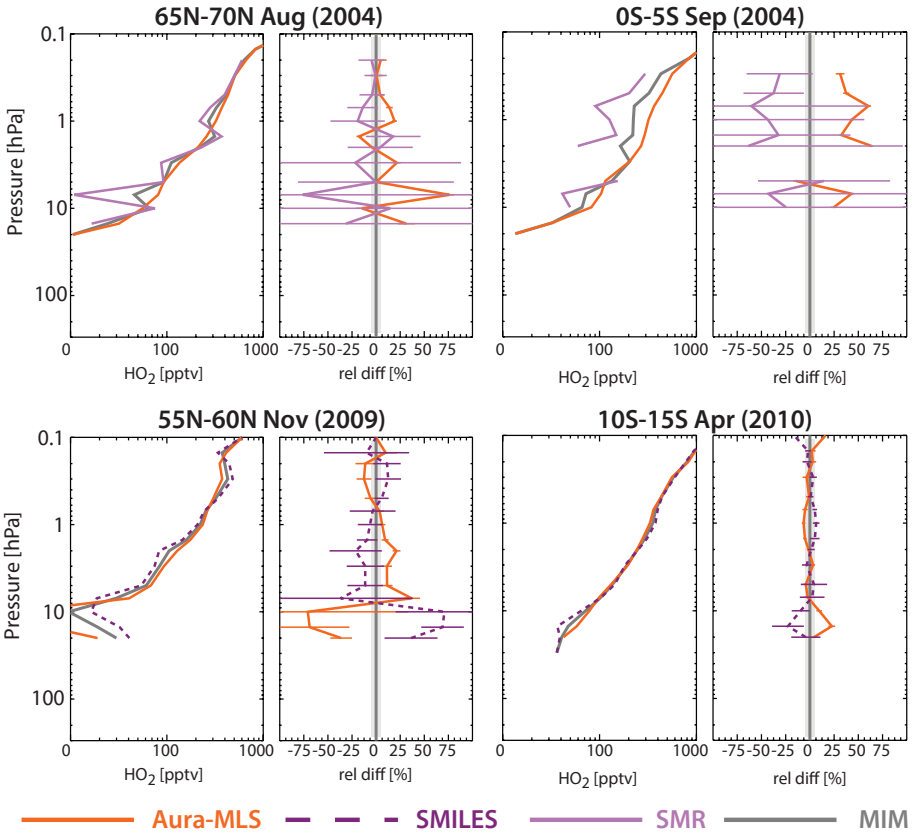

Figure 4.23.3: Altitudinal profiles of zonal mean HO_2. *Altitudinal zonal mean HO_2 profiles are shown along with their differences from the MIM for 65°N-70°N in August and 0°S-5°S in September 2004 for SMR and Aura-MLS (upper panels), and for 55°N-60°N in November 2009 and 10°S-15°S in April 2010 for SMILES and Aura-MLS (lower panels). Error bars in the difference plots indicate the uncertainties in each climatological mean based on the SEM. The grey shaded area indicates that there are few regions where relative differences are smaller than ±5%.*

within 20%, comparable to the *Khosravi et al.*, [2013] results for the tropical region). SMR measurements exhibit larger deviations from these other two instruments, most likely attributable to using unscaled climatologies that are derived from measurements at higher solar zenith angles, but maybe also because a smaller number of SMR profiles are used in the climatologies presented here.

We note also that a recent offline retrieval dataset consisting of daily zonal averages for Aura-MLS HO_2 has been created [see *Millán et al.*, 2015], with some advantages over the MLS routine production data (in the spatial and vertical coverage as well as in the night-time values).

4.24 Formaldehyde – CH_2O

Formaldehyde (CH_2O) is the simplest aldehyde in the atmosphere. CH_2O is an important intermediate in the oxidation of methane and other hydrocarbons, involving sunlight and oxygen. In the stratosphere, its main source is the oxidation of methane. CH_2O is destroyed in the reaction with OH or via photolysis [*Brasseur and Solomon*, 1986]. CH_2O exhibits a small diurnal cycle at least in the middle and upper stratosphere, shown for three different pressure levels derived with a chemical box model [*McLinden et al.*, 2010] in **Figure 4.24.1**. In the troposphere, sources in addition to CH_4 oxidation include oxidation of non-methane hydrocarbons resulting from biomass and fossil

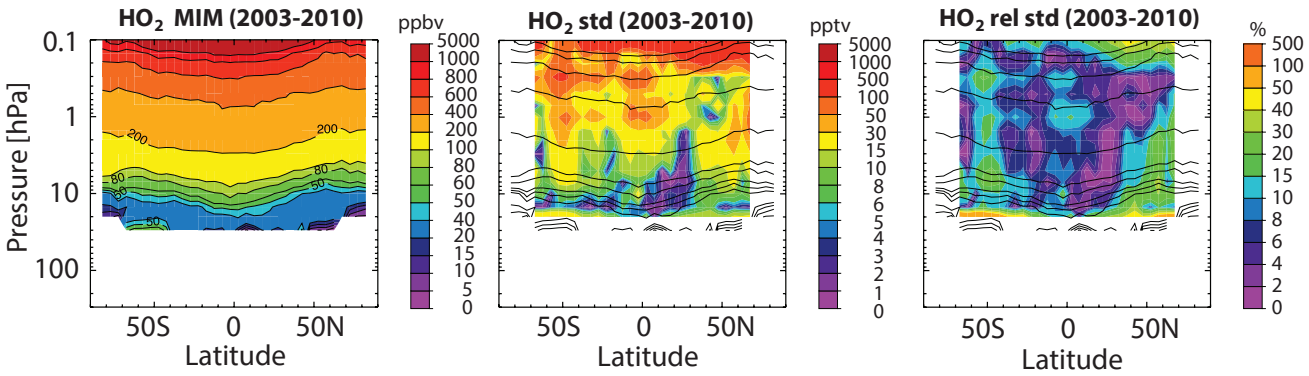

Figure 4.23.4: Summary of HO_2 annual zonal mean state for 2003-2010. *The figures show the annual zonal mean cross sections for 2003-2010 including the MIM, the absolute standard deviation, and the relative standard deviation over the HO_2 fields (from left to right, respectively). Black contours in the middle and right-hand panels repeat the MIM distribution. Instruments considered are Aura-MLS and SMILES. SMR is not included in the MIM due to its limited sampling.*

fuel burning. There are also industrial sources from manufacturing of building materials and household products. Smoking also produces CH_2O. CH_2O is highly toxic to humans and animals, causing allergic reactions, eye, nose, and lung irritations, and potentially cancer.

4.24.1 Availability of CH_2O measurements

CH_2O climatologies are available to the SPARC Data Initiative from the MIPAS and ACE-FTS instruments, which measure in the mid-IR (see **Table 2.2**). MIPAS provided measurements only during the first years of its mission, when the instrument was operating in the high spectral resolution mode [*Steck et al.*, 2008]. It obtains measurements from the upper troposphere to the upper stratosphere. ACE-FTS on the other hand extends into the mid troposphere while its upper bound is limited to the lower stratosphere [*Coheur et al.*, 2007; *Dufour et al.*, 2009]. SMR produced a CH_2O product for the upper stratosphere [*Ricaud et al.*, 2007], however, these observations are not available here.

Tables 4.24.1 and **4.24.2** compile information on the availability of CH_2O measurements, including time period, altitude range, vertical resolution, and references relevant for the data product used in this report.

4.24.2 CH_2O evaluations: Annual zonal mean cross sections

Annual mean zonal mean cross sections are here analysed to investigate mean biases between the two available datasets. **Figure 4.24.2** shows the annual zonal mean CH_2O climatologies for MIPAS (2002-2004) and ACE-FTS (2004-2009), along with the differences of ACE-FTS to the MIM. Note there is an overlap of only one month (March 2004) between the instruments.

The MIM in the upper stratosphere (here defined by MIPAS only) shows a clear maximum in the annual mean cross section with values that are higher than in the tropical upper troposphere. The strong maximum in CH_2O found in the tropics is present all year and is consistent with model calculations [see also *Ricaud et al.*, 2007]. In the lower

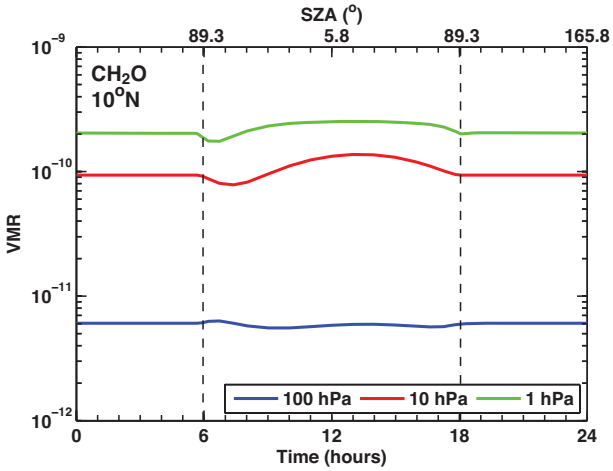

Figure 4.24.1: Diurnal cycle of CH_2O. *CH_2O variations as a function of LST or SZA are shown at 10°N at 1, 10 and 100 hPa for March 15. The diurnal cycle is derived using a chemical box model [McLinden et al., 2010].*

stratosphere, MIPAS shows minima in CH_2O located above the subtropical jets of each hemisphere. These minima are not seen in the ACE-FTS annual mean climatology, which instead shows tropopause-following isopleths. MIPAS averaging kernels [*Steck et al.*, 2008] indicate that CH_2O measurements below 18 km do not contain substantial altitude-resolved information in the UTLS. Thus the differences between MIPAS and ACE-FTS resulting from a comparison without application of averaging kernels should not be over-interpreted. In the tropical and mid-latitudinal lower stratosphere, ACE-FTS exhibits mostly larger mixing ratios (more than 100%) than MIPAS, except in the subtropical jet regions where the ACE-FTS measurements indicate lower values than MIPAS. At higher latitudes and at the upper end of the observational range, ACE-FTS measurements show also lower values than MIPAS. In the UTLS, inter-annually varying sources of CH_2O may contribute to the differences seen between the two instruments.

4.24.3 CH_2O evaluations: Meridional profiles

Meridional profile comparisons are shown in **Figure 4.24.3** and illustrate the details in the differences between the MIPAS

Table 4.24.1: Available CH_2O measurement records from limb-sounding satellite instruments between 1978 and 2010. *The red filling of the grid boxes indicates the temporal and vertical coverage of the respective instrument.*

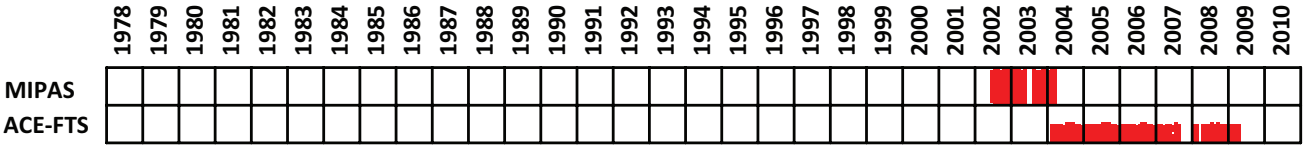

Table 4.24.2: Time period, vertical range, vertical resolution, references and other comments for CH_2O measurements.

Instrument	Time period	Vertical range	Vertical resolution	References	Additional comments
ACE-FTS V2.2	Mar 04 –	5 – 25 km (500 – 25 hPa)	3 – 4 km	*Dufour et al.*, 2009	Research product from v2.2 used here
MIPAS V2	Jul 02 – Mar 04	10 – 60 km (250 – 0.2 hPa)	11 km	*Steck et al.*, 2008	Data only in high spectral resolution mode available

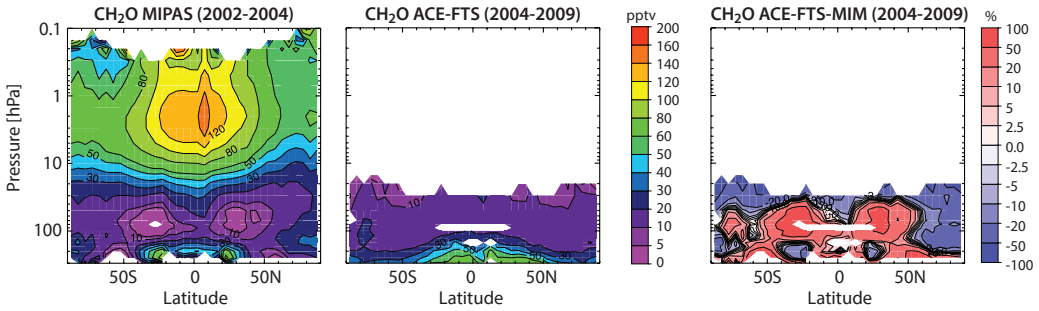

Figure 4.24.2: Cross sections of annual zonal mean CH_2O. *Annual zonal mean CH_2O cross sections are shown for MIPAS (2002-2004) and ACE-FTS (2004-2009), as well as the difference of ACE-FTS from the MIM.*

and ACE-FTS annual mean climatologies on a monthly basis. Note again that due to the low altitude resolution of MIPAS for this trace gas species and altitude range, the differences between MIPAS and ACE-FTS should be interpreted with care.

The measurements show smaller (or based on the SEM statistically less significant) differences in the SH than in the NH high latitudes, similar to the results found by *Steck et al.* [2008] for higher altitudes in comparisons with SMR. Relative differences in the NH between the two instruments are larger for March (up to 100%) than for September (mostly smaller than 50%). This result may be partially explained by higher interannual variability at polar latitudes during winter/spring than summer/autumn months together with the fact that ACE-FTS and MIPAS monthly means were not averaged over the same years. In contrast to the annual mean and March evaluations, ACE-FTS shows positive differences from the MIM at higher latitudes in September that are however statistically less significant.

4.24.4 Seasonality in CH_2O

Monthly zonal mean cross sections are compared for January, April, July, and October in order to illustrate the seasonal cycle found in CH_2O and to investigate the consistency of inter-instrument differences throughout the year in more detail (**Figure 4.24.4**). The monthly zonal mean differences are generally consistent with those derived from the annual mean evaluation, although the differences show somewhat more varying structures.

For a focus on seasonality in CH_2O in the MS and US, vertical profiles of MIPAS data are shown in **Figure 4.24.5** for

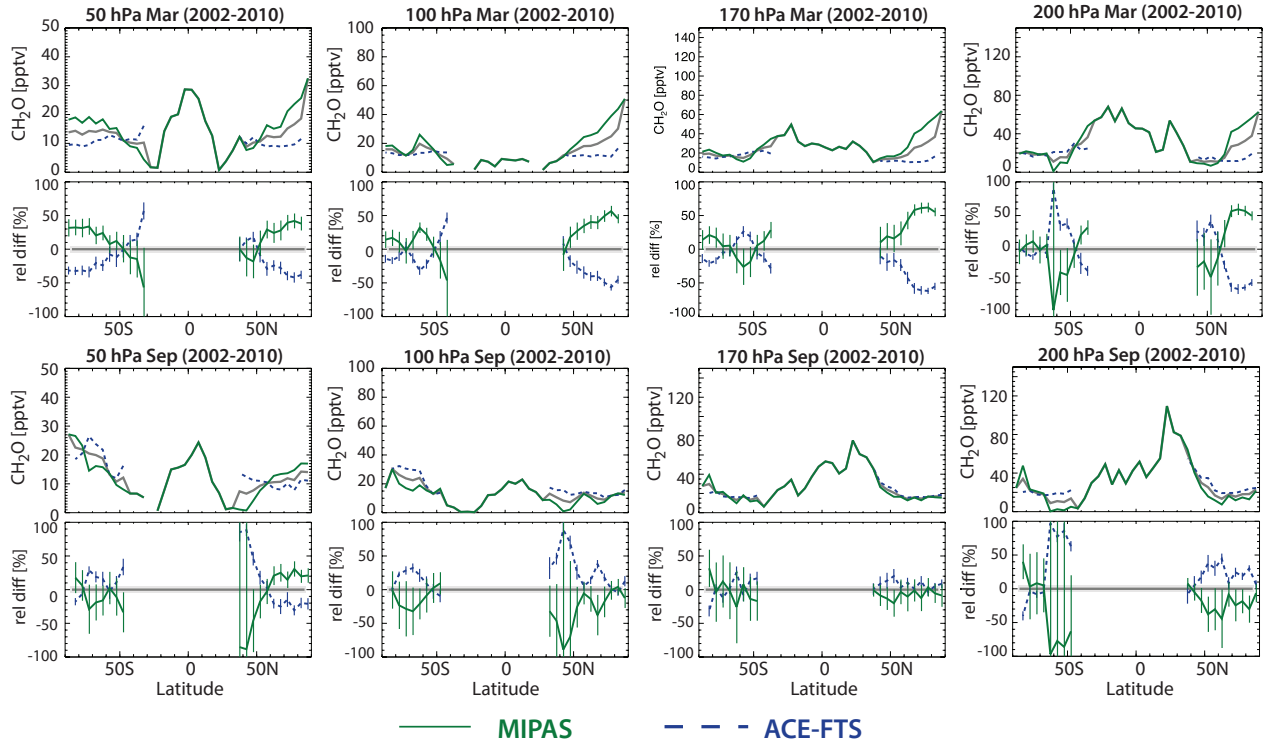

Figure 4.24.3: Meridional profiles of zonal monthly mean CH_2O. *Meridional zonal monthly mean CH_2O profiles for March (upper panels) and September (lower panels) are shown together with their differences from the MIM at 50, 100, 170, and 200 hPa. Error bars in the difference plots indicate the uncertainties in each climatological mean based on the SEM. The grey shaded area indicates where relative differences are smaller than ±5%.*

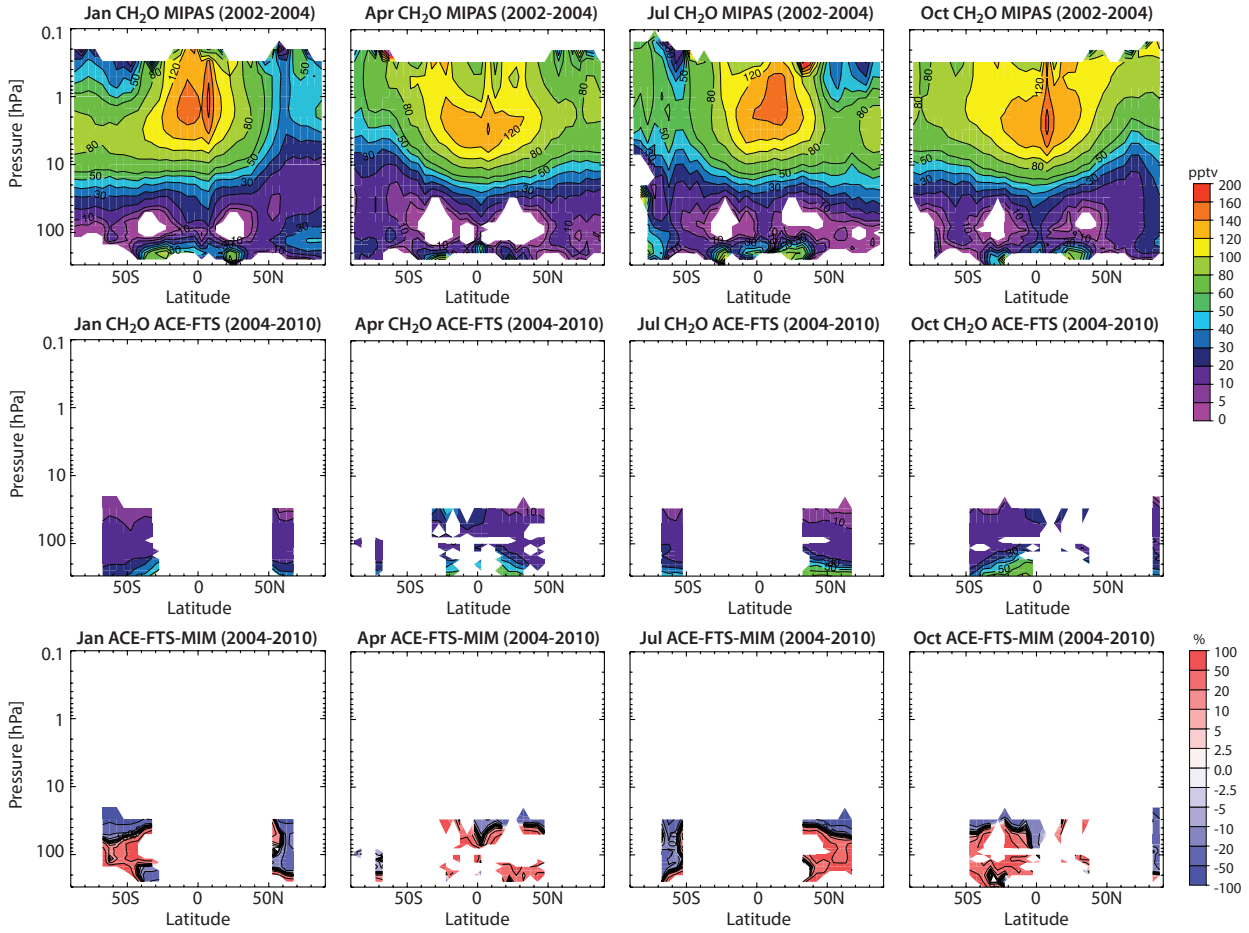

Figure 4.24.4: Monthly zonal mean cross sections of CH_2O. *Monthly zonal mean cross sections for MIPAS (2002-2004; upper row) and ACE-FTS (2004-2009; middle row) are shown for January, April, July, and October. Also shown (lower row) are the relative differences of ACE-FTS to the MIM.*

different latitudes. CH_2O in the extratropical LS and MS exhibits lowest values during autumn and winter. Maxima in extratropical CH_2O mixing ratios are found in the US during spring and summer when available sunlight triggers the production of CH_2O.

4.24.5 Summary and conclusions: CH_2O

CH_2O climatologies are available in the SPARC Data Initiative from MIPAS and ACE-FTS. The measurements were obtained in different years, with ACE-FTS focusing on

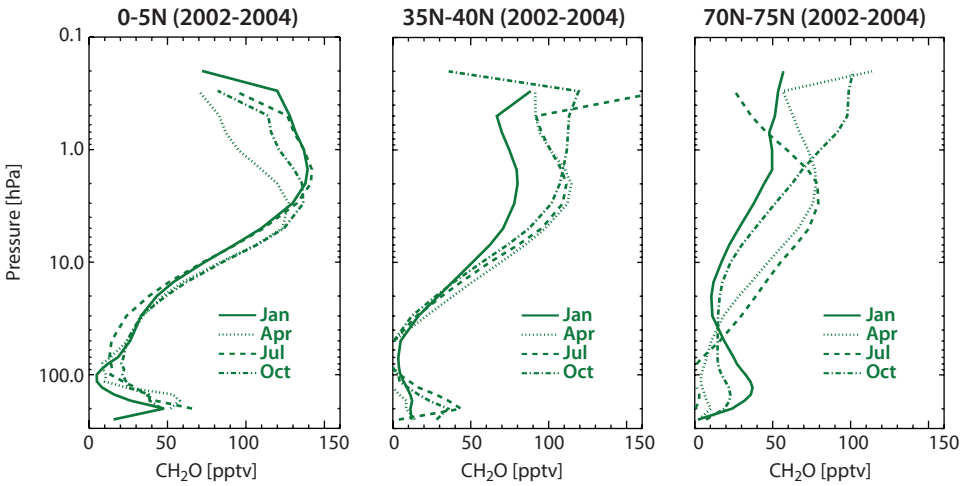

Figure 4.24.5: Altitude profiles of CH_2O. *Zonal monthly mean altitude profiles from MIPAS are shown for three different latitude bands in the tropics (0°N-5°N), at mid-latitudes (35°N-40°N) and in polar regions (70°N-75°N) for January, April, July and October.*

the troposphere/lower stratosphere, while MIPAS obtained measurements into the upper stratosphere. Differences in regions of overlap are relatively large and reach from 40% to over 100%. Largest differences are found in the subtropical LS and attributable to the relatively low vertical resolution of MIPAS, which is not adequate to resolve the distinct structures in CH_2O tracer fields around the tropopause and jet regions. In general, ACE-FTS shows mostly higher values than MIPAS with the exception of the subtropical jet regions and towards the upper limit of its measurement range.

4.25 Acetonitrile - CH_3CN

Acetonitrile (CH_3CN) is an organic trace gas in the atmosphere, which is relatively long-lived (lifetime of around 20 years at 20 km). Its main source is biomass burning [*Arijs and Brasseur*, 1986], with ocean uptake believed to be the dominant sink of the constituent [*de Gouw et al.*, 2003]. Chemical loss occurs with the hydroxyl radical (OH), however, this reaction is known to be rather slow. Tropospheric background levels are between 50 and 200 pptv [*de Gouw et al.*, 2003], while greatly enhanced values are found in biomass burning regions. Early measurements from UARS-MLS pointed to the possible existence of an additional low latitude stratospheric source of CH_3CN between 30-10 hPa (25-30 km) [*Livesey et al.*, 2001], which has not been fully explained.

4.25.1 Availability of CH_3CN measurements

Measurements of CH_3CN are available to the SPARC Data Initiative from one instrument only, SMILES, and hence only cover a few months. The first satellite-based global CH_3CN observations were made by UARS-MLS [*Livesey et al.*, 2001; 2004], and more CH_3CN products/analyses have now become available. ACE-FTS offers also measurements of global, lower stratospheric CH_3CN, which are described by *Harrison and Bernath* [2013]. While Aura-MLS measurements of CH_3CN exist, this noisy product has not been sufficiently characterised and some high biases appear to exist in the lower stratosphere [*Livesey et al.*, 2013]. Significant enhancements in lower stratospheric CH_3CN, as well as CO and HCN, were observed by Aura-MLS in the Southern Hemisphere, after the large Australian bush fires in February, 2009 [*Pumphrey et al.*, 2011].

Tables 4.25.1 and **4.25.2** compile information on the availability of CH_3CN measurements, including time period, height range, vertical resolution, and references relevant for the data product used in this report.

4.25.2 CH_3CN evaluations: Zonal mean cross sections

Zonal monthly mean cross sections are shown in **Figure 4.25.1** for selected months over the SMILES mission period (2009-2010). The cross sections reveal a strong maximum between 10 and 2 hPa, located in the SH tropics just off the equator. This maximum is at somewhat higher altitudes in the atmosphere than that identified in the early UARS-MLS measurements [*Livesey et al.*, 2001]. However, mixing ratios are similar to those found in these early measurements with maximum values between 50-60 pptv. ACE-FTS has an observational range that is limited to the lower stratosphere, and shows no indications of a tropical maximum at these altitudes [*Harrison and Bernath*, 2013]. Rather, it shows values decreasing from about 150 ppt at 11.5 km to less than 40 ppt at 25.5–29.5 km, the upper limit of its observational range.

No such maximum is seen in the extra-tropics as also illustrated in **Figure 4.25.2**. The vertical profiles reveal only a small seasonality in the tropics, increasing towards higher latitudes. At 45°N-50°N, lowest values are found in early spring, and highest in early winter at 10 hPa, although the full amplitude of the seasonal cycle cannot be determined due to the limited observation period.

4.25.3 Summary and conclusions: CH_3CN

CH_3CN climatologies are available to the SPARC Data Initiative from the SMILES instrument only. The monthly zonal mean CH_3CN climatologies from SMILES have limited temporal and vertical coverage, but reveal a maximum in the tropical upper stratosphere. Monthly profiles also indicate some seasonality that is increasing towards higher latitudes. No comparisons have been made with other instruments, however CH_3CN mixing ratios are comparable with those found in the literature on early UARS-MLS observations [*Livesey et al.*, 2001]. CH_3CN observations are now also available from Aura-MLS [*Livesey et al.*, 2013] and

Table 4.25.1: Available CH_3CN measurement record from limb-sounding satellite instruments between 1978 and 2010. *The red filling of the grid boxes indicates the temporal and vertical coverage of the respective instrument.*

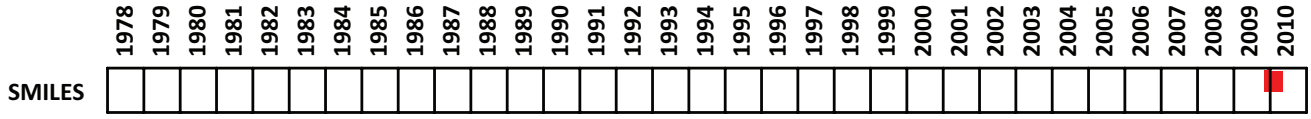

Table 4.25.2: Time period, vertical range, vertical resolution, references and other comments for CH_3CN measurements.

Instrument	Time period	Vertical range	Vertical resolution	References	Additional comments
SMILES V2.1.5	Nov 2009 – Apr 2010	16 – 0.1hPa	3 – 5 km	See **http://smiles.nict.go.jp/index-e.html** for information	Here, the total CH_3CN product is used

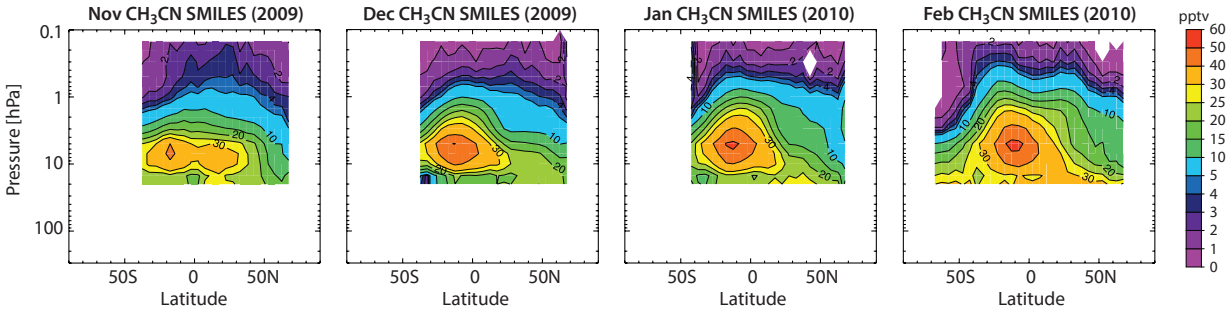

Figure 4.25.1: Cross sections of monthly zonal mean CH_3CN for 2009/2010. *Monthly zonal mean CH_3CN cross sections for November and December 2009, and January and February 2010 as obtained from SMILES observations.*

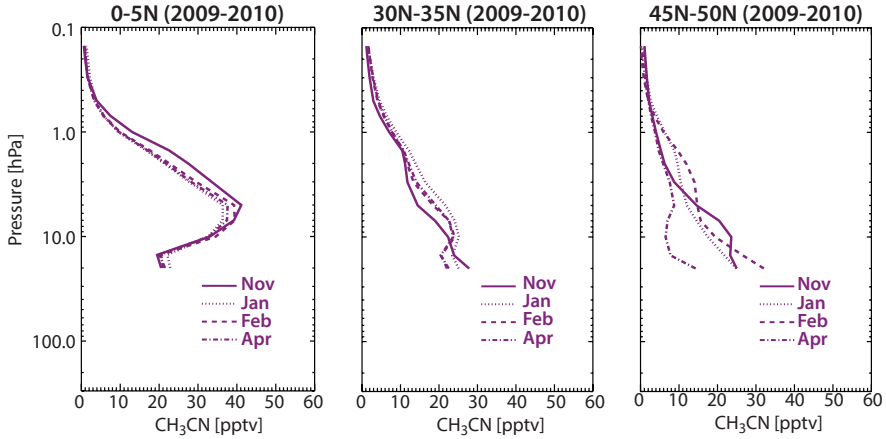

Figure 4.25.2: Vertical profiles of CH_3CN. *Zonal mean vertical profiles of CH_3CN from SMILES are shown for different months and latitude bands (equator, subtropics, and mid-latitudes).*

ACE-FTS (although these measurements are limited to the lower stratosphere)[*Harrison and Bernath*, 2013].

4.26 Aerosol

Aerosol has both natural and anthropogenic sources. Stratospheric aerosol consists primarily of liquid hydrated sulfuric acid droplets with an effective radius in the submicrometer range [*Carslaw et al.,* 1997]. The dominant source gases of stratospheric aerosol are (in order of importance) OCS, SO_2, CS_2 and Di-Methyl-Sulfide (DMS), entering the stratosphere primarily in the tropics [*SPARC*, 2006]. Natural sources of these precursors are ocean spray and desert dust, biological activity in oceans, meteoritic material, and volcanoes, the latter being capable of injecting material directly into the stratosphere in both the tropics and extra-tropics. The most important human source is fossil fuel combustion (in particular from air traffic) and biomass burning. Stratospheric aerosol has a key role in chemistry and the radiation budget of the atmosphere [*McCormick et al.*, 1995]. It offers a surface for heterogeneous reactions, controlling abundances of stratospheric NO_x [*Angell et al.*, 1985; *Hofmann and Solomon*, 1989]. NO_x in turn helps determining abundances of ClO_x and HO_x, species that are involved in stratospheric ozone depletion [*Wennberg et al.*, 1994; *Solomon et al.*, 1996]. Direct radiative forcing caused by increased aerosol loadings after volcanic eruptions leads to stratospheric warming [*Labitzke and McCormick*, 1992] and tropospheric cooling [*Manabe and Wetherald*, 1967]. Aerosol also serves as cloud condensation nuclei in the upper troposphere and the polar vortex regions [*Laaksonen et al.*, 2000], leading to an indirect radiative forcing effect. The stratospheric aerosol layer [*Junge et al.*, 1961], also called the Junge layer, has been shown to be highly variable resulting from both major and minor volcanic eruptions that reach the stratosphere [*Vernier et al.*, 2011].

4.26.1 Availability of aerosol measurements

Measurements of aerosol since 1984 are available to the SPARC Data Initiative, with the longest time series of 20 years from SAGE II ending in 2005. HALOE provides aerosol measurements from 1991 to 2005. Aerosol measurements over shorter time periods and with more limited latitude coverage are also available from SAGE III, POAM II, and POAM III. The newer generation of satellite instruments includes data from OSIRIS, GOMOS (two data products, AERGOM and v6.01, the latter hereafter simply referred to as GOMOS), and SCIAMACHY with measurements starting in the early 2000s. The data presented in this report are representative but not comprehensive. A number of valuable aerosol products can also be obtained from SAGE I [*Chu and McCormick*, 1979], SAM II [*McCormick et al.*, 1979; 1981], CLAES [*Roche et al.*, 1993], SME [*Eparvier et al.*, 1994; *Rusch et al.*, 1994], ORA [*Fussen et al.*, 2001], ILAS and ILAS II [*Sasano*, 2002], ISAMS [*Taylor et al.*, 1993; *Lambert et al.*, 1993], ACE imager [*Vanhellemont et al.*, 2008], HIRDLS [*Gille and Gray*, 2011] and CALIPSO [*Winker et al.*, 2003].

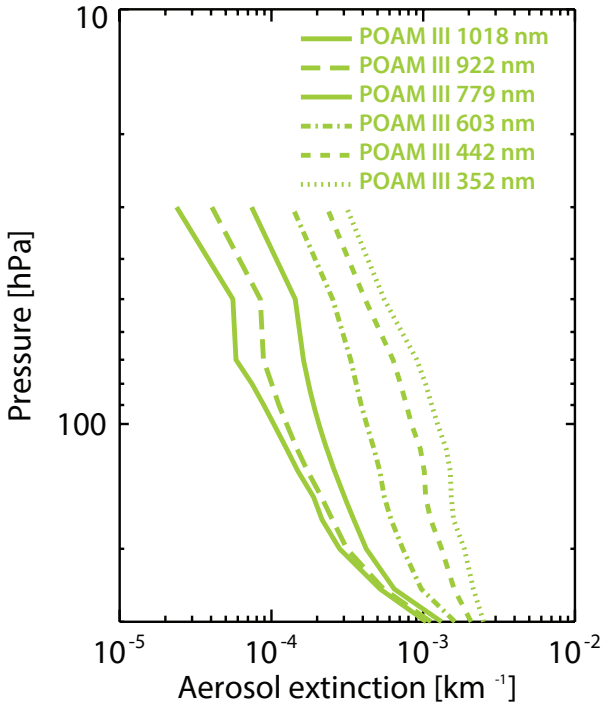

Figure 4.26.1: Aerosol extinction for April 2003. *Shown are the zonal monthly mean altitude profiles of aerosol extinction from POAM III at 60°N as derived from measurements at different wavelengths. The longer the wavelength, the smaller are the aerosol extinction values.*

The most frequently measured aerosol parameter from space that is evaluated in this report is aerosol extinction (with the unit km^{-1}). Full characterisation of aerosol on the other hand would rely on knowledge of size distribution and composition. The retrieved extinction coefficients are a measure of the attenuation of the light passing through the atmosphere due to scattering and absorption by aerosol particles. The extinction varies substantially with wavelength - longer wavelengths have smaller values as can be seen in **Figure 4.26.1**. This complicates multi-instrument comparisons, such as those included in this report, since the instruments measure over a wide range of wavelengths (see **Table 4.26.2**). HALOE products for example are retrieved at much longer wavelengths than products from other instruments, which does not allow for a direct comparison.

It should be noted that there exist fundamental differences between the aerosol extinction products from occultation and limb scattering instruments. Generally, solar, lunar, or stellar occultation sounders are able to provide a direct measurement of the atmosphere's optical depth, which can be translated into aerosol extinction without requiring assumptions on aerosol composition or size. Limb scattering instruments, on the other hand, only provide a derived quantity and require assumptions for aerosol properties in order to characterise the scattering properties of the measured light. A clear benefit of the limb scattering instruments is, however, much better geographical coverage. Note that the two SCIAMACHY products at 470 nm and 750 nm are not independent climatologies. The ratio between the extinction coefficients at these wavelengths is prescribed by the assumed particle size distribution and is not changed by the retrieval. The results at 750 nm are considered to be more reliable due to the much stronger sensitivity at this wavelength. Note also that this is essentially the same technique as used by OSIRIS.

In this report, the monthly zonal mean climatologies of aerosol extinction will be validated using two different approaches. The first approach is to compare aerosol climatologies that are derived from observations at similar wavelengths. These evaluations have to be interpreted with care, since disagreement between two instruments may be attributable to differences in the wavelengths used for the retrieval, while agreement may merely reflect the result of compensating errors. A second approach, which is introduced in more detail by *Hegglin et al.* (in preparation), applies a normalisation factor derived from each climatology during quiescent periods to the available time series. This scaling of the aerosol extinction (AE) to obtain relative anomalies follows the equation:

$$AE_{rel\_ano} = (AE/f\ -1)*100$$

where *f* is a scaling factor and represents the mean aerosol loading in 2004.

This approach has the advantage that all climatologies (even when retrieved at very different wavelengths) can be compared to each other at the same time. The normalisation factor is in principle dependent on the particle size distribution of the aerosol, which is neglected here and may introduce some error in the comparison. However, this error is considered to be of second-order importance compared to other systematic inter-instrument differences including those arising from the wavelength dependency even at similar wavelengths. Only a few examples of this new validation approach will be shown here. An assessment using standard validation approaches between the earlier satellite and ground-based measurements has been provided in the *SPARC ASAP Report* [2006].

Tables **4.26.1** and **4.26.2** compile information on the availability of aerosol measurements used in this report, including time period, altitude range, vertical resolution, relevant references, and list of aerosol retrieval wavelengths.

4.26.2 Aerosol evaluations: Vertical and meridional profiles at similar wavelengths

The available aerosol climatologies are evaluated using zonal monthly means rather than annual means in order to prevent large sampling biases, which would be expected in annual mean comparisons due to the high variability found in aerosol distributions along with the limited geographical coverage solar occultation instruments offer. In the following, we compare aerosol climatologies retrieved at similar wavelengths. To this end the climatologies are classified into five categories according to the wavelength used for the retrievals:

Table 4.26.1: Available aerosol measurement records from limb-sounding satellite instruments between 1978 and 2010. *The red filling in each grid box indicates the temporal and vertical coverage (within the pressure range 300-0.1 hPa) of the respective instrument.*

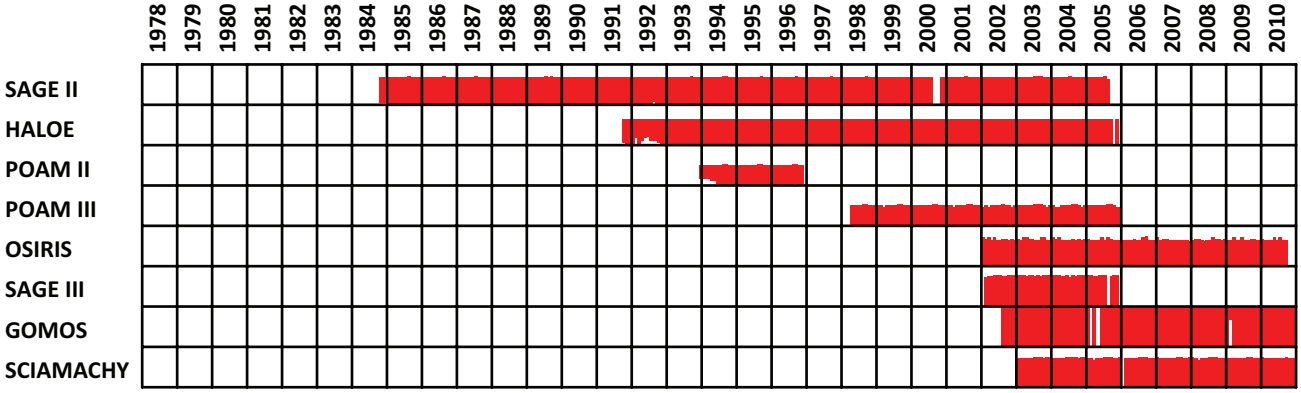

Table 4.26.2: Time period, vertical range, vertical resolution, references and other comments for aerosol extinction measurements.

Instrument	Time period	Vertical range	Vertical resolution	References	Additional comments
POAM II V6.0	Oct 1993 – Nov 1996	10 – 30 km	1 – 1.5 km	*Lumpe et al.,* 1997 *Randall et al.,* 2000	Retrieved/available at 352, 442, 601, 781, 921, 1060 nm
POAM III V4.0	Apr 1998 – Dec 2005	5 – 25 km	1 – 1.5 km	*Lumpe et al.,* 2002 *Randall et al.,* 2001	Retrieved/available at 353, 442, 603, 779, 922, 1018 nm
GOMOS V6.01 AERGOM	Aug 2002 – Apr 2012	10 – 40 km	4 km	*Vanhellemont et al.,* 2010; 2016	Retrieved/available at 500 nm (v6.01), and 350, 450, 470, 500, 525, 600, 750 nm (AERGOM)
	Aug 2002 – Apr 2012	15 – 32 km	3 – 5 km	*von Savigny et al.,* 2015	Retrieved/available at 750 (470) nm
SAGE II V7.0	Jan 1985 – Aug 2005	~5 – 40 km (channel dependent)	1 km	*Damadeo et al.,* 2013	Retrieved/available at 386, 452, 525, 1020 nm
SAGE III V4.0	Feb 2002 – Dec 2005	~5 – 40 km (channel dependent)	1 km	*Thomason,* 2010	Retrieved/available at 520, 755, 1020 nm
HALOE V19	Oct 1991 – Nov 2005	*dependent on aerosol loading	~2 km	*Hervig et al., 1996b Hervig and Deshler, 2002*	Retrieved/available at 2450, 3400, 3460, 5260 nm
OSIRIS V5.07	Nov 2001 – present	15 – 30 km	2.2 km	*Bourassa et al.,* 2007; 2012	Retrieved/available at 750 nm

- **~350 nm:** 350-390 nm
- **~450 nm:** 440-470 nm
- **~550 nm:** 500-610 nm
- **~750 nm:** 750-780 nm
- **~1050 nm:** 1010-1060 nm

Note that no such comparisons could be made for HALOE, since it derives aerosol extinction only at longer wavelengths (2450-5260 nm).

SAGE II, POAM III, and AERGOM (2003, wavelenghs ~350 nm)

Figure 4.26.2 shows the zonal monthly mean cross sections for aerosol extinction climatologies are available from measurements retrieved at wavelengths around 350 nm. Aerosol extinction climatologies from SAGE II are retrieved at 386 nm, AERGOM at 350 nm, and POAM III at 353 nm. Note the different vertical range (300-10 hPa) used in the following figures when compared to previous, monthly zonal mean cross sections in this report.

Figure 4.26.2 reveals the general features of the stratospheric aerosol layer, with high aerosol extinction values in the tropical UT that leak into the tropical LS, and mostly tropopause following aerosol isolines similar as expected from a longer-lived tropospheric source gas. Due to higher sensitivity to temperature, chemistry, and transport and its effects on aerosol, variability however is much higher than for other long-lived chemical trace gases. Towards 10 hPa, the atmosphere is becoming much 'cleaner' and the instruments start to reach their detection limit.

AERGOM (SAGE II) shows higher (lower) values than the MIM by around 10% in the middle stratosphere, and by around 50% in the UT and LS. Note that in the following the MIM has been constructed using all products shown in

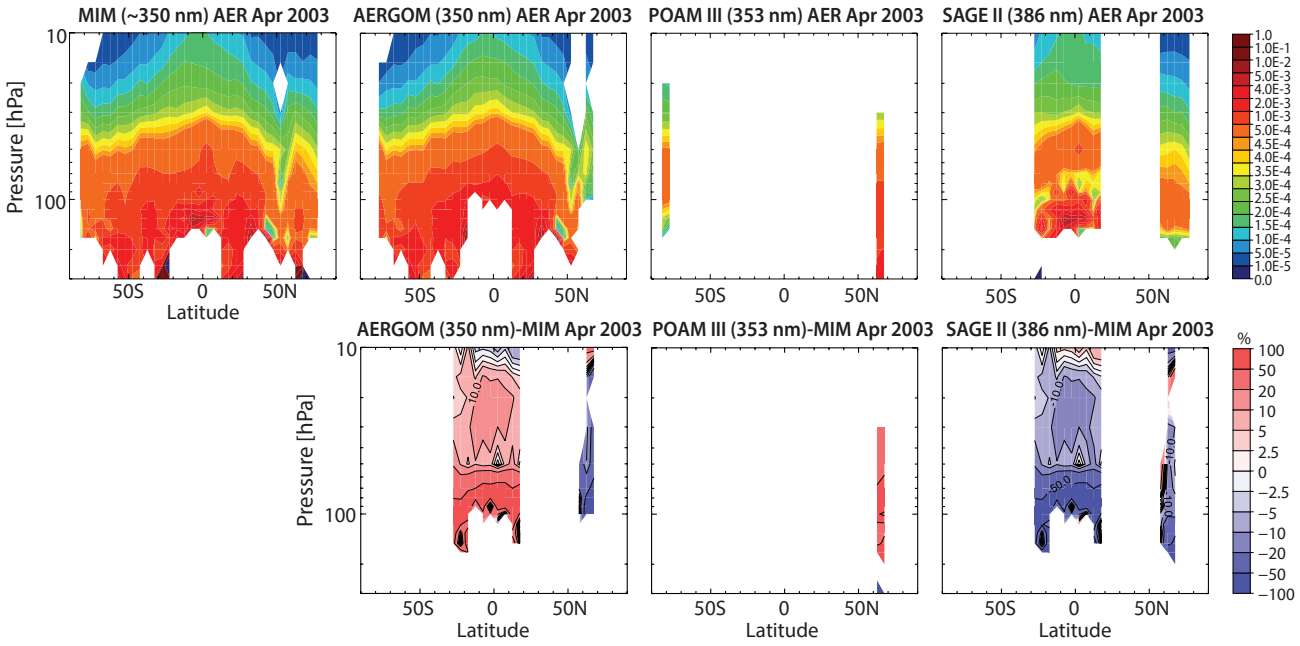

Figure 4.26.2: Cross sections of monthly zonal mean aerosol extinction (retrieved at around 350 nm) for April 2003. *The cross sections are shown for the MIM, AERGOM (at 350 nm), POAM III (at 353 nm), and SAGE II (at 386 nm)(upper row). Also shown are the relative differences of each instrument from the MIM (lower row). Note, the aerosol extinction climatologies are ordered according to rising retrieval wavelength.*

each figure, even though a particular instrument may offer more than one product in the considered wavelength range. The differences can be at least partially explained by the difference in wavelengths the two instruments use for the aerosol extinction retrieval (with SAGE II retrieving at longer wavelengths that yield lower extinction values). POAM III however, which retrieves the aerosol at a similar wavelength as AERGOM, indicates more positive values than both of these other instruments.

SAGE II, POAM III, AERGOM, and SCIAMACHY (2003, wavelengths ~450 nm)

Figure 4.26.3a and **b** show the zonal monthly mean cross sections for aerosol extinction climatologies and their differences from the MIM as deduced from measurements at wavelengths around 450 nm. Aerosol extinction climatologies are available from SAGE II retrieved at 452 nm, AERGOM at 450 and 470 nm, SCIAMACHY at 470 nm, and POAM III at 442 nm. Note that the SCIAMACHY climatologies at 470 nm have a very low information content and basically just represent a scaled 750 nm product.

AERGOM and SAGE II retrieve at very similar wavelengths in this category with their 450 and 452 nm products, respectively. Nevertheless, they show relatively large differences comparable to those seen in the previous comparison. Differences from the MIM are around ±10%, with AERGOM on the positive side and SAGE II on the negative side. Note that the AERGOM product retrieved at 470 nm still shows higher values than SAGE II (against expectations from wavelength considerations), indicating a real negative bias in SAGE II (or high bias in AERGOM). SCIAMACHY, which has a product at 470 nm as well, shows also quite large negative differences from the MIM through most of the tropical/subtropical MS. These are partially expected due to the wavelength-dependency. However, when compared to the AERGOM product at 470 nm, the differences are still much larger. In the UT and LS, SCIAMACHY shows strong positive differences from the MIM, attributable to the fact that here data were used to produce the zonal means that were not filtered for cloud occurrence. The only overlap with POAM III is seen in the Northern Hemisphere, where the POAM III retrieval shows positive deviations from the MIM, in best agreement with SAGE II and SCIAMACHY. The relatively strong negative differences from the MIM in AERGOM at these higher latitudes indicate that the products have likely a latitudinal structure in their biases, potentially arising from sampling issues that are more severe during the late winter/spring season where the polar vortex may have generated large and persisting horizontal gradients in the aerosol fields.

SAGE II, SAGE III, POAM III, GOMOS, and AERGOM (2003, wavelengths ~550 nm)

Figure 4.26.4a shows the zonal monthly mean cross sections for aerosol extinction climatologies for measurements retrieved at wavelengths around 550 nm. Available are GOMOS v6.01 aerosol extinction climatologies retrieved at 500 nm, and AERGOM at 500, 525, and 600 nm, SAGE II at 525 nm, SAGE III at 520 nm, and POAM III at 603 nm. Differences between single instruments and the MIM are shown in **Figure 4.26.4b**.

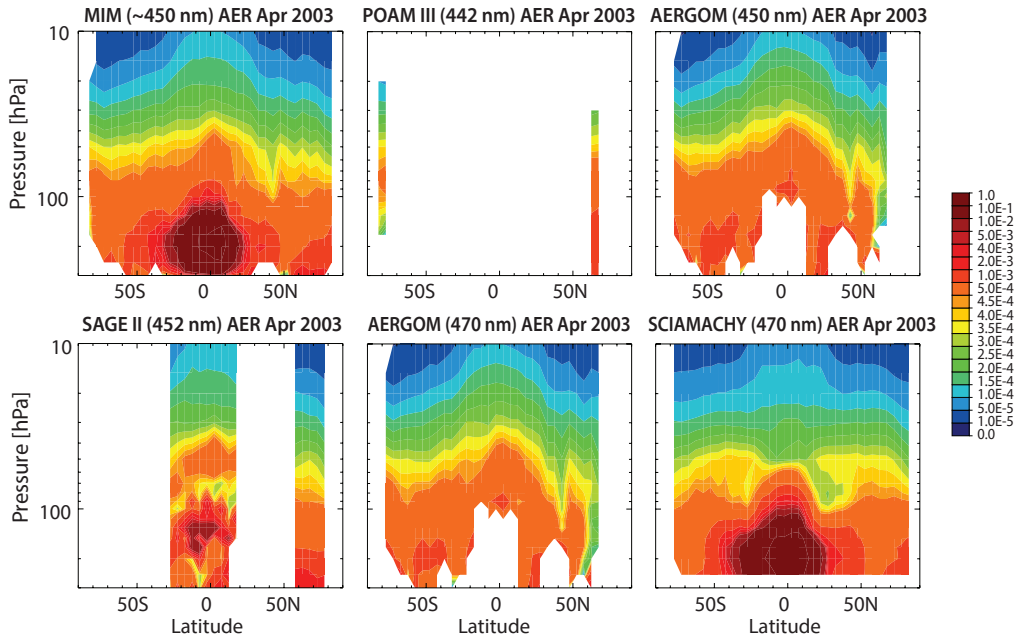

Figure 4.26.3a: Cross sections of monthly zonal mean aerosol extinction (retrieved at around 450 nm) for April 2003. *The cross sections are shown for the MIM, POAM III (442 nm), AERGOM (450 nm) (upper row), SAGE II (452 nm), AERGOM (470 nm) , and SCIAMACHY (470 nm) (lower row).*

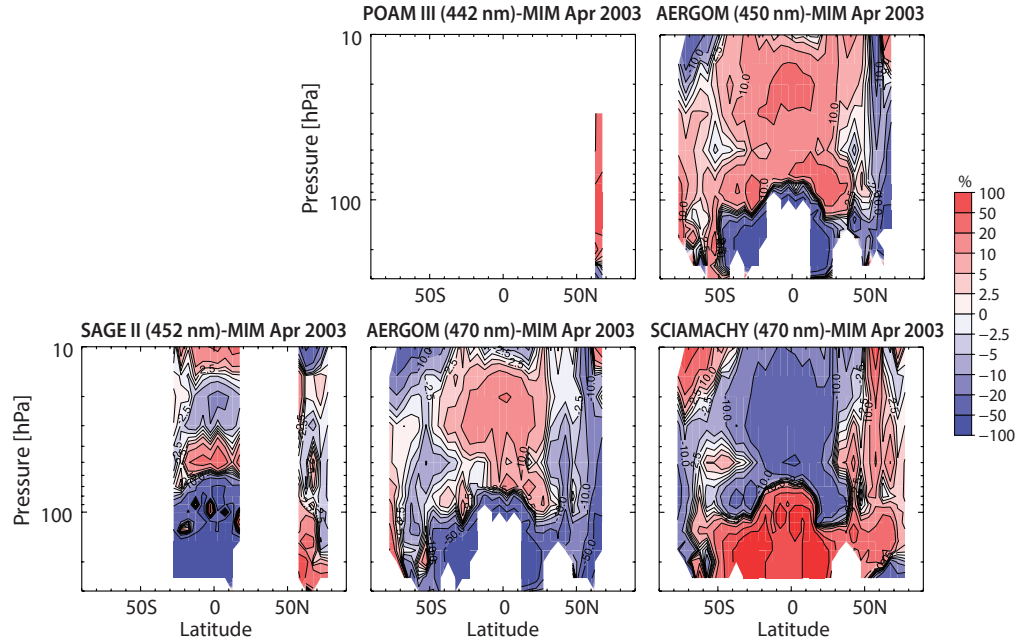

Figure 4.26.3b: Cross sections of monthly zonal mean differences in aerosol extinction (retrieved at around 450 nm) for April 2003*. Monthly zonal mean relative differences between the individual instruments and the MIM are shown.*

A strong wavelength-dependency is obvious in this comparison category with large positive deviations from the MIM for measurements obtained at 500 nm (GOMOS and AERGOM) and large negative deviations from the MIM at 600 nm (AERGOM). POAM III shows in contrast only moderate and mostly positive differences from the MIM, despite measuring at 600 nm as well. The other instruments retrieving at similar wavelengths show reasonably good agreement with differences of mostly below ±10% throughout the LS and MS (also SAGE III at 520 nm, and SAGE II and AERGOM at 525 nm). Only in the tropical upper troposphere, differences increase to above ±20%.

SAGE III, POAM III, OSIRIS, SCIAMACHY, and AERGOM (2003, wavelengths around 750)

Figure 4.26.5a shows the zonal monthly mean cross sections for aerosol extinction climatologies from measurements retrieved at wavelengths around 750 nm. OSIRIS retrieves its aerosol extinction at 750 nm, SCIAMACHY at 750 nm, AERGOM at 750 nm, SAGE III at 755 nm, and POAM II at 779 nm. OSIRIS, SCIAMACHY, and AERGOM fields are hence directly comparable, and even the wavelength used for SAGE III retrievals is close enough so that derived

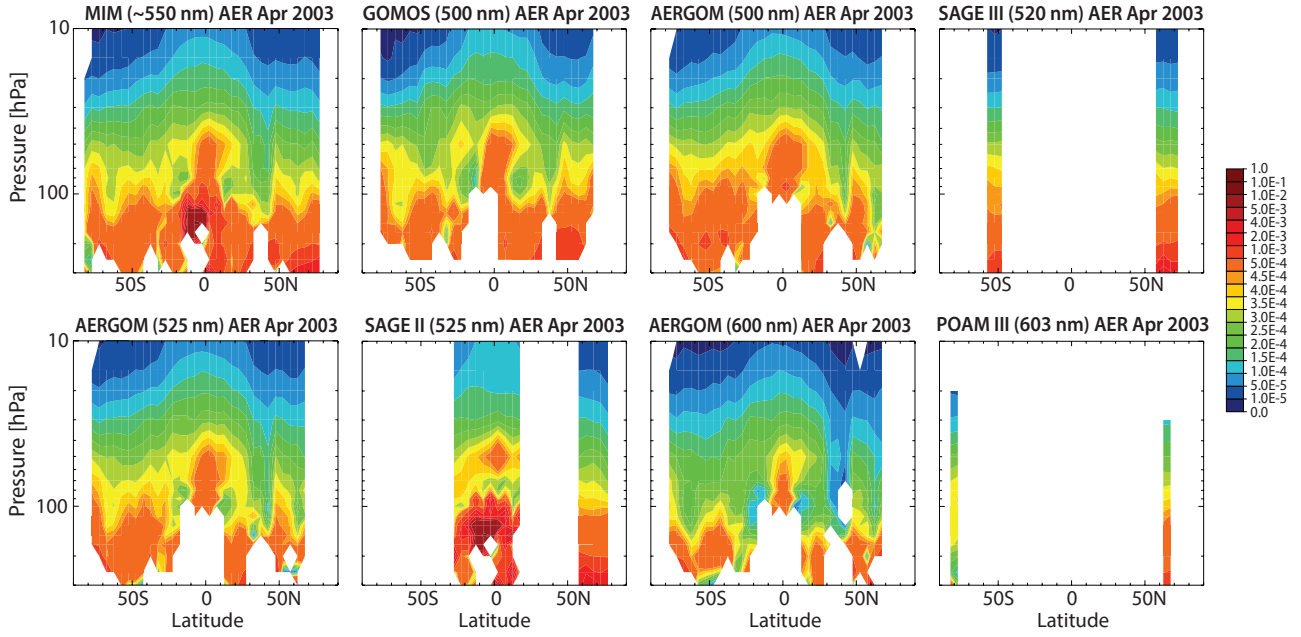

Figure 4.26.4a: Cross sections of monthly zonal mean aerosol extinction (retrieved at around 500 nm) for April 2003. *The cross sections are shown for the MIM (upper left panel), GOMOS (500 nm), AERGOM (500 nm), SAGE III (520 nm), AERGOM (525 nm), SAGE II (525 nm), AERGOM (600 nm), and POAM III (603 nm).*

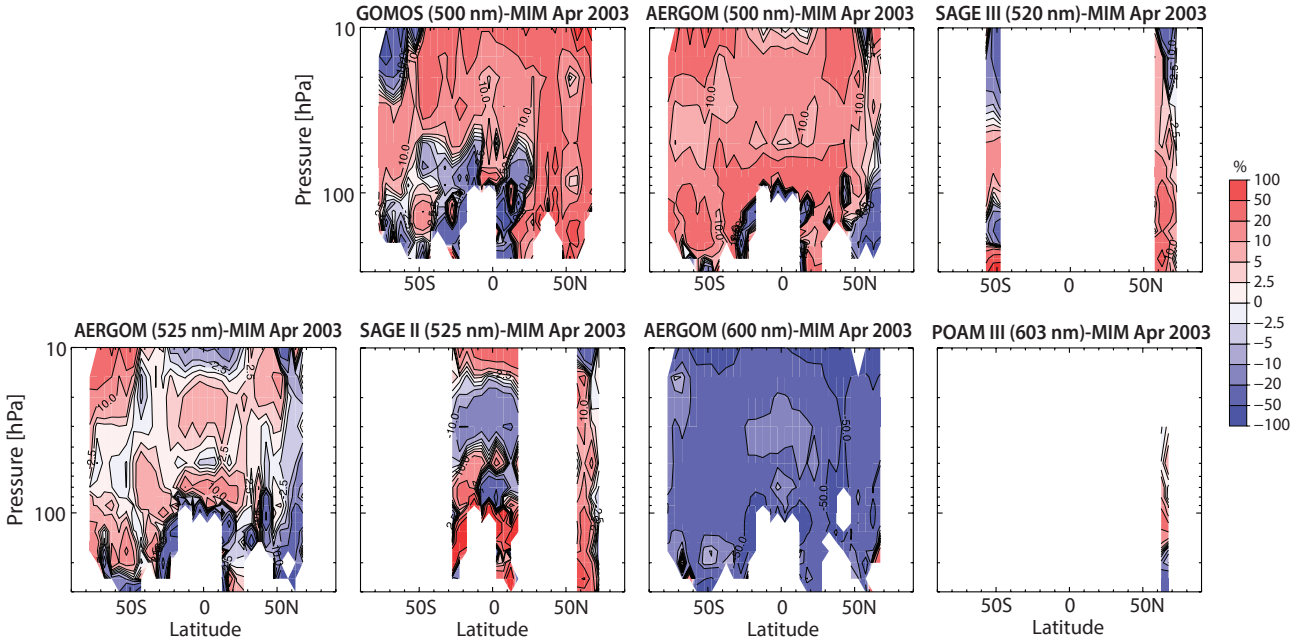

Figure 4.26.4b: Cross sections of monthly zonal mean differences in aerosol extinction (retrieved at around 550 nm) for April 2003. *Monthly zonal mean relative differences between the individual instruments and the MIM are shown.*

differences can be interpreted as real instrument differences.

A distinct feature of high aerosol extinction values is seen by all instruments in the Southern Hemisphere polar vortex (here early spring is shown), which is caused by the presence of polar stratospheric clouds [*e.g.*, *Benson et al.*, 2006].

Through most of the tropical and mid-latitude middle stratosphere, OSIRIS and SCIAMACHY show good to very good agreement (within ±5-10%). Relative differences increase towards the LS (±20%), the UT (±50%), and towards the polar region of the winter hemisphere (here the SH) (±50%) where dynamical variability and aerosol extinction values are larger. SAGE III compares very well with the MIM (mostly within ±5%), except below 100 hPa where differences from the MIM increase slightly. POAM III shows positive differences in the SH of 20% (however here agreeing better with SCIAMACHY), and a negative bias in the NH of up to 20% in the MS, which is partially expected given the higher wavelength its product is retrieved at. Differences from the MIM increase towards the LS where negative biases of up to 50% are found. The AERGOM product at 750 nm was expected to yield less accurate results and hence was excluded from the calculation of the MIM. Indeed, the differences from the MIM are as large as -50% (and worse) through most of the stratosphere, with equally large positive differences in the tropical lower stratosphere.

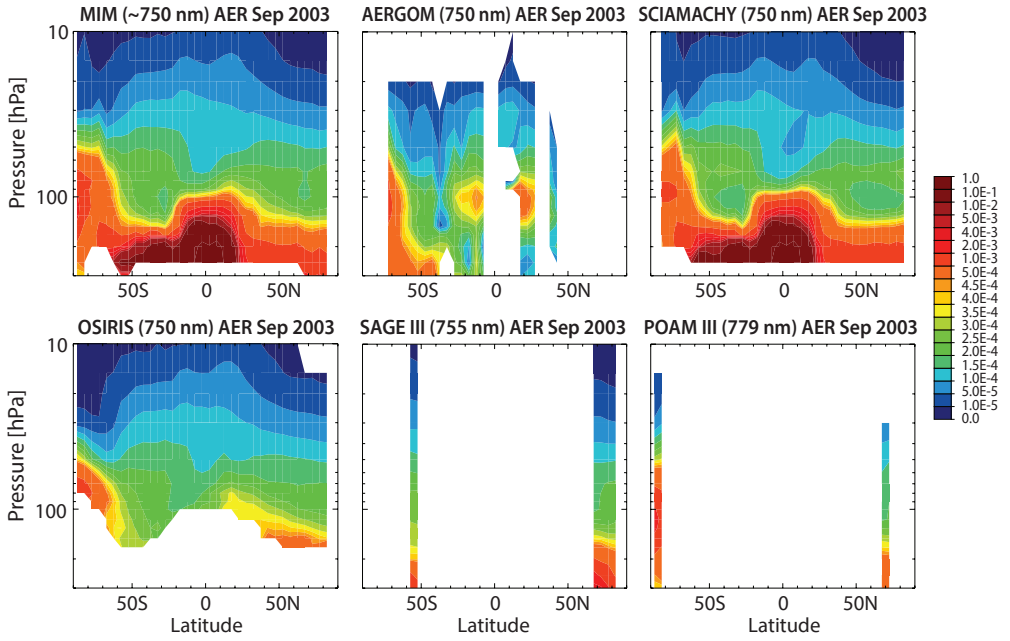

Figure 4.26.5a: Cross sections of monthly zonal mean aerosol extinction (retrieved at around 750 nm) for September 2003. *The cross sections are shown for the MIM (upper left panel), and for AERGOM (750 nm), SCIAMACHY (750 nm), OSIRIS (750 nm), SAGE III (755 nm), and POAM III (779 nm). Note that AERGOM is excluded from the MIM.*

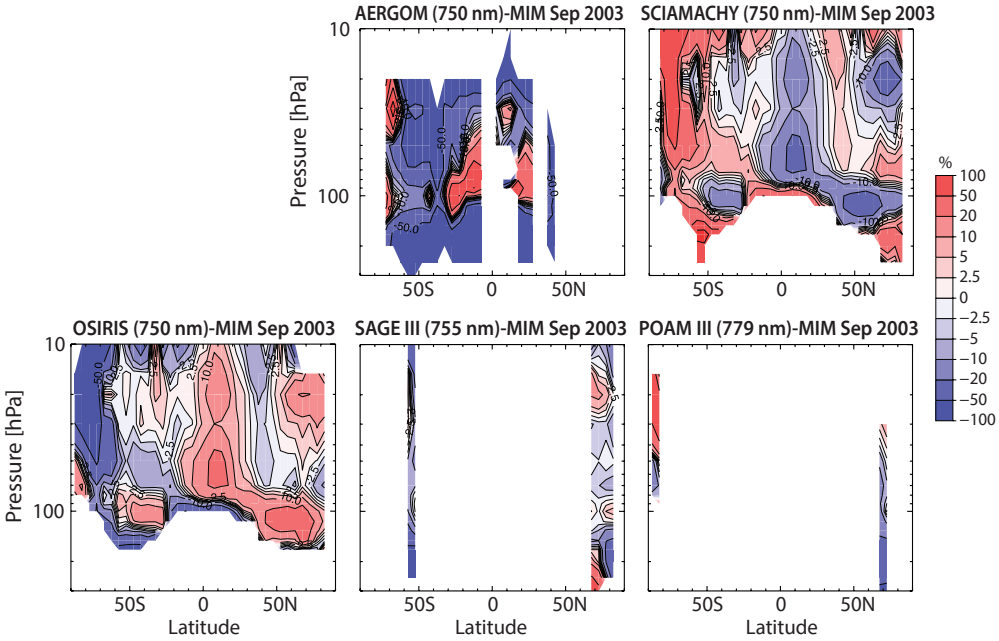

Figure 4.26.5b: Cross sections of monthly zonal mean differences in aerosol extinction (retrieved at around 750 nm) for September 2003. *Monthly zonal mean relative differences between the individual instruments and the MIM are shown.*

SAGE II, SAGE III, and POAM III (2003, wavelengths around 1050 nm)

Figure 4.26.6 finally shows the zonal monthly mean cross sections for aerosol extinction climatologies from measurements retrieved at wavelengths around 1050 nm. The instruments offering products retrieved in this wavelength region are SAGE II and SAGE III (with observations at 1020 nm) and POAM III (with observations at 1018 nm). All three aerosol extinction products are hence very well comparable to each other and show relative differences from the MIM of mostly less than ±10%, indicating good agreement between the climatologies.

4.26.3 Aerosol evaluations: Altitude profiles

Given the limitations of comparing aerosol extinction products retrieved at different wavelengths with each other, we here show only a few more evaluations of vertical profiles in addition to the above monthly zonal mean evaluations using this comparison approach. The examples are chosen to provide additional seasonal information and to perform comparisons between instruments that due to limited overlap with respect to geographical coverage were not considered above.

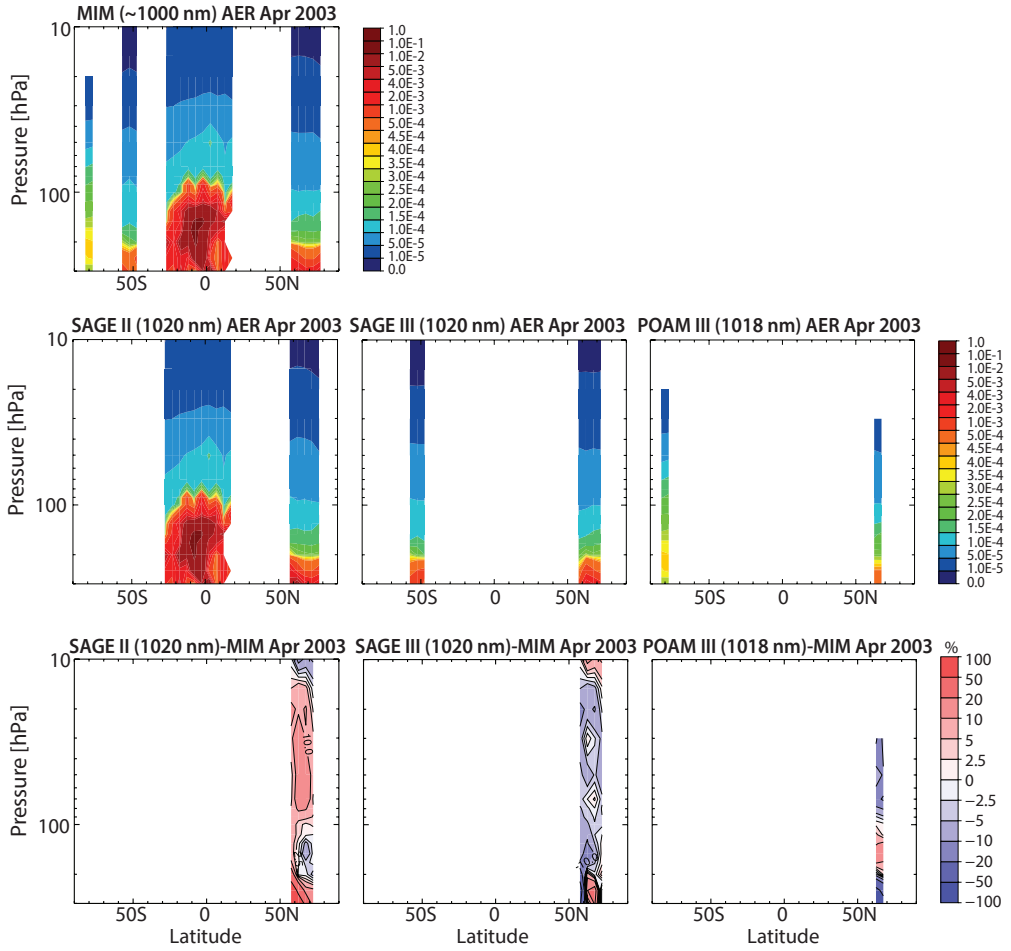

Figure 4.26.6: Cross sections of monthly zonal mean aerosol extinction (retrieved at around 1050 nm) for April 2003. *The cross sections are shown for the MIM (upper left panel), and for the instruments SAGE II, SAGE III, and POAM III (middle row). Also shown are the relative differences of each instrument to the MIM (lower row).*

Figure 4.26.7 shows a comparison between SAGE II and POAM II, with the latter not having been considered above. Two sets of products retrieved at different wavelengths are compared, SAGE II at 452 nm with POAM II at 442 nm, and SAGE II at 1020 nm with POAM II at 1060 nm. While for the first set, SAGE II should show slightly lower values than POAM II in the 450 nm comparison given above discussed wavelength dependency, SAGE II should show slightly higher values than POAM II in the 1050 nm comparison. However, this is not the case. The instruments show good agreement (between ±10%) in most examples, except for the 450 nm case in the Southern Hemisphere in February, where differences are up to ±25%. The fact that the instruments do not show the same sign in the difference from the MIM in the two hemispheres indicates a hemisphere-dependent instrument bias. These results are consistent with the POAM II/SAGE II validation analysis of *Randall et al.* [2000]. Differences were smaller in 1994, but by 1995-1996, with a cleaner atmosphere, hemispheric biases showed up that are thought to be caused by altitude registration errors in one or both datasets.

Figure 4.26.8 shows comparisons in the wavelength category of products retrieved at around 450 nm for April 2003. In the Northern Hemisphere high latitudes, the AERGOM products at 450 and 470 reveal extremely good agreement with the SAGE II product at 452 nm through most of the lower and middle stratosphere between 70 hPa and 15 hPa. While POAM III retrieved at 442 nm exhibits a high bias in the Northern Hemisphere, it shows excellent agreement with AERGOM in the Southern Hemisphere over the same altitude range. At altitudes below 70 hPa, however, AERGOM (SAGE II and POAM III) exhibit large negative (positive) differences from the MIM in the Northern Hemisphere and large positive (negative) differences from the MIM in the Southern Hemisphere, respectively.

Figure 4.26.9 shows comparisons in the wavelength category of products retrieved at around 550 nm. Good agreement between most instrument products is found throughout the LS above 100 hPa and MS below 15 hPa. Only the AERGOM product at 600 nm seems to be somewhat an outlier with much stronger negative differences from the MIM than what could be expected from the wavelength difference to other products. Even at altitudes below 100 hPa, there is generally good agreement between GOMOS, POAM, and AERGOM, while the SAGE II and III data products show rather large positive differences from the MIM. Note that the cross sections in **Figure 4.26.4b** yield a more complete picture on inter-instrument differences, given that these show varying behaviour with latitude.

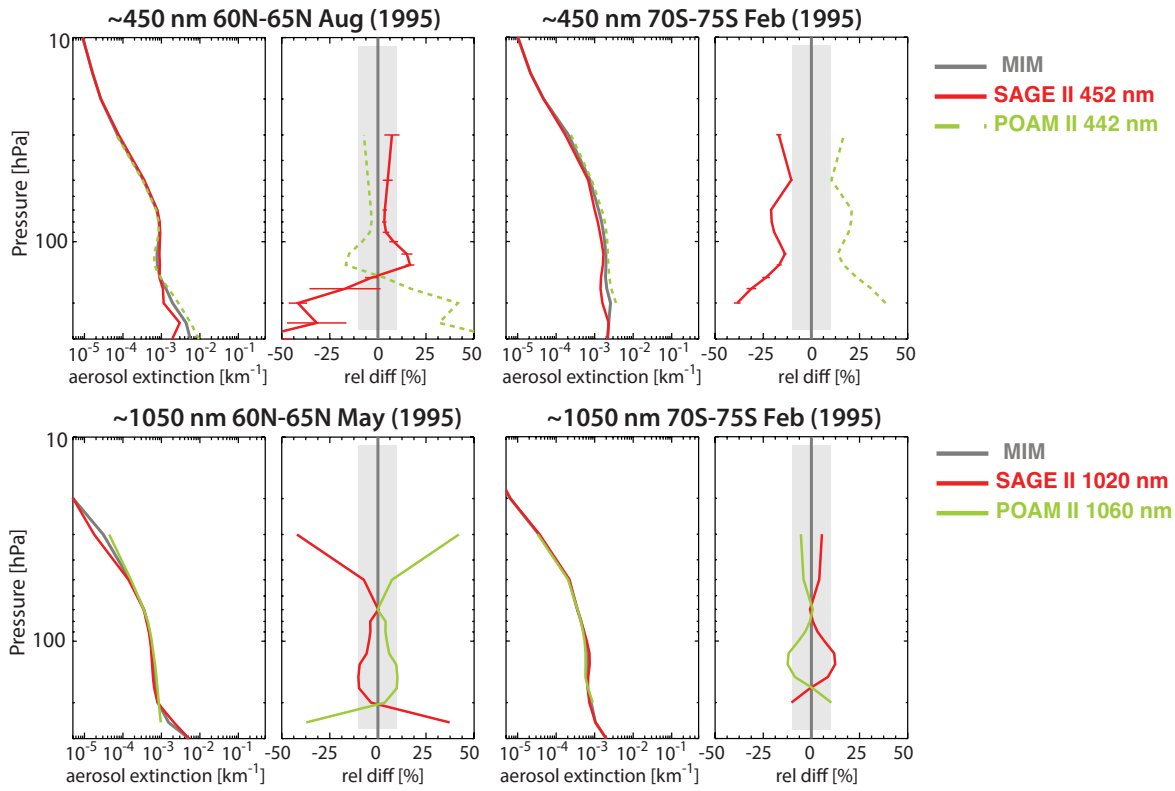

Figure 4.26.7: Vertical profiles of zonal monthly mean aerosol extinction in 1995. *The aerosol extinction profiles are shown for SAGE II and POAM II at 60°N-65°N and 70°S-75°S on the left and right, and for products retrieved at wavelengths around 450 nm and 1000 nm in upper and lower panels, respectively. The relative differences between the individual instruments and the MIM are shown in the right-hand panels. Error bars indicate the uncertainty in the relative differences based on the SEM of each instrument. The grey shaded area indicates where relative differences are smaller than 10%.*

Finally, **Figure 4.26.10** shows comparisons in the wavelength category of products retrieved at around 750 nm. At these wavelengths, the instruments again show good to reasonably good agreement through most of the LS and MS above 100 hPa, except for AERGOM, which shows large negative deviations from the MIM and the other instruments. Note that it was anticipated that the 750 nm data product would yield poorer results, and AERGOM hence was excluded from the MIM calculation. SCIAMACHY shows the tendency to be higher than the other instruments below 100 hPa (possibly due to the fact that unfiltered climatologies were used in this comparison). Finally, note the remarkable agreement between SAGE III and OSIRIS.

4.26.4 Aerosol evaluations: Interannual variability

Another important aspect of instrument performance apart from the representation of the climatological mean structure is the instruments' capability to capture interannual variability. For this evaluation, we now turn to the second approach introduced above for the comparison of the aerosol extinction climatologies (see also *Hegglin et al.*, in preparation), which uses scaling factors applied to the different wavelength products to make them better comparable to each other and also to be able to include HALOE in the comparison.

The upper panel in **Figure 4.26.11** shows the original time series of aerosol extinction in the tropics at 50 hPa averaged over 20°S-20°N as derived from a set of instruments at different retrieval wavelengths. A large spread between the different time series is apparent, illustrating once more the wavelength-dependency of aerosol extinction retrievals described above (see **Figure 4.26.1**). Note that we included only three products from AERGOM (at 350, 500, and 600 nm) so to keep the figure better readable.

The lower panel in Figure **4.26.11** shows each instrument's time series now scaled following equation (1) and using the year 2004 as reference year. The applied scaling largely removes the differences between the time series and collapses the curves on top of each other. The time series derived from different wavelengths become thereby comparable to each other. At least after 1999 and during episodes of relatively low aerosol loading, the agreement between the instruments is mostly good and lies within ±10%. During episodes with higher aerosol loading, discrepancies between the datasets increase.

In particular towards the earlier years of the comparison, the differences between the time series increase to more than 300%. In the mid to late 1990s, SAGE II at 1020 nm is a clear outlier, showing a different relaxation timescale towards background aerosol extinctions than its other wavelength products and also HALOE. However, this SAGE II product shows good agreement with the other aerosol extinction products available from 2002 onwards, indicating that the enhanced aerosol loading and changing aerosol

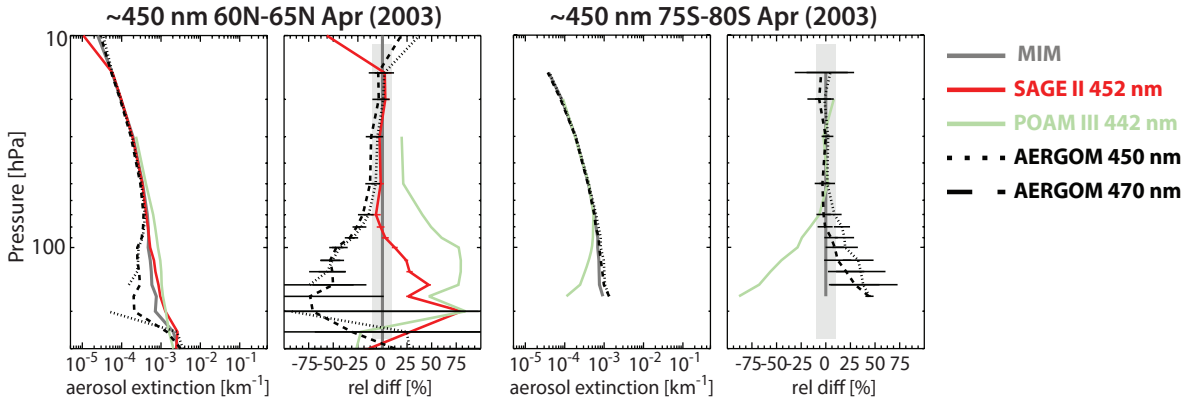

Figure 4.26.8: Vertical profiles of zonal monthly mean aerosol extinction in 2003 (retrieved at around 450 nm). *The aerosol extinction profiles are shown for different instruments (SAGE II, POAM III, and AERGOM) at 60°N-65°N and 75°S-80°S during April 2003 on the left and right, respectively. The relative differences between the individual instruments and the MIM are shown in the right-hand panels. Error bars indicate the uncertainty in the relative differences based on the SEM of each instrument. The grey shaded area indicates where relative differences are smaller than 10%.*

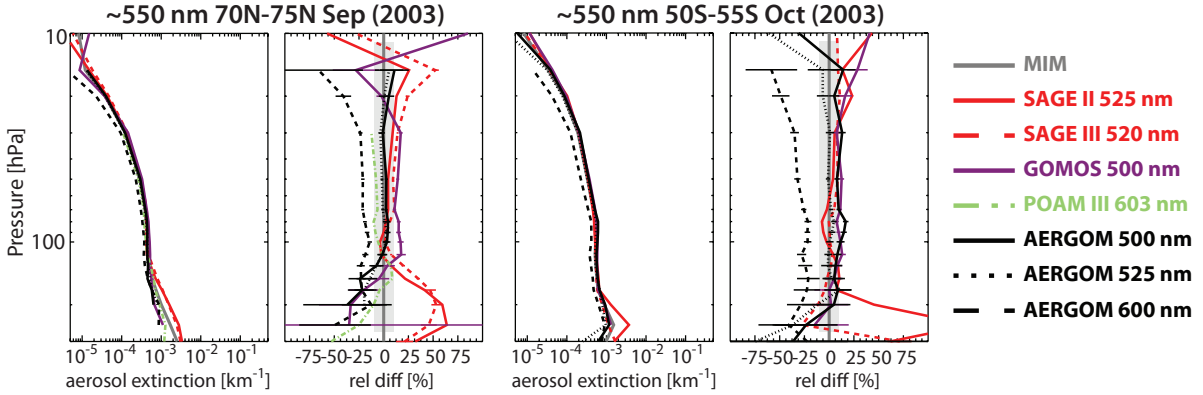

Figure 4.26.9: Vertical profiles of zonal monthly mean aerosol extinction in 2003 (retrieved at around 550 nm). *The aerosol extinction profiles are shown for different instruments and data products (SAGE II, SAGE III, POAM III, GOMOS, and AERGOM) at 70°N-75°N during September and 50°S-55°S during October on the left and right, respectively. The relative differences between the individual instruments and the MIM are shown in the right-hand panels. Error bars indicate the uncertainty in the relative differences based on the SEM of each instrument. The grey shaded area indicates where relative differences are smaller than 10%.*

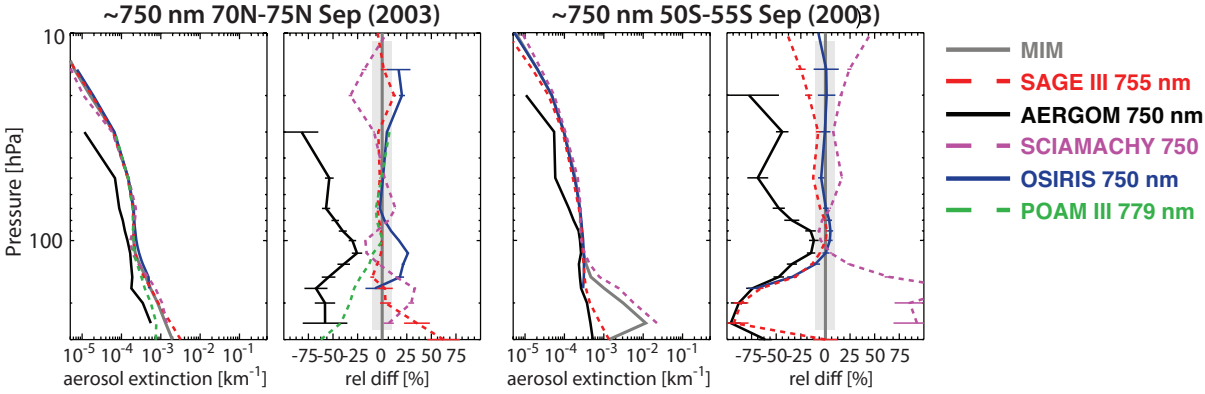

Figure 4.26.10: Vertical profiles of zonal monthly mean aerosol extinction in 2003 (retrieved at around 750 nm). *The aerosol extinction profiles are shown for different instruments (SAGE III, AERGOM, SCIAMACHY, OSIRIS, and POAM III) at 70°N-75°N and 50°S-55°S on the left and right, respectively. The relative differences between the individual instruments and the MIM are shown in the right-hand panels. Error bars indicate the uncertainty in the relative differences based on the SEM of each instrument. The grey shaded area indicates where relative differences are smaller than 10%. Note AERGOM is not included in the MIM calculation.*

size distribution may affect the comparisons made here using scaled products adversely during the early years. Note that with increasing wavelength the time series of SAGE II (increasing relative anomalies) and HALOE (decreasing relative anomalies) show opposite behaviour. The dependency on aerosol size distribution may have been especially an issue within aged aerosol particles long after the Mount Pinatubo eruption. On the other hand, the aerosol

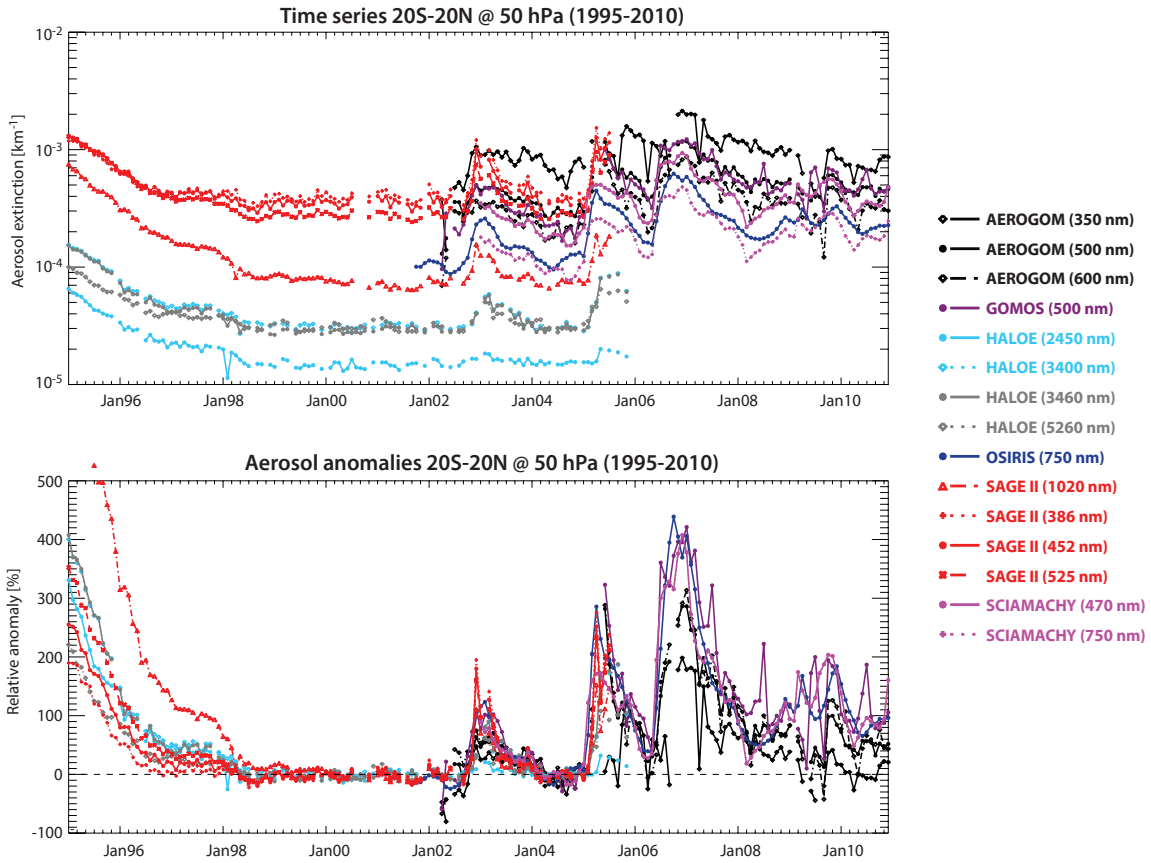

Figure 4.26.11: Tropical aerosol time series at 50 hPa. *Time series of aerosol extinction (upper panel) and deseasonalised and normalised aerosol extinction anomalies (lower panel) are shown for the latitude band 20°S-20°N at 50 hPa.*

extinction products of SAGE II at 452 and 525 nm and of HALOE at 3400 and at 3460 nm agree all fairly well with each other. HALOE at 2450 and 5260 nm seem to underestimate relative anomaly values during 2003 and 2005 when other products seem to agree well with each other. A problem in the HALOE 2450 and 5260 nm products has also been pointed out in a study by *Thomason* [2012], thereby lending support to our approach taken here.

In the later time period from 2002 onwards, GOMOS, while generally agreeing well with SCIAMACHY and OSIRIS, exhibits some strong spikes in its time series, which may be attributable to small sampling sizes. AERGOM disagrees with OSIRIS and SCIAMACHY (but not GOMOS) most strikingly during 2009, and all of its products tend towards lower aerosol extinctions than those from other instruments. The AERGOM product at 350 nm yields largest discrepancies.

Figure 4.26.12 shows the same as the previous figure, but for 80 hPa in the tropics. At this altitude, the scaled time series show somewhat larger disagreement (mostly within ±20-25%), although the main feature of a double-peaked structure with maxima during May and November is captured by most of them. Larger disagreement is expected since at these levels the retrievals are most influenced by high geophysical variability, inhomogeneous sampling, or cloud effects. SAGE II at 1020 nm shows somewhat higher variability than its other wavelength products. It remains to be investigated whether this indicates a potential retrieval problem or real natural variability that the longer wavelengths at these altitudes can capture better than the shorter wavelengths. Both GOMOS and AERGOM do not agree with the rest of the instruments during 2009. SCIAMACHY on the other hand shows too high values when compared to the other instruments in the beginning of its record.

Finally, **Figure 4.26.13** shows the same evaluation for the extra-tropics between 50°N-70°N. At these latitudes, POAM II and POAM III measurements can also be included in the comparison. Note that POAM II has been scaled using the scaling factor derived from POAM III measurements, which are measured at very similar wavelengths (see **Table 4.26.2**), since there are no POAM II measurements in the reference year 2004 available. POAM II exhibits the same wavelength dependency as SAGE II, with increasing relative anomalies with increasing wavelength, and the two instruments agree generally reasonably well with each other (mostly within 30% for POAM II at 921 and 1060 nm when compared to SAGE II at 1020 nm, and also for POAM II at 601 nm compared to SAGE II at 386, 452, and 525 nm). POAM III shows also a similar wavelength dependency during years with lower aerosol loading, and agrees well with HALOE and SAGE II overall. Finally after 2005, SCIAMACHY shows somewhat stronger maximum-to-minimum fluctuations than the other instruments. At least part of this behaviour may be attributed to the fact that the SCIAMACHY data have not undergone filtering to PSCs and clouds before inclusion in the monthly mean

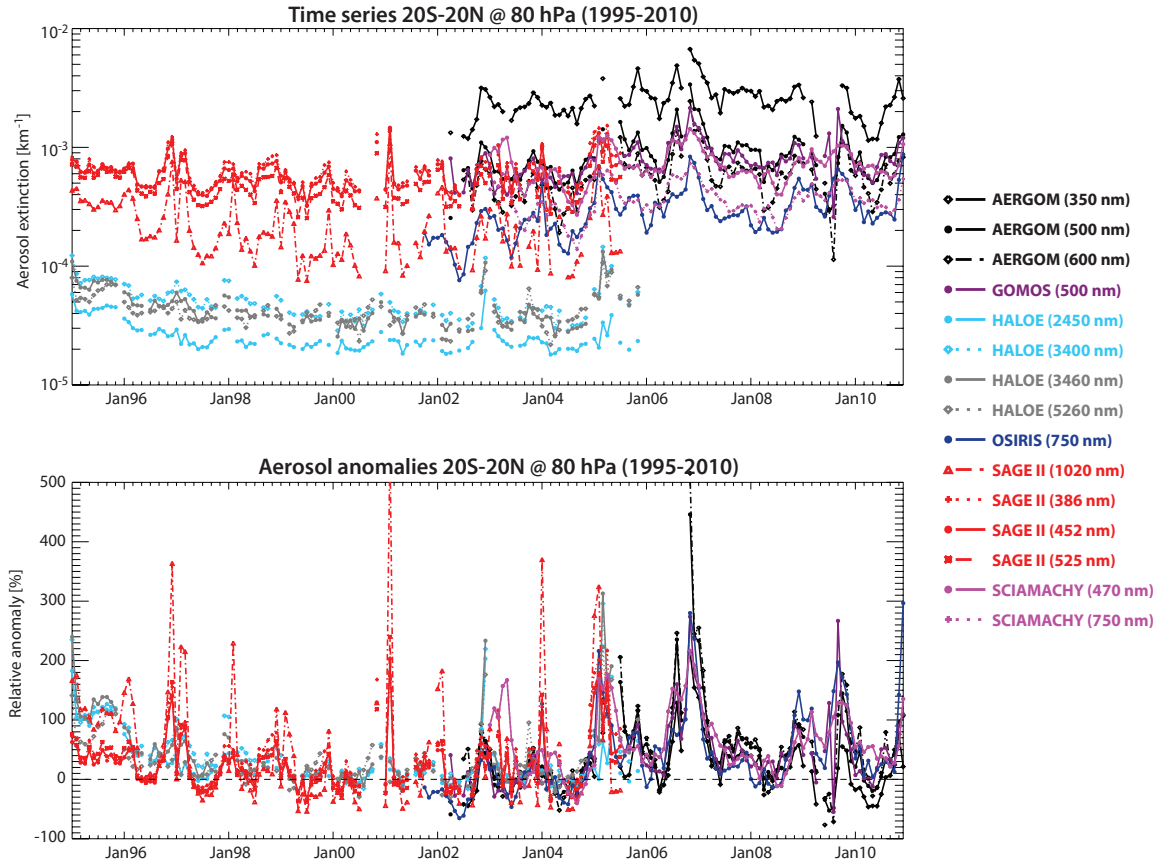

Figure 4.26.12: Tropical aerosol time series at 80 hPa. *Timeseries of aerosol extinction (upper panel) and deseasonalised and normalised aerosol extinction anomalies (lower panel) are shown for the latitude band 20°S-20°N at 80 hPa.*

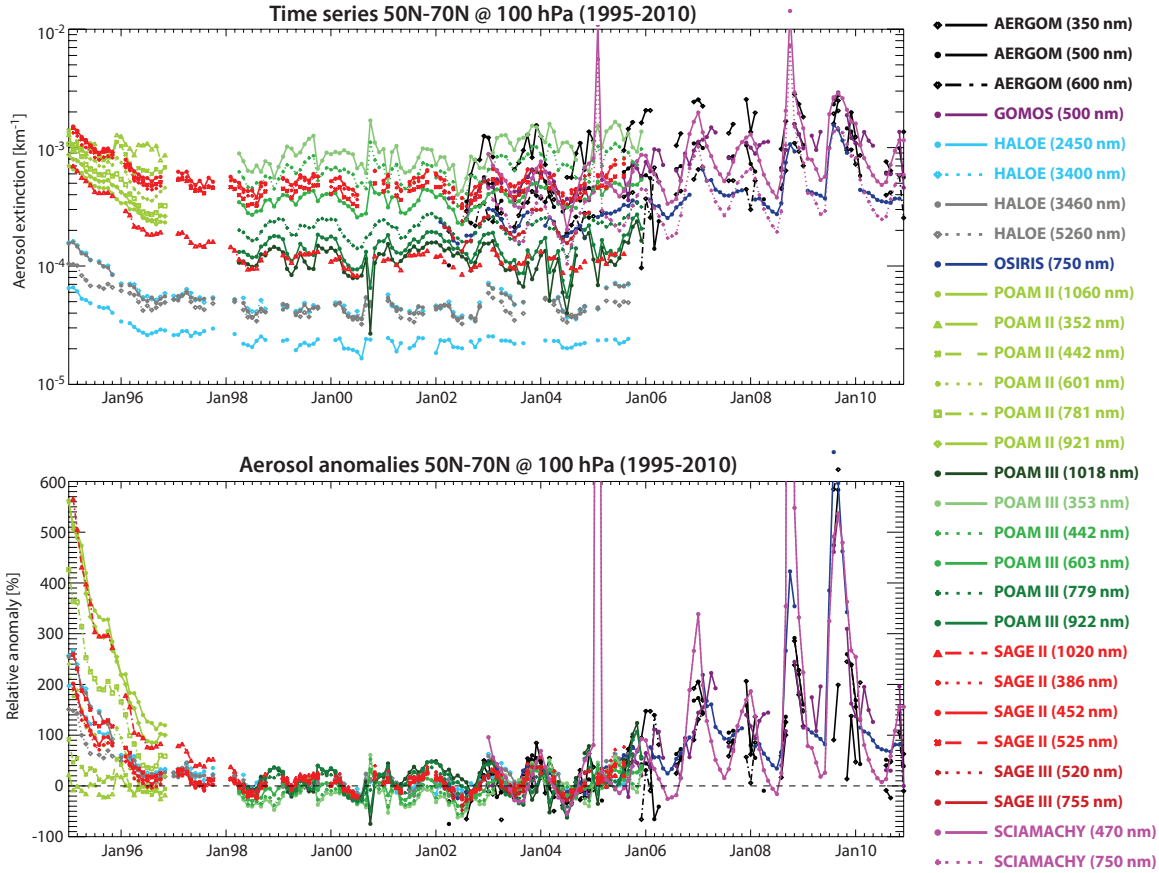

Figure 4.26.13: Extra-tropical aerosol time series at 100 hPa. *Timeseries of aerosol extinction (upper panel) and deseasonalised and normalised aerosol extinction anomalies (lower panel) are shown for the latitude band 50°N-70°N at 100 hPa.*

climatologies. GOMOS and AERGOM (except at 350 nm) indicate mostly good agreement with OSIRIS even during 2009, however show some spikes in its time series as noted for other levels/latitudes above.

Figure 4.26.14 shows the evolution of relative anomalies as derived from Equation 1 for the different instrument observations and for the MIM (upper left) now as a function of time and altitude. The original, unscaled data can be seen in **Figure A4.26.1** in *Appendix A4*. Note, the MIM is not to be mistaken for a climate data record, but merely represents a reference, since it includes all the available aerosol climatologies and not only those considered to be of high quality.

The MIM anomaly time series clearly reveals distinct pulses of enhanced stratospheric aerosol after the Nevado del Ruiz (1985), Kelut (1990), and Mount Pinatubo (1991) volcanic eruptions, a phase of relaxation towards background aerosol extinction values towards the late 1990s, and a relatively 'clean' background stratosphere between 1998 and 2004. After that a period marked by some intermediate aerosol influence following the eruptions of some smaller volcanoes such as Manam (2005), Soufrière Hills and Tavurvur (2006) occured [see *Vernier et al.*, 2011]. The source of aerosol in 2009 may indicate the impact of the Australian 'Black Saturday' bushfires on the stratospheric aerosol layer [*Siddaway et al.*, 2011].

The comparison of the different instrument products with the timeseries of the MIM reveals overall good agreement in terms of the structures seen. Note that the high values in the tropical upper troposphere in SCIAMACHY are due to the fact that the observations had not been filtered for clouds before they were included in the monthly zonal mean climatologies. Above around 100 hPa, the structures in the SCIAMACHY anomalies however resemble those found in the MIM well. The AERGOM time series from retrievals at 350, 600, and 750 nm seem somewhat noisier than the AERGOM products derived at other wavelengths and hence do not represent the structures as well as the other instruments' time series.

In order to be more quantitative about the inter-instrument differences, **Figure 4.26.15** shows the relative differences between each instrument's anomaly time series and the MIM. We first focus on the SAGE II and HALOE products during the rather clean phase of stratospheric aerosol loading after 1998 up to 2005. Smallest deviations from the MIM are seen in the SAGE II products at 452 and 525 nm, and the HALOE products at 3400 and 3460 nm with values mostly between ±5%. SAGE II at 1020 nm largely agrees with these products except for altitudes above 20 hPa, where it shows larger positive differences from the MIM of +10 to +20%. HALOE at 3400 nm shows increasing deviations below around 50 hPa. Both HALOE products at 2450 and 5260 nm show somewhat larger differences with respect to the MIM of ±10%. These findings are mostly consistent with the findings by *Thomason* [2012], who stated that the HALOE products at 2450 and 5260 should not be used, and the product at 3460 nm may suffer from a NO_2 contamination in the retrieval below 19 km.

During the years with high aerosol loading following the Mt. Pinatubo eruption, the different products however show large differences that exhibit in some cases even a vertical structure to them that complicates the interpretation. SAGE II at 1020 nm is consistently high when compared to the MIM, while SAGE II at 386 and 452 nm, and HALOE at 5260 nm are low. SAGE II at 525 nm shows positive/negative deviations above/below approximately 30 hPa, and HALOE at 2450, 3400, and 3460 nm approximately the opposite behaviour. The products during this time period seem to suffer from inconsistencies most likely attributable to the differences in aerosol size distributions assumed in the different retrievals.

The comparison with the newer generation of limb-scattering and limb occultation instruments show largely encouraging results, although with somewhat larger biases even during quiescent years. For OSIRIS, SCIAMACHY at 750 nm (or 470 nm), GOMOS, and AERGOM at 450, 470, 500, and 525 nm differences to the MIM are of around ±10%, while for AERGOM at 350, 600, and 750 nm differences increase to more than ±20%. During the time period with higher aerosol loading, the differences to the MIM increase, with mostly negative features in most AERGOM products and SCIAMACHY, and positive features in GOMOS and OSIRIS. Note that the alternating positive/negative departures from the MIM in GOMOS, OSIRIS, and SCIAMACHY may point towards sampling issues of these instruments, while the mostly negative departures in AERGOM seem to reflect a systematic low bias in the retrievals compared to the other instruments' aerosol extinction products.

The equivalent anomaly time series as in **Figure 4.26.14** are shown in **Figure 4.26.16** but for the northern mid- to high-latitudes (50°N-70°N). At these latitudes, we can also include POAM II and POAM III measurements into the comparison. In the early years of the comparison, high aerosol extinction values after the Mt. Pinatubo eruption relax to lower background values, with similar features as seen in the tropics. The MIM after 2000 shows two different layers of enhanced aerosol, one above 30 hPa, which most likely reflects aerosol from the Mt. Pinatubo eruption transported within the deep branch of Brewer-Dobson circulation to higher altitudes and latitudes, and one below 70 hPa, which rather stems from more recent volcanic injections of aerosol precursors into the LS at higher latitudes.

The different aerosol extinction products from the instruments show overall similar features, but the overall agreement is much worse than in the tropics. Much of these differences may be explainable by differences in sampling, which are considered to affect aerosol measurements more than long-lived trace gas species due to less homogeneous distributions in the stratosphere. However, differences between products of the same instrument reveal that major problems in certain wavelength products exist that must be real and

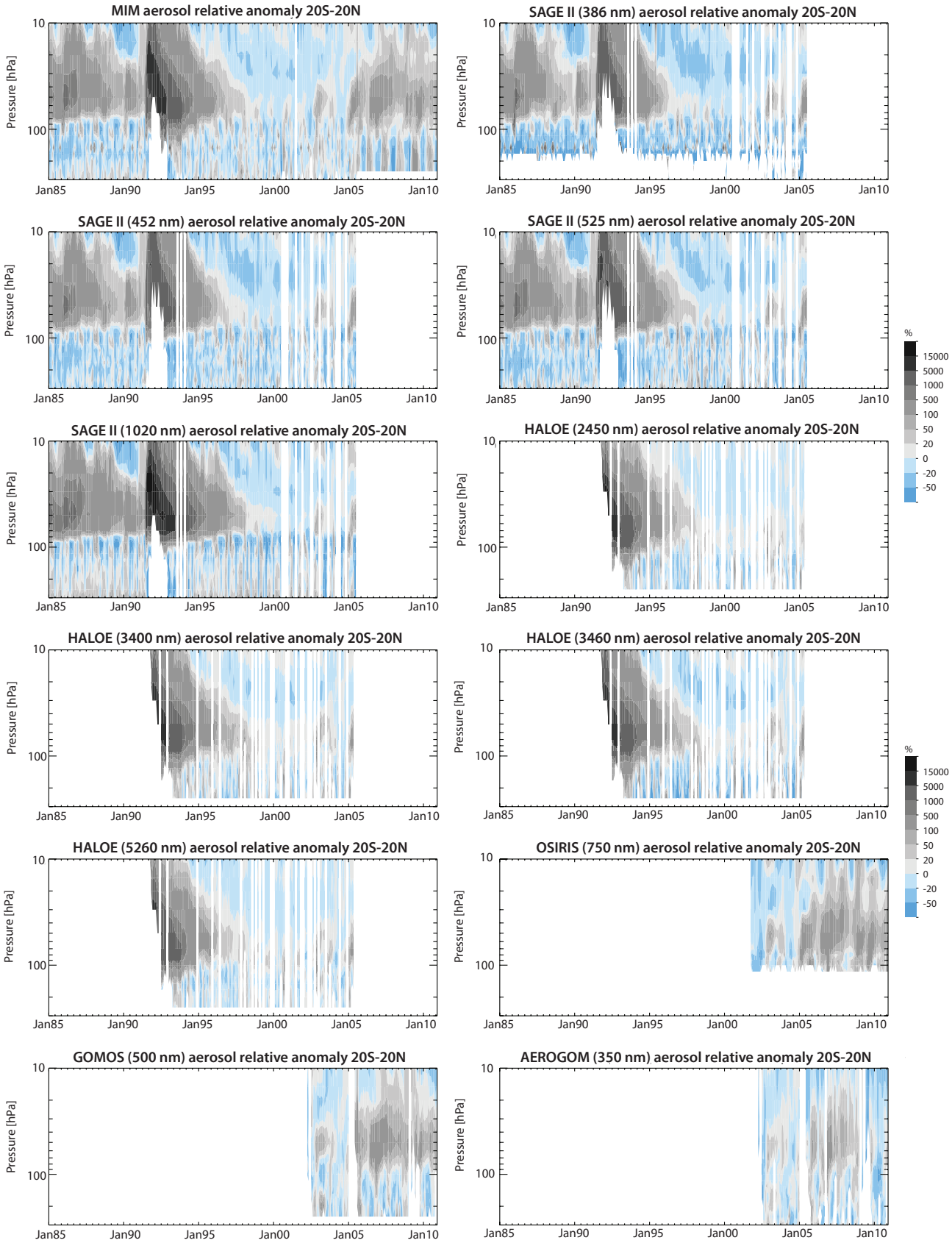

Figure 4.26.14: Time-altitude evolution of aerosol anomalies in the tropics. *The time-altitude evolution of normalised aerosol anomalies averaged over 20°S-20°N is shown for the MIM and all retrieval products of the different limb satellite sounders.*

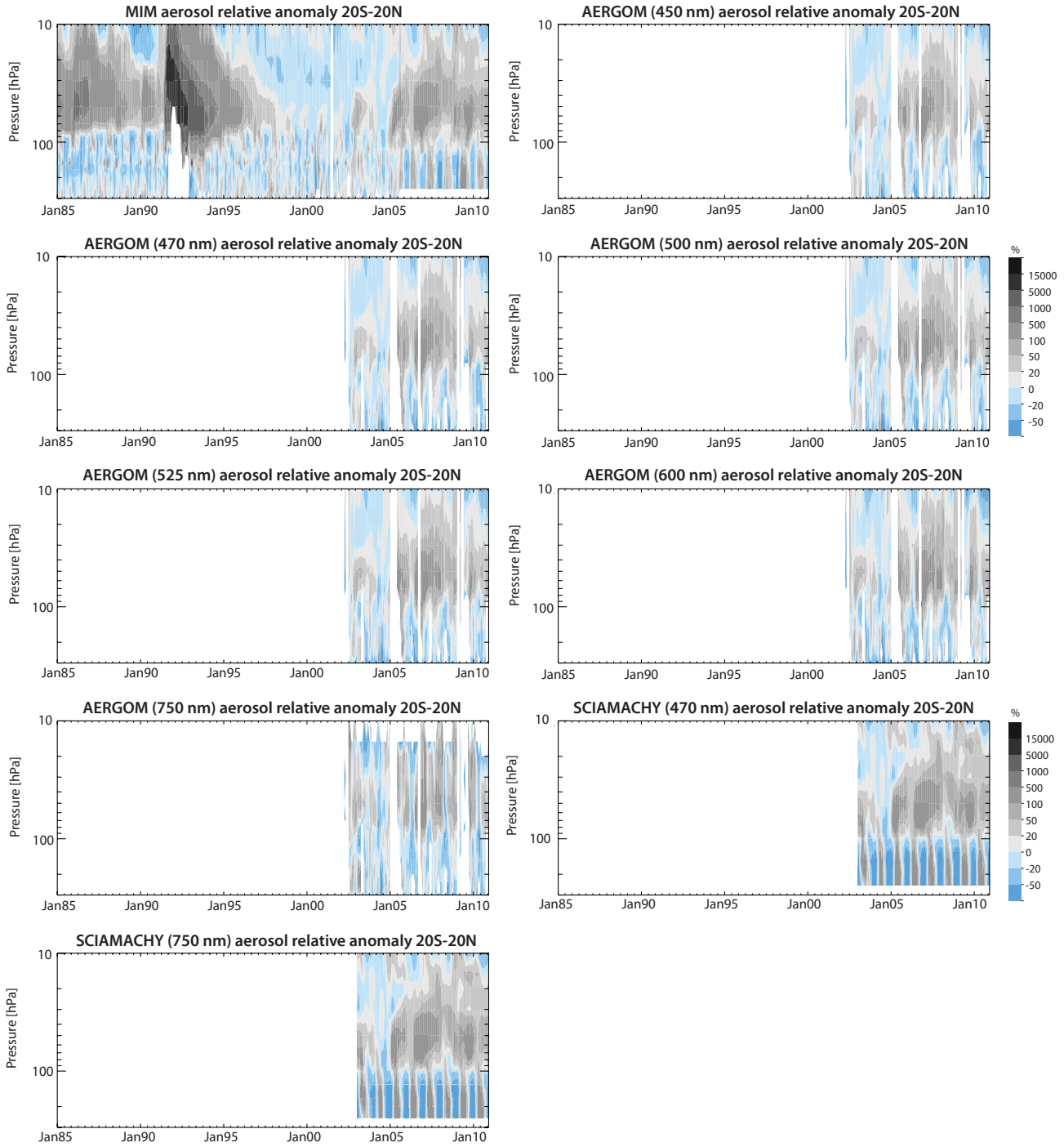

Figure 4.26.14 continued.

cannot be attributed to sampling differences. Most striking differences are found in HALOE at 2450 and 5260 nm, with both products not showing an enhanced aerosol extinction layer above 30 hPa. Also, POAM II at 352 nm seems not to show the same physical features as seen in the other time series. AERGOM time series at these latitudes have only intermittent coverage, but indicate also two layers of aerosol as seen in the other time series. Both POAM III products at 603 and 779 nm show very good to excellent agreement when compared to the MIM through most of the lower and middle stratosphere, along with slightly higher differences for the other products, which may be reflective of the limitation of the comparison methodology.

Relative differences from the MIM are shown for each anomaly time series in **Figure 4.26.17**. It is notable that these do not necessarily show the same behaviour as in the tropics. While SAGE II at 1020 nm shows positive deviations between 200 and 30 hPa in the beginning of the record as in the tropics, it here now shows negative differences above 30 hPa. All the other SAGE II products now show negative differences in the LS, and positive deviations in the MS. Also, the differences between the time series are here much larger with values around ±10% during 2000-2004, but with patches of larger and increasing differences that reach up to ±20 to ±50% towards the end of the time-series. The less reliable products from AERGOM at 600 and

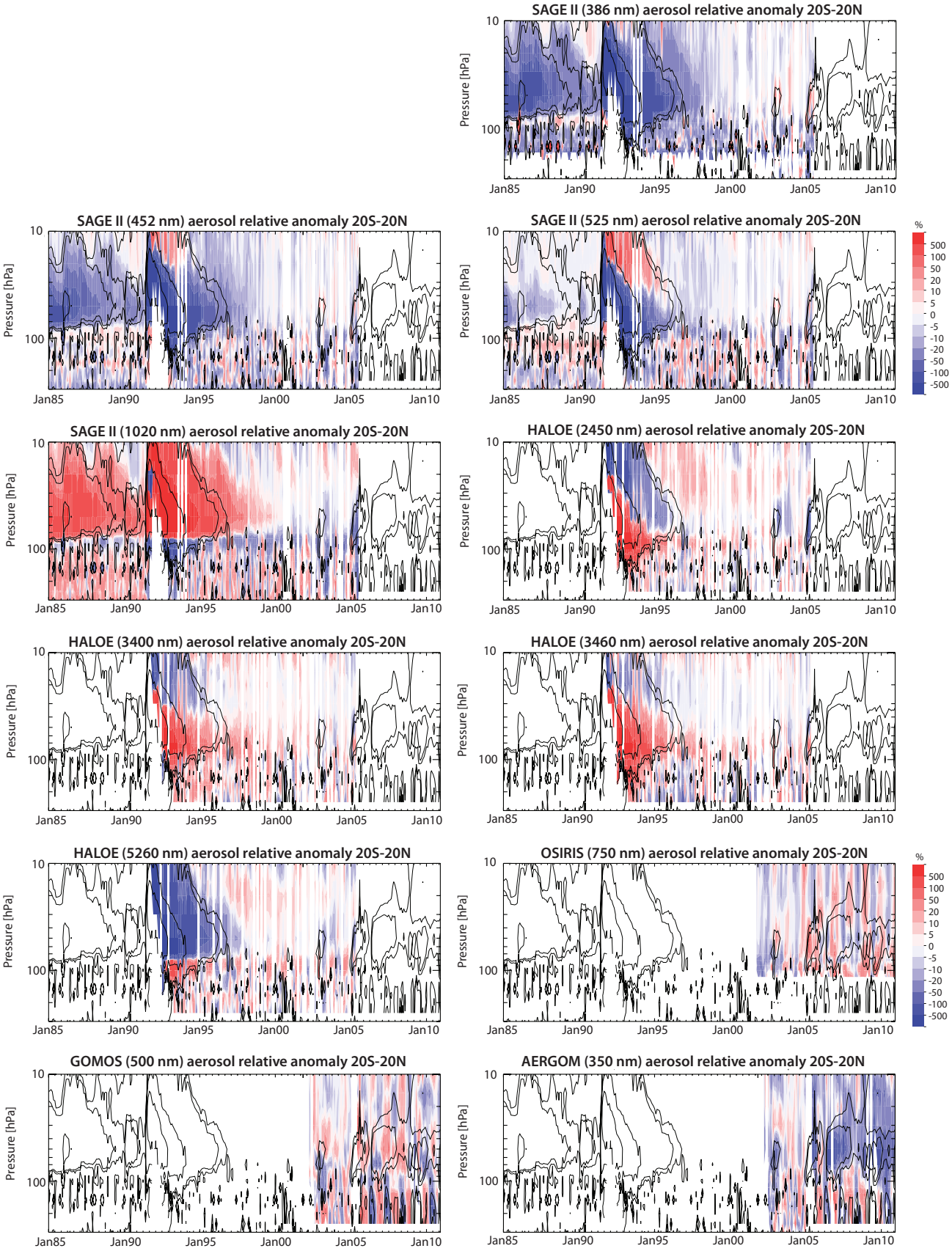

Figure 4.26.15: Time-altitude evolution of aerosol anomaly differences in the tropics. *The time-altitude evolution of normalised aerosol anomaly differences averaged over 20°S-20°N with respect to the MIM is shown for all retrieval products of the different limb satellite sounders.*

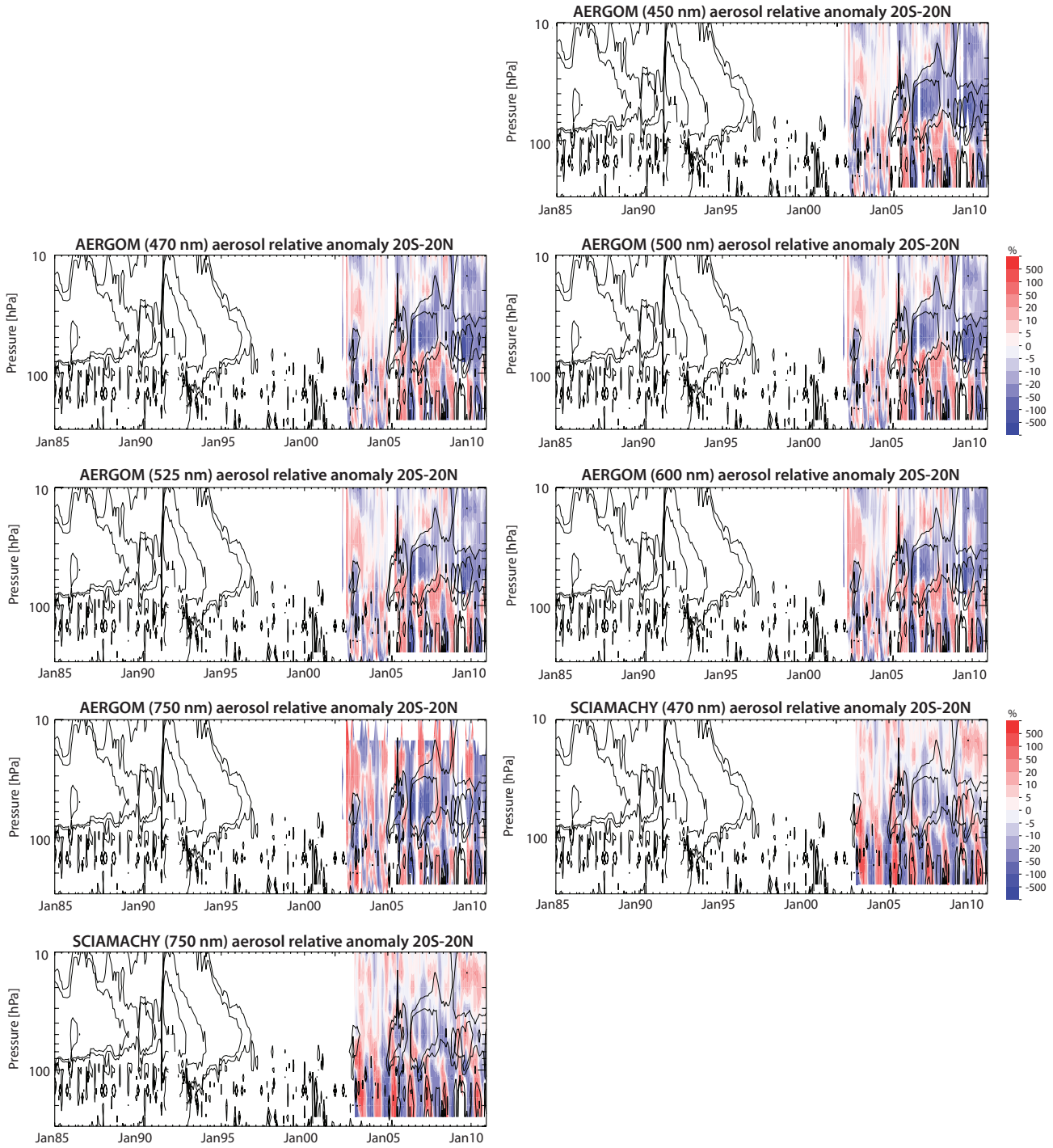

Figure 4.26.15 continued.

750 nm show mostly negative deviations as also shown in the evaluations considering similar wavelengths only (see **Figures 4.26.9** and **4.26.10**). Note, the original unscaled time series of aerosol extinction for the extra-tropics can be found in Figure **A4.26.2** in *Appendix A4.*

4.26.5 Summary and conclusions: Aerosol

Within the SPARC Data Initiative, a first overall comparison of available aerosol monthly zonal mean climatologies based on aerosol extinction profile measurements from 8 satellite instruments (SAGE II, HALOE, POAM II, POAM III, OSIRIS, SAGE III, SCIAMACHY, and GOMOS) has been carried out. From these instruments a total of 34 products are available, all retrieved at different wavelengths ranging from 350 to 5260 nm. Given the wavelength-dependency of aerosol extinction retrievals, the available products cannot all be directly compared to each other. Two different approaches have hence been chosen to compare the aerosol extinction products to each other to gain information on their quality and physical consistency. Note, interpretation of the findings from the two comparison approaches remains difficult and needs to be used with caution.

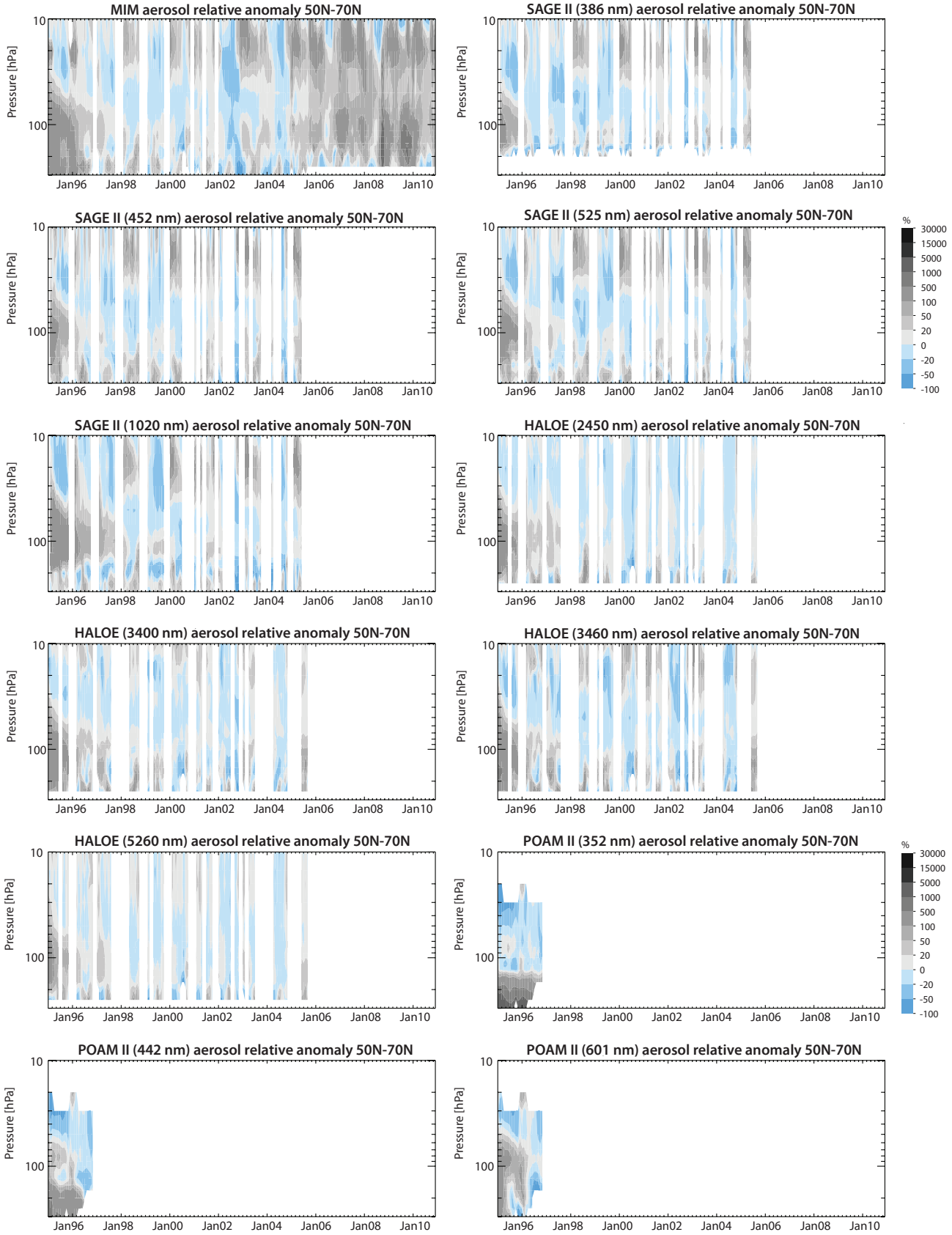

Figure 4.26.16: Time-altitude evolution of aerosol anomalies in the extra-tropics. *The time-altitude evolution of normalised aerosol anomalies averaged over 50°N-70°N with respect to the MIM is shown for all retrieval products of the different limb satellite sounders.*

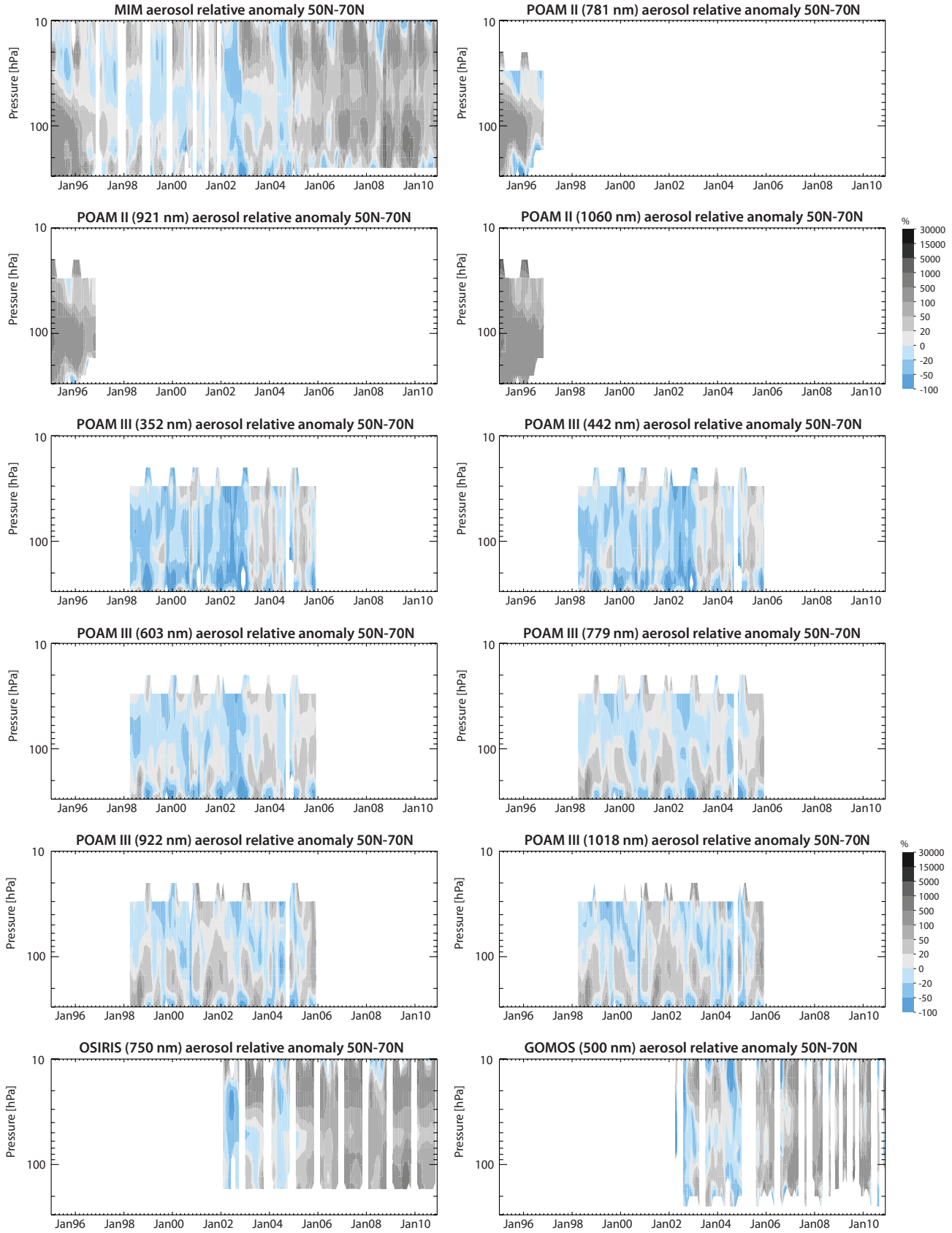

Figure 4.26.16 continued.

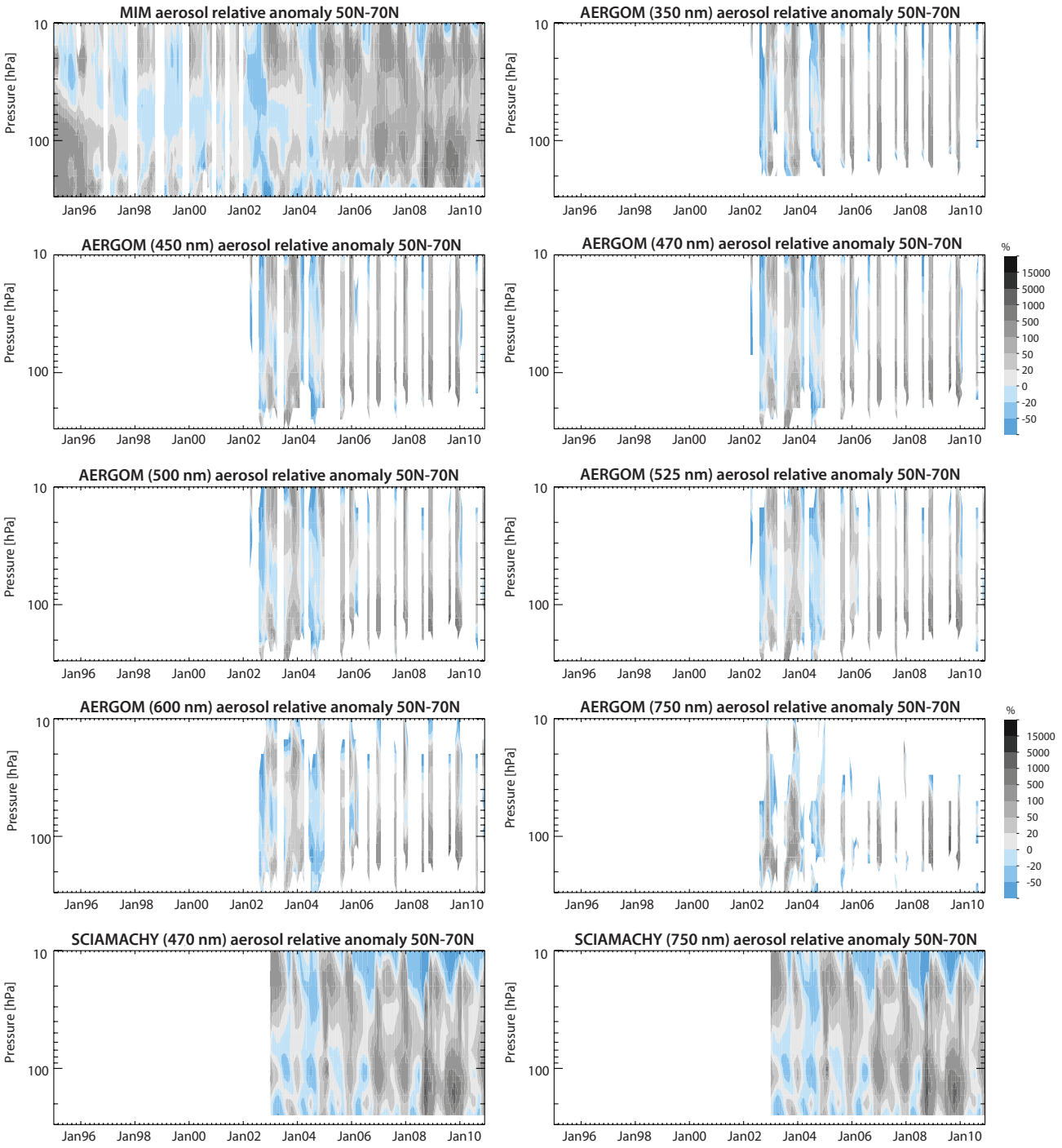

Figure 4.26.16 continued.

In the first approach, original aerosol extinction products retrieved at similar wavelengths are compared. Here, generally the aerosol extinction products show biases that at least partially reflect expected wavelength-dependencies. Some real inter-product differences however are revealed. For example, the AERGOM and SCIAMACHY products at 470 nm do show relatively large differences from the MIM in the tropics of around 30% (with AERGOM/SCIAMACHY on the high/low side) and *vice versa* in the mid-latitudes. The POAM III product at 603 nm shows mostly positive differences from the MIM, despite the fact that it was the product retrieved at the highest wavelength (and hence should show negative differences from the MIM). At 750 nm, AERGOM shows a clear negative bias when compared to the MIM (which consists mostly of products retrieved at the same wavelength). OSIRIS and SCIAMACHY at 750 nm on the other hand agree well with each other throughout the tropical and mid-latitude MS and LS, with differences largely within ±10% of the MIM. SAGE III at 755 nm compares even very well to OSIRIS (±5%).

In the second approach, a normalisation using the mean aerosol extinction value derived from each product's climatology during a quiescent period as scaling factor is applied to each product's time series. This approach neglects the spectral dependence of the normalisation factor on aerosol-size distributions, which we assume to

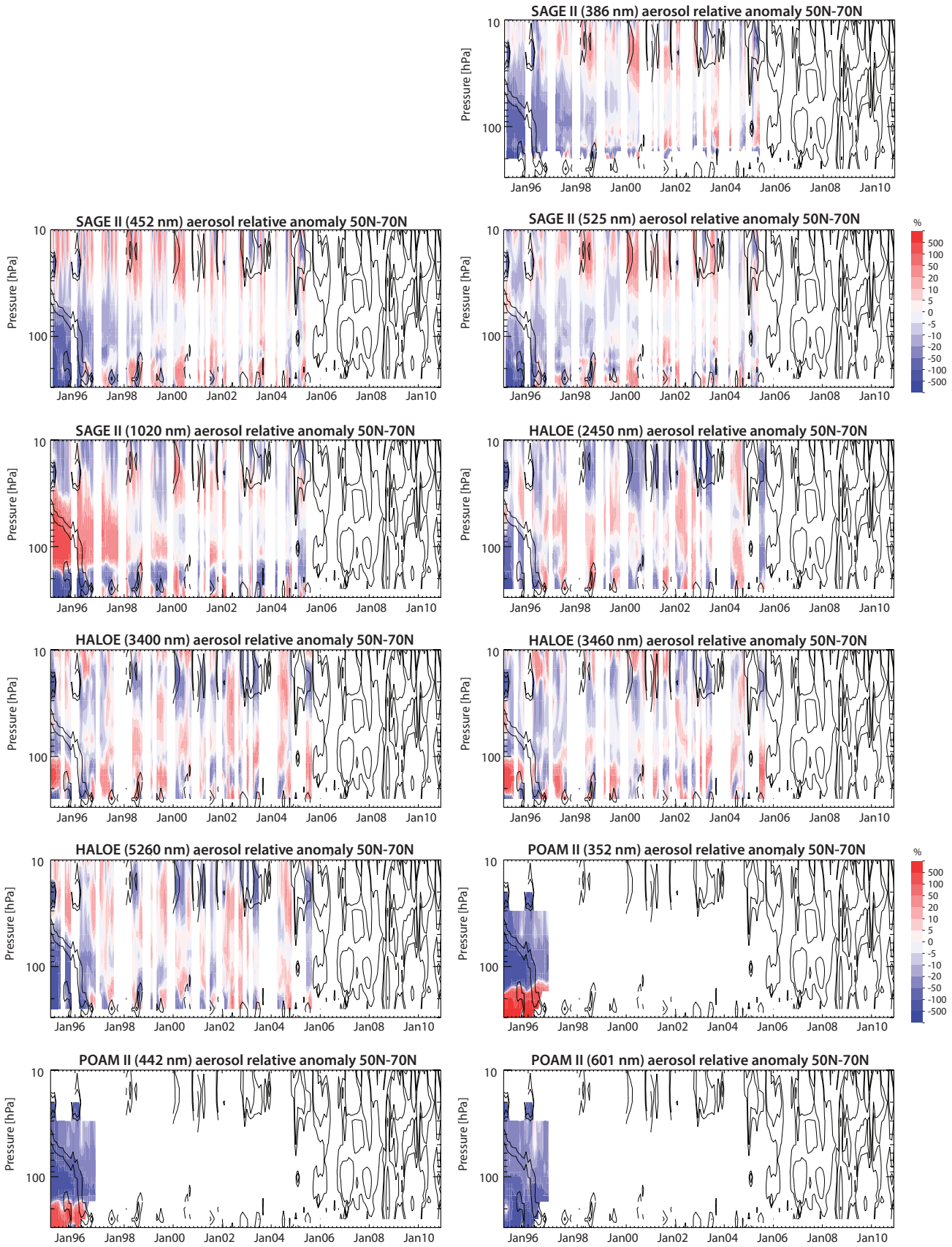

Figure 4.26.17: Time-altitude evolution of aerosol anomaly differences in the extra-tropics. *The time-altitude evolution of normalised aerosol anomaly differences averaged over 50°N-70°N with respect to the MIM is shown for all retrieval products of the different limb satellite sounders.*

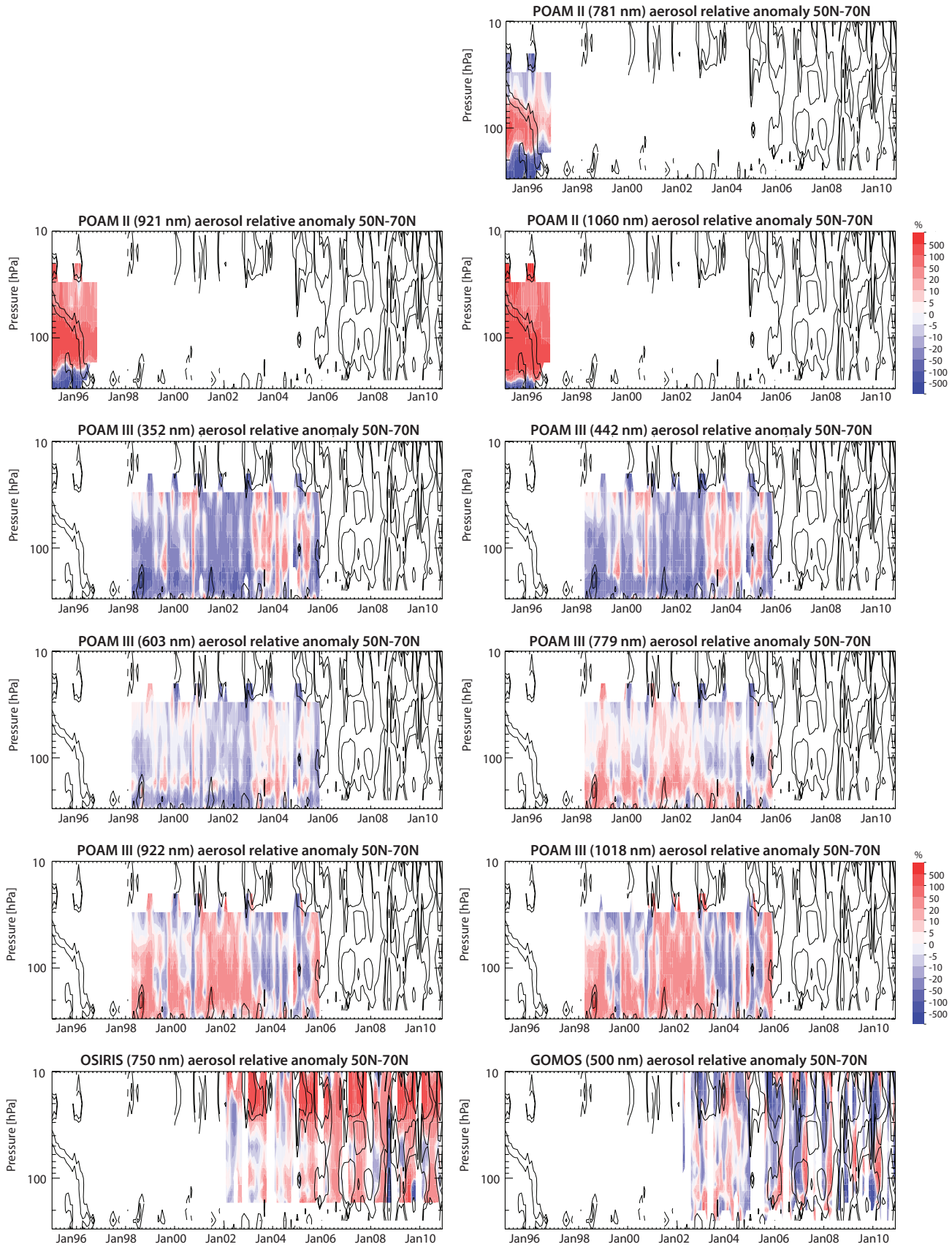

Figure 4.26.17 continued.

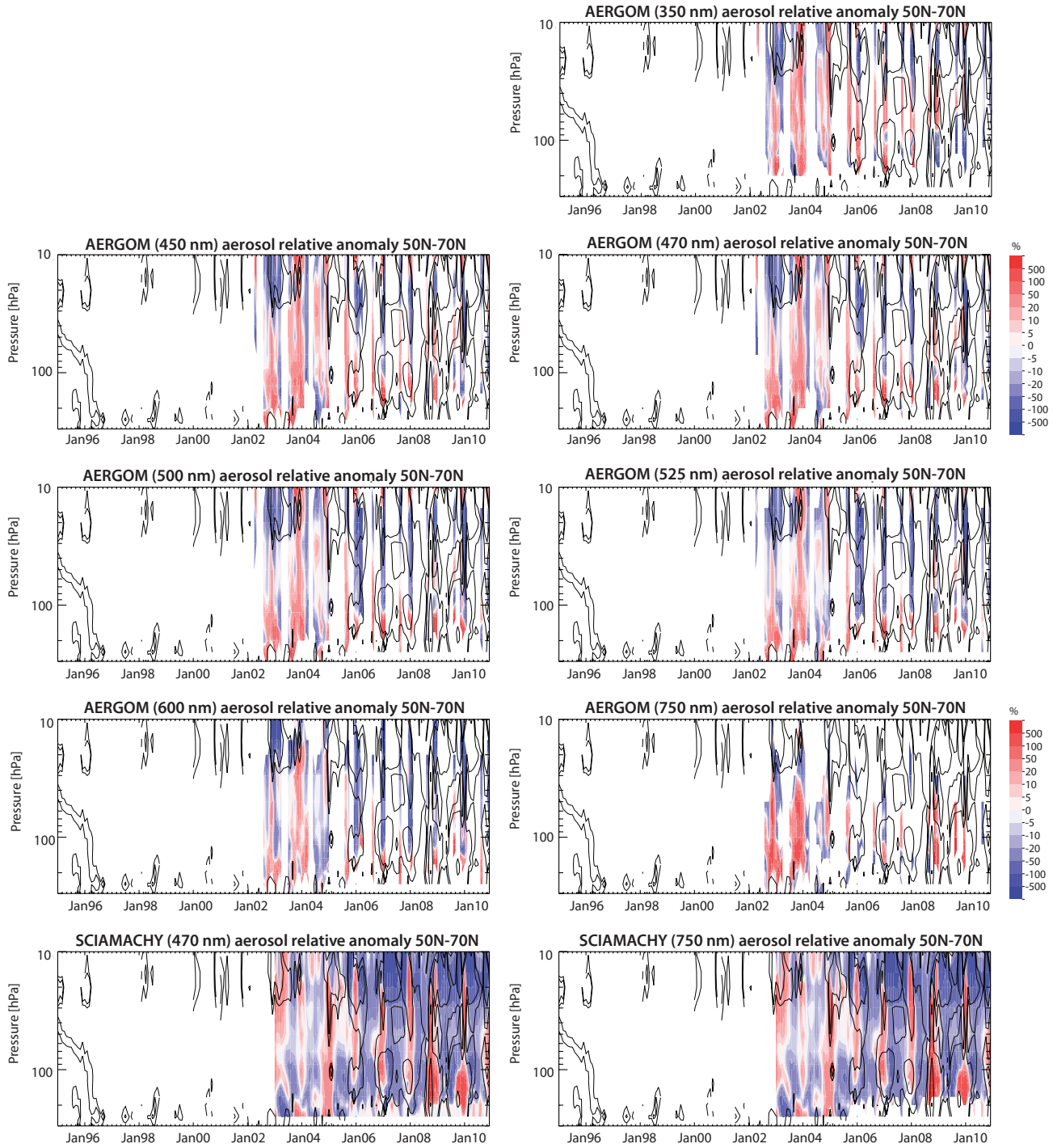

Figure 4.26.17 continued.

be of second-order importance (see also *Thomason*, 2012). Results from these comparisons can be summarised as follows.

Evaluation of anomaly time series in both the tropics and the extra-tropics reveal that most of the aerosol products capture the physical structures in the evolving aerosol layer of the stratosphere well. The comparison of the different instrument products with the time series of the MIM reveals overall good agreement in terms of the physical structures seen in the evolving stratospheric aerosol layer. Exceptions are HALOE at 2450 and 5260 nm, with both products missing to show an enhanced aerosol extinction above 30 hPa, and POAM II at 352 nm, which does not show the expected vertical structure. AERGOM time series at 350, 600, and 750 nm seem somewhat noisier than AERGOM products derived at other wavelengths and as a consequence capture the physical structure less well.

During the time period 1998-2004 with conditions of relatively low aerosol loading, most aerosol products agree very well to within ±5-10% from the MIM in the MS. At altitudes below around 70 hPa, the differences increase somewhat, but still remain largely within ±10-20%. Exceptions are the HALOE products at 2450 nm and 5260 nm, which show both somewhat larger (and also time-dependent) differences. These results confirm earlier findings

from *Thomason* [2012] who deemed these products as less reliable. The comparison with the newer generation limb-scattering and limb occultation instruments shows also encouraging results, although with somewhat larger biases, especially when moving into the extra-tropics. For OSIRIS, SCIAMACHY at 470 and 700 nm, GOMOS at 500 nm, and AERGOM at 450, 470, 500, and 525 nm differences to the MIM are of around ±10%, while for AERGOM at 350, 600, and 750 nm differences increase to up to ±20%. Note that the larger differences found in the extra-tropics between the instruments may at least partially be explained by larger sampling biases.

During the years with high aerosol loading following the Mt. Pinatubo eruption, the different products show increasing differences that exhibit often a vertical structure. This finding points towards problems in either the retrievals during periods with high aerosol loading, or problems with the comparison method that may over-simplify the wavelength-dependent sensitivity of the retrieval on aerosol size distributions.

4.27 Upper troposphere / lower stratosphere (UTLS) ozone evaluations based on TES averaging kernels

Section 4.1 provides a detailed description and comparison of the ozone climatologies from limb-viewing instruments, with a primary focus on the stratosphere. In this section we consider the distribution of ozone in the UTLS (300-70 hPa) and compare ozone measurements from six limb-viewing instruments (ACE-FTS, Aura-MLS, HIRDLS, MIPAS, OSIRIS, and SCIAMACHY) to those from the nadir-viewing Tropospheric Emission Spectrometer (TES) for 2005-2010. These results are also presented in *Neu et al.* [2014a]. TES is the only nadir-viewing instrument in this initiative, as well as the only instrument with a focus on tropospheric composition. Its ozone measurements have good sensitivity from the surface to 10 hPa and are well-validated against ozonesondes in the UTLS [*Nassar et al.*, 2008; *Boxe et al.*, 2010], as discussed in *Section 4.27.2*. Because TES is nadir viewing, it has relatively coarse vertical resolution (~6-7 km; **Figure 4.27.1a**) compared to the limb-viewing instruments discussed here, most of which have vertical resolutions of ~2-4 km. While TES has much finer horizontal resolution (<10 km) than the limb sounders (~200 km), the spacing between measurements is 182 km; thus its ability to resolve horizontal features is not much different than that of the limb sounders.

Given the strong gradients and small-scale structure of trace gas fields in the UTLS, differences in sampling and in vertical and horizontal resolution among instruments can lead to large differences that reflect sampling or smoothing error rather than systematic bias. *Toohey et al.* [2013] (see also *Section 3.2*) addresses the issue of sampling bias and shows, for example, that the construction of the zonal mean climatologies used here can lead to biases of a few percent in the subtropical jet regions (~30°N and 30°S) due to a combination of the sloping ozone surfaces in these regions and the increase in sampling density with latitude. Throughout the rest of this report, a simplified approach of directly comparing the limb-sounding climatologies without accounting for differences in vertical resolution has been used. However, because the vertical resolution of TES is so much

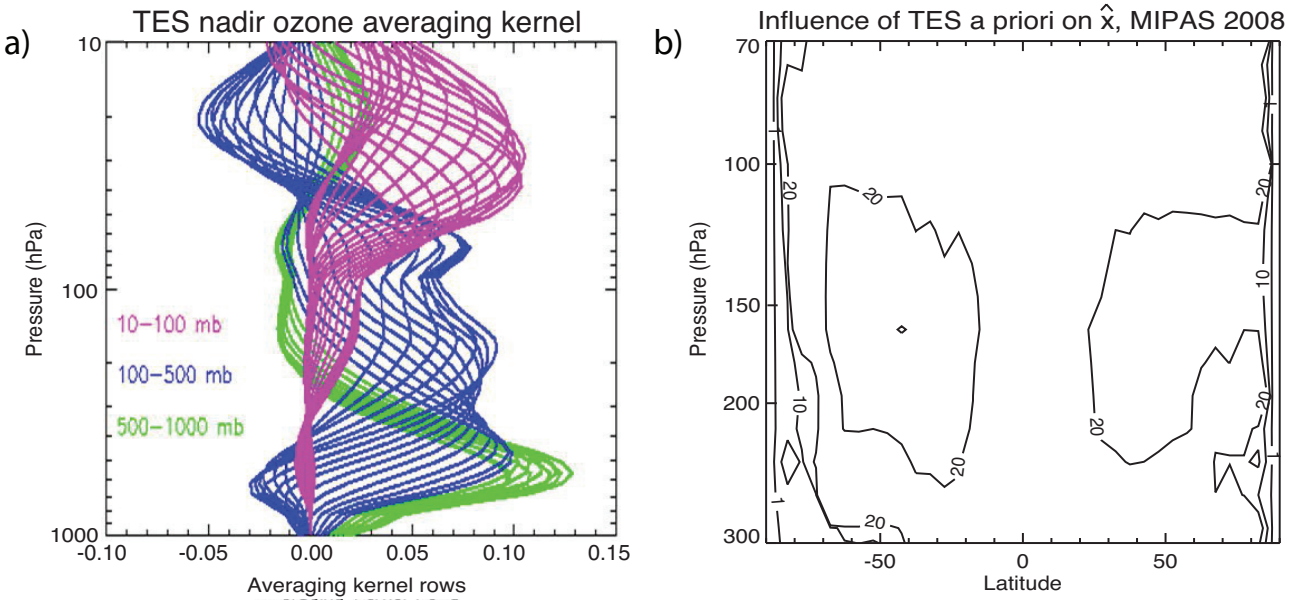

Figure 4.27.1: a) Sample TES averaging kernel. *The lines show the relative contribution of the "true" mixing ratio at each pressure level to the retrieved mixing ratio at 500-1000 hPa (green), 100-500 hPa (blue) and 10-100 hPa (purple). TES ozone averaging kernels vary with temperature, surface properties, clouds, and ozone.* ***b) Influence of the TES a priori on the virtual retrieval for MIPAS.*** *Annual mean value of the ratio of* Ax *(the contribution of the original climatology to the virtual retrieval) to* $x^a - Ax^a$ *(the contribution of the TES a priori to the virtual retrieval) for MIPAS for 2008. Results are very similar for other instruments and years. When the ratio is close to 1, the terms are of similar magnitude, so that the a priori and true profiles contribute equally to the retrieved ozone; values less than ~20 indicate a significant contribution of the a priori to the retrieval. Contour values of 1, 10, and 20 are shown.*

coarser than that of the limb viewing instruments and because vertical resolution is so critical in the UTLS, in this section we apply the TES observational operator (averaging kernel + constraint) to ozone climatologies from the limb-viewing instruments. This minimises the impact of vertical resolution disparities and allows identification of systematic differences in the large-scale structure and variability of UTLS ozone among the instruments. At the same time, the approach smooths the finer-scale vertical gradients present in the limb measurements and therefore represents a loss of this information. We thus include in this section an extensive analysis of the impact of the TES observational operator on the limb-viewing climatologies.

Ozone is the third largest component of radiative forcing [*Solomon et al.*, 2007], with maximum radiative effect in the UTLS [*Forster and Shine*, 2002]. Yet the processes that control the UTLS distribution of ozone and its trends and variability, including the exchange of air between the stratosphere and troposphere, are not well quantified [*WMO*, 2011]. The UTLS region is characterised by strong ozone gradients and complex and rapidly evolving small-scale features such as tropopause folds [*Gettelman et al.*, 2011 and references therein]. Aircraft measurements are well-suited for characterizing UTLS chemistry and dynamics because of their high spatial and temporal resolution. However, aircraft have only sparsely sampled the UTLS, raising questions about the representativeness of these measurements for applications such as evaluating free-running global chemistry-climate models [*SPARC*, 2010; *Hegglin et al.*, 2010]. Current satellite instruments lack the spatio-temporal resolution to resolve some UTLS features, such as thin, highly dynamic filaments. Furthermore, they can have low signal-to-noise in the UTLS because of the small ozone abundance there relative to the middle stratosphere, and clouds can interfere with trace gas retrievals. However, satellites provide much greater spatial and temporal coverage than aircraft, at a vertical resolution that is commensurate with that of most models [*SPARC*, 2010; *Hegglin et al.*, 2010], and their measurements have provided extensive improvements in our understanding of UTLS structure and processes [*e.g.*, *Hegglin et al.,* 2009; *Manney et al.,* 2011; *Peevey et al.*, 2012]. Assessing the differences between satellite measurements in the UTLS is critical to advancing our understanding of this region and evaluating UTLS processes in models because uncharacterised biases in satellite data can lead to incorrect conclusions about UTLS chemistry or radiative forcing.

We include TES data in this comparison and use it to evaluate measurements from the limb sounders in part because TES ozone data have been extensively validated against ozonesondes for a wide range of geophysical states and latitudes. Studies have shown that there are no observable changes in biases in the TES ozone data over time, and the bias is well characterised as a function of latitude [*Worden et al.*, 2007; *Verstraeten et al.*, 2013]. In addition, the sonde comparisons indicate that the calculated random errors are in agreement with actual errors. This means that evaluating other satellite measurements against TES provides an assessment of instrument bias rather than unquantified errors in the TES retrieval. TES is extensively used for the evaluation of upper tropospheric ozone and its precursors in chemistry transport models [*e.g.*, *Jones et al.*, 2009]. In addition, since TES measures over the entire wavelength range of ozone infrared absorption, it can provide the sensitivity of outgoing longwave radiation (OLR) to the vertical distribution of ozone [*Worden et al.*, 2008; *Worden et al.*, 2011]. As part of the Atmospheric Chemistry Climate Model Intercomparison Project (ACCMIP) TES tropospheric ozone and its effect on OLR have been compared to the same quantities derived from models and used to reduce uncertainties in ozone radiative forcing [*Bowman et al.*, 2013]. Assessing the differences between TES and other instruments measuring ozone in the UTLS region will provide a better understanding of the ozone gradients and variability that TES fails to capture due to its coarse resolution. Furthermore, improved characterisation of satellite measurements of ozone in this region will allow us to better quantify the significance of model-measurement differences in precursor emissions and radiative forcing in the UTLS.

4.27.1 Availability of UTLS ozone satellite datasets

The time period used for this analysis is determined by the availability of TES data and covers July 2005 to December 2010. TES provides global coverage from July 2005 through May 2008. To extend the life of the instrument, the latitudinal coverage was reduced in June 2008 to 60°S-82°N and in July 2008, to 50°S-70°N. From January to April 2010, the instrument went offline due to problems with the scanning mechanism. When operations resumed in May 2010, the latitude coverage was further reduced to 30°S-50°N. A second data gap of ~3 weeks occurred in October 2010, with only two Global Surveys conducted that month. **Tables 4.27.1** and **4.27.2** provide information of the availability of UTLS ozone measurements for 2005-2010 as well as the data version, vertical range, vertical resolution, and references for the instruments discussed in this section.

4.27.2 TES ozone and operational operator

TES ozone measurements have been extensively validated against ozonesondes [*Nassar et al.*, 2008; *Boxe et al.*, 2010; *Verstraeten et al.*, 2013]. In the 300-70 hPa region evaluated here, TES is positively biased with respect to sondes in all latitude regions except the southern low- and mid-latitudes (15°S-60°S), where it is negatively biased. The mean bias is smaller than 20% in all latitude regions. In the northern mid-latitudes, the bias is +15-20% for 100 hPa < p < 300 hPa and <+5% for 70 hPa < p < 100 hPa. The bias curve is "c-shaped" in the southern mid-latitude UTLS, with near-zero bias at 300 and 70 hPa and a maximum value of -20% at 150 hPa. In the tropical UTLS, TES shows a small positive bias (<10%) with respect to sondes. An analysis of seasonal variations in the northern mid-latitude (35°N-56°N) bias showed relatively small seasonal differences, except during summer when the bias decreases to <10% everywhere. Here, we include a comparison of the SPARC Data Initiative climatologies to a

Table 4.27.1: Available ozone measurements between 2005 and 2010 from limb-sounding satellite instruments and the nadir-viewing TES instrument. *The red filling of the grid boxes indicates the temporal (January to December) and vertical (300 to 70 hPa) coverage of the respective instruments.*

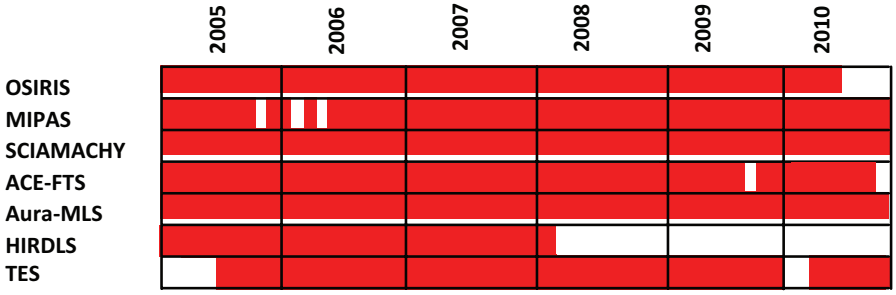

Table 4.27.2: Data version, vertical range, vertical resolution, and references for ozone datasets used for UTLS evaluations.

Instrument and data version	Vertical range	Vertical resolution	References
ACE-FTS V2.2update	5 – 95 km	3 – 4 km	*Dupuy et al.,* 2009
Aura-MLS V2.2	12 – 75 km	3 km	*Froidevaux et al.,* 2008; *Jiang et al.,* 2007
HIRDLS V6.0	10 – 55 km	1 km	*Nardi et al.,* 2008; *Gille et al.,* 2008
MIPAS V220	6 – 70 km	2.7 – 3.5 km	*von Clarmann et al.,* 2009a
OSIRIS V5-0	10 – 60 km	2 km	*Degenstein et al.,* 2009
SCIAMACHY V2.5	10 – 60 km	3 – 5 km	*Mieruch et al.,* 2012
TES V4	0 – 35 km	6 – 7 km	*Worden et al.,* 2004; *Boxe et al.,* 2010

"zonal mean" ozonesonde climatology (*Sections 4.27.3* and *4.27.4*) and find different biases for the TES climatology than those reported in the TES validation literature in some regions. These differences likely result from not accounting for 1) the sampling locations of the ozonesonde profiles and 2) the difference in vertical resolution between TES and the sondes in the climatological comparisons.

Use of zonal mean monthly mean averaging kernels

TES retrievals use the optimal estimation technique [*Rodgers*, 2000], with the retrieved profile, $\hat{x}$(ln(vmr)), given by:

$$\hat{x} = x^a + A^{xx}(x - x^a)$$

where x(ln(vmr)) is the true state, x^a(ln(vmr)) is the *a priori* profile, and A^{xx} is the averaging kernel matrix. For the comparisons shown here, the climatologies of the higher vertical resolution limb viewing instruments are taken to be the "true" state, x, and the TES observational operator (*a priori* and averaging kernel) are used to simulate a "virtual" TES retrieval, $\hat{x}$. Normally, this type of comparison is done on a profile-by-profile basis. However, due to the large number of instruments involved in this comparison and the focus on zonal mean climatologies, we apply the monthly mean zonal mean observational operator to the monthly mean zonal mean SPARC Data Initiative climatologies. The use of monthly mean zonal mean averaging kernels can be justified by the fact that the variations in TES averaging kernels are not highly correlated with variations in ozone. In the troposphere, ozone explains less than 25% of the variance in the averaging kernel diagonal at all latitudes due to the strong dependence of the averaging kernels on clouds, water vapor, and temperature, as discussed by *Aghedo et al.* [2011]. In the UTLS region, ozone explains up to 35% of the variance in the averaging kernel diagonal in mid-latitudes, with a minimum value at ~150-200 hPa where the sensitivity is relatively low and the *a priori* has a significant impact on the retrievals (see *Section 4.27.3*). In the tropical UTLS, ozone explains 20-60% of the variance in the averaging kernel diagonal, with maximum correlation at ~150 hPa. However, at all latitudes the dependence of the averaging kernel diagonal on ozone abundance is weak for ozone within ±40% of the mean value at each level; the correlations are primarily driven by ozone abundances more than 40% higher than the mean value. In the mid-latitudes, ozone abundances that are twice as large as the mean value at a given pressure level have a ~30% higher averaging kernel diagonal value. In the tropics, the slope of the relationship is somewhat higher, and a 100% increase in ozone over the mean value is associated with a 45% larger averaging kernel diagonal.

Aghedo et al. [2011] examined the error associated with using monthly mean averaging kernels in two climate models for p ≥ 100 hPa. They found differences in ozone of at most 3% when using monthly mean as compared to time-varying averaging kernels. To test the error involved in applying zonal mean averaging kernels to zonal mean data, we examined the difference between TES and Aura-MLS measurements for 2006. In the first case, we use 5°x10° gridded TES averaging kernels to smooth 5°x10° gridded Aura-MLS measurements and calculate zonal mean differences afterwards. In the second case, we use zonal mean TES averaging kernels to smooth zonal mean Aura-MLS data. The difference between the two cases is always smaller than 10%, and the difference in the zonal mean datasets is always smaller than the difference in gridded datasets (except in high southern latitudes during October). In addition, the difference between using zonal

mean averaging kernels aggregated from individual profiles and using the zonal mean of the gridded averaging kernels is negligible (< 2% everywhere). We therefore conclude that using zonal mean averaging kernels with zonal mean data provides a lower estimate that is within ~10% of the true difference between each instrument and TES. However, we note that because the averaging kernels are not fully independent of the ozone abundance, comparison using the TES observational operator may not accurately reflect the difference between TES and another instrument if there are large systematic differences between them. Given the fact that the averaging kernels depend only weakly on the ozone abundance for ozone within 40% of the mean value, we do not expect this to be an issue except where instruments differ from TES by more than 40%. In such cases, which are rare (see the discussion of **Figure 4.27.4** below), the error associated with using an averaging kernel that has sensitivity not appropriate for the ozone observed by the other instrument can only be quantified by recalculating the averaging kernel to "match" the instrument's ozone, which is beyond the scope of this report.

Applying the TES observational operator

For each instrument, we interpolate the monthly mean zonal mean climatologies from the SPARC pressure grid to the TES retrieval levels (67 levels between the surface and 0.1 hPa). We fill in the levels below the lowest measurement in each latitude bin (at pressure p_{max}) using the monthly mean, zonal mean TES *a priori* as a "fill profile". The "virtual" TES retrievals are calculated and then interpolated back to the SPARC pressure grid, and we average over all of the available data from 2005-2010 to create the climatologies shown here. We use the *a priori* as a fill profile because it makes $A(x - x^a) = 0$ in the "troposphere" (defined as $p \geq p_{max}$ for each instrument) since $x = x^a$ there, which is equivalent to applying the observational operator only to the levels where the limb-viewing instruments provide measurements. However, the fill profile can still impact the comparison to TES due to the vertical smearing of the averaging kernels. The difference between the virtual retrieval for a given instrument ($\hat{x}_{INST}$) and TES ($\hat{x}_{TES}$) can be written as

$$\hat{x}_{INST} - \hat{x}_{TES} = A^{SS}(x_{True}^{STRAT} - x_{INST}^{STRAT}) - A^{ST}(x_{True}^{TROP} - x_{INST}^{TROP})$$

where A^{SS} is the "stratospheric" component of the averaging kernel matrix ($p < p_{max}$), x_{INST}^{STRAT} the ozone profile measured by the limb-viewing instrument, A^{ST} represents the cross-terms of the averaging kernel that define the tropospheric influence on the stratosphere, and x_{INST}^{TROP} is the fill profile. To test the sensitivity of our results to our approach of using the TES *a priori* to fill in the profiles below the lowest measurement level, we have also calculated virtual retrievals in which we scale the TES *a priori*. We do so by multiplying the *a priori* profile by the percent difference between the individual instrument's ozone value and the TES *a priori* ozone at p_{max} for each latitude bin. Comparison of the virtual retrievals using the two different filling methods allows us to identify regions where our results are highly dependent on our assumptions for $p > p_{max}$, as discussed below.

4.27.3 UTLS ozone evaluations: Zonal mean cross sections, vertical and meridional profiles

As throughout *Chapter 4*, we use a series of diagnostics to evaluate differences in the vertical, latitudinal, and temporal structure of ozone as represented by the SPARC Data Initiative climatologies. However, rather than examining differences from the multi-instrument mean, we use the TES climatology as the standard to which the other climatologies are compared and, in some cases, include climatological ozonesonde measurements as an additional validation tool. We also analyse the impact of the TES observational operator on the climatologies from the limb-viewing instruments and assess how the use of the observational operator affects the ozone inter-comparison.

The second column of **Figure 4.27.2** shows the zonal mean ozone climatology for each instrument from 300 to 70 hPa averaged over 2005-2010 (2005-2007 for HIRDLS) using the data directly from the SPARC Data Initiative archive. All of the instruments show similar features, including the typical low tropical values, strong subtropical gradients, and relatively flat mid-latitude isopleths that reflect the competing effects of the stratospheric overturning circulation and mixing with the troposphere. The instruments also all show lower ozone values in the Southern Hemisphere than in the Northern Hemisphere in the annual mean due to the asymmetry in the overturning circulation. A few instruments show features not seen in the climatologies from any of the other instruments. The MIPAS climatology has an unusual contour shape in the tropics between ~200 and 100 hPa, with a slight "double ear" structure in the subtropics and a deep minimum near the equator, and Aura-MLS has very flat, tightly spaced contours near 100 hPa. It is likely that some of the differences in the climatologies in the upper tropical troposphere arise from differences in the impact of clouds on the retrievals and in criteria used for cloud screening, which can cause sampling artefacts. The OSIRIS climatology has an unusually strong zonal gradient at ~75°N below 250 hPa, which appears to reflect sampling bias in the climatology resulting from a lack of measurements in polar winter [*Toohey et al.*, 2013].

Impact of TES observational operator

The third column of **Figure 4.27.2** shows the virtual retrievals using the TES observational operator, and the fourth column shows the percent difference between the virtual TES retrieval (VTR) and the original climatology (OC) for each instrument (shown in the left column) (100*(VTR-OC)/OC). Hatched regions in the right column indicate where the choice of fill profile (TES *a priori* or scaled *a priori*) has a significant impact on the VTR, quantified (arbitrarily) as where the difference between the VTRs using the two fill profiles exceeds 10%. The HIRDLS climatology shows the

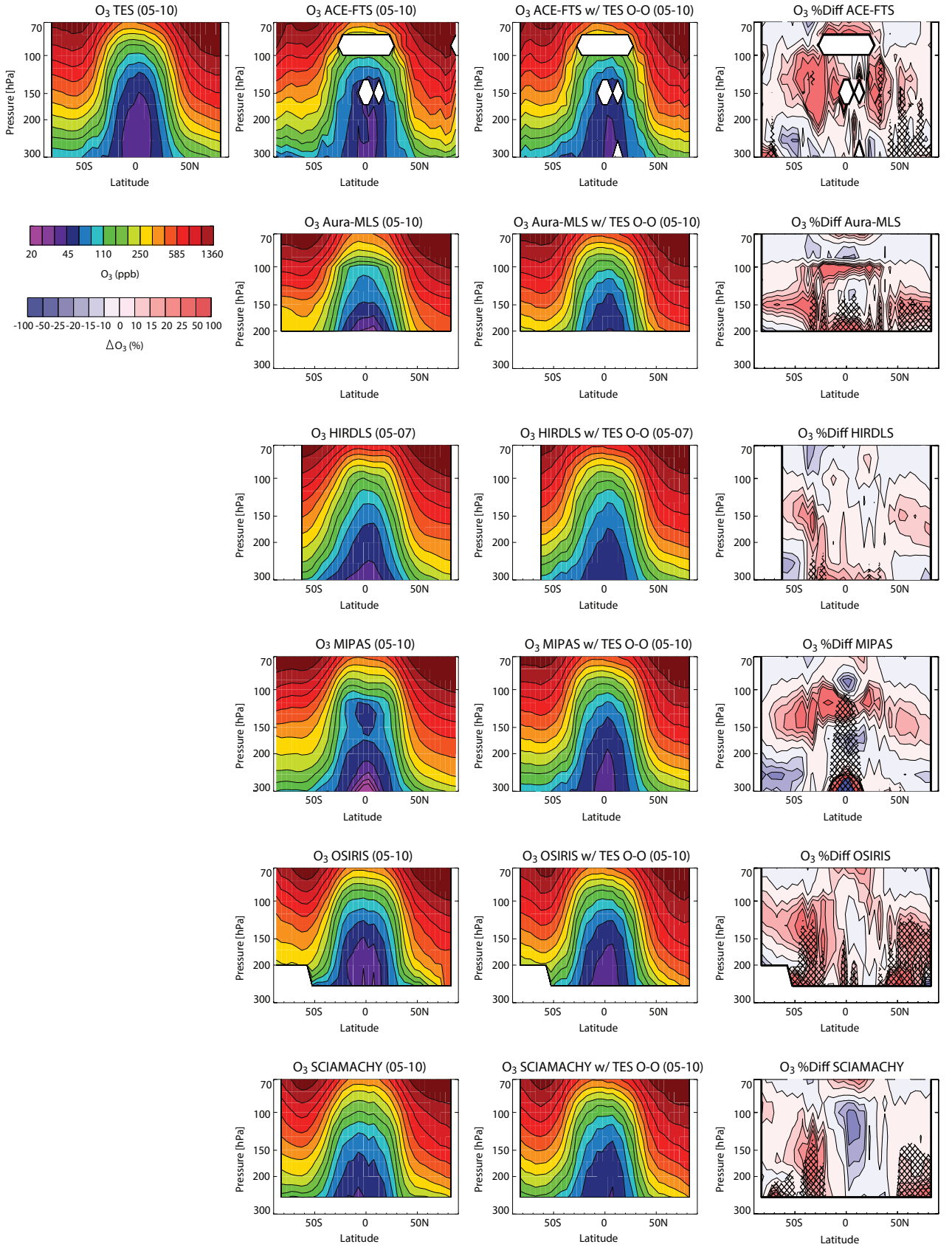

Figure 4.27.2: Cross sections of annual mean zonal mean ozone from 300 to 70 hPa for 2005-2010. *First column: Ozone cross section from TES. Second column: Ozone cross sections from ACE-FTS, Aura-MLS, HIRDLS (2005-2007), MIPAS, OSIRIS, SCIAMACHY. Third column: Cross sections from ACE-FTS, Aura-MLS, HIRDLS, MIPAS, OSIRIS, SCIAMACHY after application of the TES observational operator. Fourth Column: Percent change in annual mean zonal mean ozone introduced by the TES observational operator (100*(VTR – OC)/OC, where VTR=virtual TES retrival and OC=Original Climatology). Hatching indicates regions where the difference between the virtual retrievals using the TES a priori as the fill profile and those using the scaled a priori as the fill profile exceeds 10%. See text for details.*

most uniform and smallest changes in ozone after the application of the TES observational operator. The operator acts to smooth out the small-scale features seen in the MIPAS, Aura-MLS, and OSIRIS climatologies, as seen in the center column, due to the vertical smearing of the broad averaging kernels. In the tropics, the observational operator tends to increase ozone for $p \leq 80$ hPa and decrease it for $p > 80$ hPa relative to the original climatologies (with strong increases at 100 hPa associated with the unusual features in MIPAS and Aura-MLS). MIPAS and Aura-MLS are the only two instruments for which the choice of the fill profile has a significant impact in the tropics. It is unclear why this is the case for Aura-MLS, but the MIPAS tropical ozone values are very low at $p > 250$ hPa compared to the other instruments, and there is a very large difference between the TES *a priori* and the *a priori* scaled using the MIPAS measurements in this region.

In the extra-tropics, the observational operator tends to increase ozone at ~150 hPa and decrease it above and below, which increases the vertical and horizontal gradients of ozone in the virtual retrievals compared to the original climatologies. This increase in gradient clearly cannot result from the TES averaging kernels, which smooth and flatten vertical gradients. Rather the increase results from the influence of the *a priori*; comparison of the terms Ax, the contribution of the "true" profile from each climatology to the virtual retrieval, and, $x^a - Ax^a$, the contribution of the TES *a priori* to the virtual retrieval, (**Figure 4.27.1b**) shows that TES's sensitivity is lowest and the *a priori* profile makes the largest contribution to $\hat{x}$ in the mid-latitudes at ~150-200 hPa, as well as in the southern high latitudes at $p > 150$ hPa.

The sensitivity to the fill profile is largest in the extra-tropics, in particular for the climatologies whose range does not extend to 300 hPa (Aura-MLS, OSIRIS, and SCIAMACHY). Between ~200 and 300 hPa there are large vertical gradients in mid-latitude ozone that are not well-represented by the TES *a priori*, so that there is a large difference between the two fill profiles (the *a priori* and the scaled *a priori*). Furthermore, the averaging kernels spread the information from 300 hPa upward to ~100 hPa in the extra-tropics, so that changing ozone at 300 hPa has a significant influence over a large vertical range.

Figure A4.27.1 in *Appendix A4* shows the difference between the VTRs and OCs for January, April, July, and October. The results for the individual months are similar to the annual mean results shown here, with the exception of October. Because TES has relatively low sensitivity in southern high latitudes (see **Figure 4.27.1b** and discussion thereof) and the *a priori* does not adequately capture the characteristics of Antarctic ozone depletion, the application of the observational operator results in strong increases in ozone for $p <$~170 hPa and strong decreases in ozone for $p >$~170 hPa at latitudes poleward of 50°S in the virtual retrievals of all of the instruments. We also note a greater tendency for the difference between the VTRs using the two fill profiles to exceed 10% in the Southern Hemisphere during January-April and in the Northern Hemisphere during July-October.

Figure 4.27.3 shows a comparison of zonal mean vertical profiles in the northern mid-latitudes (April), tropics (annual mean), and southern mid-latitudes (October). The left column is once again the original SPARC Data Initiative climatology for each instrument, while the centre and right columns show the virtual retrievals using the TES observation operator and the percent difference between the virtual retrievals and the original data (100*(VTR-OC)/OC), respectively. Dashed lines in the right column indicate where the choice of fill profile affects the VTR by more than 10%. In the mid-latitudes, the observational operator smoothes the vertical profiles; it decreases ozone for $p >$150 hPa and increases it for $p <$ 150 hPa for all instruments for which the virtual retrievals do not depend strongly on the fill profile. In the tropics, as discussed above, the observational operator acts to slightly increase ozone at $p <$ 80 hPa and slightly decrease it at $p >$ 80 hPa, as well as to smooth small-scale vertical structures.

Percent difference from TES

Figure 4.27.4 shows the percent difference between the annual mean climatology for each instrument and TES (100*(OC-TES)/TES, left column) and the percent difference between the virtual retrievals for each instrument and TES (100*(VTR-TES)/TES, right column). The hatched regions in the right column indicate where differences in the VTR due to the choice of fill profile exceed 50% of the difference between the VTR and TES for each instrument. While 50% is an arbitrary choice, it highlights a combination of regions where the fill profile has a relatively large impact on the virtual retrievals (see **Figure 4.27.2** above) and regions where differences between the virtual retrievals and TES are small so that even small differences due to the fill profile are large relative to VTR-TES. The original climatologies from all instruments except ACE-FTS and OSIRIS show positive differences of more than 25% with respect to TES in the tropics. However, except for HIRDLS, which is affected by uncorrected emission from aerosol in the tropics (J. Gille, private communication, 2013), the biases are not uniform in pressure and there are some regions with negative biases, including for $p <$ 70 hPa (which can impact the region of interest when the TES observational operator is applied). The virtual retrievals represent the combined influence of the vertical smoothing of the TES averaging kernel and the *a priori*, whose influence is not negligible due to TES's imperfect sensitivity. Together these act to both vertically smooth the differences from TES and reduce them to ≤ 25% for the virtual retrievals from all instruments except HIRDLS. However, for the Aura-MLS and MIPAS virtual retrievals, the biases with respect to TES are robust (*i.e.,* not strongly dependent on the fill profile) only for $p <$ ~100 hPa. For ACE-FTS, which is a solar occultation instrument and has very sparse sampling in the tropics due to its orbit, the difference from TES may largely reflect a >5% tropical sampling bias in the climatology [*Toohey et al.*, 2013].

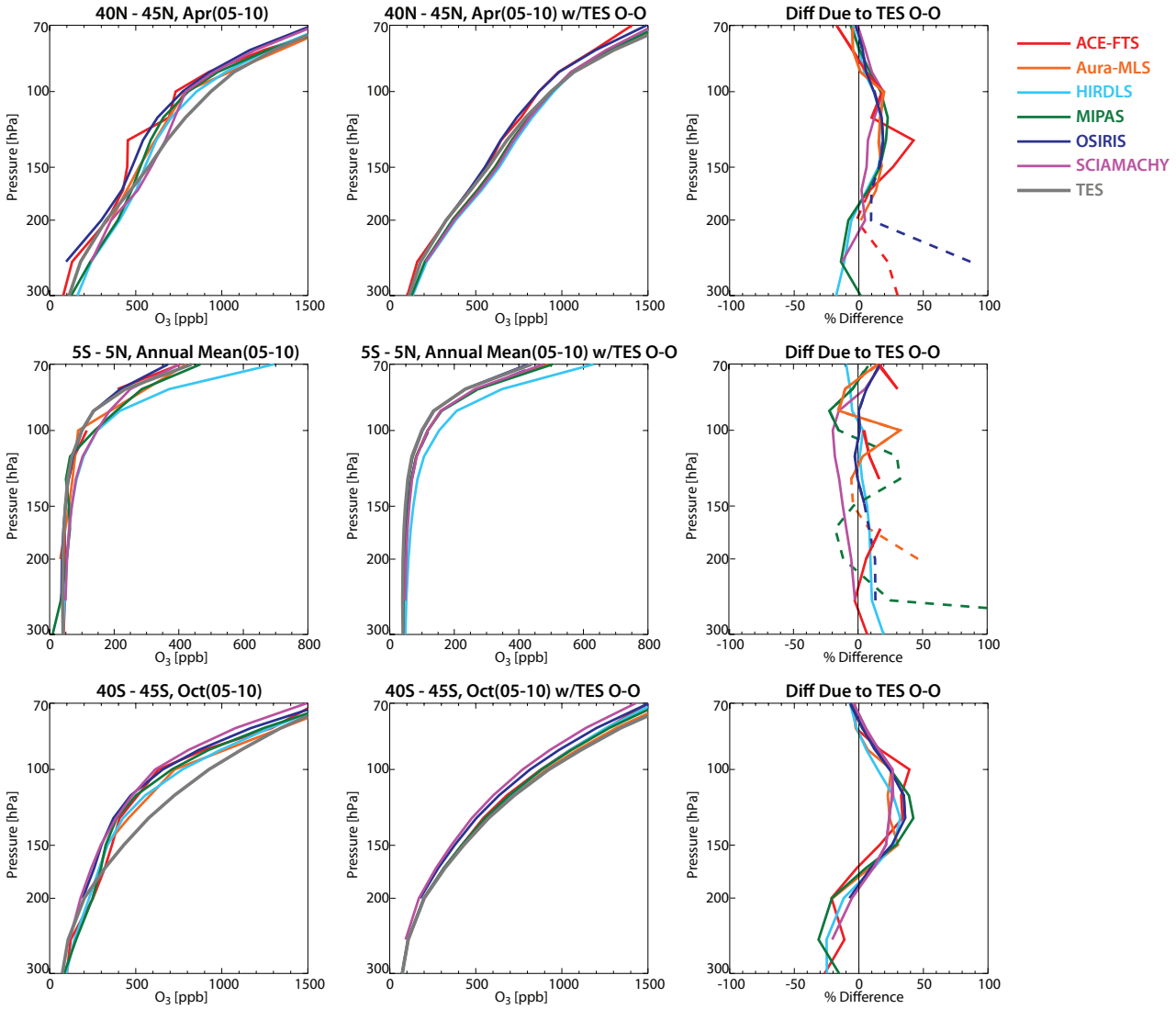

Figure 4.27.3: Vertical profiles of zonal mean ozone for 2005-2010. *Left column: Ozone profiles from the original climatology for each instrument. Centre column: Ozone profiles after application of the TES observational operator. TES measurements are the same as in the left column. Right column: The percent change in the ozone profiles introduced by the TES observational operator for all instruments except TES (100*(VTR-OC)/OC). Dashed lines indicate portions of the profile where the difference between the virtual retrievals using the TES a priori as the fill profile and those using the scaled a priori as the fill profile exceeds 10%. Top row: Zonal mean ozone profiles and differences for 40°N-45°N for April 2005-2010. Centre row: Annual mean zonal mean ozone profiles and differences for 5°S-5°N for 2005-2010. Bottom row: Zonal mean ozone profiles and differences for 40°S-45°S for October 2005-2010.*

HIRDLS and MIPAS also have annual mean positive differences of 10-30% with respect to TES at $p \geq 150$ hPa in the northern mid- and high latitudes. Again, the differences with respect to TES can be seen in the original climatologies, but the vertical extent of the positive biases is greater in the virtual retrievals. The climatologies from the other instruments also show positive differences from TES in the same region, but for the most part these are not seen in the original climatologies and are an artefact of the impact of the fill profile. In the Southern Hemisphere, the original climatologies are generally negatively biased with respect to TES, especially above 200 hPa. The TES observational operator strongly reduces the difference between the original datasets and TES in the Southern Hemisphere, such that the virtual retrievals agree with the TES climatology to within ~10%. This is likely because the differences between the original climatologies and TES occur largely in the region where TES has low sensitivity and the *a priori* plays an important role in the virtual retrievals (**Figure 4.27.1b**). OSIRIS and SCIAMACHY, which measure only in the sunlit portion of the atmosphere, have >5% negative sampling biases in their climatologies in the southern mid- and high-latitudes [*Toohey et al.*, 2013], which may at least partially explain their larger differences with respect to TES relative to the climatologies from other instruments.

Figure A4.27.2 in *Appendix A4* shows the percent difference between the virtual retrievals for each instrument and TES for the same months as shown in **Figure A4.27.1** in *Appendix A4*. The differences for individual months are generally similar to those for the annual mean (**Figure 4.27.4** right column). The positive difference between MIPAS and

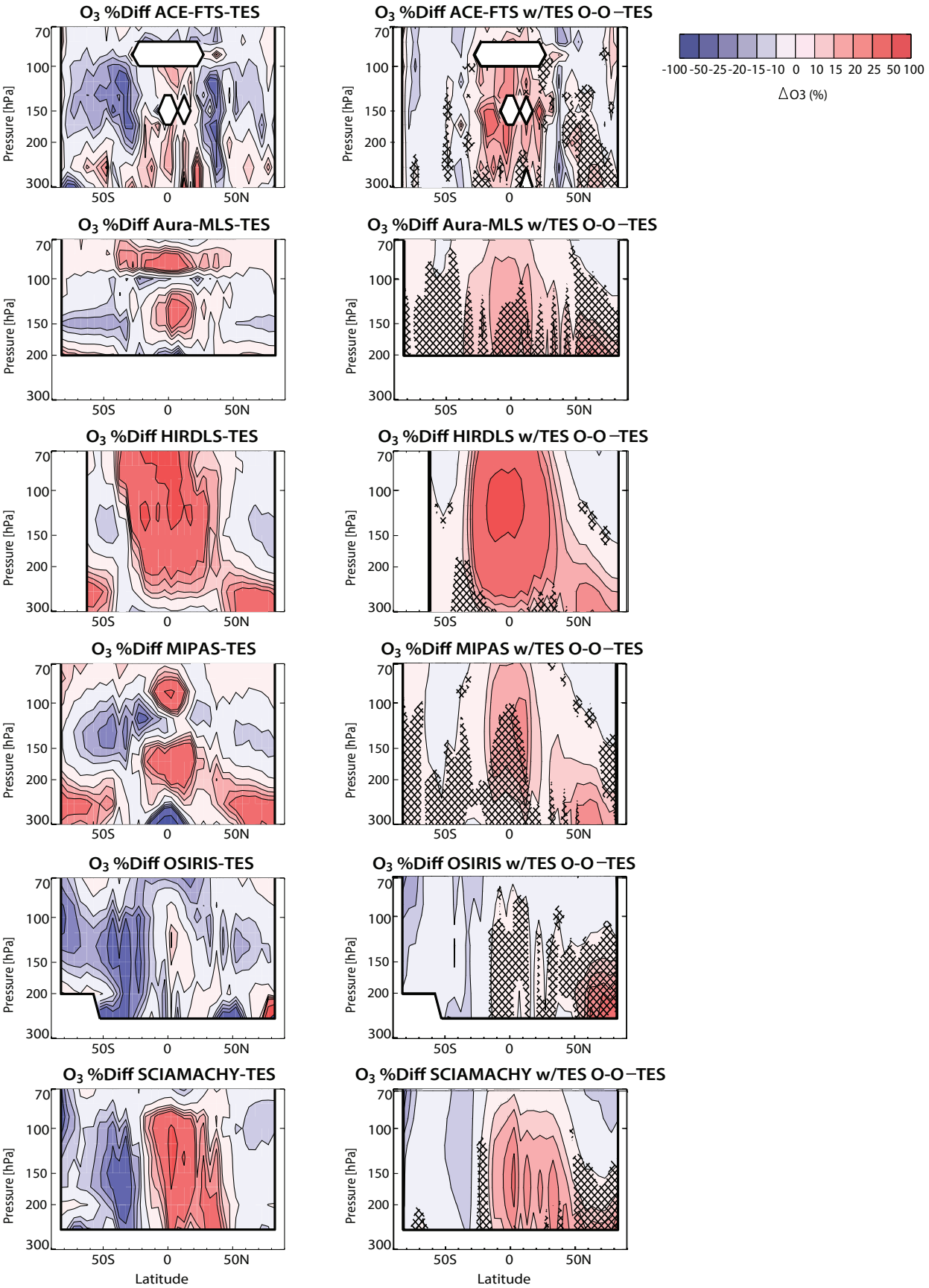

Figure 4.27.4: Cross sections of annual mean zonal mean ozone differences from 300 to 70 hPa for 2005-2010. *Left column: Annual mean zonal mean ozone percent differences between the climatology from each instrument and TES for 2005-2010 (HIRDLS: 2005-2007) (100*(OC-TES)/TES). Right column: Percent differences between the virtual retrieval from each instrument and TES after application of the TES observational operator (100*(VTR-TES)/TES). Hatched regions indicate where the difference in the virtual retrieval using the two different fill profiles exceeds 50% of the difference between the virtual retrieval and TES.*

TES in the tropics is larger in January than throughout the rest of the year, and the positive difference between both HIRDLS and MIPAS and TES in the northern mid- and high latitudes is largest in July. SCIAMACHY is the only instrument with a large (positive) difference with respect to TES in southern high latitudes during October, despite the fact that the virtual retrieval is strongly influenced by the *a priori* in that region and thus not expected to differ greatly from TES (see discussion above). The SCIAMACHY climatology has the highest October ozone values of any of the climatologies from ~150 hPa ≤ p ≤ ~100 hPa and ~70-80°S (see **Figure A4.27.5** in *Appendix A4*, discussed below), where there is a local maximum in TES Southern Hemisphere sensitivity (see **Figure 4.27.1b**). This maximum in sensitivity preserves the high ozone values in the SCIAMACHY virtual retrieval and spreads them vertically throughout the UTLS.

Latitudinal gradients on pressure surfaces

Figure 4.27.5 shows the 2005-2010 mean April ozone from each instrument as a function of latitude on four pressure surfaces. The original datasets (first column), virtual retrievals (second column), and percent differences between the original datasets and TES (100*(OC-TES)/TES, third column) and virtual retrievals and TES (100*(VTR-TES)/TES, fourth column) are all shown. Dashed lines in the fourth column indicate where differences in the VTR due to the choice of fill profile exceed 50% of the difference between the VTR and TES for an instrument. In addition to the satellite climatologies, the first column also includes a "zonal mean" ozone climatology from ozonesonde measurements at 48 stations from the datasets described by *Logan* [1999] (representative of 1980–1993) and *Thompson et al.* [2003] (representative of 1997–2011) (**Table 4.27.3**). We note that there are at most 4 ozonesonde stations in a given latitude band, and many latitude bands contain only one station, likely leading to large sampling biases. Furthermore, no attempt has been made to account for differences in vertical resolution between the satellites and the sondes, primarily because it is unclear whether the use of zonal mean averaging kernels would exacerbate the sampling bias. Nevertheless, we include the ozonesonde climatology to demonstrate the good agreement between the satellites and the sondes and to provide an additional tool to investigate biases in the satellite climatologies.

At p ≤ 200 hPa, the absolute differences between the climatologies are mostly small, except at high latitudes (>50°N/S, **Figure 4.27.5**, first column). Given the large ozone abundance at high latitudes, however, the absolute differences between the instruments translate to small relative differences; the limb-viewing instruments agree with each other and with TES (**Figure 4.27.5**, third column) to within ~30% at mid- and high latitudes for p ≤ 200. The ozonesonde measurements suggest that the TES climatology is positively biased by ~20% in the Northern Hemisphere extra-tropics for 80 < p < 200 hPa, in good agreement with the TES validation studies. In the Southern Hemisphere extra-tropics, the TES climatology shows positive biases of 20-30% with respect to the ozonesonde climatology for p > 100 hPa and negative biases of 20-30% for p < 100 hPa. The inconsistency between this comparison and the validation results discussed in *Section 4.27.2* likely arises from the sparse ozonesonde coverage in the Southern Hemisphere, the fact that we have not applied the TES operator to the ozonesonde measurements, and the comparison here being limited to a single month (results for the seasonal cycle are discussed in *Section 4.27.4*). For latitudes > ~40°N/S and p ≤ 200 hPa, it appears that the differences between the climatologies from the limb instruments and the TES climatology likely reflect biases in TES rather than any significant bias in the limb sounders' climatologies. The direct comparison of the satellite climatologies to TES, using the TES operational operator, results in agreement of all of the satellite climatologies at the 10% level for this region (**Figure 4.27.5**, fourth column). However, in reducing the difference between the limb sounders and TES, the use of the observational operator also introduces some of the TES bias into the virtual retrievals.

In the tropics, where ozone abundances are low, small absolute differences translate into large relative differences, as also seen in **Figure 4.27.4.** The limb-viewing instruments differ from one another and from TES by up to 90% in the tropics and subtropics (**Figure 4.27.5**, third column). The TES climatology does not differ systematically from the ozonesonde climatology in the tropics for p < 200 hPa, except at 150 hPa, where it is positively biased by ~25% in April. Thus, the greater ozone abundances in the limb sounder climatologies represent an over-estimate of tropical ozone throughout most of the UTLS for this month. However, although differences between the annual mean climatologies are generally similar to or smaller than the differences shown here for April, the annual mean TES climatology at 150 hPa is actually biased low by >20% relative to the annual mean ozonesonde climatology over much of the tropics (see also *Section 4.27.4*, discussion of **Figures A4.27.3-A4.27.5** in *Appendix A4* below). Again, this contradicts coincident validation studies showing a small positive bias for TES throughout the tropical UTLS. The annual mean positive differences between the limb sounder climatologies and TES seen in **Figure 4.27.4** thus likely reflect true positive biases for the limb climatologies only for p < 150 hPa. With the exception of HIRDLS, which has high ozone values over a deep vertical extent (thus limiting the impact of smoothing), the TES observational operator greatly reduces the differences between the climatologies, with agreement to within ~30% in the tropics and subtropics. The comparison to TES is most robust for p < 100 hPa, where the virtual retrievals are relatively free of influence from the fill profile. While the annual mean pattern of differences between HIRDLS and TES is more or less centred at the equator (**Figure 4.27.4**), the HIRDLS climatology shows the largest differences from TES and from the other climatologies in the southern subtropics in April, suggesting perhaps a seasonal variability in the aerosol effect on the ozone retrievals.

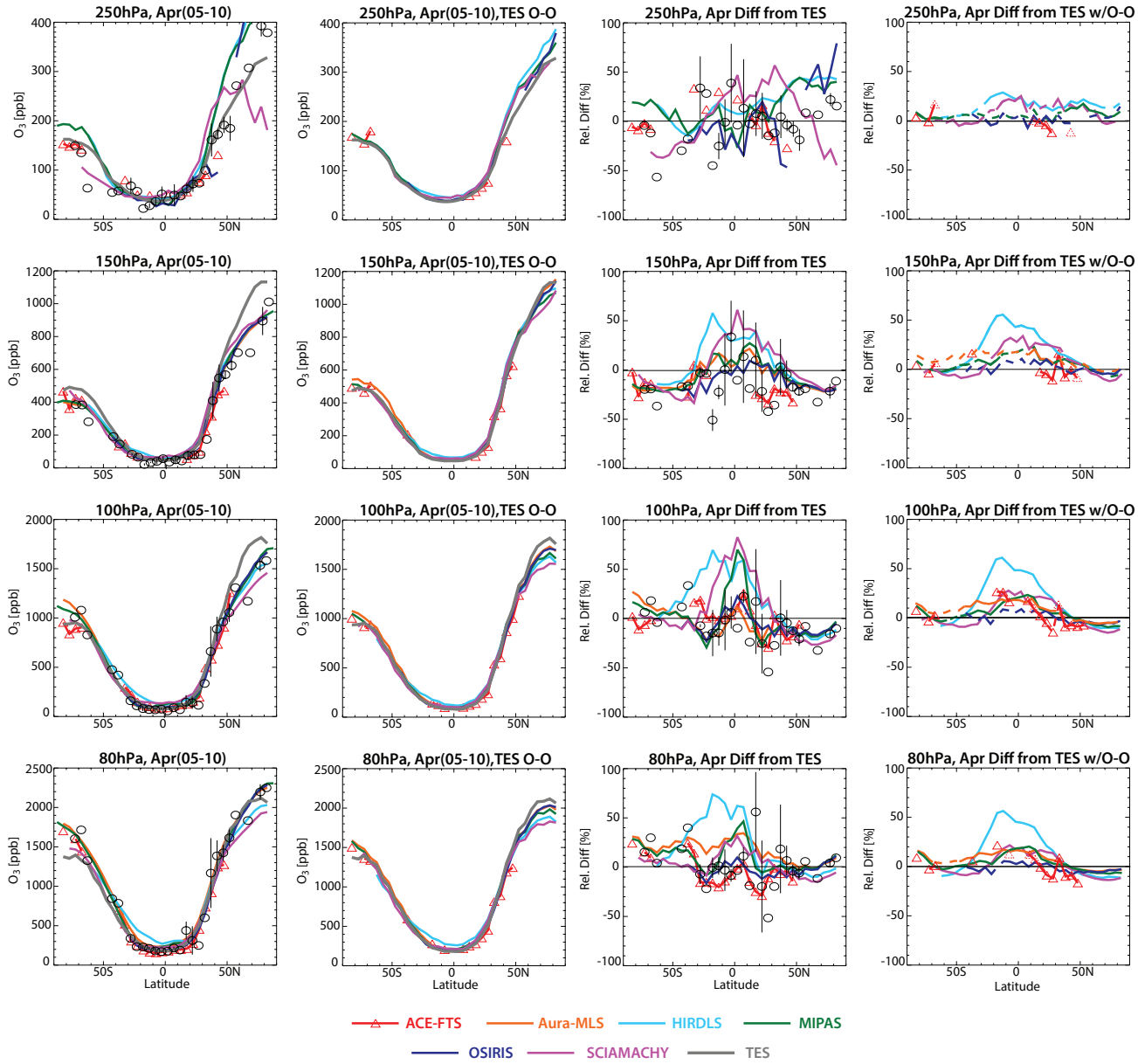

Figure 4.27.5: Meridional profiles of monthly mean zonal mean ozone for April 2005-2010. *First column: Meridional zonal mean ozone profiles from the climatology for each instrument at 250 hPa (top row), 150 hPa (second row), 100 hPa (third row), and 80 hPa (bottom row) for April 2005-2010. Black circles show the ozonesonde climatology; vertical bars represent the standard deviation of climatological mean values for latitude bands with more than one station. Second column: Meridional profiles after application of the TES observational operator to climatologies from each instrument. The TES measurements are the same as in the first column. Third column: Percent difference between each instrument and TES as a function of latitude on each pressure surface. (100*(OC-TES)/TES) Black circles show the ozonesonde climatology; vertical bars are as above. Fourth column: Same as third column, but for virtual retrievals with the TES observational operator applied (100*(VTR -TES)/TES). Dashed lines indicate portions of the virtual retrieval where the difference in the virtual retrieval using the two different fill profiles exceeds 50% of the difference between the virtual retrieval and TES.*

Figures A4.27.3-A4.27.5 in *Appendix A4* show results for January, July, and October. As discussed above, TES is biased low relative to the tropical sonde measurements at 150 hPa in each of these months, while the limb sounders are in good agreement with the sondes. In January, TES is also biased high relative to the sondes in the southern extra-tropics at this same pressure level; the limb sounders again agree well with the sonde measurements. July shows the best overall agreement among the climatologies in the tropics, both for the original climatologies and the virtual TES retrievals. During October the limb sounders are in much better agreement with the sondes in the southern extra-tropics than TES is, and the decrease in ozone for $p > 170$ hPa and increase in ozone for $p < 170$ hPa resulting from application of the TES observational operator at southern high latitudes (see discussion of **Figure A4.27.1** in *Appendix A4*) introduces negative biases and positive biases, respectively, in the VTRs.

Table 4.27.3: Station information for the ozonesonde climatology. *The latitude, longitude, average number of soundings per month and length of data record for each ozonesonde station used in the climatology is given, along with the zonal mean latitude bins (which are the same as those used for the satellite climatologies). The data are from Logan et al. [1999] (denoted by *), and Thompson et al. [2003] (denoted by †). Black rectangles show the stations that are averaged to calculate the seasonal cycle in the tropics (15°S-15°N) and northern and southern mid-latitudes (40°N-45°N and 40°S-45°S) in Figure 4.27.6. We include Asp. Laverton, located at 38°S, in the calculation of the southern mid-latitude seasonal cycle to avoid the use of a single station.*

Station name	Latitude	Longitude	Soundings/ month	Data record	Latitude bin
Forster*	71°S	12°E	28	1985-1991	70-75°S
Syowa*	69°S	39°E	18	1986-1993	65-70°S
Marambio*	64°S	57°W	20	1988-1995	60-65°S
Lauder*	45°S	170°E	24	1986-1990	45-50°S
Asp. Laverton*	38°S	145°E	24	1980-1995	35-40°S
Pretoria*	26°S	28°E	11	1990-1993	25-30°S
Irene†	26°S	28°E	19	1998-2012	25-30°S
La Reunion†	21°S	56°E	31	1998-2012	20-25°S
Suva†	18°S	178°E	22	1998-2011	15-20°S
Tahiti†	18°S	149°W	6	1998-1999	15-20°S
Am. Samoa†	14°S	170°W	37	1998-2012	10-15°S
Am. Samoa*	14°S	170°W	13	1986-1996	10-15°S
Ascension Island†	8°S	14°W	45	1998-2010	5-10°S
Watukosek†	8°S	113°E	24	1998-2012	5-10°S
Natal*	6°S	35°W	23	1978-1992	5-10°S
Natal†	5°S	35°W	39	1998-2011	5-10°S
Brazzaville*	4°S	14°E	7	1990-1992	0-5°S
Malindi†	3°S	40°E	8	1999-2006	0-5°S
Nairobi†	1°S	37°E	46	1998-2012	0-5°S
San Cristobal†	1°S	89.6°W	31	1998-2012	0-5°S
Kuala Lumpur†	3°N	102°E	23	1998-2012	0-5°N
Paramaribo†	6°N	55°W	33	1999-2012	5-10°N
Cotonou†	6°N	2°E	7	2005-2007	5-10°N
Panama*	9°N	80°W	4	1966-1969	5-10°N
Heredia†	10°N	84°W	6	2005-2012	10-15°N
Poona*	19°N	74°E	11	1966-1986	15-20°N
Hilo†	19°N	155°W	50	1998-2012	15-20°N
Hilo*	20°N	155°W	30	1985-1993	20-25°N
Ha Noi†	21°N	106°E	9	2004-2012	20-25°N
Naha*	26°N	128°E	15	1989-1995	25-30°N
Kagoshima*	32°N	131°E	19	1980-1995	30-35°N
Tateno*	36°N	140°E	37	1980-1995	35-40°N
Azores*	38°N	29°W	22	1983-1995	35-40°N
Cagliari*	39°N	9°E	25	1968-1980	35-40°N
Boulder*	40°N	105°W	27	1985-1993	40-45°N
Sapporo*	43°N	141°E	21	1980-1995	40-45°N
Sofia*	43°N	23°E	16	1982-1991	40-45°N
Biscarosse*	44°N	1°W	28	1976-1993	40-45°N
Payerne*	47°N	7°E	95	1980-1993	45-50°N
Hohenpeissenberg*	48°N	11°E	135	1980-1993	45-50°N

Table 4.27.3 continued.

Station name	Latitude	Longitude	Soundings/ month	Data record	Latitude bin
Lindenberg*	52°N	99°E	18	1980-1995	50-55°N
Edmonton*	53°N	114°W	41	1980-1993	50-55°N
Goose Bay*	53°N	60°W	45	1980-1993	50-55°N
Churchill*	59°N	147°W	43	1980-1993	55-60°N
Sodankyla*	67°N	27°E	20	1989-1992	65-70°N
Resolute*	75°N	95°W	45	1980-1993	75-80°N
Ny Alesund*	79°N	12°E	19	1990-1993	75-80°N
Alert*	83°N	62°W	29	1988-1993	80-85°N

4.27.4 UTLS ozone evaluations: Seasonal cycles

Figure 4.27.6 shows the seasonal cycle of ozone in the southern mid-latitudes, tropics, and northern mid-latitudes averaged over 2005-2010 for the original climatologies as well as for the virtual retrievals using the TES observational operator. Dashed lines in the right column of plots for each latitude region again indicate where differences in the VTR due to the choice of fill profile exceed 50% of the difference between the VTR and TES for an instrument. The ozonesonde climatology is included in the left column for each region. The seasonal variability of ozone is largely driven by seasonal changes in the Brewer-Dobson circulation [*Folkins et al.*, 2006; *Randel et al.*, 2007]. In the mid-latitudes, there is an annual cycle in ozone at all pressure levels, with maxima and minima in September and March, respectively, in the Southern Hemisphere and March and August, respectively, in the Northern Hemisphere [*Logan et al.*, 1999]. In the tropics, there is a weak semi-annual cycle driven primarily by mixing below ~150 hPa [*Konopka et al.,* 2010; *Ploeger et al.*, 2012], with maxima in June and September, transitioning to a strong single peak with a maximum in August at 100 hPa and above.

There are large differences among the climatologies in the timing and magnitude of the seasonal cycle in the tropical UT ($p \geq 100$ hPa). The OSIRIS climatology has the largest difference in peak-to-peak amplitude (>100%) relative to TES, while the SCIAMACHY climatology has the largest difference in timing, with a single broad peak from March to September. However, while the TES climatology seasonal cycle shows reasonable agreement with the sonde climatology at these levels (though with a general negative bias), the station-to-station variability in ozone from the sonde measurements is so large that the sonde climatology encompasses all of the satellite climatologies. The differences between the satellite climatologies are reduced in the comparison with the TES observational operator, so that the differences in seasonal cycle amplitude among all of the virtual retrievals are less than 50%, but are still much larger than in any other region. We note that the choice of fill profile significantly impacts most of the virtual retrievals in the tropical upper troposphere, so that, combined with the large variability in the sonde climatology, our conclusions are less robust here than anywhere else. We also note that, as discussed in *Section 4.27.3*, the difference between the TES and ozonesonde climatologies is smaller in April than any other time of the year at 150 hPa and that the TES climatology is negatively biased with respect to the sondes for $p \geq 150$ hPa.

In the tropics between 100 and 70 hPa, there are also large discrepancies between the satellite climatologies, with differences in the magnitude of the seasonal cycle of up to 85% relative to TES for the original climatologies. Here, however, the TES seasonal cycle agrees very well with that from the ozonesondes, and the variability in the ozonesonde climatology is largely diminished. The smoothing by the TES observational operator greatly improves the consistency in the seasonal cycle amplitude (to within 20% except for HIRDLS, which differs in peak-to-peak amplitude from TES by 25-45% at these pressure levels), with the largest impact at 100 hPa. In the original datasets, there are differences of up to 2 months in the timing of the ozone minimum and maximum; with the observational operator the consistency is improved to ±1 month. The changes in timing result from some combination of smoothing the seasonal cycle signal over a deep layer, with differences in phase throughout the layer, and the influence of the seasonal cycles in the TES a priori and averaging kernel.

There is excellent agreement among the satellite climatologies regarding the timing and magnitude of the seasonal cycle in northern mid-latitudes for $p < 200$ hPa; additionally, they all agree well with the ozonesonde climatology. For all instruments except ACE-FTS (which has limited sampling), the seasonal cycle peak-to-peak amplitude is consistent to within 25% for the original climatologies and for all instruments including ACE-FTS it is consistent within <5% using the TES observational operator. At $p \geq 200$ hPa, the MIPAS, SCIAMACHY, and HIRDLS climatologies have a 50-75% larger seasonal cycle than TES, whose climatology agrees well with the sondes. However, the magnitudes of the seasonal cycle in the satellite climatologies are consistent to within 5% when they are compared with the TES observational operator, with only

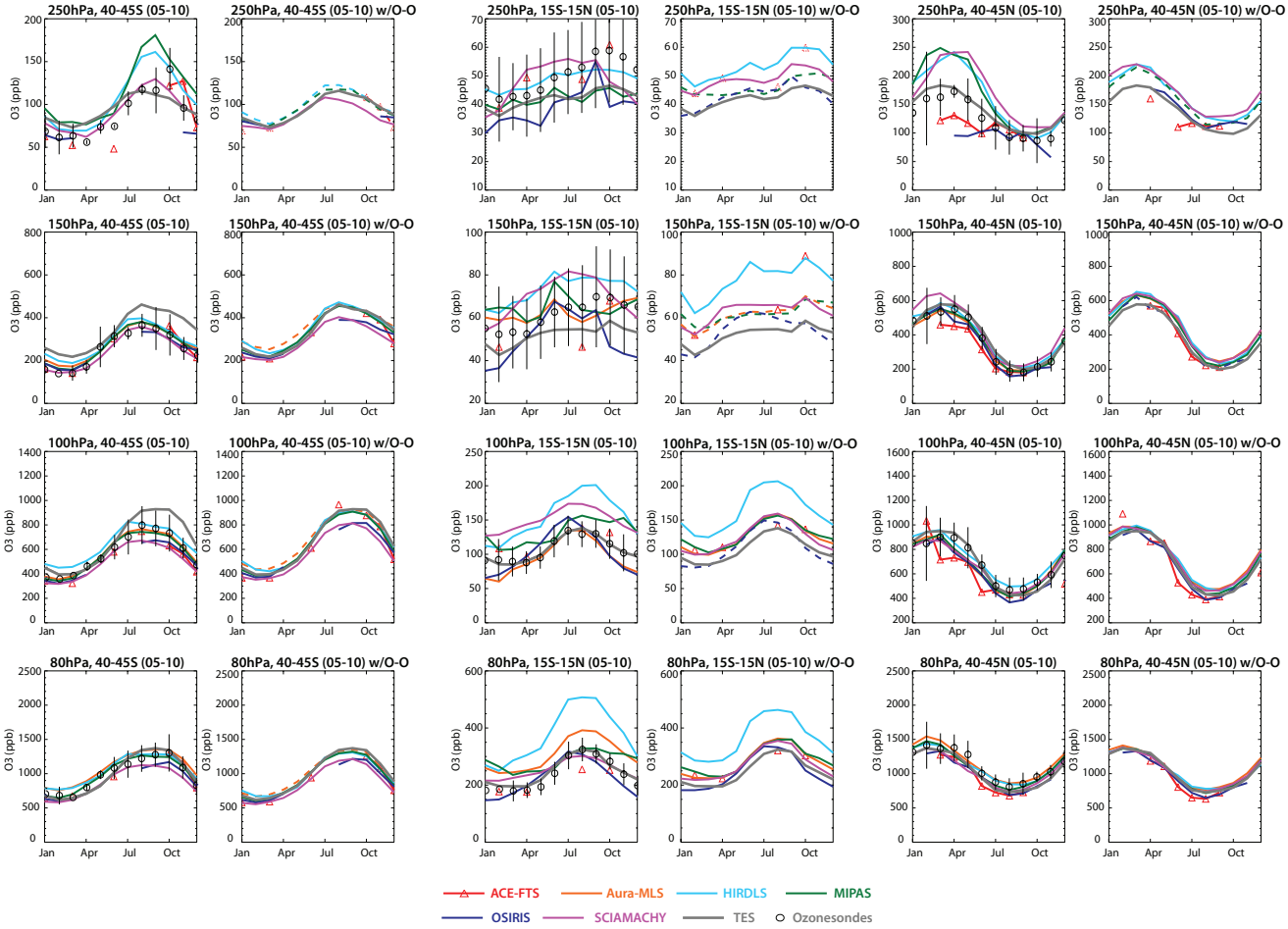

Figure 4.27.6: Seasonal cycle of ozone in the UTLS for 2005-2010. *Seasonal cycle of ozone from 40°S-45°S (two left columns), 15°S-15°N (two centre columns), and 40°N-45°N (two right columns) at 250 hPa (first row), 150 hPa (second row), 100 hPa (third row), and 80 hPa (fourth row). The left column in each grouping shows the seasonal cycle for each climatology, the right column in each grouping shows the seasonal cycle after application of the TES observational operator. The TES measurements are the same in both left and right columns of each group. Dashed lines in the figures in the right column of each group indicate portions of the virtual retrieval where the difference in the virtual retrieval using the two different fill profiles exceeds 50% of the difference between the virtual retrieval and TES in the annual mean. Black circles in the left columns of each grouping show the ozonesonde climatology; vertical bars represent the standard deviation of the climatological ozonesonde measurements from the stations in each latitude band.*

the MIPAS virtual retrievals being strongly dependent on the fill profile. In the southern mid-latitudes, the amplitude and timing of the TES seasonal cycle agree well with the ozonesonde climatology (though with a positive bias throughout the year at 150 hPa) at all levels except 100 hPa, where the ozone maximum in the TES climatology is almost 150 ppb larger than that seen in the ozonesondes and HIRDLS, MIPAS, and Aura-MLS climatologies. At $p \leq 100$ hPa, SCIAMACHY and OSIRIS have a 15% smaller seasonal cycle than those of the other instruments and sondes; the flatness results from an underestimate of the ozone maximum relative to the other climatologies and may be due to their limited sampling during winter. When the TES observational operator is applied to the climatologies, they agree to within 5% except for SCIAMACHY and OSIRIS. The vertical smoothing of the TES operator in fact spreads the low winter values in these climatologies to all of the pressure levels. We note that the increases in ozone at 150 and 100 hPa in the HIRDLS, MIPAS, and Aura-MLS virtual retrievals relative to the original climatologies represent another example of the TES operator introducing possible biases in the virtual retrievals.

Figure A4.27.6 in *Appendix A4* shows the seasonal cycles for high latitudes. In the northern high latitudes, results are generally similar to those for mid-latitudes; there is relatively good agreement between the climatologies for $p < 200$ hPa, particularly for the VTRs. However, TES is biased high relative to the limb sounders and to the sondes during the first half of the year for $p \leq 150$ hPa, and the observational operator transfers this bias to the limb sounder VTRs. In the southern high latitudes, the seasonal cycles at 250 hPa and $p \leq 150$ hPa are very different, with maximum values in January/February at 250 hPa and in July/August for $p \leq 150$ hPa. TES does a very poor job of reproducing the seasonal cycle from the sondes and the other instruments at 150 hPa. At $p \leq 100$ hPa, all of the instruments except ACE-FTS agree very well. ACE-FTS is much lower than the other instruments for August and September, but is in very good agreement with the sonde

climatology for these months. However, given the fact that only one sonde station is included here and that ACE-FTS samples this region less frequently than many of the other instruments, it is difficult to say anything conclusive about sampling differences versus biases in this case.

4.27.5 UTLS ozone evaluations: Interannual variability

Figure 4.27.7 shows the deviations from the 2005-2010 climatological monthly mean ozone for each instrument in the southern mid-latitudes, tropics, and northern mid-latitudes using the original climatologies as well as the virtual retrievals with the TES observational operator. As for the seasonal cycle, the differences between the climatologies are largest in the tropics and the TES observational operator damps out much of the smaller scale variability particularly for $p \geq 100$ hPa, and greatly improves the consistency in this region. Overall, the interannual variability in ozone is relatively low in the tropics, as expected, and the only signal that is observed by all of the instruments is a pronounced minimum in early 2010 throughout the UTLS region. This minimum can be seen in the original climatologies and is not an artefact of the TES observational operator. The low ozone values result from changes in convection and an increase in the Brewer-Dobson circulation associated with the 2009-2010 El Niño and coincident strong Easterly shear phase of the stratospheric quasi-biennial oscillation (QBO) [*Neu et al.*, 2014b]. While a tropical QBO signal is not particularly apparent for other years due to the noise in individual climatologies and the spread between them at these levels, we note that the timing of the minima and maxima in the HIRDLS climatology at $p \leq 100$ hPa is consistent with the QBO phase for 2005-2008 and that because the HIRDLS measurements are averaged over a shorter time period than the other instruments, the QBO signal is amplified in the HIRDLS record. However, it is not clear whether this fully explains the very large differences between HIRDLS and the other instruments for $p \leq 100$ hPa, or whether there might be an additional signal from QBO-related variability of the aerosol that affects the HIRDLS ozone retrievals. Regardless of the explanation, the TES observational operator spreads the information from $p \leq 100$ hPa downward so that it increases the apparent differences between HIRDLS and the other instruments for $p > 100$ hPa in the virtual retrievals. ACE-FTS also shows large differences in interannual variability from the other instruments at $p \leq 100$ hPa, likely due to its sparse sampling of the tropics. The interannual variability in OSIRIS ozone is somewhat noisier than that of the other instruments, even with the TES observational operator, but it is generally consistent with the other climatologies for $p < 100$ hPa, where the fill profile has little influence on the virtual retrieval.

The interannual variability is more consistent between the various climatologies in the northern and southern mid-latitudes than in the tropics, both in the original datasets and in the vertically smoothed virtual retrievals. As was the case for the seasonal cycle, the HIRDLS climatology and virtual retrievals agree very well with those from the other instruments in mid-latitudes, despite their large differences from the other instruments in the tropics. The largest discrepancies in mid-latitude interannual variability can be seen in the climatologies from ACE-FTS and OSIRIS in the Southern Hemisphere. In the case of ACE-FTS, the sampling is likely to blame, though we note that there may be a contribution from the fact that the lowest retrieval level (and thus the influence of the fill profile) varies throughout the year and between years more for ACE-FTS than for any other instrument. OSIRIS does not continuously sample the 40°S-45°S latitude band, so that the climatological monthly mean and deviations from the mean are not well-defined in Southern Hemisphere winter. The TES observational operator reduces the ozone variability somewhat in mid-latitudes, but the major deviations in northern mid-latitude ozone in 2008 and 2010 are well-preserved, except during the Jan-April 2010 TES data gap. The northern mid-latitude ozone minimum in 2008 and maximum in 2010 result from changes in the Brewer-Dobson circulation associated with La Niña / Westerly shear QBO and El Niño / Easterly shear QBO, respectively [*Neu et al.*, 2014b]. In the southern mid-latitudes, the climatologies all show maxima in 2005 and 2007 and minima in 2006 at $p \leq 100$ hPa. The TES observational operator reduces the maxima in the virtual retrievals due to the vertical smearing. TES stopped sampling south of 30°S in January 2010.

Figure A4.27.7 in *Appendix A4* shows the interannual variability at high latitudes. northern high latitudes have similar interannual variability as that seen in mid-latitudes, with the exception of noticeably low ozone values during 2005. Southern Hemisphere high latitude ozone variability is considerably larger than that in mid-latitudes, with pronounced minima in late 2006 and 2008 and maxima in late 2007 and 2010. While the TES southern high latitude record is quite short, the main features of the limb sounder climatologies are preserved in the virtual retrievals.

4.27.6 Summary and conclusions: UTLS ozone

While the use of zonal mean climatologies for detailed UTLS process studies is obviously limited, the SPARC Data Initiative climatologies nevertheless represent our best knowledge of the abundance and temporal variability of ozone in the UTLS and the characterisation of the datasets presented here will provide valuable information for model evaluation. Overall findings are presented in the following summary, and **Figure 4.27.8** is a synopsis plot showing the median, median absolute deviation, and standard deviation of monthly mean relative differences between measurements from the limb viewing instruments and TES in the tropics and mid-latitudes, both for the original climatologies and the virtual TES retrievals. **Figure 4.27.8** clearly shows the reduction in the difference between the limb sounders and TES as well as the reduction in variance when using the TES observational operator. It also highlights the better agreement among the instruments in mid-latitudes relative to the tropics.

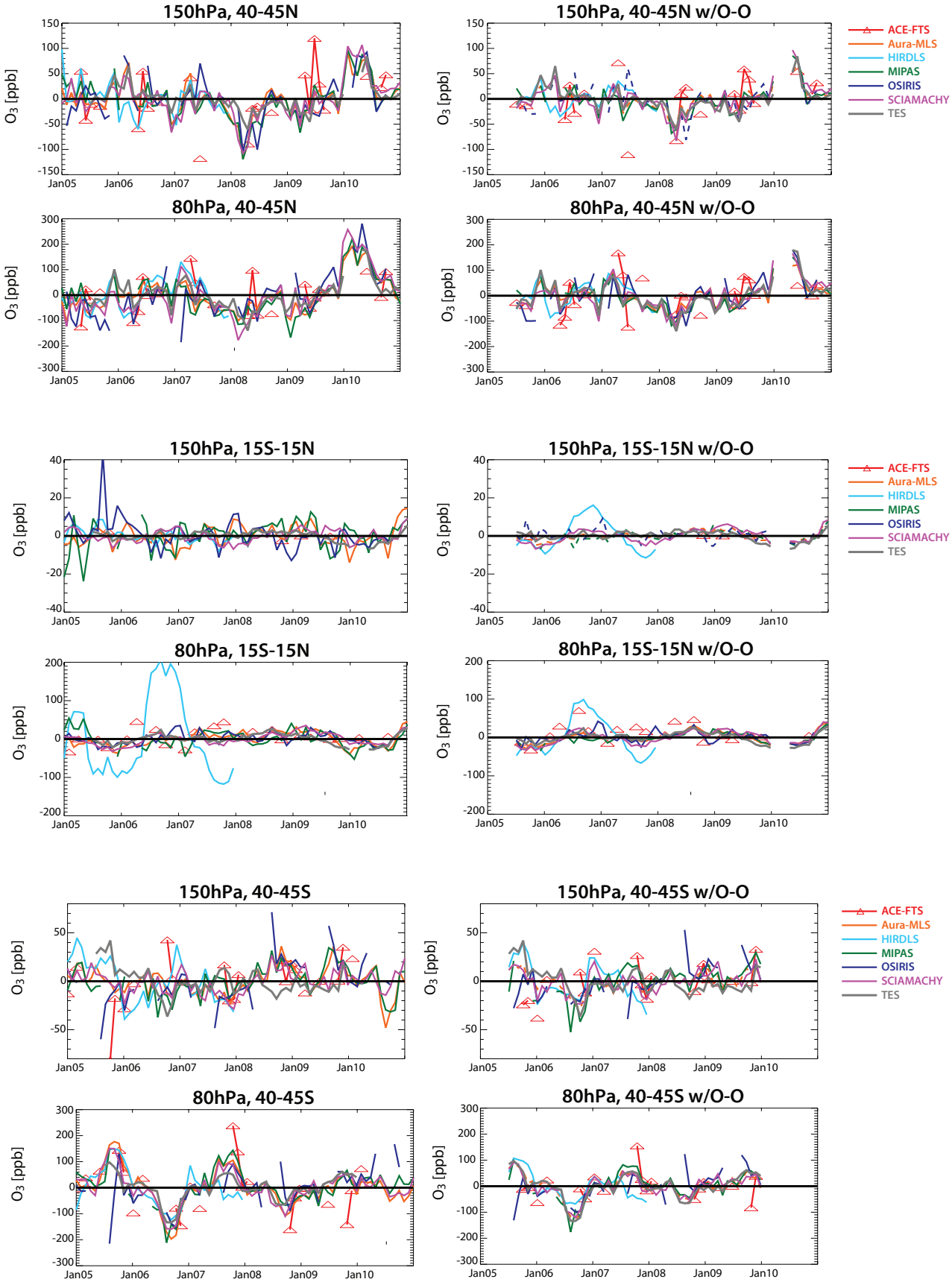

Figure 4.27.7: Interannual variability of ozone in the UTLS for 2005-2010. *Deseasonalised ozone anomalies at 150 hPa and 80 hPa for 40°N-45°N (top 4 panels), 15°S-15°N (middle 4 panels), and 40°S-45°S (bottom 4 panels). The left column shows the original climatologies, the right column shows the climatologies after application of the TES observational operator. Dashed lines in the figures in the right column indicate portions of the virtual retrieval where the difference in the virtual retrieval using the two different fill profiles exceeds 50% of the difference between the virtual retrieval and TES in the annual mean.*

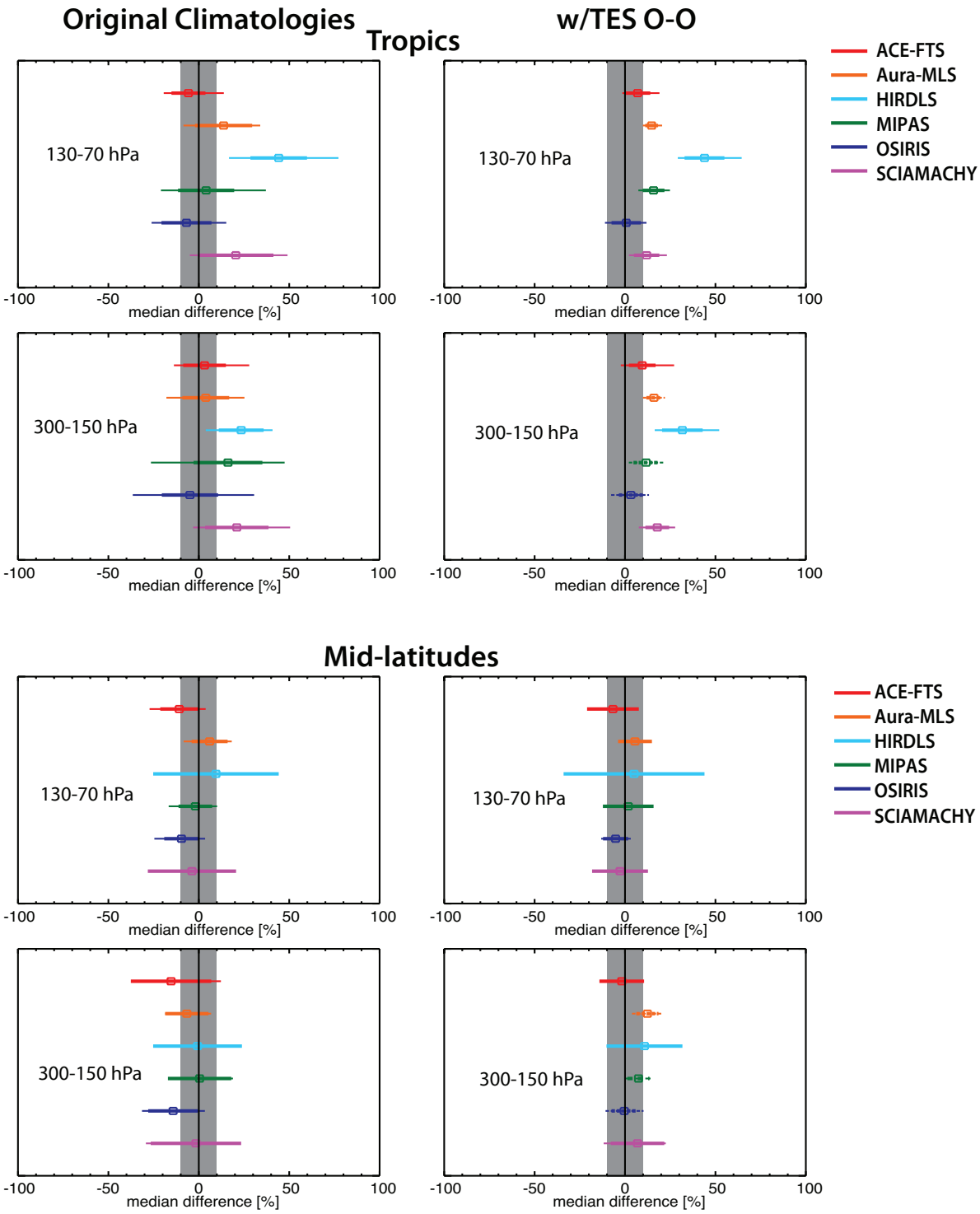

Figure 4.27.8: Summary plot of UTLS ozone. *Summary plot showing the median (square), median absolute deviation (thick line), and standard deviation (thin line) of monthly mean relative differences from TES. Here, the tropics are defined as 20°S-20°N, and mid-latitudes include 30°S-50°S and 30°N-50°N. Shaded grey regions show 10% difference from TES for reference. Left column shows results for the original climatologies, while the right column shows the results for the virtual TES retrievals.*

Key findings: nadir- and limb-viewing instruments comparisons

- Using the TES observational operator to vertically smooth the climatologies from the higher resolution limb-viewing instruments provides a common basis for comparison of the large-scale ozone morphology as well as the seasonal and interannual variability of ozone within the UTLS.
- However, this approach has several limitations, including:
  1) that the virtual retrievals can be sensitive to how one chooses to "fill in" the profiles below the lowest measurement level of the limb sounders,
  2) that the TES sensitivity varies in the UTLS such that the *a priori* profile has a significant influence near 150 hPa in the extra-tropics,

3) that the averaging kernels are not fully independent of the ozone abundance, resulting in errors in the virtual retrievals that are difficult to quantify.

We have tried to account for these factors when possible, and to focus on robust differences in the UTLS climatologies.

- The TES observational operator smoothes small-scale ozone structures and due to the influence of the *a priori* tends to increase tropical-extra-tropical ozone gradients as well as mid-latitude vertical ozone gradients in the climatologies from the limb-viewing instruments.
- The TES observational operator also reduces and vertically smoothes the differences between the limb climatologies and TES.
- The TES observational operator reduces the temporal variability of the ozone climatologies from the high-resolution instruments but also greatly improves the consistency between them. This indicates that the differences in vertical resolution among the limb-viewing instruments make a substantial contribution to differences in their retrieved ozone distributions both relative to TES and relative to one other.

Atmospheric mean state and variability

- Most of the limb-viewing instruments have climatological-mean positive differences (ranging from 5-75%) relative to TES ozone in the tropics, though for several instruments the differences depend strongly on the fill profile below ~100 hPa.
- For $p \leq 100$ hPa, the positive difference from TES likely reflect true positive biases for the climatologies given TES's lack of bias with respect to the ozonesonde climatology.
- In the Northern Hemisphere extra-tropics, only the HIRDLS and MIPAS climatologies have differences with respect to TES that are >15% and are also independent of the fill profile.
- In the southern extra-tropics, the TES observational operator greatly reduces differences between the limb-sounder climatologies and TES due to TES's low sensitivity at the pressure levels where the differences between the original climatologies and TES are largest.
- There are large differences in the timing and magnitude of the seasonal cycle in the tropical upper troposphere.
- At $p \leq 100$ hPa, the climatologies show a more consistent tropical seasonal cycle, particularly when smoothed to the TES vertical resolution. The TES observational operator reduces the differences in seasonal cycle amplitude to within 20% of TES for all instruments except HIRDLS.
- In general, there is very good agreement among the climatologies regarding both the timing and magnitude of the seasonal cycle in mid- and high latitudes, except that ozone from the OSIRIS and SCIAMACHY climatologies is ~15% low relative to the other instruments during the southern mid-latitude maximum, likely due to their limited sampling of this region. In southern high latitudes, all of the instruments except ACE-FTS overestimate the October ozone minimum relative to the ozonesonde climatology, but a definitive assessment of biases is precluded by sampling differences.
- All of the climatologies show low interannual variability in the tropics (except for HIRDLS) and higher variability in mid- and high latitudes.
- Northern mid-latitude interannual variability greatly exceeds that in southern mid-latitudes for $p > 80$ hPa, but variability in southern high latitudes is larger than that in northern high latitudes. The sampling of the ACE-FTS instrument is insufficient to capture interannual variability on monthly time scales in the tropics.
- The TES observational operator greatly reduces the interannual variability in ozone from the limb-sounder climatologies for $p > 100$ hPa in the tropics and $p > 200$ hPa in mid-latitudes. This improves the consistency between the datasets but may limit the usefulness of the virtual retrievals for quantifying UTLS variability.

Instrument-specific conclusions

- While the ACE-FTS climatology agrees well with the climatologies from TES and the other limb-viewing instruments for the annual mean ozone distribution, the instrument's sampling pattern impacts its ability to fully capture seasonal and interannual variability, particularly in the tropics.
- The HIRDLS climatology shows large positive differences from TES and the other limb sounders in the tropics, as well as a smaller positive difference in the NH extra-tropics for $p \geq 150$ hPa. The seasonal cycle amplitude is larger and the interannual variability is quite different in the tropics when compared to the other climatologies. However, both the seasonal and interannual variability are in very good agreement with the other climatologies in mid-latitudes. The large tropical ozone values are likely due to uncorrected emission from aerosol, and the differences in temporal variability relative to the other climatologies suggest that this aerosol effect may vary with time.
- The MIPAS climatology has a different morphology than is seen in the climatologies from the other instruments in the tropics between 200 and 100 hPa and much lower ozone values than any other climatology in the tropical upper troposphere. It is positively biased with respect to TES for $p < 100$ hPa in the tropics and for $p \geq 150$ hPa in the northern extra-tropics but agrees relatively well elsewhere.
- The MLS climatology has unrealistically "flat" contours in the tropics near 100 hPa, but otherwise agrees quite well with the climatologies from TES and the other limb sounders.
- The OSIRIS climatology shows the best overall agreement with TES. The limited sampling in polar winter results in unrealistic horizontal ozone gradients in the

northern high latitude lowermost stratosphere and in the southern mid-latitudes results in a slightly underestimated seasonal cycle and problems capturing the interannual variability of UTLS ozone in some months.

- The SCIAMACHY climatology is positively biased with respect to TES in the tropics. As for OSIRIS, the limited sampling during polar night leads to a smaller amplitude southern mid-latitude seasonal cycle than is seen in the other climatologies.

4.27.7 Recommendations: UTLS ozone

- A much more detailed UTLS inter-comparison using high spatial and temporal resolution measurements of multiple species is needed to fully characterise differences between instruments in this region, and has been proposed as a follow-on to the SPARC Data Initiative.
- Such an inter-comparison will require diagnostic tools that minimise geophysical variability and differences in sampling and resolution such as tracer-tracer correlations, probability distribution functions, tropopause-relative vertical coordinates, and jet-based coordinates [*e.g.*, *Hegglin et al.*, 2008; *SPARC*, 2010; *Manney et al.*, 2011].
- The proposed follow-on analysis promises to not only provide a detailed assessment of the quality of the satellite data, but also to improve our understanding of UTLS structure and processes.

Chapter 5: Implications of results

5.1 Implications for model-measurement intercomparison

Satellite trace gas datasets are crucial for the evaluation of transport and chemistry in numerical models. Datasets available from different satellite instruments vary in terms of measurement method, geographical coverage, spatial and temporal sampling and resolution, time period, and retrieval algorithm and thus have different strengths and shortcomings. Comparing numerical model output to different chemical datasets can lead to conflicting results depending on the particular application. Issues arising from the use of different observational datasets for model evaluations have been identified in the CCMVal report [*SPARC*, 2010]. It became clear that the characteristics of the satellite datasets, including quality, resolution, and representativeness, need to be known prior to their use and prior to the interpretation of model evaluation results. The CCMVal report's recommendations that "*A systematic comparison of existing observations is required in order to underpin future model evaluation efforts, by providing more accurate assessments of measurement uncertainty*" directly motivated the work for the SPARC Data Initiative presented in this report. While *Chapter 4* provides basic information on quality and consistency of the various data products, the following *Chapter 5* focuses on summarizing some implications of the results for model-measurement inter-comparisons. Examples of how knowledge of uncertainty and inter-instrument differences can be used to improve comparisons are given and particular diagnostics appropriate for model evaluations are recommended.

For the CCMVal report, the observational mean values and uncertainty range served as input for the performance metrics. Such metrics are used to quantify the ability of models to reproduce key stratospheric processes. One widely applied metric:

$$g = 1 - \frac{1}{n_g} \frac{|\mu_{mod} - \mu_{obs}|}{\sigma_{obs}} \qquad (5.1)$$

uses a scaling factor n_g as well as the observational uncertainty σ_{obs} and climatological mean μ_{obs} for the evaluation of the model climatological mean μ_{mod} [*Douglass et al.*, 1999; *Waugh and Eyring*, 2008; *SPARC*, 2010]. In the past, the observational uncertainty has most often been derived using the interannual variability of a single instrument only.

Our approach is to provide an alternative, more comprehensive uncertainty range derived from all available datasets, instead of recommending one particular satellite dataset for the model-measurement comparison. The selection of the data points suitable for the construction of the new climatological mean values and uncertainty range is based on their agreement with the mean state of the atmosphere as given by all instruments and on the specific satellite characteristics such as sampling patterns. The following general guidelines are applied for the selection process.

- The agreement of each individual dataset with the mean state of the atmosphere is determined based on the 1σ standard deviation over all instruments. For trace gases observed by more than five instruments, individual data points will be removed if they are outside of the $\pm 1\sigma$ standard deviation range. For trace gases observed by five or less instruments, the data points will be removed if they are outside of the $\pm 2\sigma$ standard deviation.
- Further specific criteria used to calculate the mean state and uncertainty range are chosen based on the instrument/retrieval performance identified in the different chapters of this report, and will change depending on the diagnostic and the trace gas. Detailed information on the evaluations is provided in the following paragraphs, structured according to evaluation diagnostic.
- For each diagnostic and even within one diagnostic, the datasets selected for the construction of the uncertainty range can be different depending on latitude, altitude, or time period considered. One example of this approach can be given for the evaluation of the ozone seasonal cycle: if one instrument presents a clear outlier for *e.g.*, March, then only the March value of this instrument is removed while the values for all other months stay included in the uncertainty range.
- The climatological mean μ_{obs} is defined as the multi-annual, multi-instrument mean value of all data points selected as suitable for the construction of the uncertainty range. Note that the climatological mean is different from the MIM used in the previous chapters which was based on all available datasets.
- The uncertainty range σ_{obs} is defined as the spread over all selected datasets and years. In general, the interannual spread needs to be accounted for when producing the uncertainty range, so that the free-running models can be compared against the observational mean state. Note however, that for model simulations nudged to meteorological reanalysis, the comparisons focus on the same years and the uncertainty range can be solely based on the spread over all selected datasets and not include interannual variations.

In summary, we derive an observational mean state and uncertainty range from multiple datasets from the SPARC Data Initiative for selected examples of evaluation diagnostics. For all evaluations listed in the following *Section 5.1*, the uncertainty range and climatological mean will be made publicly available through the SPARC Data Center.

5.1.1 Seasonal cycles

The seasonal cycle of long-lived atmospheric trace gases such as water vapor and ozone is often used as a diagnostic of transport processes in the stratosphere and in particular in the UTLS.

Ozone – O_3

The ozone seasonal cycle in the UTLS in mid-latitudes is determined by the seasonality of two processes: air mass transport with the Brewer-Dobson circulation and mixing with tropical air masses. In order to evaluate the model's representation of these large-scale transport and mixing processes, a comparison of the ozone seasonal cycle for the latitude bands 40°S/N-60°S/N at 100 and 200 hPa has been used [*SPARC*, 2010; *Hegglin et al.*, 2010]. While the calculation of the quantitative performance metric in the CCMVal report was based on MIPAS data alone, we will provide a new climatological mean state and uncertainty range derived from multiple datasets. The method (illustrated in **Figure 5.1.1**) is explained below for 40°N-60°N, 200 hPa.

Step 1: The ozone seasonal cycles for satellite datasets are derived from 2005-2010 multi-annual mean values. The time period has been chosen based on a maximum number of active satellite limb instruments. The uncertainty range (grey shading in **Figure 5.1.1**) is calculated as the $\pm 1\sigma$ standard deviation over all instruments' multi-annual mean values.

Step 2: All data points outside of the $\pm 1\sigma$ standard deviation from step 1 are removed. Additionally, data points from instruments with a very large interannual spread need to be excluded. Therefore, all multi-annual mean values with an interannual variability (vertical bars in the uppermost left panel of **Figure 5.1.1**) larger than the $\pm 2\sigma$ standard deviations from step 1 are removed. The new mean values and uncertainty range are calculated.

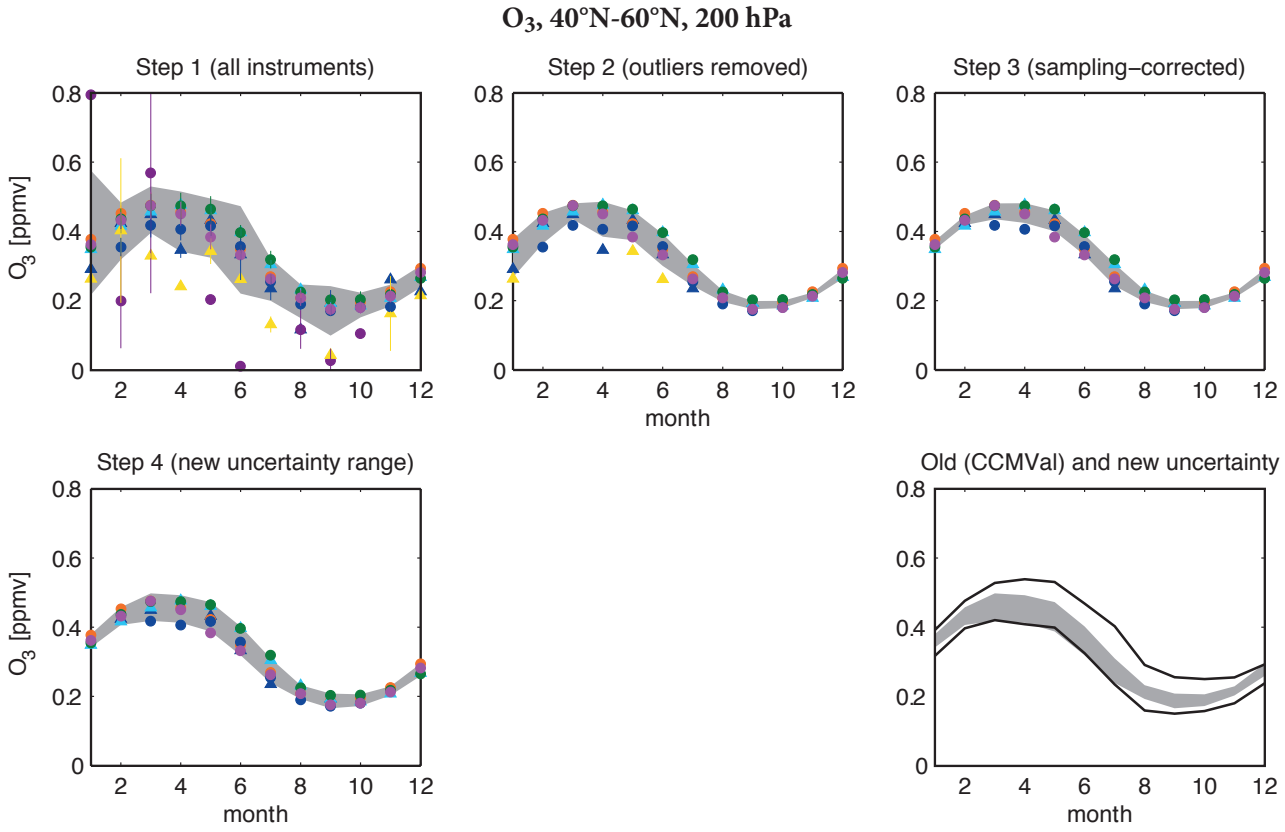

Figure 5.1.1: Ozone seasonal cycle diagnostic for 40°N-60°N at 200 hPa. *The individual steps of deriving the ozone seasonal cycle diagnostic are shown. The uncertainty range (grey shading) is given for each month by the standard deviation over all multi-annual means of the selected datasets. In the uppermost left panel the vertical bars indicate the interannual spread of each instrument calculated as the standard deviations over all years. For the selection of the datasets, outliers and data points strongly impacted by sampling are removed as illustrated in steps 1 to 3 and explained in detail in the text. In step 4 the uncertainty due to interannual variations is added to the uncertainty range. In the lower rightmost panel the old uncertainty range given in the CCMVal report and the new uncertainty range are compared.*

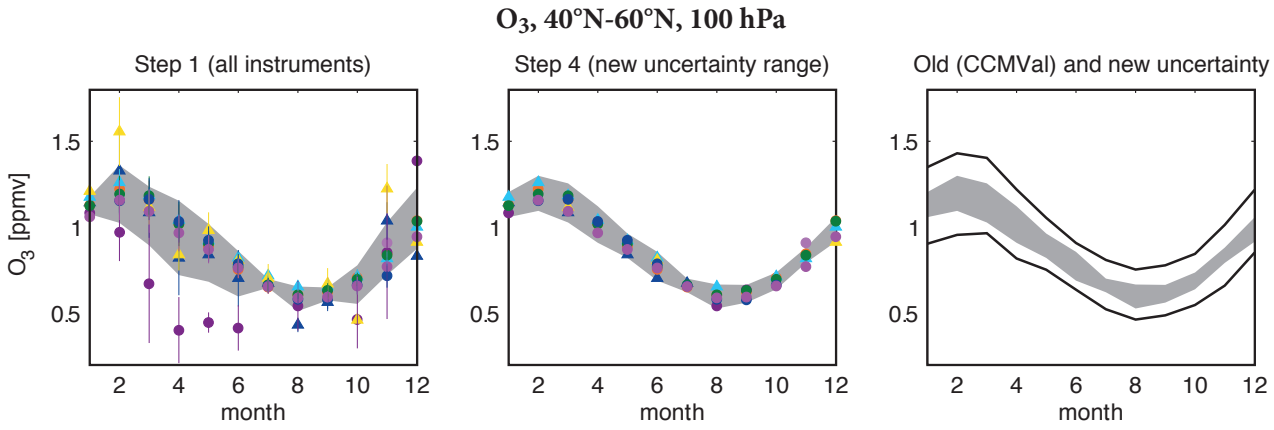

Figure 5.1.2: Ozone seasonal cycle diagnostic for 40°N-60°N at 100 hPa. *Steps 1 and 4 of deriving the ozone seasonal cycle diagnostic are shown. The uncertainty range (grey shading) is given for each month by the standard deviation over all selected datasets. In the rightmost panels the old uncertainty range given in the CCMVal report and the new uncertainty range are compared.*

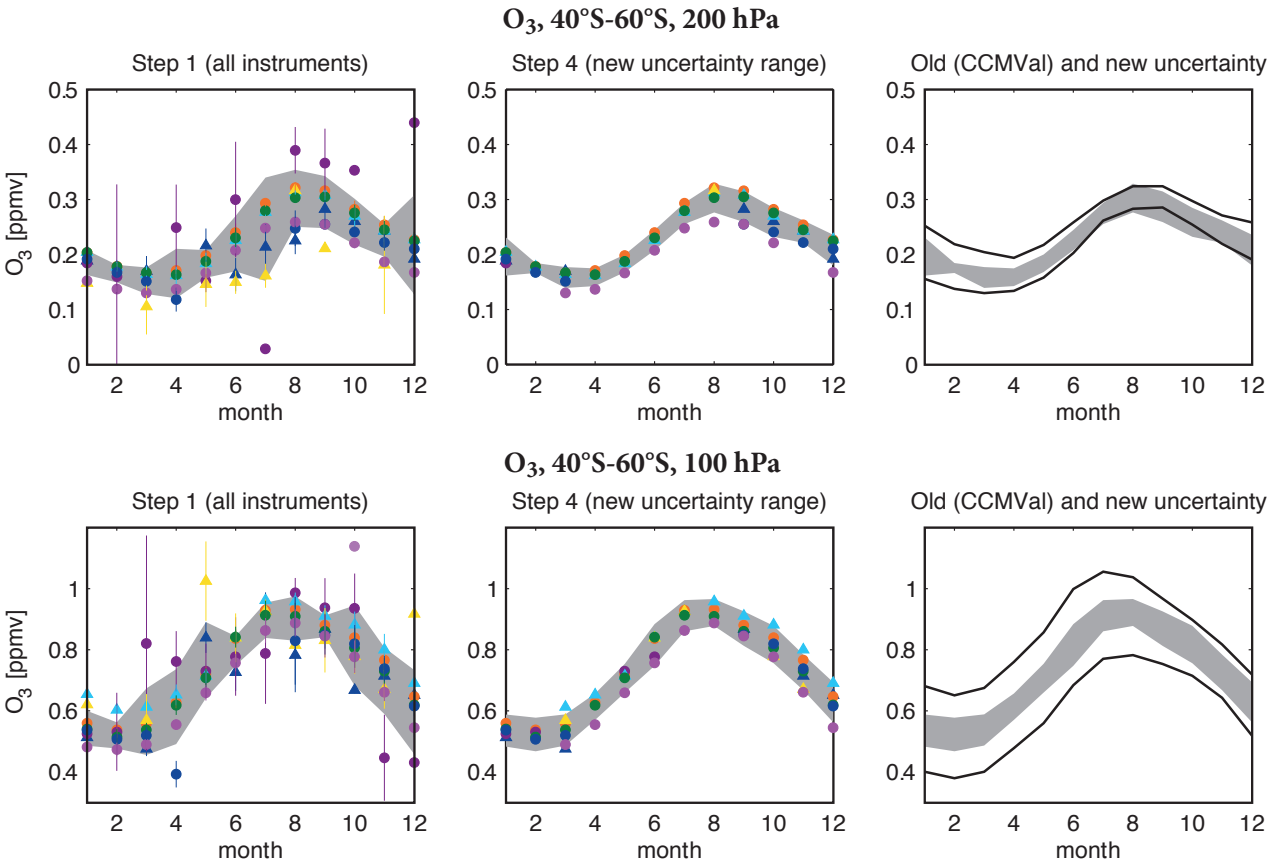

Figure 5.1.3: Ozone seasonal cycle diagnostic for 40°S-60°S at 200 and 100 hPa. *Same as Figure 5.1.2 but for 200 and 100 hPa at 40°S-60°S.*

Step 3: All data points impacted by a sampling bias estimated to be larger than 10% are removed. Such sampling bias can arise when averaging binned atmospheric measurements due to non-uniform sampling in time or space. These sampling biases have been identified by applying the sampling patterns of the satellite instruments to O_3 fields from coupled chemistry climate models (see *Chapter 3*; *Toohey et al.* [2013]). In the tropics, comparisons to ozonesondes are used to remove data points that show large deviations. The new mean values and uncertainty range are calculated.

Step 4: The uncertainty range is recalculated as the $\pm 1\sigma$ standard deviation over all remaining instruments and years, now taking not only the inter-instrument but also the inter-annual spread into account. Including the latter in this final step increases the uncertainty range for most cases, but is nevertheless important in order to produce an uncertainty that free-running models can be compared against.

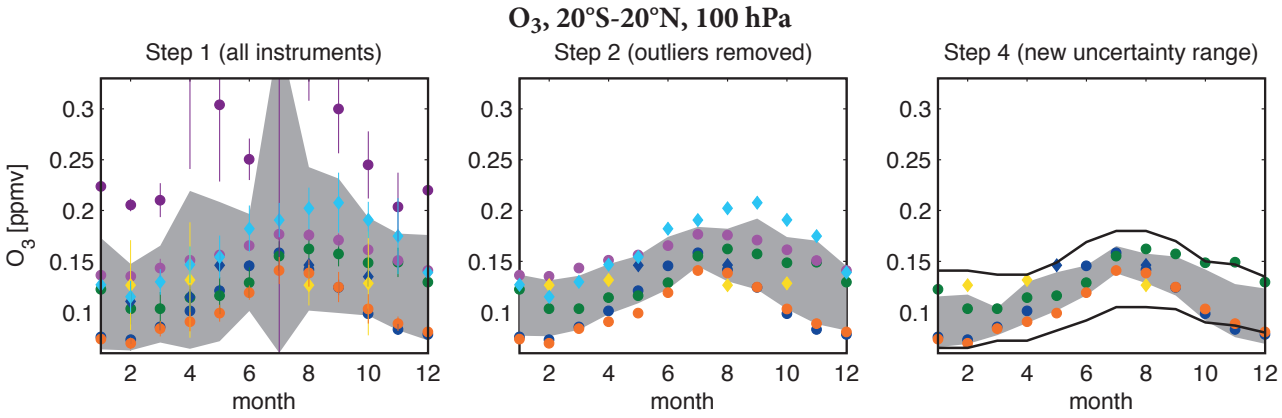

Figure 5.1.4: Ozone seasonal cycle diagnostic for 20°S-20°N at 100 hPa. *Steps 1, 2 and 4 of deriving the ozone seasonal cycle diagnostic are shown. The uncertainty range (grey shading) is given for each month by the standard deviation over all selected data points.*

To summarise, the final ozone seasonal cycle for the 2005-2010 period is calculated from the instruments' multi-annual mean values remaining after the removal of outliers and data points impacted by sampling bias (steps 1-3). The uncertainty range is calculated accordingly as the ±1σ standard deviation over all those instruments and over all years. The new uncertainty range is generally smaller than the old uncertainty range used in the CCMVal report (lower right panel in **Figure 5.1.1**). For some months, the uncertainty has been reduced by more than 50%. This reduced uncertainty range applied to the quantitative performance metric (**Eq. 5.1**) will provide a powerful constraint on the model results and thus the model representations of the ozone seasonal cycle can be differentiated more clearly than before. Additionally, the climatological mean is now shifted to lower values. The new lower mean values agree better with the CCMVal models whose multi-model mean values were found to be too low compared to the old climatological mean values (see Figure 7.22 in the *CCMVal report*; also Figure 11 in *Hegglin et al.* [2010]). The improved agreement suggests that most of the CCMVal models perform better than previously thought with regard to the ozone seasonal cycle in the UTLS.

For the presentation of the improved seasonal cycle diagnostic for other regions and trace gases, only step 1 and 4 and for some regions also step 2 as well as the comparison with the old CCMVal uncertainty range will be displayed. Figures containing each step of the derivation of the new uncertainty range are provided in *Appendix A5*. At 100 hPa in the Northern Hemisphere (NH) mid-latitudes (40°N-60°N), the ozone seasonal cycle is derived from the 2005-2010 multi-annual mean of 9 satellite instruments (**Figure 5.1.2**). Reducing the satellite datasets according to their agreement with the multi-instrument mean value and their sampling biases results in a much reduced uncertainty range in particular during NH winter and spring. For these months, most of the new uncertainty is caused by inter-annual variations and not by inter-instrument variations as becomes clear from the multi-annual mean values clustering in the center of the new uncertainty range. Similar to our results for 200 hPa, the new uncertainty range is much reduced when compared to the one used in the CCMVal report, and hence will be much better suited to identify badly performing models. For the NH summer and autumn, the reduction is about 2/3 of the old range. The climatological mean value, however, did not change systematically.

The evaluation of the Southern Hemisphere (SH) mid-latitude ozone seasonal cycle (**Figure 5.1.3**) follows the same steps as described above for the NH based on 2005-2010 multi-annual mean datasets from 9 satellite instruments. At 200 hPa, the new uncertainty range is very similar to the old one based on MIPAS observations only. Except for January, this uncertainty results mostly from the inter-instrument spread (and not from the inter-annual spread) with one instrument having particularly lower values than all other datasets. Despite this instrument seeming to be an outlier for some months, it agrees very well with SAGE II and HALOE ozone for the overlap time period 2003 (not included here) confirming this as the lower end of our uncertainty range. At 100 hPa, the new uncertainty range is reduced over the whole year compared to the old one based on MIPAS observations, with strongest improvement for SH summer, autumn and winter. The climatological mean values increase slightly for August-October, but do not change systematically for the rest of the year.

Tropical ozone exhibits a large annual cycle near and above the tropopause which is related to seasonal changes in vertical transport acting on the strong vertical ozone gradient in this region [*Randel et al.*, 2007] and in quasi-horizontal mixing [*Ploeger et al.*, 2012]. Although the annual cycle extends over only a narrow vertical range from approximately 100 to 50 hPa, it is an important characteristic of tropical ozone in the LS and has been used to analyse transport and mixing processes. The SPARC CCMVal evaluation of the seasonal cycle in tropical ozone is based on a comparison to the observational NIWA dataset [*Hassler et al.*, 2008] at 100 hPa for 20°S-20°N. A new uncertainty range based on the SPARC Data Initiative datasets is presented in **Figure 5.1.4.** After the removal of the outliers the uncertainty range (middle panel of **Figure 5.1.4**) is still relatively large and comparable to the

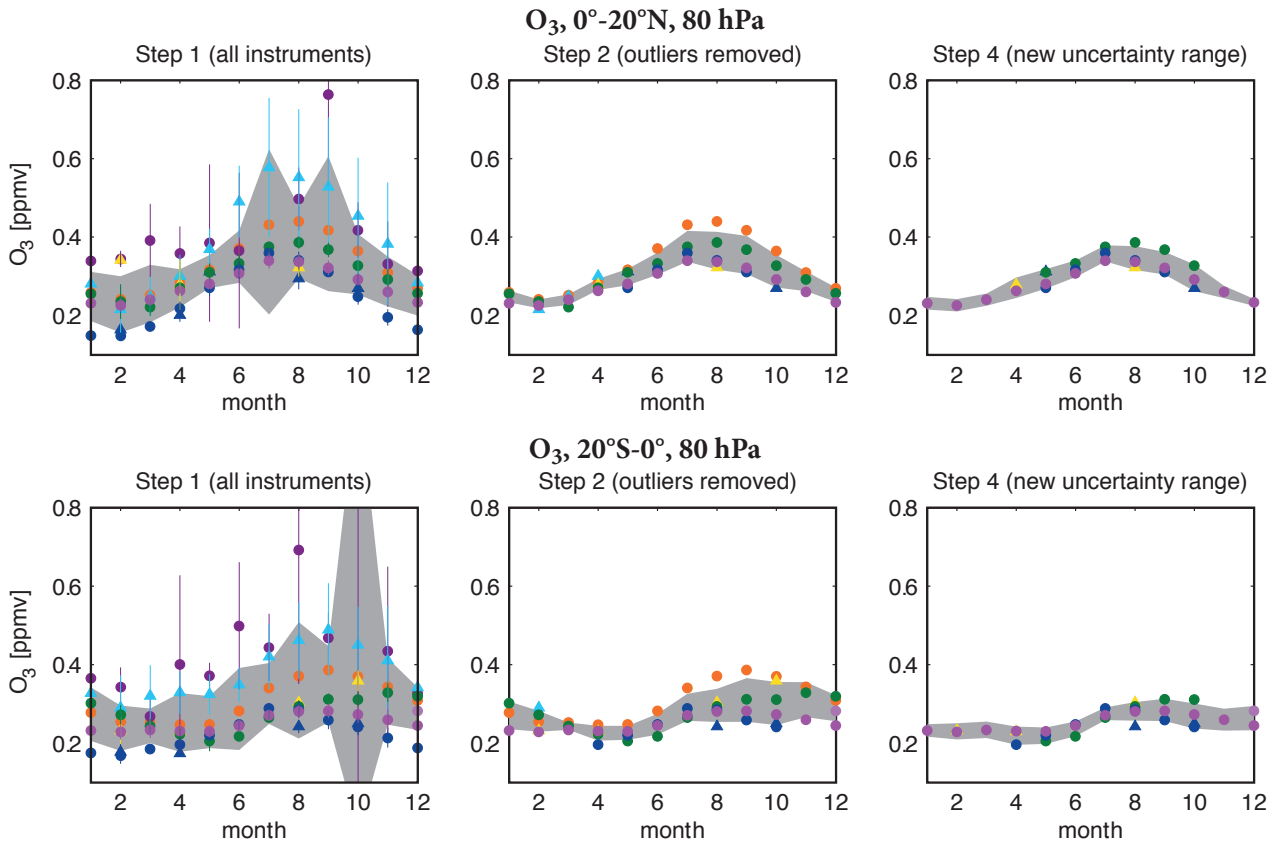

Figure 5.1.5: Ozone seasonal cycle diagnostic for 0°-20°N and 20°S-0° at 80 hPa. *Same as Figure 5.1.4 but for 80 hPa at 0°-20°N and 20°S-0°.*

NIWA-based uncertainty range (black lines in right panel of **Figure 5.1.4**). Evaluations of UTLS ozone after the application of the TES observational operator [*Section 4.27*; *Neu et al.*, 2014a] including a comparison to a "zonal mean" ozonesonde climatology indicate that in the tropics below 100 hPa most instruments have a positive bias. Removing all datasets that are outside of the ±1σ standard deviation of the climatological ozonesonde measurements (see **Figure 4.27.6** for details) results in a lower mean and also a reduced uncertainty range (right panel of **Figure 5.1.4**). Note that for November, the criteria has not been applied in order to avoid inconsistencies with the October and December uncertainty ranges. In particular for the time period from March to October the uncertainty range has been substantially reduced and is now smaller than the NIWA-based one.

Most studies analyzing the seasonal cycle of long-lived trace gases treat the tropics as a horizontally homogeneous region without differentiating between NH and SH. Very recently differences between the ozone seasonal cycles in the NH and SH tropics, related to hemispheric differences in the seasonal strength of vertical transport and horizontal mixing, have been pointed out by *Stolarski et al.* [2014]. Here, we follow their approach and derive uncertainty ranges for the ozone seasonal cycle at 80 hPa for the NH tropics (0°-20°N) and the SH tropics (20°S-0°) as illustrated in **Figure 5.1.5**. For both regions, the number of overall applicable datasets decreases substantially when identifying outliers and comparing to ozonesondes resulting in a new, narrow uncertainty range. Confirming the results from *Stolarski et al.* [2014] the seasonal cycle of tropical ozone is substantially different in the two hemispheres with a less pronounced and later occurring maximum in the SH. Model-evaluations of the ozone seasonal cycle should thus be based on two diagnostics differentiating between the NH and SH tropics.

Nitric acid – HNO_3

The HNO_3 seasonal cycle in the UTLS is used to evaluate transport and mixing processes in the models on typical time scales of weeks to months. Like ozone, HNO_3 is mostly produced in the stratosphere and thus has a similar seasonal cycle with some differences caused by chemistry and microphysics. **Figure 5.1.6** shows the evaluation diagnostics of the HNO_3 seasonal cycle for 40°N-60°N at 100 and 200 hPa. The seasonal cycles of five satellite instruments are derived from multi-annual mean (2005-2010) values. At both levels, but in particular at 100 hPa, the instruments are clustered together with only little inter-instrument spread (left panels in **Figure 5.1.6**). Compared to the ozone seasonal cycle, we have fewer instruments available (the ozone evaluations are based on 9 instruments) and thus choose a different criterion to identify outliers. Only data points outside of the ±2σ standard deviation calculated in step 1 will be removed. Note that the grey shading in **Figure 5.1.6** corresponds to the ±1σ standard deviation. At both levels, the agreement between the multi-annual mean states of the five instruments is very

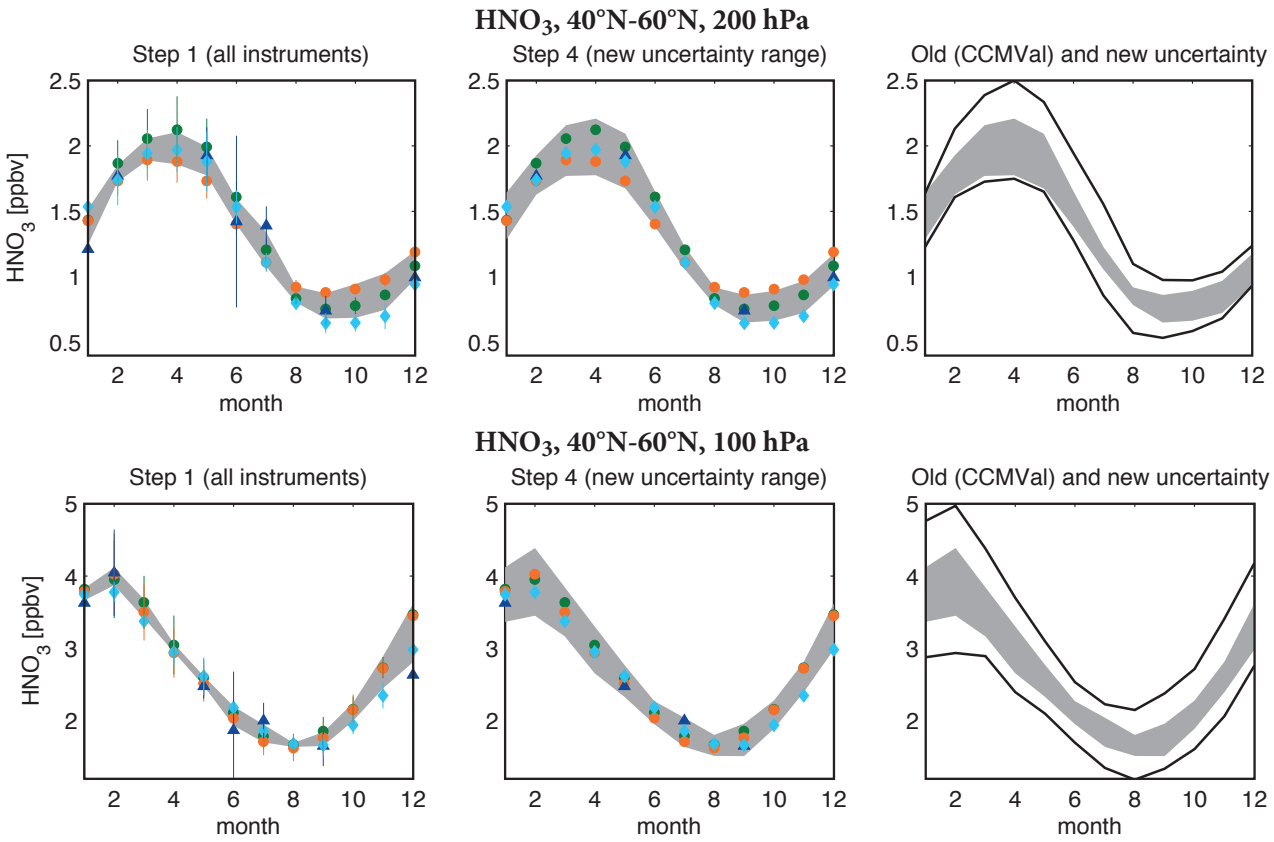

Figure 5.1.6: HNO_3 seasonal cycle diagnostic for 40°N-60°N at 200 and 100 hPa. *Steps 1 and 4 of deriving the HNO_3 seasonal cycle diagnostic are shown. The uncertainty range (grey shading) is given for each month by the standard deviation over all selected data points. In the rightmost panels the old uncertainty range given in SPARC (2010) and the new uncertainty range are compared.*

good and thus no data points are identified as outliers and excluded from the calculation of the uncertainty range. However, some instruments are removed due to their large interannual variability (illustrated by the vertical bars in the left panels). At 200 hPa, the uncertainty is more driven by the instrument spread than by the interannual variability and is smallest during NH summer. Compared to the CCMVal report the new climatological mean values during NH winter and spring are lower. The new lower mean values agree also better with most of the CCMVal models which were found to be too low when compared to the old climatological mean (see Figure 7.22 in *SPARC*, 2010). At 100 hPa, the new uncertainty range is largest during the NH winter as a result of the inter-annual variability of the remaining data. Comparisons to the uncertainty used in the CCMVal report and in *Hegglin et al.* [2010] show that the new uncertainty range is much reduced.

Similarly to the HNO_3 seasonal cycle in the NH UTLS, we derive a new uncertainty range and climatological mean (see **Figure A5.1.4** in *Appendix A5*) for the HNO_3 seasonal cycle in the SH UTLS (30°S-60°S, 100 and 200 hPa) as applied in the UTLS chapter of the CCMVal report. The strongest reduction of the uncertainty range with respect to the one used in the SPARC report is found at 100 hPa in the form of an 80% decrease.

Water vapour – H_2O

The H_2O seasonal cycle in the tropical tropopause region (at 80 hPa) is a key diagnostic to evaluate the amount of water vapour entering the stratosphere [*Gettelman et al.*, 2010]. Water vapour affects stratospheric ozone through HO_x-chemistry as well as the formation of polar stratospheric clouds, and also the radiative budget of the UTLS [*SPARC*, 2000]. The seasonal cycle in water vapour is closely related to the seasonal cycle in tropical coldpoint tropopause temperature, which in turn is dominated by the seasonally varying strength of the stratospheric Brewer-Dobson circulation.

Figure 5.1.7 shows the evaluation diagnostics of the H_2O seasonal cycle for 20°S-20°N at 80 hPa. The seasonal cycles of seven satellite instruments are derived from multi-annual means averaged over the time period 1996-2010. Choosing a shorter time period for which the instruments would show exact overlap does not improve the comparison between the instruments (see *Chapter 4*; *Hegglin et al.* [2013]), but would limit the number of instruments and information on interannual variability needed in step 4 to calculate an improved uncertainty range.

The instruments do not agree well on the mean values and hence the uncertainty range is relatively large.

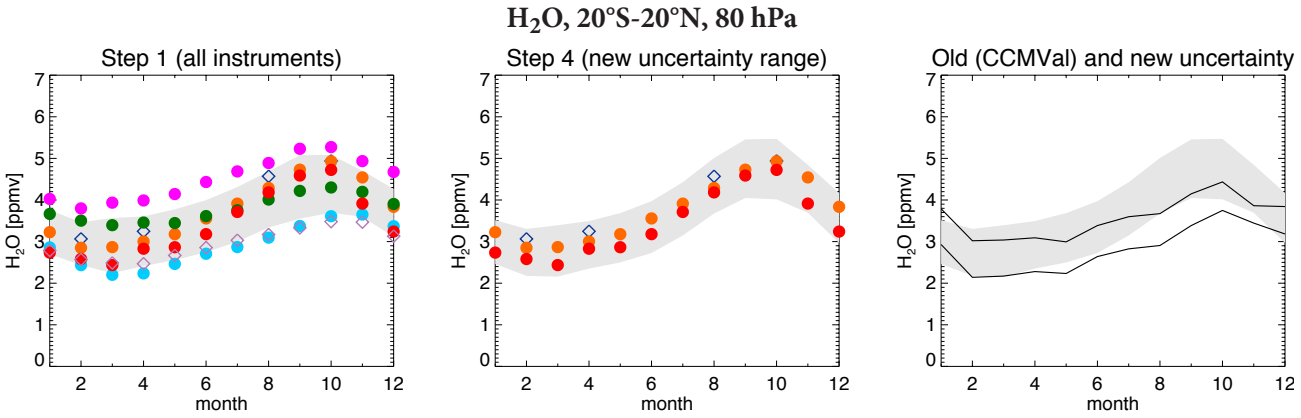

Figure 5.1.7: H_2O seasonal cycle diagnostic for 20°S-20°N at 80 hPa. *Steps 1 and 4 of deriving the H_2O seasonal cycle diagnostic are shown. The uncertainty range (grey shading) is given for each month by the 1σ standard deviation over all selected datasets (left panel). The middle panel shows the sub-selected datasets, but with the new uncertainty range accounting for interannual variability. In the right panel the new uncertainty range is compared to the uncertainty range given in the CCMVal report.*

Following the approach introduced in this chapter, we exclude instruments that lie outside the ±1σ uncertainty range given by the seven available satellite datasets. The instruments excluded were already identified in *Chapter 4.2* to have weaknesses, with SMR and HALOE showing a distinct low bias and SCIAMACHY showing a high bias due to too low resolution in the altitude range considered. In addition, we also remove MIPAS, since its averaging kernels are state-dependent (measuring with better altitude resolution in a more humid atmosphere), which leads to a seasonal cycle that exhibits too small an amplitude. The remaining instruments agree very well with each other, even though ACE-FTS has very limited sampling in the tropics. Thus no further data points are removed from the calculation and the new uncertainty range is calculated including interannual variability. The new mean seasonal cycle and its uncertainty imply that the models have been evaluated in the CCMVal report against a too low water vapour reference in terms of both mean values and seasonal cycle amplitude, while the old uncertainty range may have underestimated the impact of interannual variability.

5.1.2 Vertical and meridional profiles

Ozone – O_3

Another important aspect of CCM validation is the evaluation of polar spring time ozone profiles. Climatological mean vertical profiles in March at 75°N-85°N and in October at 75°S-85°S are compared between models and observations in order to test the models' representation of transport and chemistry in the polar regions. In contrast to the strong ozone decline driven by anthropogenically emitted ozone depleting substances until the mid-1990s, the Antarctic ozone hole has been controlled primarily by variations in stratospheric temperature and dynamical processes since 1997 [*WMO*, 2011]. In order to avoid the impact of the strong trend before the mid-1990s, we choose the time period 1997-2010 for the ozone profile evaluation in the polar regions. Over this long time period eight ozone datasets provide profile information for the Antarctic spring (**Figure 5.1.8**, left panel). Although some of the datasets cover only part of the time period, most of the profiles cluster together closely. We find one clear outlier with large deviations on the positive side, which is removed in step 2 (**Figure 5.1.8**, middle panel). In the last step, interannual variations are included in the construction of the uncertainty range resulting in slightly larger uncertainties (**Figure 5.1.8**, right panel). Overall in the MS and US, a well-defined mean ozone profile with a relatively narrow uncertainty range is derived for the Antarctic spring. In the LS, however, the spread is quite large which given the overall very small ozone abundances during this time of the Antarctic ozone hole, results in very large relative differences (see also *Chapter 4.1.6*; *Tegtmeier et al.* [2013]). The ozone hole with near-zero ozone values extends from 300 to nearly 50 hPa. Particularly between 100 and 50 hPa, the uncertainty is much higher than in other altitude ranges with similarly low abundance (above 0.3 hPa) or during other times of the year (not shown here). Such differences might be related to the different sampling patterns of the individual instruments and for detailed evaluations of high-latitude ozone in the LS we recommend the use of coincident measurement comparisons, polar vortex coordinates and the use of *in-situ* measurements.

Ozone evaluations can depend on the time period chosen. If we limit the ozone profile comparisons to shorter time periods such as 2000-2010 or 2005-2010 we get very similar mean profiles but a somewhat smaller uncertainty range. In particular, for the latter time period, the uncertainty range in the lower and middle stratosphere can be substantially reduced (see **Figure A5.1.5** in *Appendix A5*). While this suggests a better agreement of the instruments covering the latter time period, one needs to keep in mind that fewer instruments go into this evaluation (five instead of eight) which have at the same time a denser sampling pattern. The evaluation of the earlier time period 1991-2000

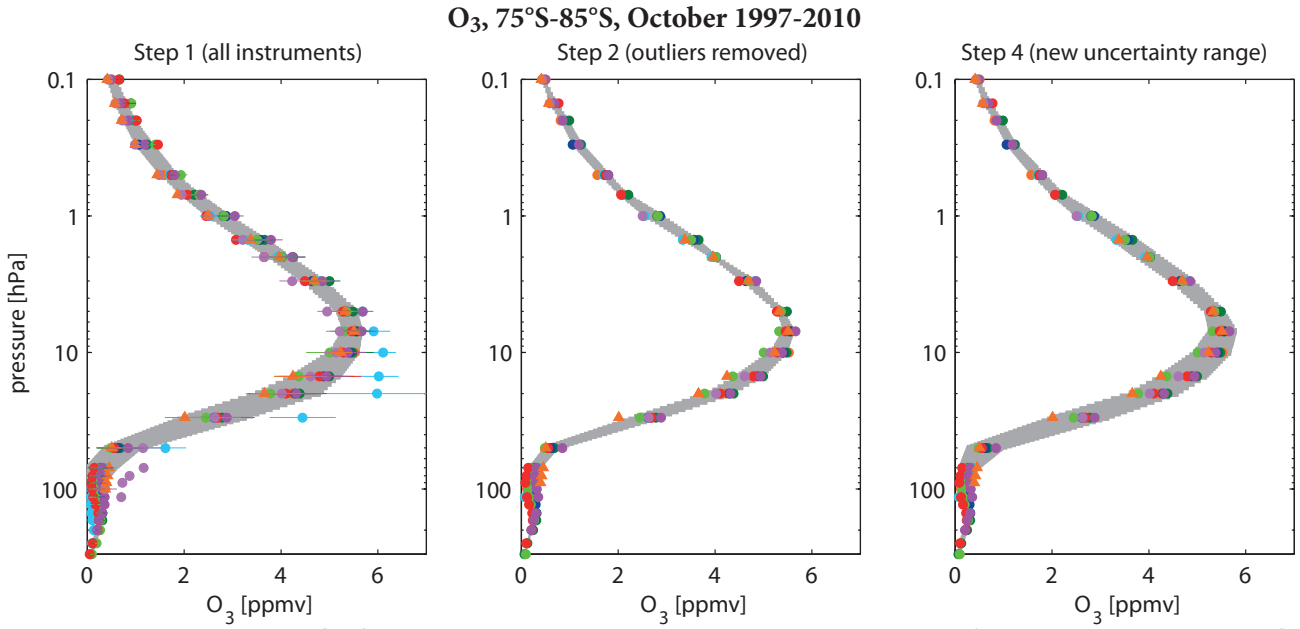

Figure 5.1.8: O_3 vertical profile for 75°S - 85°S in October 1997-2010. *Steps 1, 2 and 4 of deriving the O_3 vertical profile diagnostic are shown. The uncertainty range (grey shading) is given for each level by the standard deviation over all selected datasets.*

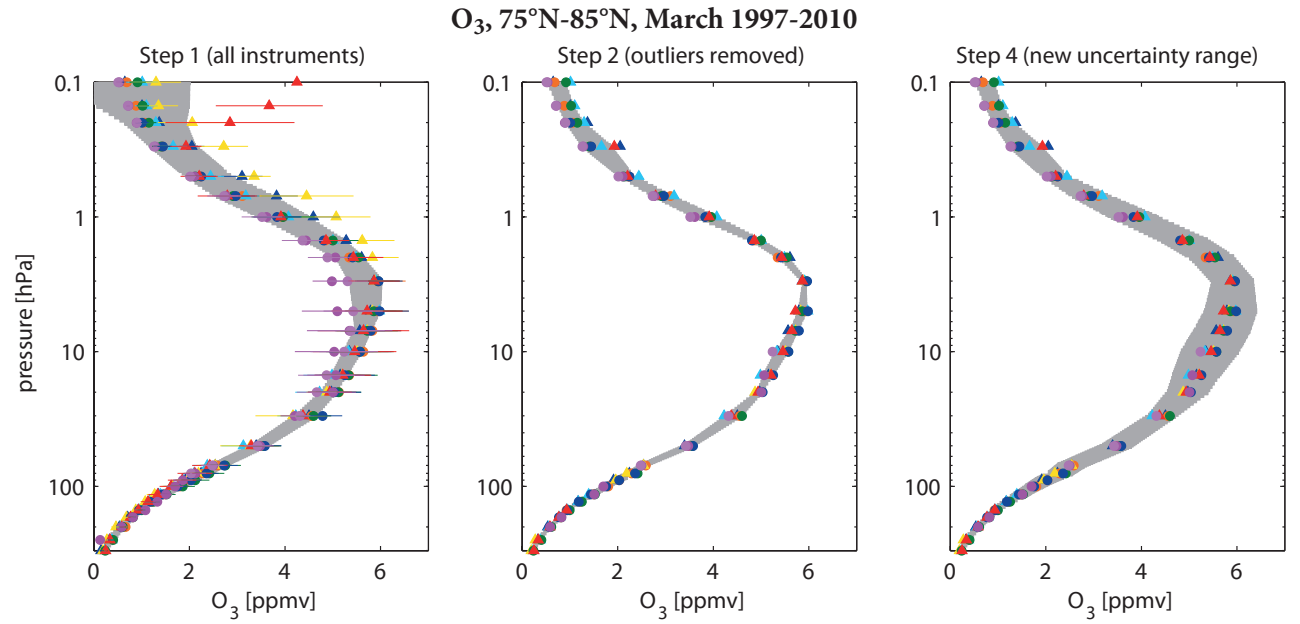

Figure 5.1.9: O_3 vertical profile for 75°N-85°N in March 1997-2010. *Same as Figure 5.1.8 but for 75°N-85°N in March.*

(**Figure A5.1.6** in *Appendix A5*), on the other hand, gives a different mean profile and a slightly larger uncertainty range due to larger interannual variability and, in comparison to 2005-2010, larger instrument-spread. In previous model evaluations focusing also on the 1990s [*SPARC*, 2010; *Eyring et al.*, 2006] the uncertainty range, based on the HALOE climatology and interannual standard deviations, was much larger than the new, multi-instrument uncertainty range introduced above.

Evaluation of the Arctic spring time ozone (here 75°N-85°N in March) shows a large inter-instrument spread, in particular in the MS/US (**Figure 5.1.9**, left panel). The spread is in most cases based on 1-2 outliers which are removed in step 2 resulting in a very narrow uncertainty range (**Figure 5.1.9**, middle panel). Due to the larger dynamical variability at the NH high latitudes, including the interannual standard deviation in the construction of the uncertainty range leads to much larger uncertainties, in particular in the MS. In contrast to the Antarctic, the inter-instrument spread in the LS is quite small leading to a well-defined profile with low uncertainties in this region.

Methane – CH_4

Methane (CH_4) meridional profiles are similarly used in model evaluation to study stratospheric transport characteristics (see *Eyring et al.* [2006]). As mentioned above, transport in the stratosphere involves both the residual mean circulation and isentropic mixing, with the

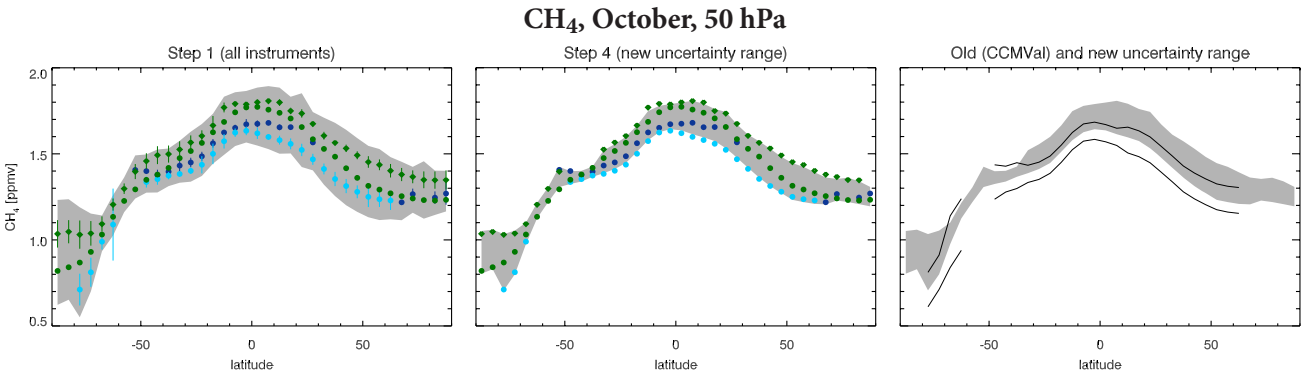

Figure 5.1.10: Climatological CH_4 meridional profile at 50 hPa in October over the time period 1998-2010. *Steps 1 and 4 of deriving the meridional profile of CH_4 are shown in the upper two panels. The uncertainty range (grey shading) is given for each month by the ±2σ standard deviation over all selected datasets (left panel). In the middle panel the newly derived uncertainty range (accounting for interannual variability) is shown, and in the right panel it is compared to the old uncertainty range given in the CCMVal report.*

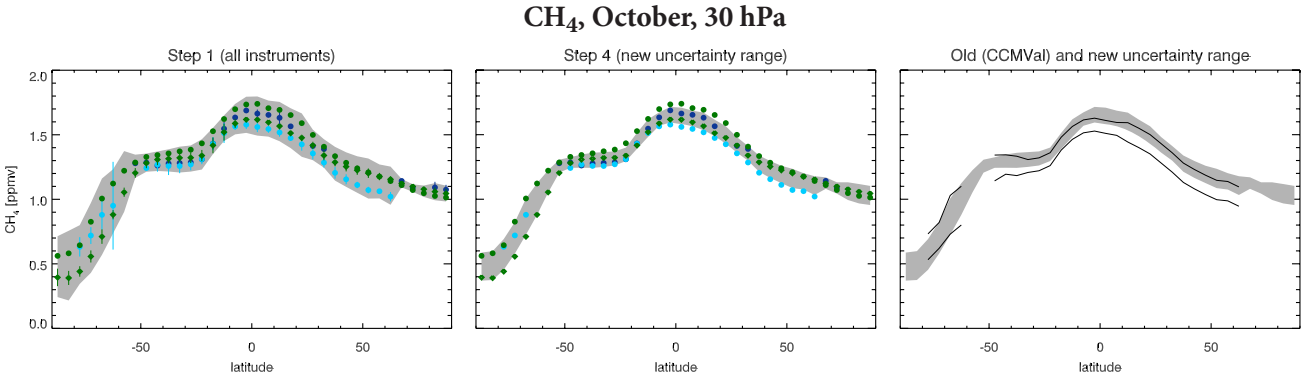

Figure 5.1.11: Climatological CH_4 meridional profile at 30 hPa in October over the time period 1998-2010. *Same as previous Figure, but for the 30 hPa level.*

latter being highly inhomogeneous in space and time. The winter hemisphere surf zone thereby constitutes a region of strong stirring and mixing, whereas the subtropical edges and the polar vortex are barriers to transport and mixing processes. Failing to reproduce the strength of these mixing barriers can lead to wrong distributions of long-lived and reactive trace gas species with potentially significant impacts on the ozone chemistry. The meridional profile of methane (or any other long-lived trace gas) reveals the existence of transport and mixing barriers in regions where tracer gradients are large. On the other hand, small tracer gradients indicate regions of strong mixing.

Only three instruments participating in the SPARC Data Initiative measured CH_4. The conclusions of *Chapter 4*, supported by other validation studies from the literature, suggest to treat the two MIPAS retrievals (high-spectral and high-spatial resolution) as two different instruments, hence **Figures 5.1.10** and **5.1.11** include four datasets each.

Figure 5.1.10 shows the meridional profile of methane at 50 hPa. The uncertainty range in step 1 is relatively large, especially in the SH polar vortex region, where the diagnostic is used to test the relative strengths of mixing across the polar vortex edge versus descent within the polar vortex. Removing multi-annual mean values with an interannual variability larger than the ±2σ standard deviations from step 1 and accounting for interannual variability yields a much smaller uncertainty range. This uncertainty range compared to the one used in *Eyring et al.* [2006] is shown to have improved in two aspects. First, the strong gradient across the polar vortex edge is much better defined than by using HALOE measurements alone. Second, HALOE mean values are much lower than the new multi-instrument mean values, in particular within the polar vortex region. The models (from Figure 5 in *Eyring et al.* [2006]) would hence compare much more favorably to the new instrument mean than to the old measurement diagnostic derived from HALOE. Note that the HALOE reference does not improve using a more limited range of years (*e.g.*, 2003-2005), but loses latitudinal coverage due to increasing sampling limitations towards the end of the mission.

Figure 5.1.11 shows the meridional profile of methane at 30 hPa. This level is chosen in order to illustrate that the comparison between the HALOE reference (as calculated in an equivalent way to that used in the CCMVal report at 50 hPa) and the multi-instrument mean and standard deviation from the SPARC Data Initiative datasets is altitude dependent. The comparison has much improved in terms of latitudinal structure, although the HALOE mean

values are still generally somewhat lower than those of the other instruments.

5.1.3 Recommendations for short-lived species

Short-lived species are characterised by chemically driven variations linked to the local solar time (LST). Limb-viewing instruments measure at LSTs that can differ from instrument to instrument, and between seasons and latitudes for the same instrument. Most of the instruments measure two distinct LSTs per latitude. These instruments are in polar sun-synchronous orbits, with one LST for the ascending portion of the orbit and one forthe descending portion. In the case of solar occultation sounders, measurements correspond to sunrise and sunset as seen from the satellite and the LSTs shift with the day of year.

The SPARC Data Initiative produced two types of climatologies for the diurnally varying species; climatologies from observations binned by LST (unscaled), and climatologies from observations scaled to a common LST. The climatologies from instruments in a sun-synchronous orbit are generally based on measurements separated into am and pm data. Climatologies from instruments that observe from non sun-synchronous orbits are generally separated into daytime and night-time measurements. Exceptions are the climatologies from solar occultation measurements which are based on data separated into local sunrise and sunset measurements. Additional climatologies are compiled using a photochemical box model to scale the measurements to a common LST, as explained in detail in *Section 3.1.2*.

When evaluating short-lived species from chemistry-climate models with the SPARC Data Initiative climatologies, the comparisons will be meaningless in most cases, if the monthly zonal mean model output is constructed in the traditional way by averaging over all longitudes at each output time step. Since most of the SPARC Data Initiative climatologies correspond to specific LSTs or times of day, the model output needs to be sampled in a similar manner. Even for instruments like SMILES, that observe species at varying LST because of their non sun-synchronous orbit, the constructed zonal mean climatologies are biased towards particular LSTs as a result of the non-homogeneous sampling patterns [*Kreyling et al.*, 2013]. Ideally, model data should be sampled with the satellite sampling patterns including the position and LST of each measurement. Trace gas climatologies derived from thus sampled model fields can be directly compared to the trace gas climatologies from the respective satellite instrument. While this approach is well suited for the comparison of short-lived species, it also means a lot of effort given that each satellite instrument has a different sampling pattern. Alternatively, the model output could be filtered according to LST in a manner similar to the SPARC Data Initiative climatologies in order to construct datasets corresponding to a particular LST, am/pm, day/night, or local sunrise/local sunset conditions. Another possibility is to restrict comparisons between model and satellite climatologies of short-lived species to latitude and altitude regions where the diurnal variations are small. Guidelines for appropriate comparisons of the individual short-lived species are given below.

- NO measurements show strong gradients at sunrise and sunset and model output should be filtered to construct sunrise and sunset (comparable to ACE-FTS or HALOE) or 10am LST (comparable to MIPAS or scaled ACE-FTS) climatologies.
- NO_2 diurnal variations are also most pronounced during sunset/sunrise. Model data should be filtered in order to construct sunrise/sunset (comparable to HALOE, SAGE II, POAM III, SAGE III and ACE-FTS) or 10am/10pm LST (comparable to MIPAS, SCIAMACHY, GOMOS or scaled OSIRIS, HIRDLS, and ACE-FTS) climatologies. If the model output is binned into daytime or night-time data instead (comparable to MIPAS, SCIAMACHY, GOMOS, OSIRIS, HIRDLS am/pm) differences of up to 20-30% can arise from the diurnal variations.
- NO_x is longer lived and has small diurnal variations in the MS. Data should be filtered to construct sunrise/sunset (comparable to HALOE and ACE-FTS) or 10am/10pm (comparable to MIPAS, SCIAMACHY, or scaled OSIRIS, and ACE-FTS) climatologies. Comparison of unfiltered monthly zonal mean climatologies can result in differences of around 20%. Binning the model output into daytime/night-time will not improve the comparison since there are no pronounced gradients at sunrise/sunset.
- HNO_3 is fairly long-lived in the UT to MS and shows a weak diurnal cycle in the US which increases further in the LM. Zonal mean climatologies can be compared directly at altitudes below 3 hPa.
- HNO_4, $ClONO_2$ and N_2O_5 climatologies show strong diurnal cycles above 10 hPa (100 hPa for N_2O_5) where model data needs to be binned according to sunrise/sunset (comparable to ACE-FTS) or 10am/10pm data (comparable to MIPAS). Below 10 hPa (100 hPa for N_2O_5), diurnal variations are weak allowing for a direct comparison of the datasets corresponding to different LSTs.
- ClO and BrO exhibit strong diurnal variations most pronounced during sunset/sunrise and with decreasing amplitude towards the USLM. Daytime variations are much smaller than night-time variations. For ClO, model data should be filtered in order to construct sunrise/sunset (comparable to SMR) or daytime climatologies (comparable to Aura-MLS pm, SMILES daytime, MIPAS am, or scaled daytime SMR climatologies). Comparisons should focus on the tropical/mid-latitude US. For BrO, model output should be filtered to construct daytime climatologies (comparable to scaled OSIRIS, scaled SCIAMACHY, or daytime SMILES climatologies). Comparisons should focus on altitude levels above 20 hPa. HOCl shows in contrast strong diurnal variations and model data need to be compiled according to instrument measurement times for a more meaningful comparison.

- HO_2 shows a strong diurnal cycle with smaller variations during daytime than during night-time. Model data can be binned into daytime climatologies (comparable to SMILES and Aura-MLS daytime) and compared in the altitude region between 10 and 0.5 hPa. OH has a strong diurnal cycle and model output should be filtered in order to construct daytime 2pm climatologies (comparable to Aura-MLS). CH_2O and CH_3CN show small diurnal variations, thus allowing for a direct comparison of datasets even if they apply to different LSTs.

5.1.4 Suggestions for new diagnostics

The monthly zonal mean SPARC Data Initiative datasets provide a unique source of observational data for model evaluation diagnostics. Here, we present suggestions for new diagnostics covering different aspects of model validation. The new diagnostics use, in addition to the monthly zonal mean climatologies, parameters from the SPARC Data Initiative datasets that describe variability, location and timing of the underlying measurements.

CFC-11 mean profiles and standard deviations

Profiles of long-lived tracers (as also shown in *Section 5.1.2* for CH_4) have been used extensively over the past to analyse the effects of diabatic descent and mixing in the polar vortex [*SPARC,* 2010]. Here, we show CFC-11 profiles at the high SH latitudes (80°S-85°S) at the beginning (June) and end (September) of the Antarctic winter for MIPAS and the Whole Atmosphere Community Climate Model (WACCM) (**Figure 5.1.12**). The comparison of June and September CFC-11 profiles provides information on the combined effects of vortex descent, bringing lower CFC-11 mixing ratios downward, and of transport from lower latitudes, bringing higher CFC-11 mixing ratios towards the pole. Between 100 and 50 hPa, WACCM shows lower mixing ratios at the beginning of the austral winter but higher mixing ratios at the end of the winter when compared to MIPAS. Thus the CFC-11 decrease is not strong enough in the model suggesting that there is too little descent and/or too much mixing across the vortex edge.

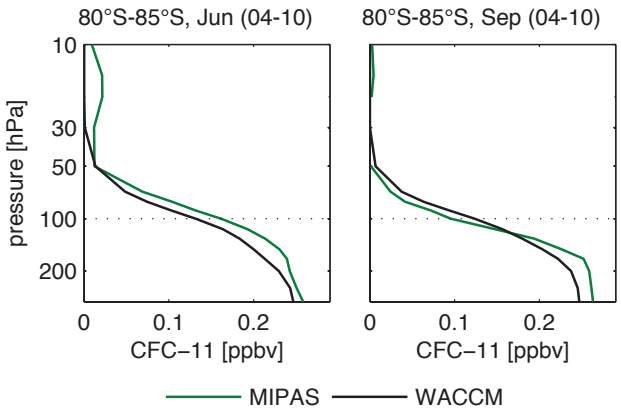

Figure 5.1.12: Vertical monthly zonal mean CFC-11 profiles for 80°S-85°S in June and September for MIPAS and WACCM.

Besides the monthly mean values, the SPARC Data Initiative datasets provide the standard deviations for each month, latitude bin and pressure level. **Figure 5.1.13** shows the standard deviation fields which describe the variability within each latitude band and month and are calculated over all given measurements in the respective bin. At 30 hPa (upper panels), elevated standard deviations at around 20°S/N indicate stronger variability in the trace gas field caused by breaking of planetary scale waves at the tropical pipe edge. The temporal extent (in the NH from December to March and in the SH from April to November) and magnitude of this event agree quite well between model and observations. Note that, at altitudes below 70 hPa, breaking synoptic scale waves cause more stirring and therefore prevent strong tracer gradients or any maxima in the standard deviation field. At 100 hPa in the tropics (~20°S-20°N), WACCM shows similar mean values but much lower standard deviations than MIPAS, which is very likely caused by the natural variability in this region being smaller than the MIPAS measurement error [*Toohey et al.*, 2010]. Most of the MIPAS variability is indeed explained by the MIPAS random error estimated to be around 17 pptv. Consequently, the standard deviation from observational fields should only be used for model evaluations in regions where the natural variability is larger than the measurement error. However, at 30 hPa the comparison reveals a striking absence of variability in the model in the SH high latitudes throughout the year, but in particular during SH winter, when the observations show high variability. This result implies a too low dynamical activity in the model, which may be related to the SH cold bias chemistry-climate models exhibit in this region [*Austin et al.*, 2003].

The comparison of the standard deviation fields from MIPAS and WACCM at 100 hPa (**Figure 5.1.13**, lower panels) reveals the absence of a mixing minimum during summer in the SH mid-latitudes in the model. The SH vortex edge region shows comparable variability during SH late winter, but higher variability in the model in early winter. The situation reverses at the very high SH latitudes, where the model has much lower variability over most of the year. In particular, the low standard deviations in the model during the winter from June to September suggest that the inner vortex south of 70°S in WACCM is less disturbed than implied by the MIPAS observations. Thus the missing decrease of the WACCM CFC-11 profiles in the vortex during winter (seen from the profile comparisons in **Figure 5.1.12**) is probably caused by too weak diabatic descent and not by too strong in-mixing. MIPAS on the other hand, shows elevated standard deviations during the winter related to zonal asymmetries in the CFC-11 field which can be either caused by asymmetric descent or by in-mixing. One to two months after the vortex breakdown the standard deviation of the CFC-11 field increases due to longitudinal asymmetries. This phenomenon can be observed earlier in MIPAS (December) than in WACCM

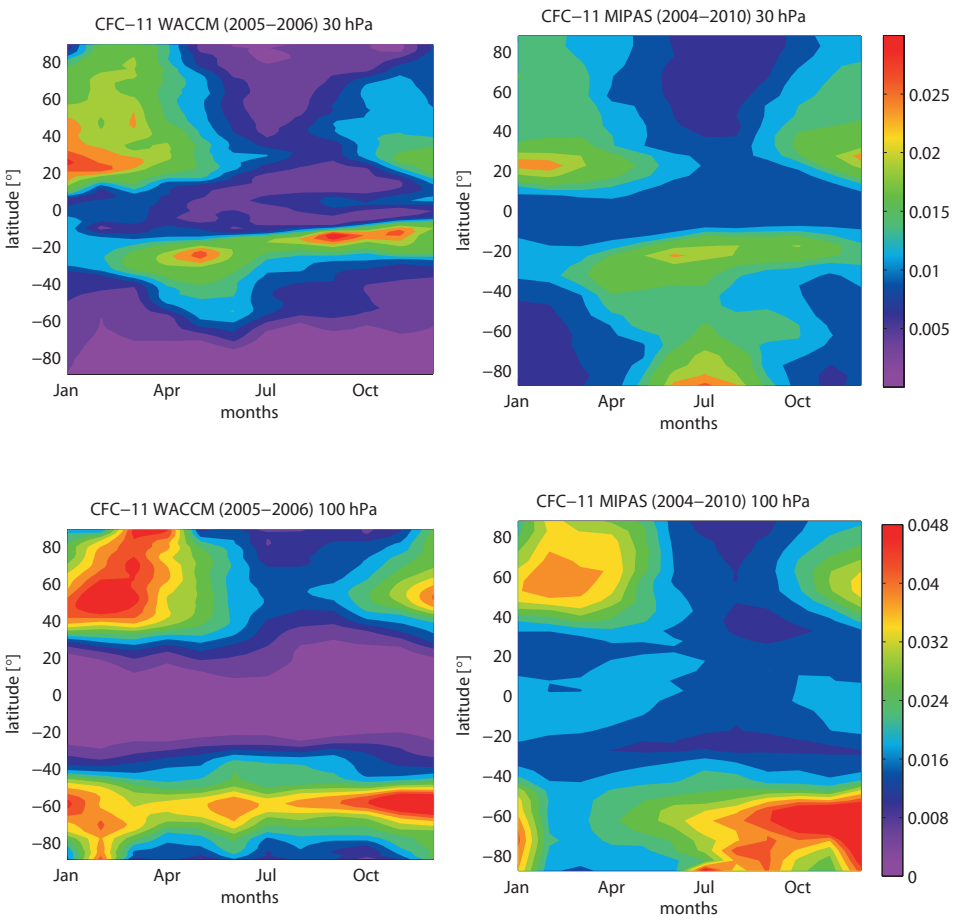

Figure 5.1.13: ***Time-latitude cross-sections of CFC-11 standard deviation fields for MIPAS and WACCM at 30 hPa (upper panels) and at 100 hPa (lower panels).*** *The standard deviation describes the variability within each latitude band and month and has been calculated over all given data points in the respective bin and month.*

(February) due to a late breakdown of the vortex in the model [*de laTorre et al.*, 2012]. At the NH high latitudes, the standard deviations show better agreement between observations and model suggesting more similarities in the dynamical situation.

CH_4 time-latitude evolution

While meridional and altitude profiles of CH_4 and N_2O have been extensively used in the past to test stratospheric transport in chemistry-climate models [*Eyring et al.*, 2006; *SPARC*, 2010; *Strahan et al.*, 2011], the SPARC Data Initiative monthly zonal mean climatologies lend themselves to also study the time evolution of these profiles. **Figure 5.1.14** shows to this end a comparison of the time-latitude evolution of CH_4 at two different pressure levels (2 and 10 hPa) between the multi-instrument mean derived from the HALOE, MIPAS, and ACE-FTS instruments, and the Canadian Middle Atmosphere Model using a simulation nudged to observed meteorology (CMAM30). As explained in more detail in *Chapter 4.3*, the feature at 2 hPa has been attributed to the equatorial Semi-Annual Oscillation (SAO) [*Choi and Holton*, 1991], with the maxima in tropical CH_4 coinciding with maxima in upwelling. The 2 hPa and 10 hPa levels are furthermore distinct in the CH_4 variability seen in the polar region. At 10 hPa, the minima in polar regions during autumn and winter coincide with the maxima in downwelling within the Brewer-Dobson circulation [*Randel et al.*, 1998]. At 2 hPa, on the other hand, the minima show up in summer/autumn as the result of photochemistry, with CH_4 lifetimes decreasing to four months at these altitudes [*Randel et al.*, 1998; *Solomon*, 1986].

Comparison of CMAM30 with the observations yields overall encouraging results, with CMAM30 clearly indicating a SAO. Furthermore, the timing and extent of the low CH_4 in polar regions correspond well between observations and model at both levels. However, some differences can also be identified. For example in both hemispheres at 2 hPa, the photochemically induced minima during autumn are not quite as pronounced as in the observations. This could be due to a problem in the chemistry, but more likely results from too strong mixing between the tropics and the higher latitudes (partially due to numerical diffusion in the rather low model resolution). Likewise, the maxima seen in the tropics are not quite as pronounced as in the observations, along with the minima in polar regions at 10 hPa, indicating that CMAM30 exhibits too weak upwelling/downwelling or again too strong horizontal mixing. The overall good agreement between CMAM30 and the observations is partially due to using a model version that is driven by the observed meteorology. Note however that the influence of the nudging to the meteorological fields weakens towards higher altitudes above 10 hPa, so that the model seems to at least partially represent the right dynamical mechanisms that produce the SAO.

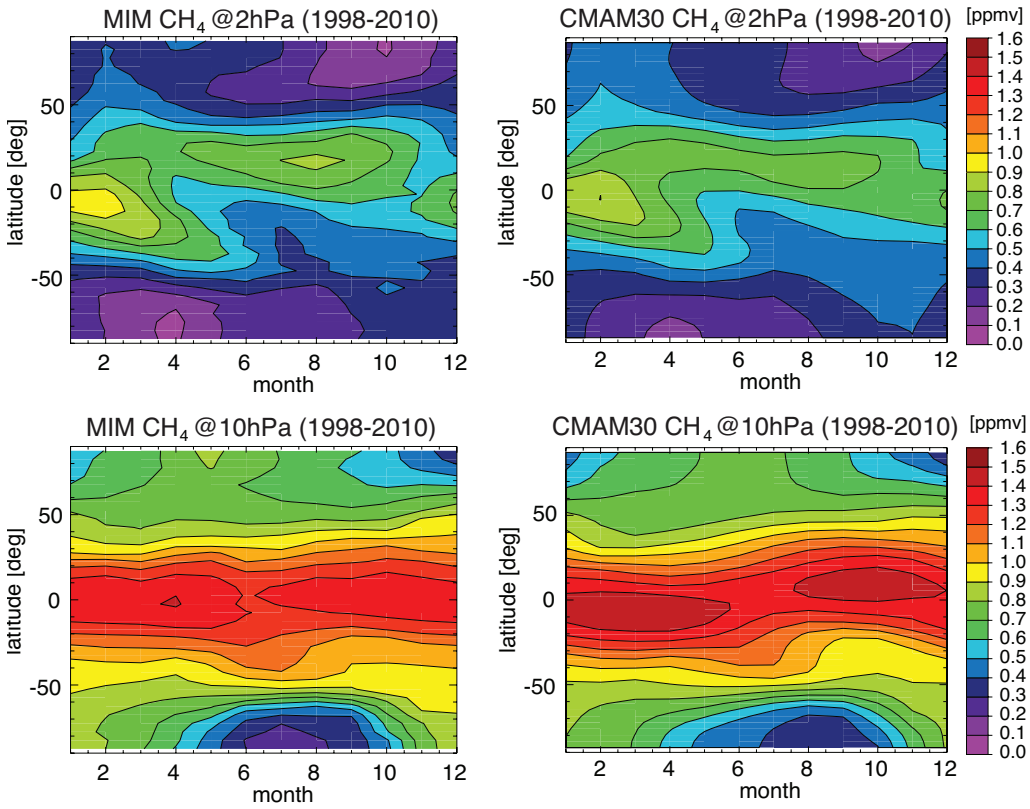

Figure 5.1.14: *Time-latitude cross-sections of CH_4 mixing ratios at 2 hPa (upper panels) and 10 hPa (lower panels) from the multi-instrument mean (left) and CMAM30 (right).*

5.2 Implications for merging activities

With monthly zonal mean time series of stratospheric constituents available from all the SPARC Data Initiative instruments, the obvious question is why these have not been merged into one homogeneous data product which globally covers multiple decades. The reason is that such a project is a challenge in itself which requires solving a number of technical and methodological problems. One needs to try to eliminate outliers or even whole datasets if many problems are discovered (*e.g.*, after a careful multi-instrument comparison). Currently, there is not even full agreement about what the most appropriate merging techniques are. Techniques range from a simple merge of two single datasets by accounting for an inter-instrument bias that is calculated over some overlap time period [*Bourrassa et al.*, 2014] to merging of multiple datasets including detailed calculations of uncertainties [*Froidevaux et al.*, 2015], statistical methods to fill in observational gaps [*Bodeker et al.*, 2013], or the use of a nudged chemistry-climate model as transfer function between the instruments [*Hegglin et al.*, 2014].

Some of the problems arising in data merging can be solved by directly using the parent datasets instead of the merged dataset and using an analysis tool that is immune against one or the other of these problems. One example is the trend estimator by *von Clarmann et al.* [2010] which is immune against biases between subsets of data. An ideal solution for the general data merging problem, however, does not yet exist. The first important step towards optimal data merging is to develop a common language and to develop schemes to evaluate and report retrieval errors, altitude resolution and content of prior information in the data in an inter-comparable manner. Given that all different merging techniques have their weaknesses and strengths, it remains important that independent research teams approach data merging so that their results can be compared and used to identify not only instrument errors but also uncertainties in the merging techniques themselves.

In the following sections we discuss the most prominent problem areas that arise in data merging.

5.2.1 Error characterisation of instruments

In the most straightforward scenario, multiple datasets are available for the same latitude bins and certain overlap time periods. In this case merging reduces to a weighted or unweighted mean of the data. The obvious advantage of weighting the data by their inverse estimated error, usually in terms of variance, is that reliable data dominate the merged product. Drawbacks and pitfalls, however, are:

- The error estimation schemes used for the different datasets may differ and different error types may be included. Thus, a better instrument can have larger error bars.
- For some instruments error covariances are reported, while for others only error bars are available. Optimal averaging, however, requires the covariance matrices.

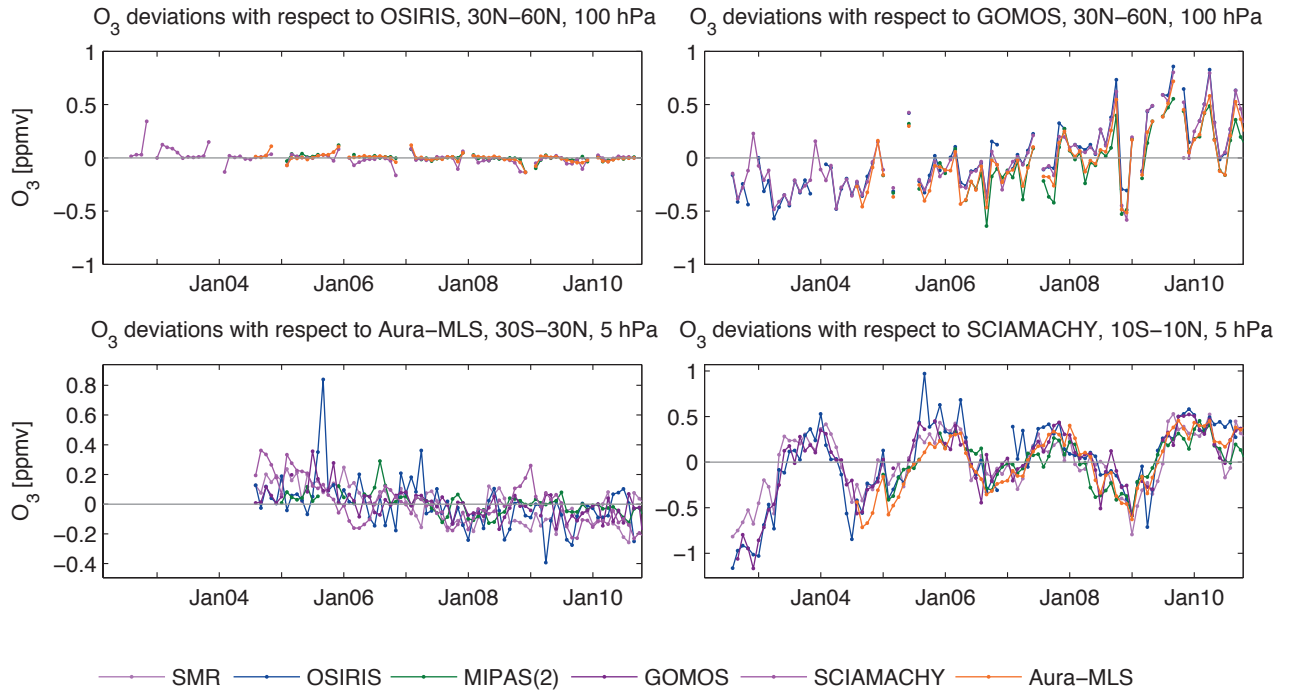

Figure 5.2.1: Time series of ozone deviations for 2002-2010. *Deviations of all instruments with respect to OSIRIS and GOMOS for 30°N-60°N at 100 hPa (upper panels), with respect to Aura-MLS for 30°S-30°N at 5 hPa (lower left panel) and with respect to SCIAMACHY for 10°S-10°N at 5 hPa (lower right panel) are shown.*

- For some instruments the error estimate includes by default the so-called smoothing error [*Rodgers*, 2000]. This quantity, however, does not follow the generalised Gaussian error propagation law [*von Clarmann,* 2014] and thus is not applicable to regridded data.

Trying to avoid these problems by using the sample standard error of the zonal mean instead of the error estimates is not as simple as one might think, because (a) in the case of regular sampling patterns measurements cannot be regarded as independent random samples and thus the standard error is not the sample standard deviation divided by the square root of the sample size [*Toohey and von Clarmann*, 2013]; and (b) sophisticated schemes are needed to distinguish the two components of the standard error of zonal means, namely measurement errors and natural variability [*Laeng et al.,* 2014; *Sofieva et al.*, 2014].

A particular problem is that the quality of the measurement can depend on the atmospheric state itself, *e.g.,* in infrared emission spectroscopy the signal is larger and thus the precision is better when it is warmer. Weighting by the inverse error variance in such a case would introduce a representativeness bias towards warmer parts of the atmosphere.

Another problem arises from denotation ambiguities. Many terms used for error characterisation are not clearly defined, used in different contexts, and have ambiguous meanings. Accuracy characterises in some cases the total error, in other cases only the systematic part, precision excluded. The systematic error in some documents includes all error sources except noise, in other cases only error terms which are - in amount and sign - time-independent. Noise often is referred to as the random part of the error while equally often it is used for the pure measurement noise only. Some total errors are more comprehensive than others. Some error budgets refer to an ideal point measurement and include the so-called smoothing error which characterises the expected difference between the atmospheric state at one idealised atmospheric point and in a finite air volume. Other error budgets refer to the atmospheric state at finite resolution and do not include the so-called smoothing error.

5.2.2 Drifts and jumps between datasets

Drifts within datasets are often unknown because, contrary to the usual validation measurements, drift estimation requires availability of long-term datasets. Even if these are available, it is not always clear which of the instruments compared to each other has a drift. For trace gases where a large number of instruments are available, such as ozone, the long-term changes of the differences can provide information on possible drifts [*Tegtmeier et al.*, 2013]. Therefore, for each instrument an analysis of the temporal variations of the differences with respect to each of the other instruments has been performed. Such time series are characterised by seasonal patterns and month-to-month variability. After removing the seasonal cycle, longer-term changes can be the dominant signal. However, for nearly all ozone datasets and regions included in this study the differences display no apparent long-term changes. One example for this consistency is shown in **Figure 5.2.1** (upper left panel) in the form of the instrument difference

with respect to OSIRIS in the NH mid-latitude LS. A few exceptions exist where clear changes of the differences over time can be identified (**Figure 5.2.1**). First, differences of all instruments with respect to GOMOS in the NH mid-latitude LS are mostly negative before 2008 and mostly positive afterwards indicating a change of GOMOS over time that is not seen by the other instruments. Note that GOMOS is excluded from the comparison to OSIRIS discussed above in order to present one example where the differences display no apparent long-term changes. For Aura-MLS, some discrepancies can be observed for the tropical US, with positive differences at the beginning and negative differences at the end of the time period, although not all instruments agree on this. SCIAMACHY differences in the tropics are dominated by the quasi-biennial oscillation (QBO) signal, while SMR (not shown here) displays larger values compared to the other datasets in 2003 but differences around zero after 2006. Note that here only drifts of a magnitude comparable to the deviations themselves have been identified; while for trend studies a more thorough analysis including possibly quite small long-term drifts is necessary.

Another option is the comparison of the instruments' time series with a model (used as a transfer function in the merging) which can yield additional evidence for which instrument is more likely to show a drift or a jump [*Hegglin et al.*, 2014]. An example for this is shown in **Figure 5.2.2**, where two data versions of SAGE II (v6.2 and v7.0) are compared to each other and a distinct difference in the beginning of the data record is revealed. The very good agreement between the maroon-coloured data version (v7.0) and the model (as seen in the bias-corrected differences fluctuating randomly around zero) provides the user with confidence that the red data version (v6.2) suffers from an inhomogeneity at the beginning of its record and therefore should not be used for merging during this time period.

Finally, the choice of well-established *in-situ* measurements as reference instruments, which usually are trusted more than remote sensing instruments, leads to the problem of often lacking statistical significance and representativeness due to low data amounts. Despite this shortcoming, ground-based measurements of ozone from sonde and lidar networks have been shown to allow for comprehensive analysis of the long-term stability of satellite ozone datasets [*Hubert et al.*, 2015]. A complication of all these types of validation studies is that the reference instrument (or model) itself needs thorough validation.

For certain regions and/or time periods, available datasets do not overlap in time. In this case, it is not clear if any jumps in the data reflect natural variability or instrument biases. A model as a transfer standard again can help here [*Hegglin et al.*, 2014]. While this approach may be seen as contaminating an otherwise purely empirical product with model information, it capitalises on our physical knowledge of the atmosphere and provides at least a best estimate of what happened during a time period when observations were not available.

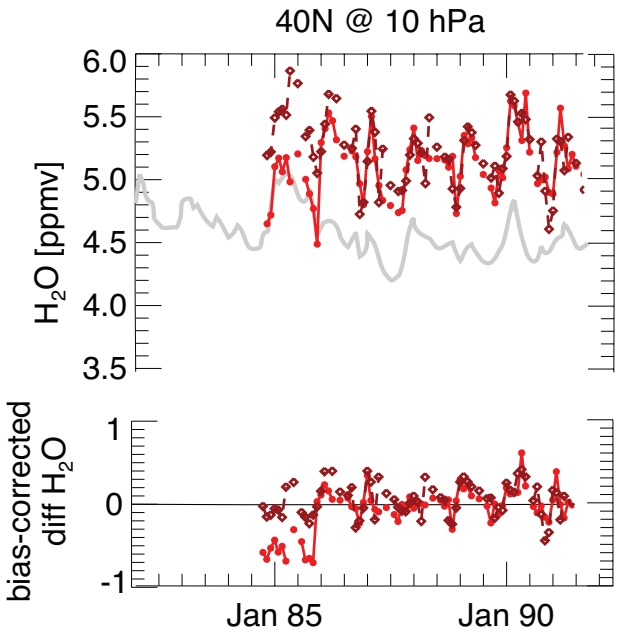

Figure 5.2.2: Model-based bias and drift estimates of observational data. *Time series of water vapour (upper panel) and bias-corrected difference to the model (lower panel) at 10 hPa and 40°N from two data versions of SAGE II water vapour (with red indicating v6.2 and maroon dots v7.0) and the Canadian Middle Atmosphere Model CMAM nudged to observed meteorology (grey line). Irregular behaviour in the bias-corrected differences reveals a problem in the red data version.*

5.2.3 Altitude resolution and a priori information

Key problems in any application where remote measurements of multiple instruments are considered are different altitude resolutions and different content of a priori information in the datasets. Some of the related problems can be solved by application of the averaging kernel matrix [*Rodgers,* 2000]; *e.g.*, the averaging kernel matrix can be used to degrade the altitude resolution of a high-resolution profile to make it comparable to a lower-resolution profile [*Rodgers and Connor*, 2003]. Such an approach has been applied in the SPARC Data Initiative when comparing the limb-viewing instruments with the nadir sounder TES in order to cross-validate ozone distributions in the UTLS with an independent dataset [*Section 4.27*; *Neu et al.*, 2014a]. TES measurements have been well-validated against ozonesondes in the UTLS and the dataset is frequently used for the evaluation of tropospheric ozone in chemistry-climate models. Observations of the higher vertical resolution limb sounders have been smoothed using the observational operator of TES. In the tropical UTLS, large positive biases of up to 50% have been identified for the limb-sounders with respect to the TES. While this study successfully provides a common basis for comparison of the large-scale ozone morphology in the UTLS, a couple of general problems remain unresolved for the general application of such comparisons:

- There exists a large number of datasets for which no averaging kernels are available, and can - due to the particular retrieval scheme used - not easily be produced.
- The application of the averaging kernel fails if the better resolved profile does not have sufficient altitude coverage to allow this operation for all relevant altitudes. There exist ad hoc solutions to this problem but these are not exact (see *Section 4.27* or *Neu et al.* [2014a]). In the SPARC Data Initiative evaluations, the TES a priori has been used to fill in the profiles below the lowest measurement level. To identify regions where the results are highly sensitive to this approach, virtual retrievals using two different filling methods have been calculated and compared.
- The situation is even worse if the altitude resolution of a measurement depends on the atmospheric state. This causes artefacts in estimated trends [*Yoon et al.*, 2013] or amplitudes of annual cycles (see *Section 4.2* or *Hegglin et al.* [2013]).

5.3 Implications for future planning of satellite limb-sounders

Past observations from limb satellite sounders have provided us with invaluable information on the chemistry (*e.g.*, *Waters et al.* [1993]; *Santee et al.* [1998]), transport (*e.g.*, *Park et al.* [2007]; *Stiller et al.* [2008]; *Hegglin et al.* [2009]; *Gille et al.* [2014]), and dynamics of the stratosphere (*e.g.*, *Randel et al.* [1993]; *Manney et al.* [2009]). This information has helped us understand many key aspects of the processes involved in stratospheric ozone depletion, the Antarctic ozone hole, and climate change. While we had a wealth of stratospheric limb observations during the past 30 years, it now has to be expected that there will be a lack of adequate limb measurements in the near future. This looming problem is due to an ageing fleet of currently still flying limb sounders (Aura-MLS, ACE-FTS, ACE-MAESTRO, OSIRIS and SMR) along with the lack of any concrete plans to launch new instruments except for SAGE III on the International Space Station (ISS) (which offers only limited spatial coverage) and the OMPS instruments (which only measure O_3, NO_2, and aerosol). These instruments may not be able to provide continuous temporal coverage, due to a nominal mission duration of Suomi NPP until 2016 and a replacement of the limb-viewing OMPS capacity on JPSS-2 in 2022 only.

The evaluations within the SPARC Data Initiative illustrate that there is no single best instrument that potentially covers all measurement needs, because instruments differ greatly in their measurement characteristics such as spatial and temporal sampling, viewing geometry, accuracy and precision, and measurement stability (*Chapters 2* and *3*). It is only through careful comparison between the instruments as done in this report that outliers can be detected, and weaknesses and strengths of instruments in measuring different species can be identified. An example is the realisation that SAGE II offers a valuable water vapour product that helps to extend the water vapour record from satellite observations (in particular HALOE) back to the late 1980s and also to improve this climate data record more generally [*Chapter 4.2*; *Hegglin et al.*, 2013; 2014].

Our evaluations also demonstrate clearly that there is no single instrument that can provide measurements of the full suite of atmospheric trace gas species with a high vertical and horizontal resolution, high accuracy and precision, and dense data coverage. Only a comprehensive set of high quality instruments that are complementary with respect to data coverage and target species allows development of a global picture of stratospheric composition. Such datasets enable among other things the analysis of temporal variations on different time scales and the quantification of important chemical budgets *e.g.*, of the chlorine family. As discussed in the previous *Section (5.2)*, data merging, even in the case of multiple overlapping instruments, poses a real challenge and complicates our understanding of long-term changes of the stratosphere in a changing climate. The future scenario we are currently facing with no overlap between instruments will render it impossible to derive reliable long-term changes of atmospheric trace constituents such as water vapor, ozone, and aerosol, and other important transport tracers.

Not only water vapour, but also other chemical trace gas species can be difficult to measure, especially when their atmospheric mixing ratios are close to the instruments' detection limits. Where agreement between instruments is found, the atmospheric mean state distributions and variability of trace gas species can be considered well-known (ozone [*Tegtmeier et al.*, 2013], water vapour [*Hegglin et al.*, 2013], N_2O, and CH_4 [*Hegglin et al.*, in prep.]). However, for other species that are measured by a few instruments only and for which not many ground-based validation measurements are available, our knowledge is still limited (many short-lived species such as HO_2, OH, BrO, ClO, *etc.*). It is key for the future planning of satellite limb sounders to design measurement systems that not only fit the purpose of covering specific measurement needs (in terms of scientific research question, region of interest, resolution, accuracy and precision, species list required), but also that offer redundancy between measurements, so that problems can be identified and adequately investigated.

References

Aghedo, A. M., *et al.*, 2011: The impact of orbital sampling, monthly averaging and vertical resolution on climate chemistry model evaluation with satellite observations. *Atmos. Chem. Phys.*, **11**, 6493-6514, doi:10.5194/acp-11-6493-2011.

Allen, D. R., *et al.*, 2000: Antarctic polar descent and planetary wave activity observed in ISAMS CO from April to July 1992. *Geophys. Res. Lett.*, **27**, 665-668, doi:10.1029/1999GL010888.

Angell, J. K., *et al.*, 1985: Ground-based and satellite evidence for a pronounced total-ozone minimum in early 1983 and responsible atmospheric layers. *Mon. Weather Rev.*, **113**, 641-646, doi:10.1175/1520-0493(1985)113<0641:GBASEF>2.0.CO;2.

Arijs, E., and G. Brasseur, 1986: Acetonitrile in the stratosphere and implications for positive ion composition. *J. Geophys. Res.*, **91**, 4003-4016, doi: 10.1029/JD091iD03p04003.

Austin, J. and N. Butchart, 2003: Coupled chemistry-climate model simulations for the period 1980 to 2020: Ozone depletion and the start of ozone recovery. *Q. J. Roy. Meteor. Soc.*, **129**, 3225-3249, doi:10.1256/qj.02.203.

Austin, J., *et al.*, 2003: Uncertainties and assessments of chemistry-climate models of the stratosphere. *Atmos. Chem. Phys.*, **3**, 1-27, doi:10.5194/acp-3-1-2003.

Austin, J., and F. Li, 2006: On the relationship between the strength of the Brewer-Dobson circulation and the age of stratospheric air. *Geophys. Res. Lett.*, **33**, L17807, doi:10.1029/2006GL026867.

Baehr, J., *et al.*, 2005: Validation of MIPAS-ENVISAT CH_4, N_2O, CFC-11 and CFC-12 by airborne in situ observations. Proceedings of the 2004 Envisat & ERS Symposium, SP-572, 6-10 September 2004, Salzburg, Austria, published by: ESA Publications Division, ESTEC, Noordwijk, The Netherlands, ISBN: 92-9092-883-2.

Baldwin, M. P., *et al.*, 2001: The quasi-biennial oscillation. *Rev. Geophys.*, **39**, 179-229, doi:10.1029/1999RG000073.

Barath, F. T., *et al.*, 1993: The Upper Atmosphere Research Satellite Microwave Limb Sounder instrument. *J. Geophys. Res.*, **98**, 10751-10762, doi:10.1029/93JD00798.

Baron, P., *et al.*, 2009: HO_2 measurements in the stratosphere and the mesosphere from the sub-millimetre limb sounder Odin/SMR. *Int. J. of Remote Sens.*, **30**, 4195-4208, http://dx.doi.org/10.1080/01431160902822831.

Baron, P., *et al.*, 2011: The Level 2 research product algorithms for the Superconducting Submillimeter-Wave Limb-Emission Sounder (SMILES). *Atmos. Meas. Tech.*, **4**, 2105-2124, doi:10.5194/amt-4-2105-2011.

Barth, C. A., 1992: Nitric oxide in the lower thermosphere. *Planet. Space Sci.,* **40**, 315-336, doi:10.1016/0032-0633(92)90067-X.

Bates, D. R., and M. Nicolet, 1950: The photochemistry of atmospheric water vapor. *J. Geophys. Res.*, **55**, 301-327, doi:10.1029/JZ055i003p00301.

Bauer, R., *et al.*, 2012: Validation of SCIAMACHY limb NO_2 profiles using solar occultation measurements. *Atmos. Meas. Tech.*, **5**, 1059-1084, doi:10.5194/amt-5-1059-2012.

Beer, R., *et al.*, 2001: Tropospheric Emission Spectrometer for the Earth Observing System's Aura satellite. *Appl. Opt.*, **40**, 2356-2367, doi:10.1364/AO.40.002356.

Beer, R., 2006: TES on the Aura mission: Scientific objectives, measurements, and analysis overview. *IEEE Trans. Geosci. Remote Sens.*, **44**, 1102-1105, doi:10.1109/TGRS.2005.863716.

Benson, C. M., *et al.*, 2006: Polar stratospheric clouds in the 1998-2003 Antarctic vortex: Microphysical modeling and Polar Ozone and Aerosol Measurement (POAM) III observations. *J. Geophys. Res.*, **111**, D18206, doi:10.1029/2005JD006948.

Bernath, P. F., *et al.*, 2005: Atmospheric Chemistry Experiment (ACE): Mission overview. *Geophys. Res. Lett.*, **32**, L15S01, doi:10.1029/2005GL022386.

Bernath, P., 2006: Atmospheric Chemistry Experiment (ACE): Analytical Chemistry from Orbit. *Trends Anal. Chem.*, **25**, 647-654, doi:10.1016/j.trac.2006.05.001.

Bertaux, J. L., *et al.*, 2010: Global ozone monitoring by occultation of stars: An overview of GOMOS measurements on Envisat. *Atmos. Chem. Phys.*, **10**, 12091-12148, doi:10.5194/acp-10-12091-2010.

Bhartia, P. K., *et al.*, 2004: Solar Backscatter Ultraviolet (SBUV) version 8 profile algorithm. Proceedings of the Quadrennial Ozone Symposium 2004, edited by: C. Zerefos, *Int. Ozone Comm.*, Athens, Greece, pp295-296.

Bodeker, G. E., *et al.*, 2013: A vertically resolved, global, gap-free ozone database for assessing or constraining global climate model simulations. *Earth Syst. Sci. Data*, **5**, 31-43, doi:10.5194/essd-5-31-2013.

Boone, C. D., *et al.*, 2005: Retrievals for the atmospheric chemistry experiment Fourier-transform spectrometer. *Appl. Opt.*, **44**, 7218-7231, doi:10.1364/AO.44.007218.

Bourassa, A. E., *et al.*, 2007: Stratospheric aerosol retrieval with optical spectrograph and infrared imaging system limb scatter measurements. *J. Geophys. Res.*, **112**, D10217, doi:10.1029/2006JD008079.

Bourassa, A. E., *et al.*, 2012: Odin-OSIRIS stratospheric aerosol data product and SAGE III intercomparison. *Atmos. Chem. Phys.*, **12**, 605-614, doi:10.5194/acp-12-605-2012.

Bourassa, A. E., *et al.*, 2014: Trends in stratospheric ozone derived from merged SAGE II and Odin-OSIRIS satellite observations. *Atmos. Chem. Phys.*, **14**, 6983-6994, doi:10.5194/acp-14-6983-2014.

Bovensmann, H., *et al.*, 1999: SCIAMACHY – Mission objectives and measurement modes. *J. Atmos. Sci.*, **56**, 127-150, doi:10.1175/1520-0469(1999)056<0127:SMOAMM>2.0.CO;2.

Bowman, K. W., *et al.*, 2002: Capturing time and vertical variability of tropospheric ozone: A study using TES nadir retrievals. *J. Geophys. Res.*, **107**, 4723, doi:10.1029/2002JD002150.

Bowman, K. W., *et al.*, 2006: Tropospheric Emission Spectrometer: Retrieval method and error analysis. *IEEE Trans. Geosci. Remote Sens.*, **44**, 1297-1307, doi:10.1109/TGRS.2006.871234.

Bowman, K. W., *et al.*, 2013: Evaluation of ACCMIP outgoing longwave radiation from tropospheric ozone using TES satellite observations. *Atmos. Chem. Phys.*, **13**, 4057-4072, doi:10.5194/acp-13-4057-2013.

Boxe, C. S., *et al.*, 2010: Validation of northern latitude Tropospheric Emission Spectrometer stare ozone profiles with ARC-IONS sondes during ARCTAS: Sensitivity, bias and error analysis. *Atmos. Chem. Phys.,* **10**, 9901-9914, doi:10.5194/acp-10-9901-2010.

Bracher, A., *et al.*, 2005: Cross comparisons of O_3 and NO_2 measured by the atmospheric ENVISAT instruments GOMOS, MIPAS, and SCIAMACHY. *Adv. Space Res.*, **36**, 855-867, doi:10.1016/j.asr.2005.04.005.

Brasseur, G. and S. Solomon, 1984: Aeronomy of the middle atmosphere: chemistry and physics of the stratosphere and mesosphere. D. Reidel Publishing Company: Hingham, MA.

Brasseur, G., *et al.*, 1998: MOZART, A global chemical transport model for ozone and related chemical tracers 1. Model description. *J. Geophys. Res.*, **103**, 28265-28289, doi:10.1029/98JD02397.

Brohede, S., *et al.*, 2007a: A Stratospheric NO_2 Climatology from Odin/OSIRIS Limb-Scatter Measurement. *Can. J. Phys.*, **85**, 1253-1274, doi:10.1139/P07-141.

Brohede, S., *et al.*, 2007b: Validation of Odin/OSIRIS Stratospheric NO_2 Profiles. *J. Geophys. Res.*, **112**, D07310, doi:10.1029/2006JD007586.

Brohede, S., *et al.*, 2008: Odin stratospheric proxy NO_y measurements and climatology. *Atmos. Chem. Phys.*, **8**, 5731-5754.

Brown, A. T., *et al.*, 2011: Trends in atmospheric halogen containing gases since 2004. *J. Quant. Spectrosc. Ra.*, **112**, 2552-2566, doi:10.1016/j.jqsrt.2011.07.005.

Bruehl, C., *et al.*, 1996: Halogen Occultation Experiment ozone channel validation. *J. Geophys. Res.*, **101**, 10217, doi:10.1029/95JD02031.

Buehler, S. A., *et al.*, 2005: ARTS, the atmospheric radiative transfer simulator. *J. Quant. Spectros. Rad. Transf.*, **91**, 65-93, http://dx.doi.org/10.1016/j.jqsrt.2004.05.051.

Burrows, J. P., *et al.*, 1995: SCIAMACHY – Scanning Imaging Absorption Spectrometer for Atmospheric Chartography. *Acta Astronautica,* **35**, 445, doi:10.1016/0094-5765(94)00278-T.

Carleer, M. R., *et al.*, 2008: Validation of water vapour profiles from the Atmospheric Chemistry Experiment (ACE). *Atmos. Chem. Phys. Discuss.*, **8**, 4499-4559, doi:10.5194/acpd-8-4499-2008.

Carslaw, K. S., *et al.*, 1994: Stratospheric aerosol growth and HNO_3 gas phase depletion from coupled HNO_3 and water uptake by liquid particles. *Geophys. Res. Lett.*, **21**, 2479-2482, doi:10.1029/94GL02799.

Carslaw, K.S. *et al.*, 1997: Modeling the composition of liquid stratospheric aerosols. *Rev. Geophys.*, **35**, 125–154, doi:10.1029/97RG00078.

Chauhan, S., *et al.*, 2009: MIPAS reduced spectral resolution UTLS-1 mode measurements of temperature, O_3, HNO_3, N_2O, H_2O and relative humidity over ice: retrievals and comparison to MLS. *Atmos. Meas. Tech.*, **2**, 337-353, doi:10.5194/amt-2-337-2009.

Chipperfield, M. P., *et al.*, 1994: A two-dimensional model study of the QBO signal in SAGE II NO_2 and O_3. *Geophys. Res. Lett.*, **21**, 589-592, doi: 10.1029/94GL00211.

Choi, W. K, and J. R. Holton, 1991: Transport of N_2O in the stratosphere related to the equatorial semiannual oscillation. *J. Geophys. Res.*, **96**, 22543-22557, doi:10.1029/91JD02263.

Chu, W. P., and M. P. McCormick, 1979: Inversion of stratospheric aerosol and gaseous constituents from spacecraft solar extinction data in the 0.38-1.0 μm wavelength region. *Appl. Opt.*, **18**, 1404-1414, https://doi.org/10.1364/AO.18.001404.

Chu, W. P., *et al.*, 1989: SAGE II Inversion Algorithm. *J. Geophys. Res.*, **94**, 8339-8351, doi:10.1029/JD094iD06p08339.

Clerbaux, C., *et al.*, 2008: CO measurements from the ACE-FTS satellite instrument: data analysis and validation using groundbased, airborne and spaceborne observations. *Atmos. Chem. Phys.*, **8**, 2569-2594, doi:10.5194/acp-8-2569-2008.

Coheur, P.-F., *et al.*, 2007: ACE-FTS observation of a young biomass burning plume: first reported measurements of C_2H_4, C_3H_6O, H_2CO and PAN by infrared occultation from space. *Atmos. Chem. Phys.*, **7**, 5437-5446, doi:10.5194/acp-7-5437-2007.

Collins, W. D., *et al.*, 2004: Description of the NCAR Community Atmosphere Model (CAM3). NCAR Technical Note, NCAR/TN-464+STR, 226 pp.

Connor, B. J., *et al.*, 2007: Comparison of ClO measurements from the Aura Microwave Limb Sounder to ground-based microwave measurements at Scott Base, Antarctica, in spring 2005. *J. Geophys. Res.*, **112**, D24S42, doi:10.1029/2007JD008792.

Conway, R. R., *et al.*, 1999: Middle atmosphere high resolution spectrograph investigation. *J. Geophys. Res.*, **104**, 16327-16348, doi:10.1029/1998JD100036.

Conway, R. R., *et al.*, 2000: Satellite observations of upper stratospheric and mesospheric OH: The HO_x dilemma. *Geophys. Res. Lett.*, **27**, 2613-2616, doi:10.1029/2000GL011698.

Crutzen, P. J., 1970: The influence of nitrogen oxides on the atmospheric ozone content. *Q. J. R. Meteorol. Soc.*, **96**, 320-325, doi:10.1002/qj.49709640815.

Cunnold, D. M., *et al.*, 1991: Validation of SAGE II NO_2 Measurements. *J. Geophys. Res.*, **96**, 12913-12925, doi:10.1029/91JD01344.

Damadeo, R. P., *et al.*, 2013: SAGE version 7.0 algorithm: Application to SAGE II. *Atmos. Meas. Tech.,* **6**, 3539–3561, doi:10.5194/amt-6-3539-2013.

Damiani, A., *et al.*, 2012: Impact of January 2005 solar proton events on chlorine species. *Atmos. Chem. Phys*., **12**, 4159-4179, doi:10.5194/acp-12-4159-2012.

Daniel, J. S., and S. Solomon, 1998: On the climate forcing of carbon monoxide. *J. Geophys. Res.*, **103**, 13249-13260, doi:10.1029/98JD00822.

Degenstein, D., *et al.*, 2002: Volume emission rate tomography from a satellite platform. *Appl. Opt.*, **42**, 1441-1450, https://doi.org/10.1364/AO.42.001441.

Degenstein, D., *et al.*, 2009: Limb scatter ozone retrieval from 10 to 60 km using a multiplicative reconstruction technique. *Atmos. Chem. Phys.*, **9**, 6521-6529, doi:10.5194/acp-9-6521-2009.

de Gouw, J. A., *et al.*, 2003: Emission sources and ocean uptake of aceotnitrile (CH_3CN) in the atmosphere. *J. Geophys. Res.*, **108**(D11), doi:10.1029/2002JD002897.

de la Torre, L., *et al.*, 2012: Climatology and characteristics of stratospheric sudden warmings in the Whole Atmosphere Community Climate Model. *J. Geophys. Res.*, **117**, D04110, doi:10.1029/ 2011JD016840.

De Mazière, M., *et al.*, 2008: Validation of ACE-FTS v2.2 methane profiles from the upper troposphere to the lower mesosphere. *Atmos. Chem. Phys.*, **8**, 2421-2435, doi:10.5194/acp-8-2421-2008.

DeMore, W. B., *et al.*, 1997: Chemical kinetics and photochemical data for use in stratospheric modeling. JPL publication 92-94, Jet Propulsion Laboratory, Pasadena, California.

Douglass, A. R., *et al.*, 1999: Choosing meteorological input for the global modeling initiative assessment of high-speed aircraft. *J. Geophys. Res.*, **104**(D22), 27,545-27,564, doi:10.1029/1999JD900827.

Drummond, J. R., *et al.*, 1980: The stratospheric and mesospheric sounder on NIMBUS-7. *Philos. T. Roy. Soc.*, **A296**, 219-241, doi:10.1098/rsta.1980.0166.

Dufour, G., *et al.*, 2009: Global upper-tropospheric formaldehyde: seasonal cycles observed by the ACE-FTS satellite instrument. *Atmos. Chem. Phys.*, **9**, 3893-3910, doi:10.5194/acp-9-3893-2009.

Dupuy, E., *et al.,* 2004: Strato-mesospheric measurements of carbon monoxide with the Odin Sub-millimetre Radiometer: Retrieval and First Results. *Geophys. Res. Lett.*, **31**, L20101, doi:10.1029/2004GL020558.

Dupuy, E., *et al.*, 2009: Validation of ozone measurements from the Atmospheric Chemistry Experiment (ACE). *Atmos. Chem. Phys.*, **9**, 287-343, doi:10.5194/acp-9-287-2009.

Ejiri, M. K., *et al.*, 2006: Validation of the improved limb atmospheric spectrometer-II (ILAS-II) Version 1.4 nitrous oxide and methane profiles. *J. Geophys. Res.*, **111**, D22S90, doi:10.1029/2005JD006449.

Ekström, M., *et al.*, 2008: Comparison of satellite limb-sounding humidity climatologies of the uppermost tropical troposphere. *Atmos. Chem. Phys.*, **8**, 309-320, doi:10.5194/acp-8-309-2008.

Ekström, M., and Eriksson, P., 2008: Altitude resolved ice-fraction in the uppermost tropical troposphere. *Geophys. Res. Lett.*, **35**, L13822, doi:10.1029/2008GL034305.

Englert, C. R., *et al.*, 2008: First results from the Spatial Heterodyne Imager for Mesospheric Radicals (SHIMMER), Diurnal variation of mesospheric hydroxyl. *Geophys. Res. Lett.*, **35**, L19813, doi:10.1029/2008GL035420.

Englert, C. R., *et al.*, 2010: Spatial Heterodyne Imager for Mesospheric Radicals on STPSat-1. *J. Geophys. Res.*, **115**, D20306, doi:10.1029/2010JD014398.

Eparvier, F. G., *et al.*, 1994: Solar Mesosphere Explorer satellite measurements of El Chichon stratospheric aerosols, 2. Aerosol mass and size parameters. *J. Geophys. Res.*, **99**, 20533-20544, doi:10.1029/94JD01841.

Eriksson, P., C. Jiménez and S. A. Buehler, 2005: Qpack, a tool for instrument simulation and retrieval work. *J. Quant. Spectrosc. Rad. Transf.*, **91**, 47-64, http://dx.doi.org/10.1016/j.jqsrt.2004.05.050.

Ernst, F., *et al.*, 2009: Retrieval of stratospheric aerosol distributions from SCIAMACHY limb measurements: first steps and methodology. Proceedings Atmospheric Science Conference, Barcelona, Spain, 7-11 Sept 2009, ESA Special Publication SP-676.

Eyring, V., *et al.*, 2006: Assessment of temperature, trace species, and ozone in chemistry-climate model simulations of the recent past. *J. Geophys. Res.*, **111**(D22), D22308.

Fahey, D. W., *et al.*, 2001: The detection of large HNO_3-containing particles in the winter Arctic stratosphere. *Science*, **291**, 1026-1031, doi:10.1126/science.1057265.

Fiorucci, I., *et al.*, 2013: Ground-based stratospheric O_3 and HNO_3 measurements at Thule, Greenland: an intercomparison with Aura MLS observations. *Atm. Meas. Tech.*, **6**, 2441-2453, doi:10.5194/amt-6-2441-2013.

Fischer, H., *et al.*, 2008: MIPAS: An instrument for atmospheric and climate research. *Atmos. Chem. Phys.,* **8**, 2151-2188, doi:10.5194/acp-8-2151-200.

Fish, D. J., *et al.*, 2000: Possible causes of stratospheric NO_2 trends observed at Lauder. *Geophys. Res. Lett.*, **20**, 3313-3316, doi:10.1029/2000GL011700.

Flocke, F, *et al.*, 1999: An examination of chemistry and transport processes in the tropical lower stratosphere using observations of long-lived and short-lived compounds obtained during STRAT and POLARIS. *J. Geophys. Res.*, **104**, 26625-26642, doi:10.1029/1999JD900504.

Folkins, I., *et al.*, 2006: Seasonal cycles of O_3, CO, and convective outflow at the tropical tropopause. *Geophys. Res. Lett.*, **33**, L16802, doi:10.1029/2006GL026602.

Forkman, P., *et al.*, 2012: Six years of mesospheric CO estimated from ground-based frequency-switched microwave radiometry at 57°N compared with satellite instruments. *Atmos. Meas. Tech.*, **5**, 2827-2841, doi:10.5194/amt-5-2827-2012.

Forster, P. M. and K. P. Shine, 2002: Assessing the climate impacts of trends in stratospheric water vapour. *Geophys. Res. Lett.,* **29**, 1086-1089, doi:10.1029/2001GL013909.

Frisk, U., *et al.*, 2003: The Odin satellite: I. Radiometer design and test. *Astron. Astrophys.*, **402**, L27(34), doi:10.1051/0004-6361:20030335.

Froidevaux, L., *et al.*, 2006: Early validation analyses of the atmospheric profiles from EOS MLS on the Aura satellite. *IEEE Trans. Geosci. Remote Sens.*, **44**, 1106-1121, doi:10.1109/TGRS.2006.864366.

Froidevaux, L., *et al.*, 2008a: Validation of Aura Microwave Limb Sounder stratospheric ozone measurements. *J. Geophys. Res.*, **113**, D15S20, doi:10.1029/2007JD008771.

Froidevaux, L., *et al.*, 2008b: Validation of Aura Microwave Limb Sounder HCl measurements. *J. Geophys. Res.*, **113**, D15S25, doi:10.1029/2007JD009025.

Froidevaux, L., *et al.*, 2015: Global Ozone Chemistry And Related trace gas Data records for the Stratosphere (GOZCARDS): methodology and sample results with a focus on HCl, H_2O, and O_3. *Atmos. Chem. Phys.*, **15**, 10471-10507, doi:10.5194/acp-15-10471-2015.

Fueglistaler, S., *et al.*, 2009: The tropical tropopause layer. *Rev. Geophys.*, **47**, RG1004, doi:10.1029/2008RG000267.

Fujiwara, M., *et al.*, 2010: Seasonal to decadal variations of water vapour in the tropical lower stratosphere observed with balloon-borne cryogenic frost point hygrometers. *J. Geophys. Res.*, **115**, D18304, doi:10.1029/2010JD014179.

Funke, B., *et al.*, 2001: A new non-LTE retrieval method for atmospheric parameters from MIPAS-Envisat emission spectra. *Adv. Space Res.*, **27**, 1099-1104, doi:10.1016/S0273-1177(01)00169-7.

Funke, B., *et al.*, 2005a: Retrieval of stratospheric NO_x from 5.3 and 6.2 μm nonlocal thermodynamic equilibrium emissions measured by Michelson Interferometer for Passive Atmospheric Sounding (MIPAS) on Envisat. *J. Geophys. Res.*, **110**, D09302, doi:10.1029/2004JD005225.

Funke, B., *et al.*, 2005b: Downward transport of upper atmospheric NO_x into the polar stratosphere and lower mesosphere during the Antarctic 2003 and Arctic 2002/2003 winters. *J. Geophys. Res.,* **110**, D24308, doi:10.1029/2005JD006463.

Funke, B., *et al.*, 2009: Carbon monoxide distributions from the upper troposphere to the mesosphere inferred from 4.7 μm nonlocal thermal equilibrium emissions measured by MIPAS on Envisat. *Atmos. Chem. Phys.*, **9**, 2387-2411, doi:10.5194/acp-9-2387-2009.

Funke, B. and von Clarmann, T., 2012: How to average logarithmic retrievals? *Atmos. Meas. Tech.*, **5**, 831-841, doi:10.5194/amt-5-831-2012.

Funke, B., *et al.*, 2014: Mesospheric and stratospheric NO_Y produced by energetic particle precipitation during 2002-2012. *J. Geophys. Res. Atmos.*, **119**, 4429-4446, doi:10.1002/2013JD021404.

Fussen, D., *et al.,* 2001: Evolution of stratospheric aerosols in the post-Pinatubo period measured by the occultation radiometer experiment ORA. *Atmos. Env.*, **35**, 5067-5078.

Garcia, R. R., *et al.*, 2007: Simulation of secular trends in the middle atmosphere, 1950-2003. *J. Geophys. Res.*, **112**, D09301, doi:10.1029/2006JD007485.

Garcia, R. R., *et al.*, 2011: On the Determination of Age of Air Trends from Atmospheric Trace Species. *J. Atmos. Sci.*, **68**, 139-154, doi:10.1175/2010JAS3527.1.

Geller, L.S., *et al.,* 1997: Tropospheric SF_6: Observed latitudinal distribution and trends, derived emissions, and interhemispheric exchange time. *Geophys. Res.*, **24**, 675-678, doi:10.1029/97GL00523.

Gettelman, A., *et al.*, 2010: Multimodel assessment of the upper troposphere and lower stratosphere: Tropics and global trends. *J. Geophys. Res.*, **115**, D00M08, doi:10.1029/2009JD013638.

Gettelman, A., *et al.*, 2011: The extra tropical upper troposphere and lower stratosphere. *Rev. Geophys.*, **49**, RG3003, doi:10.1029/2011RG000355.

Gille, J., and J. M. Russell III, 1984: The Limb Infrared Monitor of the Stratosphere (LIMS) experiment: Experiment description, performance, and results. *J. Geophys. Res.*, **88**, 5125-5140.

Gille, J., and J. Barnett, 1992: The High-Resolution Dynamics Limb Sounder (HIRDLS). An instrument for the study of global change. The Use of EOS for Studies of Atmospheric Physics, J. Gille and G. Visconti (Eds.), North-Holland, pp433-450.

Gille, J., *et al.*, 2008: The High Resolution Dynamics Limb Sounder (HIRDLS): Experiment overview, results and validation of initial temperature data. *J. Geophys. Res.*, **113**, D16S43, doi:10.1029/2007JD008824.

Gille, J., and L. Gray, 2011: High Resolution Dynamics Limb Sounder, Earth Observing System (EOS), Data Description and Quality. Version 6 (V6), available from **www.eos.ucar.edu/hirdls/**, **http://disc.sci.gsfc.nasa.gov/data-holdings**, or **http://badc.nerc.ac.uk/browse/badc/hirdls**.

Gille, J., *et al.*, 2014: The role of midlatitude mixing barriers in creating the annual variation of total ozone in high northern latitudes. *J. Geophys. Res. Atmos.*, **119**, 9578-9595, doi:10.1002/2013JD021416.

Glaccum, W., *et al.*, 1996: The Polar Ozone and Aerosol Measurement (POAM II) Instrument. *J. Geophys. Res.*, **101**, 14479-14487, doi:10.1029/96JD00576.

Glatthor, N., *et al.*, 1998: Airborne remote sensing of NO_2 in the Arctic winter of 1994-1995 and comparison with a three-dimensional chemical transport model. *J. Geophys. Res.*, **103**, 13315-13326., doi:10.1029/98JD00521.

Glatthor, N., *et al.,* 1999: Intercomparison of the KOPRA and the RFM radiative transfer codes. Proc. European Symposium on Atmospheric Measurements from Space, ESAMS'99, 18-22 Jan 1999, Noordwijk, European Space Agency, ESTEC, Noordwijk, The Netherlands, pp757-764.

Glatthor, N., *et al.*, 2004: Spaceborne ClO observations by the Michelson Interferometer for Passive Atmospheric Sounding (MIPAS) before and during the Antarctic major warming in September/October 2002. *J. Geophys. Res.*, **109**, D11307, doi:10.1029/2003JD004440.

Glatthor, N., *et al.*, 2005: Mixing processes during the Antarctic vortex split in September/October 2002 as inferred from source gas and ozone distributions from ENVISAT-MIPAS. *J. Atmos. Sci.*, **62**, 787-800, doi:10.1175/JAS-3332.1.

Glatthor, N., *et al.*, 2006: Retrieval of stratospheric ozone profiles from MIPAS/ENVISAT limb emission spectra: A sensitivity study. *Atmos. Chem. Phys.*, **6**, 2767-2781, doi:10.5194/acp-6-2767-2006.

Gordley, L. L., *et al.*, 1996: Validation of nitric oxide and nitrogen dioxide measurements made by the Halogen Occultation Experiment for UARS platform. *J. Geophys. Res.*, **101**, 10241-10266, doi:10.1029/95JD02143.

Griesfeller, A., *et al.*, 2008: Intercomparison of ILAS-II Version 1.4 and Version 2 target parameters with MIPAS-Envisat measurements. *Atmos. Chem. Phys.*, **8**, 825-843, doi:10.5194/acp-8-825-2008.

Grooß, J.-U., and J. M. Russell III, 2005: Technical note: A stratospheric climatology for O_3, H_2O, CH_4, NO_x, HCl and HF derived from HALOE measurements. *Atmos. Chem. Phys.*, **5**, 2797-2807, doi:10.5194/acp-5-2797-2005.

Gunson, M., *et al.*, 1996: The Atmospheric Trace Molecule Spectroscopy (ATMOS) experiment: Deployment on the ATLAS Space Shuttle missions. *Geophys. Res. Lett.*, **23**, 2333-2336, doi:10.1029/96GL01569.

Haley, C., *et al.*, 2004: Retrievals of stratospheric O_3 and NO_2 profiles from Odin Optical Spectrograph and InfraRed Imager System (OSIRIS) limb-scattered sunlight measurements. *J. Geophys. Res.*, **109**, D16303, doi:10.1029/2004JD004588.

Haley, C. and S. Brohede, 2007: Status of the Odin/OSIRIS Stratospheric O_3 and NO_2 Data Products. *Can. J. Phys.*, **85**, 1177-1194, doi:10.1139/P07-114.

Hanson, D. R. and K. Mauersberger, 1988: Laboratory studies of the nitric acid trihydrate: implications for the south polar stratosphere. *Geophys. Res. Lett.*, **15**, 855-858, doi:10.1029/GL015i008p00855.

Harries, J. E., *et al.*, 1996: Validation of water vapor measurements from the Halogen Occultation Experiment. *J. Geophys. Res.*, **101**, 10205, doi:10.1029/95JD02933.

Harrison, J. J. and P. F. Bernath, 2013: ACE-FTS observations of acetonitrile in the lower stratosphere. *Atmos. Chem. Phys.*, **13**, 7405-7413, doi:10.5194/acp-13-7405-2013.

Hartmann, G. K., *et al.*, 1996: Measurements of O_3, H_2O and ClO in the middle atmosphere using the Millimeter-Wave Atmospheric Sounder (MAS). *Geophys. Res. Lett.*, **23**, 2313-2316, doi:10.1029/96GL01475.

Hasebe, F., 1994: Quasi-biennial oscillations of ozone and diabatic circulation in the equatorial stratosphere. *J. Atmos. Sci.*, **51**, 729-745, doi:10.1175/1520-0469(1994)051<0729:QBOOOA>2.0.CO;2.

Hassler, B., G.E. Bodeker, and M. Dameris, 2008: Technical Note: A new global database of trace gases and aerosols from multiple sources of high vertical resolution measurements. *Atmos. Chem. Phys.*, **8**, 5403-5421, doi:10.5194/acp-8-5403-2008.

Hauchecorne, A., *et al.*, 2005: First simultaneous global measurements of nighttime stratospheric NO_2 and NO_3 observed by Global Ozone Monitoring by Occultation of Stars (GOMOS)/ENVISAT in 2003. *J. Geophys. Res.*, **110**, D18301, doi:10.1029/2004JD005711.

Hauchecorne, A., *et al.*, 2010: Response of tropical stratospheric O_3, NO_2 and NO_3 to the equatorial Quasi-Biennial Oscillation and to temperature as seen from GOMOS/Envisat. *Atmos. Chem. Phys.*, **10**, 8873-8879, doi:10.5194/acp-10-8873-2010.

Hedin, A. E., 1991: Extension of the MSIS thermosphere model into the middle and lower atmosphere. *J. Geophys. Res.*, **96**(A2), 1159, Document ID: 19910040911.

Hegglin, M. I., *et al.*, 2008: Validation of ACE-FTS satellite data in the upper troposphere/lower stratosphere (UTLS) using non-coincident measurements. *Atmos. Chem. Phys.*, **8**, 1483-1499, doi:10.5194/acp-8-1483-2008.

Hegglin, M. I., *et al.*, 2009: A global view of the extratropical tropopause transition layer from Atmospheric Chemistry Experiment Fourier Transform Spectrometer O_3, H_2O, and CO. *J. Geophys. Res.*, **114**, D00B11, doi:10.1029/2008JD009984.

Hegglin, M. I., *et al.,* 2010: Multimodel assessment of the upper troposphere and lower stratosphere: Extratropics. *J. Geophys. Res.*, **115**, D00M09, doi:10.1029/2010JD013884.

Hegglin, M. I., *et al.*, 2013: SPARC Data Initiative: Comparison of water vapor climatologies from international limb satellite sounders. *J. Geophys. Res. Atmos.*, **118**, doi:10.1002/jgrd.50752.

Hegglin, M. I., *et al.*, 2014: Vertical structure of stratospheric water vapour trends derived from merged satellite data. *Nature Geoscience*, **7** (10), 768-776, ISSN 1752-0894 doi:10.1038/ngeo2236.

Hegglin, M. I., *et al.*, in prep.: SPARC Data Initiative: Comparison of aerosol climatologies from international limb satellite sounders.

Hervig, M. E., *et al.*, 1996a: Validation of temperature measurements from the Halogen Occultation Experiment. *J. Geophys. Res.*, **101**, 10277-10285, doi:10.1029/95JD01713.

Hervig, M. E., *et al.*, 1996b: Validation of aerosol measurements from the Halogen Occultation Experiment. J. *Geophys. Res.*, **101**, 10267-10275, doi:10.1029/95JD02464.

Hervig, M. E., and T. Deshler, 2002: Evaluation of aerosol measurements from SAGE II, HALOE, and balloonborne optical particle counters. *J. Geophys. Res.*, **107**, 4031, doi:10.1029/2001JD 000703.

Hocke, K., *et al.*, 2007: Comparison and synergy of stratospheric ozone measurements by satellite limb sounders and the ground-based microwave radiometer SOMORA. *Atmos. Chem. Phys.*, **7**, 4117-4131, doi:10.5194/acp-7-4117-2007.

Hofmann, D. J., and S. Solomon,1989: Ozone destruction through heterogeneous chemistry following the eruption of El Chichón. *J. Geophys. Res.*, **94**, 5029-5041, Paper No.: 88JD04231.

Holton, J. R., and W.-K. Choi, 1988: Transport circulation deduced from SAMS trace species data. *J. Atmos. Sci.*, **45**, 1929–1939.

Höpfner, M., *et al.*, 2004: First spaceborne observations of Antarctic stratospheric $ClONO_2$ recovery: Austral spring 2002. *J. Geophys. Res.*, **109**, doi:10.1029/2004JD004609.

Höpfner, M., *et al.*, 2007: Validation of MIPAS $ClONO_2$ measurements. *Atmos. Chem. Phys.*, **7**, 257-281, doi:10.5194/acp-7-257-2007.

Hoor, P., *et al.*, 2010: Transport timescales and tracer properties in the extratropical UTLS. *Atmos. Chem. Phys.*, **10**, 7929-7944, doi:10.5194/acp-10-7929-2010.

Hubert, D., *et al.*, 2016: Ground-based assessment of the bias and long-term stability of 14 limb and occultation ozone profile data records. *Atmos. Meas. Tech.*, **9**, 2497-2534, doi:10.5194/amt-9-2497-2016.

Hurst, D. F., *et al.*, 2011: Stratospheric water vapour trends over Boulder, Colorado: Analysis of the 30 year Boulder record. *J. Geophys. Res.*, **116**, D02306, doi:10.1029/2010JD015065.

Isaksen, I. S. A., *et al.*, 2009: Atmospheric composition change: Chemistry-climate interactions. *Atmos. Env.,* **43**, 5138-5192, doi:10.1016/j.atmosenv.2009.08.003.

Jackman, C. H., *et al.*, 2008: Short and medium-term atmospheric constituent effects of very large solar proton events. *Atmos. Chem. Phys.*, **8**, 765-785, doi:10.5194/acp-8-765-2008.

Jiang, J. H., *et al.*, 2005: Comparison of GPS/SAC-C and MIPAS/ENVISAT temperature profiles and its possible implementation for EOS MLS observations. Earth Observation with CHAMP: Results from Three Years in Orbit, C. Reigber, H. Lühr, P. Schwintzer, and J. Wickert (Eds.), Springer-Verlag Berlin Heidelberg New York, pp573-578.

Jiang, Y. B., *et al.*, 2007: Validation of aura microwave limb sounder ozone by ozonesonde and lidar measurements. *J. Geophys. Res.*, **112**, D24S34, doi:10.1029/2007JD008776.

Jin, J. J., *et al.*, 2009: Comparison of CMAM simulations of carbon monoxide (CO), nitrous oxide (N_2O), and methane (CH_4) with observations from Odin/SMR, ACE-FTS, and Aura/MLS. *Atmos. Chem. Phys.*, **9**, 3233-3252, doi:10.5194/acp-9-3233-2009.

Johnson, D. G., *et al.*, 1995: Estimating the abundance of ClO from simultaneous remote sensing measurements of HO_2, OH, and HOCl.*Geophys. Res. Lett.*, **22**, 1869-1871, doi:10.1029/95GL01249.

Johnston, H., 1971: Reduction of stratospheric ozone by nitrogen oxide catalysts from supersonic transport exhaust. *Science*, **173**, 517-522, doi:10.1126/science.173.3996.517.

Jones, R. L., and J. A. Pyle, 1984: Observations of CH_4 and N_2O by the NIMBUS 7 SAMS: A comparison with *in situ* data and two-dimensional numerical model calculations. *J. Geophys. Res.*, **89**, 5263-5279, doi:10.1029/JD089iD04p05263.

Jones, R. L., *et al.*, 1986: The water vapour budget of the stratosphere studied using LIMS and SAMS satellite data. *Quarterly J. Royal Meteorol. Soc.*, **112**, doi:10.1256/smsqj.47411.

Jones, A., *et al.*, 2009: Evolution of stratospheric ozone and water vapor time series studied with satellite measurements. *Atmos. Chem. Phys.*, **9**, 6055-6075, doi:10.5194/acp-9-6055-2009.

Jones, D. B. A., *et al.*, 2009: The zonal structure of tropical O_3 and CO as observed by the Tropospheric Emission Spectrometer in November 2004. Part I. Inverse modeling of CO emissions. *Atmos. Chem. Phys.*, **9**, 3547-3562, doi:10.5194/acp-9-3547-2009.

Jones, A., *et al.*, 2011: A global inventory of stratospheric NO_y from ACE-FTS. *J. Geophys. Res.*, **116**, D17304, doi:10.1029/2010JD015465.

Jones, A., *et al.*, 2012: Technical Note: A trace gas climatology derived from the Atmospheric Chemistry Experiment Fourier Transform Spectrometer (ACE-FTS) dataset. *Atmos. Chem. Phys.*, **12**, 5207-5220, doi:10.5194/acp-12-5207-2012.

Jucks, K. W., *et al.,* 1998: Observations of OH, HO_2, H_2O, and O_3, in the upper stratosphere: Implications for HO_x photochemistry. *Geophys. Res. Lett.*, **25**, 3935-3938, doi:10.1029/1998GL900009.

Junge, C. E., C. W. Chagnon, and J. E. Manson, 1961: Stratospheric aerosols. *J. Meteorol.*, **18**, 81-108., http://dx.doi.org/10.1175/1520-0469(1961)018<0081:SA>2.0.CO;2

Kanzawa, H., *et al.*, 2003: Validation and data characteristics of nitrous oxide and methane profiles observed by the Improved Limb Atmospheric Spectrometer (ILAS) and processed with the Version 5.20 algorithm. *J. Geophys. Res.*, **108**, 8003, doi:10.1029/2002JD002458.

Kar, J., *et al.*, 2007: Initial comparison of ozone and NO_2 profiles from ACE-MAESTRO with balloon and satellite data. *J. Geophys. Res.*, **112**, D16301, doi:10.1029/2006JD008242.

Kasai, Y., *et al.*, 2013: Validation of stratospheric and mesospheric ozone observed by SMILES from International Space Station. *Atmos. Meas. Tech.*, **6**, 2311-2338, doi:10.5194/amt-6-2311-2013.

Kellmann, S., *et al.*, 2012: Global CFC-11 (CCl_3F) and CFC-12 (CCl_2F_2) measurements with the Michelson Interferometer for Passive Atmospheric Sounding (MIPAS): Retrieval, climatologies and trends. *Atmos. Chem. Phys.*, **12**, 11857-11875, doi:10.5194/acp-12-11857-2012.

Kerzenmacher, T., *et al.*, 2008: Validation of NO_2 and NO from the Atmospheric Chemistry Experiment (ACE). *Atmos. Chem. Phys.*, **8**, 5801-5841, doi:10.5194/acp-8-5801-2008.

Khosravi, R., *et al.*, 2009: Overview and characterization of retrievals of temperature, pressure, and atmospheric constituents from the High Resolution Dynamics Limb Sounder (HIRDLS) measurements. *J. Geophys. Res.*, **114**, D20304, doi:10.1029/2009JD011937.

Khosravi, M., *et al.*, 2013: Diurnal variation of stratospheric and lower mesospheric HOCl, ClO and HO_2 at the equator: comparison of 1-D model calculations with measurements by satellite instruments. *Atmos. Chem. Phys.*, **13**, doi:10.5194/acp-13-7587-2013.

Kiefer, M., *et al.,* 2010: Impact of temperature field inhomogeneities on the retrieval of atmospheric species from MIPAS IR limb emission spectra. *Atmos. Meas. Tech.*, **3**, 1487-1507, doi:10.5194/amt-3-1487-2010.

Kikuchi, K., *et al.*, 2010: Overview and early results of the Superconducting Submillimeter-Wave Limb-Emission Sounder (SMILES). *J. Geophys. Res.*, **115**, D23306, doi:10.1029/2010JD014379.

Kinnison, D.E., *et al.*, 2007: Sensitivity of chemical tracers to meteorological parameters in the MOZART-3 chemical transport model. J. *Geophys. Res.*, **112**, D20302, doi:10.1029/2006JD007879.

Ko, M. K. W., *et al.*, 1993: Atmospheric sulfur hexafluoride: Sources, sinks and greenhouse warming. *J. Geophys. Res.*, **98**, 10499-10507, doi:10.1029/93JD00228.

Kohri, W.J., 1981: LRIR Observations of the Structure and Propagation of the Stationary Planetary Waves in the Northern Hemisphere during December 1975. Cooperative Thesis No. 63, Drexel University and National Center for Atmospheric Research.

Konopka, P., *et al.*, 2010: Annual cycle of ozone at and above the tropical tropopause: observations versus simulations with the Chemical Lagrangian Model of the Stratosphere (CLaMS). *Atmos. Chem. Phys.*, **10**, 121-132, doi:10.5194/acp-10-121-2010.

Kreyling, D., *et al.*, 2013: SMILES zonal and diurnal variation climatology of stratospheric and mesospheric trace gasses: O_3, HCl, HNO_3, ClO, BrO, HOCl, HO_2, and temperature. *J. Geophys. Res. Atmos.*, **118**, 11888-11903, doi:10.1002/2012JD019420.

Krüger, K., B. Naujokat, and K. Labitzke, 2005: The unusual midwinter warming in the Southern Hemisphere stratosphere of 2002: A comparison to Northern Hemisphere phenomena. *J. Atmos. Sci*., **62**, 603-613, doi:10.1175/JAS-3316.1.

Kulawik, S. S., *et al.*, 2006a: TES atmospheric profile retrieval characterization: An orbit of simulated observations. *IEEE Trans. Geosci. Remote Sens.*, **44**, 1324– 1333, doi:10.1109/TGRS.2006.871207.

Kulawik, S. S., *et al.*, 2006b: Calculation of altitude-dependent Tikhonov constraints for TES nadir retrievals. *IEEE Trans. Geosci. Remote Sens.*, **44**, 1334–1342, doi:10.1109/TGRS.2006.871206.

Kuribayashi, K., *et al.,* 2014: Direct estimation of the rate constant of the reaction ClO + HO_2 -> HOCl +O_2 from SMILES atmospheric observations. *Atmos. Chem. Phys.*, **14**, 255-266, doi:10.5194/acp-14-255-2014.

Kyrölä, E., *et al.*, 2006: Night-time ozone profiles in the stratosphere and mesosphere by the Global Ozone Monitoring by Occultation of Stars on Envisat. *J. Geophys. Res.*, **111**, D24306, doi:10.1029/2006JD007193.

Kyrölä, E., *et al.*, 2010a: GOMOS O_3, NO_2, and NO_3 observations in 2002-2008. *Atmos. Chem. Phys.*, **10**, 7723-7738, doi:10.5194/acp-10-7723-2010.

Kyrölä, E., *et al.*, 2010b: Retrieval of atmospheric parameters from GOMOS data. *Atmos. Chem. Phys.*, **10**, 11881-11903, doi:10.5194/acp-10-11881-2010.

Laaksonen, A., *et al.*, 2000: Upper tropospheric SO_2 conversion into sulfuric acid aerosols and cloud condensation nuclei. *J. Geophys. Res.*, **105**, 1459-1469, doi:10.1029/1999JD900933.

Labitzke, K., and M. P. McCormick, 1992: Stratospheric temperature increases due to Pinatubo aerosols. *Geophys. Res. Lett*., **19**, 207-210, doi:10.1029/91GL02940.

Laeng, A., *et al.*, 2014: Validation of MIPAS IMK/IAA V5R_O3_224 ozone profiles. *Atmos. Meas. Tech.*, **7**, 3971-3987, doi:10.5194/amt-7-3971-2014.

Lambert, A., *et al.*, 1993: Measurements of the evolution of the Mount Pinatubo aerosol clouds by ISAMS. *Geophys. Res. Lett*., **20**, 1287-1290, doi:10.1029/93GL00827.

Lambert, A., *et al.*, 2007: Validation of the Aura Microwave Limb Sounder middle atmosphere water vapor and nitrous oxide measurements. *J. Geophys. Res.*, **112**(D24S36), doi:10.1029/2007JD008724.

Lary, D. J., *et al.*, 2007: Variations in stratospheric inorganic chlorine between 1991 and 2006. *Geophys. Res. Lett.*, **34**, L21811, doi:10.1029/2007GL030053.

Leblanc, T., *et al.*, 2011: Measurements of Humidity in the Atmosphere and Validation Experiments (MOHAVE)-2009: Review of campaign operations and results. *Atmos. Meas. Tech.*, **4**, 2579-2605, doi:10.5194/amt-4-2579-2011.

Ling, X.-D., and J. London, 1986: The quasi-biennial oscillation of ozone in the tropical middle stratosphere: A one-dimensional model. *J. Atmos. Sci*., **43**, 3122-3137, doi:10.1175/1520-0469(1986)043<3122:TQBOOO>2.0.CO;2.

Livesey, N. J., and W. G. Read, 2000: Direct retrieval of line-of-sight atmospheric structure from limb sounding observations. *Geophys. Res. Lett.*, **27**, 891-894, doi:10.1029/1999GL010964.

Livesey, N. J., et al., 2001: Stratospheric CH_3CN from the UARS Microwave Limb Sounder. *Geophys. Res. Letts.*, **28**, 779-782, doi:10.1029/2000GL012144.

Livesey, N. J., *et al.*, 2003: The UARS Microwave Limb Sounder version 5 dataset: Theory, characterization and validation. *J. Geophys. Res.,* **108**, 4378, doi:10.1029/2002JD002273.

Livesey, N. J., *et al.*, 2004: Enhancements in lower stratospheric CH_3CN observed by UARS MLS following boreal forest fires. *J. Geophys. Res.*, **109**, D06308, doi:10.1029/2003JD004055.

Livesey, N. J., *et al.*, 2006: Retrieval algorithms for the EOS Microwave Limb Sounder (MLS) instrument. *IEEE Trans. Geosci. Remote Sens.*, **44**, 1144-1155, doi:10.1109/TGRS.2006.872327.

Livesey, N. J., *et al.*, 2008: Validation of Aura Microwave Limb Sounder O_3 and CO observations in the upper troposphere and lower stratosphere. *J. Geophys. Res.*, **113**, D15S02, doi:10.1029/2007JD008805.

Livesey, N. J., *et al.*, 2011: EOS MLS Version 3.3 Level 2 data quality and description document. Tech. rep., D-33509, Jet Propulsion Laboratory.

Livesey, N. J., *et al.,* 2013: EOS MLS Version 3.3/3.4 Level 2 data quality and description document. Tech. rep., Jet Propulsion Laboratory, available from **http://mls.jpl.nasa.gov/**.

Llewellyn, E., *et al.*, 2004: The OSIRIS Instrument on the Odin Spacecraft. *Can. J. Phys.*, **82**, 411-422, doi:10.1139/p04-005.

Logan, J.A., 1999: An analysis of ozonesonde data for the troposphere: Recommendations for testing 3-D models, and development of a gridded climatology for tropospheric ozone. *J. Geophys. Res.*, **104**, 16115-16149, doi:10.1029/1998JD100096.

Lossow, S., *et al.*, 2009: Wintertime water vapor in the polar upper mesosphere and lower thermosphere – first satellite observations by Odin/SMR. *J. Geophys. Res.*, **114**, D10304, doi:10.1029/2008JD011462.

Lowe, D., and R. MacKenzie, 2008: Review: Polar stratospheric cloud microphysics and chemistry. *J. Atmos. Sol.-Terr. Phys.*, **70**, 13-40, http://dx.doi.org/10.1016/j.jastp.2007.09.011.

Lucke, R. L., *et al.*, 1999: The Polar Ozone and Aerosol Measurement (POAM III) Instrument and Early Validation Results. *J. Geophys. Res.*, **104**, 18785-18799, doi:10.1029/1999JD900235.

Lumpe, J. D., *et al.*, 1997: POAM II Retrieval Algorithm and Error Analysis. *J. Geophys. Res.*, **102**, 23593-23614, doi:10.1029/97JD00906.

Lumpe, J. D., *et al.*, 2002: POAM III retrieval algorithm and error analysis. *J. Geophys. Res.*, **107**, 4575, doi:10.1029/2002JD002137.

Lumpe, J., *et al.*, 2006: Validation of Polar Ozone and Aerosol Measurement (POAM) III version 4 stratospheric water vapour. *J. Geophys. Res.*, **111**, D11301, doi:10.1029/2005JD006763.

Mahieu, E., *et al.*, 2008: Validation of ACE-FTS v2.2 measurements of HCl, HF, CCl_3F and CCl_2F_2 using space-, balloon- and ground-based instrument observations. *Atmos. Chem. Phys.*, **8**, 6199-6221, doi:10.5194/acp-8-6199-2008.

Manabe, S., and R. T. Wetherald, 1967: Thermal equilibrium of the atmosphere with a given distribution of relative humidity. *J. Atmos. Sci.*, **24**, 241 pp., http://dx.doi.org/10.1175/1520-0469(1967)024<0241:TEOTAW>2.0.CO;2.

Manney, G. L., *et al.*, 2009: Satellite observations and modelling of transport during the 2006 major stratospheric sudden warming. *Atmos. Chem. Phys.*, **9**, 4775-4795.

Manney, G. L., *et al.*, 2011: Jet characterization in the upper troposphere/lower stratosphere (UTLS): Applications to climatology and transport studies. *Atmos. Chem. Phys.*, **11**, 6115-6137, doi:10.5194/acp-11-6115-2011.

McCormick, M. P., *et al.*, 1979: Satellite studies of the stratospheric aerosol. *Bull. Am. Meteor. Soc.*, **60**, 1038-1046, http://dx.doi.org/10.1175/1520-0477(1979)060<1038:SSOTSA>2.0.CO;2.

McCormick, M. P., *et al.*, 1981: High-latitude stratospheric aerosols measured by the SAM II satellite system in 1978 and 1979. *Science*, **214**, 328-331, doi:10.1126/science.214.4518.328.

McCormick, M. P., *et al.*, 1989: An overview of SAGE-I and II ozone measurements. *Planetary and Space Science*, **37**, 1567-86, doi:10.1016/0032-0633(89)90146-3.

McCormick, M. P., *et al.*, 1995: Atmospheric effects of the Mt. Pinatubo eruption. *Nature*, **373**, 399-404, doi:10.1038/373399a0.

McElroy, C. T., *et al.*, 2007: The ACE-MAESTRO instrument on SCISAT: description, performance, and preliminary results. *Appl. Opt.*, **46**, 4341-4356, doi:10.1364/AO.46.004341.

McHugh, M. J., *et al.*, 2003: Improved mesospheric temperature, water vapor and polar mesospheric cloud extinctions from HALOE. *Geophys. Res. Lett.*, **30**, 1440, doi:10.1029/2002GL016859.

McHugh, M., *et al.*, 2005: Comparison of atmospheric retrievals from ACE and HALOE. *Geophys. Res. Lett.*, **32**, L15S10, doi:10.1029/2005GL022403.

McLinden, C. A., *et al.*, 2000: Stratospheric ozone in 3-D models: A simple chemistry and the cross-tropopause flux. *J. Geophys. Res.*, **105**, 14653-14665, doi:10.1029/2000JD900124.

McLinden, C. A., *et al.*, 2001: Understanding trends in stratospheric NO_y and NO_2. *J. Geophys. Res.*, **106**, 27787-27793, doi:10.1029/2000JD000100.

McLinden, C. A., S. Tegtmeier, and V. Fioletov, 2009: Technical Note: A SAGE-corrected SBUV zonal-mean ozone data set. *Atmos. Chem. Phys.*, **9**, 7963-7972, doi:10.5194/acp-9-7963-2009.

McLinden, C. A., *et al.*, 2010: Odin/OSIRIS observations of stratospheric BrO: Retrieval methodology, climatology, and inferred Br_y. *J. Geophys. Res.*, **115**, D15308, doi:10.1029/2009JD012488.

Mengistu Tsidu, G., *et al.*, 2004: Stratospheric N_2O_5 in the austral spring 2002 as rerieved from limb emission spectra recorded by the Michelson Interferometer for Passive Atmospheric Sounding (MIPAS). *J. Geophys. Res.*, **109**, D18301, doi:10.1029/2004JD004856.

Mengistu Tsidu, G., *et al.*, 2005: NO_y from Michelson Interferometer for Passive Atmospheric Sounding on Environmental Satellite during the southern hemisphere polar vortex split in September/October 2002. *J. Geophys. Res.,* **110**, D11301, doi:10.1029/2004JD005322.

Mieruch, S., *et al.,* 2012: Global and long-term comparison of SCIAMACHY limb ozone profiles with correlative satellite data (2002-2008). *Atmos. Meas. Tech.*, **5**, 771-788, doi:10.5194/amt-5-771-2012.

Millán, L., 2012: New Aura Microwave Limb Sounder observations of BrO and implications for Bry. *Atmos. Meas. Tech.*, **5**, 1741–1751, doi:10.5194/amt-5-1741-2012.

Milz, M., *et al.*, 2005: Water vapor distributions measured with the Michelson Interferometer for Passive Atmospheric Sounding on board Envisat (MIPAS/Envisat). *J. Geophys. Res*., **110**, D24307, doi:10.1029/2005JD005973.

Milz, M., *et al.*, 2009: Validation of water vapour profiles (version 13) retrieved by the IMK/IAA scientific retrieval processor based on full resolution spectra measured by MIPAS on board Envisat. *Atmos. Meas. Tech*., **2**, 379-399, doi:10.5194/amt-2-379-2009.

Millán, L., *et al.*, 2015: Stratospheric and mesospheric HO_2 observations from the Aura Microwave Limb Sounder. *Atmos. Chem. Phys.*, **15**, 2889-2902, doi:10.5194/acp-15-2889-2015.

Molina, L. T. and M.J. Molina, 1987: Production of Cl_2O_2 from the self-reaction of the ClO radical. *J. Phys. Chem*. **91**, 433-436, doi: 10.1021/j100286a035.

Moré, J. J., 1977: The Levenberg-Marquardt algorithm: Implementation and theory. *Proc. Biennial Conf. Numerical Analysis*, pp105-116, doi:10.1007/BFb0067700.

Morris, R. A., *et al.*, 1995: Effects of electron and ion reactions on atmospheric lifetimes of fully fluorinated compounds. *J. Geophys. Res.,* **100**, 1287-1294, doi:10.1029/94JD02399.

Mote, P.W., *et al.*, 1996: An atmospheric tape recorder: The imprint of tropical tropopause temperatures on stratospheric water vapour. *J Geophys. Res.*, **101**, 3989-4006, doi:10.1029/95JD03422.

Murtagh, D., *et al.*, 2002: An overview of the Odin atmospheric mission. *Can. J. Phys.*, **80**, 309-319, doi:10.1139/p01-157.

Nardi, B., *et al.*, 2008: Initial validation of ozone measurements from the High Resolution Dynamics Limb Sounder. *J. Geophys. Res.*, **113**, D16S36, doi:10.1029/2007JD008837.

Nassar, R., *et al.*, 2008: Validation of Tropospheric Emission Spectrometer (TES) nadir ozone profiles using ozonesonde measurements. *J. Geophys. Res.*, **113**, D15S17, doi:10.1029/2007JD008819.

Nedoluha, G. E., *et al.*, 2007: A comparison of middle atmospheric water vapour as measured by WVMS, E_S-MLS, and HALOE. *J. Geophys. Res.*, **112**, D24S39, doi:10.1029/2007JD008757.

Nedoluha, G. E., *et al.*, 2009: Water vapour measurements in the mesosphere from Mauna Loa over solar cycle 23. *J. Geophys. Res.*, **114**, D23303, doi:10.1029/2009JD012504.

Nedoluha, G. E., *et al.*, 2011: Ground-based measurements of ClO from Mauna Kea and intercomparisons with Aura and Uars MLS. *J. Geophys. Res.*, **116**, D02307, doi:10.1029/2010JD014732.

Neu, J. L., *et al.*, 2014a: The SPARC Data Initiative: Comparison of upper troposphere / lower stratosphere ozone climatologies from limb-viewing instruments and the nadir-viewing Tropospheric Emission Spectrometer (TES). *J. Geophys. Res.*, **119**, 6971-6990, doi:10.1002/2013JD020822.

Neu, J. L., *et al.*, 2014b: Tropospheric ozone variations governed by changes in stratospheric circulation. *Nature Geosci.*, **7**, 340-344, doi:10.1038/ngeo2138.

Newman, P. A., *et al.*, 2006: When will the Antarctic ozone hole recover? *Geophys. Res. Lett*., **33**, L12814, doi:10.1029/2005GL025232.

Niwano, M., *et al.*, 2003: Seasonal and QBO variations of ascent rate in the tropical lower stratosphere as inferred from UARS HALOE trace gas data, *J. Geophys. Res.*, **108**, 4794, doi:10.1029/2003JD003871.

Olberg, M., *et al.*, 2003: The Odin satellite: II. Radiometer data processing and calibration. *Astron. Astrophys.,* **402**, L35, http://dx.doi.org/10.1051/0004-6361:20030336.

Orsolini, Y., *et al.*, 2010: Descent from the polar mesosphere and anomalously high stratopause observed in 8 years of water vapor and temperature satellite observations by the Odin Sub-Millimeter Radiometer. *J. Geophys. Res.*, **115**, doi:10.1029/2009JD013501.

Pardo, J. R., *et al.*, 2001: Submillimeter atmospheric transmission measurements on Mauna Kea during extremely dry El Niño conditions: Implications for broadband opacity contributions. *J. Quant. Spectrosc. Rad. Transf.*, **68**, 419-433, doi:10.1016/S0022-4073(00)00034-0.

Park, J. H., *et al.*, 1996: Validation of halogen occultation experiment CH_4 measurements from the UARS. *J. Geophys. Res.*, **101**, 10183-10204, doi:10.1029/95JD02736.

Park, M., *et al.*, 2004: Seasonal variations of methane, water vapor, ozone, and nitrogen dioxide near the tropopause: Satellite observations and model simulations. *J. Geophys. Res.*, **109**, D03302, doi:10.1029/2003JD003706.

Park, M., *et al.*, 2007: Transport above the Asian summer monsoon anticyclone inferred from Aura MLS tracers. *J. Geophys. Res.*, **112**, D16309, doi:10.1029/2006JD008294.

Peevey, T. R., *et al.*, 2012: Investigation of double tropopause spatial and temporal global variability utilizing High Resolution Dynamics Limb Sounder temperature observations. *J. Geophys. Res.*, **117**, D01105, doi:10.1029/2011JD016443.

Peter, T., 1997: Microphysics and heterogeneous chemistry of polar stratospheric clouds. *Annu. Rev. Phys. Chem.*, **48**, 785-822, doi:10.1146/annurev.physchem.48.1.785.

Pickett, H. M., *et al.*, 2006: Validation of Aura MLS HO_x measurements with remote-sensing balloon instruments. *Geophys. Res. Lett.*, **33**, doi:10.1029/2005GL024048.

Pickett, H. M., *et al.*, 2008: Validation of Aura Microwave limb sounder OH and HO_2 measurements. *J. Geophys. Res.*, **113**, doi:10.1029/2007JD008775.

Ploeger, F., *et al.*, 2012: Horizontal transport affecting trace gas seasonality in the Tropical Tropopause Layer (TTL). *J. Geophys. Res.*, **117**, 1-16, doi:10.1029/2011JD017267.

Plummer, D. A., *et al.*, 2010: Quantifying the contributions to stratospheric ozone changes from ozone depleting substances and greenhouse gases. *Atmos. Chem. Phys.*, **10**, 8803-8820, doi:10.5194/acp-10-8803-2010.

Prather, M. J., 1992: Catastrophic loss of stratospheric ozone in dense volcanic clouds. *J. Geophys. Res.*, **97**, 10187-10191, doi:10.1029/92JD00845.

Pumphrey, H. C., 1999: Validation of a new prototype water vapor retrieval for the UARS Microwave Limb Sounder. *J. Geophys. Res.*, **104**, 9399-9412, doi:10.1029/1998JD200113.

Pumphrey, H. C., *et al.*, 2000: Lower stratospheric water vapor measured by UARS MLS. *Geophys. Res. Lett.*, **27**, 1691-1694, doi:10.1029/1999GL011339.

Pumphrey, H. C., *et al.*, 2007: Validation of middle-atmosphere carbon monoxide retrievals from the Microwave Limb Sounder on Aura. *J. Geophys. Res.*, **112**, doi:10.1029/2007JD008723.

Pumphrey, H. C., *et al.*, 2011: Microwave Limb Sounder observations of biomass-burning products from the Australian bush fires of February 2009. *Atmos. Chem. Phys.*, **11**, 6285-6296, doi:10.5194/acp-11-6285-2011.

Pumphrey, H. C., *et al.*, 2013: EOS MLS Version 3.3/3.4 Level 2 data quality and description document. Tech. Rep., Jet Propulsion Laboratory, available from **http://mls.jpl.nasa.gov/**.

Randall, C. E., *et al.*, 1998: POAM II measurements of stratospheric NO_2, 1993-1996. *J. Geophys. Res.*,**103**, 28361-28371, doi:10.1029/98JD02092.

Randall, C. E., *et al.*, 2000: Comparison of Polar Ozone and Aerosol measurement (POAM) II and Stratospheric Aerosol and Gas Experiment (SAGE) II aerosol extinction measurements from 1994 to 1996. *J. Geophys. Res.*, **105**, 3929-3942, doi: 10.1029/1999JD901024.

Randall, C. E., *et al.*, 2001: Validation of POAM III Aerosols: Comparison to SAGE II and HALOE. *J. Geophys. Res.*, **106**, 27525-27536, doi:10.1029/2001JD000528.

Randall, C. E., *et al.*, 2002: Validation of POAM III NO_2 measurements. *J. Geophys. Res.*, **107**, 4432, doi:10.1029/2001JD001520.

Randall, C. E., *et al.*, 2003: Validation of POAM III ozone: Comparisons with ozonesonde and satellite data. *J. Geophys. Res.*, **108**, 4367, doi:10.1029/2002JD002944.

Randel, W. J., 1990: Kelvin wave induced trace constituent oscillations in the equatorial stratosphere. *J. Geophys. Res.*, **95**, 18641-18652, doi:10.1029/JD095iD11p18641.

Randel, W. J., 1993: Global variations of zonal mean ozone during stratospheric warming events. *J. Atmos. Sci.*, **50**, 3308-3321.

Randel, W. J., *et al.*, 1998: Seasonal cycles and QBO variations in stratospheric CH_4 and H_2O observed in UARS HALOE data. *J. Atmos. Sci.,* **55**, 163-185, doi:10.1175/1520-0469(1998)055<0163:SCAQVI>2.0.CO;2.

Randel, W. J., *et al.*, 2004: Interannual changes of stratospheric water vapor and correlations with tropical tropopause temperatures. *J. Atmos. Sci.*, **61**, 2133-2148, http://dx.doi.org/10.1175/1520-0469(2004)061<2133:ICOSWV>2.0.CO;2.

Randel, W. J., *et al.*, 2006: Decreases in stratospheric water vapor since 2001: Links to changes in the tropical tropopause and the Brewer-Dobson circulation. *J. Geophys. Res.*, **111**, D12312, doi:10.1029/2005JD006744.

Randel,W. J., *et al.*, 2007: A large annual cycle in ozone above the tropical tropopause linked to the Brewer-Dobson circulation. *J. Atmos. Sci.*, **64**, 4479-4488, doi:10.1175/2007JAS2409.1.

Ravishankara, A. R., *et al.*, 1993: Atmospheric lifetimes of long-lived halogenated species. *Science*, **259**, 194-199, doi:10.1126/science.259.5092.194.

Ravishankara, A. R., *et al.*, 2009: Nitrous Oxide (N_2O): The dominant ozone-depleting substance emitted in the 21st century. *Science*, **326**, 123-125, doi:10.1126/science.1176985.

Ray, E. A., *et al.*, 1994: The tropical semiannual oscillation in temperature and ozone as observed by MLS. *J. Atmos. Sci.*, **51**, 3045-3052, doi:10.1175/1520-0469(1994)051<3045:TTSOIT>2.0.CO;2.

Read, W. G., *et al.*, 2006: The clear-sky unpolarized forward model for the EOS Microwave Limb Sounder (MLS). *IEEE Trans. Geosci. Remote Sens.*, **44**, 1367-1379.

Read, W. G., *et al.*, 2007: Aura Microwave Limb Sounder upper tropospheric and lower stratospheric H_2O and relative humidity with respect to ice validation. *J. Geophys. Res.*, **112**, D24S35, doi:10.1029/2007JD008752.

Reber, C. A., *et al.*, 1993: The Upper Atmosphere Research Satellite (UARS) mission. *J. Geophys. Res.*, **98**, 10643-10647, doi:10.1029/92JD02828.

Reddmann, T., *et al.*, 2001: Three-dimensional model simulations of SF_6 with mesospheric chemistry. *J. Geophys. Res.*, **106**, 14525-14537, doi:10.1029/2000JD900700.

Reddmann, T., *et al.*, 2010: Modeling disturbed stratospheric chemistry during solar-induced NO_x enhancements observed with MIPAS/ENVISAT. *J. Geophys. Res.*, **115**, D00I11, doi:10.1029/2009JD012569.

Remsberg E. E., et. al., 1990: Estimation of synopic fields of middle atmosphere parameters from Nimbus-7 LIMS profile data. *J. Atmos. Oceanic Tech.*, **7**, 689-705, doi:10.1175/1520-0426(1990)007<0689:EOSFOM>2.0.CO;2.

Remsberg, E. E., *et al.*, 2004: The Nimbus 7 LIMS Version 6 radiance conditioning and temperature retrieval methods and results. *J. Quant. Spectrosc. Rad. Transf.*, **86**, 395-424, doi:10.1016/j.jqsrt.2003.12.007.

Remsberg, E. E., *et al.*, 2007: On the quality of the Nimbus 7 LIMS version 6 ozone for studies of the middle atmosphere. *J. Quant. Spectrosc. Rad. Transf.*, **105**, 492-518, doi:10.1016/j.jqsrt.2006.12.005.

Remsberg, E. E., *et al.*, 2009: On the quality of the Nimbus 7 LIMS Version 6 water vapor profiles and distributions. *Atmos. Chem. Phys.*, **9**, 9155-9167, doi:10.5194/acp-9-9155-2009.

Remsberg, E. E., *et al.*, 2010: Improvements in the profiles and distributions of nitric acid and nitrogen dioxide with the LIMS version 6 dataset. *Atmos. Chem. Phys.*, **10**, 4741-4756, doi:10.5194/acp-10-4741-2010.

Remsberg, E. E., 2015: Methane as a diagnostic tracer of changes in the Brewer–Dobson circulation of the stratosphere. *Atmos. Chem. Phys.*, **15**, 3739-3754, doi:10.5194/acp-15-3739-2015.

Ricaud, P., *et al.*, 2007: Measurements of mid-stratospheric formaldehyde from the Odin/SMR instrument. *J. Quant. Spectroscop. Radiat. Transfer*, **107**, 91-104, http://dx.doi.org/10.1016/j.jqsrt.2007.01.058.

Riese, M., *et al.*, 1999: Cryogenic Infrared Spectrometers and Telescopes for the Atmosphere (CRISTA) data processing and atmospheric temperature and trace gas retrieval. *J. Geophys. Res.*, **104**, 16349-16368, doi:10.1029/1998JD100057.

Roche, A. E., *et al.*, 1993: The Cryogenic Limb Array Etalon Spectrometer (CLAES) on UARS: Experiment description and performance. *J. Geophys. Res.,* **98**, 10763-10775, doi:10.1029/93JD00800.

Rodgers, C. D., 1976: Retrieval of atmospheric temperature and composition from remote measurements of thermal radiation. *Rev. Geophys.*, **14**, 609-624, doi:10.1029/RG014i004p00609.

Rodgers, C., 2000: Inverse Methods for Atmospheric Sounding: Theory and Practice. World Scientific, London.

Rodgers, C. D., and B. J. Connor, 2003: Intercomparison of remote sounding instruments. *J. Geophys. Res.*, **108**, 4116, doi:10.1029/2002JD002299.

Rothman, L. S., *et al.*, 2005: The HITRAN 2004 molecular spectroscopic database. *J. Quant. Spectrosc. Rad. Transf.*, **96**, 139-204, doi:10.1016/j.jqsrt.2004.10.008.

Rousseeuw, P. J., and Croux, C., 1993: Alternatives to the median absolute deviation. *J. Amer. Statist. Assoc.,* **88**, 1273-1283, http://dx.doi.org/10.1080/01621459.1993.10476408.

Rozanov, A., *et al.*, 2005: NO_2 and BrO vertical profile retrieval from SCIAMACHY limb measurements: Sensitivity studies. *Advances in Space Research*, **36**, 846-854, doi:10.1016/j.asr.2005.03.013.

Rozanov, A., *et al.*, 2011a: BrO vertical distributions from SCIAMACHY limb measurements: comparison of algorithms and retrieval results. *Atmos. Meas. Tech.*, **4**, 1319-1359, doi:10.5194/amt-4-1319-2011.

Rozanov, A., *et al.*, 2011b: Retrieval of water vapor vertical distributions in the upper troposphere and the lower stratosphere from SCIAMACHY limb measurements. *Atmos. Meas. Tech.*, **4**, 933-954, doi:10.5194/amt-4-933-2011.

Rusch, D. W., *et al.*, 1994: Solar Mesosphere Explorer satellite measurements of El Chichon stratospheric aerosols 1. Cloud morphology. *J. Geophys. Res.*, **99**, 20525-20532, doi:10.1029/94JD01842.

Rusch, D.W., *et al.*, 1997: Validation of POAM II Ozone Measurements with Coincident MLS, HALOE, and SAGE II Observations. *J. Geophys. Res.*, **102**, 23615-23627, doi:10.1029/97JD00458.

Russell III, J. M., *et al.*, 1984: The variability of stratospheric and mesospheric NO_2 in the polar winter night observed by LIMS. *J. Geophys. Res.*, **89**, 7267-7275, doi:10.1029/JD089iD05p07267.

Russell III, J. M., *et al.*, 1993: The Halogen Occultation Experiment. *J. Geophys. Res.*, **98**, 10777-10797, doi:10.1029/93JD00799.

Russell III, J. M., *et al.*, 1996a: Validation of hydrogen fluoride measurements made by the Halogen Occultation Experiment from the UARS platform. *J. Geophys. Res.*, **101**, 10163-10174, doi:10.1029/95JD01705..

Russell III, J. M., *et al.*, 1996b: Validation of hydrogen chloride measurements made by the Halogen Occultation Experiment from the UARS platform. *J. Geophys. Res.*, **101**, 10151-10162, doi:10.1029/95JD01696..

Ruth, S., *et al.*, 1997: Seasonal, semiannual, and interannual variability seen in measurements of methane made by the UARS Halogen Occultation Experiment. *J. Geophys. Res.,* **102**, 16189-16199, doi:10.1029/97JD00868.

Sagawa, H., *et al.*, 2013: Comparison of SMILES ClO profiles with satellite, balloon-borne and ground-based measurements. *Atmos. Meas. Tech.*, **6**, 3325-3347, doi:10.5194/amt-6-3325-2013.

SAGE-III, 2002: SAGE III Algorithm Theoretical Base Document, Solar and Lunar Algorithm, Earth Observing System Project science Office web site, **http://eospso.gsfc.nasa.gov**.

Salby, M. L., *et al.*, 1990: Chemical fluctuations associated with vertically propagating equatorial Kelvin waves. *J. Geophys. Res.*, **95**, 20491-20505, doi:10.1029/90JD01371.

Santee, M. L., *et al.*, 1998: UARS Microwave Limb Sounder HNO_3 observations: Implications for Antarctic polar stratospheric clouds. *J. Geophys. Res.*, **103**(D11), 13285-13313, doi:10.1029/98JD00365.

Santee, M. L., *et al.*, 2003: Variations and climatology of ClO in the polar lower stratosphere from UARS Microwave Limb Sounder measurements. *J. Geophys. Res.*, **108**, D15, 4454 pp., doi:10.1029/2002JD003335.

Santee, M. L., *et al.*, 2007: Validation of Aura Microwave Limb Sounder HNO_3 Measurements. *J. Geophys. Res.*, **112**, D24S40, doi:10.1029/2007JD008721.

Santee, M.L., *et al.*, 2008: A study of stratospheric chlorine partitioning based on new satellite measurements and modeling. *J. Geophys. Res.*, **113**, D12307, doi:10.1029/2007JD009057.

Sasano, Y., *et al.*, 1999: Improved Limb Atmospheric Spectrometer (ILAS) for stratospheric ozone layer measurements by solar occultation technique. *Geophys. Res. Lett.*, **26**, 197-200, doi:10.1029/1998GL900276.

Sasano, Y., 2002: Preface. *J. Geophys. Res.*, **107**, 8204, doi:10.1029/2002JD002155.

Sato, T. O., *et al.*, 2012: Strato-mesospheric ClO observations by SMILES: Error analysis and diurnal variation. *Atmos. Meas. Tech.*, **5**, 2809-2825, doi:10.5194/amt-5-2809-2012.

Schneider, N., *et al.*, 2005: Seasonal and diurnal ozone variations: observations and modeling. *J. Atmos. Chem.*, **50**, 25-47, doi:10.1007/s10874-005-1172-z.

Schwartz, M. J., *et al.*, 2006: EOS MLS forward model polarized radiative transfer for Zeeman-split oxygen lines. *IEEE Trans. Geosci. Remote Sens.,* **44**, 1182-1191, doi:10.1109/TGRS.2005.862267.

Seinfeld, J. H., and S. N. Pandis, 2006: Atmospheric chemistry and physics: From air pollution to climate change. 2nd ed., John Wiley&Sons, New York, NY.

Seppälä, A., *et al.*, 2007: Arctic and Antarctic polar winter NO_x and energetic particle precipitation in 2002-2006. *Geophys. Res. Lett.*, **34**, L12810, doi:10.1029/2007GL029733.

Sheese, *et al.*, 2013: Odin observations of Antarctic nighttime NO densities in the mesosphere-lower thermosphere and observations of a lower NO layer, *J. Geophys. Res.*, **118**, 7414–7425, doi:10.1002/jgrd.50563.

Siddaway, J. M., and S. V. Petelina, 2011: Transport and evolution of the 2009 Australian Black Saturday bushfire smoke in the lower stratosphere observed by OSIRIS on Odin. *J. Geophys. Res.*, **116,** D06203, doi:10.1029/2010JD015162.

Sinnhuber, B.-M., *et al.*, 2009: The contribution of anthropogenic bromine emissions to past stratospheric ozone trends: a modelling study. *Atmos. Chem. Phys.*, **9**, 2863–2871, doi:10.5194/acp-9-2863-2009.

Siskind, D. E., *et al.*, 2013: Comparison of a photochemical model with observations of mesospheric hydroxyl and ozone. *J. Geophys. Res. Atmos.*, **118**, 195-207, doi:10.1029/2012JD017971.

Sofieva, V. F., *et al.*, 2004: Ozone profile smoothness as a priori information in the inversion of limb measurements. *Ann. Geophys.*, **22**, 3411-3420, doi:10.5194/angeo-22-3411-2004.

Sofieva, V., *et al.*, 2009: Influence of scintillation on quality of ozone monitoring by GOMOS. *Atmos. Chem. Phys.*, **9,** 9197-9207, doi:10.5194/acp-9-9197-2009.

Sofieva, V. F., *et al.*, 2010: Retrievals from GOMOS stellar occultation measurements using characterization of modeling errors. *Atmos. Meas. Tech.*, **3**, 1019-1027, doi:10.5194/amt-3-1019-2010.

Sofieva, V. F., *et al.*, 2014: Validation of GOMOS ozone precision estimates in the stratosphere. *Atmos. Meas. Tech.*, **7**, 2147-2158, doi:10.5194/amt-7-2147-2014.

Solomon, S., *et al.*, 1982: Photochemical coupling between the thermosphere and the lower atmosphere, I. Odd nitrogen from 50 to 120 km. *J. Geophys. Res.*, **87**, 7206-7220, doi:10.1029/JC087iC09p07206.

Solomon, S., *et al.*, 1986: On the depletion of Antarctic ozone. *Nature*, **321**, 755-758, doi:10.1038/321755a0.

Solomon, S., *et al.*, 1996: The role of aerosol variability in anthropogenic ozone depletion at northern midlatitudes. *J. Geophys. Res.*, **101**, 6713-6727, doi:10.1029/95JD03353.

Solomon, S., 1999: Stratospheric ozone depletion: A review of concepts and history. *Rev. Geophys.*, **37**, 275-316, doi:10.1029/1999RG900008.

Solomon, S., *et al.* (eds), 2007: Contribution of Working Group I to the Fourth Assessment Report of the Intergovernmental Panel on Climate Change, Cambridge Univ. Press, Cambridge.

Sonkaew, T., *et al.*, 2009: Cloud sensitivity studies for stratospheric and lower mesospheric ozone profile retrievals from measurements of limb-scattered solar radiation. *Atmos. Meas. Tech.*, **2**, 653-678, doi:10.5194/amt-2-653-2009.

SPARC, 2000: Upper Tropospheric and Stratospheric Water Vapour (WAVAS). D. Kley, J. M. Russell III, and C. Phillips (eds.), SPARC Report No. 2, WMO/TD-No. 1043, **www.sparc-climate.org/publications/sparc-reports/sparc-report-no2**.

SPARC, 2006: Assessment of stratospheric aerosol properties (ASAP). L. Thomason and T. Peter (eds.), SPARC Report No. 4, WCRP-124, WMO/TD-No. 1295., **www.sparc-climate.org/publications/sparc-reports/sparc-report-no4**.

SPARC, 2010: SPARC Report on the Evaluation of Chemistry-Climate Models. V. Eyring, T. G. Shepherd, D. W. Waugh (eds.), SPARC Report No. 5, WCRP-132, WMO/TD-No. 1526, **www.sparc-climate.org/publications/sparc-reports/sparc-report-no5**.

Steck, T., and T. von Clarmann, 2001: Constrained profile retrieval applied to the observation mode of the Michelson Interferometer for Passive Atmospheric Sounding. *Appl. Opt.,* **40**, 3559-3571, https://doi.org/10.1364/AO.40.003559.

Steck, T., *et al.*, 2007: Bias determination and precision validation of ozone profiles from MIPAS-Envisat retrieved with the IMK-IAA processor. *Atmos. Chem. Phys.*, **7**, 3639-3662, doi:10.5194/acp-7-3639-2007.

Steck, T., *et al.*, 2008: Retrieval of global upper tropospheric and stratospheric formaldehyde (H_2CO) distributions from high-resolution MIPAS-Envisat spectra. *Atmos. Chem. Phys.*, **8**, 463-470, doi:10.5194/acp-8-463-2008.

Stephens, G. L., *et al.*, 2002: The CloudSat mission and the A-train: A new dimension of space-based observations of clouds and precipitation. *Bull. Amer. Meteor. Soc.*, **83**, 1771-1790, http://dx.doi.org/10.1175/BAMS-83-12-1771.

Stiller, G. P., *et al.*, 2002: Sensitivity of trace gas abundances retrievals from infrared limb emission spectra to simplifying approximations in radiative transfer modelling. *J. Quant. Spectrosc. Radiat. Transfer*, **72**, 249-280, doi:10.1016/S0022-4073(01)00123-6.

Stiller, G. P., *et al.*, 2007: Global distributions of HO_2NO_2 as observed by the Michelson Interferometer for Passive Atmospheric Sounding (MIPAS). J. *Geophys. Res.*, **112**, D09314, doi:10.1029/2006JD007212.

Stiller, G. P., *et al.*, 2008: Global distribution of mean age of stratospheric air from MIPAS SF_6 measurements. *Atmos. Chem. Phys.*, **8**, 677-695, doi:10.5194/acp-8-677-2008.

Stiller G. P., *et al.*, 2012: Validation of MIPAS IMK/IAA temperature, water vapour, and ozone profiles with MOHAVE-2009 campaign measurements. *Atmos. Meas. Tech.*, **5**, 289-320, doi:10.5194/amt-5-289-2012.

Stolarski, R. S., *et al.*, 2014: Seasonal variation of ozone in the tropical lower stratosphere: Southern tropics are different from northern tropics. *J. Geophys. Res. Atmos.*, **119**, 6196-6206, doi:10.1002/2013JD021294.

Strong, K., *et al.*, 2008: Validation of ACE-FTS N2O measurements. *Atmos. Chem. Phys.*, **8**, 4759-4786, doi:10.5194/acp-8-4759-2008.

Taha, G., *et al.*, 2004: Comparison of Stratospheric Aerosol and Gas Experiment (SAGE) II version 6.2 water vapor with ballon-born and space-based instruments. *J. Geophys. Res.*, **109**, D18313, doi:10/1029/2004/2004JD004859.

Tamminen, J., *et al.*, 2010: GOMOS data characterisation and error estimation. *Atmos. Chem. Phys.*, **10**, 9505-9519, doi:10.5194/acp-10-9505-2010.

Taylor, F. W., 1987: Infrared remote sensing of the middle atmosphere from satellites: The stratospheric and mesospheric sounder experiment 1978-1983. *Surveys in Geophysics*, **9**, 123-148, doi:10.1007/BF01904119.

Taylor, F. W., *et al.*, 1993: Remote sensing of atmospheric structure and composition by pressure modulator radiometry from space: The ISAMS experiment on UARS. *J. Geophys. Res.*, **98**, 10799-10814, doi:10.1029/92JD03029.

Taylor, K. E., 2001: Summarizing multiple aspects of model performance in a single diagram. *J. Geophys. Res.*, **106**, 7183-7192, doi:10.1029/2000JD900719.

Tegtmeier, S., *et al.*, 2013: SPARC Data Initiative: A comparison of ozone climatologies from international satellite limb sounders. *J. Geophys. Res. Atmos.*, **118**, 12229-12247, doi:10.1002/2013JD019877.

Tikhonov, A. N., 1963: О решении некорректно поставленных задач и методе регуляризации. *Doklady Akademii Nauk SSSR*, **151**, 501-504. Translated in "Solution of incorrectly formulated problems and the regularization method". *Soviet Mathematics*, **4**, 1035-1038.

Thomason, L. W., and G. Taha, 2003: SAGE III aerosol extinction measurements: Initial results. *Geophys. Res. Lett.*, **30**, 1631, doi:10.1029/ 2003GL017317.

Thomason, L. W., *et al.*, 2004: A revised water vapor product for the Stratospheric Aerosol and Gas Experiment (SAGE) II version 6.2 data set. *J. Geophys. Res.*, **109**, D06312, doi:10.1029/2003JD004465.

Thomason, L. W., *et al.*, 2010: An evaluation of the SAGE III version 4 aerosol extinction coefficient and water vapour data products. *Atmos. Chem. Phys.*, **10**, 2159-2173, doi:10.5194/acp-10-2159-2010.

Thompson, A. M., *et al.*, 2003: Southern Hemisphere Additional Ozonesondes (SHADOZ) 1998-2000 tropical ozone climatology 1. Comparison with Total Ozone Mapping Spectrometer (TOMS) and ground-based measurements. *J. Geophys. Res.*, **108**, 8238, doi:10.1029/2001JD000967.

Toohey, M., *et al.*, 2010: Validating the reported random errors of ACE-FTS measurements. *J. Geophys. Res.*, **115**, D20304, doi:10.1029/2010JD014185.

Toohey, M., and von Clarmann,T., 2013: Climatologies from satellite measurements: The impact of orbital sampling on the standard error of the mean. *Atmos. Meas. Tech.*, **6**, 937-948, doi:10/5194/amt-6-937-2013.

Toohey, M., *et al.*, 2013: Characterizing sampling biases in the trace gas climatologies of the SPARC Data Initiative. *J. Geophys. Res.*, **118**, 11847-11862, doi:10.1002/jgrd.50874.

Toon, O. B., 1986: Condensation of HNO_3 and HCl in winter polar stratospheres. *Geophys. Res. Lett.*, **13**, 1284-1287, doi:10.1029/GL013i012p01284.

Toon, G. C., 1991: The JPL MkIV Interferometer. *Opt. Photonics News*, **2**, 19-21, https://doi.org/10.1364/OPN.2.10.000019.

Twomey, S., 1975: Comparison of constrained linear iversion and an iterative non-linear algorithm applied to the indirect estimation of particle size distribution. *J. Comput. Phys.*, **18**, 188-198, doi:10.1016/0021-9991(75)90028-5.

Urban, J., *et al.*, 2004: MOLIERE (v5): A versatile forward- and inversion model for the millimeter and sub-millimeter wavelength range. *J. Quant. Spectrosc. Rad. Transf.*, **83**, 529-554, http://dx.doi.org/10.1016/S0022-4073(03)00104-3.

Urban, J., *et al.*, 2005a: Odin/SMR limb observations of stratospheric trace gases: Level 2 Processing of ClO, N_2O, O_3, and HNO_3. *J. Geophys. Res.*, **110**, D14307, doi:10.1029/2004JD005741.

Urban, J., *et al.*, 2005b: Odin/SMR limb observations of stratospheric trace gases: Validation of N_2O. *J. Geophys. Res.*, **110**, D09301, doi:10.1029/2004JD005394.

Urban, J., *et al.*, 2006: Odin/SMR Limb Observations of Trace Gases in the Polar Lower Stratosphere during 2004-2005. In: Proc. ESA First Atmospheric Science Conference, 8-12 May 2006, Frascati, Italy. Lacoste, H. (ed.), ESA-SP-628 Noordwijk: European Space Agency. ISBN-92-9092-939-1.

Urban, J., *et al.*, 2007: Global observations of middle atmospheric water vapour by the Odin satellite: An overview. *Planet. Space Sci.*, **55**, 1093-1102, http://dx.doi.org/10.1016/j.pss.2006.11.021.

Urban, J., 2008: Tropical ascent of lower stratospheric air analysed using measurements of the Odin Sub-Millimetre Radiometer. Proc. Reunion Island Int. Symp. Tropical Stratosphere – Upper Troposphere, 5-9 November 2007, St. Gilles, Reunion Island, France. Bencherif, H. (ed.), publisher: Université de la Réunion, pp29-34.

Urban, J., *et al.*, 2009: Nitric acid in the stratosphere based on Odin observations from 2001 to 2009 – Part 1: A global climatology. *Atmos. Chem. Phys.*, **9**, 7031-7044, doi:10.5194/acp-9-7031-2009.

Urban, J., *et al.*, 2012: Evolution and variability of water vapour in the tropical tropopause and lower stratosphere region derived from satellite measurements. In: Proc. ATMOS 2012, Advances in Atmospheric Science and Applications, ESA SP-708 (CD-ROM), ESA Communications, European Space Agency, Noordwijk, The Netherlands.

Vanhellemont, F., *et al.*, 2010: Optical extinction by upper tropospheric/stratospheric aerosols and clouds: GOMOS observations for the period 2002-2008. *Atmos. Chem. Phys.*, **10**, 7997-8009, doi:10.5194/acp-10-7997-2010.

Vanhellemont, F., *et al.*, 2016: AerGOM, an improved algorithm for stratospheric aerosol extinction retrieval from GOMOS observations – Part 1: Algorithm description. *Atmos. Meas. Tech.*, **9**, 4687-4700, doi:10.5194/amt-9-4687-2016.

Vernier, J.-P., *et al.*, 2011: Major influence of tropical volcanic eruptions on the stratospheric aerosol layer during the last decade. *Geophys. Res. Lett.*, **38**, L12807, doi:10.1029/2011GL047563.

Verronen, P. T., *et al.*, 2005: A comparison of night-time GOMOS and MIPAS ozone profiles in the stratosphere and mesosphere. *Adv. Space Res.,* **36**, 958-966, doi:10.1016/j.asr.2005.04.073.

Verstraeten, W. W., *et al.*, 2013: Validation of six years of TES tropospheric ozone retrievals with ozonesonde measurements: implications for spatial patterns and temporal stability in the bias. *Atmos. Meas. Tech.*, **6**, 1413-1423, doi:10.5194/amt-6-1413-2013.

Voemel, H., *et al.*, 2007: Validation of Aura Microwave Limb Sounder water vapour by balloon-borne Cryogenic Frost Point Hygrometer measurements. *J. Geophys. Res.*, **112**, D24S37, doi:10.1029/2007JD008698.

Vogel, B., *et al.*, 2008: Model simulations of stratospheric ozone loss caused by enhanced mesospheric NO_x during Arctic Winter 2003/2004. *Atmos. Chem. Phys.*, **8**, 5279-5293, doi:10.5194/acp-8-5279-2008.

von Clarmann, T., *et al.*, 2002: Intercomparison of radiative transfer codes under nonlocal thermodynamic equilibrium conditions. *J. Geophys. Res.*, **107**, 4631, doi:10.1029/2001JD001551.

von Clarmann, T., *et al.*, 2003a: A blind test retrieval experiment for infrared limb emission spectrometry. *J. Geophys. Res.*, **108**, 4746, doi:10.1029/2003JD003835.

von Clarmann, T., *et al.*, 2003b: Retrieval of temperature and tangent altitude pointing from limb emission spectra recorded from space by the Michelson Interferometer for Passive Atmospheric Sounding (MIPAS). *J. Geophys. Res.*, **108**, 4736, doi:10.1029/2003JD003602.

von Clarmann, T., *et al.*, 2003c: Modelling of atmospheric mid-infrared radiative transfer: the AMIL2DA algorithm intercomparison experiment. *J. Quant. Spectrosc. Radiat. Transfer*, **78**, 381-407, doi:10.1016/S0022-4073(02)00262-5.

von Clarmann, T., *et al.*, 2005: Experimantal evidence of perturbed odd hydrogen and chlorine chemistry after the October 2003 solar proton events. *J. Geophys. Res.*, **110**, A09S45, doi:10.1029/2005JA011053.

von Clarmann, T., *et al.*, 2006: Global stratospheric HOCl distributions retrieved from infrared limb emission spectra recorded by the Michelson Interferometer for Passive Atmospheric Sounding (MIPAS). *J. Geophys. Res.*, **111**, D05311, doi:10.1029/2005JD005939.

von Clarmann, T., *et al.*, 2009a: Retrieval of temperature, H_2O, O_3, HNO_3, CH_4, N_2O, $ClONO_2$ and ClO from MIPAS reduced resolution nominal mode limb emission measurements. *Atmos. Meas. Tech.*, **2**, 159-175, doi:10.5194/amt-2-159-2009.

von Clarmann, T., *et al.*, 2009b: HOCl chemistry in the Antarctic Stratospheric Vortex 2002, as observed with the Michelson Interferometer for Passive Atmospheric Sounding (MIPAS). *Atmos. Chem. Phys.*, **9**, 1817-1829, doi:10.5194/acp-9-1817-2009.

von Clarmann, T., *et al.*, 2010: Technical Note: Trend estimation from irregularly sampled, correlated data. *Atmos. Chem. Phys.*, **10**, 6737-6747, doi:10.5194/acp-10-6737-2010.

von Clarmann, T., *et al.*, 2012: The MIPAS HOCl climatology. *Atmos. Chem. Phys.*, **12**, 1965-1977, doi:10.5194/acp-12-1965-2012.

von Clarmann, T., 2014: Smoothing error pitfalls. *Atmos. Meas. Tech.*, **7,** 3023-3034, doi:10.5194/amt-7-3023-2014.

von Savigny, C., *et al.*, 2015: Improved stratospheric aerosol extinction profiles from SCIAMACHY: Validation and Sample results. *Atmos. Meas. Tech.*, **8**, 5223-5235, doi:10.5194/amt-8-5223-2015.

Wang, H. J., *et al.*, 1996: A critical analysis of SAGE ozone trends. *J. Geophys. Res.*, **101**, 12495-12514, Paper No. 96JD00581.

Wang, H. J., *et al.*, 2002: Assessment of SAGE version 6.1 ozone data quality. *J. Geophys. Res.*, **107**, 4691, doi:10.1029/2002JD002418.

Wang, D.-Y., *et al.*, 2004: Cross-validation of MIPAS/ENVISAT and GPS-RO/CHAMP temperature profiles. *J. Geophys. Res.,* **109**, D19311, doi:10.1029/2004JD004963.

Wang, D.-Y., *et al.*, 2005a: Comparisons of MIPAS/ENVISAT ozone profiles with SMR/ODIN and HALOE/UARS observations. *Adv. Space Res.*, **36**, 927-931, doi:10.1016/j.asr.2005.03.015.

Wang, D. Y., *et al.*, 2005b: Validation of stratospheric temperatures measured by Michelson Interferometer for Passive Atmospheric Sounding MIPAS on Envisat. *J. Geophys. Res.*, **110**, D08301, doi:10.1029/2004JD005342.

Wang, H.-J., *et al.*, 2006: SAGE III solar ozone measurements: Initial results. *Geophys. Res. Lett.*, **33**, L03805, doi:10.1029/2005GL025099.

Wang, D. Y., *et al.*, 2007: Validation of nitric acid retrieved by the IMK/IAA processor from MIPAS/ENVISAT measurements. *Atmos. Chem. Phys.*, **7**, 721-738, doi:10.5194/acp-7-721-2007.

Wang, S., *et al.*, 2008: Validation of Aura Microwave Limb Sounder OH measurements with Fourier Transform Ultra-Violet Spectrometer total OH column measurements at Table Mountain, California. *J. Geophys. Res.*, **113**, D22301, doi:10.1029/2008JD009883.

Wang, S., *et al.*, 2013: Midlatitude atmospheric OH response to the most recent 11-y solar cycle. *Proc. Nat. Acad. Sci.*, **110**, 2023-2028, doi:10.1073/pnas.1117790110.

Waters, J. W., *et al.*, 1993: Stratospheric ClO and ozone from the Microwave Limb Sounder on the Upper Atmosphere Research Satellite. *Nature*, **362**, 597-602, doi:10.1038/362597a0.

Waters, J. W., *et al.*, 1999: The UARS and EOS Microwave Limb Sounder (MLS) Experiments. *J. Atmos. Sci.*, **56**, 194-218, http://dx.doi.org/10.1175/1520-0469(1999)056<0194:TUAEML>2.0.CO;2.

Waters, J. W., *et al.*, 2006: The Earth Observing System Microwave Limb Sounder (EOS MLS) on the Aura satellite. *IEEE Trans. Geosci. Remote Sens.,* **44**, 1075-1092, doi:10.1109/TGRS.2006.873771.

Waugh, D. W., and V. Eyring, 2008: Quantitative performance metrics for stratospheric-resolving chemistry-climate models. *Atmos. Chem. Phys.*, **8**, 5699-5713, doi:10.5194/acp-8-5699-2008.

Waugh, D. W., *et al.*, 2009: Impacts of climate change on stratospheric ozone recovery. *Geophys. Res. Lett.*, **36**, L03805, doi:10.1029/2008GL036223.

Weinstock, E. M., *et al.*, 2009: Validation of the Harvard Lyman-a in situ water vapour instrument: Implications for the mechanisms that control stratospheric water vapour. *J. Geophys. Res.*, **114**, D23301, doi:10.1029/2009JD012427.

Wennberg, P. O., *et al.*, 1994: Removal of stratospheric O_3 by radicals: In situ measurements, of OH, HO_2, NO, NO_2, ClO, and BrO. *Science*, **266**, 398-404, doi:10.1126/science.266.5184.398.

Winker, D. M., *et al.*, 2003: The CALIPSO mission: Spaceborne lidar for observation of aerosols and clouds. *Proc. SPIE Int. Soc. Opt. Eng.*, **4893**, 1-11, doi:10.1117/12.466539.

WMO, 2011: World Meteorological Organization Scientific Assessment of Ozone Depletion: 2010. Report 52, Global Ozone Research and Monitoring Project.

WMO, 2014: World Meteorological Organization Scientific Ozone Assessment of Ozone Depletion: 2014, Report 55, Global Ozone Research and Monitoring Project..

Wolff, M. A., *et al.*, 2008: Validation of HNO_3, $ClONO_2$ and N_2O_5 from the Atmospheric Chemistry Experiment Fourier Transform Spectrometer (ACE-FTS). *Atmos. Chem. Phys.*, **8**, 3529-3562, doi:10.5194/acp-8-3529-2008.

Worden, J. S., *et al.*, 2004: Predicted errors of Tropospheric Emission Spectrometer nadir retrievals from spectral window selection. *J. Geophys. Res.*, **109**, D09308, doi:10.1029/2004JD004522.

Worden, H. M., *et al.*, 2007: Comparisons of Tropospheric Emission Spectrometer (TES) ozone profiles to ozonesodes: methods and initial results. *J. Geophys. Res.*, **112**, D03309, doi:10.1029/2006JD007258.

Worden, H. M., *et al.*, 2008: Satellite measurements of the clear-sky greenhouse effect from tropospheric ozone. *Nature Geosci.*, **1**, 305-308, doi:10.1038/ngeo182.

Worden, H. M., *et al.*, 2011: Sensitivity of outgoing longwave radiative flux to the global vertical distribution of ozone characterized by instantaneous radiative kernels from Aura TES. *J. Geophys. Res.*, **116**, D14115, doi:10.1029/2010JD015101.

Worden, H. M., *et al.*, 2013: Decadal record of satellite carbon monoxide observations. *Atmos. Chem. Phys.*, **13**, 837-850, doi:10.5194/acp-13-837-2013.

Yoon, J., *et al.*, 2013: Technical Note: Temporal change in averaging kernels as a source of uncertainty in trend estimates of carbon monoxide retrieved from MOPITT. *Atmos. Chem. Phys.*, **13**, 11307-11316, doi:10.5194/acp-13-11307-2013.

Zawodny, J. M., and M. P. McCormick, 1991: Stratospheric aerosol and gas experiment II measurements of the quasi-biennial oscillation of ozone and nitrogen dioxide. *J. Geophys. Res.*, **96**, 9371-9377.